Direct synthesis of nanoparticles with spatial heterogeneity for tailored cellular interactions

UNIVERSITY OF LIVERPOOL

Thesis submitted in accordance with the requirements of the University of Liverpool for the degree of Doctor in Philosophy

by

Faye Yvette Hern

October 2017

Dedicated to my wonderful Dad

Acknowledgements

Firstly, I would like to thank my supervisor, Prof. Steve Rannard, for his encouragement, guidance and kindness over the course of my PhD, and for giving me the opportunity to carry out this research. His support has been incredibly valuable to me; particularly over the last few months, which have been especially difficult.

I would like to thank all current and past members of the Rannard group, who have provided a friendly and supportive working environment. Particular thanks go to Steph Edwards for her unwavering enthusiasm and for being a fantastic lab partner; Dr Pierre Chambon, Dr Andy Dwyer and Sean Flynn for the GPC maintenance and advice; Dr Helen Cauldbeck and Dr Alison Savage for their help with the radiolabelled nanoparticle synthesis and analysis, and Dr Lee Tatham for carrying out the pharmacological studies.

I am extremely grateful to Oliver Andrén at the KTH Royal Institute of Technology, Stockholm, for MALDI-TOF mass spectrometry data which provided an invaluable addition for the full analysis of my materials.

Thank you to Mike Craven, Mike Davidson, Dr Casper Kunstmann, Alex Hill (extra thanks for the GNP synthesis!), Ste Danks, Dr Chris Thomas, Bob Smith and Dr Dan Bradley, for not being too serious and for letting me be one of the lads!

Finally, huge thanks go to my family. To my siblings; I would like to thank Shana for her constant support and encouragement, Kyle for keeping me grounded and Chloe for being the one I wanted to inspire. To my wonderful husband Steven, without whom I don't think I could have done any of this, you are my strength, my courage and my best friend; thank you for everything. Mum, thank you for only ever asking me to try my best – I'm still trying! And Dad, thank you for showing me how important it is to be myself. Race in peace, Daddy Cool.

Abstract

Forming patterned nanoparticles with modified biological interactions is of wide academic interest, generating a fine level of control at the nano- and bio-interface. Targeted and combinatorial nanoscale therapies are the future of personalised disease therapy, with recent advances providing information about molecular profiles and biomarkers of various diseases. This information will aid the fabrication of novel multifunctional nanoscale delivery systems with the potential to integrate imaging, targeting and treatment moieties on the surface and in the core, resulting in precise targeted drug delivery to the disease site.

The complexity of reported patterned nanoparticle syntheses results in prohibitively high predicted associated cost; direct syntheses may therefore facilitate scalable synthetic processes. The novel polymer architecture, hyperbranched polydendrons (HPDs), combines the benefits of dendrimers and branched vinyl polymerisation; with recent mixed initiation studies introducing a new concept for controlled chain-end chemistry. Here, different HPD strategies for zoned and statistical functionality have been investigated, utilising xanthate chemistry for the controlled introduction of multifunctionality. Simple nanoprecipitation of HPDs was applied for nanoparticle (NP) synthesis (~60 nm); the novel direct surface imaging of functional group patterning using 3 nm gold nanoparticles (GNPs) showed statistically higher grouping of GNPs for patchy HPD NPs (60% ≥twos) than statistical HPD NPs (31% ≥twos). Direct cellular accumulation comparisons of nanoparticles with patchy and statistical distributions of surface functional groups (benzyl- and dimethylamino- groups) showed >3-fold higher accumulation of patchy particles in phagocytic and non-phagocytic cells.

This direct synthesis approach was not trivial; however, it demonstrates the value of NPs with zoned surface chemistry and suggests truly scalable syntheses combining commercial dendron synthesis, vinyl chemistry and nanoprecipitation could be developed.

Contents

Abbreviations

AIDS	acquired immunodeficiency syndrome
ART	antiretroviral therapy
ATHP-1	monocyte-derived macrophages
ATRP	atom transfer radical polymerisation
Caco-2	human epithelial colorectal adenocarcinoma cell line
CAR	cellular accumulation ratio
CI	chemical ionisation
CRP	controlled radical polymerisation
CuAAC	copper catalysed azide-alkyne cycloaddition
Đ	dispersity (GPC)
DLS	dynamic light scattering
D_n	average size by number
DP_n	number-average degree of polymerisation
D_z	Z-average diameter
EPR	enhanced permeation and retention
ESI	electrospray ionisation
G_x	generation x (dendron/dendrimer)
HAART	highly active antiretroviral therapy
HIV	human immunodeficiency virus
HPD	hyperbranched polydendron
LDH	linear dendritic hybrid
MALDI-TOF	matrix-assisted laser desorption ionisation time of flight
M_n	number average molecular weight
MPS	mononuclear phagocyte system
MS	mass spectrometry
MW	molecular weight
M_w	weight average molecular weight
NMR	nuclear magnetic resonance
PdI	polydispersity index (DLS)
ppm	parts per million
RALS	right-angle light scattering
RI	refractive index
SEC	size exclusion chromatography
TEM	transmission electron microscopy
THP-1	human monocytic cells
TLC	thin layer chromatography

Chemical abbreviations

^{3}[H]	tritium
Am	2-(dimethylamino)ethyl
BHA	benzhydryl amide
Bis-MPA	2,2-bis(hydroxymethyl)propionic acid
Bpy	2,2'-bipyridyl
Bz	benzyl
CDI	1,1'-carbonyldiimidazole
DAB	diaminobutane
DBU	1,8-diazabicyclo[5.4.0]undec-7-ene
DCC	N,N'-dicyclohexylcarbodiimide
DCU	dicyclohexylurea
DMAEA	2-(dimethylamino)ethyl acrylate
DMAP	4-dimethylaminopyridine
DMF	dimethylformamide
DMSO	dimethyl sulfoxide
DPTS	4-(dimethylamino)pyridinium *p*-toluenesulfonate
EBiB	ethyl α-bromoisobutyrate
EDA	ethylene diamine
EGDMA	ethylene glycol dimethacrylate
GNP	gold nanoparticle
HEBiB	2-hydroxyethyl 2-bromoisobutyrate
HPMA	2-hydroxypropyl methacrylate
IPA	propan-2-ol
nBMA	*n*-butylmethacrylate
PAMAM	poly(amidoamine)
PEG	poly(ethylene glycol)
PMMH	phenoxymethyl methylhydrazone
*p*TsOH	*p*-toluenesulfonic acid
tBMA	*tert*-butylmethacrylate
TEA	triethylamine
THF	tetrahydrofuran
THPE	1,1,1-tris(hydroxyphenyl)ethane
TMS	tetramethylsilane
TSe	*p*-toluenesulfonyl ethyl

CHAPTER 1

Introduction

1.1 Dendritic macromolecules

Dendritic (Greek: branched) macromolecules are highly branched polymer architectures with a high number of functional groups and a complex tertiary structure. They can be divided into monodisperse dendrons and dendrimers, and polydisperse hyperbranched polymers, dendrigrafts and linear-dendritic hybrids (LDHs) (Fig. 1.1).[1]

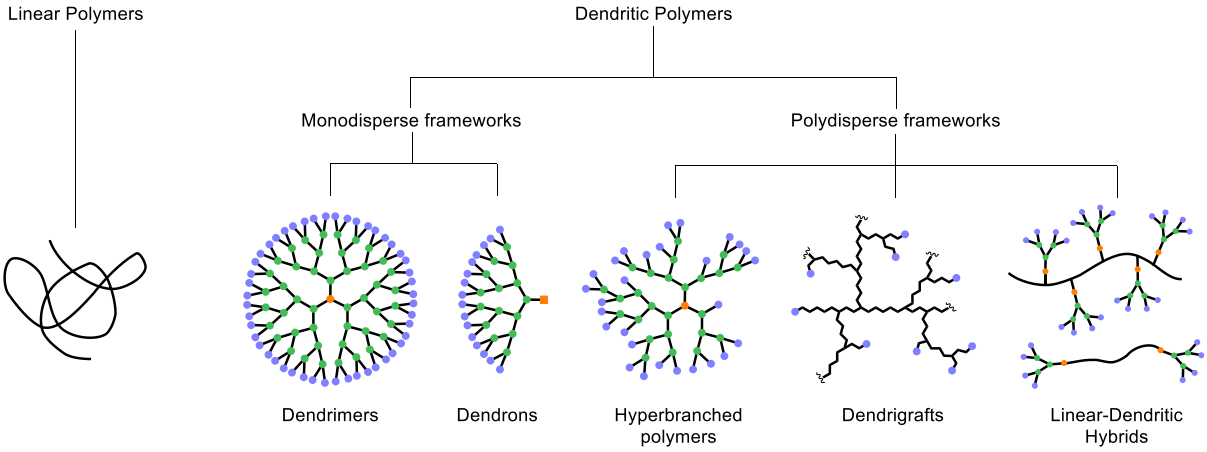

Fig. 1.1 Schematic representation of dendritic polymer subclasses (adapted from Walter and Malkoch)[1]

These subgroups reflect differing relative degrees of structural control over their architectures. Dendrons and dendrimers are highly symmetric macromolecules synthesised in the same manner, with or without a core molecule. Hyperbranched polymers are irregularly branched polymeric architectures with varying degrees of branching, polydisperse structure and size.[2] Dendrigraft polymers, also known as arborescent polymers, possess a multi-level branched architecture assembled from macromolecular branching units. Linear-dendritic hybrids are comprised of two dissimilar polymer architectures; a flexible linear polymer chain and a dense, rigid dendron segment.

Since the first reported synthesis by Vögtle and coworkers in 1978[3], "cascade molecules" or dendrimers (from Greek: *dendros*; tree and *meros*; part), have gained increasing interest due to their quantised nanoscale dimensions, dictated by generation number (approximately 2-10

nm in diameter)[4], perfectly branched structures, formed as a result of carefully controlled iterative coupling reactions. Dendrimers are monodisperse macromolecules and are typically symmetric around the core, adopting a spherical, three-dimensional morphology consisting of a core, branch points and peripheral groups and are usually described in terms of generation (G); the number of layers of repeat units (Fig. 1.2).[5]

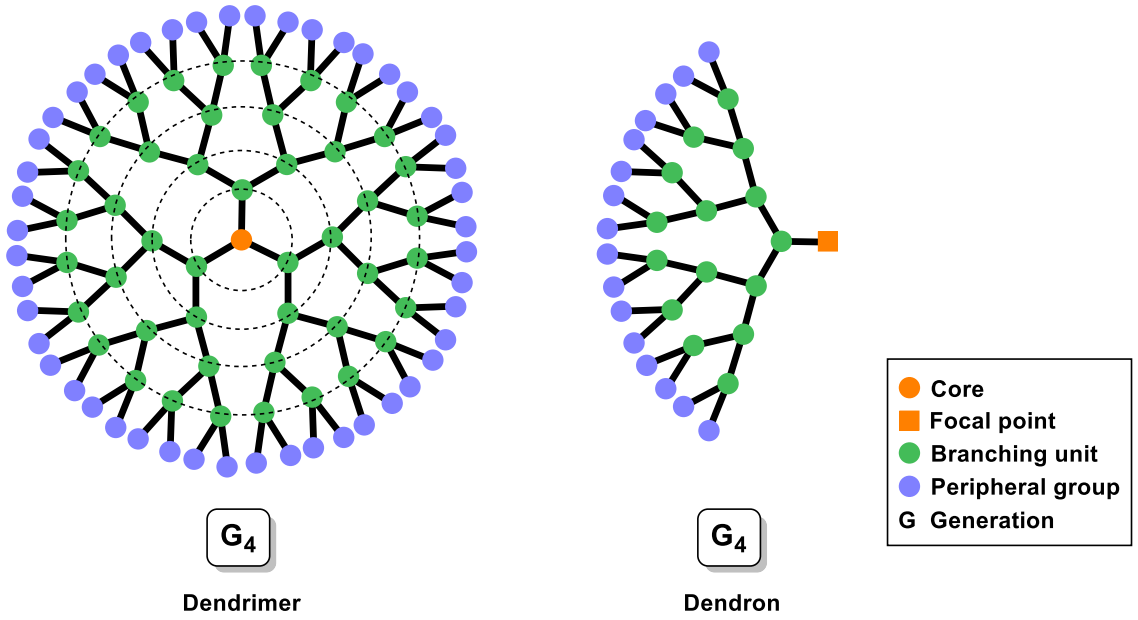

Fig. 1.2 Schematic representation of a generation 4 (G_4) dendrimer and corresponding dendron

Control over chemical functionality at the periphery and within dendrimers can be achieved at any step during the growth process, enabling incorporation of desired functionality for pharmaceutical, chemical, electronic and materials applications.[6,7] Their multivalency, modifiable surface functionality and internal cavity also makes them attractive for drug delivery applications.[4] However, multivalency of higher generations requires precisely controlled, target-specific regioselective functionalisation.[8] A major drawback of these perfectly branched polymers is their limited industrial viability due to lengthy syntheses and high manufacturing costs.

1.1.1 Dendrimer synthesis

Dendrimers are synthesised via a complex series of iterative reactions involving protection/deprotection and coupling reactions, which becomes increasingly complicated and expensive with higher generation numbers. Synthesis involves the repetition of a sequence of reactive steps, producing dendrimers one generation larger with each repetition. Mono- or multi-functional core molecules and AB_n ($n \geq 2$) monomers are used - where A and B denote different functional groups; with either focal point or peripheral protecting groups, depending upon the synthetic route employed. The choice of AB_n monomer helps determine physical properties including solubility and viscosity.[9] Synthetic methodologies for dendrimer construction are based on two defined approaches: The divergent approach, described as "starburst" and "arborol" structures by Tomalia *et al.*[10] and Newkome *et al.*[11] respectively, reported independently in 1985; and the convergent approach reported by Hawker and Fréchet in 1990[12]. These two approaches to dendrimer synthesis can be considered as complimentary, with respect to dendrimer size, purity and functionality. These developments gave rise to a new class of polymer topology which rapidly expanded to a diverse array of chemical structures, applications and modifications.

1.1.1.1 Divergent approach

Divergent synthesis (core first) starts from a multifunctional core molecule, B_n ($n \geq 2$) and involves at least a two-step process; the activation of surface functional groups and reaction with branching monomer units, AB_n ($n \geq 2$), creating a new generation. Repetition of this addition process leads to the synthesis of dendrimers of successive generations. The final step involves the addition of surface functional groups, as shown in Scheme 1.1. This method usually involves the protection of reactive groups, which once coupled to the core are deprotected for the next reactive step.

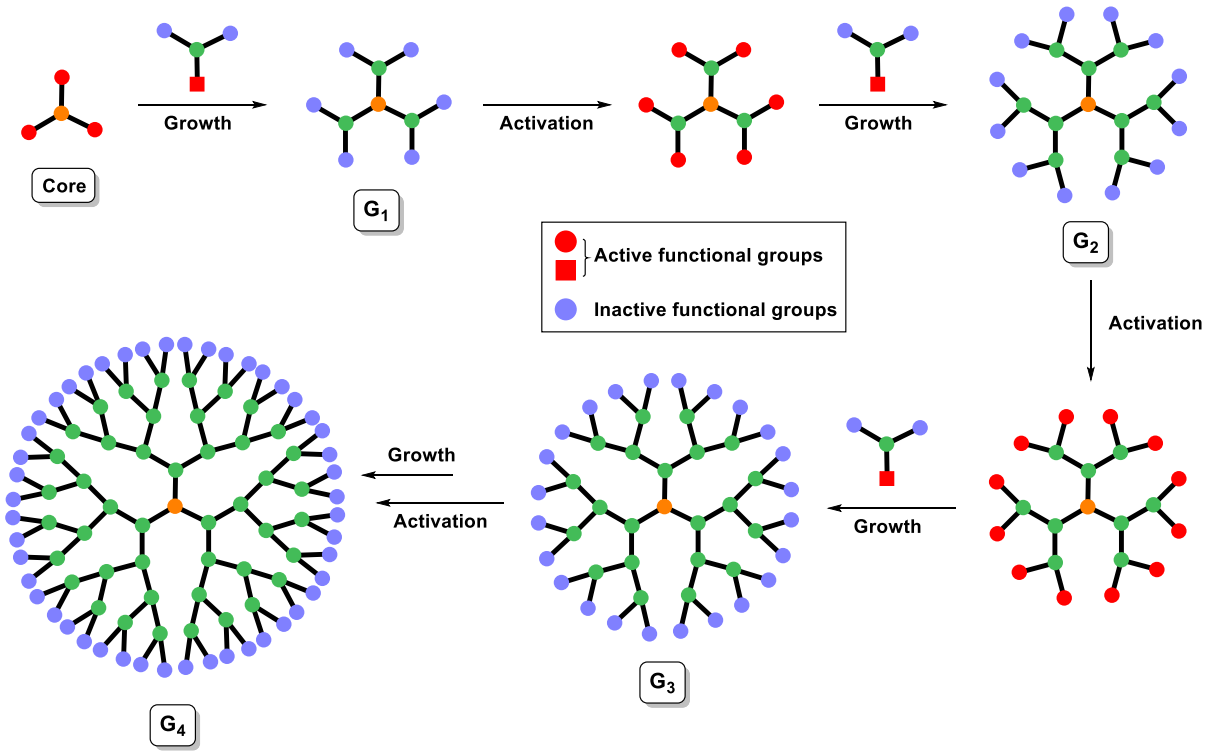

Scheme 1.1 Schematic representation of divergent dendrimer synthesis (adapted from Sowinska and Urbanczyk-Lipkowska)[8]

The first example of an iterative synthetic procedure to produce well-defined branched architectures was reported by Buhleier *et al*. (1978) who applied it to the construction of non-cyclic low molecular weight dendritic amines and described the method as a "cascade"

approach.[3] This approach was also adopted by a number of research groups including Denkewalter, Tomalia and Newkome.[3,10,11,13]

The first publication describing the synthesis of "dendrimers" was presented in 1985 by Tomalia *et al.*[10], describing the synthesis of a series of poly(amidoamine) (PAMAM) dendrimers. The originally reported synthesis of PAMAM dendrimers, trademarked as "Starburst™ polymers" (Dow Chemical Company), was so successful that it remains the preferred commercial route.[14]

The synthesis of PAMAM dendrimers involves the reaction of an amine-functional core molecule (e.g. ammonia, NH_3) with an excess of methyl acrylate via exhaustive Michael addition, followed by complete amidation of the terminal ester functionalities with a large excess of ethylenediamine (EDA) (to avoid cross-linking terminal groups and cycle formation), yielding primary amines at the surface, Scheme 1.2. This reaction sequence can be repeated to produce dendrimers with very high molecular weights. An EDA core can also be applied in the first step to yield dendrimers via a divergent growth approach up to the 10^{th} generation, G_{10} (molecular weight, MW = 934,720 g mol^{-1}; 4,096 peripheral amine groups), although an extremely large excess of reagents is required in order to prevent gelation via dendrimer bridging during amidation.[10,15]

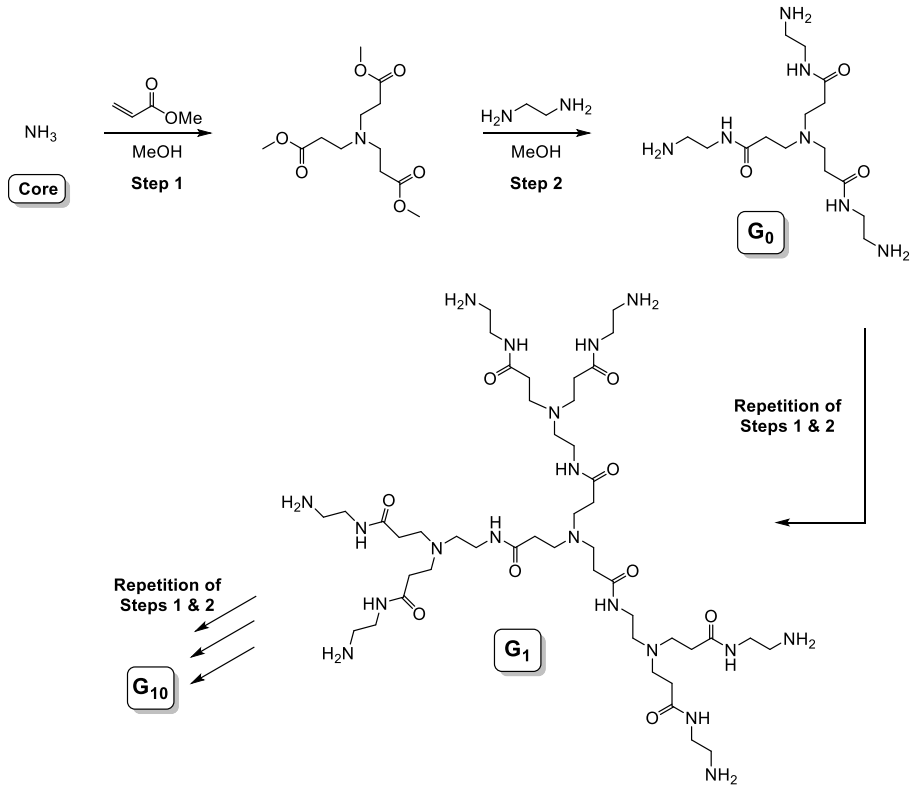

Scheme 1.2 Divergent synthesis of ammonia-core PAMAM dendrimers

The divergent growth approach can be used to quickly synthesise a library of various generation dendrimers, however, it does have some disadvantages. As the number of terminal groups increases exponentially with each generation, the volume of the dendrimer increases (proportional to the cube of the radius, $V = \frac{4}{3}\pi r^3$) much more rapidly than the surface area (proportional to the square of the radius, $S = 4\pi r^2$), resulting is dense packing and hence, steric hindrance, as predicted by de Gennes and Hervet.[16] Therefore, dendrimers adopt a globular architecture at higher generation numbers.[17] As a result of de Gennes dense packing, the possibility of 100% conversion for each reactive step decreases with increasing dendrimer generation. Any incomplete reactions during a chemical step can lead to imperfections or failure sequences in the subsequent generation. In order to assure completion and to prevent possible side reactions, an extremely large excess of reagents is required, however, a small number of statistical defects cannot be avoided, leading to difficulties during purification due

to the small differences in properties (e.g. polarity, molecular mass, size) of the products. A convergent approach was therefore developed in response to the limitations of divergent growth.

1.1.1.2 Convergent approach

The convergent synthesis method (periphery first), developed by Hawker and Fréchet in 1990,[12,18] starts from the surface functional groups of the resulting dendrimer and proceeds towards the core, where dendritic segments (dendrons) are selectively activated at the focal point and coupled to a polyfunctional core, as shown in Scheme 1.3.

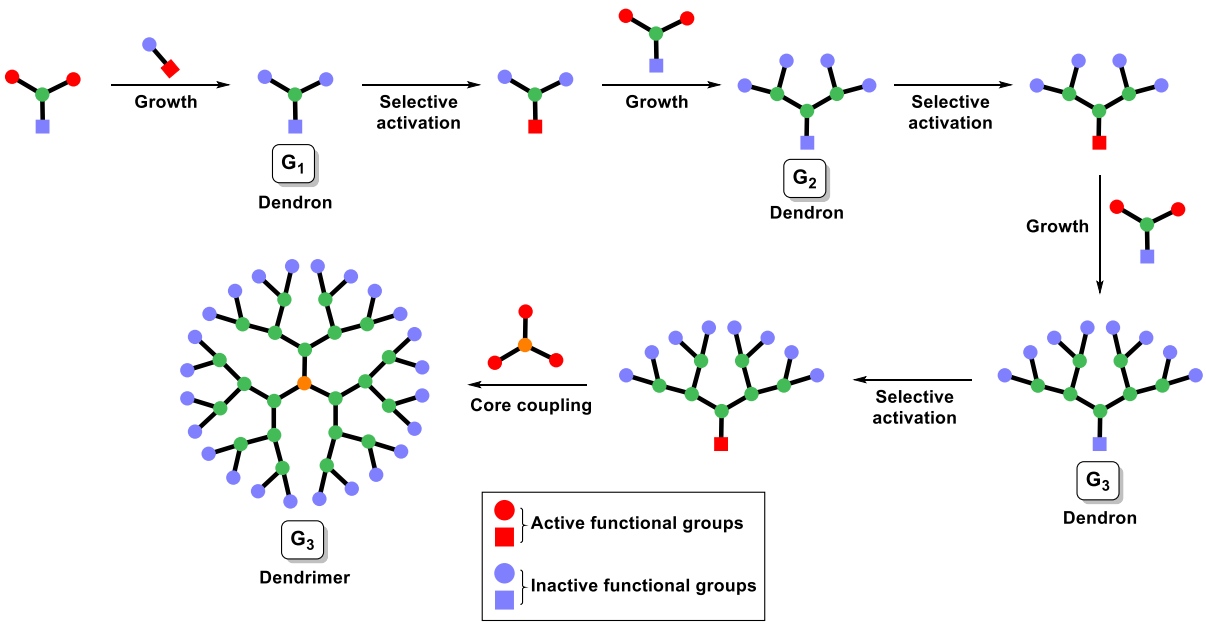

Scheme 1.3 Schematic representation of convergent dendrimer synthesis (adapted from Sowinska and Urbanczyk-Lipkowska)[8]

The convergent approach affords outstanding control over growth and structure due to the relatively low number of coupling reactions at each growth step, less imperfections and without the need of a large excess of reagents[8], in contrast to divergent growth.[10] Imperfect growth leads to significant differences in molecular weight and polarity, whereas

imperfections in divergent growth have little effect on polarity, number of surface groups or molecular weight. As a result, dendrimers obtained via convergent growth tend to be of higher structural purity as materials with imperfect branching can be removed much more easily during purification, e.g. by liquid chromatography.

Hawker and Fréchet reported convergent dendrimer synthesis up to the sixth generation (G_6), based upon the branching 'monomer' unit 3,5-dihydroxybenzyl alcohol to form poly(aryl ether) dendrimers, or Fréchet-type dendrimers, Scheme 1.4.[12,18,19]

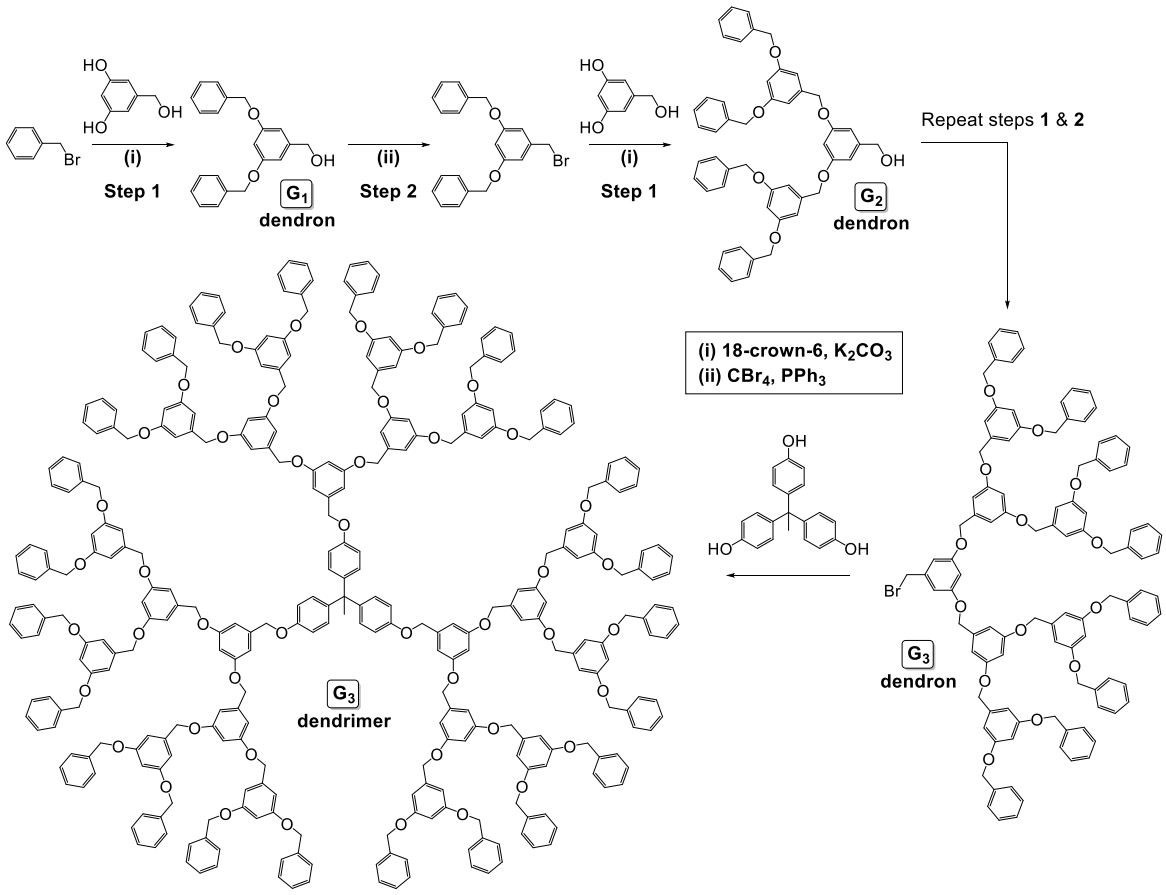

Scheme 1.4 Convergent synthesis of a G_3 poly(aryl ether) dendrimer[12,18]

The dendrimer bears a series of ether linkages between aromatic rings formed via Williamson etherification reactions between benzyl bromide and 3,5-dihydroxybenzyl alcohol. The focal point of the first generation dendron is then activated with carbon tetrabromide (CBr_4) and triphenyl phosphine (PPh_3), then coupled to 3,5-dihydroxybenzyl alcohol to yield the deactivated second generation dendron. This sequence of reactive steps is repeated until the

desired dendron generation is achieved. Dendrimers are formed by coupling dendrons to a multifunctional phenolic (Fréchet) core.

The convergent route allows exceptional control over location of functionality as the core is installed during the final step, enabling incorporation of a range of functionalities with regional variation in the final dendrimer (dendrons with different molecular composition and/or generation), giving rise to numerous novel architectures. This has led to the synthesis of dendrimers consisting of different blocks, chemically varied layers, encapsulated functionalities, differentiated surface functionalities and the opportunity to synthesise linear-dendritic hybrid materials and “dendronised” macromolecules.[20-22] An example of this is "Janus dendrimers" which are constructed from two different dendrons, resulting in macromolecules with two distinct parts either with different polymer backbones, or bearing different functional groups.

The major limitation of convergent synthesis is that as the size of dendrons increase, steric hindrance restricts coupling to the core and hence decreases yield. The convergent method is therefore restricted to the synthesis of lower generation dendrimers (i.e. below G_6). Variations of the convergent approach and its combination with divergent dendrimer synthesis has led to the development of synthetic strategies which reduce the number of reactive steps required to produce high generation dendrimers.[9] These "accelerated syntheses"[1] include: The hypermonomer approach[23], in which an AB_4 or AB_8 monomer is typically employed; Double-stage convergent synthesis[24] where a larger core, known as a "hypercore", is reacted with smaller dendrons to reduce steric hindrance; Double-exponential growth and orthogonal approaches which take advantage of chemoselectivity to orthogonally protect/deprotect reactive groups and quickly build dendrons which are later coupled to a core (orthogonal protection is a synthetic strategy which affords independent deprotection of functional groups).

1.1.2 Dendrimers based on 2,2'-bis(hydroxymethyl)propionic acid

Since the work presented within this thesis is mainly focussed on materials based on the monomer 2,2-bis(hydroxymethyl)propionic acid (bis-MPA), it is prudent to look in more detail at literature examples of this family of dendrimers.

Bis-MPA dendrimers have been proven to be non-toxic and non-invasive and are therefore promising candidates for drug delivery applications.[25-27] The polyester dendrimer scaffold possesses hydrolytically labile ester linkages and is therefore biodegradable.[28,29]

The first example of dendrimers based on the AB_2 monomer bis-MPA was presented by Ihre *et al*. in the mid-1990s.[30] In this first iteration, a convergent route was applied to synthesise a fourth generation (G_4) dendrimer with a trisphenolic core and 48 peripheral acetyl groups. In this case, oxalyl chloride was used to activate the focal point at each growth step, with 10 reactive steps and an overall yield of 15%.[31] Unfortunately, attempts to remove peripheral acetyl protecting groups resulted in degradation of the dendrimer backbone. To alleviate this problem, a double-exponential growth strategy was developed, employing acetonide protecting groups which can be removed under milder conditions, without damage to the dendrimer backbone and yielding a dendrimer with reactive surface groups, Scheme 1.5.

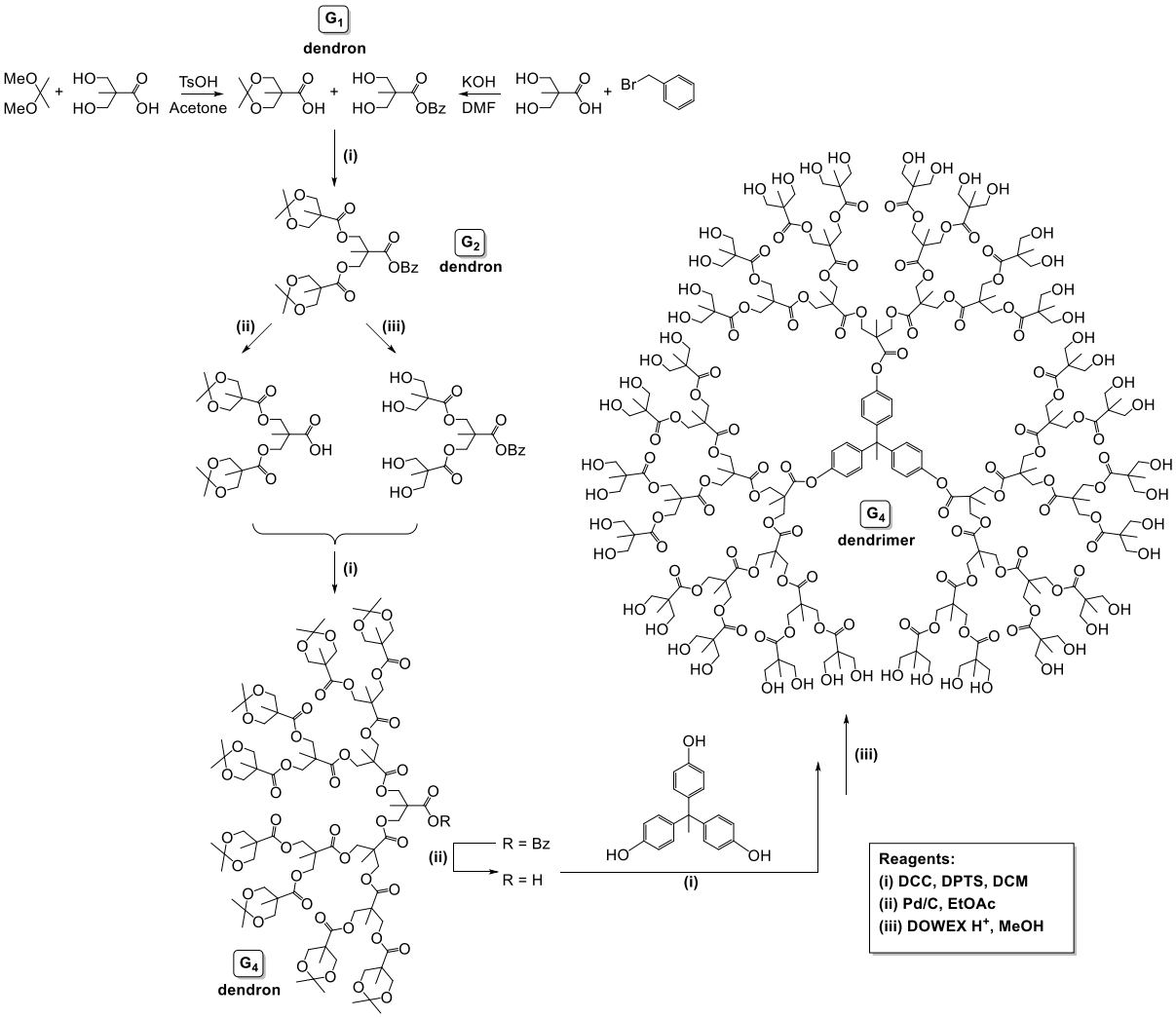

Scheme 1.5 Preparation of a G_4 polyester dendrimer using 2,2-bis(hydroxymethyl)propionic acid (bis-MPA)[31]

Fourth generation bis-MPA dendrimers with 48 peripheral hydroxyl groups were synthesised in high recovered yields (56% in 7 reactive steps) using *N,N'*-dicyclohexylcarbodiimide (DCC) as the esterification agent for coupling acetonide protected bis-MPA to hydroxyl functional groups.[32] The presence of 4-(dimethylamino)pyridinium 4-toluenesulfonate (DPTS), which is formed from an equimolar ratio of DMAP and *p*-toluenesulfonic acid monohydrate[33], suppresses the formation of inactive *N*-acylurea byproducts. Although this method was successful, it suffered low yields at high dendrimer generations, resulting in the introduction of a novel anhydride monomer unit based on bis-MPA.[34] The application of anhydride chemistry to the synthesis of dendrimers has proven to be an efficient strategy due to their greater tolerance of water residues than acid chlorides and acid bromides, enhanced

reactivity towards hydroxyl groups and high recovered yields, facilitating dendrimer synthesis on a large scale. Reactions between anhydrides and alcohols to yield polyester dendrimers are normally carried out at ambient temperature in the presence of catalytic DMAP, thus minimising transesterification and degradation.[35] The synthesis of a 2nd generation bis-MPA based dendrimer using the anhydride approach is shown in Scheme 1.6, below.

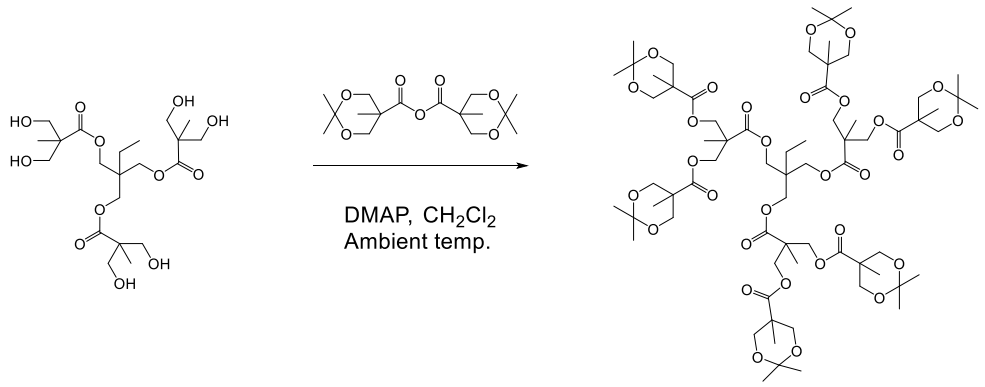

Scheme 1.6 Preparation of a G_2 polyester dendrimer using 2,2-bis(hydroxymethyl)propionic anhydride[34]

1.1.3 Dendrimers in therapeutic applications

Due to the structural properties of dendrimers, hydrophobic drugs can be loaded into the hydrophobic internal cavity, whilst hydrophilic drugs, antibodies, DNA, reactive chemical groups or other desired ligands can be attached to the multivalent surface via covalent conjugation or electrostatic interaction.[36,37] Dendrimers have shown to be promising candidates for the treatment of neurodegenerative disease and as antiviral agents for the treatment of Human Immunodeficiency Virus (HIV) due to their ability to disrupt protein aggregates.[38] Starpharma Holdings Ltd developed SPL7013 gel (VivaGel®); a 4th generation dendrimer with a benzhydryl amide (BHA) core and polylysine backbone, capped with 32 naphthalene disulphonic acid groups which provide hydrophobicity and high anionic charge

to the surface of the dendrimer.[39] VivaGel® is a vaginal microbicide for the prevention of HIV and HSV infections.[40] This water based antimicrobial/antiviral gel has EU regulatory approval for the topical treatment of bacterial vaginosis (BV) and is under clinical development for the prevention of recurrent BV. VivaGel® has also been shown to have potent antiviral activity against the Zika virus in laboratory studies.[41] Dendrimer-enhanced (DEP™) drug delivery (passive and targeted) of existing drugs is also under development, with a dendrimer-enhanced version of docetaxel (marketed under the name Taxotere®) for treatment of solid tumours in the advanced stages of Phase 1 clinical testing (Trial ID: ACTRN12614000171617). Docetaxel is attached to the surface of the dendrimer with a linker which controls its release. In pre-clinical studies, DEP™ docetaxel was shown to have enhanced efficacy and reduced toxicity compared to docetaxel alone, with an absence of neutropenia, a major dose-limiting factor of the drug.[42]

1.1.4 Limitations of dendrimers

Dendrimers display interesting materials properties due to their compact, globular structure and very high surface functionality, as a result of complete synthetic control. Although there are a wide range of potential applications of dendrimers, their future applications rely on efficient and practical synthetic procedures.

Divergent dendrimer growth is generally limited to the 10th generation, with the exception of a G_{13} dendrimer, with dimensions comparable to small viruses, reported by Lim *et al*. in 2013.[43] This synthesis utilises a hypermonomer approach to incorporate two generations per iteration, yielding G_{13} dendrimers with a theoretical molecular weight exceeding 8.4 MDa, and 16,384 amine groups at the surface. This triazine dendrimer platform utilises 18 flexible atoms per branching unit (P = 18), resulting in a limiting generation (the maximum generation achieved before defects) of 13 when applied to Eq. 1.1.[16]

$$limiting\ generation = 2.88(lnP + 1.5) \qquad \text{(Eq. 1.1)}$$

This limitation is due to steric hindrance, as described by de Gennes dense packing[16], resulting in self-limiting dendrimer dimensions as a function of generation unit length. Ideal dendritic growth without branching defects is only possible for generation numbers below the limiting generation, also known as the *dense packed state*. By application of site-specific stable isotope labelling of $G_{1\text{-}5}$ benzyl ether dendrimers, distances between the chain ends (^{13}C) and focal point (^{19}F) were evaluated with rotational-echo double resonance (REDOR) NMR.[44] At higher generation numbers ($G_{3\text{-}5}$), inward-folding of the chain ends and interpenetration between dendrimers occurs; decreasing interpenetration is observed with increasing generation.

Another major limitation in the commercialisation of dendrimers is the large excess of reagents often required to achieve perfect growth, particularly for divergent dendrimer synthesis, Fig. 1.3. Convergent dendrimer synthesis suffers from steric hindrance when coupling large dendrons to a small core molecule, often resulting in incomplete reactions.

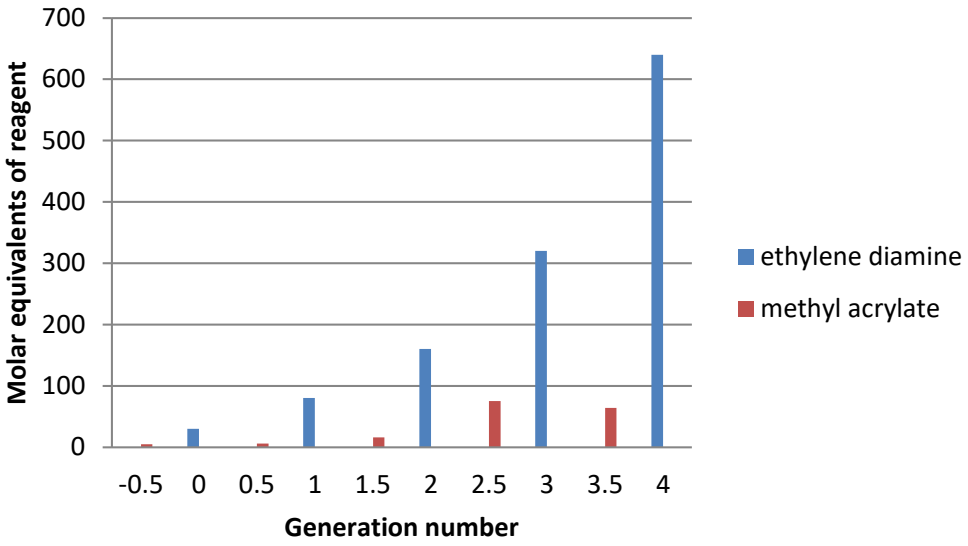

Fig. 1.3 Reagent excess for divergent synthesis of aniline-cored PAMAM dendron up to G_4 (32 terminal groups)[45]

Both convergent and divergent approaches have the disadvantage of time consuming and expensive syntheses, limiting their commercial applications. There are currently only a small number of commercially available dendrimers; PAMAM®, DAB®, Phosphorus PMMH and bis-MPA dendrimers[46], therefore, a continuous improvement in synthetic procedures is key to their commercial success.

Materials such as hyperbranched polymers possess similar characteristics to dendrimers, with highly branched polymer structures, but lack the same structural uniformity due to statistical branching of AB_n ($n \geq 2$) monomers during their one-pot synthesis.[47] They are often used as dendrimer "mimics", due to their similar structural and globular properties, without the need for multistep synthetic strategies[2], however their poorly controlled structure contains both dendritic and linear sites. Hyperbranched polymers will not be discussed further in this introduction, instead the reader is directed to a recent review of these types of materials.[48]

1.2 Dendritic hybrid architectures

Dendrons and dendrimers provide a high degree of structural uniformity, however, despite synthetic advances in this field, dendrimers remain exceptionally difficult to synthesise in high purity. New synthetic protocols for the construction of more sophisticated functional dendritic hybrids have been developed in order to combine well-defined dendritic architectures with the synthetic ease of traditional polymer synthesis, as discussed below.

1.2.1 Linear dendritic hybrids

Linear dendritic hybrids (LDHs) are macromolecular copolymers consisting of two or more structurally dissimilar blocks; linear polymer chains (L) and dendrons (D). This difference in

structure is reflected in their differing physical properties; linear polymer chains display a higher viscosity and hydrodynamic volume than corresponding dendritic structures with the same molecular weight.[49] Covalent bonding of two or more blocks of sufficient size (linear block ≥1000 g mol^{-1}, dendron block ≥G_2) gives rise to novel qualities of the resulting copolymer, with higher generation dendritic blocks significantly altering solid state and solution properties.[50] These materials have shown promise for applications in catalysis, as bioreactors and in the biomedical field.[51-53]

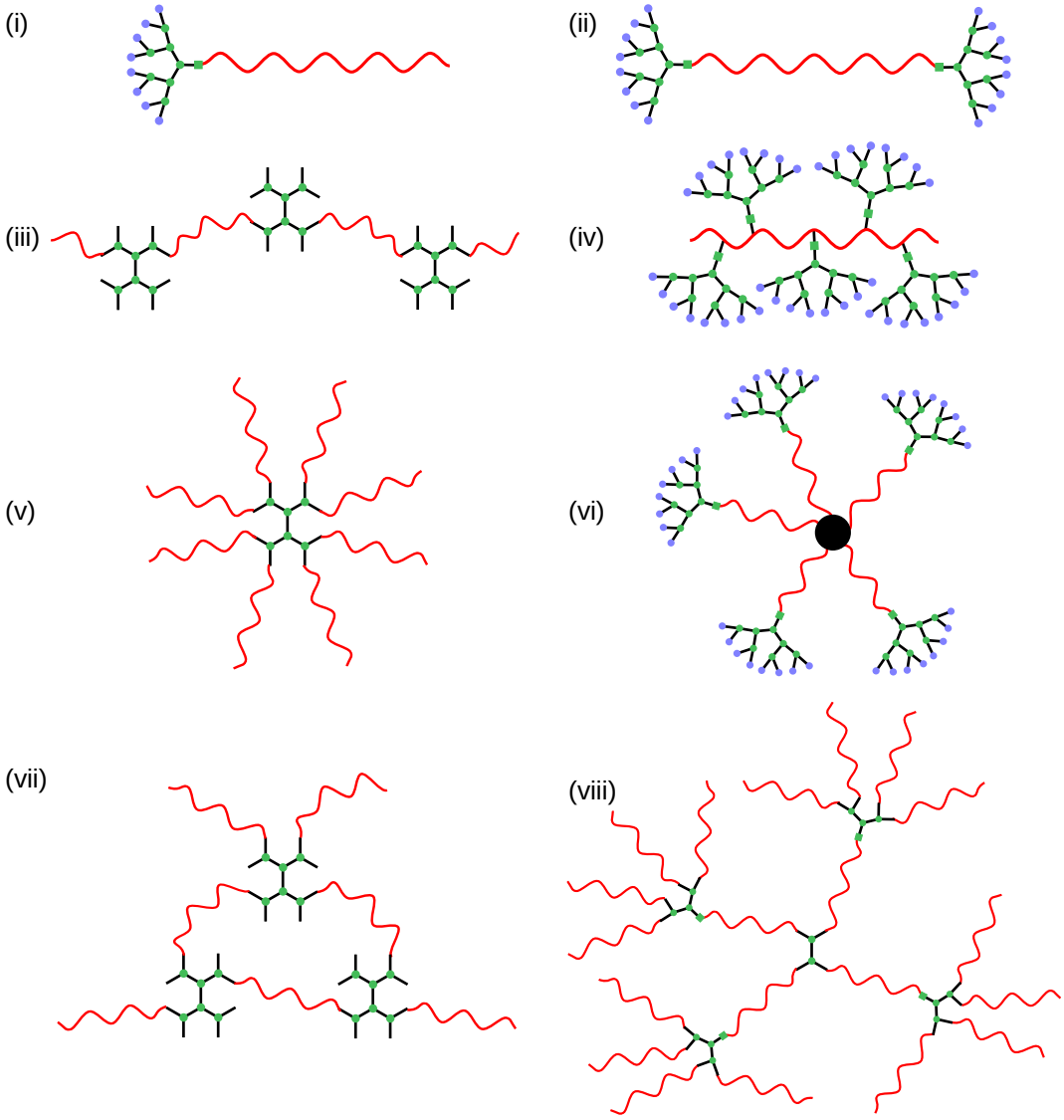

Fig. 1.4 Possible architectural types of linear(red) dendritic(black) hybrids (LDHs): (i) LD; (ii) DLD; (iii) LD_n; (iv) L-*graft*-D; (v) star-$D(L)_n$; (vi) star-$(LD)_n$; (vii) network D_nL_m m≥n; (viii) superdendrimer D^1-$[L(DL_n)]_m$ (focal point of dendrons represented by green squares)

A range of structures can be achieved depending upon the relative position of the linear (L) and dendritic (D) blocks, outlined in Fig. 1.4. As can be seen in Fig 1.4, LDHs can be synthesised from dendrons that possess a reactive group at the focal point and dendrimers with reactive groups at the surface. The combination of linear polymers with dendrons will be the focus of this discussion. Synthetic routes to LDHs include: (a) coupling of preformed linear and dendron blocks; (b) growth of dendritic structures on linear chains with reactive groups along the backbone or at the ends ("chain-first"); (c) linear chain growth by dendritic macroinitiators ("dendron-first") and (d) polymerisation of dendritic macromonomers.[52] To preserve the monodisperse nature of the dendritic block, efficient coupling chemistries and controlled polymerisation techniques are typically used.

(a) Coupling of preformed linear and dendron blocks

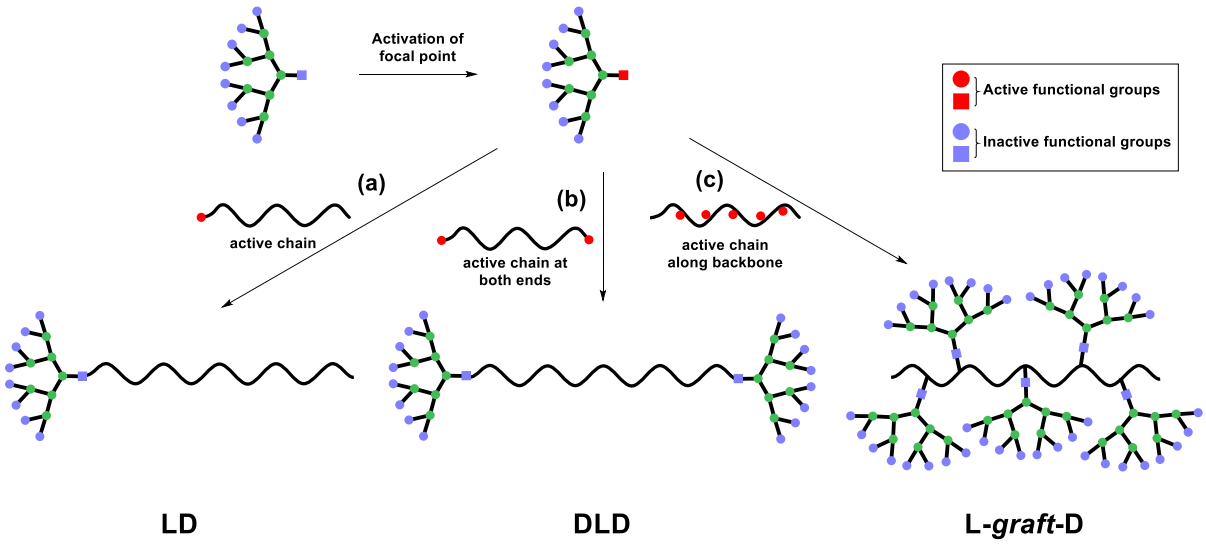

Scheme 1.7 Schematic representation of LDHs synthesised by coupling of preformed linear and dendron blocks: (a) LD; (b) DLD and (c) L-*graft*-D type

Coupling of preformed reactive linear and dendron blocks was the first method of LDH synthesis utilised and could theoretically be used to synthesise all macromolecular structures

from (i)-(vii) (Fig. 1.4), Scheme 1.7. In the first reported synthesis by Gitsov *et al*., poly(styrene) was initially synthesised via "living" polymerisation with potassium naphthalene, modified with 1,1-diphenylethylene, then terminated with poly(benzyl ether) dendrons possessing a benzyl bromide at the focal point, generating a DLD-type hybrid (Fig. 1.4 (ii)).[54,55] This method of LDH formation benefits from a one-step synthesis, easy purification by extraction/precipitation or liquid chromatography and unambiguous structure analysis by a combination of SEC, MALDI-TOF, FTIR and NMR. However, limited reaction chemistries and difficulties associated with the detection of a low number of covalent bond formations in large structures limits this approach.[52,54]

(b) Growth of dendritic structures on linear chains with reactive groups along the backbone or at the ends ("chain-first")

LD, DLD and L-*graft*-D (Fig. 1.4 (i), (ii) and (iv)) structures may also be synthesised via a "chain first" route, whereby dendrons are divergently grown from the end or at specific reactive sites along the backbone of a preformed linear polymer chain, Scheme 1.8. This method suffers from the same drawbacks as traditional divergent dendrimer synthesis; a large excess of reagents is required in order to avoid branching defects - a problem encountered by Yin *et al*. when synthesising dendronised polymers based on PAMAM dendrons, using the "graft-from" approach.[56] PAMAM dendrons up to the 4th generation were constructed at the side chains of poly(ethylene imine) linear chains formed by "living" cationic polymerisation (number average degree of polymerisation, DP_n = 10-500), however, a 10,000 fold excess of ethylene diamine (EDA) was required for complete amidation, with reaction times of 5-8 days.

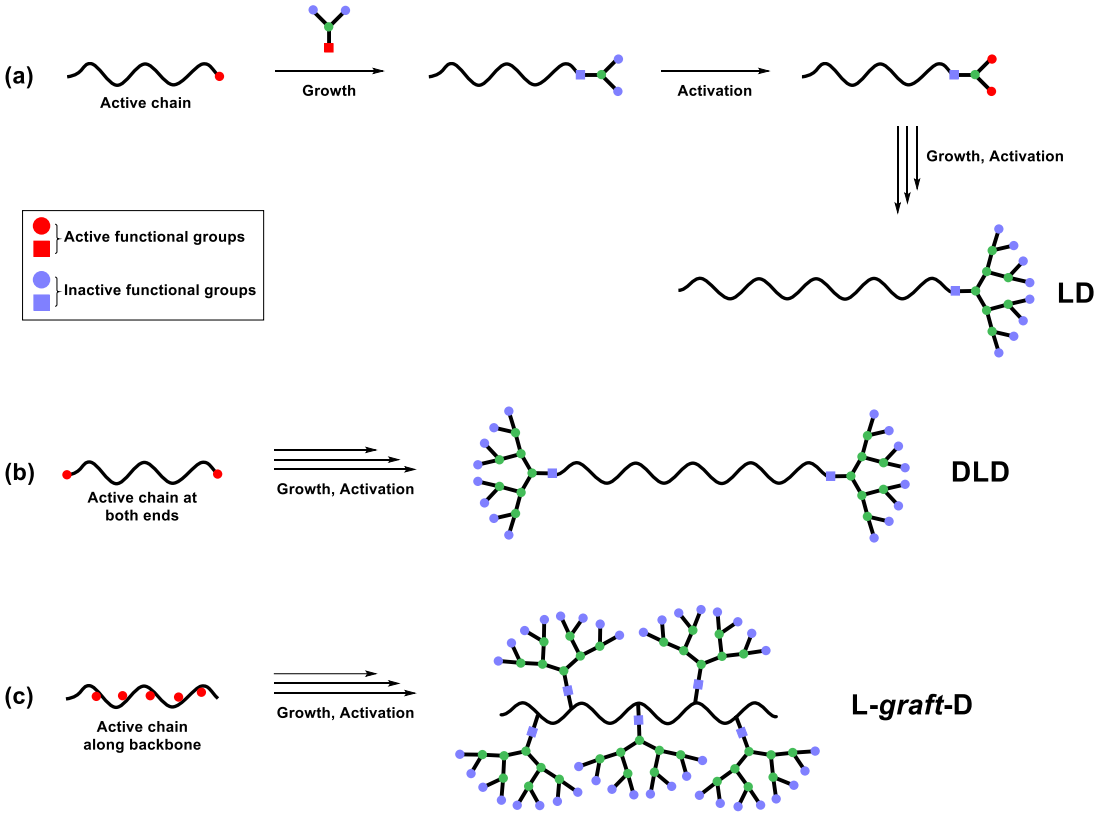

Scheme 1.8 Schematic representation of "chain-first" LDH synthesis: (a) LD; (b) DLD and (c) L-*graft*-D

(c) Linear chain growth by dendritic macroinitiators ("dendron-first")

The "dendron-first" method of LD synthesis is based on a macroinitiator approach, which involves focal point modification of the dendron block to incorporate functionality to initiate polymerisation, Scheme 1.9. Polymerisation techniques such as anionic ring-opening polymerisation (ROP) and controlled radical polymerisation (CRP) methods such as ATRP (for more information, see section 2.8.1), RAFT and NMP ensure good control over chain length and monomer composition of the linear block. It is also possible to tailor the nature of the end groups by various polymerisation techniques and modification chemistries.

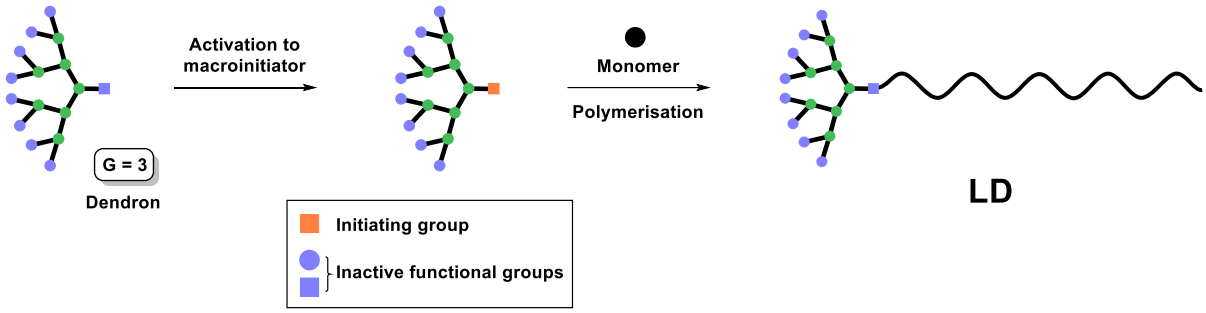

Scheme 1.9 Schematic representation of "dendron-first" synthesis of LD hybrid

This method of LDH synthesis was first reported by Gitsov *et al.*[57] and involved the ring-opening polymerisation (ROP) of ε-caprolactone with poly(benzyl ether) dendrons possessing a benzyl alcohol functionality at the focal point. LDHs with high molecular weights and narrow dispersities were obtained.

(d) Polymerisation of dendritic macromonomers

Dendronised polymers, or L-*graft*-D hybrids (Fig. 1.4 (iv)), can also be synthesised via the macromonomer approach, Scheme 1.10.[58,59]

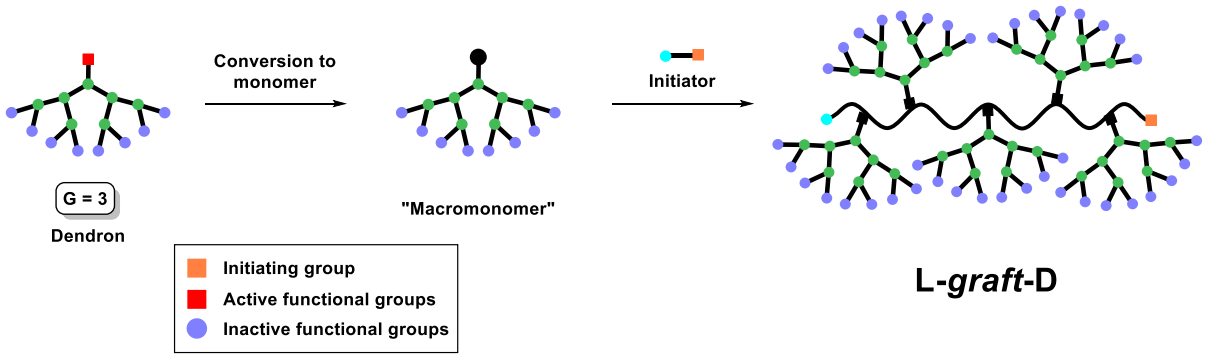

Scheme 1.10 Schematic representation of macromonomer approach to L-*graft*-D dendronised polymer hybrids

In the macromonomer route, first reported by Hawker and Fréchet in 1992[60], dendrons of desired generations are modified at the focal point to introduce polymerisable functionality. This macromonomer is then utilised in a polymerisation reaction, yielding a dendronised polymer with the desired dendron present in every repeat unit, giving rise to an extremely

high density of functionality at the surface. However, the macromonomers are increasingly difficult to synthesise with increasing generation and must be highly reactive with respect to propagation, the comonomer (if used) must have a small and favourable shape and the polymer backbone must be reasonably stiff.[52,58]

1.2.2 Hyperbranched polydendrons

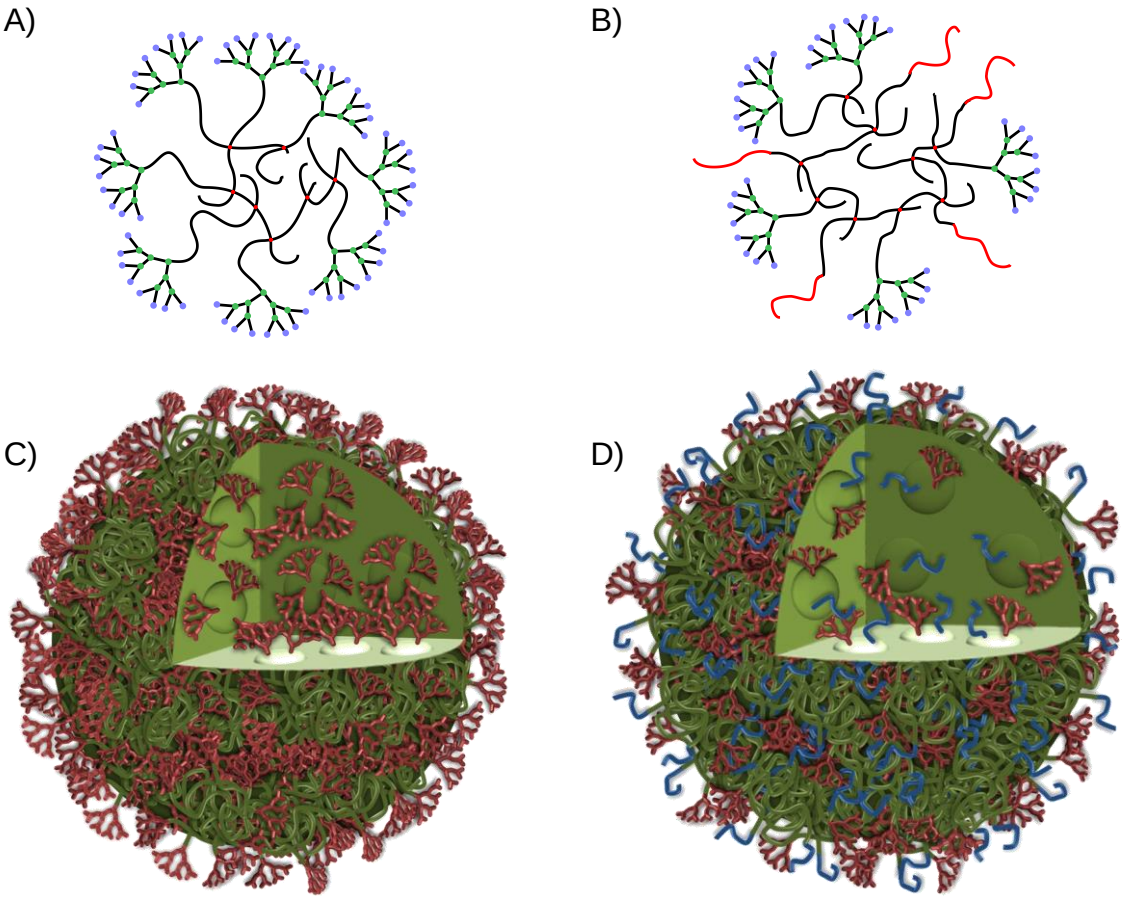

Fig. 1.5 Schematic representation of: A) A hyperbranched polydendron (HPD); B) a co-initiated HPD; and nanoparticles formed via nanoprecipitation of C) HPD; and D) coinitiated HPD

A new dendritic-polymer hybrid architecture known as hyperbranched polydendrons (HPDs) (Fig. 1.5A) was recently reported by Hatton *et al.*[61]; these structures consist of multiple dendron blocks attached to a soluble, branched polymer core, synthesised via the macroinitiator route. First and second generation ATRP macroinitiators were prepared using

the secondary symmetrical alcohol 1,3-dibenzyloxy-2-propanol and modified at the focal point with α-bromoisobutyryl bromide. These macroinitiators were then utilised in the ATRP of 2-hydroxypropyl methacrylate (HPMA) in the presence of bifunctional monomer ethylene glycol dimethacrylate (EGDMA), with a ratio of <1 brancher unit per intitiator molecule to avoid cross-linking the core, resulting in very high molecular weight polymers. These hyperbranched polydendron structures were able to form remarkably uniform nanoparticles in water via nanoprecipitation (see section 1.6.2), despite their very high molecular weight and broad dispersities. These materials offer an alternative to dendrimers, maintaining desirable surface chemistry at molecular sizes not currently achievable by convergent or divergent growth strategies. Hyperbranched polydendrons also hold the potential to overcome the disadvantage of limited drug payload of dendrimer systems as physical encapsulation into the core is an additional option for these materials. It was hypothesised that these polymeric nanoparticles contain a hydrophobic core for the non-covalent encapsulation of hydrophobic guest molecules and dendron moieties to introduce high surface functionality, thus emulating dendrimer-like structures on a much larger scale (Fig. 1.5C). Encapsulation provides a significant advantage as there is no need to chemically modify the structure of the drug molecule.

In another report[62], the G_2 dendron macroinitiator was utilised in a co-initiated polymerisation with a poly(ethylene glycol)-derived (PEG_{16}) ATRP initiator for the copolymerisation of HPMA and EGDMA (Fig. 1.5B). It was found that by varying the ratio of the dendron and PEG initiator molecules, nanoparticles with varying surface and internal chemistry could be formed via nanoprecipitation (Fig. 1.5D), resulting in the ability to tailor particles for encapsulation of hydrophobic molecules and permeation through a gut epithelium model.

1.3 Nanomedicine

The application of nanotechnology to medical and pharmaceutical challenges has led to the broad field of nanomedicine which targets the diagnosis, screening, prophylaxis and treatment of diseases with unprecedented precision and accuracy.[63-65] This development is in response to unsuitable physicochemical properties of existing drug molecules, such as poor solubility, and hence low bioavailability, and to provide different routes of administration with safer and more effective therapies compared to conventional methods. One of the primary goals of nanomedicine is to achieve localised drug delivery and specific targeting, which is essential in tumour treatment and gene therapy. The use of nanomedicine facilitates the creation of a differential drug distribution between the disease site and the rest of the body, thus maximising the therapeutic effect whilst minimising off-target adverse effects (Fig. 1.6 (i)).

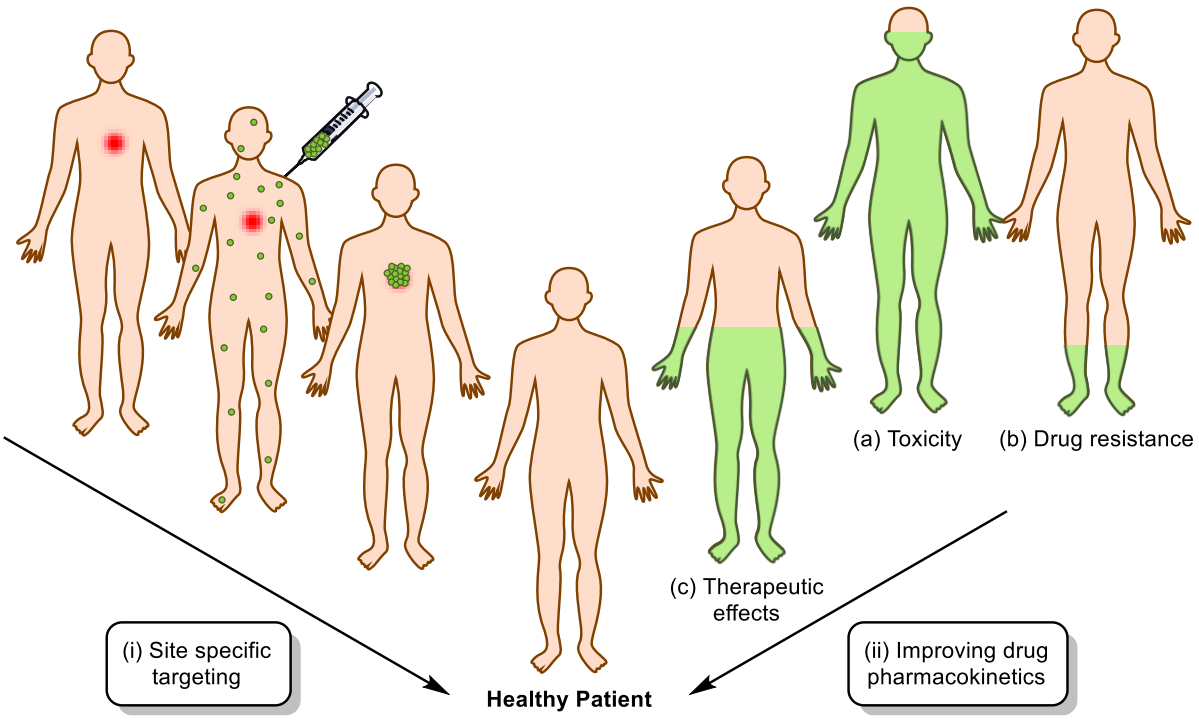

Fig. 1.6 Drug delivery approaches of nanomedicines: (i) Site specific targeting and (ii) Improving pharmacokinetics[66]

Improving drug pharmacokinetics (Fig. 1.6 (ii)) by increasing bioavailability, distribution or residence time within systemic circulation aims to reduce toxicity or drug resistance as a result of incorrect dosing. This is of particular importance when treating chronic diseases such as HIV; where toxicity leads to negative side-effects and ultimately poor adherence to drug regimes, and drug resistance requires modifying the anti-retroviral drug therapy combination to prevent proliferation of the virus.[67] Sustained release of antiretroviral drugs is desirable for the treatment or prevention of HIV, reducing the number and frequency of doses taken by patients.[68]

The goal of sophisticated drug delivery systems is to carry sufficient drug loads and efficiently cross various physiological barriers. Targeted delivery systems are designed to reach specific disease sites intact via a medium that can control administration by means of a chemical or physical trigger.[69] As most physiological barriers prohibit permeation or internalisation of particles or drug molecules with large sizes and undesirable surface chemistry, nanomedicine aims to miniaturise and multifunctionalise drug carriers for improved drug delivery in a controlled, site-specific manner. Polymeric nanoparticles made from natural and synthetic polymers have gained interest recently for applications in the pharmaceutical industry as a mode of targeted drug delivery due to their stability and ease of surface modification.[70] Nanosized drug delivery vehicles can be divided into; polymeric nanoparticles, liposomes, solid lipid nanoparticles, polymeric micelles and dendrimers. Polymeric nanoparticles are submicron-sized colloidal particles and can be in the form of nanospheres; matrix systems in which drugs are dispersed throughout the particles, or nanocapsules; where the drug is confined in an aqueous or oily cavity surrounded by a polymeric membrane (a core-shell structure) (Fig. 1.7), resulting in differing release profiles.

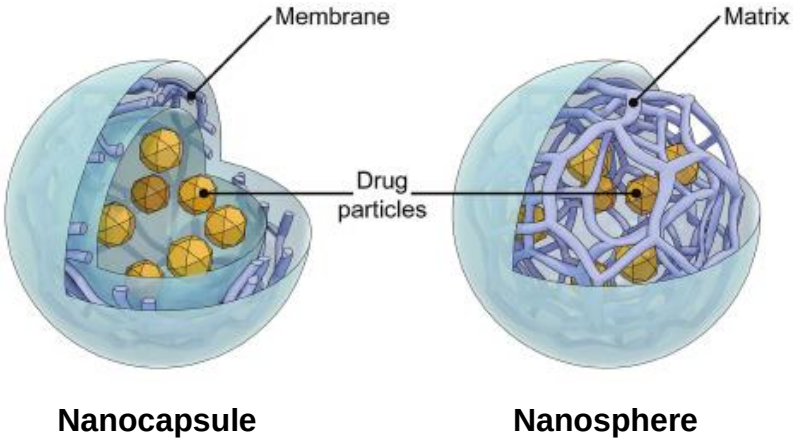

Fig. 1.7 Schematic representation of a nanocapsule and a nanosphere[71]

Polymer-based nanoparticles should be biocompatible (non-toxic) and biodegradable in order for them to serve as viable carriers for site specific drug delivery. Route of administration either by intravenous or oral intake can initiate different immune reactions.[72] PEG is a biocompatible, non-toxic polymer which is often used to modify the surface of nanoparticles to introduce "stealth" character at the surface, reducing protein (opsonin) adsorption by masking undesired charge or surface properties.[73] Opsonisation, enhanced by the hydrophobicity of a particle's surface, is a rapid process for mononuclear phagocyte system (MPS) recognition and clearance whereby particles are marked with proteins (opsonins) to enhance interactions with cell surface receptors on phagocytes; this can result in increased uptake of nanoparticles by the phagocytic cells of the MPS, which in turn determines the route of nanoparticle internalisation. These factors highlight the importance of surface effects for nanoparticles to be used as a carrier for drug delivery.

1.4 Active vs. Passive targeting

Targeted drug delivery refers to drug accumulation in a specific site of disease, independent of the method and route of administration.[74] For drug delivery vehicles to work, they should be able to reach the desired location within the body, either by passive or active targeting, through the various routes and biological barriers with minimal loss of their volume and functional integrity. Once in the desired location, they should be able to release their drug cargo without creating negative side effects in the surrounding healthy cells or tissue via controlled and targeted release mechanisms. If successful, these delivery systems would improve patient survival rates, reduce adverse side effects associated with the administered drug, reduce dosage frequency and size, and hence wastage, and improve the overall therapeutic effect. Targeted drug carriers can be designed to incorporate different physical and chemical properties including hydrophobicity/hydrophilicity, charge, size, morphology and targeting ligands.

Passive targeting of nanocarriers is based on a size-flow-filtration phenomenon, usually limited to tumours, the MPS and lymph nodes.[75] In cancer therapy, passive targeting takes advantage of the leaky vasculature in tumour tissue and compromised lymphatic drainage, resulting in higher accumulation; this is known as the enhanced permeation and retention (EPR) effect. This effect allows macromolecules/nanoparticles to enter and preferentially accumulate in the tumour interstitial fluid whilst suppressed lymphatic filtration blocks their clearance from the tumour.[76] Extravasation of nanoparticles from systemic circulation can occur by convection (dominant, blood pressure dependant) or diffusion (slower, concentration dependant). However, the EPR effect is influenced by factors such as the structure of the tumour (vascular bed, stroma and extracellular matrix), tumour size, the

presence or absence of functional lymphatics, interstitial pressure and location, resulting in variability across patients.

An advantage of active targeted drug delivery is that the drug is internalised and released intracellularly, dramatically diminishing the efflux of drug.

1.5 Treatment of chronic disease

Healthcare systems face a number of extremely costly and burdensome chronic medical conditions, such as arthritis, asthma, heart disease, diabetes, cancer and HIV/AIDS; accounting for 70% of deaths and 75% of direct healthcare costs in the United States in 2005.[77] Chronic drug regimens for conditions which generate long-term morbidity often require frequent dosing through daily administration of single or combination drug therapies. Current research focuses heavily on the development of nanomedicine platforms for the treatment of cancer[78], although few have been approved due to strict approval procedures.[79] Research aims to decrease dosage and hence toxicity, whilst increasing drug concentrations at the tumour site; avoiding exposure of healthy tissue to toxic drug levels.[80] Cancer presents an obvious target for nanomedicines which can take advantage of the EPR effect; increasing drug accumulation around a tumour in a localised disease site. However with diseases such as HIV, for which there is no cure, the viral infection occupies cellular and tissue sites widely distributed throughout the body and in systemic circulation.[81] According to the World Health Organisation (WHO), 36.7 million people globally were living with HIV at the end of 2015.[82] Highly active antiretroviral therapy (HAART) provides effective treatment for HIV by combining different classes of antiretroviral agents, transforming a lethal disease into a chronic pathology; maintaining the function of the immune system and preventing opportunistic infections that often result in death.[83] HAART provides effective treatment

options for treatment-experienced and new patients. Several classes of antiretroviral agents currently exist:

- Nucleoside reverse transcriptase inhibitors (NRTIs)
- Non-nucleoside reverse transcriptase inhibitors (NNRTIs)
- Protease inhibitors (PIs)
- Integrase strand transfer inhibitors (INSTIs)/Allosteric integrase inhibitors (ALLINIs)
- Fusion inhibitors (FIs)
- Chemokine receptor antagonists (CCR5 or CXCR4 antagonists)

Most current HAART drug regimens consist of a combination of 3 antiretroviral agents; two NRTIs and one PI/NNRTI/INSTI.[84] Strict adherence to antiretroviral therapy (ART) is critical for sustained HIV suppression and reduced risk of drug resistance.[85]

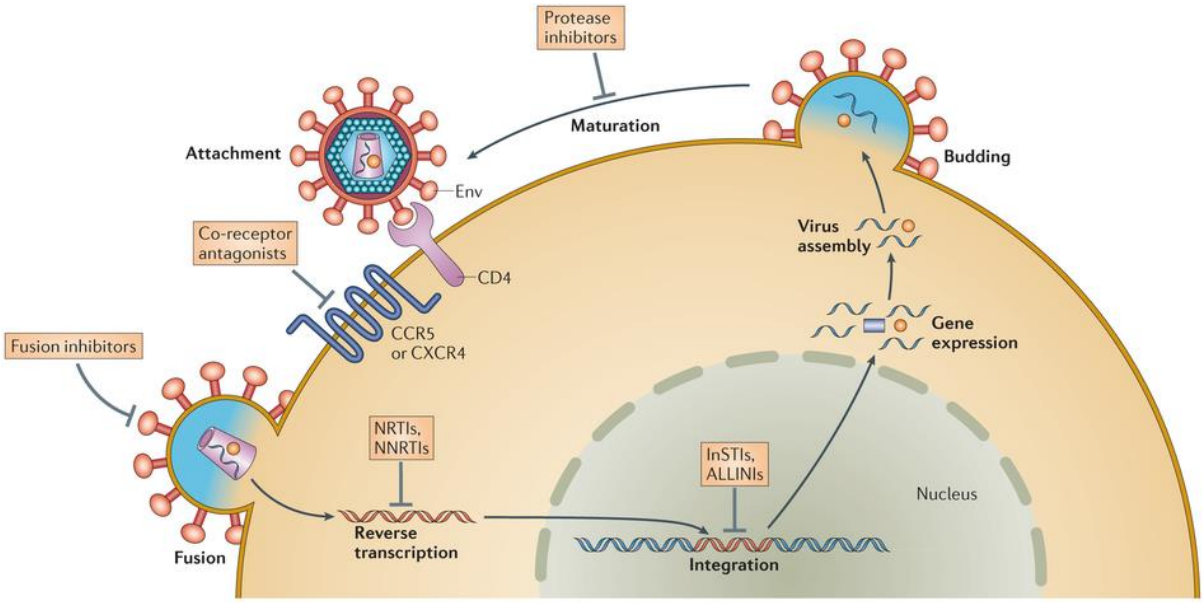

Fig. 1.8 Stages of the HIV-1 life cycle targeted by antiretroviral drugs[86]

Restricted access of antiretroviral drugs to sanctuary sites such as the brain and the lymphatic system impedes viral clearance and is believed to be the main cause of resurgence of

suppressed HIV replication from below detection level in patients with interrupted treatment.[87,88] The narrow therapeutic index – the ratio between the therapeutic and toxic dose of a drug – of many antiretroviral drugs such as efavirenz (NNRTIs), lopinavir/ritonavir (PIs), maraviroc (CCR5 inhibitor) and tenofovir (NRTIs), often limits their effectiveness as they are administered to patients in sub-optimal doses to prevent side-effects. Some antiretroviral therapies have considerable interpatient pharmacokinetic variability while others have known drug concentrations associated with efficacy and/or toxicity.[89] To overcome these problems, smart nanocarriers with targeting moieties and stimuli responsive release are being developed for the delivery of antiretrovirals.[90-93] Orally dosed nanomedicine formulations aim to reduce drug dose whilst maintaining therapeutic exposure, leading to a decrease in side-effects and cost per dose.

1.5.1 Passive targeting of macrophages

Passive targeting takes advantage of the inherent biophysicochemical properties of the nanoparticle such as size, shape, charge and flexibility to influence tissue accumulation, adhesion and cell uptake.[94] Passive targeting of nanocarriers to lymph nodes, an important induction and HIV-1 replication site, is key to improved drug delivery for the treatment of HIV/AIDS.[75] Macrophages are also an important replication and sanctuary site which play a significant role in the pathogenesis of HIV-1. Once infected, macrophages generate new virus, have low drug permeation, die during rapid viral replication and negatively impact immune system activity.[95] HIV infected macrophages are more phagocytic than non-infected macrophages[96], thus providing a potential passive targeting option for drug delivery vehicles. Long-term successful treatment of HIV infected macrophages requires potent strategies to prevent entry and persistence in these cells.[97] Several research groups[98-102] have used

macrophages to target the MPS, particularly lymph nodes. Drug-loaded nanocarriers are engulfed by macrophages, which then migrate to the lymph nodes (or other MPS tissues); the drugs slowly diffuse out of the macrophages, producing a sustained high drug concentration within the lymph node. In all cases, frequency of administration of the drug carriers was decreased, total amount of drugs delivered is low, resulting in reduced toxicity, yet the efficacy is high. One study involved the intravenous (IV) injection of indinavir (IDV) nanoparticles entrapped in macrophages *in vitro* into humanised mice; the *in vivo* studies showed accumulation in the lung, liver and spleen. This resulted in a reduction of HIV-infected cells in plasma, lymph nodes, spleen, liver and lung, as well as $CD4^+$ T-cell protection.[100]

Reliance on passive diffusion limits effective drugs to those that are soluble in both polar extracellular environments and non-polar cell membrane environments.

1.5.2 Opportunities for active targeting of HIV

Physical targeting of nanomaterials makes use of external sources or fields to guide nanoparticles to target sites and to control the therapeutic effect, for example in photothermal and magnetic hyperthermia therapy.[103]

Targeted delivery of nanocarriers for the treatment of HIV requires specific ligands that interact with specific HIV receptor targets. This approach has been applied extensively in preclinical studies of cancer targeting where certain receptors are over-expressed at various stages of the disease.[78,104,105] HIV receptor targets are lacking on infected cells, however, the disease only targets a limited number of cell types ($CD4^+$ T cells, $CD4^+$ monocytes/macrophages, dendritic cells). HIV receptor CD4, co-receptors CCR5 and

CXCR4, and others (e.g. folate) relatively specific to macrophages provide potentially valuable surface targets for drug delivery to all HIV-susceptible cells in patients.[75]

A combination of both active and passive targeting may ultimately prove to be the most effective when targeting the treatment of HIV.

1.6 Nanoparticles with heterogeneous surface functionality for drug delivery

Nanoparticles are solid, colloidal particles with dimensions of less than 1 μm, in which therapeutic agents can be encapsulated or attached onto the surface.[106,107] The preparation of well-defined particles on the scale of nanometers to micrometers can be achieved using a range of techniques such as self-assembly, (mini/micro)emulsion systems, suspension and interfacial polymerisation.[108] Nanoparticles can be biodegradable, biocompatible and functionalised depending upon material selection and manufacturing technique. The choice of technique depends upon the desired material properties; solubility, morphology, size and dispersity can be tailored for the targeted application.[109,110]

Multivalent interactions occur naturally in many biological systems and are characterised by the simultaneous binding of multiple ligands to multiple receptors.[111] Nanoparticles with numerous targeting ligands can provide multivalent binding with cells that present a high density of receptors at the surface, e.g. cancer cells, providing enhanced interactions over single targeting ligands of molecular conjugates (Fig. 1.9).[112]

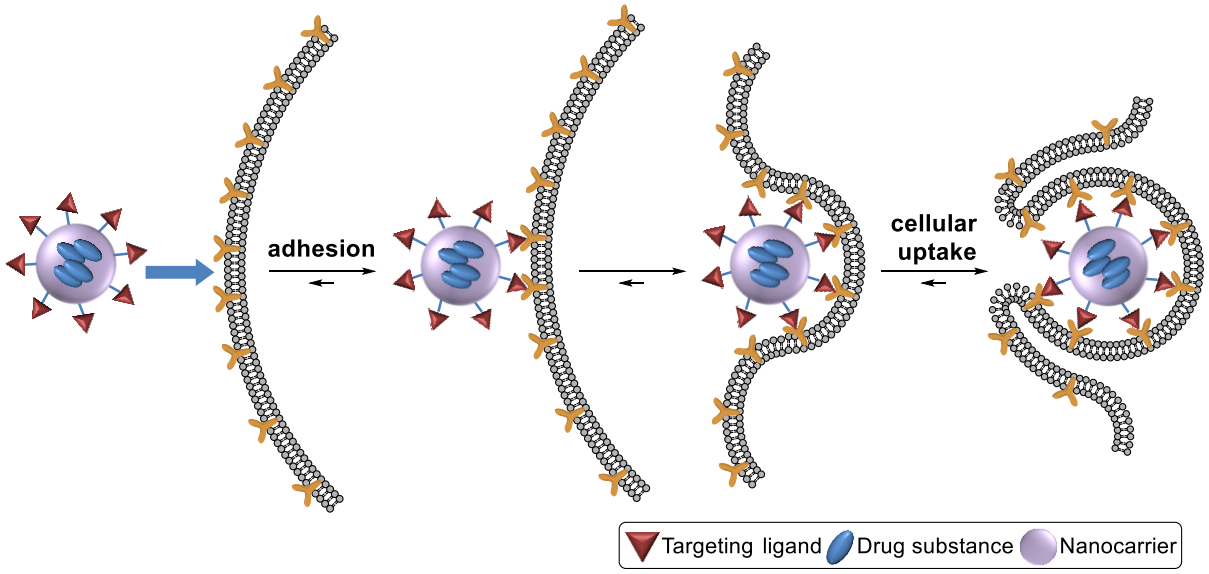

Fig. 1.9 Multivalent interaction between nanocarriers possessing multiple targeting ligands and multiple receptors on a cell surface leading to endocytosis

Drug delivery systems are specifically engineered to deliver therapeutic agents in a targeted and/or controlled manner and must therefore; avoid capture by the immune system, target diseased tissue, infiltrate the diseased tissue, release the drug, avoid drug resistance mechanisms and avoid releasing drug in healthy tissue, as this would lead to side effects.[69,113] Therefore, particles with multiple surface chemistries (denoted as "patches") are required to aid navigation through the body. Various inorganic and organic colloids (objects with at least one dimension in the order of 1 nm – 1 μm, dispersed in a continuous medium)[114] can be produced with good control over dispersity of size and shape, however, their surfaces remain chemically homogeneous.[115] Janus particles, which possess two distinct regions of contrasting polarity or surface chemistry (Fig. 1.10), have been widely studied as a subcategory of patchy particles, after being popularised by de Gennes in 1992.[116]

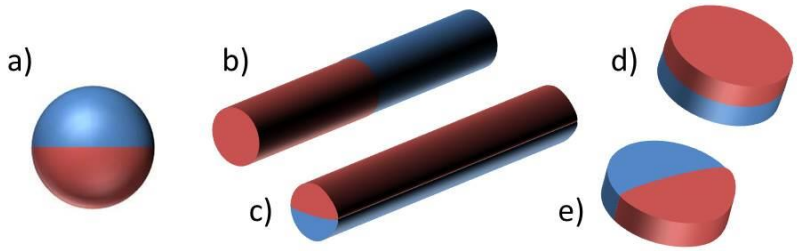

Fig. 1.10 Possible Janus particle architectures; (a) sphere, (b,c) cylinders and (d,e) discs

Two-faced Janus particles introduce asymmetry and directionality within a single particle for self-assembly[117-119] or emulsion stabilisation at fluid-fluid interfaces[120]. Three main strategies are employed for the synthesis of Janus particles; masking, phase separation and self-assembly.[121] Masking involves protection of one side of a particle, followed by modification of the unprotected side by evaporative deposition[122] or suspension at an interface[123]. Preparation of Janus particles by phase separation involves the mixing of two incompatible substances, usually either two polymers or a polymer and an inorganic material, that separate into their own domains within a single particle. Synthesis via self-assembly of block copolymers was first described in 2001 by Erhardt *et al*.[124], and involved the self-organisation of a polystyrene-*block*-polybutadiene-*block*-poly(methyl methacrylate) triblock copolymer into spherical Janus micelles possessing polystyrene and poly(methyl methacrylate) hemispheres.

Patchy particles are defined as having 1 or more patches of less than 50% of the total surface area of the particle which exhibit different properties.[125] Patchy particles are colloidal particles with an anisotropic distribution of surface functional groups, resulting from tailoring the particle's surface or modification of components during fabrication.[126] As a result of the heterogeneously patterned surface, patches are able to form highly directional and specific bonding interactions, Fig. 1.11.[127]

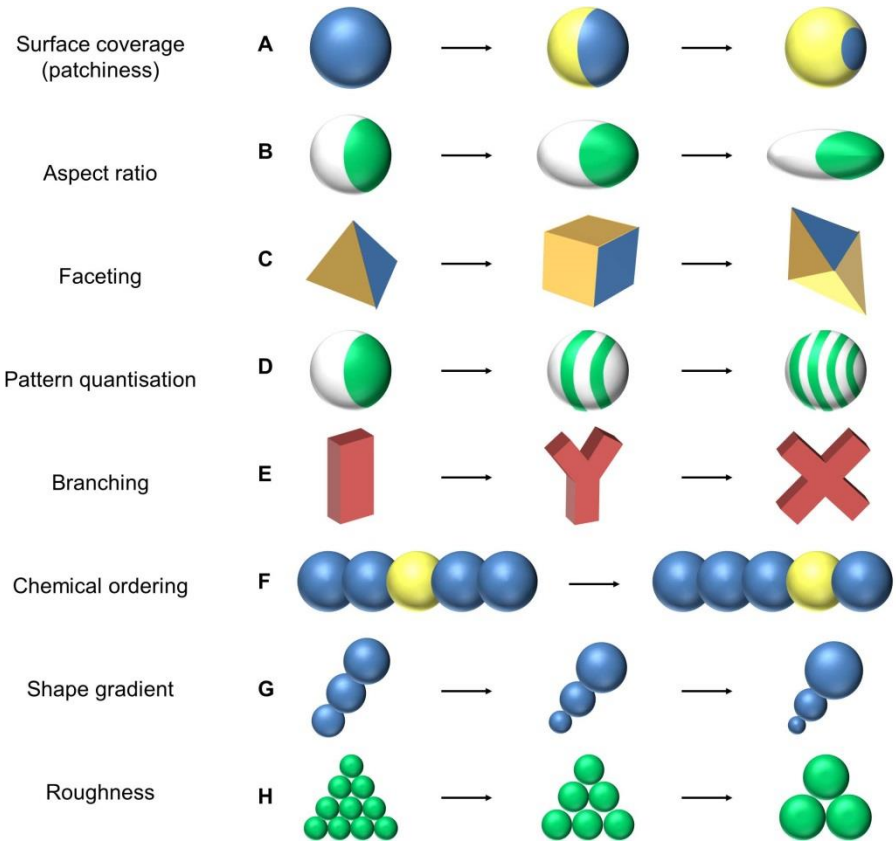

Fig. 1.11 Patchy particles (adapted from Glotzer *et al.*)[127]

Patchiness is introduced onto the surface of colloidal particles via a range of chemical and physical processes, including: templating or masking (as described for Janus particles)[125]; particle lithography, which involves attaching small particles to larger particles[128]; glancing angle deposition (GLAD) where vapour deposition is carried out at an inclined angle with respect to the particle monolayer[125]; colloidal clusters, where microspheres are attached to the surface of liquid emulsion droplets, followed by removal of the liquid, leading to packing of the spheres[129]; nanosphere lithography, involving three dimensional close-packed arrays of particles where the top layer of particles acts as a mask which determines the patterning of metal deposited on the lower layer(s)[130].

Experimental simulations have concluded that the size and nature of the patches of functionality on the surface of nanoparticles affects insertion and penetration across a flat membrane.[131] It has been shown that particles of similar size and overall surface composition

with patterned and non-patterned surfaces display remarkably different membrane penetration behaviour. Gold nanoparticles (~6 nm) with ordered, ribbon-like domains of hydrophobic and hydrophilic moieties on the surface were shown to penetrate cell membranes at 37°C and 4°C without evidence of membrane disruption; whereas particles lacking structural order showed no evidence of cell membrane penetration.[132]

The combination of different functionalities onto one single particle may lead to the development of multifunctional nanomedical platforms for simultaneous targeting, imaging and therapy administration.[133] The availability of multiple terminal groups allows dendritic structures to carry a higher payload of functional moieties, enhancing targeted toxicity.

1.6.1 Surface modifications

Multifunctional materials are often required for advanced applications.[134] The highly branched nature of dendrimers provides enormous surface functionality with well-defined interior and exterior regions, enabling multifunctionality on the same macromolecule and therefore multivalent interactions with microorganisms *in vivo*. The interior environment of dendrimers is usually unreactive and therefore unavailable for post-synthesis modification, however there are some examples where dendrimers have been treated with strong acids[135] or super bases[136] to generate active sites within the dendrimer interior for further modification. The incorporation of "temporary" groups, or protected precursors, into the dendrimer structure allows for selective transformation post-synthesis.[137-139] McGrath and coworkers presented dendrimers with dormant hydroxyl functional groups in the interior, which can be activated under moderate acidic conditions.[140,141] However, the most common modifications take place at the surface where a large number of terminal groups are presented. Many of the properties that dendrimers exhibit are determined by end-group chemistry, e.g.

hydrophobicity/hydrophilicity, solubility, thermal stability.[142] Due to the equivalent nature of these end groups, only reagents with high reactivity and selectivity can be used. Some examples of reactions that have been established for the surface modification of bis-MPA dendrimers include copper-catalysed azide-alkyne cycloaddition (CuAAC) click chemistry[143] and incorporation of peripheral hydroxyl groups that can be converted to reactive intermediates including alkenes[144,145], alkynes[143,146,147] and *p*-nitrophenyl carbonates[26,148]. CuAAC click chemistry combines exceptional chemoselectivity with a lack of byproducts and high yields, and has been used to efficiently functionalise dendrimers with peptides[149] and carbohydrates[150,151]. However, highly reactive, potentially explosive and toxic azide substrates, and the strict purification procedures required for removal of cytotoxic copper used in the synthesis, has limited the application of CuAAC click chemistry and resulted in the development of alternative click reactions including retro Diels-Alder cycloaddition and thiol-based click reactions.

1.6.2 Nanoprecipitation

Nanoparticle formation by nanoprecipitation, also known as solvent displacement or interfacial deposition, was developed by Fessi *et al.* in 1989[152], and involves the addition of a polymer in a "good" solvent (e.g. THF, acetone) to a miscible anti-solvent (usually water) with stirring. Nanoprecipitation occurs by rapid desolvation of the polymer in the anti-solvent by diffusion and evaporation of the "good" solvent, resulting in a decrease in interfacial tension and subsequent phase separation. Nanoprecipitation offers the advantage of simple and mild formulation under ambient conditions without the use of chemical additives and harsh chemical or physical processes. Nanoprecipitation is insensitive to the chemical

specificity of the components, making it a widely applicable nanoparticle formation technique.

Lince *et al.*[153] described nanoprecipitation in terms of three stages; nucleation, growth and aggregation. The rate of each step determines the resulting particle size distribution and relies on super-saturation, defined as the ratio of polymer concentration and the solubility of the polymer in the solvent mixture. Nanoparticle size may be controlled by; addition speed of solvent to anti-solvent, mixing velocity, the concentration and/or ratio of polymer(s) and other components (e.g. drug molecules) in the "good" solvent, types of solvent used, and the ratio of solvent to anti-solvent.

Hatton *et al.* recently demonstrated that nanoprecipitation can be directed by large, highly branched macromolecules, even in polymer samples with very broad molecular weight distributions, containing a significant linear portion.[154] This has implications for materials used in a medical setting; significantly reducing the need for stringent control over polymer synthesis and nanoparticle formation, to obtain nanoparticles with controlled size and narrow polydispersities.

1.7 Research hypothesis

Properties such as nanoparticle size, surface charge, solubility, and surface functionality influence uptake and clearance by macrophages.[155] In several cases, the passive targeting of macrophages may be highly beneficial to therapeutic outcomes and one such opportunity has been highlighted through the observation that HIV-infected macrophages are more phagocytic than uninfected macrophages.[96] This potentially offers a higher statistical delivery of drug-containing nanoparticles to target cells in a mixed population containing healthy and infected cells.

Polymer nanoparticles can be specifically designed to achieve both controlled drug release and site-specific localisation by tuning the polymer properties and surface chemistry.[156] Important characteristics for drug delivery using nanoparticles include; high water solubility and drug loading capacity, biodegradability, low toxicity, favourable retention and biodistribution characteristics, specificity and appropriate bioavailability.[157] Dendrimers are considered as promising drug delivery vehicles as they enable simultaneous incorporation of drugs and biological ligands at the surface for active targeting. However, their complex and expensive synthesis and purification procedures as well as poor drug loading efficiency render them not widely commercially viable. It has also been shown that flexible, elongated nanocarriers might be more successful in drug delivery applications than dense, radially symmetric dendrimers.[158,159] HPDs provide a promising alternative to dendrimers as they maintain a high level of surface functionality with a tuneable polymer core. These materials have also been shown to nanoprecipitate to form nanoparticles which display exceptional size control, stability and uniformity of behaviour, despite the broad dispersity and high molecular weight of the branched polymer structures.[61] HPDs can potentially improve the carrier-to-active ratio, compared to dendrimers, whilst maintaining surface functionality for multivalent

interactions.[160] Multivalent interactions between nanoparticles and macrophages may result in enhanced cellular uptake via the simultaneous binding of multiple ligands at the nanoparticle periphery with multiple receptors on the cell surface. In addition, patchy particles simultaneously present multiple different surface functionalities on the same construct, making them promising for multivalent guest-host interactions. Controlling the size and distribution of patches on nanocarriers may enhance efficacy and specificity of targeted delivery.[161]

The HPD platform provides a relatively simple method of connecting multiple chain ends bearing diverse chemistry by branching between primary polymer chains, thereby producing materials with very high molecular weight and surface functionality. In previous studies, tailoring the initiator feed ratio of two different functional macroinitiators (dendron- and PEG-derived) resulted in materials with varying nanoparticle size and permeation through a human gut epithelium model.[62] The presented hypothesis suggests an opportunity to expand this concept to include multiple-initiation of a PEG macroinitiator with more than one functional dendron initiator, potentially of different generations, to induce "patchiness" on the surface of nanoprecipitates. Using this modular synthesis approach, it may be possible to build patchy, multifunctional nanoparticles with isolated functional groups and aqueous stabilisation which enable targeting of infected macrophages, Fig. 1.12.

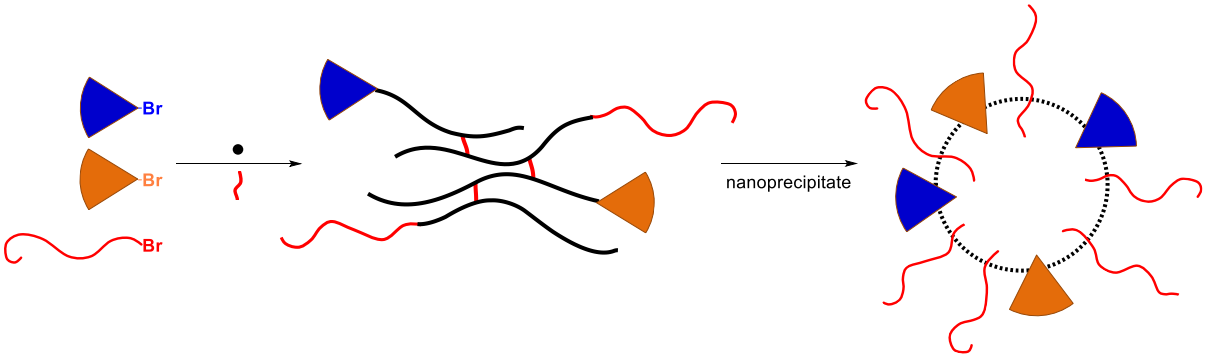

Fig. 1.12 Co-initiation of two dendron macroinitiators with different peripheral functionality with a PEG-derived macroinitiator to synthesise patchy multifunctional nanoparticles

Increasing the generation number of the dendron, and hence the number of functional groups per "patch", it may be possible to maximise the avidity of multivalent ligands, Fig. 1.13. The precise, spatial control of functionalities may result in directional interactions with receptors on the macrophage surface.

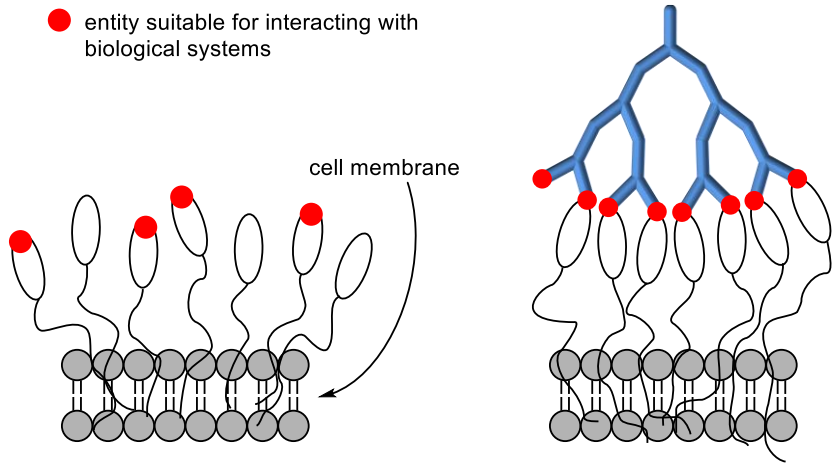

Fig. 1.13 Schematic representation of the multivalency effect that may occur with biological systems in the presence of dendritic structures compared to monomeric interactions (adapted from Caminade and Turrin)[162]

1.8 Research objectives

To systematically and rigorously investigate the presented research hypothesis, a combination of dendrimer chemistry for the construction of dendron macroinitiators, controlled radical polymerisation (CRP) for the rapid formation of HPDs, and facile thiol-Michael addition reactions will be required. This builds considerably on the previous advances in HPD synthesis and allows access to the unique opportunities for simple, modular nanoparticle design and production. The potential for targeted nanocarriers for drug delivery applications is clearly enabled by the simplicity of this synthesis strategy if the targeted biological benefits can be realised.

ATRP (see section 2.8.1), which has been successfully applied to the formation of LDHs[163] and the recently reported HPDs[61], was selected for the synthesis of these specifically engineered polymer structures. ATRP is compatible with a wide range of monomers, initiators, functional groups and solvent systems, and allows good control over molecular architecture. Surface modification by incorporation of xanthate functional groups at the dendron periphery has previously been reported.[163,164] These xanthate groups are able to undergo facile orthogonal deprotection and functionalisation with a range of hydrophobic, hydrophilic and polymeric acrylates to introduce different functionalities into complex polymer structures and offer the potential to create feedstock materials that can be readily modified to generate a range of test materials without the need for repeated synthesis.

1.8.1 Develop a control strategy; statistical multifunctionalisation

In order to test the research hypothesis, a series of materials is required that vary only in the spatial arrangement of surface functionality, with as little variation in other physical and chemical properties as possible. This is shown schematically in Fig. 1.14, where structures with the same molar ratio of functionality either statistically mixed or grouped into “patches” across the HPD structure are presented. Modification of the cellular interactions of nanoparticles with either patchy or statistical multifunctionalisation could therefore be compared directly within appropriate biological assays.

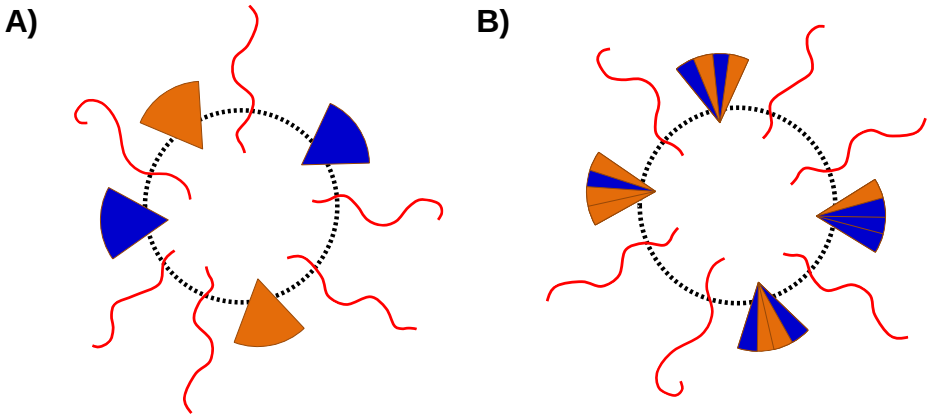

Fig. 1.14 Target materials: A) Patchy; and B) Statistically multifunctional HPDs

To establish a statistical functionalisation of the nanoprecipitates is not a trivial synthetic challenge as final analytical confirmation of the distribution is difficult to achieve. By combining previously reported work for the synthesis of HPDs via ATRP[61] and the use of xanthate functional groups for surface modification of dendritic materials[163,164], xanthate functional HPDs which can be statistically modified after polymerisation using mixtures of functional acrylates are achievable, Fig. 1.15.

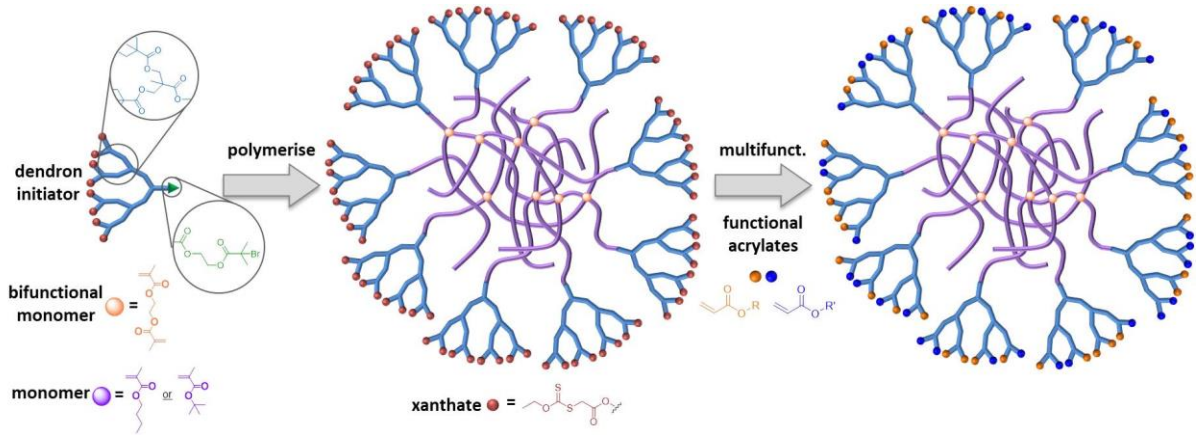

Fig. 1.15 Schematic representation of the aims of this project; HPD synthesis, post-functionalisation

Model studies that establish the outcomes of such a statistical modification are not readily available within the literature, therefore, a key aim of this research is to study this process. A detailed understanding of the statistical nature of the functionalisation is required in order to

provide evidence of the statistical distribution and confidence that the approach will create materials able to address the main research hypothesis.

1.8.2 Probing the distribution of surface functional groups

As seen previously in Fig. 1.11 (section 1.6), a wide range of patchy particles have been reported. Within each material, it is a key issue to develop analytical methods that probe the functional group distribution and, if possible, generate clear evidence that "patchiness" has been created. This can be achieved through imaging the distribution of surface functional groups but this is extremely difficult at the single functional group scale. The xanthate functionality does present a clear opportunity as once deprotected, the resulting thiols are able to bind gold nanoparticles. In this case, it may be possible to utilise a combination of nanoparticle binding and electron microscopy imaging to directly quantify the differences between statistical and patchy thiol spatial arrangements, Fig. 1.16.

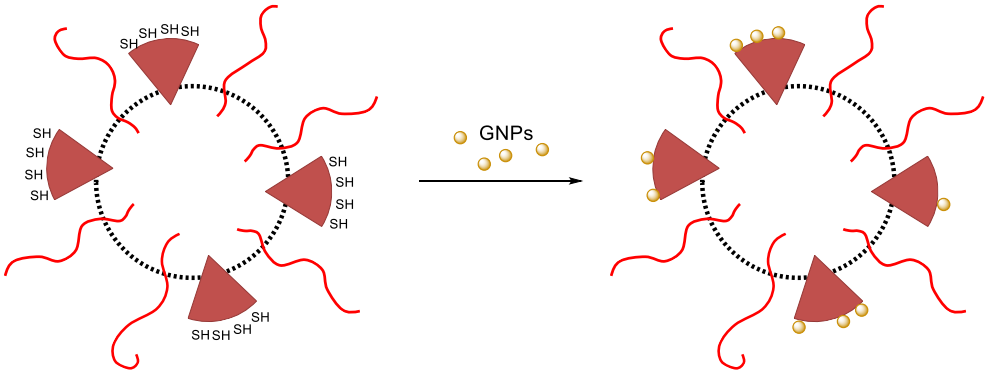

Fig. 1.16 Probing the distribution of surface functional groups by coordination of GNPs to thiol-functional HPD nanoprecipitates

Confirming the distribution of xanthate functional groups at the nanoparticle surface would provide confidence that patchy particles with other functional groups could also be generated in a "bottom-up" HPD synthesis approach.

1.8.3 Preparation of patchy particles with mixed functional groups and interaction with macrophages

If incorporation of functional dendron initiators, isolation of surface groups by varying PEG:dendron ratios in a branched polymerisation, and post-polymerisation modification of xanthate functional HPDs is possible, a statistically multifunctionalised HPD and a corresponding patchy multifunctionalised HPD should also be possible, Fig. 1.17. Tailoring of the mixed initiator feed will allow the same molar functionality to be maintained between these multifunctional materials and nanoparticle structures varying predominantly in the spatial arrangement of functional groups should be achievable.

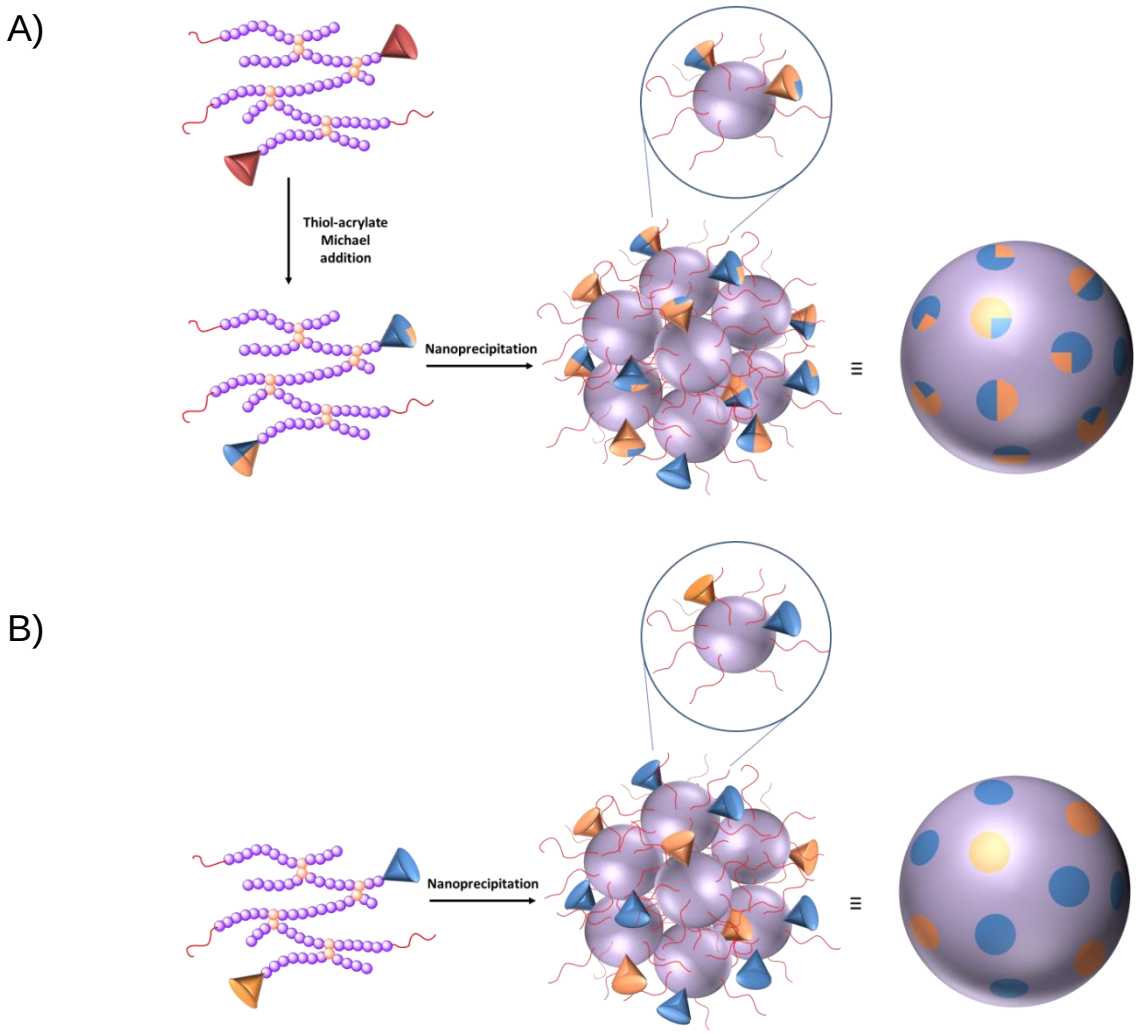

Fig. 1.17 Schematic representation of the construction of; A) statistically multifunctional, and B) patchy multifunctional nanoparticle formation

This is highly speculative and depends on the ability to synthesise and multifunctionalise xanthate functional HPDs and probe the distribution of surface functional groups to confirm "patchiness".

The rational design and combinatorial synthesis of co-initiated HPDs with regions of distinct chemical surface heterogeneity will be applied for systematic evaluation and optimisation of nanocarriers. Whilst most drug delivery systems aim to avoid uptake by the MPS – part of the immune system that consists of phagocytic cells such as monocytes and macrophages – we are targeting the treatment of HIV, which resides in macrophages. This project aims to elucidate the synergism of functional group co-localisation and multivalency on particle-cell interaction and uptake into monocyte derived macrophages (ATHP-1). The detection of polymer nanoparticles and monitoring their uptake into cells (cellular accumulation ratio; CAR) may be achieved using fluorescence or dye labelling, however, such modifications may alter the chemistry of the nanoparticle. Through the application of radiochemistry, polymer nanoparticles containing significant amounts of the ^{3}[H] isotope would allow quantification of nanoparticle uptake without significant chemical modification of the polymer structure, limiting the potential for interference of the biological assay by the presence of new chemical moieties. Radiolabelling of the patchy and statistically multifunctionalised polymers before nanoprecipitation, therefore, enables the monitoring of the nanocarriers directly. An idealised biological assay outcome after quantifying the CAR of patchy and statistically multifunctionalised nanocarriers is shown in Fig. 1.18, and would strongly indicate the difference between the cellular interactions of these materials with phagocytic cells.

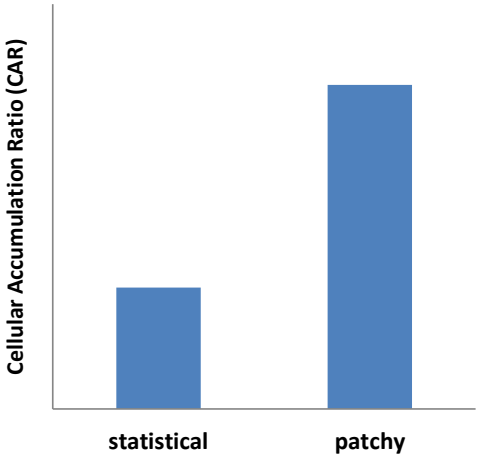

Fig. 1.18 Predicted difference in CAR of patchy and statistically multifunctionalised nanocarriers as a result of multivalency effect

1.9 References

1. M. V Walter and M. Malkoch, *Chem. Soc. Rev.*, 2012, **41**, 4593–4609.
2. A. Hult, M. Johansson, and E. Malmström, *Adv. Polym. Sci.*, 1999, **143**, 1–34.
3. E. Buhleier, W. Wehner, and F. Vögtle, *Synthesis*, 1978, **2**, 155–158.
4. S. Svenson and D. A. Tomalia, *Adv. Drug Deliv. Rev.*, 2012, 64, 102–115.
5. J. M. J. Frechet and D. A. Tomalia, *Dendrimers and other Dendritic Polymers*, John Wiley and Sons Inc., 2001.
6. F. Zeng and S. C. Zimmerman, *Chem. Rev.*, 1997, **97**, 1681–1712.
7. A. W. Bosman, H. M. Janssen, and E. W. Meijer, *Chem. Rev.*, 1999, **99**, 1665–1688.
8. M. Sowinska and Z. Urbanczyk-Lipkowska, *New J. Chem.*, 2014, **38**, 2168–2203.
9. K. Inoue, *Prog. Polym. Sci.*, 2000, **25**, 453–571.
10. D. A. Tomalia, H. Baker, J. Dewald, M. Hall, G. Kallos, S. Martin, J. Roeck, J. Ryder, and P. Smith, *Polym. J.*, 1984, **17**, 117–132.
11. G. R. Newkome, Z. Yao, G. R. Baker, and V. K. Gupta, *J. Org. Chem.*, 1985, **50**, 2003–2004.

12. C. Hawker and J. M. J. Frechet, *J. Chem. Soc. Chem. Commun.*, 1990, 1010–1013.

13. R. G. Denkewalter, J. Kolc, and W. J. Lukasavage, *US Pat. 4289872*, 1981.

14. D. A. Tomalia and J. M. J. Fréchet, *J. Polym. Sci. Pol. Chem.*, 2002, **40**, 2719–2728.

15. D. A. Tomalia, H. Baker, J. Dewald, M. Hall, G. Kallos, S. Martin, J. Roeck, J. Ryder, and P. Smith, *Macromolecules*, 1986, **19**, 2466–2468.

16. P. G. de Gennes and H. Hervet, *J. Phys. Lettres*, 1983, **44**, 351–360.

17. S. M. Grayson and J. M. J. Fréchet, *Chem. Rev.*, 2001, **101**, 3819–3868.

18. C. J. Hawker and J. M. J. Frechet, *J. Am. Chem. Soc.*, 1990, **112**, 7638–7647.

19. J. M. J. Frechet, C. J. Hawker, and A. E. Philippides, *US Pat. 5041516*, 1991.

20. K. L. Wooley, C. J. Hawker, and J. M. J. Frechet, *J. Chem. Soc. Perk. T. 1*, 1991, 1059–1076.

21. C. J. Hawker and J. M. J. Frechet, *Macromolecules*, 1990, **23**, 4726–4729.

22. K. L. Wooley, C. J. Hawker, and J. M. J. Frechet, *J. Am. Chem. Soc.*, 1993, **115**, 11496–11505.

23. K. L. Wooley, C. J. Hawker, and J. M. J. Fréchet, *Angew. Chem. Int. Edit.*, 1994, **33**, 82–85.

24. K. L. Wooley, C. J. Hawker, and J. M. J. Frechet, *J. Am. Chem. Soc.*, 1991, **113**, 4252–4261.

25. E. R. Gillies, E. Dy, J. M. J. Fréchet, and F. C. Szoka, *Mol. Pharm.*, 2005, **2**, 129–138.

26. O. L. Padilla De Jesús, H. R. Ihre, L. Gagne, J. M. J. Fréchet, and F. C. Szoka, *Bioconjug. Chem.*, 2002, **13**, 453–461.

27. N. Feliu, M. V. Walter, M. I. Montañez, A. Kunzmann, A. Hult, A. Nyström, M. Malkoch, and B. Fadeel, *Biomaterials*, 2012, **33**, 1970–1981.

28. J. Twibanire and T. B. Grindley, *Polymers*, 2014, **6**, 179–213.

29. W. Cao, J. Zhou, A. Mann, Y. Wang and L. Zhu, *Biomacromolecules*, 2011, **12**, 2697–2707.

30. H. Ihre, A. Hult, and E. Söderlind, *J. Am. Chem. Soc.*, 1996, **118**, 6388–6395.

31. A. Carlmark, E. Malmstrom, and M. Malkoch, *Chem. Soc. Rev.*, 2013, **42**, 5858–5879.

32. H. Ihre, A. Hult, J. M. J. Fréchet, and I. Gitsov, *Macromolecules*, 1998, **31**, 4061–4068.

33. J. S. Moore and S. I. Stupp, *Macromolecules*, 1990, **23**, 65–70.

34. H. Ihre, O. L. Padilla De Jesús, and J. M. J. Fréchet, *J. Am. Chem. Soc.*, 2001, **123**, 5908–5917.

35. M. Malkoch, E. Malmström, and A. Hult, *Macromolecules*, 2002, **35**, 8307–8314.

36. E. R. Gillies and J. M. J. Fréchet, *Drug Discov. Today*, 2005, **10**, 35–43.

37. A. Florence, *Adv. Drug Deliv. Rev.*, 2005, **57**, 2104–2105.

38. V. Gajbhiye, V. K. Palanirajan, R. K. Tekade, and N. K. Jain, *J. Pharm. Pharmacol.*, 2009, **61**, 989–1003.

39. D. Tyssen, S. A. Henderson, A. Johnson, J. Sterjovski, K. Moore, J. La, M. Zanin, S. Sonza, P. Karellas, M. P. Giannis, G. Krippner, S. Wesselingh, T. McCarthy, P. R. Gorry, P. A. Ramsland, R. Cone, J. R. A. Paull, G. R. Lewis, and G. Tachedjian, *PLoS One*, 2010, **5**, e12309.

40. C. F. Price, D. Tyssen, S. Sonza, A. Davie, S. Evans, G. R. Lewis, S. Xia, T. Spelman, P. Hodsman, T. R. Moench, A. Humberstone, J. R. A. Paull, and G. Tachedjian, *PLoS One*, 2011, **9**, e24095.

41. *Starpharma website*, 2016, www.starpharma.com/news/281

42. *Starpharma website*, 2015, www.starpharma.com/drug_delivery/dep_docetaxel

43. J. Lim, M. Kostiainen, J. Maly, V. C. P. Da Costa, O. Annunziata, G. M. Pavan, and E. E. Simanek, *J. Am. Chem. Soc.*, 2013, **135**, 4660–4663.

44. K. L. Wooley, C. A. Klug, K. Tasaki, and J. Schaefer, *J. Am. Chem. Soc.*, 1997, **119**, 53–58.

45. A. S. H. King, I. K. Martin, and L. J. Twyman, *Polym. Int.*, 2006, **55**, 798–807.

46. P. Antoni, D. Nyström, C. J. Hawker, A. Hult, and M. Malkoch, *Chem. Commun.*, 2007, 2249–2251.

47. C. Gao and D. Yan, *Prog Polym Sci*, 2004, **29**, 183–275.

48. B. I. Voit and A. Lederer, *Chem. Rev.*, 2009, **109**, 5924–73.

49. C. J. Hawker, E. E. Malmström, C. W. Frank, and J. P. Kampf, *J. Am. Chem. Soc.*, 1997, **119**, 9903–9904.

50. I. Gitsov, in *Advances in Dendritic Macromolecules, Volume 5*, ed. G. R. Newkome, Elsevier Science, Amsterdam, 2002, 45–87.

51. F. Wurm and H. Frey, *Prog. Polym. Sci.*, 2011, **36**, 1–52.

52. I. Gitsov, *J. Polym. Sci. Pol. Chem.*, 2008, **46**, 5295–5314.

53. C. M. Dong and G. Liu, *Polym. Chem.*, 2013, **4**, 46–52.

54. I. Gitsov, K. L. Wooley, C. J. Hawker, and J. M. J. Frechet, *Polym. Prep.*, 1991, **32**, 631–2.

55. I. Gitsov and J. M. J. Frechet, *Macromolecules*, 1994, **27**, 7309–7315.

56. R. Yin, Y. Zhu, D. A. Tomalia, and H. Ibuki, *J. Am. Chem. Soc.*, 1998, **120**, 2678–2679.

57. I. Gitsov, P. T. Ivanova, and J. M. J. Fréchet, *Macromol. Rapid Comm.*, 1994, **15**, 387–393.

58. A. D. Schlüter and J. P. Rabe, *Angew. Chem. Int. Edit.*, 2000, **39**, 864–883.

59. M. Malkoch, A. Carlmark, A. Woldegiorgis, A. Hult, and E. E. Malmström, *Macromolecules*, 2004, **37**, 322–329.

60. C. J. Hawker and J. M. J. Fréchet, *Polymer*, 1992, **33**, 1507–1511.

61. F. L. Hatton, P. Chambon, T. O. McDonald, A. Owen, and S. P. Rannard, *Chem. Sci.*, 2014, **5**, 1844–1853.

62. F. L. Hatton, L. M. Tatham, L. R. Tidbury, P. Chambon, T. He, A. Owen, and S. P. Rannard, *Chem. Sci.*, 2015, **6**, 326–334.

63. K. J. Morrow, R. Bawa, and C. Wei, *Med. Clin. N. Am.*, 2007, **91**, 805–843.

64. K. Riehemann, S. W. Schneider, T. A. Luger, B. Godin, M. Ferrari, and H. Fuchs, *Angew. Chem. Int. Ed. Engl.*, 2009, **48**, 872–897.

65. M. Pautler and S. Brenner, *Int. J. Nanomedicine*, 2010, **5**, 803–809.

66. F. L. Hatton, *Hyperbranched Polydendrons*, Springer, Liverpool, 2014, 21–22.

67. P. Masikini and B. C. T. Mpondo, *Clin. Case Reports*, 2015, **3**, 353–356.

68. A. Owen and S. Rannard, *Adv. Drug Deliv. Rev.*, 2016, **103**, 144–156.

69. S. K. Tiwari, G., Tiwari, R., Sriwastawa, B., Bhati, L., Pandey, S., Pandey, P., & Bannerjee, *Int. J. Pharm. Invest.*, 2012, **2**, 2–11.

70. J. M. Chan, P. M. Valencia, L. Zhang, R. Langer, and O. C. Farokhzad, *Methods Mol. Biol.*, 2010, **624**, 163–175.

71. G. Suffredini, J. E. East, and L. M. Levy, *Am. J. Neuroradiol.*, 2014, **35**, 1246–1253.

72. M. A. Dobrovolskaia and S. E. McNeil, *Nat. Nano.*, 2007, **2**, 469–478.

73. T. M. Allen, *Science*, 2004, **303**, 1818–1822.

74. Y. H. Bae and K. Park, *J. Control. Release*, 2011, **153**, 198–205.

75. S. Gunaseelan, K. Gunaseelan, M. Deshmukh, X. Zhang, and P. J. Sinko, *Adv. Drug Deliv. Rev.*, 2010, **62**, 518–531.

76. Y. Matsumura and H. Maeda, *Cancer Res.*, 1986, **46**, 6387–6392.

77. J. H. Thrall, *Radiology*, 2005, **235**, 9–12.

78. A. Wicki, D. Witzigmann, V. Balasubramanian, and J. Huwyler, *J. Control. Release*, 2015, **200**, 138–157.

79. V. J. Venditto and F. C. Szoka, *Adv. Drug Deliv. Rev.*, 2013, **65**, 80–88.

80. K. K. Jain, *The Handbook of Nanomedicine*, Humana Press, New York, 3rd edn., 2017.

81. A. Owen and S. Rannard, *Nanomedicine*, 2015, **10**, 3103–3107.

82. *World Health Organisation (WHO)*, 2015, www.who.int/gho/hiv/en/

83. R. D. Moore and R. E. Chaisson, *AIDS*, 1999, **13**, 1933–1942.

84. *National Institutes of Health (NIH), AIDSinfo website*, 2016, 1–288, https://aidsinfo.nih.gov/contentfiles/lvguidelines/adultandadolescentgl.pdf

85. M. A. Chesney, *J. Acq. Immun. Def. Synd.*, 2006, **43**, 149–155.

86. S. B. Laskey and R. F. Siliciano, *Nat. Rev. Microbiol.*, 2014, **12**, 772–780.

87. L. Varatharajan and S. A. Thomas, *Antivir. Res.*, 2009, **84**, 99–109.

88. V. Le Douce, A. Janossy, H. Hallay, S. Ali, R. Riclet, O. Rohr, and C. Schwartz, *J. Antimicrob. Chemoth.*, 2012, **67**, 1063–1074.

89. E. Pretorius, H. Klinker, and B. Rosenkranz, *Ther. Drug Monit.*, 2011, **33**, 265–274.

90. R. R. Adhikary, P. More, and R. Banerjee, *Nanoscale*, 2015, **7**, 7520–7534.

91. B. R. Matthews and G. Holan, *US Pat. 6190650*, 2001.

92. J. C. Imperiale, P. Nejamkin, M. J. del Sole, C. E. Lanusse, and A. Sosnik, *Biomaterials*, 2015, **37**, 383–394.

93. A. Kaushik, R. D. Jayant, and M. Nair, *Int. J. Nanomedicine*, 2016, **11**, 4317–4325.

94. N. Kamaly, Z. Xiao, P. M. Valencia, A. F. Radovic-Moreno, and O. C. Farokhzad, *Chem. Soc. Rev.*, 2012, **41**, 2971–3010.

95. W. Abbas, M. Tariq, M. Iqbal, A. Kumar, and G. Herbein, *Viruses*, 2015, **7**, 1578–1598.

96. V. Schäfer, H. von Briesen, R. Andreesen, A. M. Steffan, C. Royer, S. Tröster, J. Kreuter, and H. Rübsamen-Waigmann, *Pharm. Res.*, 1992, **9**, 541–546.

97. H. Koppensteiner, R. Brack-Werner, and M. Schindler, *Retrovirology*, 2012, **9**, 82.

98. L. Kinman, T. Bui, K. Larsen, C. C. Tsai, D. Anderson, W. R. Morton, S. L. Hu, and R. J. Y. Ho, *J. Acq. Immun. Def. Synd.*, 2006, **42**, 155–161.

99. L. Kinman, S. J. Brodie, C. C. Tsai, T. Bui, K. Larsen, A. Schmidt, D. Anderson, W. R. Morton, S. L. Hu, and R. J. Y. Ho, *J. Acq. Immun. Def. Synd.*, 2003, **34**, 387–397.

100. H. Dou, C. J. Destache, J. R. Morehead, R. L. Mosley, M. D. Boska, J. Kingsley, S. Gorantla, L. Poluektova, J. A. Nelson, M. Chaubal, J. Werling, J. Kipp, B. E. Rabinow, and H. E. Gendelman, *Blood*, 2006, **108**, 2827–2835.

101. A. T. Palamara, E. Garaci, G. Rotilio, M. R. Ciriolo, A. Casabianca, A. Fraternale, L. Rossi, G. F. Schiavano, L. Chiarantini, and M. Magnani, *AIDS Res. Hum. Retrov.*, 1996, **12**, 1373–1381.

102. M. Aouadi, G. J. Tesz, S. M. Nicoloro, M. Wang, M. Chouinard, E. Soto, G. R. Ostroff, and M. P. Czech, *Nature*, 2009, **458**, 1180–1184.

103. X. Yu, I. Trase, M. Ren, K. Duval, X. Guo, and Z. Chen, *J. Nanomater.*, 2016, **2016**, 1–15.

104. M. E. Davis, Z. Chen, and D. M. Shin, *Nat. Rev. Drug Discov.*, 2008, **7**, 771–782.

105. M. Ferrari, *Nat. Rev. Cancer*, 2005, **5**, 161–171.

106. J. Kreuter, *Eur. J. Drug Metab. Ph.*, 1994, **19**, 253–256.

107. R. A. Petros and J. M. DeSimone, *Nat. Rev. Drug Discov.*, 2010, **9**, 615.

108. C. Vauthier and K. Bouchemal, *Pharm. Res.*, 2009, **26**, 1025–1058.

109. M. Goldberg, R. Langer, and X. Jia, *J. Biomater. Sci. Polym. Ed.*, 2007, **18**, 241-268.

110. Y. Zhang, H. F. Chan and K. W. Leong, *Adv. Drug Deliv. Rev.*, 2013, **65**, 104–120.

111. M. Mammen, S. K. Choi, and G. M. Whitesides, *Angew. Chem. Int. Edit.*, 1998, **37**, 2754–2794.

112. M. E. Davis, Z. Chen, and D. M. Shin, *Nat. Rev. Drug Discov.*, 2008, **7**, 771–782.

113. D. Liu, F. Yang, F. Xiong and N. Gu, *Theranostics*, 2016, **6**, 1306–1323.

114. IUPAC, *Compendium of Chemical Terminology: Gold Book*, 2012.

115. R. J. Hunter, *Introduction to Modern Colloid Science*, Oxford University Press, 1993.

116. P. G. de Gennes, *Rev. Mod. Phys.*, 1992, **64**, 645–648.

117. L. Hong, A. Cacciuto, E. Luijten, and S. Granick, *Nano Lett.*, 2006, **6**, 2510–2514.

118. S. K. Smoukov, S. Gangwal, M. Marquez, and O. D. Velev, *Soft Matter*, 2009, **5**, 1285–1292.

119. J. Yan, M. Bloom, S. C. Bae, E. Luijten, and S. Granick, *Nature*, 2012, **491**, 578–581.

120. B. P. Binks and P. D. I. Fletcher, *Langmuir*, 2001, **17**, 4708–4710.

121. A. Walther and A. H. E. Müller, *Soft Matter*, 2008, **4**, 663–668.

122. Z. He and I. Kretzschmar, *Langmuir*, 2012, **28**, 9915–9919.

123. S. Jiang, Q. Chen, M. Tripathy, E. Luijten, K. S. Schweizer, and S. Granick, *Adv. Mater.*, 2010, **22**, 1060–1071.

124. R. Erhardt, A. Böker, H. Zettl, H. Kaya, W. Pyckhout-Hintzen, G. Krausch, V. Abetz, and A. H. E. Müller, *Macromolecules*, 2001, **34**, 1069–1075.

125. A. B. Pawar and I. Kretzschmar, *Macromol. Rapid Comm.*, 2010, **31**, 150–68.

126. E. Bianchi, R. Blaak, and C. N. Likos, *Phys. Chem. Chem. Phys.*, 2011, **13**, 6397–6410.

127. S. C. Glotzer and M. J. Solomon, *Nat. Mater.*, 2007, **6**, 557–562.

128. C. E. Snyder, A. M. Yake, J. D. Feick, and D. Velegol, *Langmuir*, 2005, **21**, 4813–4815.

129. V. N. Manoharan, *Science*, 2003, **301**, 483–487.

130. G. Zhang, D. Wang, and H. Möhwald, *Nano Lett.*, 2005, **5**, 143–146.

131. Y. Li, X. Zhang, and D. Cao, *Soft Matter*, 2014, **10**, 6844–56.

132. A. Verma, O. Uzun, Y. Hu, Y. Hu, H. S. Han, N. Watson, S. Chen, D. J. Irvine, and F. Stellacci, *Nat. Mater.*, 2008, **7**, 588–595.

133. E. Blanco, H. Shen and M. Ferrari, *Nat. Biotechnol.*, 2015, **33**, 941–951.

134. W. Senaratne, L. Andruzzi, and C. K. Ober, *Biomacromolecules*, 2005, **6**, 2427–2448.

135. C. Galliot, C. Larré, A. M. Caminade, and J. P. Majoral, *Science*, 1997, **277**, 1981–1984.

136. L. Lochmann, L. K. Wooley, P. T. Ivanova, and J. M. J. Fréchet, *J. Am. Chem. Soc*, 1993, **115**, 7043–7044.

137. S. Hecht, *J. Polym. Sci. Pol. Chem.*, 2003, **41**, 1047–1058.

138. C. O. Liang and J. M. J. Fréchet, *Macromolecules*, 2005, **38**, 6276–6284.

139. P. Antoni, Y. Hed, A. Nordberg, D. Nyström, H. von Holst, A. Hult, and M. Malkoch, *Angew. Chem. Int. Edit.*, 2009, **48**, 2126–2130.

140. J. R. McElhanon, M. J. Wu, M. Escobar, U. Chaudhry, C. L. Hu, and D. V McGrath, *J. Org. Chem.*, 1997, **62**, 908–915.

141. J. R. McElhanon and D. V McGrath, *J. Org. Chem.*, 2000, **65**, 3525–3529.

142. N. W. Suek and M. H. Lamm, *Macromolecules*, 2006, **39**, 4247–4255.

143. M. Malkoch, K. Schleicher, E. Drockenmuller, C. J. Hawker, T. P. Russell, P. Wu, and V. V Fokin, *Macromolecules*, 2005, **38**, 3663–3678.

144. M. I. Montañez, L. M. Campos, P. Antoni, Y. Hed, M. V Walter, B. T. Krull, A. Khan, A. Hult, C. J. Hawker, and M. Malkoch, *Macromolecules*, 2010, **43**, 6004–6013.

145. P. Antoni, M. J. Robb, L. Campos, M. Montanez, A. Hult, E. Malmström, M. Malkoch, and C. J. Hawker, *Macromolecules*, 2010, **43**, 6625–6631.

146. P. Wu, M. Malkoch, J. N. Hunt, R. Vestberg, E. Kaltgrad, M. G. Finn, V. V. Fokin, K. B. Sharpless, and C. J. Hawker, *Chem. Commun.*, 2005, 5775–5777.

147. P. A. Ledin, F. Friscourt, J. Guo, and G. J. Boons, *Chem. Eur. J.*, 2011, **17**, 839–846.

148. E. R. Gillies and J. M. J. Fréchet, *J. Am. Chem. Soc.*, 2002, **124**, 14137–14146.

149. C. B. Yim, O. C. Boerman, M. de Visser, M. de Jong, A. C. Dechesne, D. T. S. Rijkers, and R. M. J. Liskamp, *Bioconjug. Chem.*, 2009, **20**, 1323–1331.

150. Y. Chabre and R. Roy, *Curr. Top. Med. Chem.*, 2008, **8**, 1237–1285.

151. S. K. Wang, P. H. Liang, R. D. Astronomo, T. L. Hsu, S. L. Hsieh, D. R. Burton, and C. H. Wong, *P. Natl. Acad. Sci.*, 2008, **105**, 3690–3695.

152. H. Fessi, F. Puisieux, J. P. Devissaguet, N. Ammoury, and S. Benita, *Int. J. Pharm.*, 1989, **55**, 1–4.

153. F. Lince, D. L. Marchisio, and A. A. Barresi, *J. Colloid Interf. Sci.*, 2008, **322**, 505–515.

154. F. L. Hatton, P. Chambon, A. C. Savage, and S. P. Rannard, *Chem. Commun.*, 2016, **52**, 3915–3918.

155. M. A. Dobrovolskaia, P. Aggarwal, J. B. Hall, and S. E. McNeil, *Mol. Pharm.*, 2008, **5**, 487–495.

156. S. M. Moghimi, J. C. Murray, and A. C. Hunter, *Pharmacol. Rev.*, 2001, **53**, 283–318.

157. J. B. Wolinsky and M. W. Grinstaff, *Adv. Drug Deliv. Rev.*, 2008, **60**, 1037–1055.

158. S. Venkataraman, J. L. Hedrick, Z. Y. Ong, C. Yang, P. L. R. Ee, P. T. Hammond, and Y. Y. Yang, *Adv. Drug Deliv. Rev.*, 2011, **63**, 1228–1246.

159. Y. Geng, P. Dalhaimer, S. Cai, R. Tsai, M. Tewari, T. Minko, and D. E. Discher, *Nat. Nano.*, 2007, **2**, 249–255.

160. S. Svenson, *Chem. Soc. Rev.*, 2015, **44**, 4131–4144.

161. Z. Poon, S. Chen, A. C. Engler, H. Lee, E. Atas, G. von Maltzahn, S. N. Bhatia, and P. T. Hammond, *Angew. Chem. Int. Edit.*, 2010, **49**, 7266–7270.

162. A. M. Caminade and C. O. Turrin, *J. Mater. Chem. B*, 2014, **2**, 4055–4066.

163. S. E. R. Auty, O. C. J. Andrén, F. Y. Hern, M. Malkoch, and S. P. Rannard, *Polym. Chem.*, 2014, **6**, 573–582.

164. S. E. R. Auty, O. Andren, M. Malkoch, and S. P. Rannard, *Chem. Commun.*, 2014, **50**, 6574–6577.

CHAPTER 2

Xanthate functional dendritic material synthesis

Recently published in part as:

"Model studies of the sequential and simultaneous statistical modification of dendritic functional groups and their implications within complex polymer architecture synthesis."

F. Y. Hern, S. E. R. Auty, O. C. J. Andrén, M. Malkoch and S. P. Rannard, *Polym. Chem.*, 2017, **8**, 1644-1653.

Individual contributions: S. E. R. Auty – Initial studies to establish xanthate chemistry;

O. C. J. Andrén – recorded MALDI-TOF spectra; M. Malkoch and S. P. Rannard – supervisors.

2.1 Introduction

Highly functional polymers for advanced applications may be prepared by the polymerisation of specifically designed functional monomers or the post-polymerisation modification of a polymer possessing reactive functional groups. Although polymerisation of functional monomers ensures a high degree of functionality, this method is hindered by solubility issues, difficulty to polymerise and incompatibility with polymerisation conditions.[1-3]

Post-polymerisation modification represents a versatile platform for the preparation of a library of diversely functionalised materials from a single well-defined precursor. Combining controlled polymerisation techniques with highly efficient coupling chemistries facilitates quantitative and orthogonal functionalisation of complex polymer architectures at the periphery and at side-chains, affording the opportunity for obtaining desired material properties. Highly efficient chemistries including "click" reactions have successfully been applied to the preparation of functional polymers via a post-polymerisation strategy.[2-9] "Click" chemistry, as described by Sharpless *et al.*, represents a range of reactions that should be equimolar, easy to purify, rapid, high yielding and, perhaps most importantly, chemoselective.[10] The ability to perform these types of reaction in the presence of other commonly reactive moieties makes "click" reactions an invaluable tool.

Xanthate functional dendrons, dendrimers and linear dendritic hybrids (LDHs) were recently shown to undergo a facile ambient temperature one-pot deprotection and surface functionalisation via thiol-acrylate Michael addition, without the need for direct handling of highly reactive thiols.[9,11] This platform presents the opportunity for extending post-modification reactions to highly complex polymer architectures, such as recently reported hyperbranched polydendrons (HPDs)[12], and for controlled multifunctionalisation of a range of dendritic materials.

In Chapter 2, the synthesis and full characterisation of four generations of xanthate peripheral dendrons (G_0, G_1, G_2, G_3) is presented. These functional dendrons were used to prepare xanthate functional dendrimers, linear dendritic hybrids (LDHs) and hyperbranched polydendrons (HPDs). ATRP polymerisation of *n*-butyl methacrylate (nBMA) and *tert*-butyl methacrylate (tBMA) is investigated with xanthate functional dendron macroinitiators, Fig. 2.1.

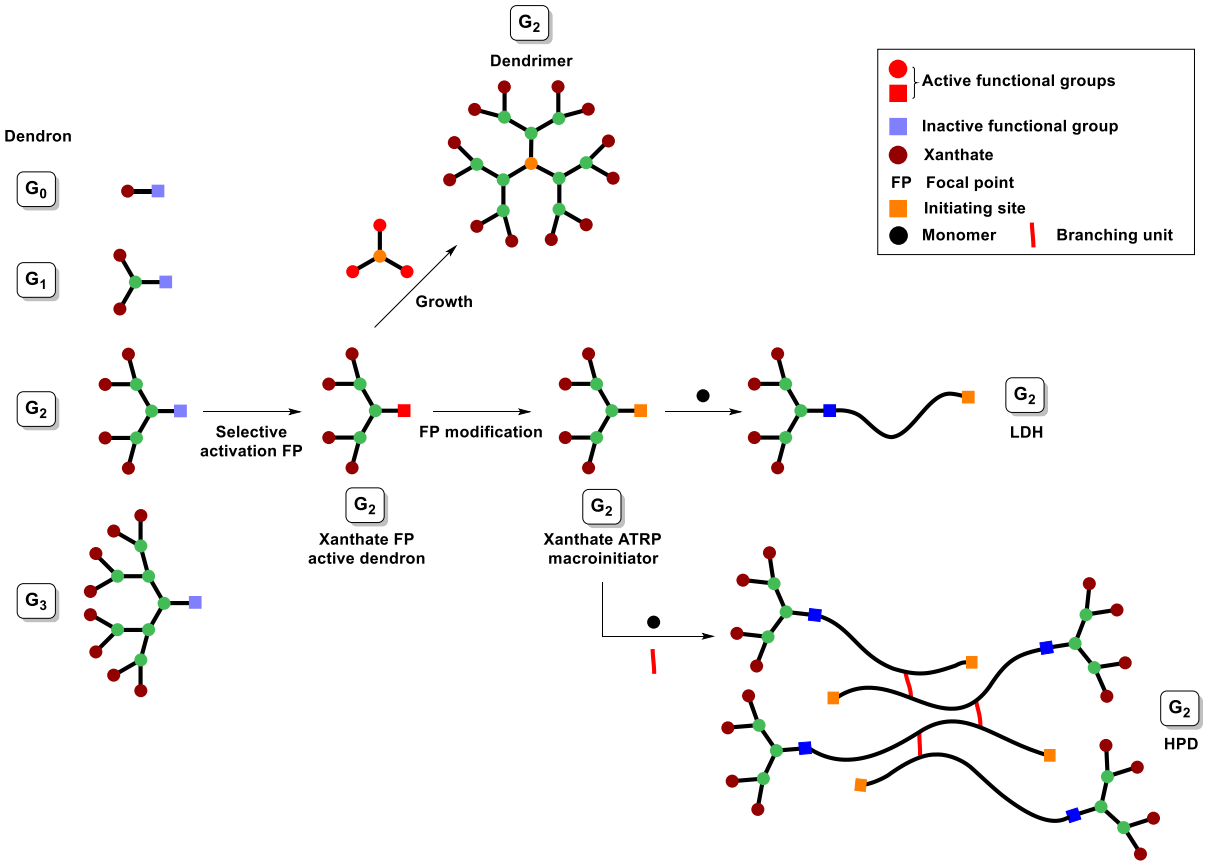

Fig. 2.1 Schematic representation of the aims within this chapter: G_0-G_3 xanthate peripheral dendrons; dendron focal point modification; dendrimer synthesis; bromoinitiator synthesis and polymerisation to form linear dendritic hybrids (LDH) and hyperbranched polydendrons (HPD)

2.2 Synthesis of bis-MPA scaffold by divergent route

Both divergent and convergent synthetic strategies offer respective advantages and disadvantages (Chapter 1.1.1). A divergent growth approach was adopted for the construction of the 2,2-bis(hydroxymethyl)propionic acid (bis-MPA) dendron scaffold with subsequent xanthate functionalisation. Focal point manipulation to produce dendrimers or macroinitiators via a convergent strategy is also possible by this route, as discussed later in this chapter (sections 2.6 and 2.7). The synthetic strategy is outlined schematically in Fig. 2.2.

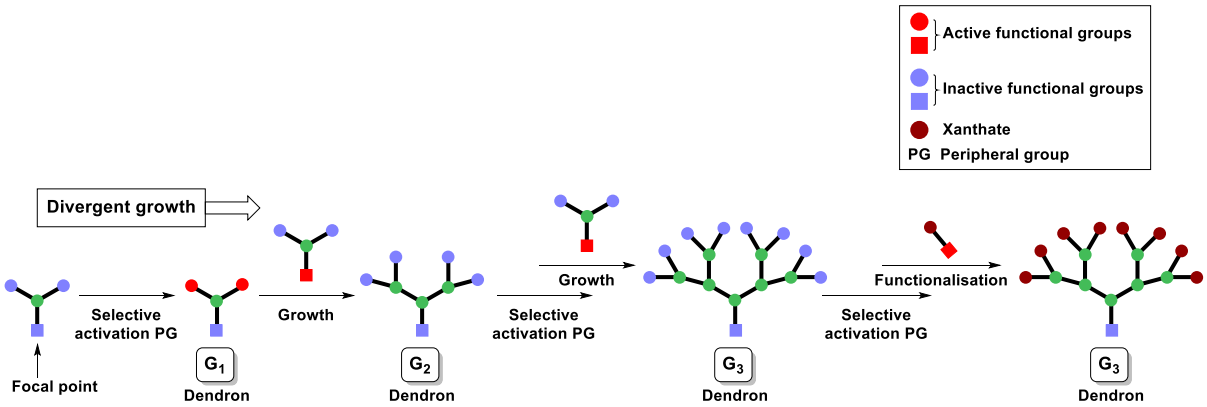

Fig. 2.2 Schematic representation of the divergent approach to polyester dendrons based on 2,2-bis(hydroxymethyl)propionic acid (bis-MPA) and subsequent xanthate functionalisation

Polyester dendrons and dendrimers based on AB_2 monomer bis-MPA have been extensively explored for biological applications as they are known to be biocompatible and biodegradable with non-toxic degradation products (Chapter 1.1.2).[13]

Dendron synthesis requires focal point and peripheral protecting groups that facilitate independent and quantitative deprotection. Focal point protecting group *para*-toluenesulfonyl ethanol (*p*-TSe) was utilised for the construction of the dendron scaffold as it is stable during activation and growth procedures developed by Ihre *et al.*[14], and is easily removed under conditions which do not degrade the xanthate peripheral groups.[9,11,15] Its facile removal is achieved using non-nucleophilic base 1,8-diazabicyclo[5.4.0]undec-7-ene (DBU).

Acetonide protected bis-MPA anhydride, which employs acid hydrolysis for acetonide removal, was used for the construction of the bis-MPA scaffold, Scheme 2.1.[16]

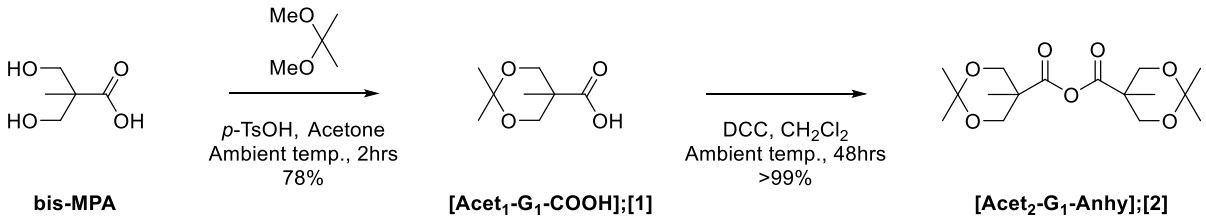

Scheme 2.1 Synthesis of acetonide protected bis-MPA anhydride **[Acet$_1$-G$_1$-Anhy];[2]**

In the first step, hydroxyl groups of the bis-MPA monomer were protected by the formation of an acetonide group with 2,2-dimethoxypropane in the presence of *p*-toluenesulfonic acid (*p*TsOH) in acetone **[Acet$_1$-G$_1$-COOH];[1]**. Acetonide protected anhydride monomer **[Acet$_2$-G$_1$-Anhy];[2]** was prepared in high yields (99%) by self-condensation of **[1]** with *N,N'*-dicyclohexylcarbodiimide (DCC). ^{13}C NMR spectroscopy was used to monitor reaction progress; the change in chemical shift of the carbonyl environment at δ = 180.3 ppm to 169.6 ppm indicating anhydride formation.

Anhydride monomer **[2]** was used to construct a range of dendritic macromolecules (**[3]-[8]**) up to the third generation hydroxyl functional dendron **[(OH)$_8$-G$_3$-TSe];[8]**, using a two-step divergent growth approach, Scheme 2.2.

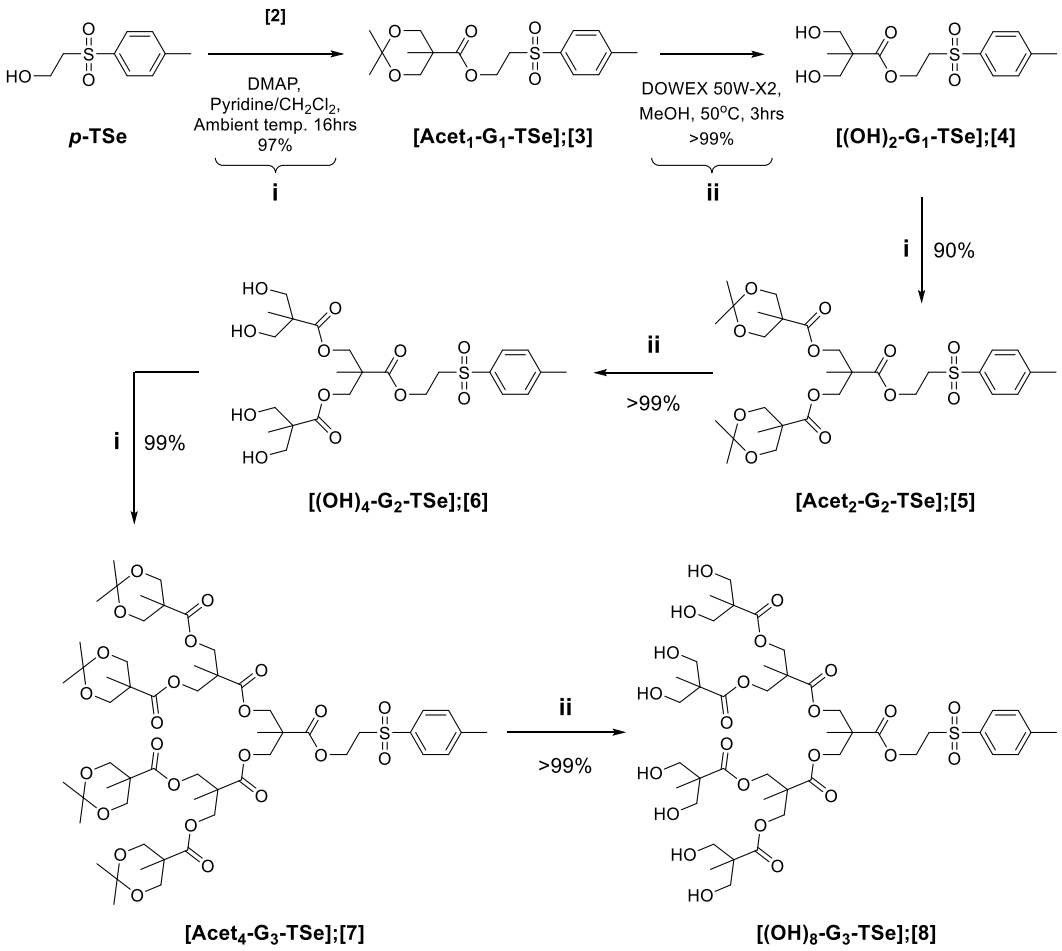

Scheme 2.2 Divergent synthesis of core-protected hydroxyl-functional G_1, G_2 and G_3 dendrons;

[(OH)$_2$-G$_1$-TSe];[4], **[(OH)$_4$-G$_2$-TSe];[6]**, **[(OH)$_8$-G$_3$-TSe];[8]**

Each growth step was achieved by reacting each hydroxyl group with 1.3-1.5 equivalents of anhydride monomer **[2]**, 0.2 equivalents of 4-dimethylaminopyridine (DMAP) and 5 equivalents of pyridine (per hydroxyl group) in a 1:3 ratio of pyridine:CH_2Cl_2 (v/v). The first generation dendron **[Acet$_1$-G$_1$-TSe];[3]** was synthesised in 97% recovered yield, with structural confirmation by electrospray mass spectrometry (ESI-MS) (Fig. S2.7), ^{1}H and ^{13}C NMR spectroscopy (Fig. S2.5 and S2.6, respectively), and elemental microanalysis.

Removal of the acetonide protecting groups was achieved using a DOWEX-50W X2 resin in methanol, heated to 50°C and stirred for 3 hours. Progress was monitored by thin layer chromatography (TLC) and resulted in quantitative recovered yields for each generation. The

structure of first generation hydroxyl functional dendron **[$(OH)_2$-G_1-TSe];[4]** was confirmed by ESI-MS, ^{1}H and ^{13}C NMR, with no evidence of TSe focal point protecting group degradation, Fig. S2.8-S2.10. Purification by liquid chromatography was required for higher generation acetonide protected bis-MPA dendrons **[5]** and **[7]** to remove lower molecular weight impurities. Structural integrity was confirmed by ^{1}H and ^{13}C NMR and mass spectrometry.

2.3 Characterisation of bis-MPA scaffold by a divergent route

Each dendritic macromolecule was characterised using ^{1}H and ^{13}C NMR spectroscopy and mass spectrometry. Although NMR was useful to indicate the presence of symmetrical chemical environments, the technique was not sensitive enough to detect structural defects in higher dendron generations. Mass spectrometry is therefore essential for full analysis of higher generation dendrons since the technique easily identifies branching defects.

2.3.1 Analysis by NMR spectroscopy

Dendritic macromolecules **[3]** to **[8]** were fully characterised by ^{1}H and ^{13}C NMR spectroscopy; acetonide protected materials were analysed in $CDCl_3$, and hydroxyl functional dendrons in CD_3OD. ^{1}H NMR analysis of acetonide protected G_3 dendron **[$Acet_4$-G_3-TSe];[7]** confirmed 12 proton environments, with expected integrals relative to the TSe focal point protecting group moiety and expected multiplicity, Fig. 2.3. Proton environments at different generations within the structure give rise to unique resonances, as seen previously[9], for example the methyl resonances at δ = 1.14, 1.18 and 1.27 ppm (environments 3, 7 and 5

respectively, Fig. 2.3). Similar features are also present in lower generation dendrons, Fig. S2.5 and S2.11.

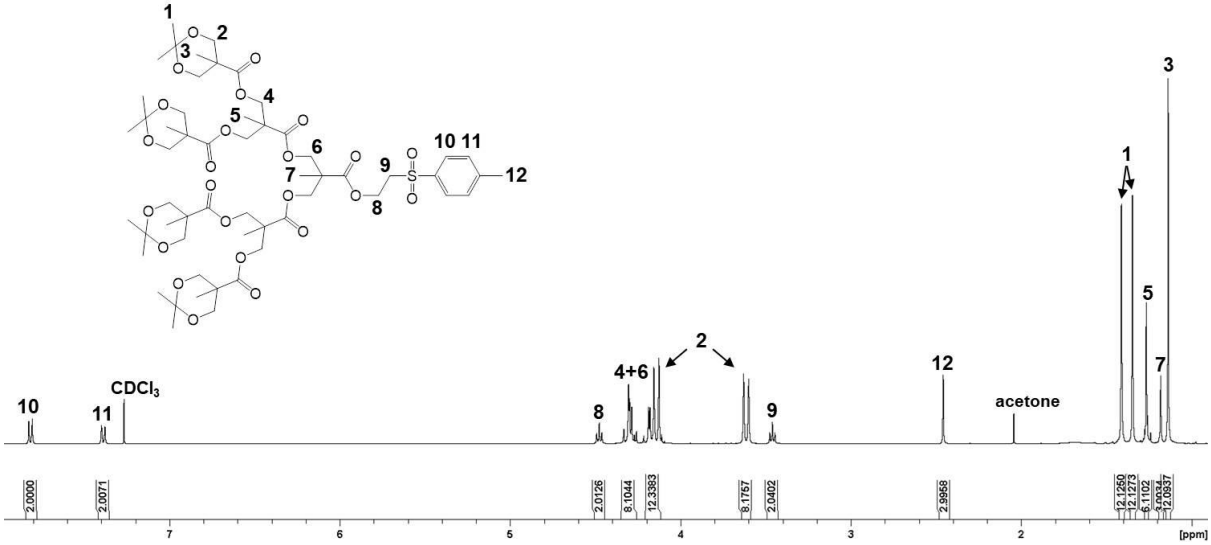

Fig. 2.3 ^{1}H NMR (400 MHz, $CDCl_3$) of **[Acet$_4$-G$_3$-TSe];[7]**

^{13}C NMR analysis of acetonide protected dendrons similarly resulted in extra resonances after each growth step. The ^{13}C NMR spectrum of acetonide protected G_3 dendron **[Acet$_4$-G$_3$-TSe];[7]** indicates 21 carbon environments, including different resonances for ester carbonyl, methyl, tertiary carbon and methylene environments for each generation within the structure, Fig. S2.17. This was also observed in lower generation acetonide protected dendrons **[3]** and **[5]**, Fig. S2.6 and S2.12.

^{1}H NMR analysis of hydroxyl functional dendrons **[4]**, **[6]** and **[8]** indicated the disappearance of a pair of singlets at approximately $\delta = 1.35$ and $\delta = 1.41$ ppm, confirming the complete removal of the acetonide protecting group, shown here for the ^{1}H NMR spectrum of **[(OH)$_8$-G$_3$-TSe];[8]**, Fig. 2.4. This is also seen for lower generation dendrons, Fig. S2.8 and S2.14.

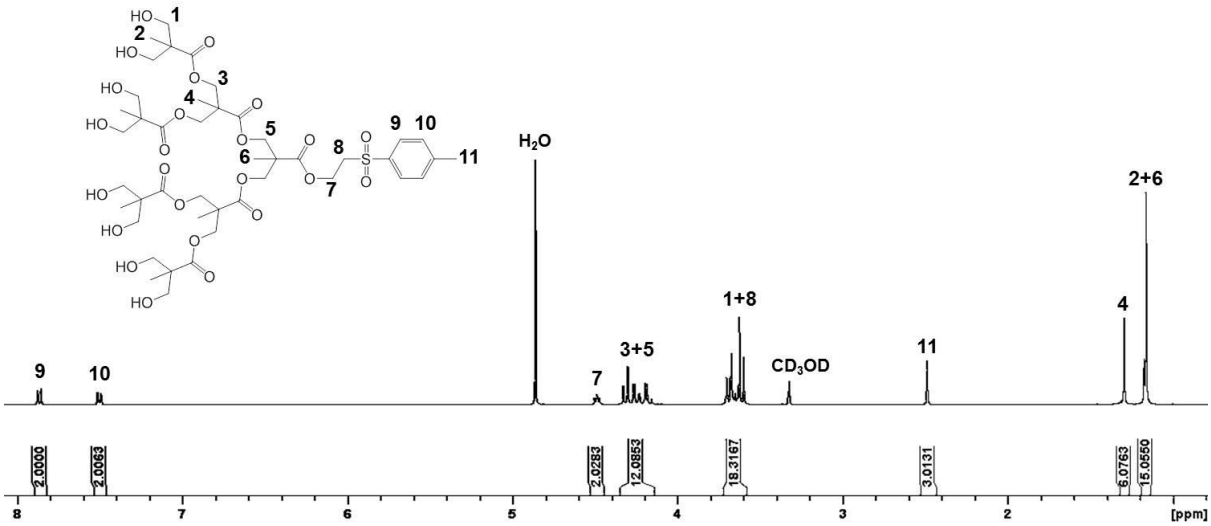

Fig. 2.4 ^{1}H NMR (400 MHz, CD_3OD) of **[$(OH)_8$-G_3-TSe];[8]**

Disappearance of the acetonide protecting group resonances is also seen in ^{13}C NMR spectra of hydroxyl functional dendrons **[4]**, **[6]** and **[8]**, with the loss of resonances at δ = 22, 25 and 98 ppm, Fig. S2.9, S2.15 and S2.18.

No degradation of the focal point protecting group functionality (TSe) was observed after deprotection of the peripheral groups in either ^{1}H or ^{13}C NMR spectra of the hydroxyl functional dendrons (**[4]**, **[6]** and **[8]**).

2.3.2 Analysis by mass spectrometry

Dendritic macromolecules **[3]** to **[8]** were analysed by ESI-MS, with desired adducts observed in each case. Acetonide protected G_1 dendron **[$Acet_1$-G_1-TSe];[3]** ([M] ($C_{17}H_{24}O_6S$) = 356.13 Da) confirmed populations at $[MNa]^+$ = 379.1 Da and $[MK]^+$ = 395.1 Da, Fig. S2.7. After acetonide protecting group removal, **[$(OH)_2$-G_1-TSe];[4]** ([M] ($C_{14}H_{20}O_6S$) = 316.10 Da) confirmed populations at $[MH]^+$ = 317.1 Da, $[MNa]^+$ = 339.1 Da and $[MK]^+$ = 355.1 Da, with no indication of lower molecular weight materials formed as a result of focal point protecting group degradation, Fig. S2.10.

Populations for G_2 dendron **[Acet$_2$-G$_2$-TSe];[5]** ([M] ($C_{30}H_{44}O_{12}S$) = 628.26 Da) were confirmed at $[MNa]^+$ = 651.2 Da and $[MK]^+$ = 667.2 Da, Fig. S2.13, and following deprotection, **[(OH)$_4$-G$_2$-TSe];[6]** ([M] ($C_{24}H_{36}O_{12}S$) = 548.19 Da) confirmed populations at $[MNa]^+$ = 571.2 Da and $[MK]^+$ = 587.2 Da, Fig. S2.16. The G_3 dendron **[Acet$_4$-G$_3$-TSe];[7]** ([M] ($C_{56}H_{84}O_{24}S$) = 1172.51 Da) indicated populations at $[MNa]^+$ = 1195.5 Da and $[MK]^+$ = 1211.5 Da, and a low intensity signal at 1013.5 Da, which may correspond to the sodium adduct of focal point acid functional material $[(M - TSe)Na]^+$ as a result of fragmentation, Fig. 2.5. After deprotection, **[(OH)$_8$-G$_3$-TSe];[8]** ([M] ($C_{44}H_{68}O_{24}S$) = 1012.38 Da) confirmed populations at $[MNa]^+$ = 1035.4 Da and $[MK]^+$ = 1051.4 Da, Fig. 2.6. Some lower molecular weight impurities can be seen (approximately 750-900 Da), which are likely to be contaminants in the mass spectrometer, as they were seen in multiple spectra.

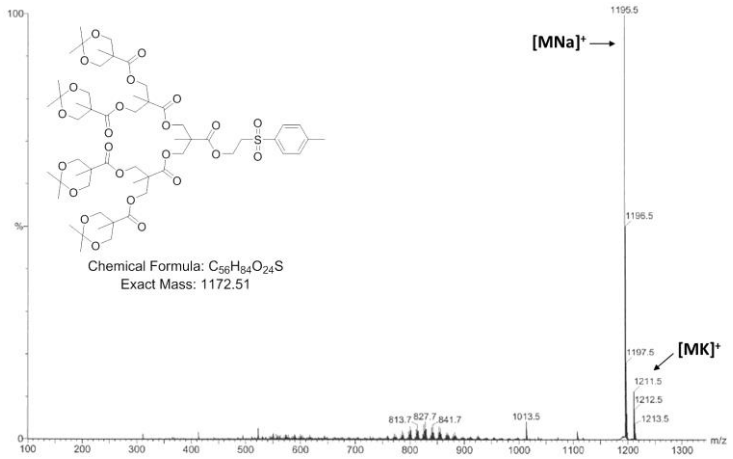

Fig. 2.5 ESI MS (MeOH) of **[Acet$_4$-G$_3$-TSe];[7]**

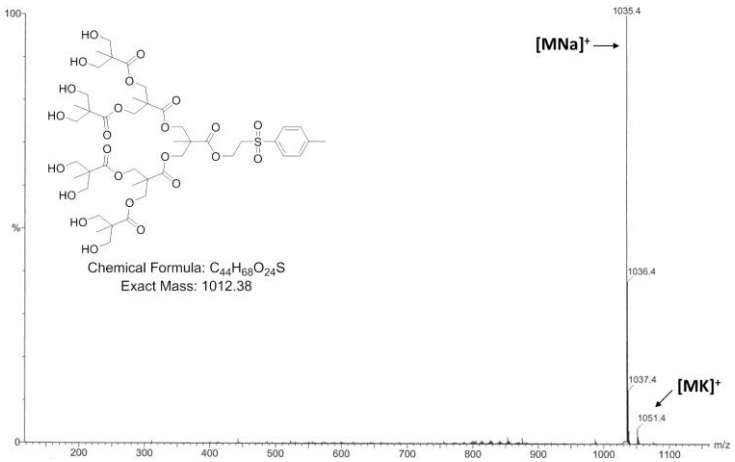

Fig. 2.6 ESI MS (MeOH) of **[(OH)$_8$-G$_3$-TSe];[8]**

2.4 Functionalisation of the scaffold with xanthate peripheral groups

Dithiocarbonates, commonly known as xanthates, have recently been used as thiol protecting groups for efficient functionalisation using thiol Michael addition chemistry.[9,11,17-19] Thiols are generated *in situ* by deprotection of xanthates with an excess of *n*-butylamine, followed by addition of a functional acrylate to perform a thiol acrylate Michael addition functionalisation. The *in situ* generation of thiols significantly reduces the chance of disulphide formation.

Xanthate functional building block **[Xan-COOH];[9]** was prepared by a simple SN_2 alkylation reaction between bromoacetic acid and potassium ethyl xanthogenate, Scheme 2.3. The material was characterised by ^{1}H and ^{13}C NMR spectroscopy.

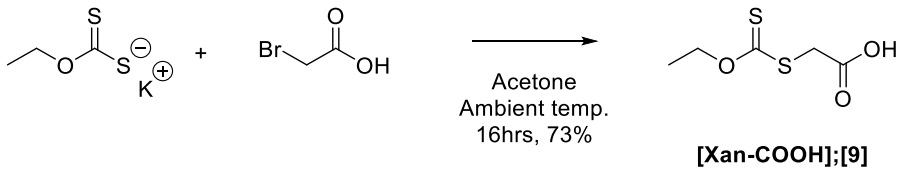

Scheme 2.3 Preparation of xanthate acid building block **[Xan-COOH];[9]**

The ^{1}H NMR spectrum of **[Xan-COOH];[9]** confirmed 3 proton environments, with expected corresponding integration ratios and multiplicity, Fig. 2.7. Analysis by ^{13}C NMR confirmed 5 carbon environments, including the acid resonance at δ = 174 ppm and the xanthate thiocarbonyl at δ = 212 ppm, Fig. S2.19.

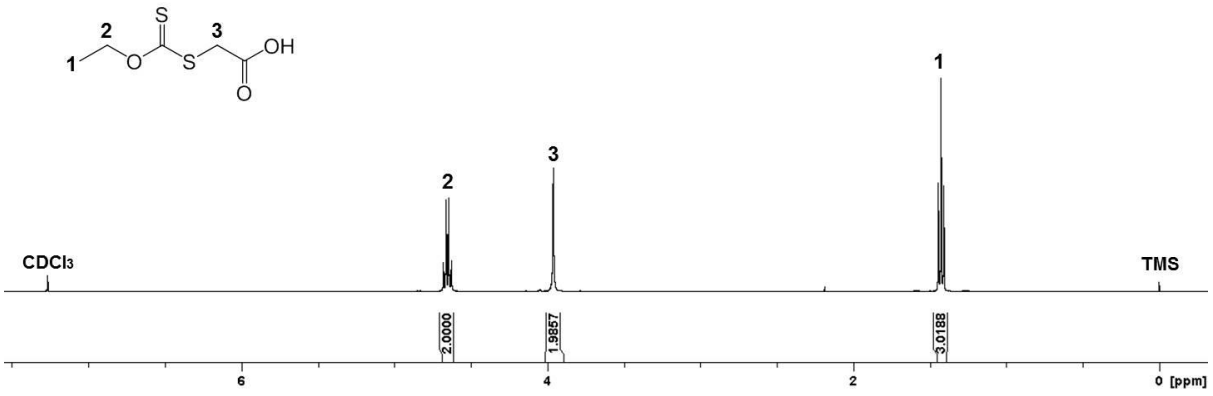

Fig. 2.7 ^{1}H NMR (400 MHz, $CDCl_3$) of **2-((ethoxycarbonothioyl)thio)acetic acid [Xan-COOH];[9]**

2.4.1 Xanthate functionalisation via DCC esterification

Xanthate functionalisation of hydroxyl-peripheral dendritic macromolecules was achieved using xanthate acid building block **[9]** for lower generation (G_0-G_2) dendrons using DCC/DPTS coupling chemistry, Scheme 2.4.[9]

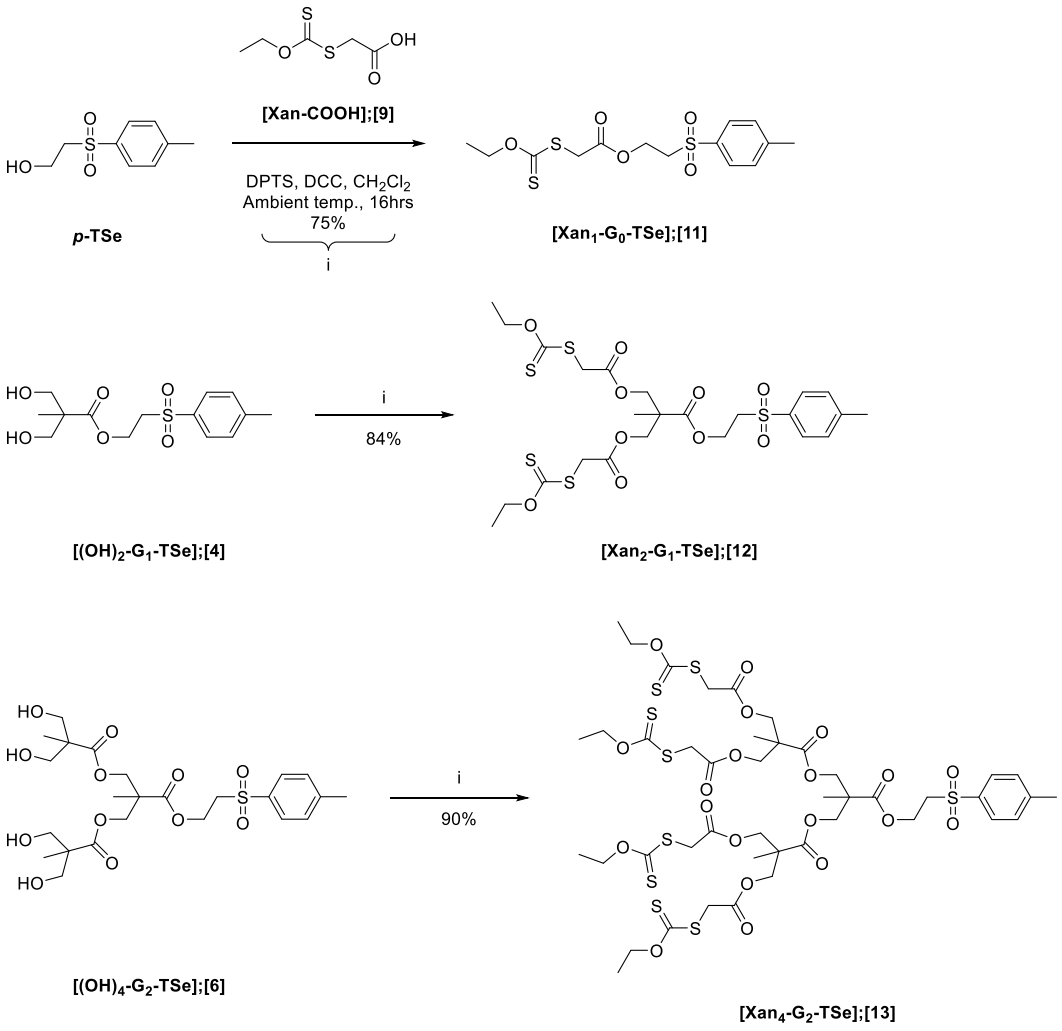

Scheme 2.4 Synthesis of **[Xan_1-G_0-TSe];[11]**, **[Xan_2-G_1-TSe];[12]** and **[Xan_4-G_2-TSe];[13]**

4-(Dimethylamino)pyridinium *p*-toluenesulfonate (DPTS) was chosen as the esterification catalyst to prevent the 1,3-rearrangement of the *O*-acyl intermediate to an unreactive *N*-acylurea by-product, by maintaining low pH.[20] The catalyst was prepared using literature procedures[21] via azeotropic distillation of *p*-toluenesulfonic acid monohydrate (pTsOH·H_2O)

in toluene, followed by addition of an equimolar ratio of DMAP, Scheme 2.5. Analysis via ^{1}H and ^{13}C NMR confirmed formation of the catalyst, Fig. S2.20 and S2.21.

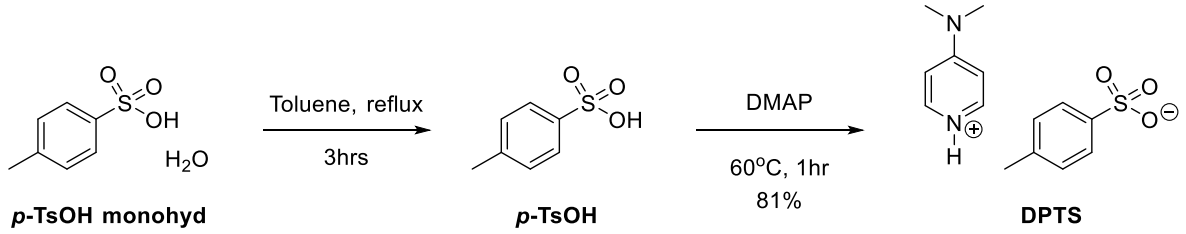

Scheme 2.5 Synthesis of 4-(dimethylamino)pyridinium *p*-toluenesulfonate (DPTS)

Xanthate functional dendrons **[Xan$_1$-G$_0$-TSe];[11]**, **[Xan$_2$-G$_1$-TSe];[12]** and **[Xan$_4$-G$_2$-TSe];[13]** were prepared by reaction of *p*-toluenesulfonyl ethanol (*p*-TSe) or hydroxyl-terminated dendrons **[4]** and **[6]** with xanthate acid **[9]** in the presence of DCC and a catalytic amount of DPTS in CH_2Cl_2, Scheme 2.4. No trace of urea side products was observed when DPTS was used. Following purification by liquid chromatography, confirmation of the target molecules was obtained using ESI-MS for G_0 and G_1 dendrons **[11]** and **[12]** (G_0 $[MNa]^+$ = 395.0 Da and G_1 $[MNa]^+$ = 663.0 Da, Fig. S2.24 and S2.27, respectively) and MALDI-TOF mass spectrometry for the G_2 dendron **[13]** ($[MNa]^+$ = 1219.1 Da, Fig. S2.29).

^{1}H NMR analysis of the xanthate functional dendrons (G_0-G_2, **[11]-[13]**) indicated the presence of a triplet at δ = 1.42 ppm and a quartet at δ = 4.64 ppm, confirming the presence of the xanthate functionality, shown here for G_2 dendron **[13]**, Fig. 2.8 (G_0 and G_1 Fig. S2.22 and S2.25, respectively).

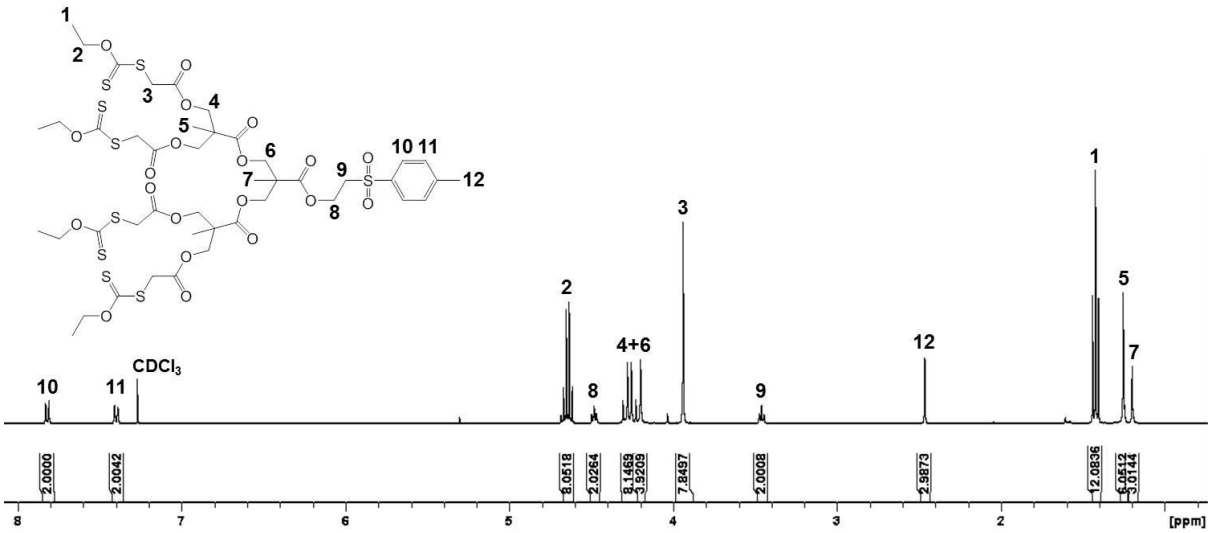

Fig. 2.8 ^{1}H NMR (400 MHz, $CDCl_3$) of **[Xan$_4$-G$_2$-TSe];[13]**

^{13}C NMR analysis confirmed 12 carbon environments for the G_0 dendron **[11]**, 16 carbon environments for the G_1 dendron **[12]** and 20 carbon environments for the G_2 dendron **[13]**, including the ester carbonyl at δ = 167 ppm and the xanthate thiocarbonyl at δ = 212 ppm, Fig. S2.23, S2.26 and S2.28.

2.4.2 Xanthate functionalisation via anhydride chemistry

Poor solubility of hydroxyl functional G_3 dendron **[(OH)$_8$-G$_3$-TSe];[8]** in CH_2Cl_2 led to the use of pyridine to act as a catalyst and co-solvent during anhydride esterification.[11] Xanthate anhydride building block **[Xan-Anhy];[10]** was synthesised by self-condensation of xanthate acid **[9]** with DCC, Scheme 2.6.

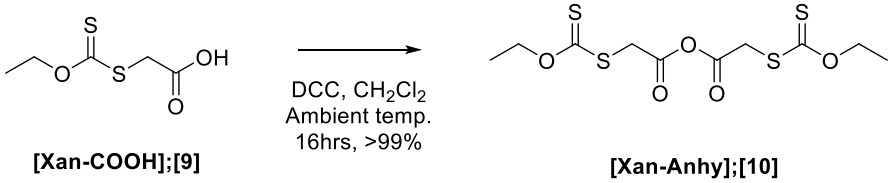

Scheme 2.6 Preparation of xanthate anhydride building block **[Xan-Anhy];[10]**

^{13}C NMR spectroscopy was used to monitor reaction progress, with the shift of acid resonance at δ = 174 ppm to 163 ppm indicating anhydride formation (Fig. S2.31). Xanthate functional G_3 dendron **[Xan$_8$-G$_3$-TSe];[14]** was prepared via anhydride esterification of hydroxyl functional G_3 dendron **[(OH)$_8$-G$_3$-TSe];[8]** with xanthate anhydride **[10]**, Scheme 2.7.

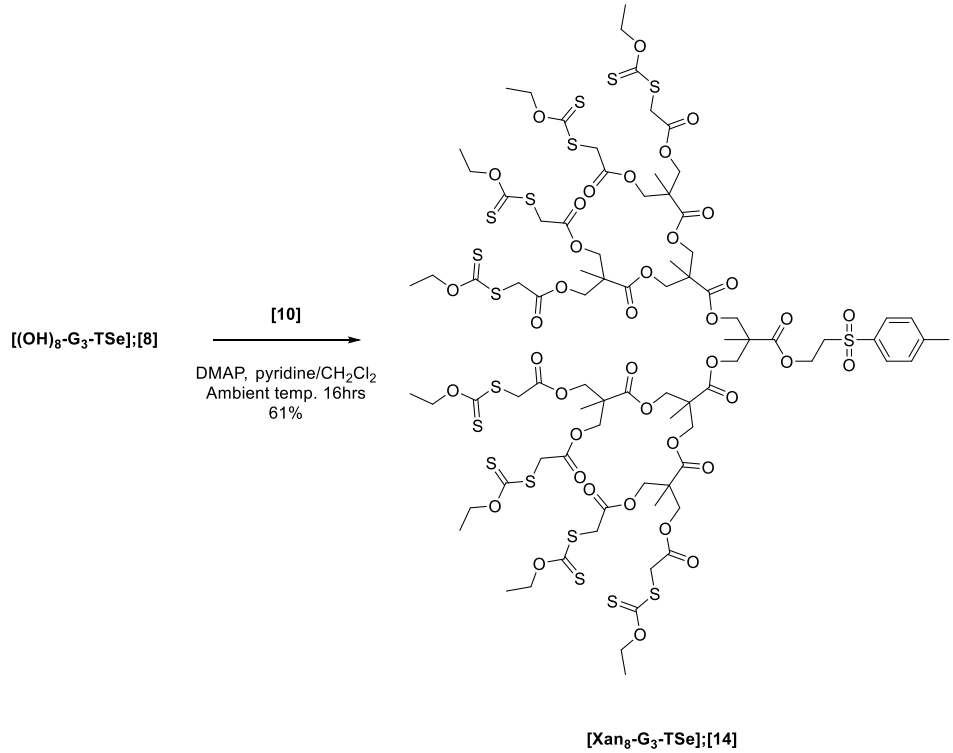

Scheme 2.7 Preparation of xanthate functional G_3 dendron **[Xan$_8$-G$_3$-TSe];[14]**

Hydroxyl functional G_3 dendron **[8]** was dissolved in a 1:2 ratio of pyridine:CH_2Cl_2 (v/v), then reacted with 1.3 equivalents (per hydroxyl group) of xanthate anhydride **[10]** and 0.2 equivalents of DMAP. Purification by liquid chromatography generated xanthate functional dendron **[Xan$_8$-G$_3$-TSe];[14]** in 61% yield. Confirmation of the target molecule was obtained by ^{1}H and ^{13}C NMR spectroscopy, MALDI-TOF mass spectrometry and elemental microanalysis.

^{1}H NMR analysis of **[14]** indicated 14 proton environments, each with corresponding expected integrals relative to the TSe focal point protecting group moiety and expected multiplicity, Fig. 2.9. Integrals of the characteristic xanthate resonances at δ = 1.42 ppm and 4.64 ppm confirmed the incorporation of 8 xanthate functional groups.

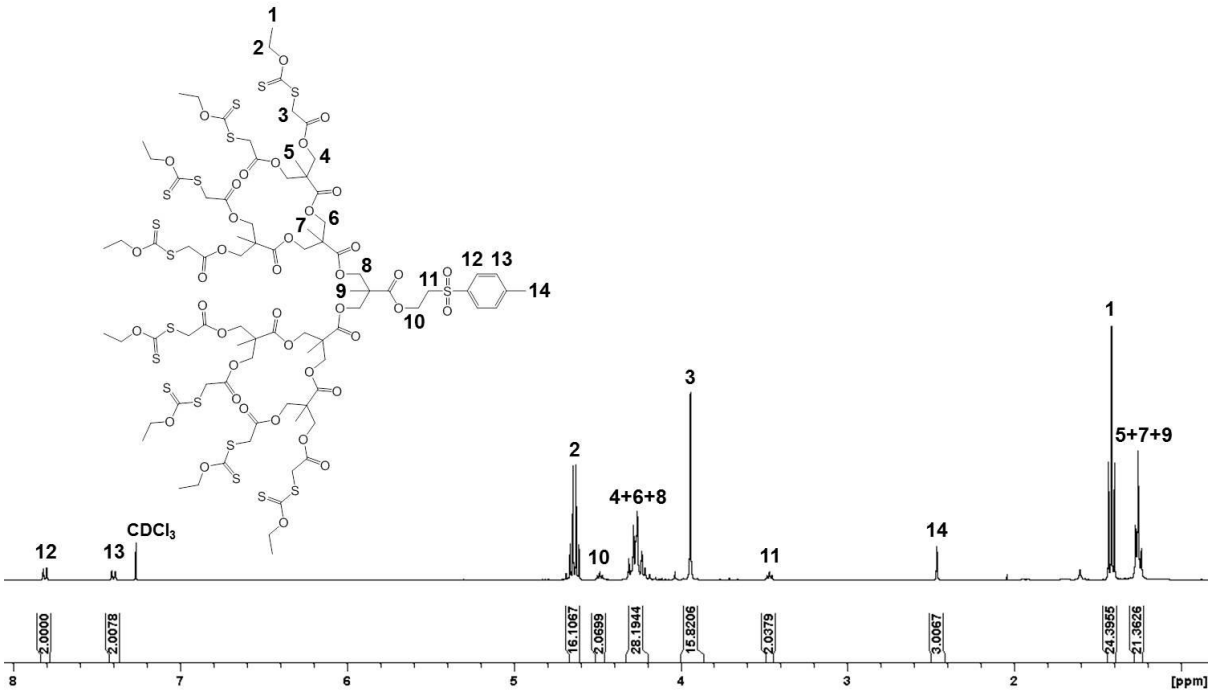

Fig. 2.9 ^{1}H NMR (400 MHz, $CDCl_3$) of **[Xan$_8$-G$_3$-TSe];[14]**

^{13}C NMR analysis confirmed 24 carbon environments, including ester carbonyl backbone resonances at δ = 171.5, 171.6 and 171.7 ppm and the xanthate thiocarbonyl at δ = 212 ppm, Fig. S2.32. Structural confirmation by MALDI-TOF analysis ([M] ($C_{84}H_{116}O_{40}S_{17}$) = 2308.23 Da) showed a major population; $[MNa]^+$ = 2331.7 Da, Fig. 2.10. Matrix-related peaks in the low mass region (m/z <1500 Da) can also be seen.

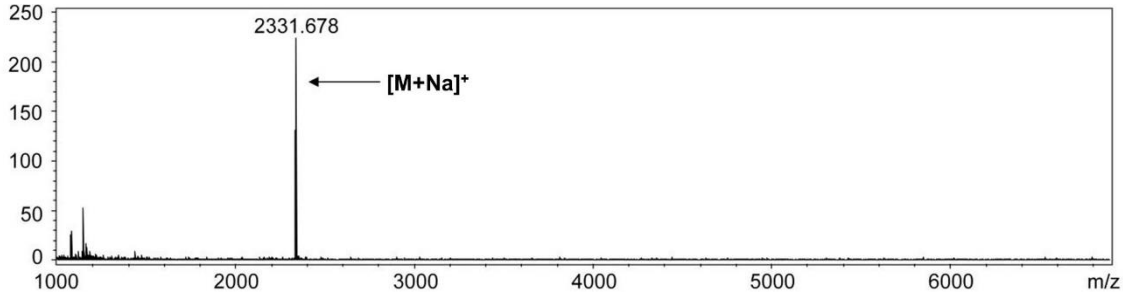

Fig. 2.10 MALDI-TOF analysis (HABA) of **[Xan$_8$-G$_3$-TSe];[14]**

2.4.3 Analysis by SEC

Triple detection size exclusion chromatography (SEC) of the xanthate functional G_1-G_3 dendrons, **[12]-[14]** with a THF/2% TEA (v/v) eluent system showed narrow dispersity (Đ) in the region 1.12-1.19 for all samples, Table 2.1. The calculated molecular weight (M_{Calc}) had a good agreement with the observed molecular weight (M_{Obs}) and the SEC-derived M_n values for each dendron, despite a lower resolution of molar mass determination using SEC. The SEC chromatograms for each dendron display a monomodal distribution, Fig. 2.11.

Table 2.1 Triple detection SEC analysis of xanthate functional G_{1-3} dendrons, **[Xan$_2$-G$_1$-TSe];[12]**, **[Xan$_4$-G$_2$-TSe];[13]** and **[Xan$_8$-G$_3$-TSe];[14]**

	MS $[MNa]^+$		SEC (THF)[a]		
Dendron	M_{Calc} (Da)	M_{Obs} (Da)	M_n	M_w	Đ
[Xan$_2$-G$_1$-TSe];[12]	640.1	663.0	626	702	1.12
[Xan$_4$-G$_2$-TSe];[13]	1196.1	1219.1	1193	1413	1.19
[Xan$_8$-G$_3$-TSe];[14]	2308.2	2331.4	2355	2697	1.15

[a]THF containing 2% TEA (v/v) at 35°C, 1mL min^{-1} flow rate.
M_n – number average molecular weight; M_w – weight average molecular weight

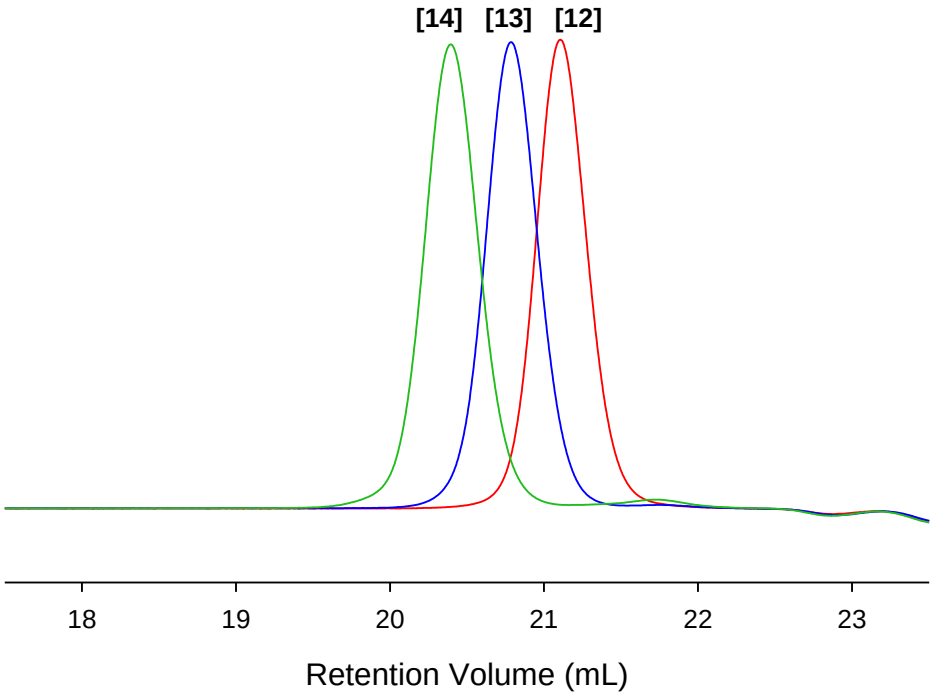

Fig. 2.11 SEC chromatogram overlay (refractive index) of xanthate functional dendrons **[Xan$_2$-G$_1$-TSe];[12]** (red), **[Xan$_4$-G$_2$-TSe];[13]** (blue) and **[Xan$_8$-G$_3$-TSe];[14]** (green)

2.5 Removal of TSe protecting group

Complete removal of focal point protecting group *p*-toluenesulfonyl ethyl (TSe) was achieved using an excess (1.3 equivalents) of 1,8-diazabicyclo[5.4.0]undec-7-ene (DBU) and stirring at ambient temperature for 16 hours, Scheme 2.8. DBU has been shown to effectively remove the focal point protecting group without degradation of the bis-MPA dendron backbone[15] or xanthate functional groups.[9,11]

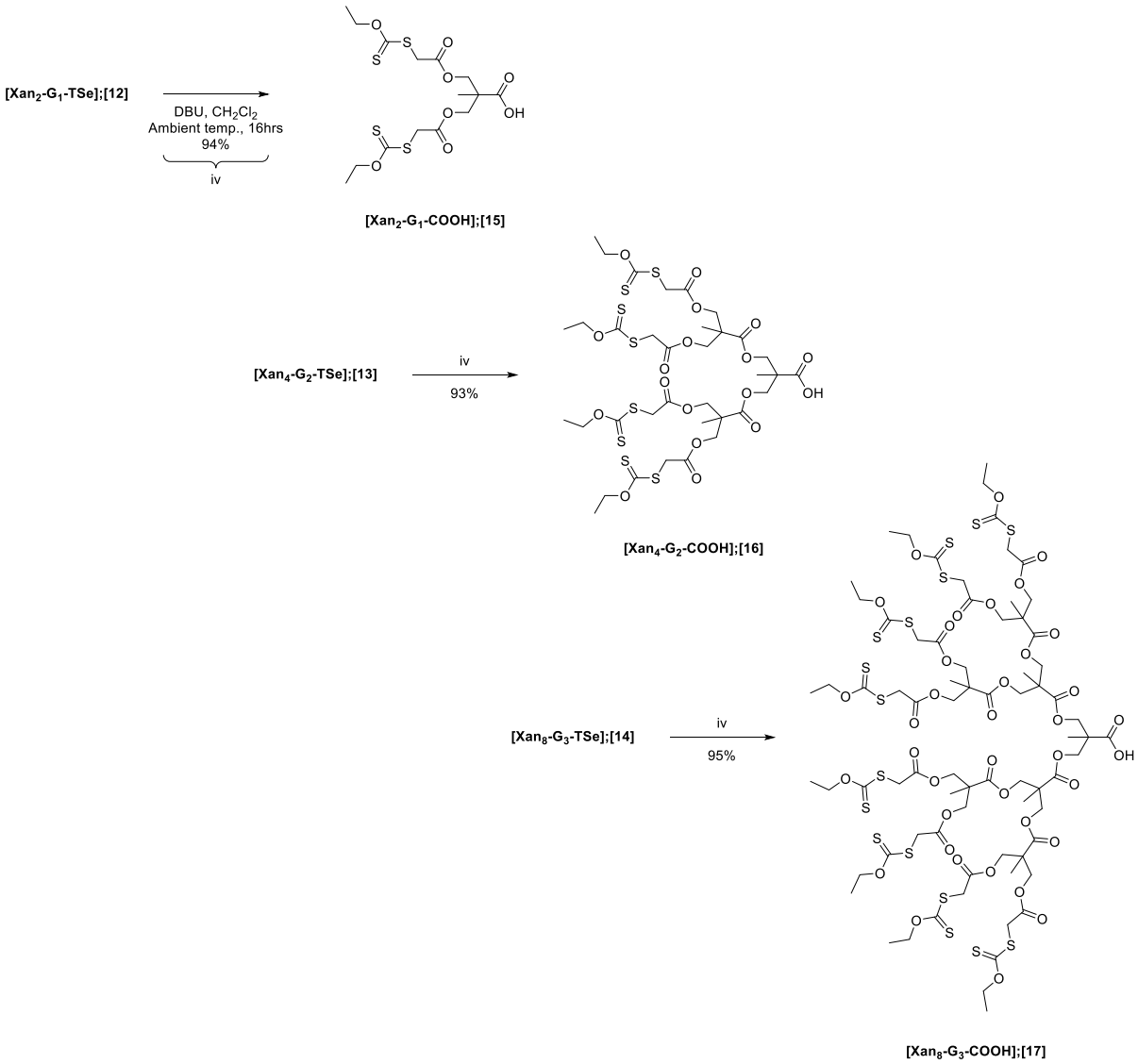

Scheme 2.8 Removal of TSe focal point protecting group, resulting in acid functional dendrons **[Xan$_2$-G$_1$-COOH];[15]**, **[Xan$_4$-G$_2$-COOH];[16]** and **[Xan$_8$-G$_3$-COOH];[17]**

Isolation of the acid functional dendron was achieved by acid washing (1M $NaHSO_4$) and precipitation into hexane:ethyl acetate (90:10). Confirmation by mass spectrometry showed no evidence of degradation of the bis-MPA backbone or peripheral xanthate functionality (**[15]** and **[16]** Fig. S2.35, S2.38 and **[17]** Fig. 2.13).

^{1}H NMR analysis of the focal point acid functional materials (**[15]-[17]**) confirmed the loss of CH_2 resonances at δ = 4.46 ppm and 3.44 ppm and aromatic resonances at δ = 7.80 ppm and 7.39 ppm, correlating to the loss of the TSe protecting group, shown here for **[17]** Fig. 2.12 (**[15]** and **[16]** Fig. S2.33 and S2.36, respectively). Some evidence of the vinyl sulfone by-product (^{1}H NMR overlay of **[14]** and **[17]**, Fig. S2.39) generated during deprotection was indicated at δ = 7.77 ppm and 7.35 ppm (aromatic resonances) and δ = 6.65, 6.44 and 6.01 ppm (vinyl resonances), although no additional purification was implemented as the by-products would not lead to side reactions and would be removed via liquid chromatography in the next step. Confirmation by ^{13}C NMR revealed a characteristic carbonyl resonance at δ = 173 ppm, corresponding to the newly formed acid functionality, Fig. S2.40 (**[15]** and **[16]** Fig. S2.34 and S2.37).

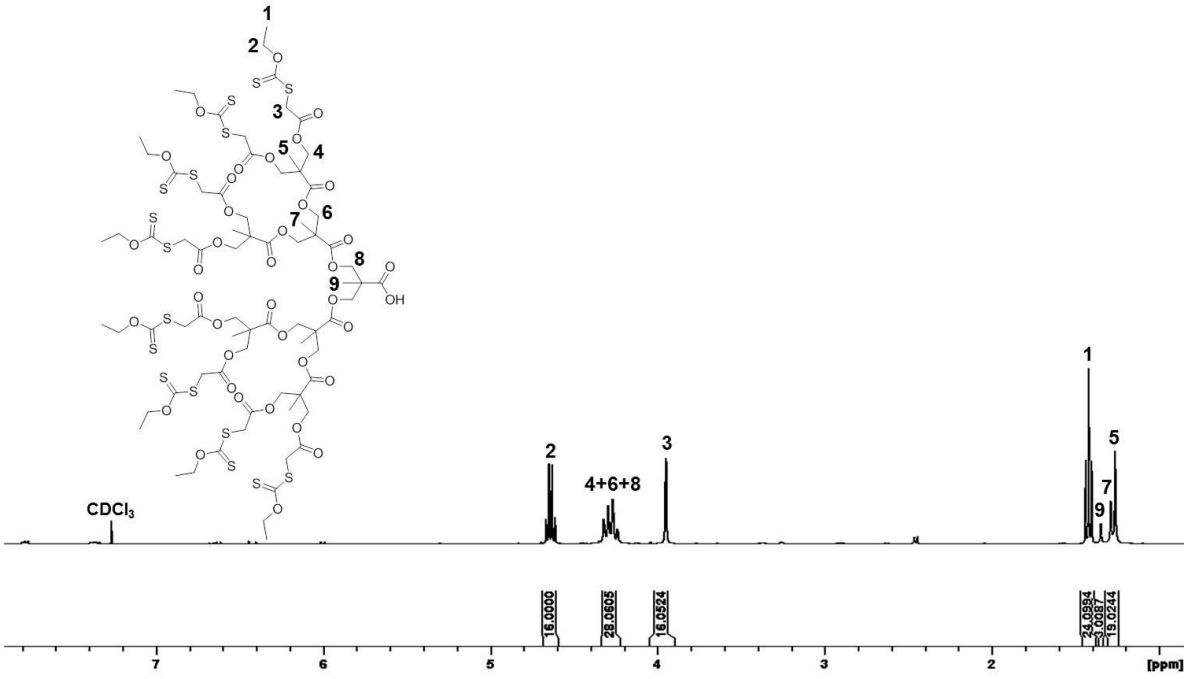

Fig. 2.12 ^{1}H NMR (400 MHz, $CDCl_3$) of **[Xan$_8$-G$_3$-COOH];[17]**

Analysis of **[Xan$_8$-G$_3$-COOH];[17]** ([M] ($C_{75}H_{106}O_{38}S_{16}$) = 2126.19 Da) by MALDI-TOF mass spectrometry confirmed a single population at $[MNa]^+$ = 2151.7 Da with no evidence of higher molecular weight species, indicating complete removal of the TSe protecting group, Fig. 2.13. No degradation of the bis-MPA dendron backbone or xanthate functionality was observed by ^1H or ^{13}C NMR analysis or mass spectrometry.

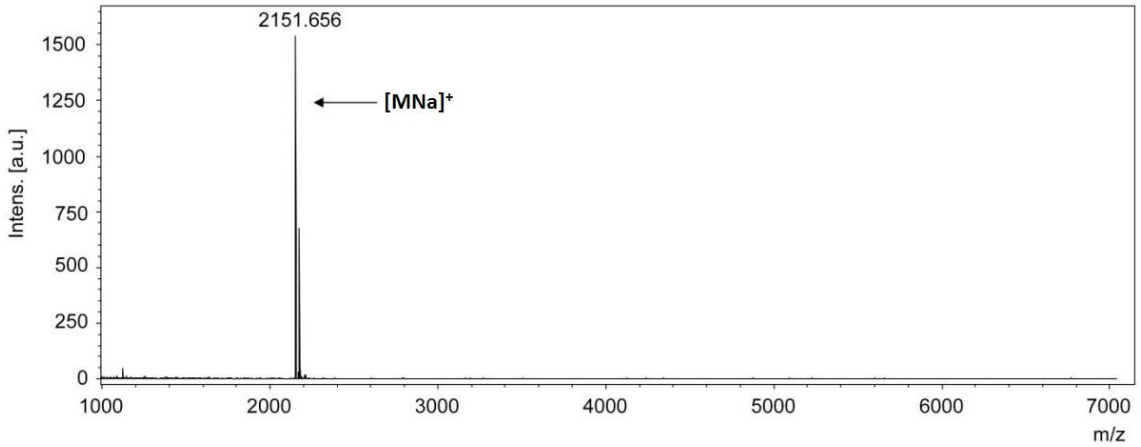

Fig. 2.13 MALDI-TOF analysis (dithranol) of **[Xan$_8$-G$_3$-COOH];[17]**

2.6 Synthesis of xanthate peripheral dendrimers

Convergent coupling of focal point acid functional G_2 xanthate dendron **[Xan_4-G_2-COOH];[16]** to trifunctional core 1,1,1-tris(4-hydroxyphenyl)ethane (THPE) yielded xanthate functional G_2 dendrimer **[Xan_{12}-G_2-THPE];[18]**, Scheme 2.9.

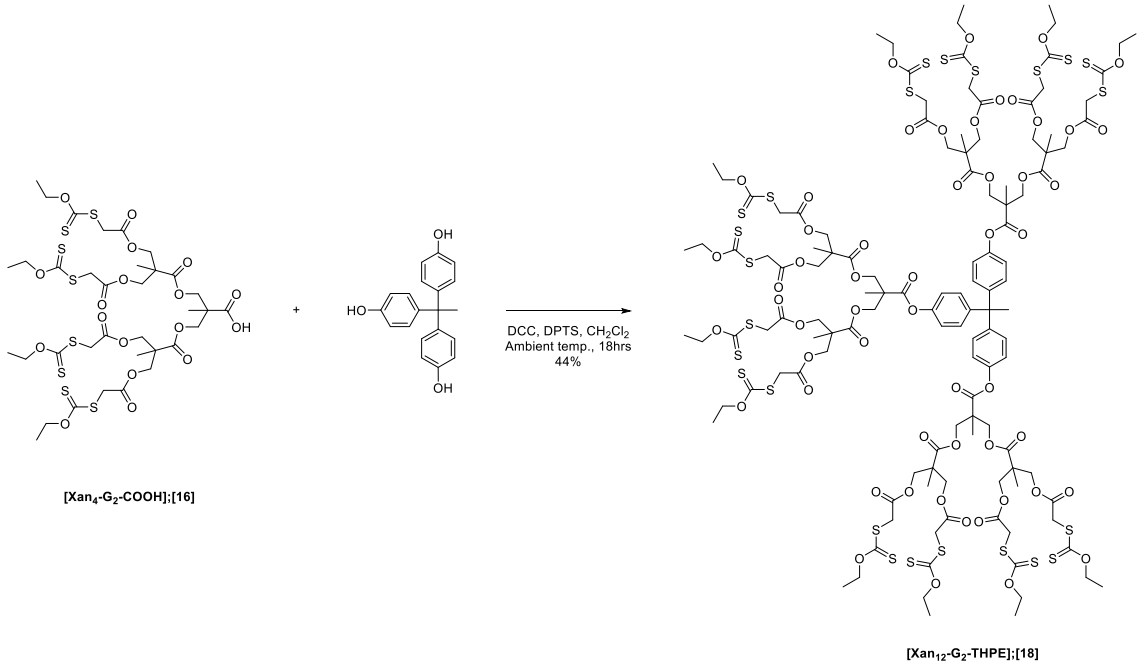

Scheme 2.9 Synthesis of G_2 dendrimer **[Xan_{12}-G_2-THPE];[18]**

1.3 equivalents of acid focal point functional dendron **[Xan_4-G_2-COOH];[16]** per hydroxyl group of trifunctional Frechét core THPE was reacted using DCC/DPTS chemistry to ensure complete coupling occurred. After purification by liquid chromatography, the xanthate functional G_2 dendrimer was obtained in 44% yield.

^{1}H NMR analysis of **[18]** indicated 10 proton environments, Fig. 2.14. Integration of the core aromatic environment at δ = 7.11 ppm (environment 9, Fig. 2.14) indicated the presence of 12 xanthate functional groups, confirmed by the integral of the characteristic xanthate resonance at δ = 4.64 ppm. Further confirmation was also illustrated by the difference in methyl resonances (environments 5 and 7, Fig. 2.14) at δ = 1.29 ppm and 1.44 ppm.

^{13}C NMR analysis of **[18]** confirmed 19 carbon environments including backbone ester carbonyl environments at δ = 171.2 and 171.7 ppm, Fig. S2.42.

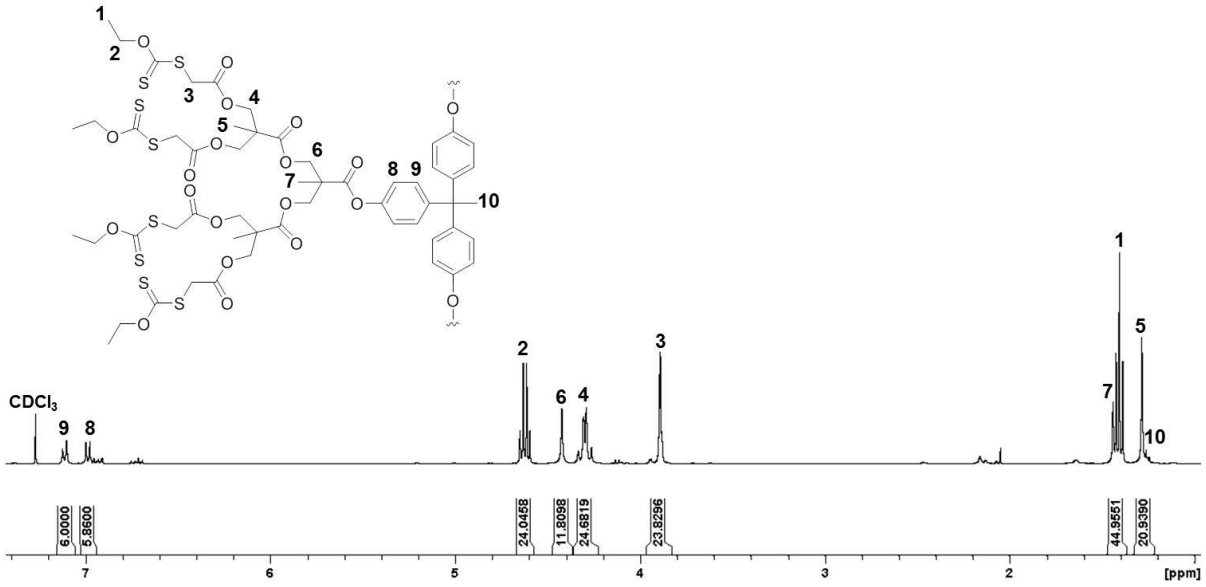

Fig. 2.14 ^{1}H NMR (400 MHz, $CDCl_3$) of **[Xan$_{12}$-G$_2$-THPE];[18]**

Extra resonances at δ = 6.68-6.77 ppm and 6.89-6.97 ppm are evident in the ^{1}H NMR spectrum of the dendrimer product, which may be due to partial reaction of the core molecule (^{1}H NMR overlay of **[16]** and **[18]**, Fig. S2.41). The xanthate functional G_2 dendrimer ([M] ($C_{125}H_{162}O_{54}S_{24}$) = 3294.32 Da) was therefore analysed by MALDI-TOF mass spectrometry to ensure structural perfection, and indicated populations at $[MNa]^+$ = 3316.4 Da, corresponding to the targeted material, and a lower intensity peak at approximately 2320 Da, which is likely to be partially reacted material with only two dendrons attached to the core molecule ($[(M-(Xan_4-G_2))Na]^+$ = 2320.25 Da), Fig. 2.15.

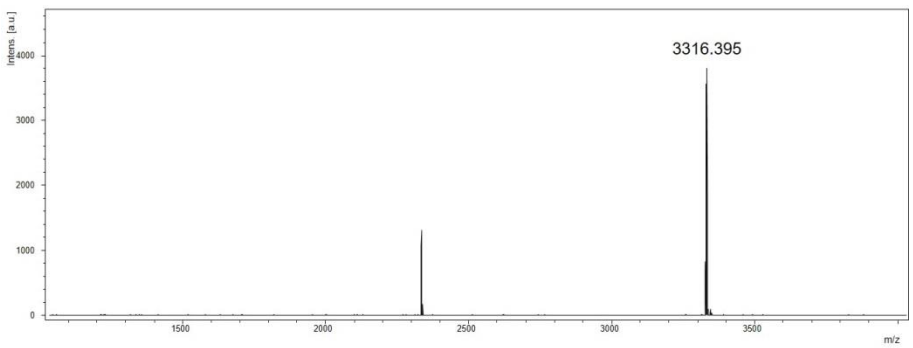

Fig. 2.15 MALDI-TOF analysis (DCTB) of **[Xan$_{12}$-G$_2$-THPE];[18]**

2.7 Dendritic ATRP macroinitiators

ATRP has previously been applied for the synthesis of dendritic hybrid architectures including linear dendritic hybrids (LDHs) and hyperbranched polydendrons (HPDs).[11,12]

2.7.1 Synthesis of xanthate functional macroinitiators

Conversion of the xanthate functional dendrons to ATRP macroinitiators involves activation of the focal point by removal of the TSe protecting group, as described earlier (Section 2.5), then conversion to a tertiary alkyl bromide ATRP initiator site. This was achieved by synthesis of 2-hydroxyethyl-2-bromoisobutyrate **[HEBiB];[19]**, via an asymmetric modification of ethylene glycol with α-bromoisobutyryl bromide, Scheme 2.10.

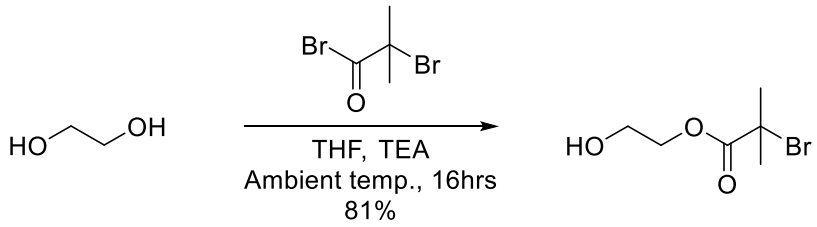

Scheme 2.10 Preparation of **[HEBiB];[19]**

[HEBiB];[19] was used to react with xanthate acid **[Xan-COOH];[9]** and focal point acid functional dendrons **[15]-[17]** using DCC/DPTS chemistry to form four generations of dendritic ATRP macroinitiators (G_0-G_3 **[20]-[23]**), in relatively high recovered yields (55-75%) after purification by liquid chromatography, Scheme 2.11.

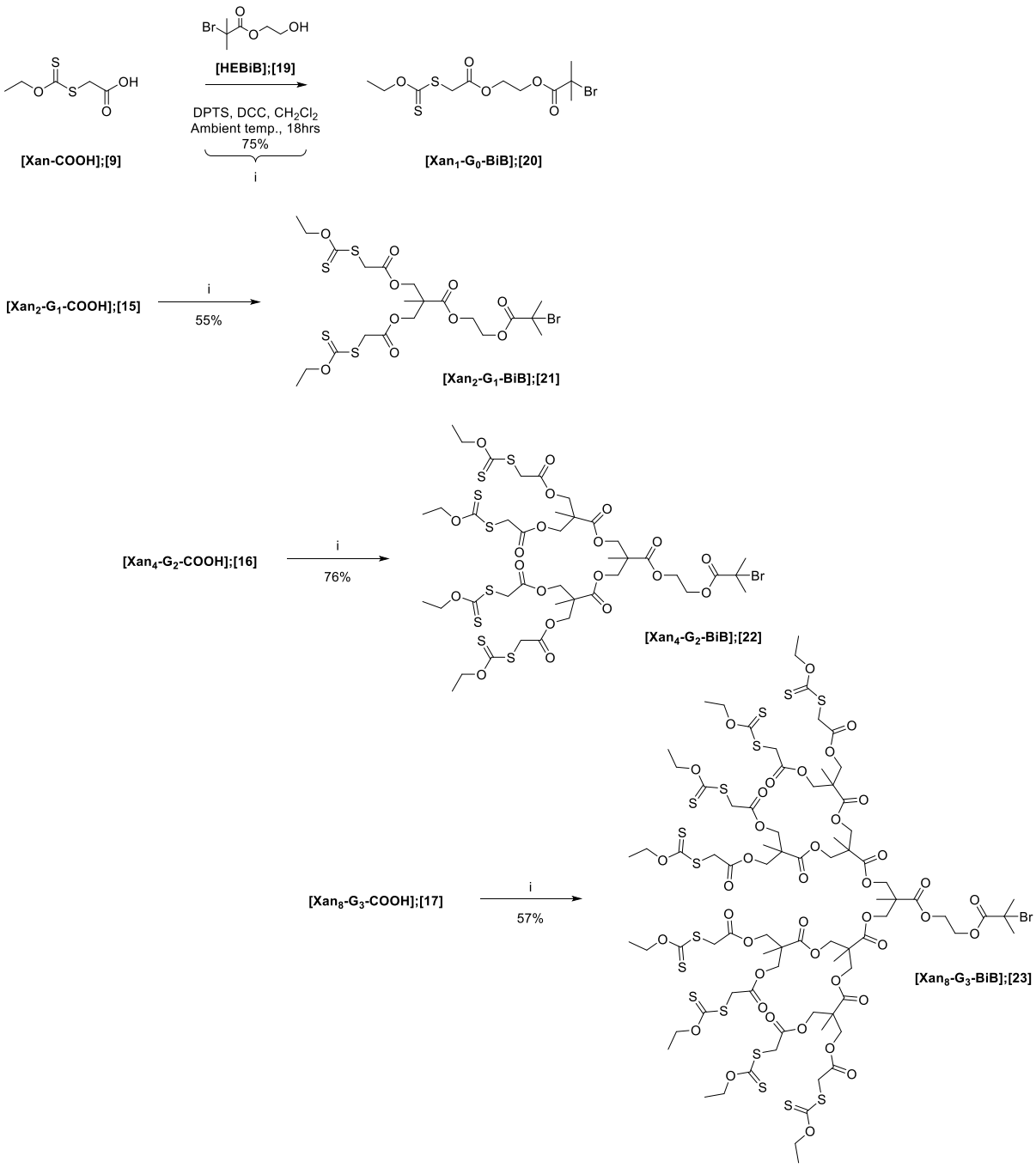

Scheme 2.11 Preparation of xanthate functional dendritic ATRP macroinitiators

[Xan$_1$-G$_0$-BiB];[20], **[Xan$_2$-G$_1$-BiB];[21]**, **[Xan$_4$-G$_2$-BiB];[22]** and **[Xan$_8$-G$_3$-BiB];[23]**

2.7.2 Characterisation of xanthate functional macroinitiators

2.7.2.1 Analysis by NMR spectroscopy

Synthesis of **[HEBiB];[19]** was confirmed by NMR spectroscopy; the ^{1}H NMR spectrum of this material indicated 3 proton environments with corresponding expected integrals, Fig. S2.43, and the ^{13}C NMR spectrum indicating 5 carbon environments, Fig. S2.44.

Characterisation of the xanthate functional dendron macroinitiators **[20]-[23]** by ^{1}H NMR spectroscopy indicated the formation of a singlet at approximately 1.90 ppm corresponding to the two symmetrical methyl environments on the bromoisobutyrate moiety, shown here for **[Xan$_8$-G$_3$-BiB];[23]**, Fig. 2.16, (**[20]-[22]** Fig. S2.45, S2.48 and S2.51). A broad resonance is also observed at approximately 4.40 ppm, corresponding to the two OC*H*$_2$ environments from the HEBiB unit.

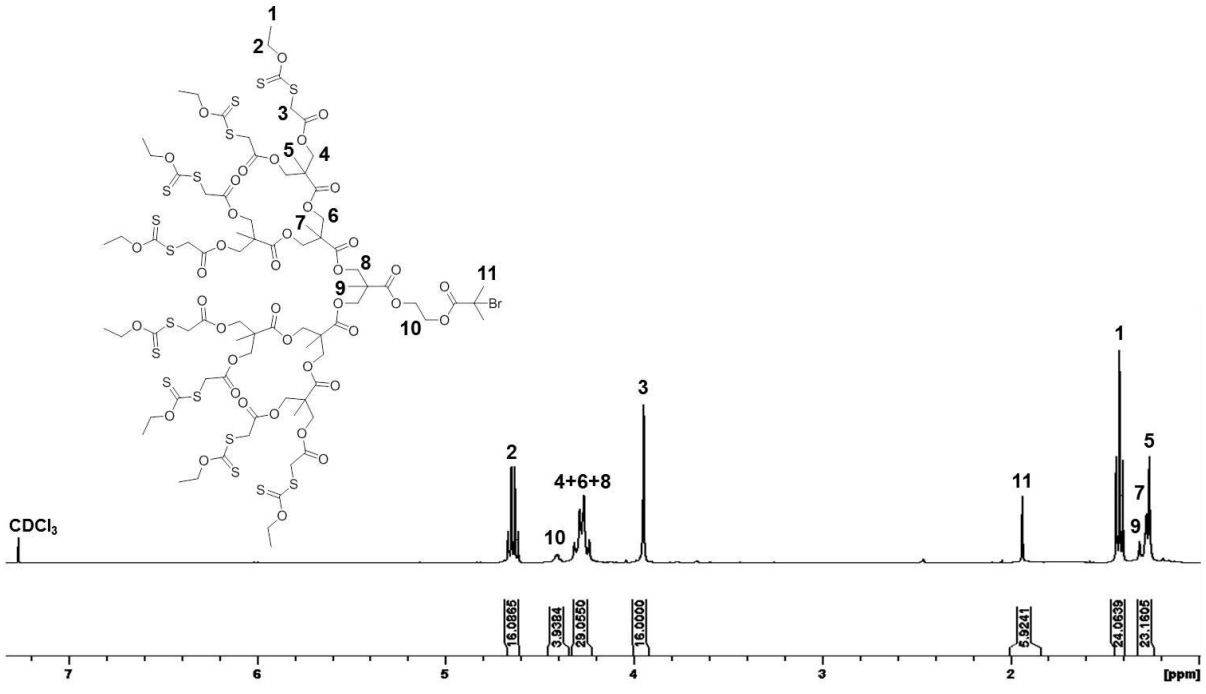

Fig. 2.16 ^{1}H NMR (400 MHz, $CDCl_3$) of **[Xan$_8$-G$_3$-BiB];[23]**

^{13}C NMR analysis indicated the presence of new resonances at δ = 34.0, 55.5 and 65.5 ppm corresponding to the HEBiB unit, the loss of the acid carbonyl resonance at approximately

δ = 173 ppm and the subsequent formation of a new ester carbonyl resonance at approximately δ = 171 ppm, confirming the incorporation of the bromoinitiator functionality, Fig. S2.46, S2.49, S2.52 and S2.54.

2.7.2.2 Analysis by mass spectrometry

Although NMR can give insight into the presence of symmetrical functional groups, mass spectrometry is a more sensitive tool for confirming the structural integrity of dendritic materials; this is increasingly important at higher dendron generations as NMR analysis becomes more complicated, and mass spectrometry techniques are able to easily identify branching defects within the structures. ESI-MS was performed on G_0 and G_1 initiators **[Xan$_1$-G$_0$-BiB];[20]** ([M] ($C_{11}H_{17}BrO_5S_2$) = 371.97 Da) and **[Xan$_2$-G$_1$-BiB];[21]** ([M] ($C_{21}H_{31}BrO_{10}S_4$) = 650.00 Da), indicating populations at $[MNa]^+$ = 395.0 Da and $[MNa]^+$ = 673.0 Da, respectively, Fig. S2.47 and S2.50. MALDI-TOF analysis was performed on G_2 and G_3 initiators **[Xan$_4$-G$_2$-BiB];[22]** ([M] ($C_{41}H_{59}BrO_{20}S_8$) = 1206.05 Da) and **[Xan$_8$-G$_3$-BiB];[23]** ([M] ($C_{81}H_{115}BrO_{40}S_{16}$) = 2318.17 Da), indicating populations at $[MNa]^+$ = 1229.2 Da and $[MNa]^+$ = 2341.4 Da, respectively, Fig. S2.53, 2.17. Some additional adducts were observed for **[23]** with increasing multiples of 16 Da, believed to have occurred during analysis due to thio-ether oxidation[22], although this can easily be mistaken for the 16 Da difference between sodium and potassium adducts. Bromine, present at the initiator focal point, has two isotopes (^{79}Br and ^{81}Br) in an approximately 1:1 ratio, resulting in two peaks in the molecular ion region, which further complicates analysis.

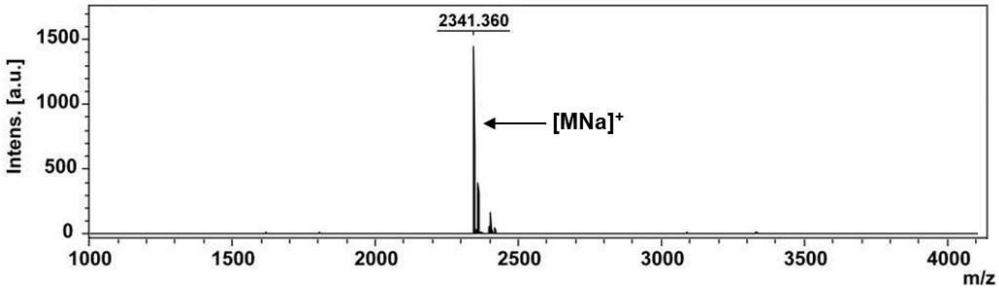

Fig. 2.17 MALDI-TOF analysis (HABA) of **[Xan$_8$-G$_3$-BiB];[23]**

2.8 Polymer synthesis

2.8.1 Atom Transfer Radical Polymerisation (ATRP)

The synthesis of well-defined macromolecules requires a combination of efficient coupling chemistries and polymerisation techniques with good control over polymer chain length, dispersity and chain-end functionality. This can be achieved by employing controlled polymerisation techniques such as atom transfer radical polymerisation (ATRP). ATRP is one of the most studied reversible-deactivation radical polymerisation (RDRP) techniques due to its versatility and compatibility with a wide range of commercially available monomers (styrenes, (meth)acrylates, meth(acrylamides), acrylonitriles, etc.), catalysts and ligands.[23]

The mechanism was first reported in 1995 by concurrent studies of Kato *et al*.[24], Wang and Matyjaszewski[25] and Percec and Barboiu[26]. In conventional radical polymerisation, continuous initiation, rapid propagation and termination reactions result in broad dispersities with no control over chain-end functionality. In ATRP, termination reactions are significantly suppressed with respect to propagation, allowing propagation to continue until all the monomer has been consumed. Rapid initiation and suppression of termination events, achieved by establishment of a dynamic equilibrium between active and dormant species, ensures polymer chains are propagating simultaneously, as outlined in Scheme 2.12 below.

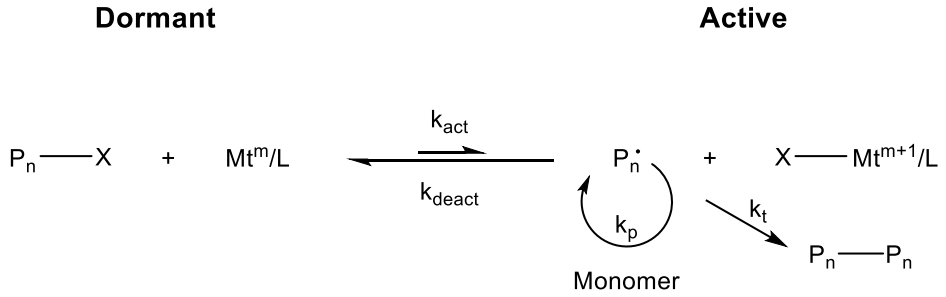

Scheme 2.12 – Dynamic equilibrium of ATRP, involving a propagating radical (P_n•) (n = number of monomers in polymer chain), transition metal catalyst (Mt^m) (m = oxidation state), ligand (L) and a halogen atom (X). k_{act}, k_{deact}, k_p and k_t represent the rate constants of activation, deactivation, propagation and termination, respectively.

The transition metal catalyst (M_t^m/L) abstracts the halogen atom from the dormant radical species (P_n-X) to generate a radical active centre P_n• and an oxidised metal complex (X-M_t^{m+1} /L), with a rate constant of activation k_{act}. This active radical species (P_n•) is then able to propagate by further reaction with monomer units with a rate constant of propagation k_p. Termination events (k_t) may also occur by combination or disproportionation, but this is minimal throughout the reaction. Success of the mechanism depends on the reversible activation of the dormant radical species. Since the dormant species is strongly preferred, the concentration of propagating radicals remains very low and equilibrium shifts towards the dormant species, suppressing possible side reactions and hence preserving the reactive nature of the end groups.[27] This control over possible side reactions allows the synthesis of polymers with narrow Đ, whose M_n is dependent upon the ratio of monomer and initiator used during the reaction. Care must be taken to ensure no oxygen is present during the polymerisation as oxygen is a potent radical scavenger and can therefore terminate the radical polymerisation and can also oxidise the transition metal catalyst.[23,28]

The high versatility of ATRP towards monomers and its tolerance to various functional groups (e.g. epoxides, hydroxyls, amines, cyanides) and solvents (can be performed in bulk or solution, using either organic or aqueous media), make this system ideal for the synthesis of a diverse range of polymers.[23] The reactive character of the chain-end allows for further polymerisation or functionalisation, with the ability to synthesise complex polymer architectures such as block or star polymers.

2.8.2 Synthesis and characterisation of xanthate functional LDHs and HPDs

Xanthate functional G_0-G_3 initiators (**[20]-[23]**) were used to synthesise either linear or branched poly(butyl methacrylate) via ATRP. Recent studies have shown that initiators bearing similar xanthate functionalities can undergo ATRP polymerisations without loss of control.[11,29] Monomers tBMA and nBMA were employed for dendritic polymer hybrid synthesis as the resulting polymer backbone and pendant methyl groups have proton resonances between approximately δ = 0.8-2.2 ppm by ^{1}H NMR spectroscopic analysis. Since the characteristic xanthate resonance is at δ = 4.64 ppm, we are able to independently observe changes in the dendritic surface groups after thiol Michael addition reactions.

The dendritic initiator functionality is present at one end of the polymer chain in linear hybrid structures, Scheme 2.13A. When a bifunctional monomer unit (ethylene glycol dimethacrylate, EGDMA) is incorporated into the polymerisation, highly branched polymer architectures result. The HPD structure is composed of a highly branched core with multiple dendritic initiator groups decorating the surface, Scheme 2.13B.

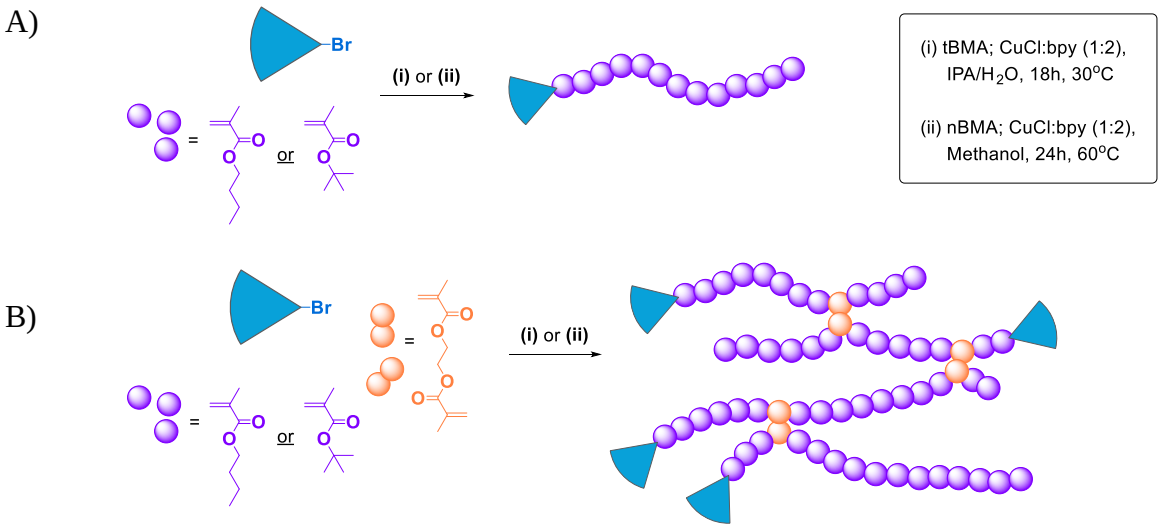

Scheme 2.13 Schematic representation of: (A) linear dendritic hybrid (LDH); and (B) hyperbranched polydendron (HPD) syntheses

A number average degree of polymerisation (DP_n) of 50 monomer units was targeted for the tBMA polymers. Two different DP_n values were targeted for the nBMA polymers; 50 and 100 monomer units per primary polymer chain. Analysis by triple detection SEC and ^{1}H NMR spectroscopy for each polymer is summarised in Table 2.2.

Table 2.2 ^{1}H NMR and SEC data for all LDHs synthesised

Initiator	Target Polymer Composition	SEC (THF)[a]					^{1}H NMR[b]	
		M_n (g mol^{-1})	M_w (g mol^{-1})	Đ	Number average number of chains[c]	Weight average number of chains[d]	DP_n	DP_n
G_1	$tBMA_{50}$	13 700	17 000	1.24	-	-	92	64
G_2	$tBMA_{50}$	12 900	15 200	1.19	-	-	82	65
G_1	$tBMA_{50}$-*co*-$EGDMA_{0.8}$	59 600	935 800	15.69	4	55	-	55
G_2	$tBMA_{50}$-*co*-$EGDMA_{0.8}$	46 500	340 700	7.29	4	22	-	59
G_1	$nBMA_{50}$	13 200	15 500	1.17	-	-	88	62
G_2	$nBMA_{50}$	14 300	16 700	1.17	-	-	92	64
G_3	$nBMA_{50}$	20 900	23 200	1.11	-	-	130	56
G_0	$nBMA_{100}$	20 200	23 900	1.18	-	-	140	136
G_0	$nBMA_{100}$	21 700[e]	26 400[e]	1.21	-	-	150	136
G_1	$nBMA_{100}$	19 200[e]	23 000[e]	1.20	-	-	130	108
G_2	$nBMA_{100}$	20 500[e]	25 200[e]	1.22	-	-	136	109
G_3	$nBMA_{100}$	26 600[e]	31 800[e]	1.19	-	-	170	93
G_0	$nBMA_{100}$-*co*-$EGDMA_{0.7}$	44 500	162 000	3.64	2	7	-	159
G_1	$nBMA_{100}$-*co*-$EGDMA_{0.8}$	628 000	3 730 000	5.94	33	162	-	168
G_2	$nBMA_{100}$-*co*-$EGDMA_{0.8}$	105 800	1 380 000	13.01	5	55	-	142
G_3	$nBMA_{100}$-*co*-$EGDMA_{0.8}$	61 600	299 700	4.86	2	9	-	121

[a]THF containing 2% TEA (v/v) at 35°C, 1mL min^{-1} flow rate. [b]Determined by ^{1}H NMR analysis in $CDCl_3$
[c]Calculated from M_n, [d]Calculated from M_w [e]Sample analysed in DMF containing 0.01 M LiBr at 60°C, 1mL min^{-1} flow rate.

2.8.3 Model reactions of polymerisation

2.8.3.1 Xanthate compatibility

In order to demonstrate that the xanthate moiety does not inhibit or induce chain transfer reactions during the ATRP of nBMA, a model polymerisation was carried out in the presence of xanthate acid **[9]**, using the commercially available ATRP initiator ethyl α-bromoisobutyrate (EBiB), Scheme 2.14.

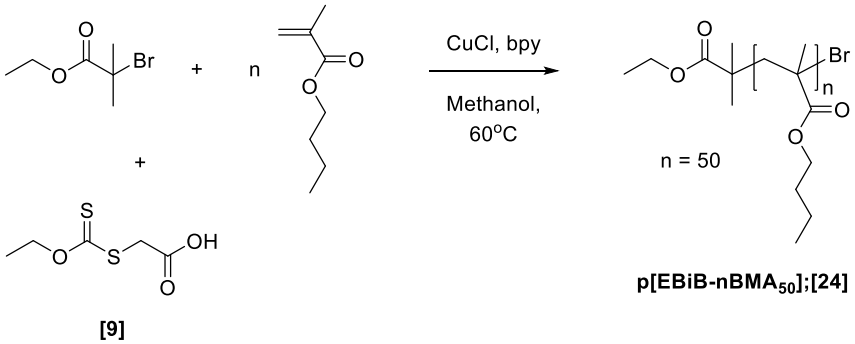

Scheme 2.14 ATRP of nBMA in the presence of xanthate acid **[9]**

The polymerisation of nBMA with targeted DP_{50} was carried out at 60°C in methanol with CuCl:bipyridyl (bpy) (1:2) as the catalytic system. The EBiB initiator proton resonances overlap with the polymer resonances in the ^{1}H NMR spectrum, and could not be adequately distinguished; anisole was therefore used as an internal reference for ^{1}H NMR end group analysis by addition at the beginning of the reaction. Analysis of resulting polymer **p[EBiB-nBMA$_{50}$];[24]** by ^{1}H NMR showed no evidence of xanthate functionality after purification, Fig. S2.55. This model reaction confirmed that the presence of xanthate acid **[9]** had no effect on the ATRP of nBMA.

Lack of initiation was also confirmed by setting up an ATRP of nBMA with targeted DP_{100} using G_0 xanthate functional initiator, but without the presence of the CuCl catalyst. After 24hrs, stirring at 60°C, no polymerisation was seen, evidenced by no decrease in the integral of methacrylate vinyl resonances at δ = 5.48 ppm and δ = 6.00 ppm, calibrated against the xanthate CH_2 resonance of the initiator at δ = 4.64 ppm Fig. S2.56.

2.8.4 Synthesis and characterisation of xanthate functional LDHs

Linear dendritic hybrid (LDH) polymers each possess the initiator functionality at one end of the polymer chain. The calculated DP_n by ^1H NMR end group analysis was less than the value obtained by SEC for all linear polymers. This discrepancy is thought to be due to <100% initiator efficiency for each dendron. Unreacted dendron remains in the sample when analysed by NMR (can be seen in SEC chromatograms at high retention volumes, Fig. 2.20), thus skewing DP_n calculations to shorter chain lengths compared to values obtained by SEC analysis. This effect has previously been reported.[30,31]

2.8.4.1 tBMA LDHs

Based on previous reports for the ATRP of tBMA,[11] an IPA/water (92.5:7.5 v/v) solvent system was used with G_1 and G_2 initiators, **[Xan$_2$-G$_1$-BiB];[21]** and **[Xan$_4$-G$_2$-BiB];[22]**, respectively, represented here by the G_2 initiator, Scheme 2.15.

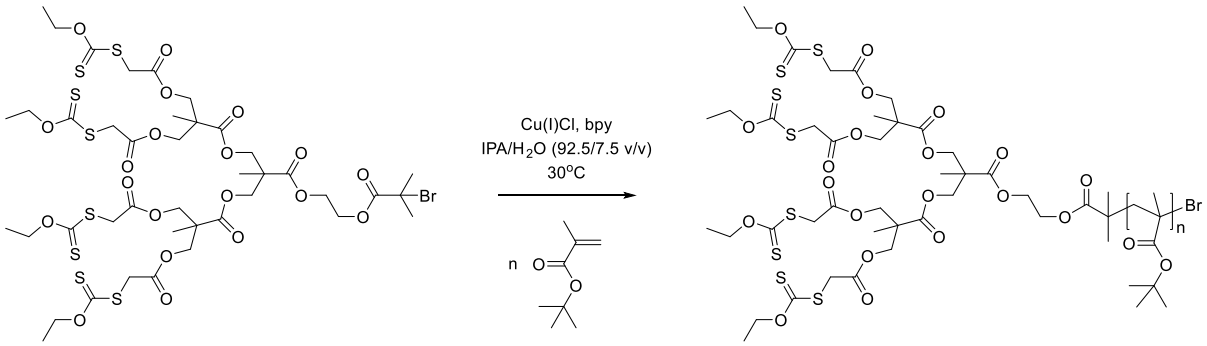

Scheme 2.15 Synthesis of LDH using G_2 initiator **[Xan$_4$-G$_2$-BiB];[22]**

Polymerisations of tBMA with a targeted DP_{50} were carried out at 30°C in IPA/water with CuCl:bpy (1:2) catalyst system. Reactions were terminated when conversion reached >95%, as indicated by integrals of the monomer vinyl resonances at δ = 5.48 and 6.00 ppm by ^1H NMR end group analysis during the reaction.

2.8.4.2 nBMA LDHs

The polymerisations of nBMA with targeted DP_{50} (G_1-G_3 dendron initiators **[21]-[23]**) and DP_{100} (G_0-G_3 dendron initiators **[20]-[23]**) were carried out at 60°C in methanol with CuCl:bpy (1:2) as the catalyst system, represented here by the G_3 initiator, Scheme 2.16. For polymerisation kinetics studies, the reaction was regularly sampled (approx. 0.2 mL) and diluted in $CDCl_3$ for ^{1}H NMR analysis and THF for SEC analysis.

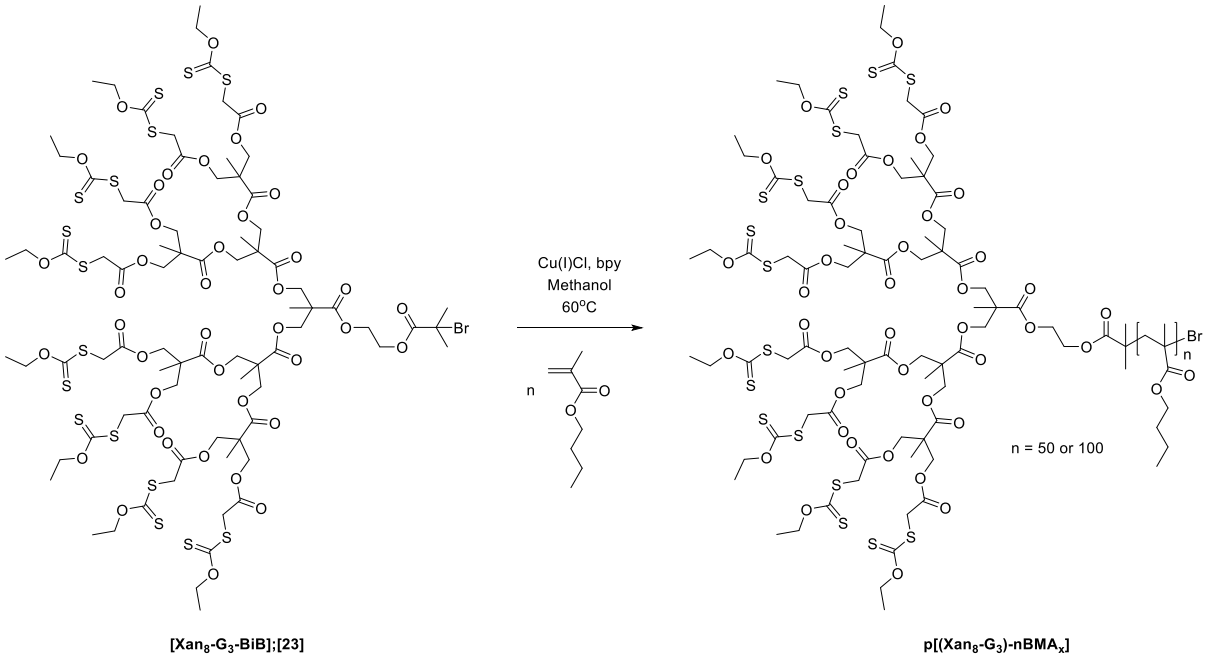

Scheme 2.16 Synthesis of LDH using G_3 initiator **[Xan_8-G_3-BiB];[23]**

Polymerisations were terminated by exposure to oxygen when conversion reached >95%, as calculated by ^{1}H NMR analysis of monomer vinyl resonances at δ = 5.56 and δ = 6.11 ppm. Kinetics studies for the polymerisation of nBMA were performed for each dendron initiator (G_0-G_3; **[20]-[23]**) to confirm that each linear polymerisation proceeds via first order kinetics with respect to monomer concentration, and to monitor the evolution of molecular weight with respect to monomer conversion Fig. 2.18.

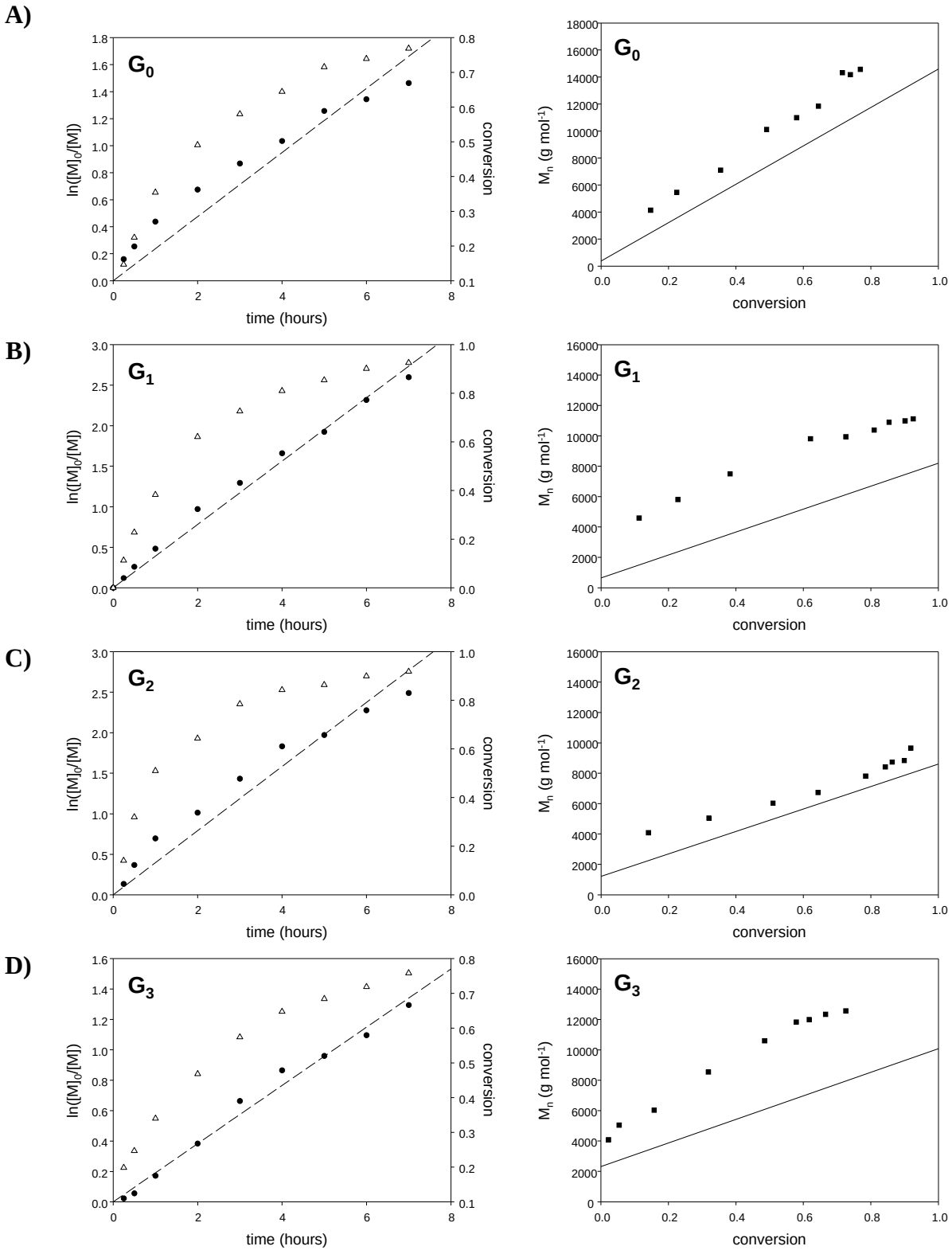

Fig. 2.18 Kinetic studies of the ATRP of nBMA: A) **p[(Xan$_1$-G$_0$)-nBMA$_{100}$];[32]**; B) **p[(Xan$_2$-G$_1$)-nBMA$_{50}$];[29]**; C) **p[(Xan$_4$-G$_2$)-nBMA$_{50}$];[30]**; D) **p[(Xan$_8$-G$_3$)-nBMA$_{50}$];[31]**. Conversion *vs*. time (open triangles) with corresponding semi-logarithmic plots (closed black circles); dashed line represents linear regression of semi-logarithmic plot. M_n *vs*. conversion (closed black squares) and theoretical M_n *vs*. conversion (solid line).

The kinetics plots for each linear polymerisation show that high conversion is achieved within 7 hours (Fig. 2.18), and follows first order kinetics, as expected.[30] A near-linear relationship between evolution of M_n and monomer conversion is observed, close to the theoretical values from targeted M_n. Variation in the refractive index increment (dn/dc) is expected during the polymerisation, although no correction was made here (carried out for linear polymerisation kinetics with PEG macroinitiator, see section 4.4.2). Triple detection SEC and ^{1}H NMR analysis of the purified G_0-G_3 LDHs was performed, Table 2.2. Conversion reached >90% for G_1 and G_2 initiated DP_{50} polymers after 6 hours and Đ remained low (≤ 1.22) for all dendron initiated polymerisations (G_0-G_3). G_3 initiated LDH (**p[(Xan$_8$-G$_3$)-nBMA$_{50}$];[31]**) had a slower rate of conversion, reaching 76% after 7 hours, due to poor solubility in the polymerisation solvent and potential steric crowding around the initiating site. This suggests that increasing dendron size has an adverse effect on the ATRP equilibrium constant ($K_{ATRP} = k_{act}/k_{deact}$).

Fig. 2.19 shows the ^{1}H NMR spectra of **p[(Xan$_4$-G$_2$)-nBMA$_{50}$]** at various time points during the polymerisation.

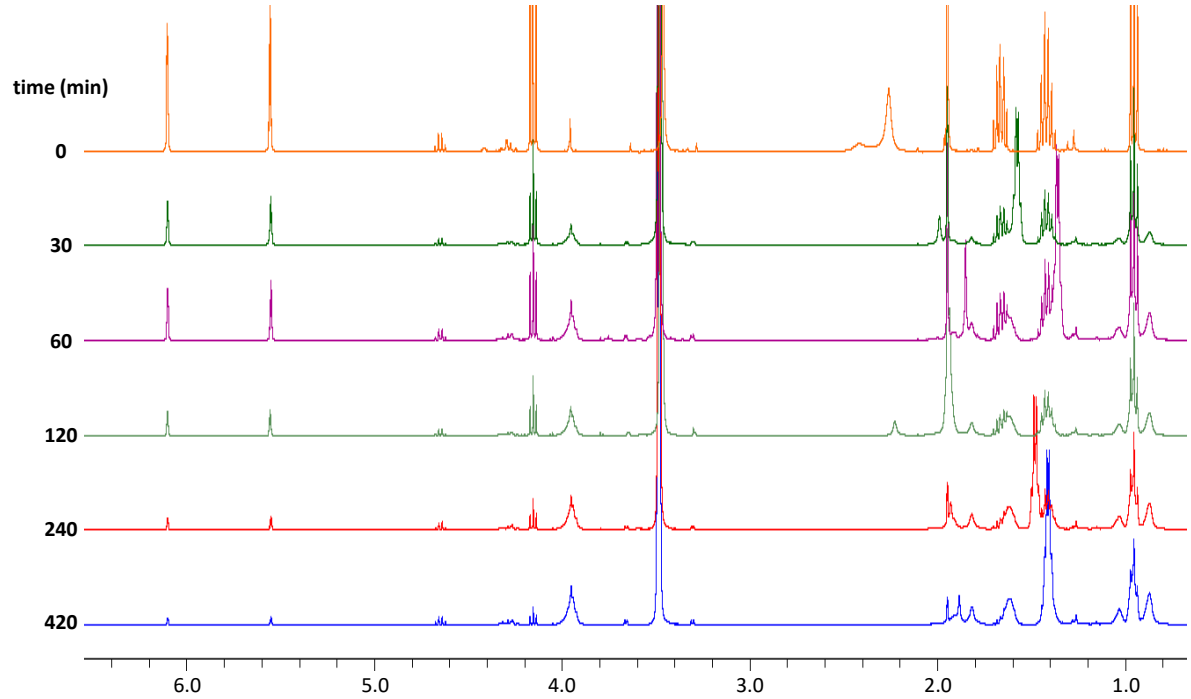

Fig. 2.19 ^{1}H NMR (400 MHz, $CDCl_3$) spectra overlay of **p[(Xan$_4$-G$_2$)-nBMA$_{50}$];[30]** kinetic time points

As the reaction proceeds, the monomer vinyl resonances at δ = 5.56 and δ = 6.11 ppm decrease as the monomer is consumed. Conversion was calculated by calibrating the integral of the vinyl resonances to 1, and comparing to the integral of the polymer resonance at δ ≈ 0.8-1.1 ppm, corresponding to backbone and pendant methyl groups.

Unreacted dendron initiator was present in each polymer sample after polymerisation had reached complete conversion. This could be seen in the refractive index (RI) SEC chromatograms, indicated by a small peak at high retention volumes (~20-22 mL), Fig. 2.20.

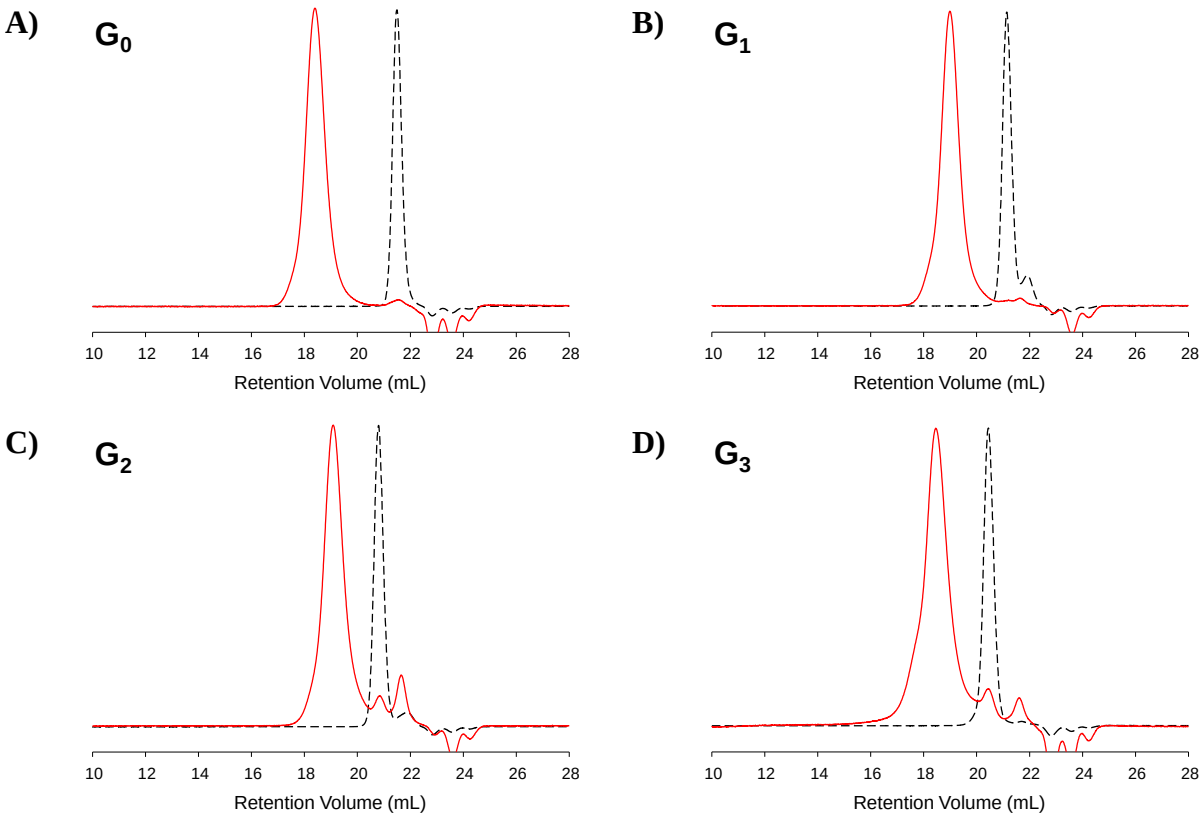

Fig. 2.20 SEC RI chromatogram overlays of LDH (red solid line) and dendron initiator (black dashed line), analysed in THF: A) **[Xan$_1$-G$_0$-BiB];[20]** with **p[(Xan$_1$-G$_0$)-nBMA$_{100}$];[32]**; B) **[Xan$_2$-G$_1$-BiB];[21]** with **p[(Xan$_2$-G$_1$)-nBMA$_{50}$];[29]**; C) **[Xan$_4$-G$_2$-BiB];[22]** with **p[(Xan$_4$-G$_2$)-nBMA$_{50}$];[30]**; and D) **[Xan$_8$-G$_3$-BiB];[23]** with **p[(Xan$_8$-G$_3$)-nBMA$_{50}$];[31]**.

The SEC chromatograms for all linear-dendritic hybrids (LDHs) (Fig. 2.20 A-D and Fig. 2.21 A-D) have monomodal distributions, indicating good control over molecular weight and composition. The G_3 initiated LDH, **p[(Xan$_8$-G$_3$)-nBMA$_{50}$];[31]**, had a lower retention volume than corresponding lower generation dendron initiated LDHs, indicating a higher average molecular weight. This is thought to be due to <100% initiator efficiency due to solubility issues in methanol and steric hindrance around the initiating site, leading to fewer chains being successfully initiated, and hence higher than expected molecular weights. A slight shoulder is also visible for the G_3 LDH with targeted DP_{50}, which could be due to coupling of chain ends at high conversion.[32]

G_0-G_3 dendron initiated LDHs, **[32]-[35]**, with a targeted DP_n of 100 monomer units were synthesised and analysed by triple detection SEC in a DMF eluent system, Fig. 2.21 A-D.

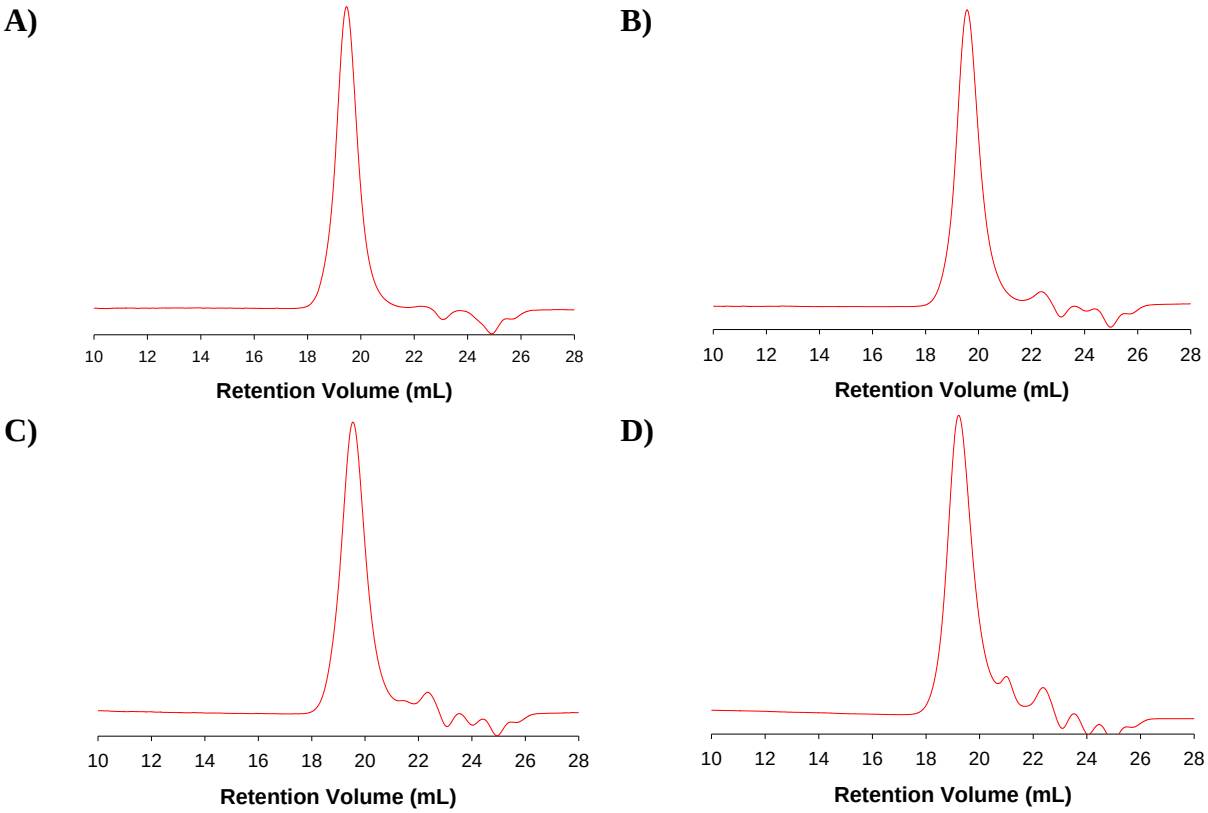

Fig. 2.21 SEC RI chromatogram traces of G_0-G_3 dendron initiated DP_{100} LDH materials, analysed in DMF: A) **p[(Xan$_1$-G$_0$)-nBMA$_{100}$];[32]**; B) **p[(Xan$_2$-G$_1$)-nBMA$_{100}$];[33]**; C) **p[(Xan$_4$-G$_2$)-nBMA$_{100}$];[34]**; and D) **p[(Xan$_8$-G$_3$)-nBMA$_{100}$];[35]**.

Although these materials appear to elute at similar retention volumes to the DP_{50} LDHs (Fig. 2.20 A-D), SEC analysis reveals much higher average molecular weights achieved for these DP_{100} LDH materials (Table 2.2). Comparison of G_0 initiated DP_{100} analysed in both THF (Fig. 2.20A) and DMF (Fig. 2.21A) eluent systems reveals very similar average molecular weights, despite the difference in elution volume seen in the SEC RI chromatogram traces (Table 2.2).

2.8.5 Synthesis and characterisation of xanthate functional HPDs

Incorporation of bifunctional monomer EGDMA into the polymerisation leads to the formation of large, high molecular weight branched polymer architectures.[12,33-35] A 1:1 initiator:brancher ratio would theoretically lead to cross-linking of the polymer chains and ultimately, macroscopic gelation.[36,37] A ratio of slightly less than 1 (e.g. 0.95) should lead to highly branched structures, however, due to the <100% initiator efficiency of the dendron macroinitiators, an optimum initiator:brancher ratio of 1:0.8 was applied for this system (identified through empirical experimentation). Polymerisation concentration is also key, with more dilute polymerisations increasing the probability of intramolecular looping, instead of the desired intermolecular branching. Therefore, polymerisations were conducted at a concentration of 50 v/v% with respect to the monomer.

2.8.5.1 tBMA HPDs

The branched copolymerisation of tBMA and bifunctional monomer EGDMA, targeting DP_{50} of the primary polymer chains of the G_1 and G_2 dendron initiated HPDs, was carried out under the same conditions as for LDHs, Scheme 2.17.

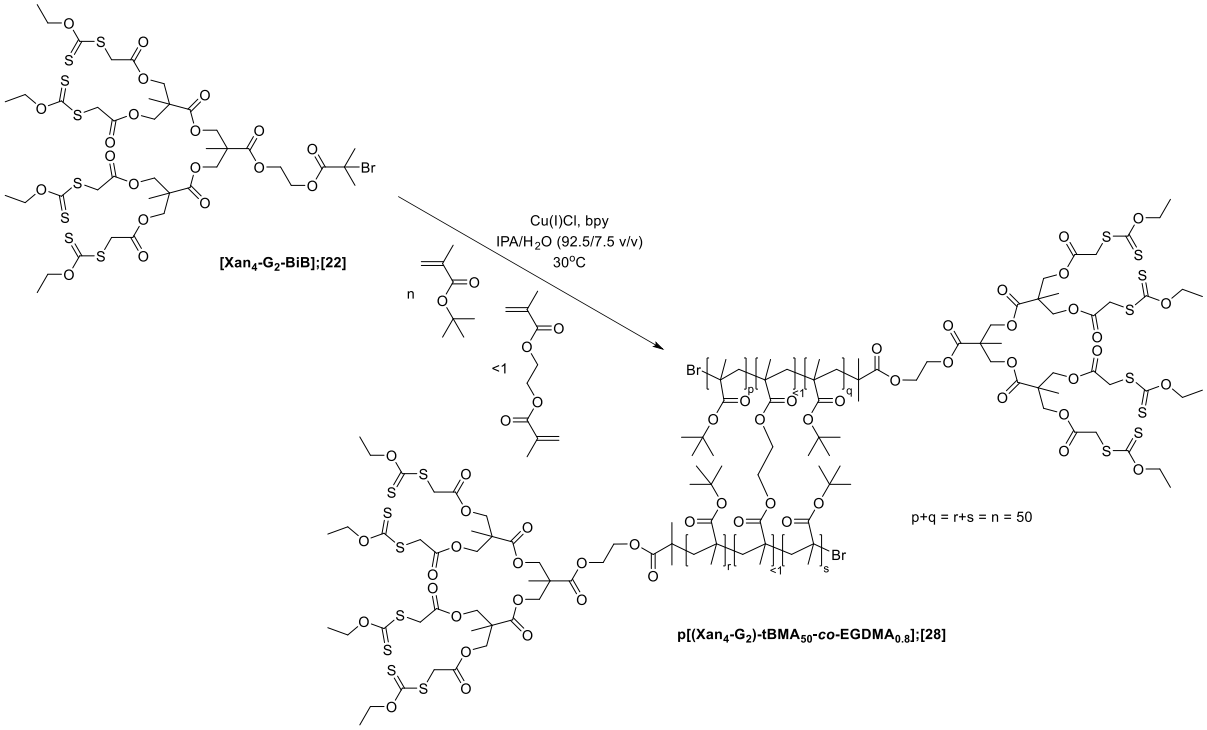

Scheme 2.17 Synthesis of HPD **p[(Xan_4-G_2)-$tBMA_{50}$-*co*-$EGDMA_{0.8}$];[28]**

The SEC chromatogram overlays of G_1 and G_2 initiated tBMA polymers highlight the difference between linear and branched architectures via the RI (Fig. 2.22A and C) and right angle light scattering (RALS) detectors (Fig. 2.22B and D). The RI detector is employed to calculate concentration, whereas the RALS detector is used to calculate the average size of polymers in solution, therefore, high molecular weight species at low concentration give rise to a small RI response, and a large RALS response as large polymers scatter much more light than smaller species in solution. Inclusion of bifunctional monomer EGDMA into the ATRP of tBMA results in high molecular weight polymers which elute at lower retention volumes than the corresponding linear polymers.

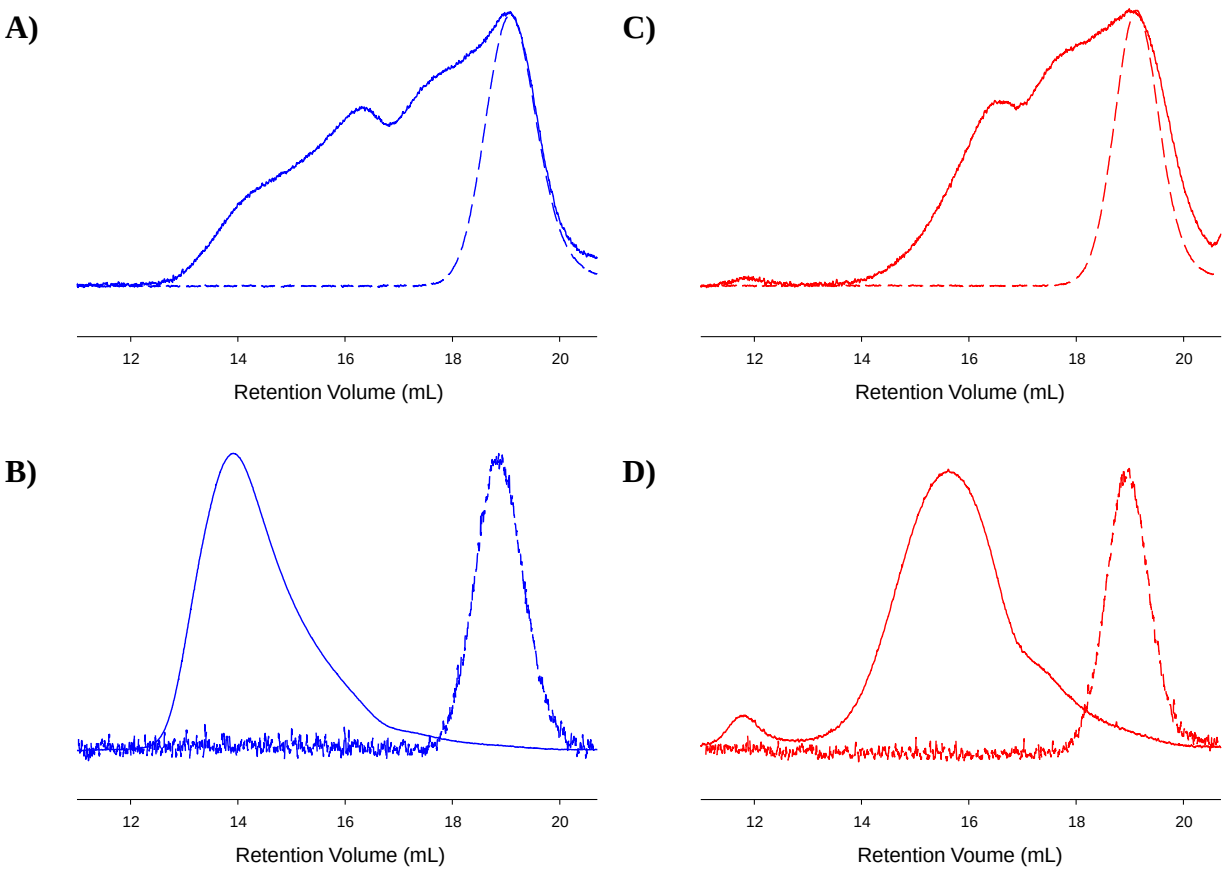

Fig. 2.22 SEC chromatogram overlays of: A) RI trace and B) RALS trace of **p[(Xan$_2$-G$_1$)-tBMA$_{50}$];[25]** (dashed blue line) with **p[(Xan$_2$-G$_1$)-tBMA$_{50}$-*co*-EGDMA$_{0.8}$];[27]** (solid blue line) and; C) RI trace and D) RALS trace of **p[(Xan$_4$-G$_2$)-tBMA$_{50}$];[26]** (dashed red line) with **p[(Xan$_4$-G$_2$)-tBMA$_{50}$-*co*-EGDMA$_{0.8}$];[28]** (solid red line)

The linear and branched polymers were analysed by ^{1}H NMR spectroscopy, as discussed previously. Fig. 2.23 shows the ^{1}H NMR spectra overlay of G_1 and G_2 dendron initiated $tBMA_{50}$ LDHs, with major peaks assigned.

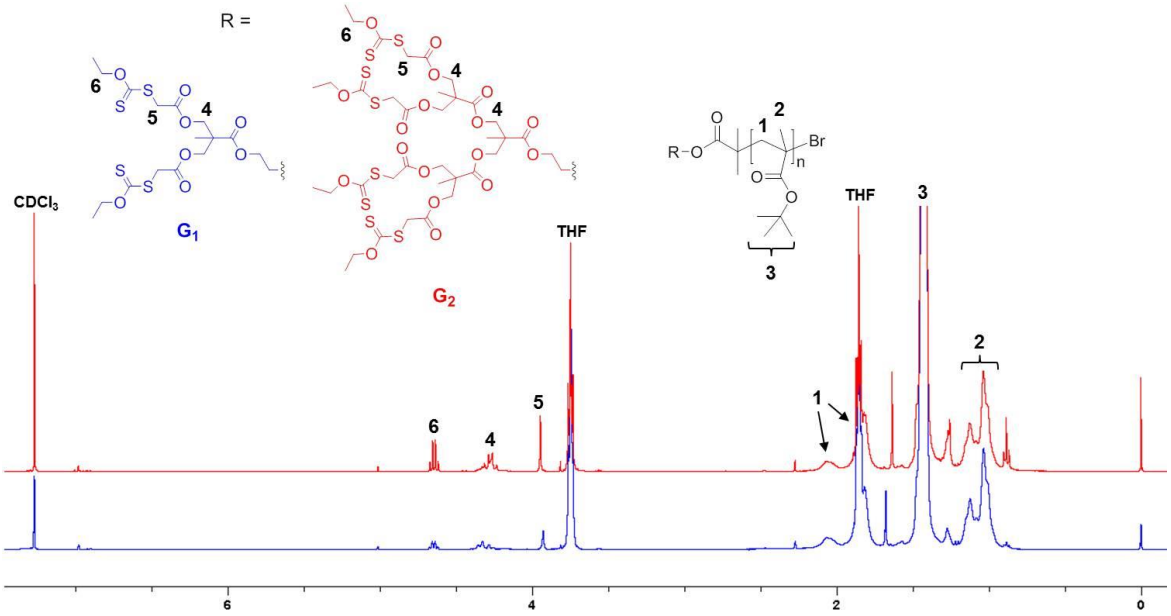

Fig. 2.23 ^{1}H NMR (400 MHz, $CDCl_3$) spectra overlay of **p[(Xan_2-G_1)-$tBMA_{50}$];[25]** (blue) and **p[(Xan_4-G_2)-$tBMA_{50}$];[26]** (red) with major peaks assigned

The G_1 and G_2 dendron initiated $tBMA_{50}$ HPD ^{1}H NMR spectra are overlaid in Fig. 2.24 with major peaks assigned. The difference between LDH and HPD species is the presence of bifunctional monomer EGDMA in branched polymers, which possess protons with similar resonances to the tBMA monomer, and are therefore indistinguishable in the ^{1}H NMR spectra.

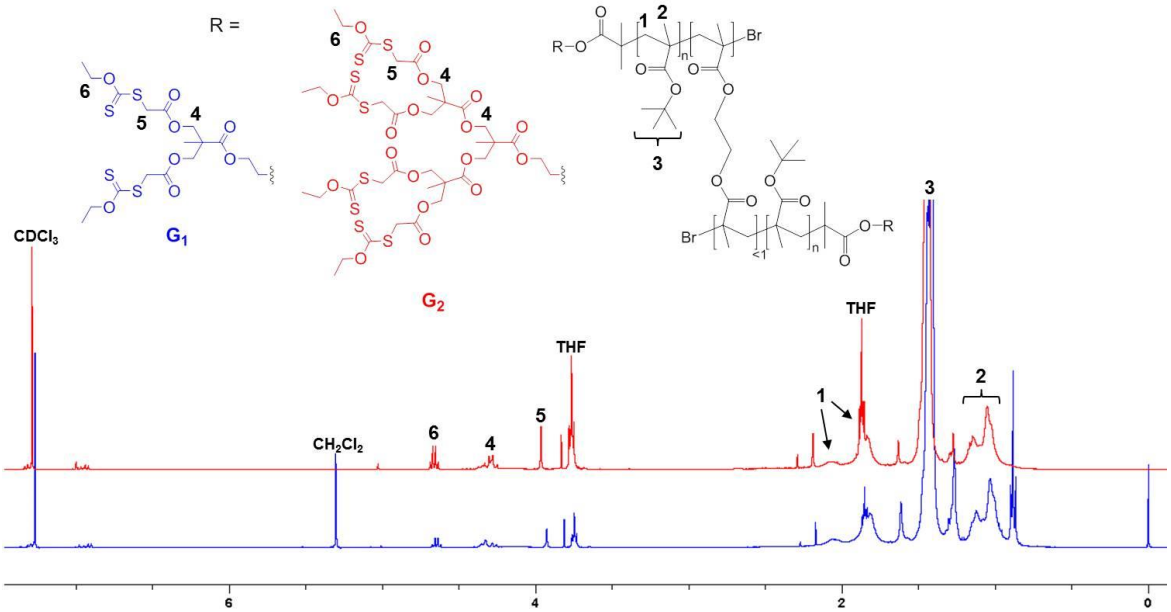

Fig. 2.24 ^{1}H NMR (400 MHz, $CDCl_3$) spectra overlay of **p[(Xan_2-G_1)-$tBMA_{50}$-*co*-$EGDMA_{0.8}$];[27]** (blue) and **p[(Xan_4-G_2)-$tBMA_{50}$-*co*-$EGDMA_{0.8}$];[28]** (red) with major peaks assigned

2.8.5.2 nBMA HPDs

The branched copolymerisation of nBMA and bifunctional monomer EGDMA, targeting DP_{100}, was conducted under the same conditions as for LDHs with G_0-G_3 dendron initiators, Scheme 2.18.

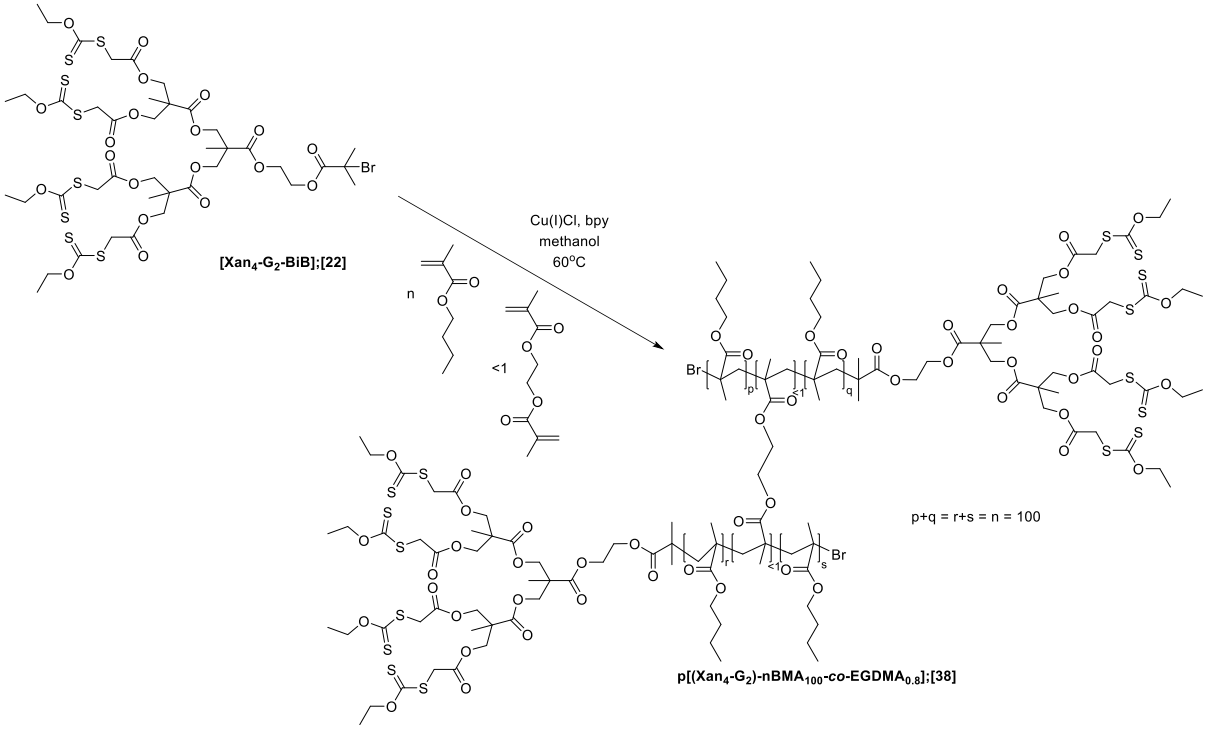

Scheme 2.18 Synthesis of HPD **p[(Xan$_4$-G$_2$)-nBMA$_{100}$-*co*-EGDMA$_{0.8}$];[38]**

The SEC chromatogram overlays of RI and RALS traces for G_0-G_3 dendron initiated HPDs shows the distribution of materials formed during the branched copolymerisation, as a result of statistical branching, Fig. 2.25. Inclusion of a bifunctional monomer results in high molecular weight branched polymers, which elute at low retention volumes. The G_2 dendron initiated branched polymerisation reaction was regularly sampled (approx. 0.2 mL) and diluted in $CDCl_3$ for ^{1}H NMR analysis and THF for SEC analysis in order to study the kinetics.

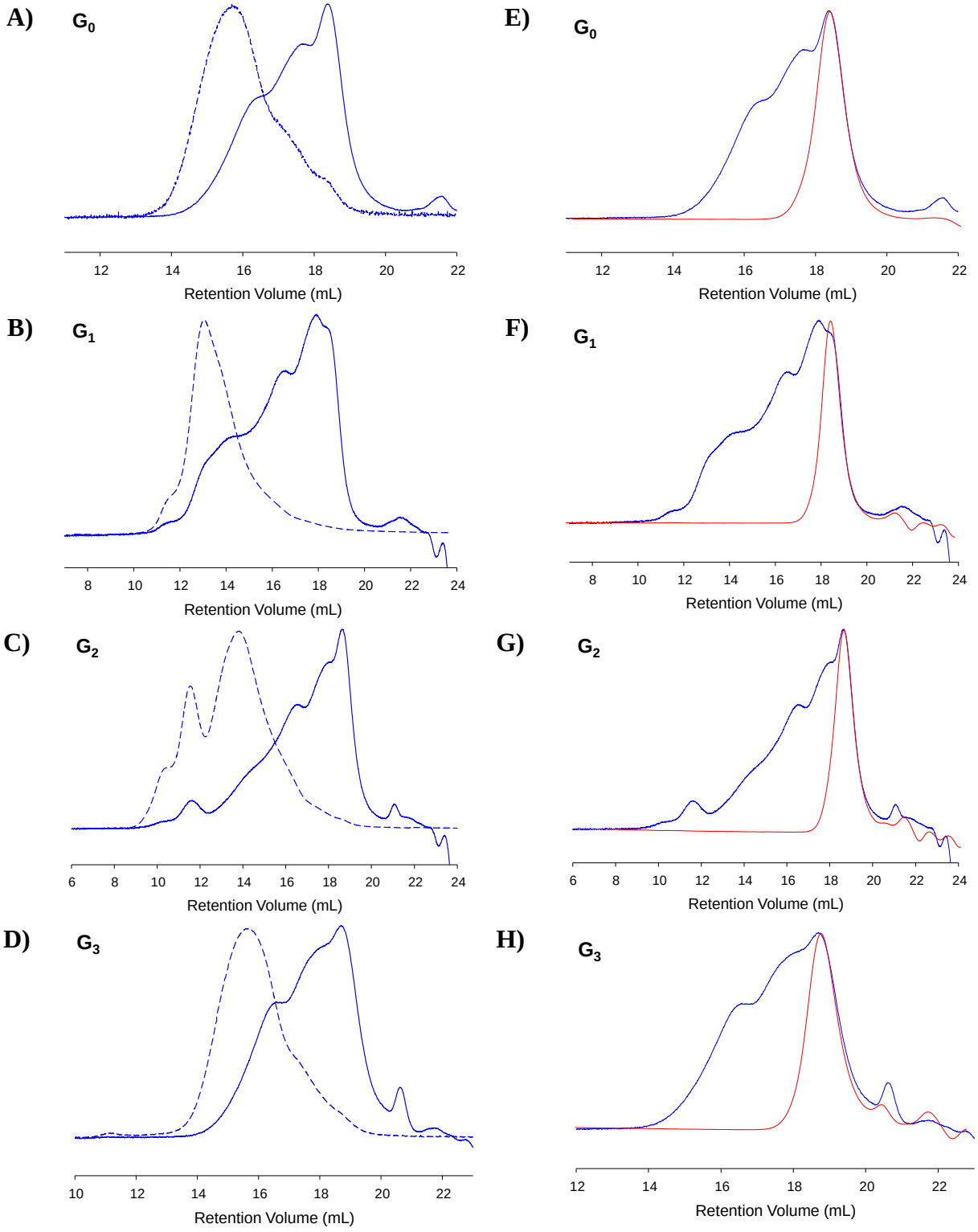

Fig. 2.25 SEC chromatogram overlays of RI (blue solid line) and RALS (blue dashed line) of HPDs and RI traces of HPDs (blue solid line) with corresponding LDHs (red solid line) of A)&E) **p[(Xan$_1$-G$_0$)-nBMA$_{100}$-*co*-EGDMA$_{0.7}$];[36]**; B)&F) **p[(Xan$_2$-G$_1$)-nBMA$_{100}$-*co*-EGDMA$_{0.8}$];[37]**; C)&G) **p[(Xan$_4$-G$_2$)-nBMA$_{100}$-*co*-EGDMA$_{0.8}$];[38];** and D)&H) **p[(Xan$_8$-G$_3$)-nBMA$_{100}$-*co*-EGDMA$_{0.8}$];[39]**.

A kinetic plot for the branched polymerisation of G_2 initiated nBMA, with targeted DP_{100}, **[(Xan$_4$-G$_2$)-nBMA$_{100}$-*co*-EGDMA$_{0.8}$];[38]**, shows the change in M_n and M_w vs. conversion, Fig. 2.26.

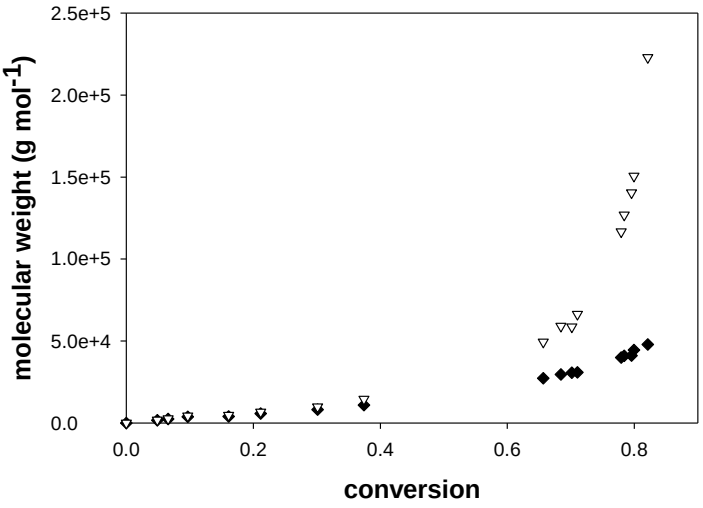

Fig. 2.26 Kinetic studies of the ATRP of nBMA-*co*-EGDMA: **p[(Xan$_4$-G$_2$)-nBMA$_{100}$-*co*-EGDMA$_{0.8}$];[38]**. Molecular weight (g mol^{-1}) *vs*. conversion; M_n (closed black diamonds) and M_w (open downward triangles).

The M_n and M_w increase linearly at the beginning of the polymerisation, until conversion reaches approximately 70%, where the M_w increases steeply, indicating intermolecular branching of linear chains to form large branched structures at high conversion. At low conversion, EGDMA is incorporated into the growing polymer chain by reaction of one of its double bonds; as monomer is consumed within the reaction mixture, the pendant vinyl group of incorporated EGDMA reacts with neighbouring polymer chains in solution, resulting in a branched polymer. Due to the statistical nature of branching during ATRP, a broad distribution of materials, from linear polymers to highly branched macromolecules, results.[33]

The M_n of a polymer distribution is a measure for the chain length, whereas M_w is a measure for the expected statistical size of the polymer, based on the weight fraction of the sample. G_2 dendron initiated HPD **p[(Xan$_4$-G$_2$)-nBMA$_{100}$-*co*-EGDMA$_{0.8}$];[38]** had an M_n value (Table 2.2) of 105,800, corresponding to a number average of 5 primary polymer chains joined

together and an M_w value of 1,380,000, corresponding to a weight average of 55 primary polymer chains joined together, when compared to the equivalent LDH. These values have been represented graphically in Fig. 2.27 below, to give a visual representation of the distribution of materials within the sample.

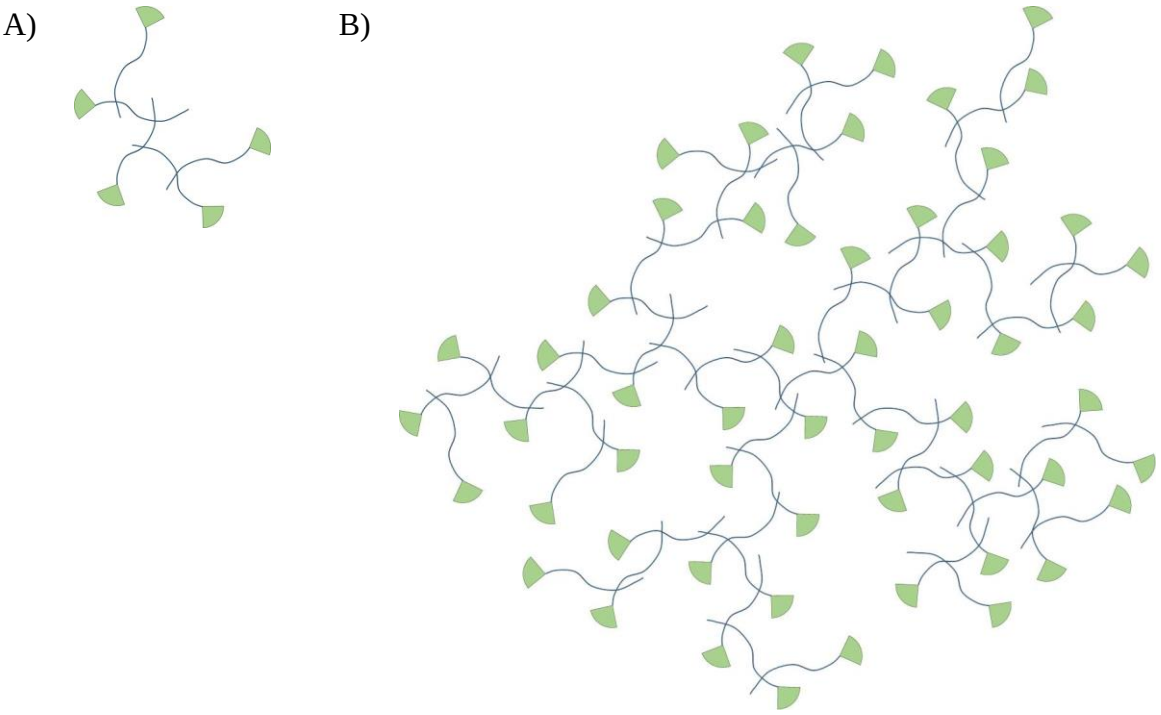

Fig. 2.27 A visual representation of; A) number average molecular weight (M_n), and B) weight average molecular weight (M_w) of **p[(Xan$_4$-G$_2$)-nBMA$_{100}$-*co*-EGDMA$_{0.8}$];[38]**

These HPD species, therefore, consist of number average molecular weight polymers each possessing 20 xanthate peripheral groups and weight average molecular weight polymers possessing 220 xanthate peripheral groups; originating from the G_2 dendron at every primary polymer chain end, each with 4 xanthate functional groups. Clearly, species with lower and much higher molecular weights are present within the polymer sample, and would represent a higher level of structural dispersity than shown here.

2.9 Conclusions

In order to test the research hypothesis outlined in Chapter 1, a library of materials has been synthesised. The application of dendrimer chemistry for the construction of four generations (G_0-G_3) of polyester dendron and addition of xanthate functionality at the periphery via DCC/DPTS coupling and anhydride chemistry has been described. These dendrons were then converted into ATRP macroinitiators by activation of the focal point and used to polymerise tBMA and nBMA at DP_n = 50 and 100 monomer units per primary polymer chain during LDH synthesis, and copolymerise with bifunctional monomer EGDMA during HPD synthesis. These polymerisations proceeded via first order kinetics, as expected, and produced LDHs with a monomodal molecular weight distribution and HPDs with a much broader distribution of polymeric species. Very high molecular weight soluble polymers were formed, containing large numbers of conjoined chains, each bearing a dendron at one chain-end. These synthesised HPD species contain, on average, a much larger number of peripheral xanthate groups than modifiable dendrimer species previously reported.[9] The ability of these materials to undergo post-synthetic modification will be investigated in Chapter 3.

2.10 References

1. A. D. Schlüter and J. P. Rabe, *Angew. Chemie Int. Ed.*, 2000, **39**, 864–883.
2. M. A. Gauthier, M. I. Gibson, and H. A. Klok, *Angew. Chemie Int. Ed.*, 2009, **48**, 48–58.
3. K. A. Günay, P. Theato, and H. A. Klok, *J. Polym. Sci. Part A Polym. Chem.*, 2013, **51**, 1–28.
4. P. L. Golas and K. Matyjaszewski, *Chem. Soc. Rev.*, 2010, **39**, 1338–1354.
5. R. K. Iha, K. L. Wooley, A. M. Nyström, D. J. Burke, M. J. Kade, and C. J. Hawker, *Chem. Rev.*, 2009, **109**, 5620–5686.
6. W. H. Binder and R. Sachsenhofer, *Macromol. Rapid Commun.*, 2007, **28**, 15–54.
7. A. S. Goldmann, M. Glassner, A. J. Inglis, and C. Barner-Kowollik, *Macromol. Rapid Commun.*, 2013, **34**, 810–849.
8. C. H. Wong and S. C. Zimmerman, *Chem. Commun.*, 2013, **49**, 1679–1695.
9. S. E. R. Auty, O. Andren, M. Malkoch, and S. P. Rannard, *Chem. Commun.*, 2014, **50**, 6574–6577.
10. H. C. Kolb, M. G. Finn, and K. B. Sharpless, *Angew. Chemie - Int. Ed.*, 2001, **40**, 2004–2021.
11. S. E. R. Auty, O. C. J. Andrén, F. Y. Hern, M. Malkoch, and S. P. Rannard, *Polym. Chem.*, 2014, **6**, 573–582.
12. F. L. Hatton, P. Chambon, T. O. McDonald, A. Owen, and S. P. Rannard, *Chem. Sci.*, 2014, **5**, 1844–1853.
13. O. L. Padilla De Jesús, H. R. Ihre, L. Gagne, J. M. J. Fréchet, and F. C. Szoka, *Bioconjug. Chem.*, 2002, **13**, 453–461.
14. H. Ihre, A. Hult, J. M. J. Fréchet, and I. Gitsov, *Macromolecules*, 1998, **31**, 4061–4068.

15. M. C. Parrott, S. R. Benhabbour, C. Saab, J. A. Lemon, S. Parker, J. F. Valliant, and A. Adronov, *J. Am. Chem. Soc.*, 2009, **131**, 2906–2916.

16. M. Malkoch, E. Malmström, and A. Hult, *Macromolecules*, 2002, **35**, 8307–8314.

17. R. Nicolaÿ, *Macromolecules*, 2012, **45**, 821–827.

18. M. Le Neindre, B. Magny, and R. Nicolaÿ, *Polym. Chem.*, 2013, **4**, 5577–5584.

19. M. Le Neindre and R. Nicolaÿ, *Polym. Int.*, 2014, **63**, 887–893.

20. C. J. Hawker and J. M. J. Frechet, *J. Am. Chem. Soc.*, 1992, **114**, 8405–8413.

21. J. S. Moore and S. I. Stupp, *Macromolecules*, 1990, **23**, 65–70.

22. K. Bahrami, M. M. Khodaei, and M. Sheikh Arabi, *J. Org. Chem.*, 2010, **75**, 6208–13.

23. K. Matyjaszewski and J. Xia, *Chem. Rev.*, 2001, **101**, 2921–2990.

24. M. Kato, M. Kamigaito, M. Sawamoto, and T. Higashimura, *Macromolecules*, 1995, **28**, 1721–1723.

25. J. S. Wang and K. Matyjaszewski, *J. Am. Chem. Soc.*, 1995, **117**, 5614–5615.

26. V. Percec and B. Barboiu, *Macromolecules*, 1995, **28**, 7970–7972.

27. K. Matyjaszewski, *Isr. J. Chem.*, 2012, **52**, 206–220.

28. H. Fischer, *Chem. Rev.*, 2001, **101**, 3581–3610.

29. M. Le Neindre and R. Nicolay, *Polym. Chem.*, 2014, **5**, 4601–4611.

30. J. Xia, S. G. Gaynor, and K. Matyjaszewski, *Macromolecules*, 1998, **31**, 5958–5959.

31. P. A. Gurr, M. F. Mills, G. G. Qiao, and D. H. Solomon, *Polymer*, 2005, **46**, 2097–2104.

32. K. Matyjaszewski, *Prog. Polym. Sci.*, 2005, **30**, 858–875.

33. I. Bannister, N. C. Billingham, S. P. Armes, S. P. Rannard, and P. Findlay, *Macromolecules*, 2006, **39**, 7483–7492.

34. R. A. Slater, T. O. McDonald, D. J. Adams, E. R. Draper, J. V. M. Weaver, and S. P. Rannard, *Soft Matter*, 2012, **8**, 9816–9827.

35. F. L. Hatton, L. M. Tatham, L. R. Tidbury, P. Chambon, T. He, A. Owen, and S. P. Rannard, *Chem. Sci.*, 2015, **6**, 326–334.

36. P. J. Flory, *J. Am. Chem. Soc.*, 1941, **63**, 3083–3090.

37. W. H. Stockmayer, *J. Chem. Phys.*, 1944, **12**, 125–131.

2.11 Appendix

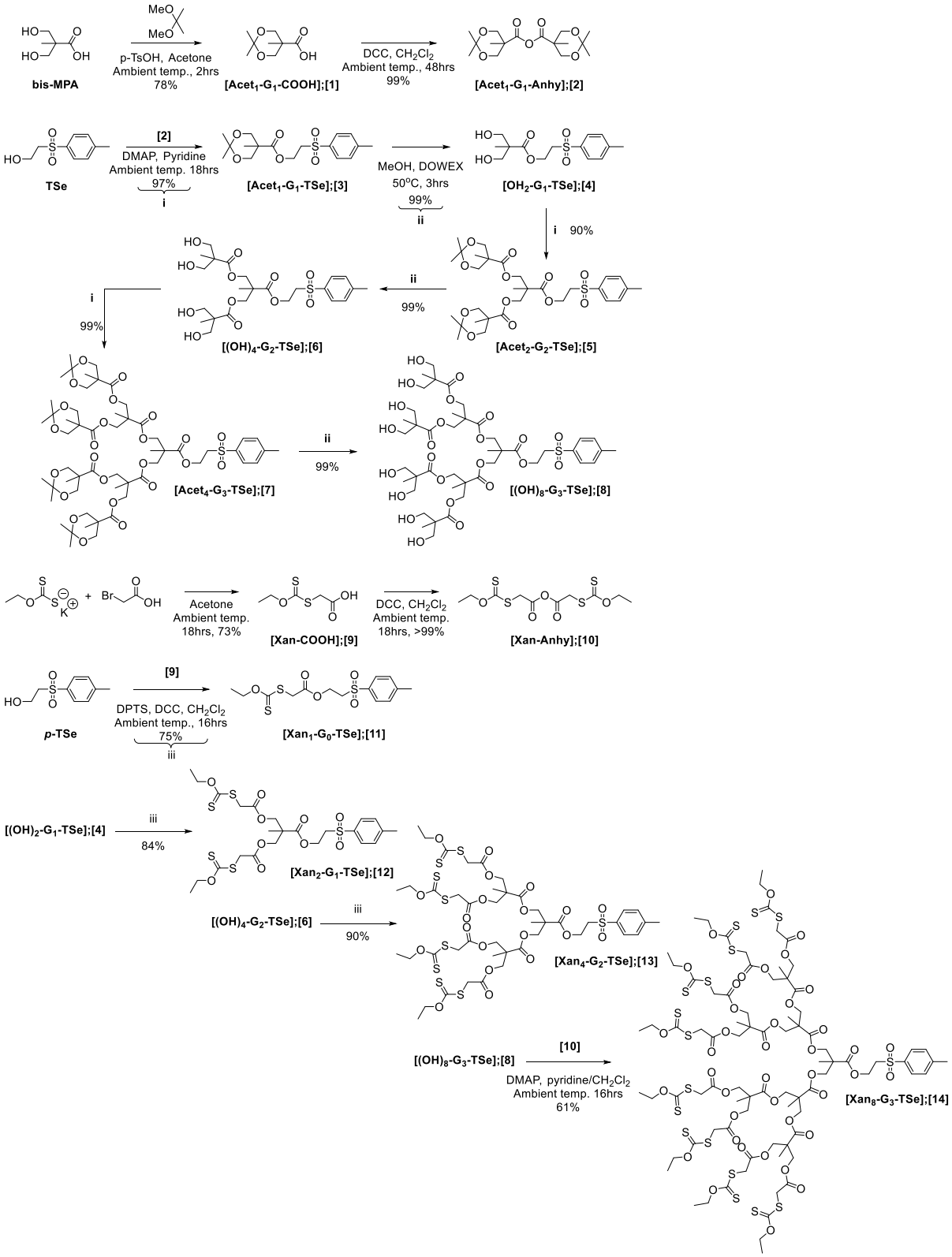

Scheme S2.1 Synthetic strategy for the synthesis of the focal-point protected dendrons used within the study

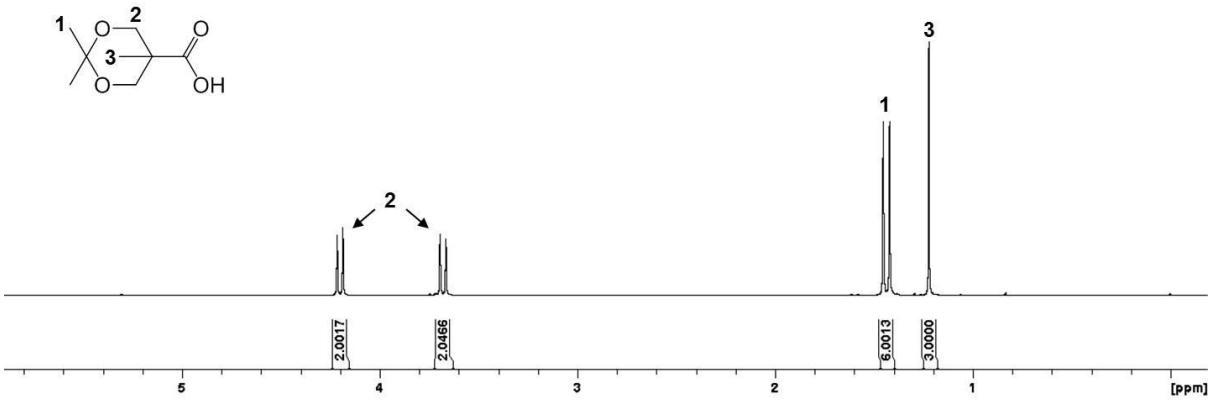

Figure S2.1 ^{1}H NMR (400 MHz, $CDCl_3$) of **[Acet$_1$-G$_1$-COOH];[1]**

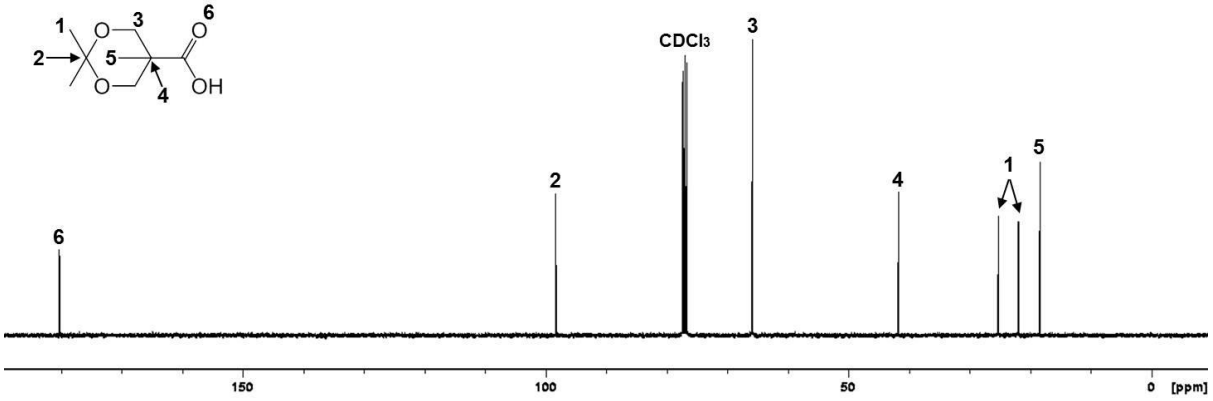

Figure S2.2 ^{13}C NMR (100 MHz, $CDCl_3$) of **[Acet$_1$-G$_1$-COOH];[1]**

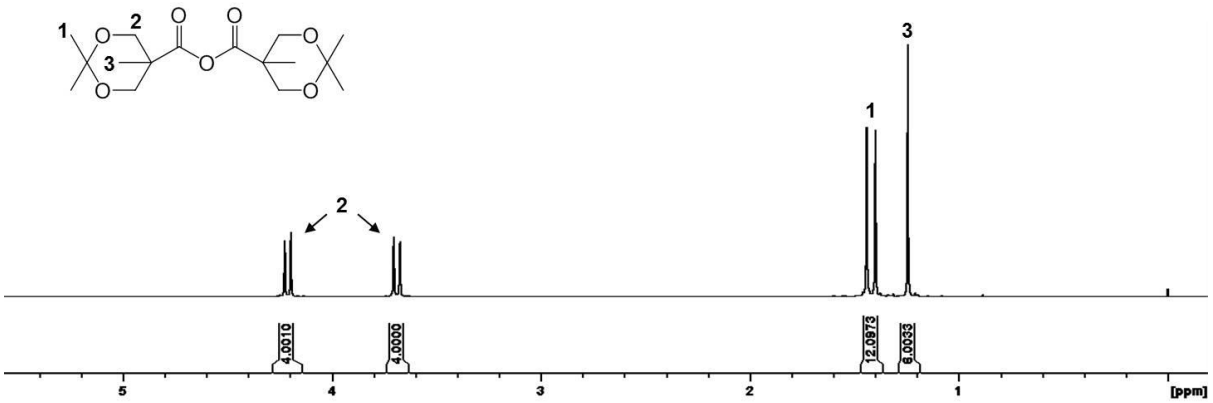

Figure S2.3 ^{1}H NMR (400 MHz, $CDCl_3$) of **[Acet$_1$-G$_1$-Anhy];[2]**

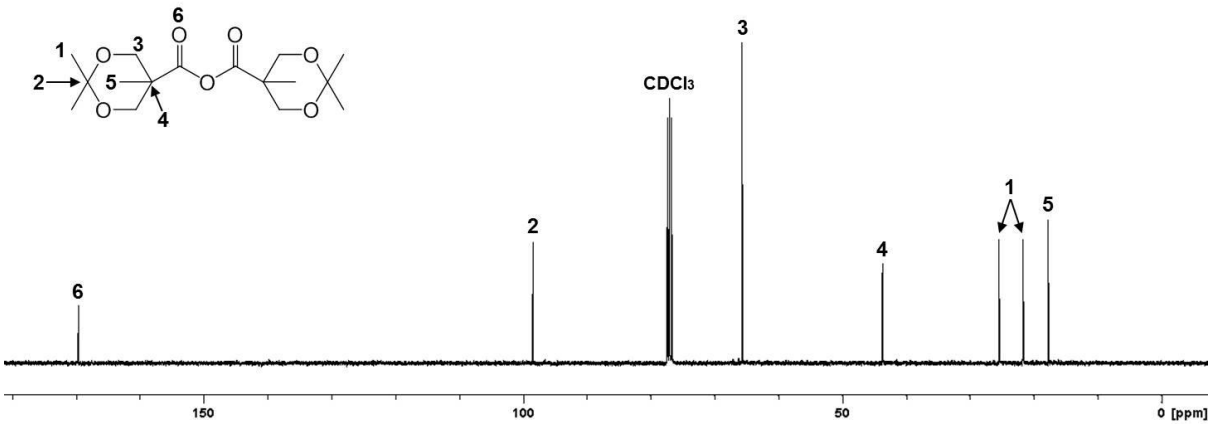

Figure S2.4 ^{13}C NMR (100 MHz, $CDCl_3$) of **[Acet$_1$-G$_1$-Anhy];[2]**

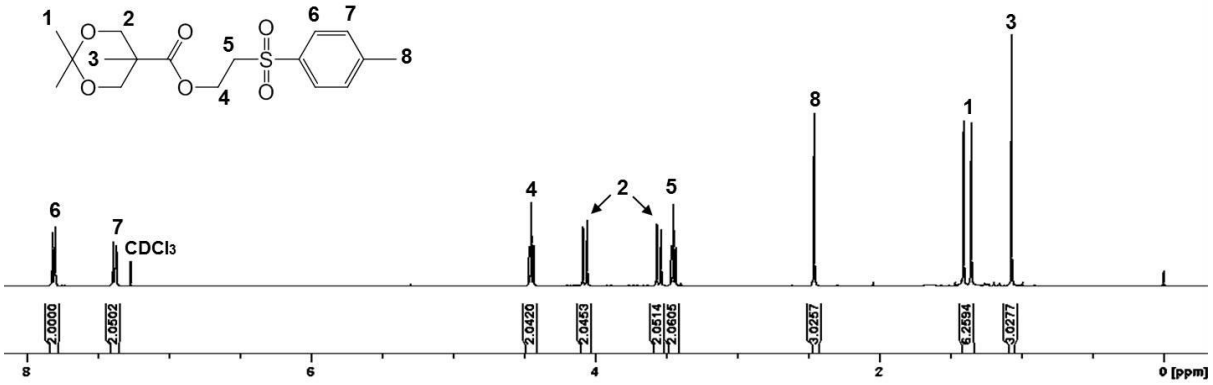

Figure S2.5 ^{1}H NMR (400 MHz, $CDCl_3$) of **[Acet$_1$-G$_1$-TSe];[3]**

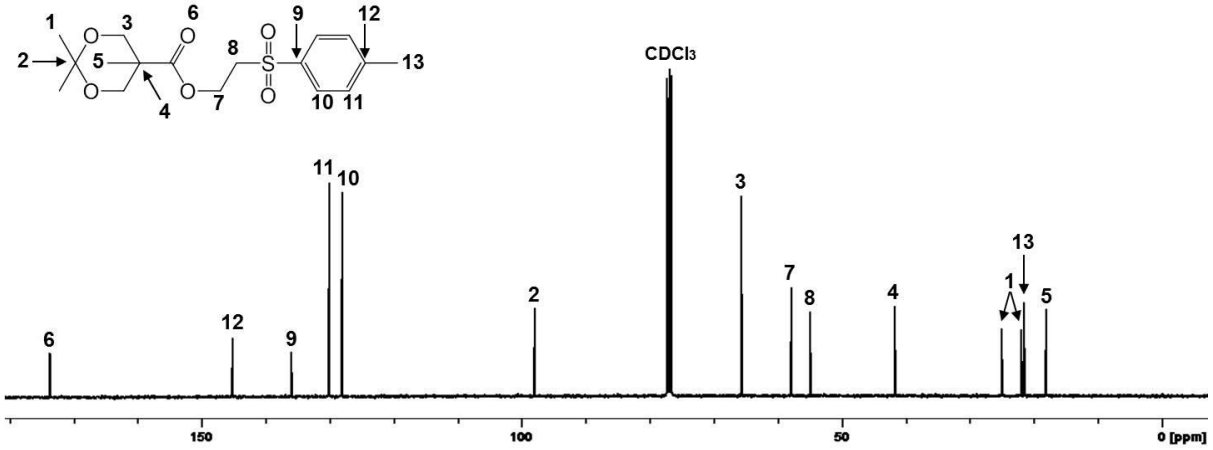

Figure S2.6 ^{13}C NMR (100 MHz, $CDCl_3$) of **[Acet$_1$-G$_1$-TSe];[3]**

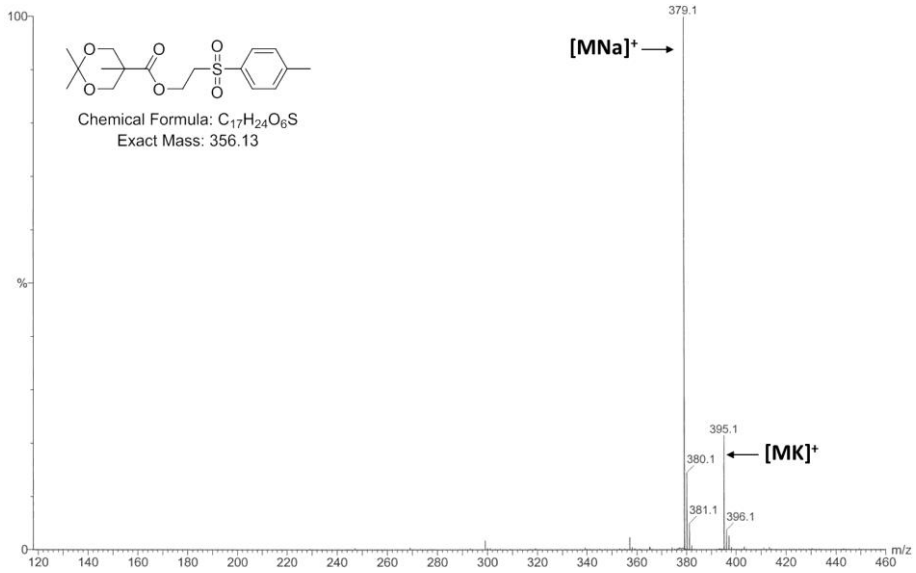

Figure S2.7 ESI MS (MeOH) of **[Acet$_1$-G$_1$-TSe];[3]**

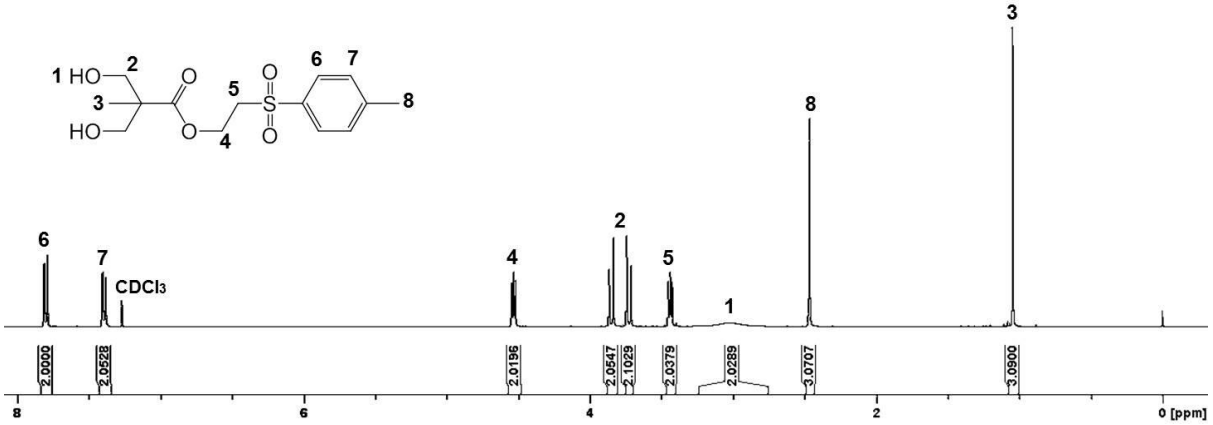

Figure S2.8 ^{1}H NMR (400 MHz, $CDCl_3$) of **[(OH)$_2$-G$_1$-TSe];[4]**

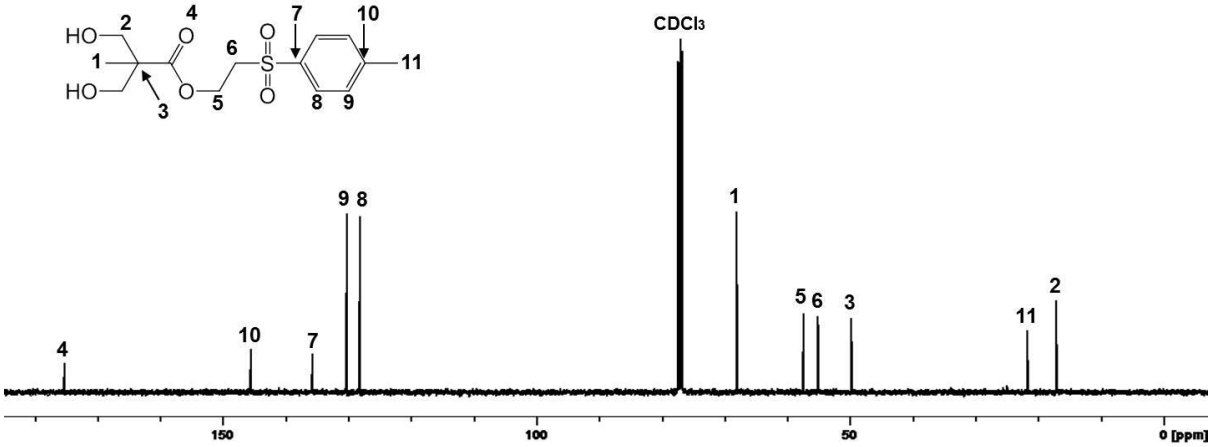

Figure S2.9 ^{13}C NMR (100 MHz, $CDCl_3$) of **[(OH)$_2$-G$_1$-TSe];[4]**

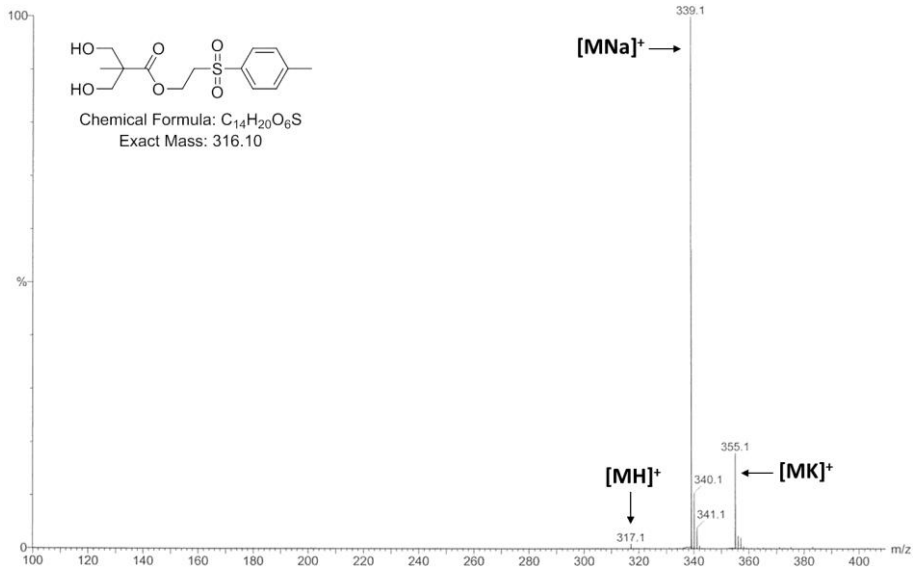

Figure S2.10 ESI MS (MeOH) of **[$(OH)_2$-G_1-TSe];[4]**

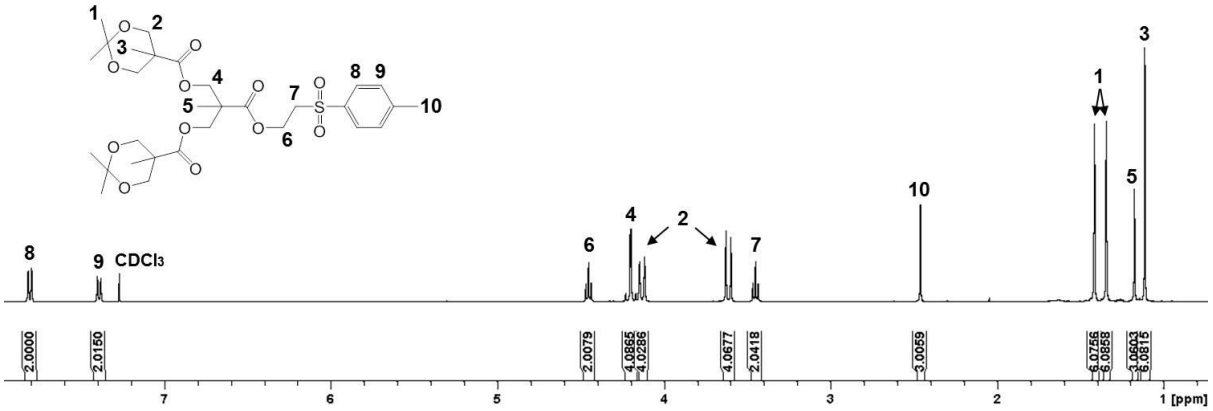

Figure S2.11 ^{1}H NMR (400 MHz, $CDCl_3$) of **[$Acet_2$-G_2-TSe];[5]**

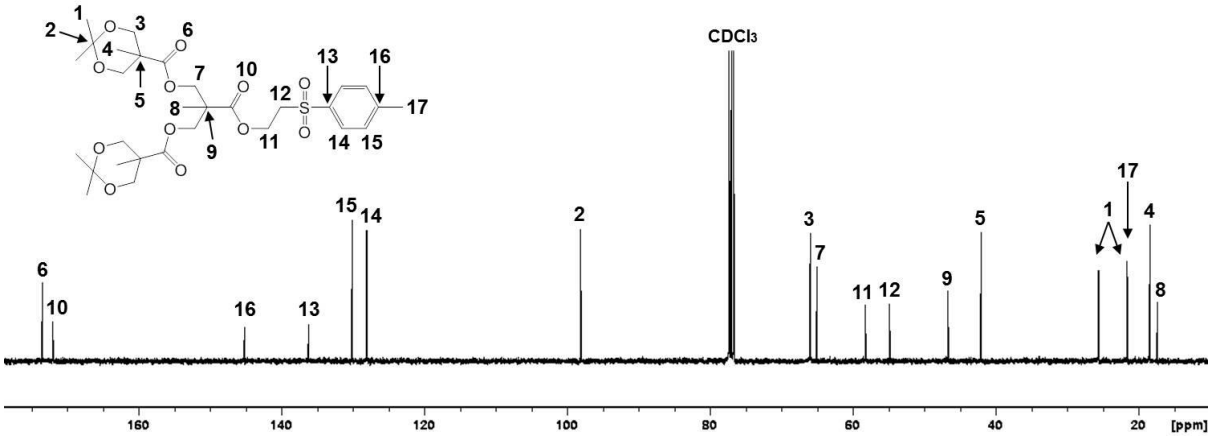

Figure S2.12 ^{13}C NMR (100 MHz, $CDCl_3$) of **[$Acet_2$-G_2-TSe];[5]**

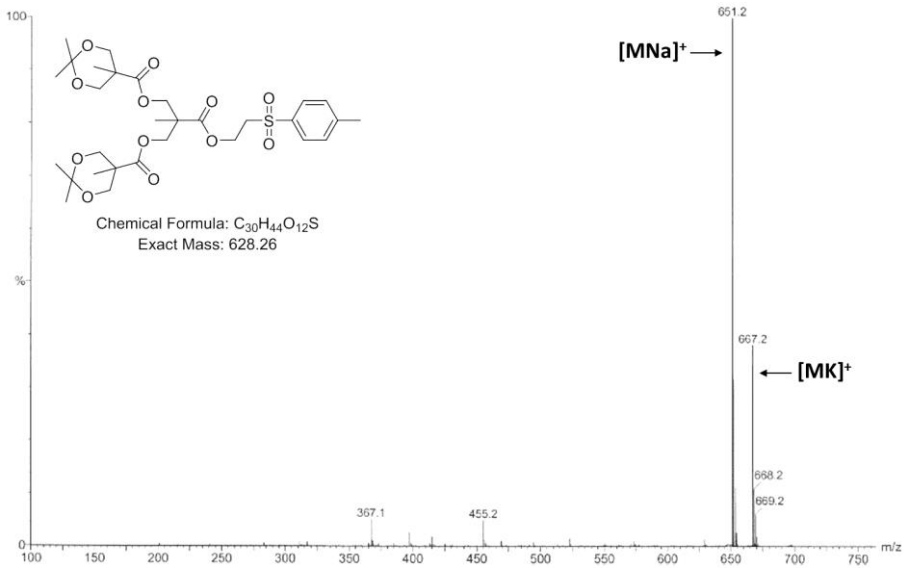

Figure S2.13 ESI MS (MeOH) of **[Acet$_2$-G$_2$-TSe];[5]**

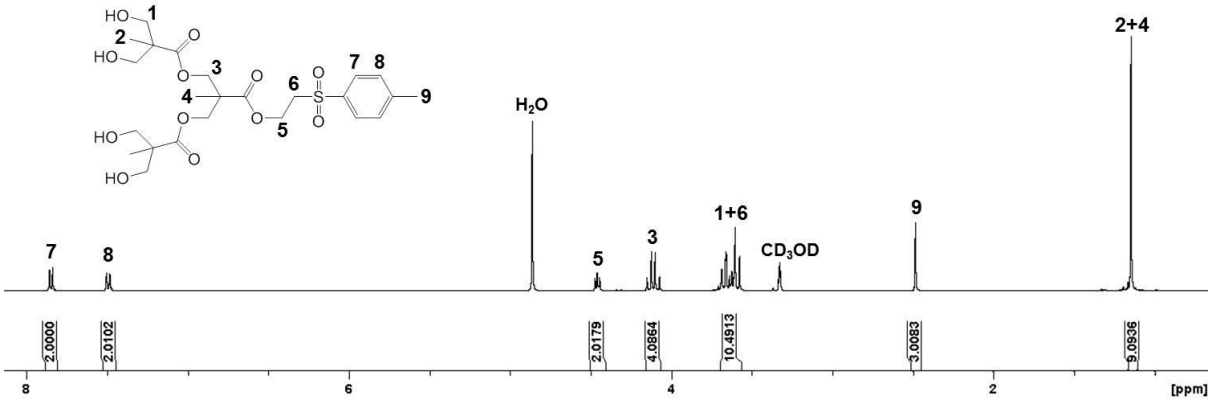

Figure S2.14 ^{1}H NMR (400 MHz, CD_3OD) of **[(OH)$_4$-G$_2$-TSe];[6]**

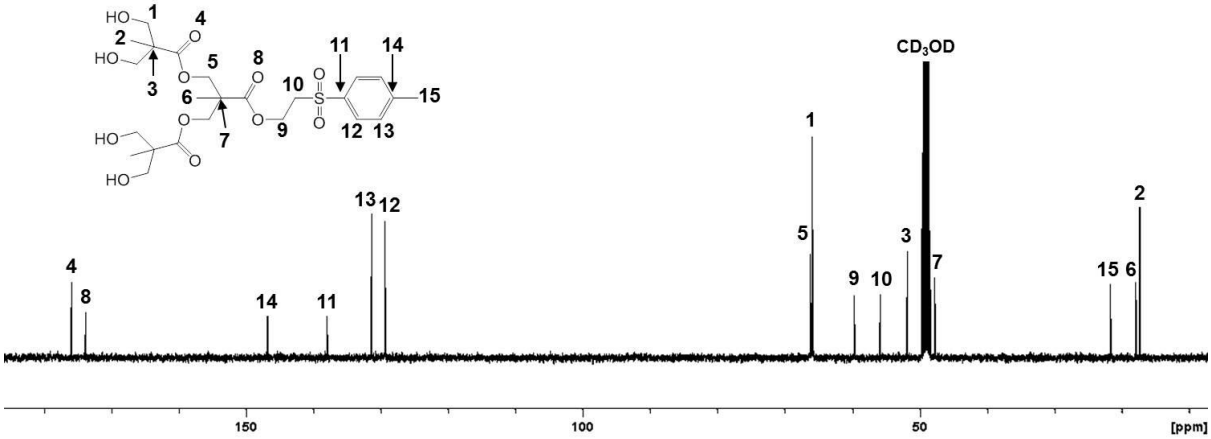

Figure S2.15 ^{13}C NMR (100 MHz, CD_3OD) of **[(OH)$_4$-G$_2$-TSe];[6]**

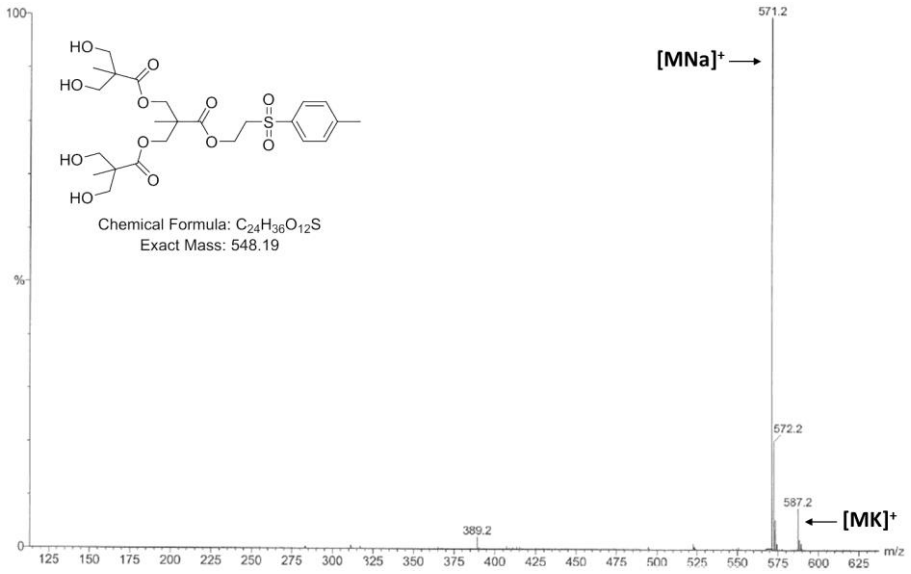

Figure S2.16 ESI MS (MeOH) of **[$(OH)_4$-G_2-TSe];[6]**

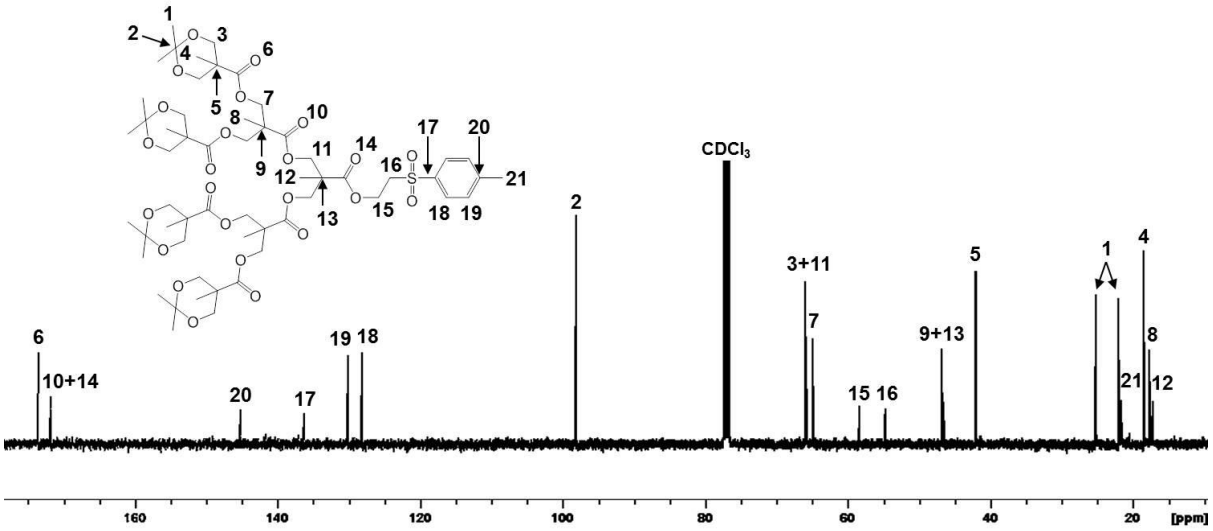

Figure S2.17 ^{13}C NMR (100 MHz, $CDCl_3$) of **[$Acet_4$-G_3-TSe];[7]**

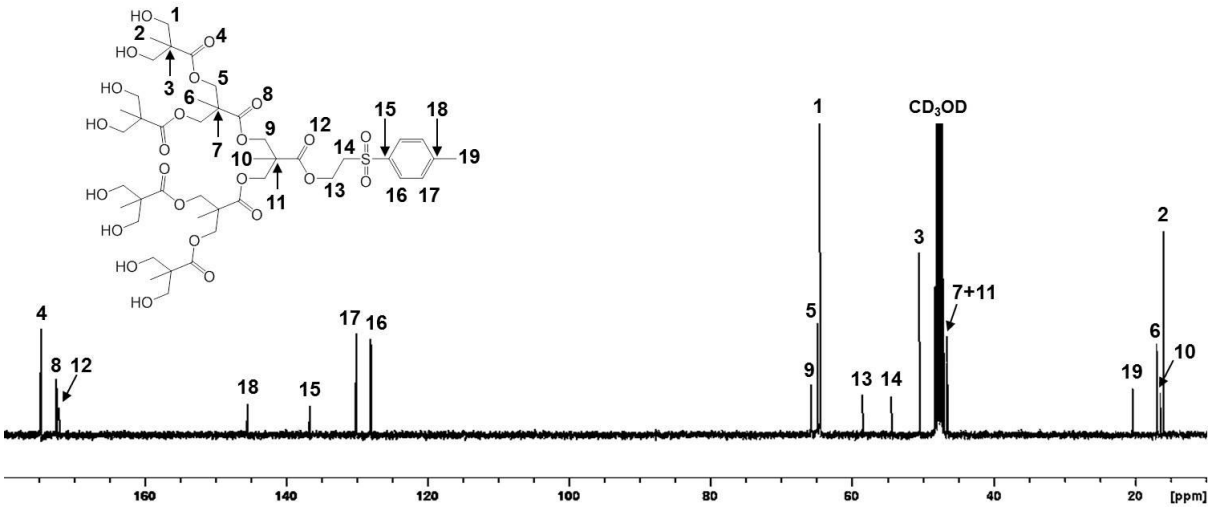

Figure S2.18 ^{13}C NMR (100 MHz, CD_3OD) of **[$(OH)_8$-G_3-TSe];[8]**

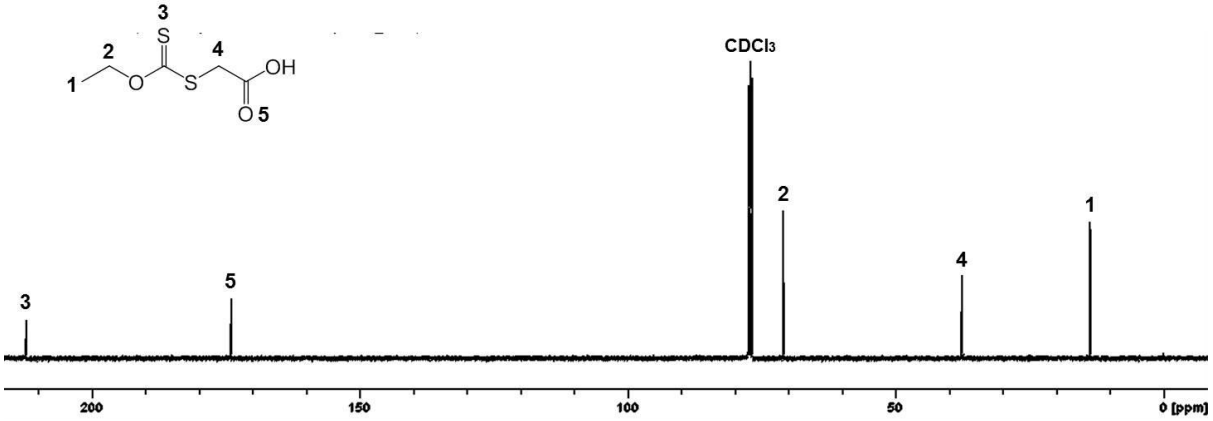

Figure S2.19 ^{13}C NMR (100 MHz, $CDCl_3$) of **2-((Ethoxycarbonothioyl)thio)acetic acid, [Xan-COOH];[9]**

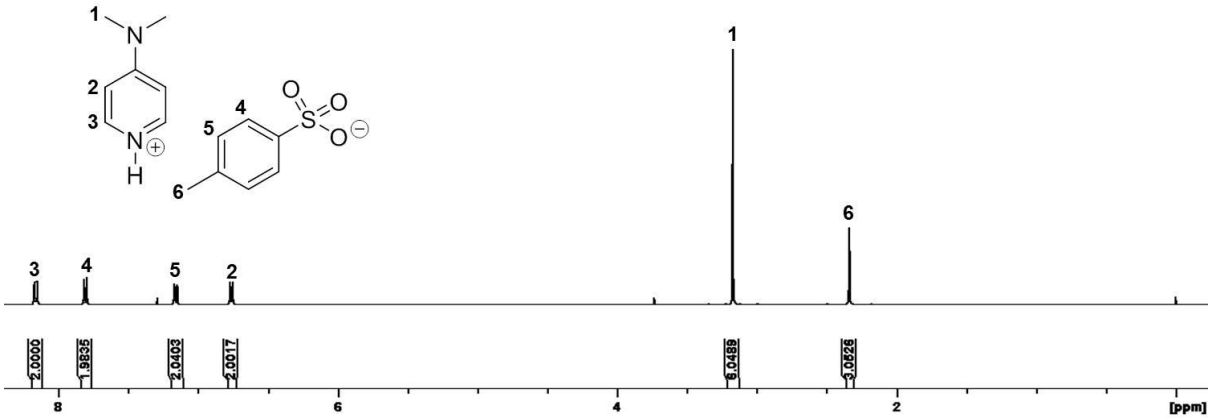

Figure S2.20 ^{1}H NMR (400 MHz, $CDCl_3$) of **DPTS**

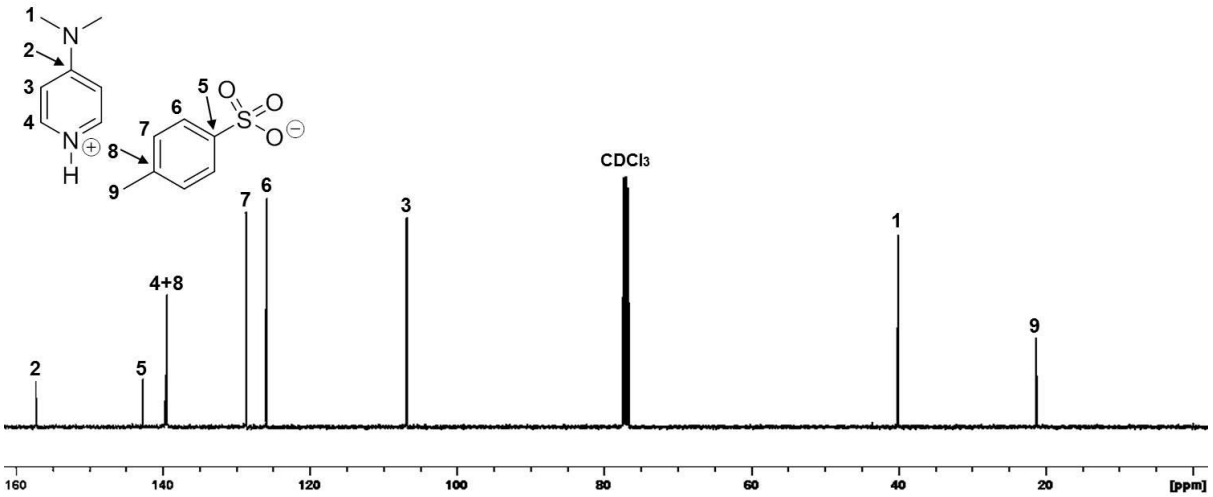

Figure S2.21 ^{13}C NMR (100 MHz, $CDCl_3$) of **DPTS**

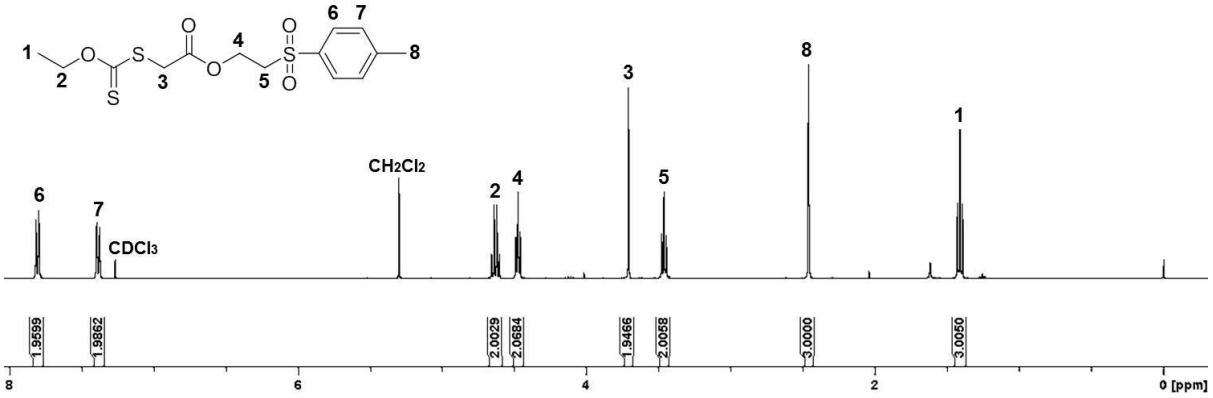

Figure S2.22 ^{1}H NMR (400 MHz, $CDCl_3$) of **[Xan_1-G_0-TSe];[11]**

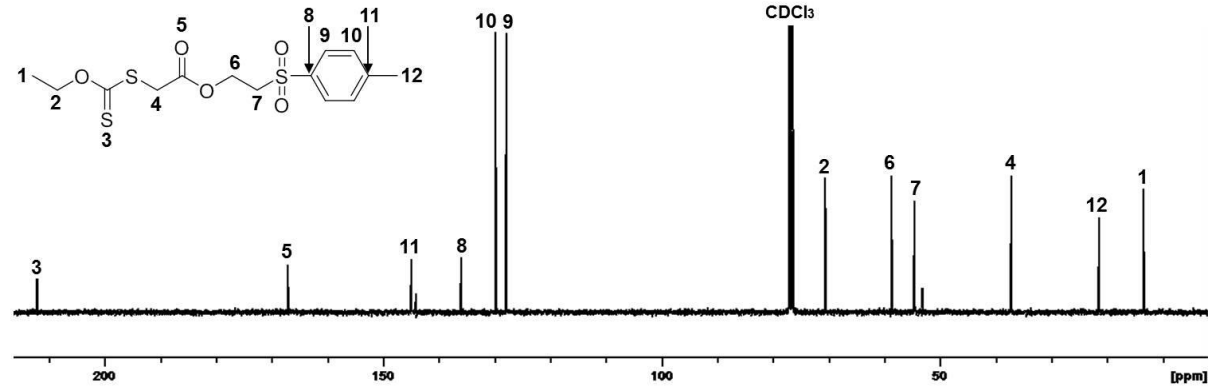

Figure S2.23 ^{13}C NMR (100 MHz, $CDCl_3$) of **[Xan_1-G_0-TSe];[11]**

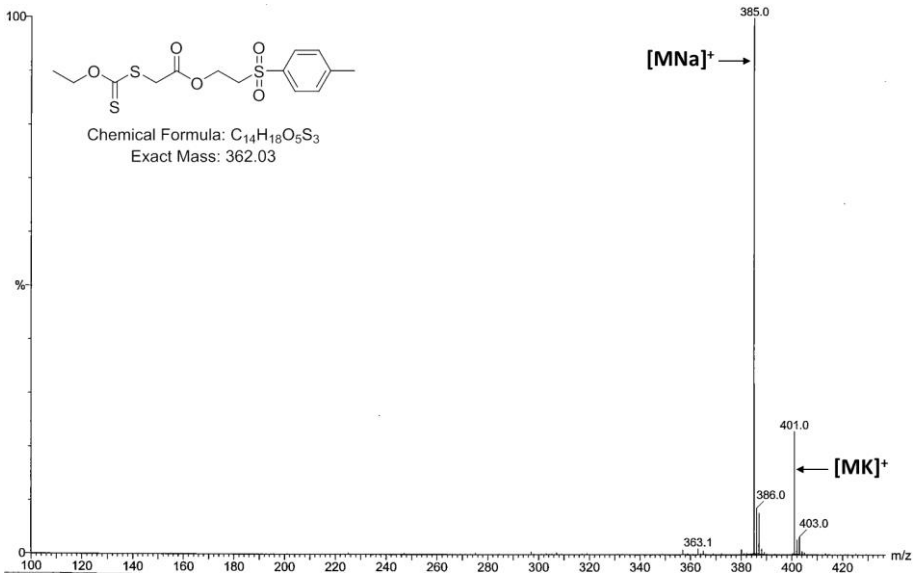

Figure S2.24 ESI-MS (MeOH) of **[Xan$_1$-G$_0$-TSe];[11]**

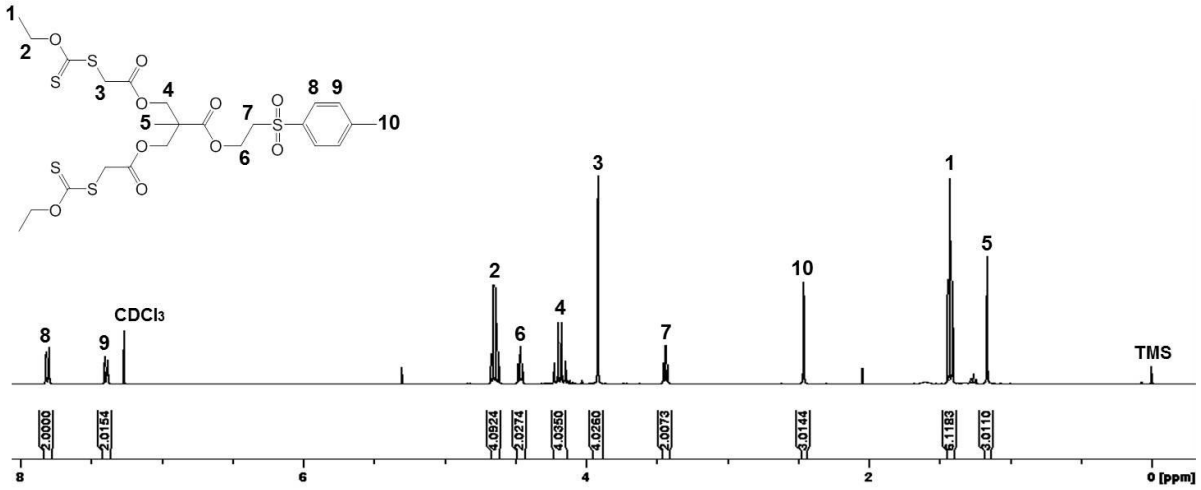

Figure S2.25 ^{1}H NMR (400 MHz, $CDCl_3$) of **[Xan$_2$-G$_1$-TSe];[12]**

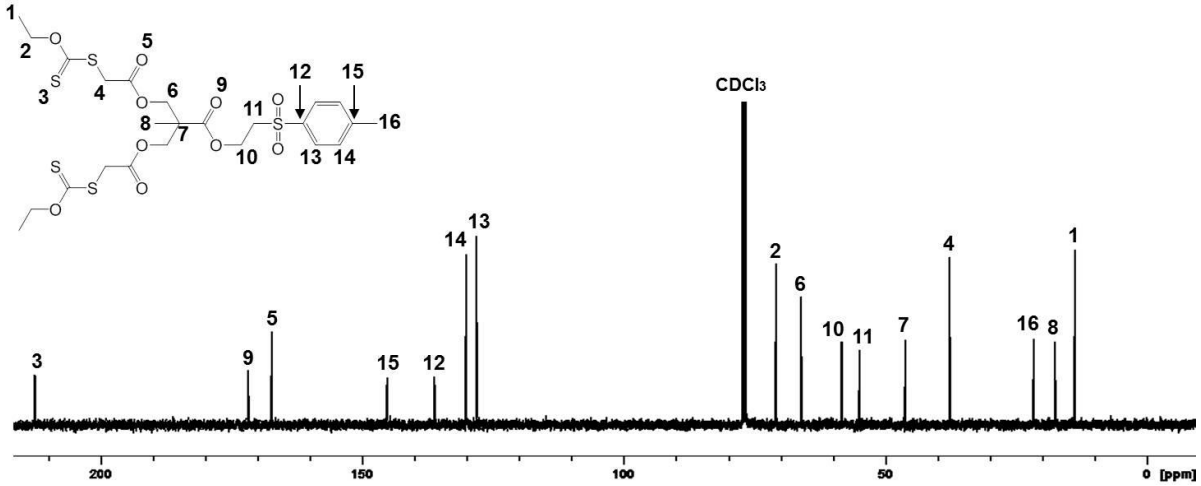

Figure S2.26 ^{13}C NMR (100 MHz, $CDCl_3$) of **[Xan$_2$-G$_1$-TSe];[12]**

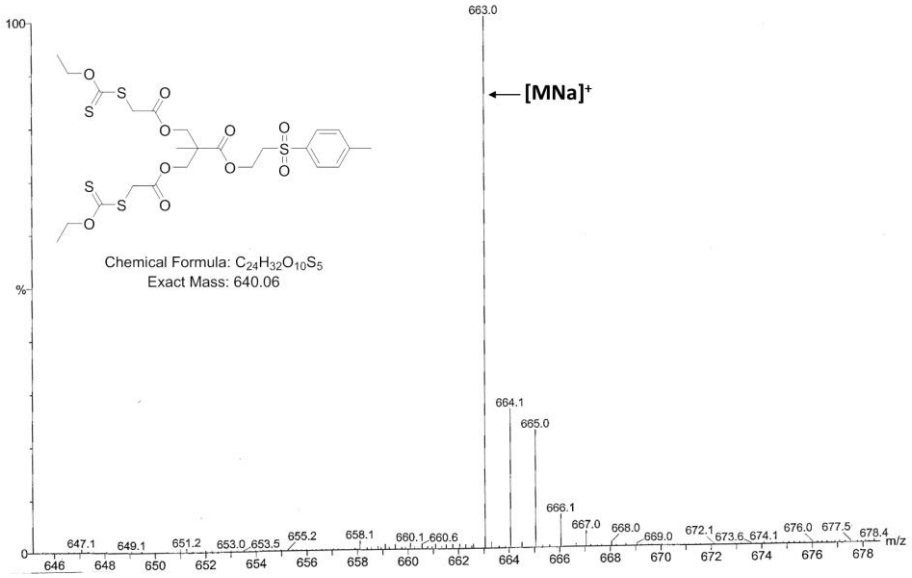

Figure S2.27 ESI-MS (MeOH) of **[Xan$_2$-G$_1$-TSe];[12]**

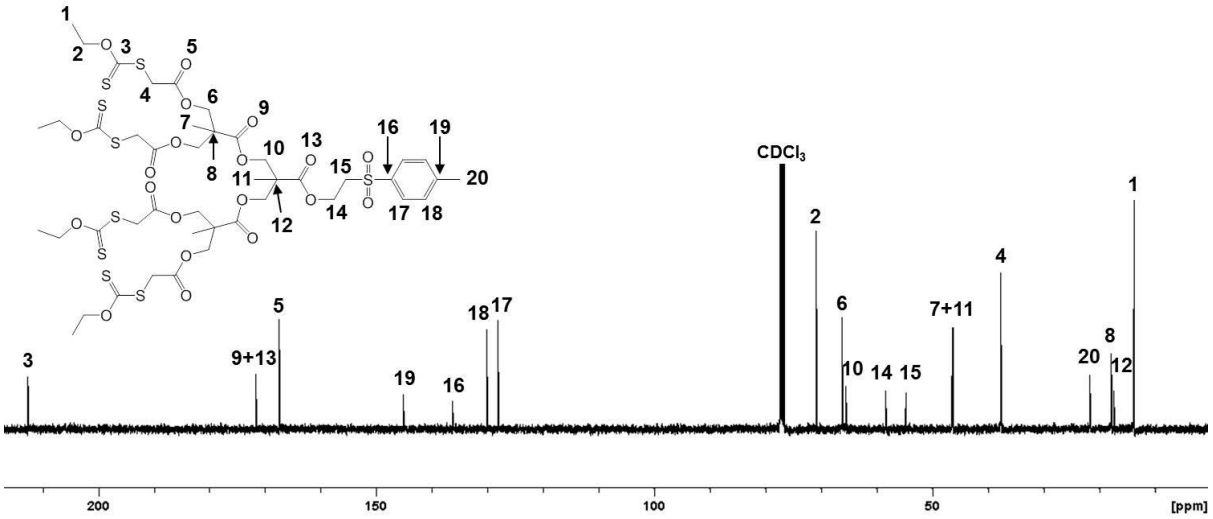

Figure S2.28 ^{13}C NMR (100 MHz, $CDCl_3$) of **[Xan$_4$-G$_2$-TSe];[13]**

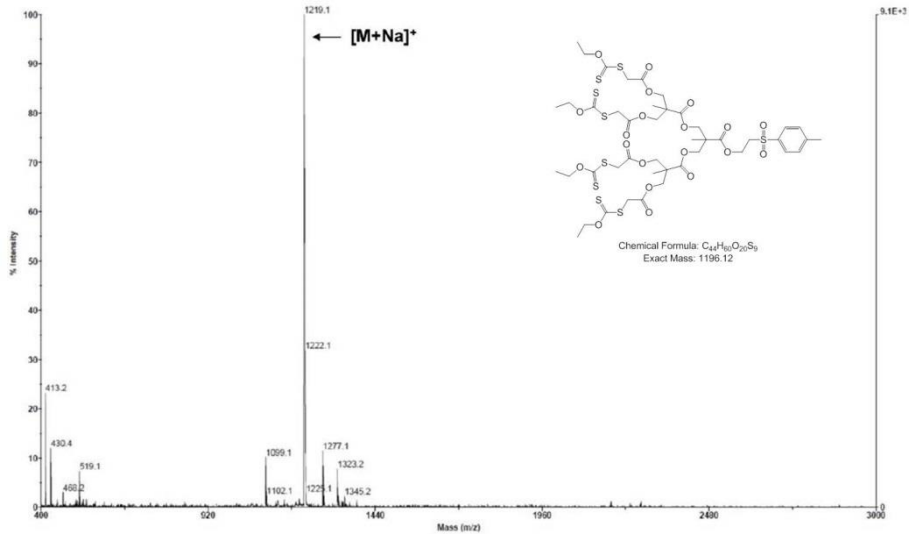

Figure S2.29 MALDI-TOF analysis (dithranol) of **[Xan$_4$-G$_2$-TSe];[13]**

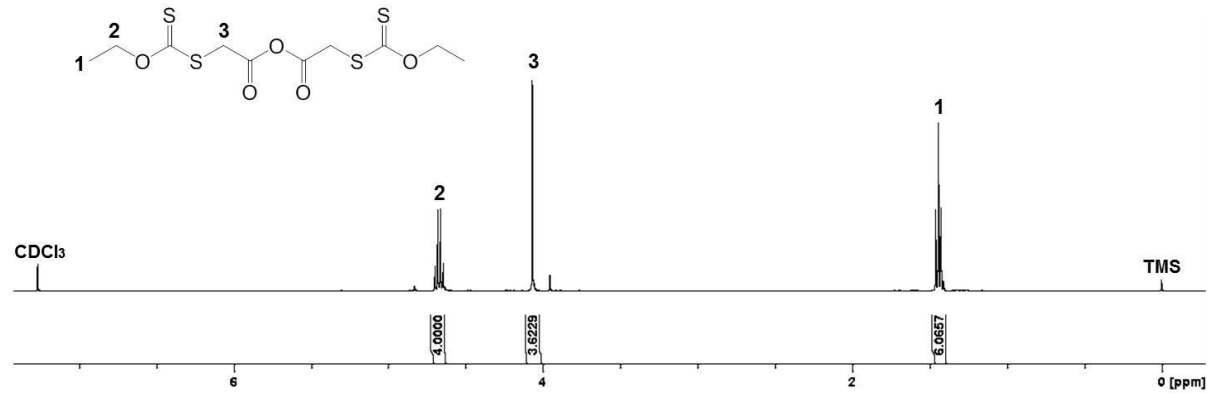

Figure S2.30 ^{1}H NMR (400 MHz, $CDCl_3$) of **2-((Ethoxycarbonothioyl)thio)acetic anhydride, [Xan-Anhy];[10]**

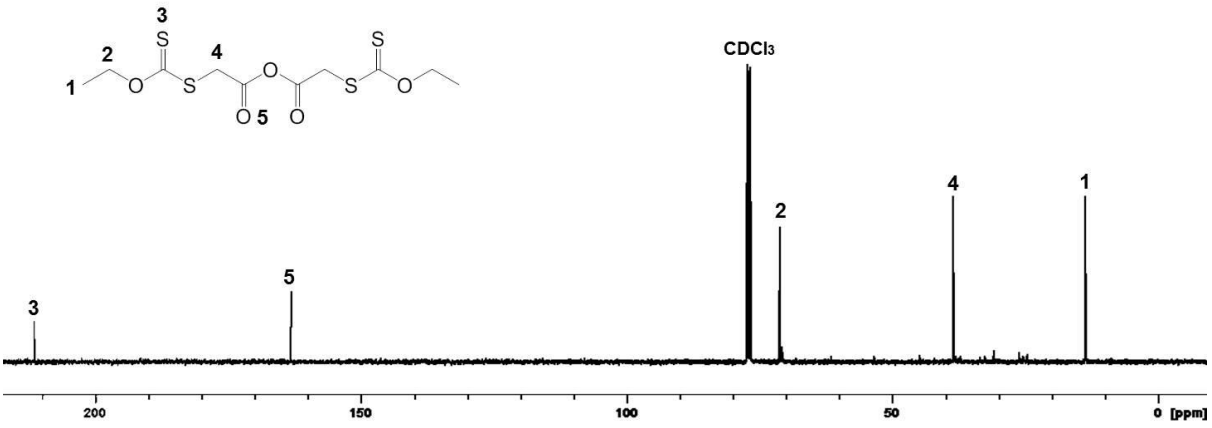

Figure S2.31 ^{13}C NMR (100 MHz, $CDCl_3$) of **2-((Ethoxycarbonothioyl)thio)acetic anhydride, [Xan-Anhy];[10]**

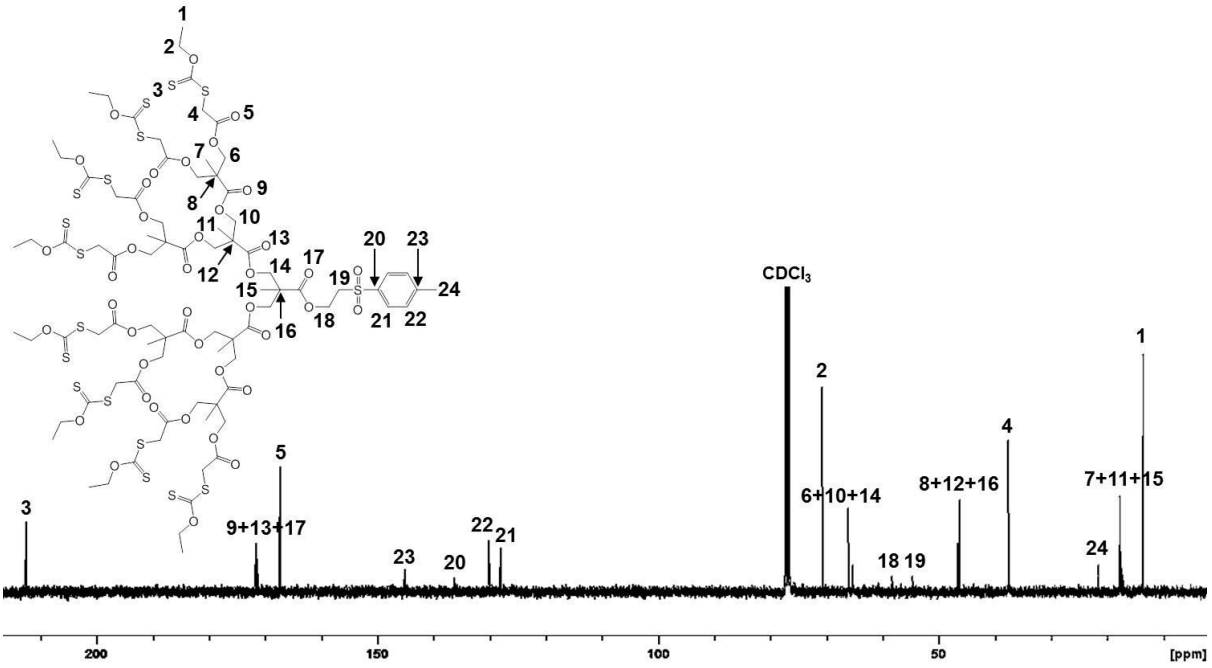

Figure S2.32 ^{13}C NMR (100 MHz, $CDCl_3$) of **[Xan$_8$-G$_3$-TSe];[14]**

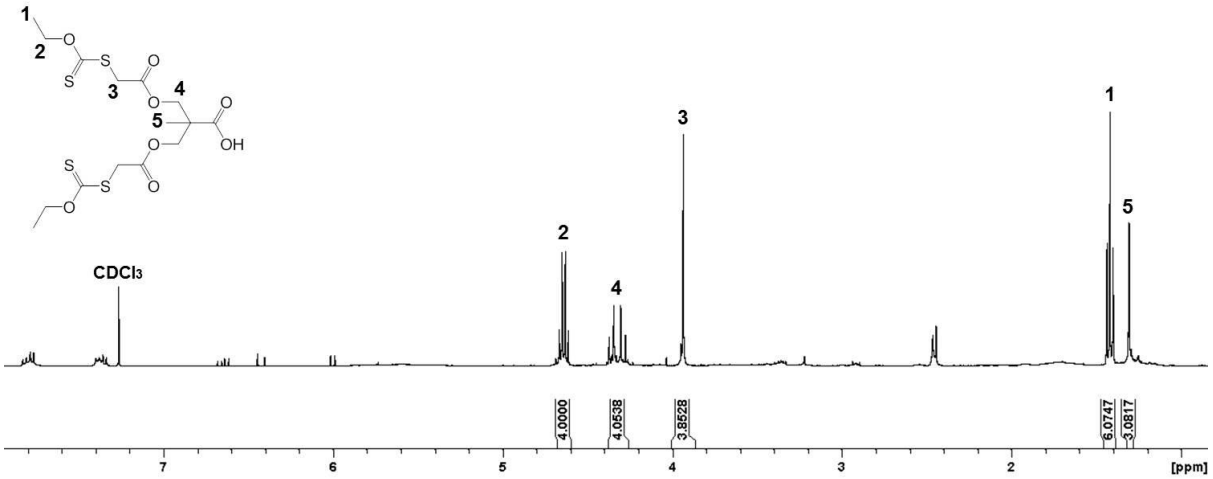

Figure S2.33 ^{1}H NMR (400 MHz, $CDCl_3$) of **[Xan_2-G_1-COOH];[15]**

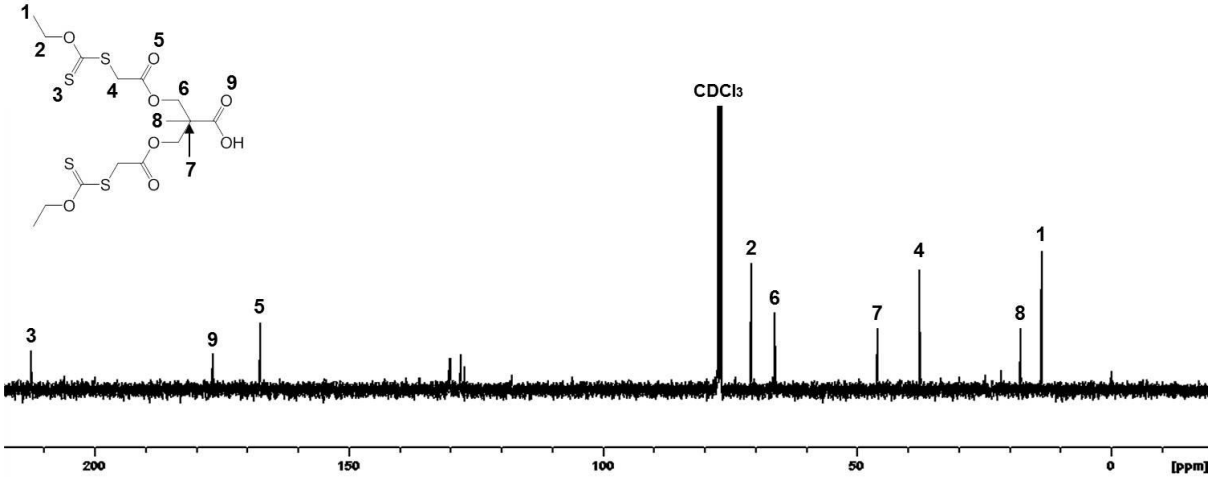

Figure S2.34 ^{13}C NMR (100 MHz, $CDCl_3$) of **[Xan_2-G_1-COOH];[15]**

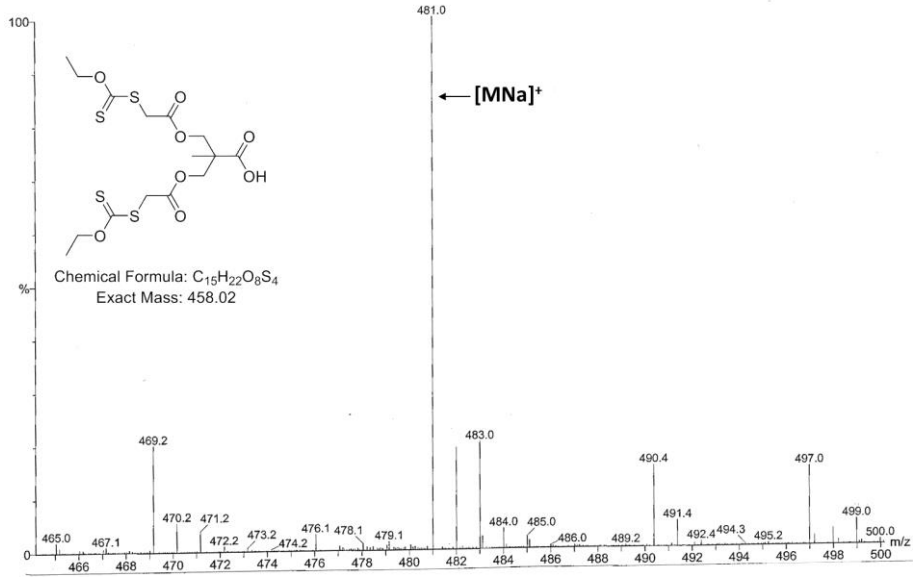

Figure S2.35 ESI MS (MeOH) of **[Xan_2-G_1-COOH];[15]**

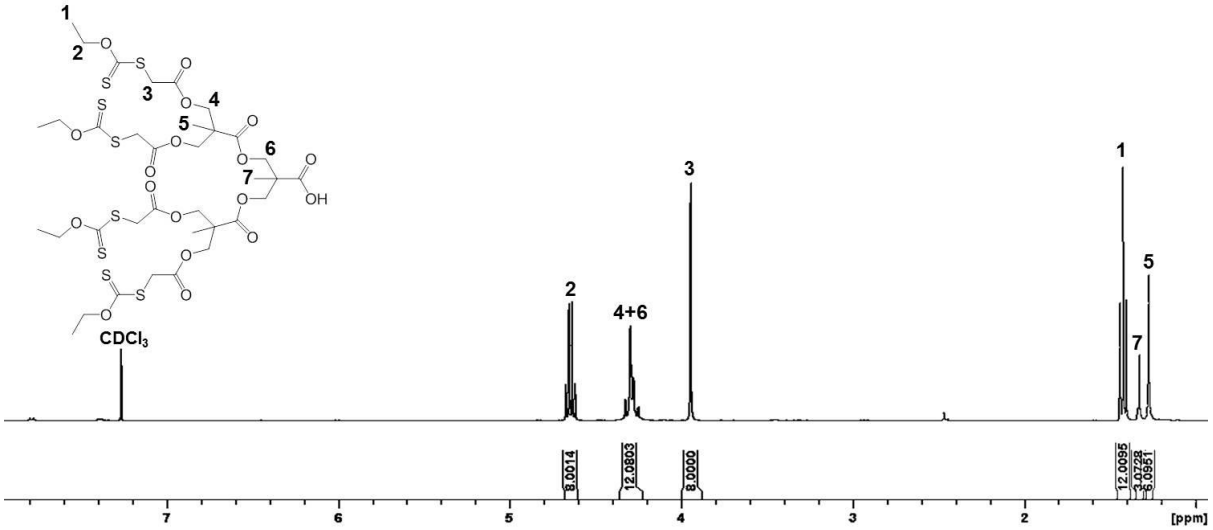

Figure S2.36 ^{1}H NMR (400 MHz, $CDCl_3$) of **[Xan$_4$-G$_2$-COOH];[16]**

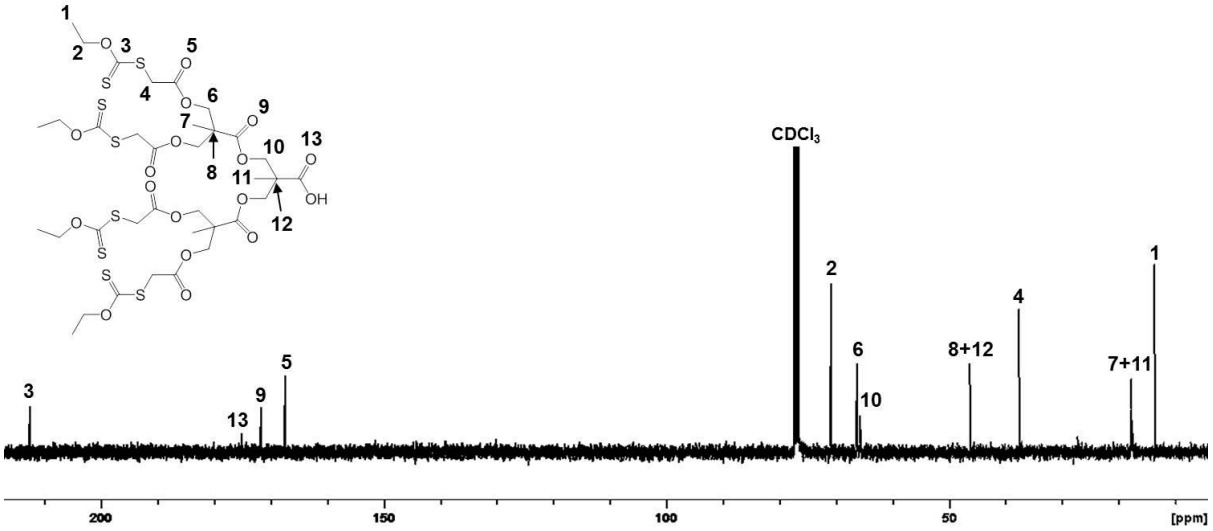

Figure S2.37 ^{13}C NMR (100 MHz, $CDCl_3$) of **[Xan$_4$-G$_2$-COOH];[16]**

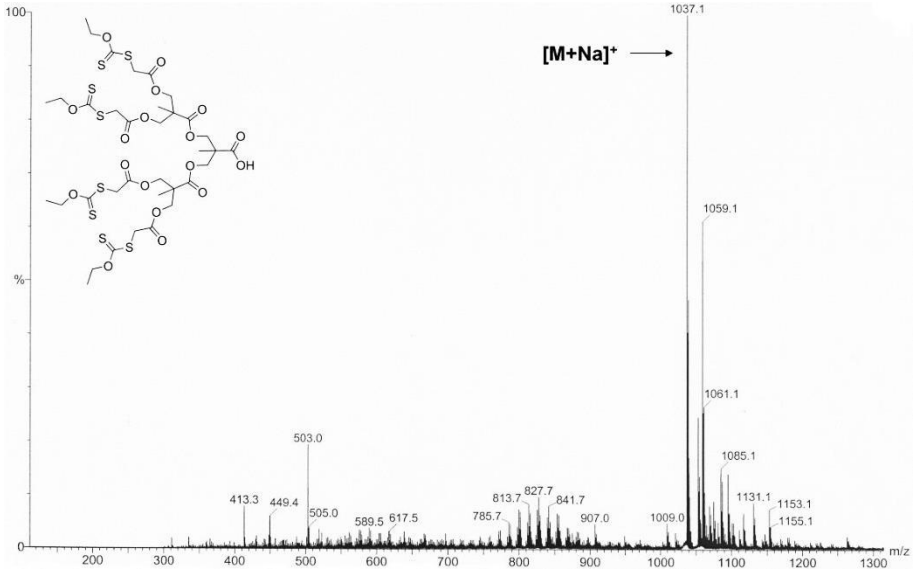

Figure S2.38 ESI MS (MeOH) of **[Xan$_4$-G$_2$-COOH];[16]**

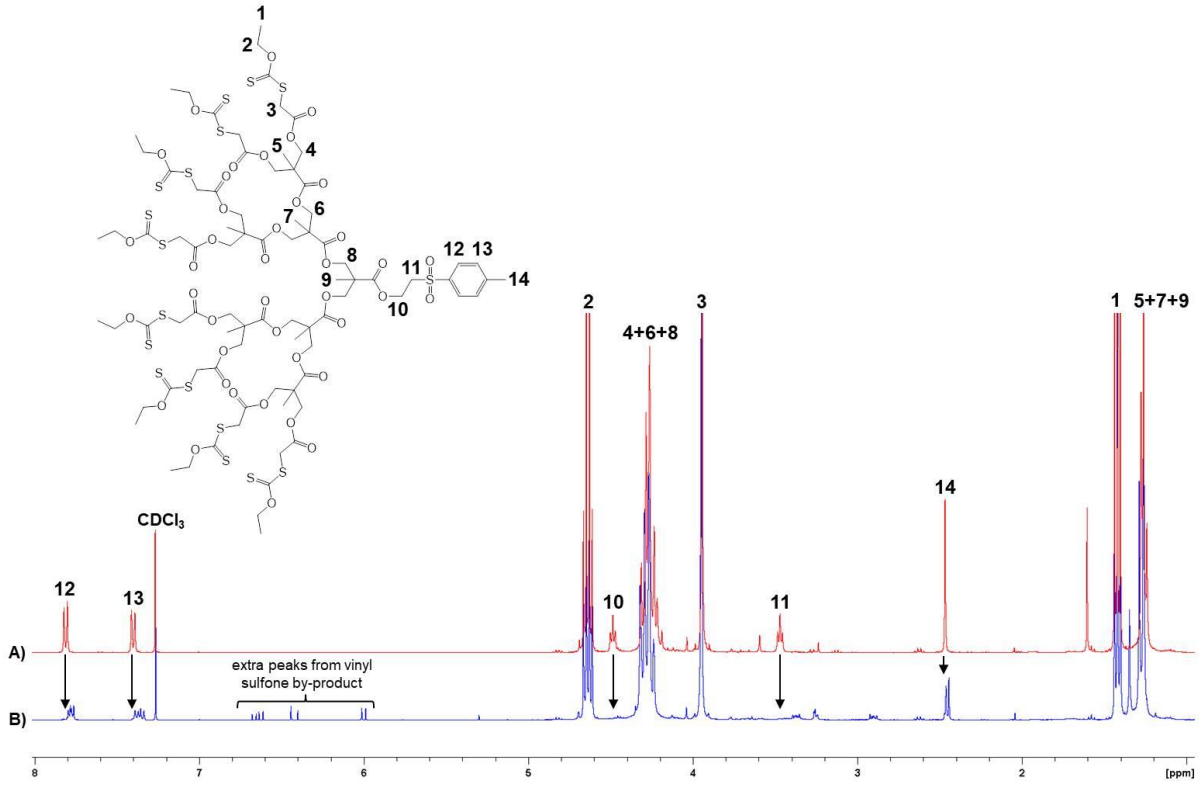

Figure S2.39 ^{1}H NMR (400 MHz, $CDCl_3$) overlay of; A) **[Xan$_8$-G$_3$-TSe];[14]**, and B) **[Xan$_8$-G$_3$-COOH];[17]**

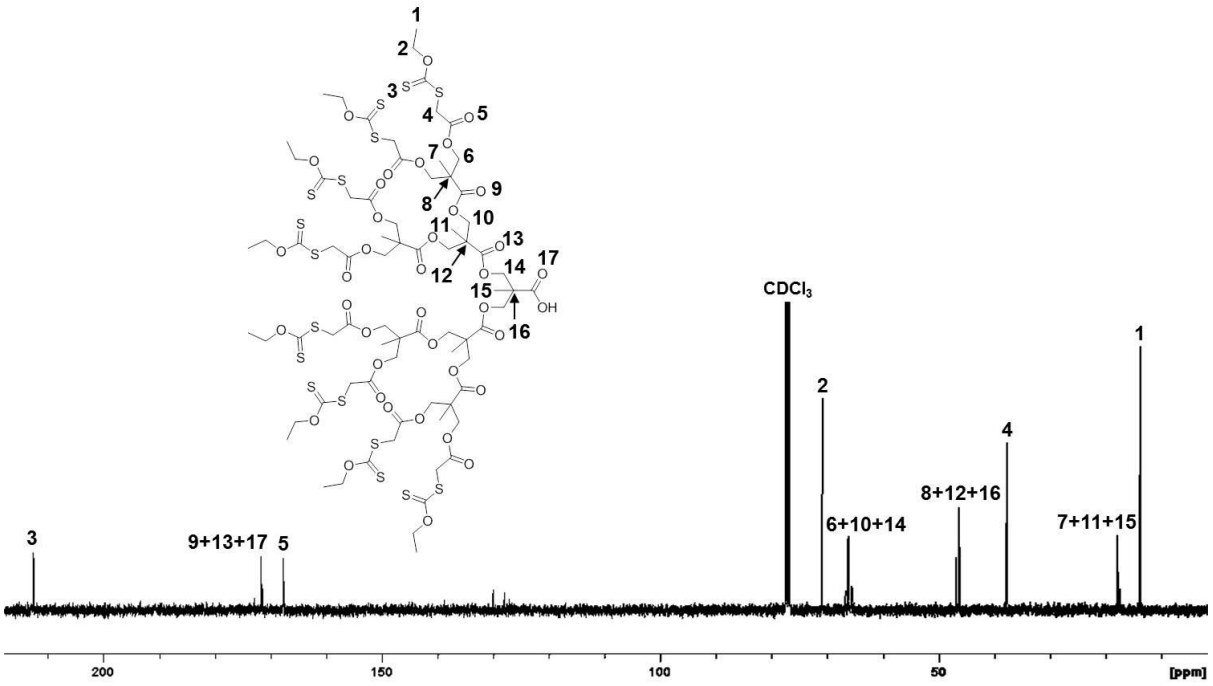

Figure S2.40 ^{13}C NMR (100 MHz, $CDCl_3$) of **[Xan$_8$-G$_3$-COOH];[17]**

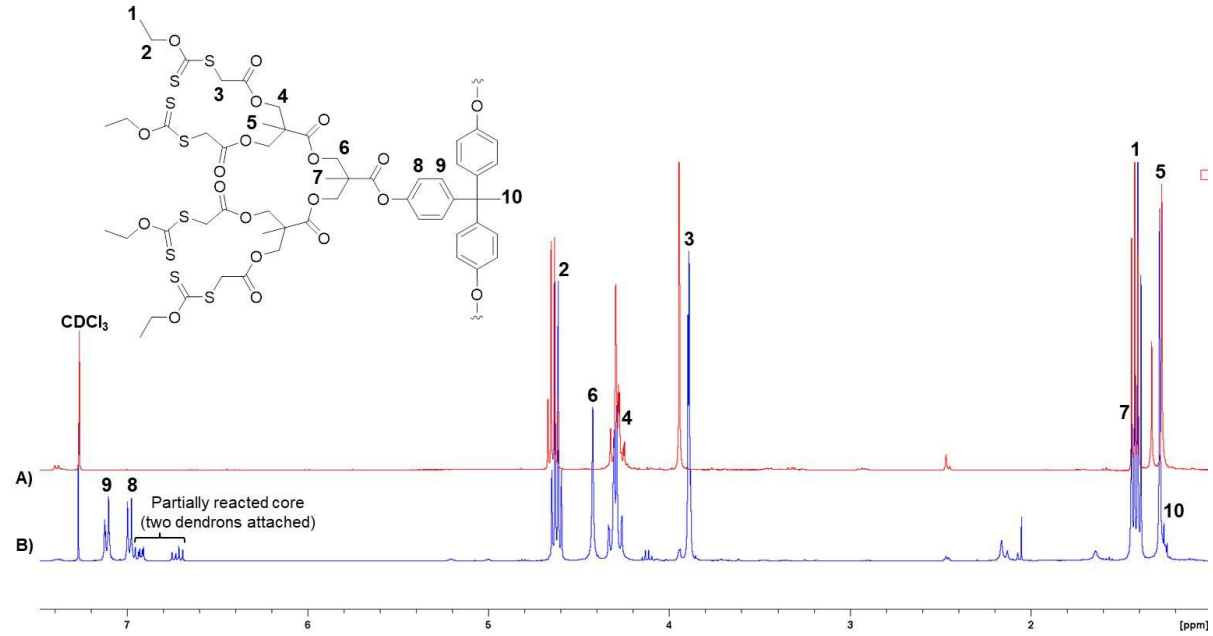

Figure S2.41 ^{1}H NMR (400 MHz, $CDCl_3$) overlay of; A) **[Xan$_4$-G$_2$-COOH];[16]**, and B) **[Xan$_{12}$-G$_2$-THPE];[18]**

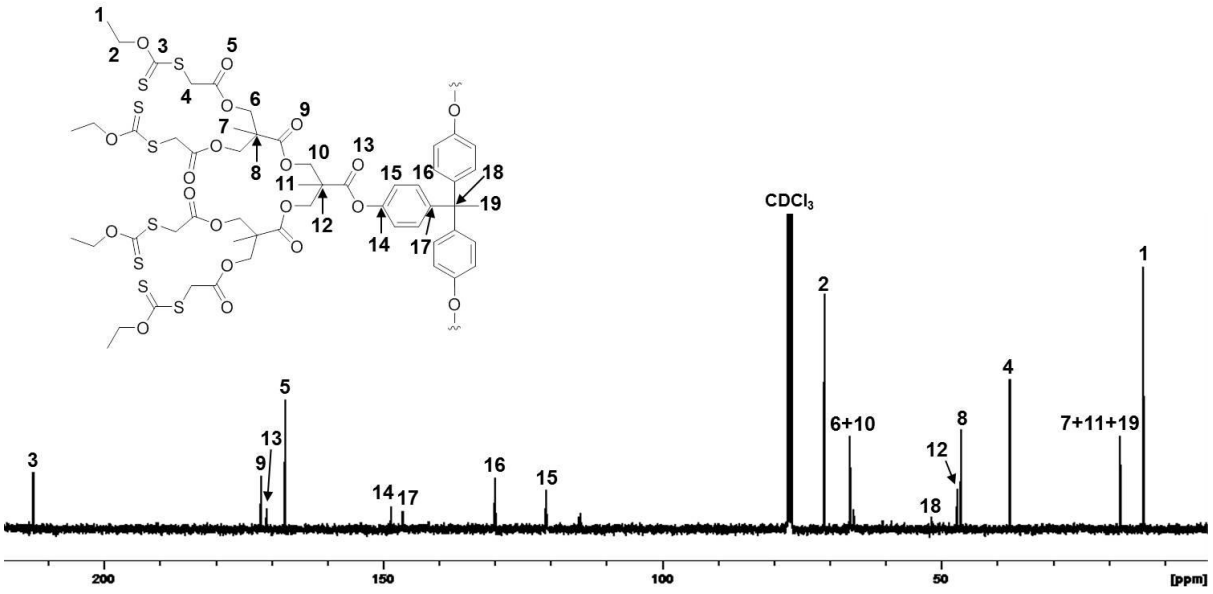

Figure S2.42 ^{13}C NMR (100 MHz, $CDCl_3$) of **[Xan_{12}-G_2-THPE];[18]**

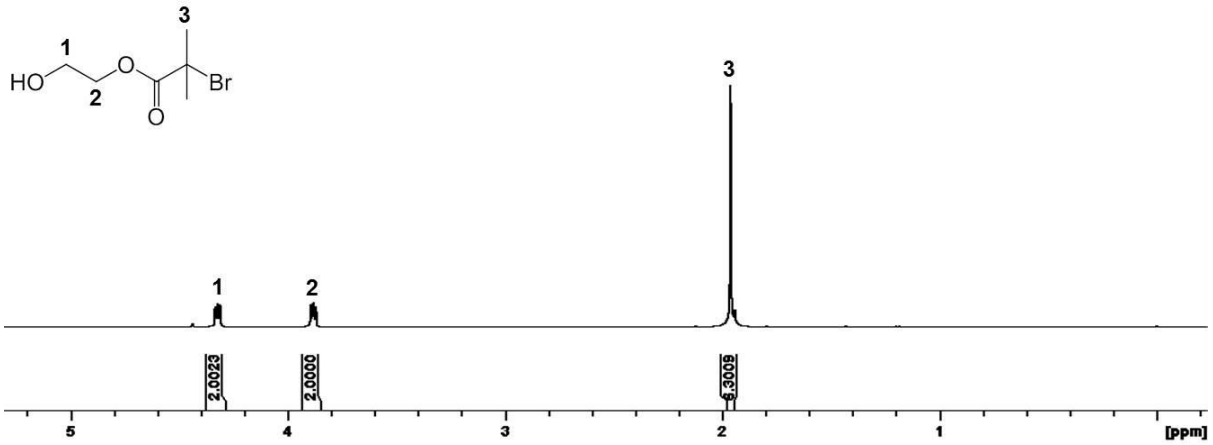

Figure S2.43 ^{1}H NMR (400 MHz, $CDCl_3$) of **[HEBiB];[19]**

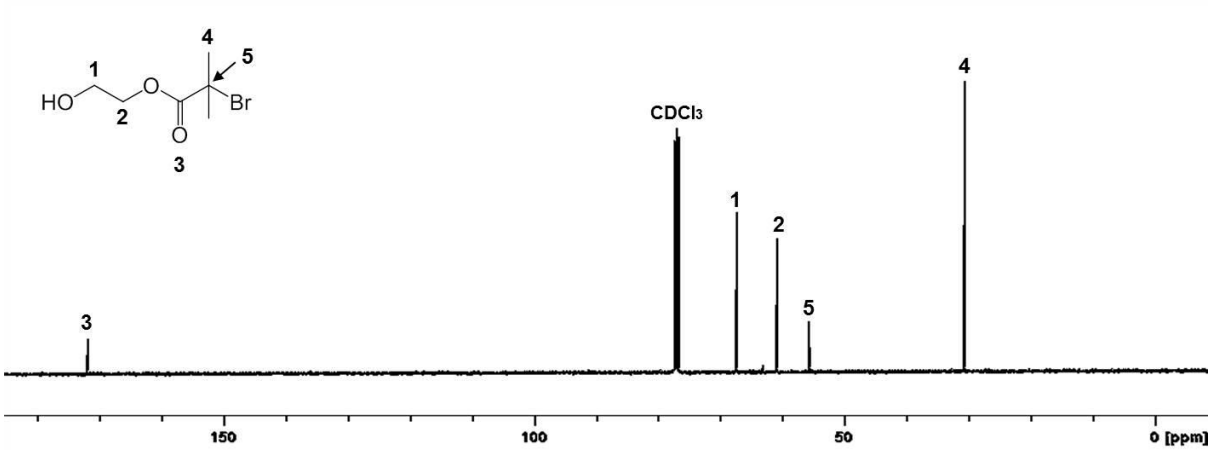

Figure S2.44 ^{13}C NMR (100 MHz, $CDCl_3$) of **[HEBiB];[19]**

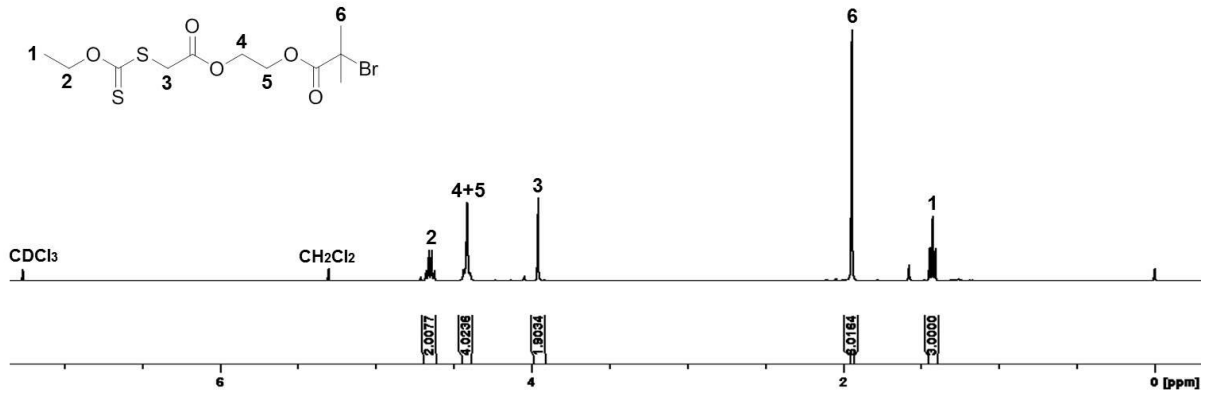

Figure S2.45 ^{1}H NMR (400 MHz, $CDCl_3$) of **[Xan$_1$-G$_0$-BiB];[20]**

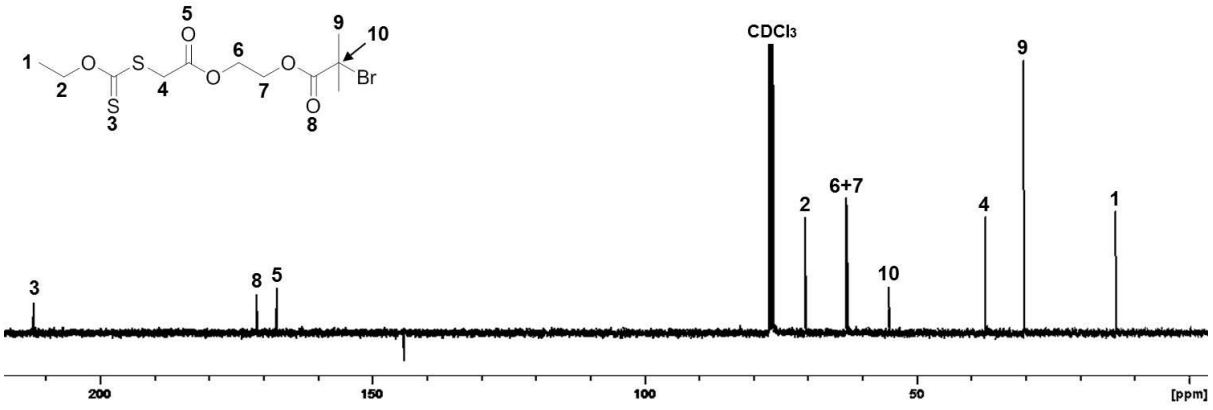

Figure S2.46 ^{13}C NMR (100 MHz, $CDCl_3$) of **[Xan$_1$-G$_0$-BiB];[20]**

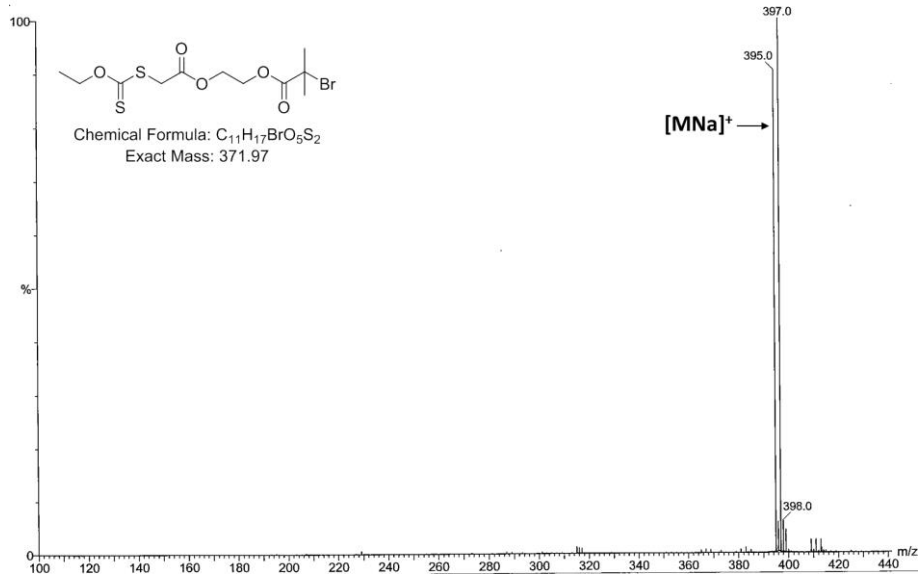

Figure S2.47 ESI-MS (MeOH) of **[Xan$_1$-G$_0$-BiB];[20]**

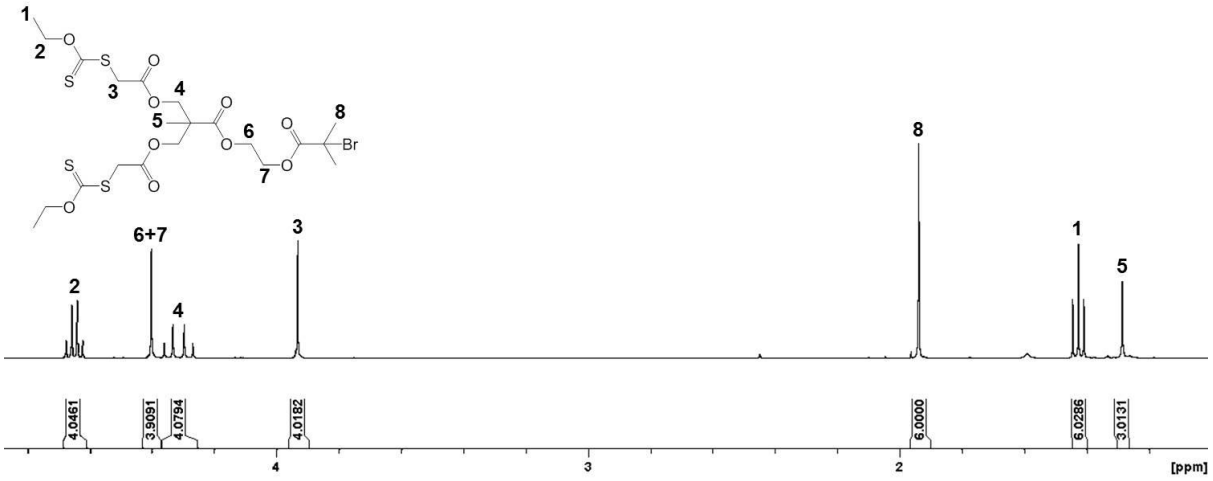

Figure S2.48 ^{1}H NMR (400 MHz, $CDCl_3$) of **[Xan$_2$-G$_1$-BiB];[21]**

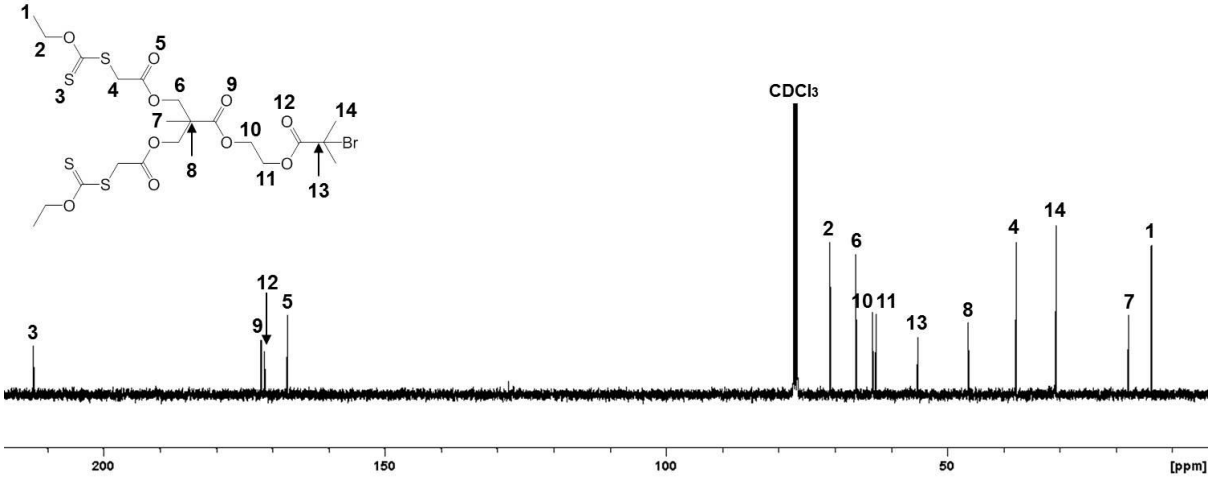

Figure S2.49 ^{13}C NMR (100 MHz, $CDCl_3$) of **[Xan$_2$-G$_1$-BiB];[21]**

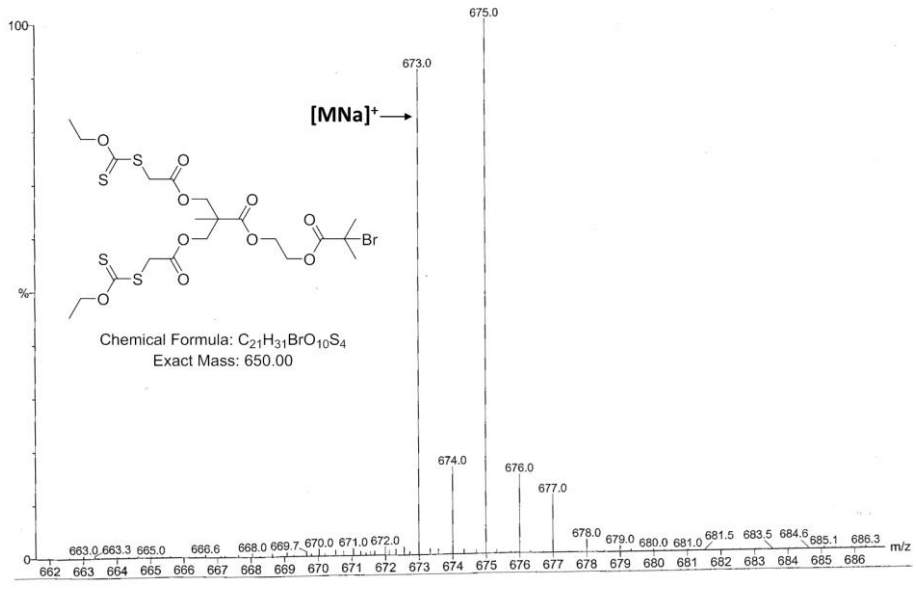

Figure S2.50 ESI MS (MeOH) of **[Xan$_2$-G$_1$-BiB];[21]**

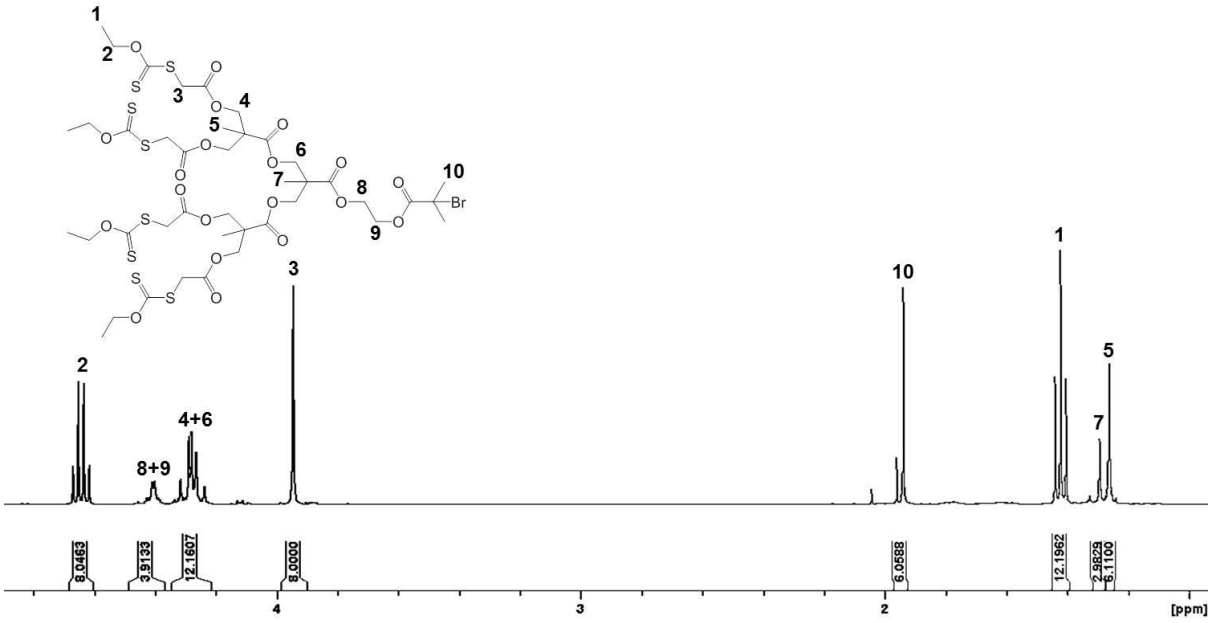

Figure S2.51 ^{1}H NMR (400 MHz, $CDCl_3$) of **[Xan$_4$-G$_2$-BiB];[22]**

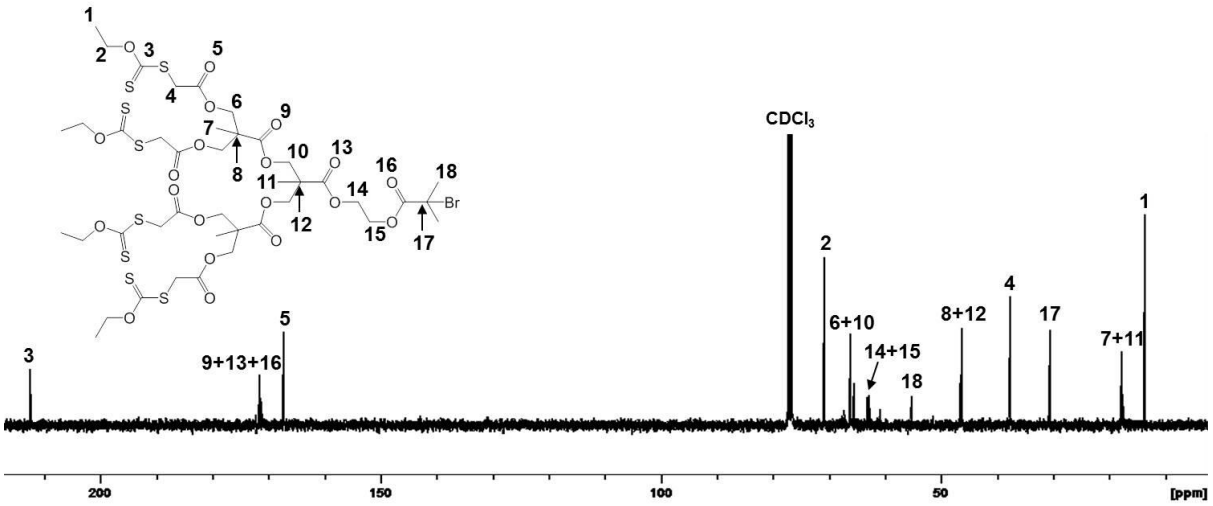

Figure S2.52 ^{13}C NMR (100 MHz, $CDCl_3$) of **[Xan$_4$-G$_2$-BiB];[22]**

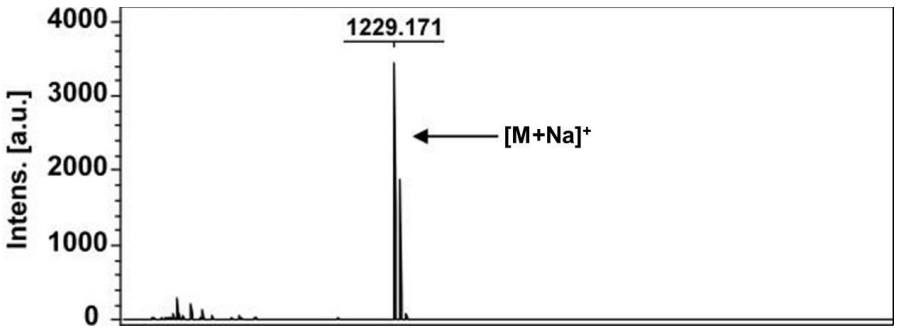

Figure S2.53 MALDI-TOF analysis (dithranol) of **[Xan$_4$-G$_2$-BiB];[22]**

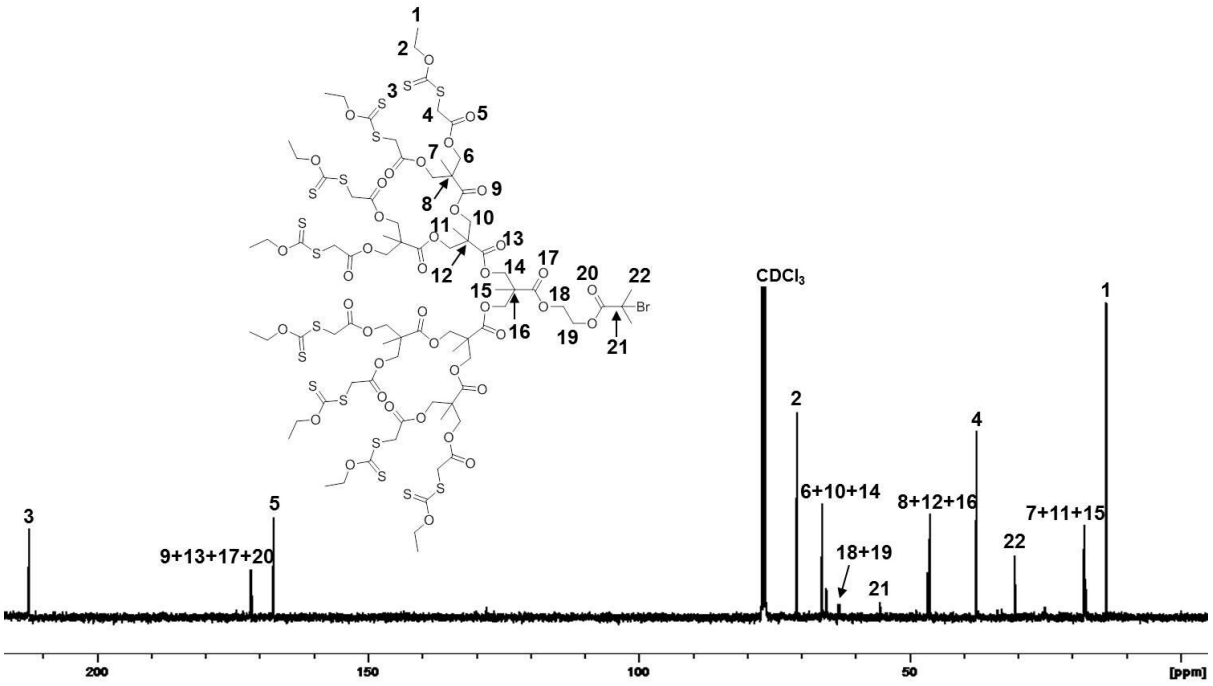

Figure S2.54 ^{13}C NMR (100 MHz, $CDCl_3$) of **[Xan$_8$-G$_3$-BiB];[23]**

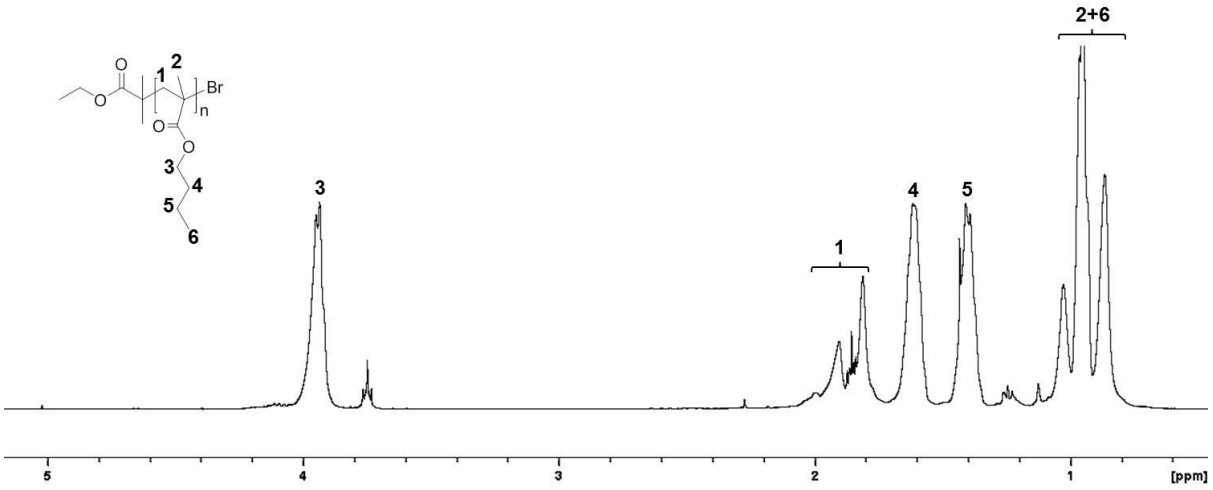

Figure S2.55 ^{1}H NMR (400 MHz, $CDCl_3$) of **p[EBiB-nBMA$_{50}$];[24]**

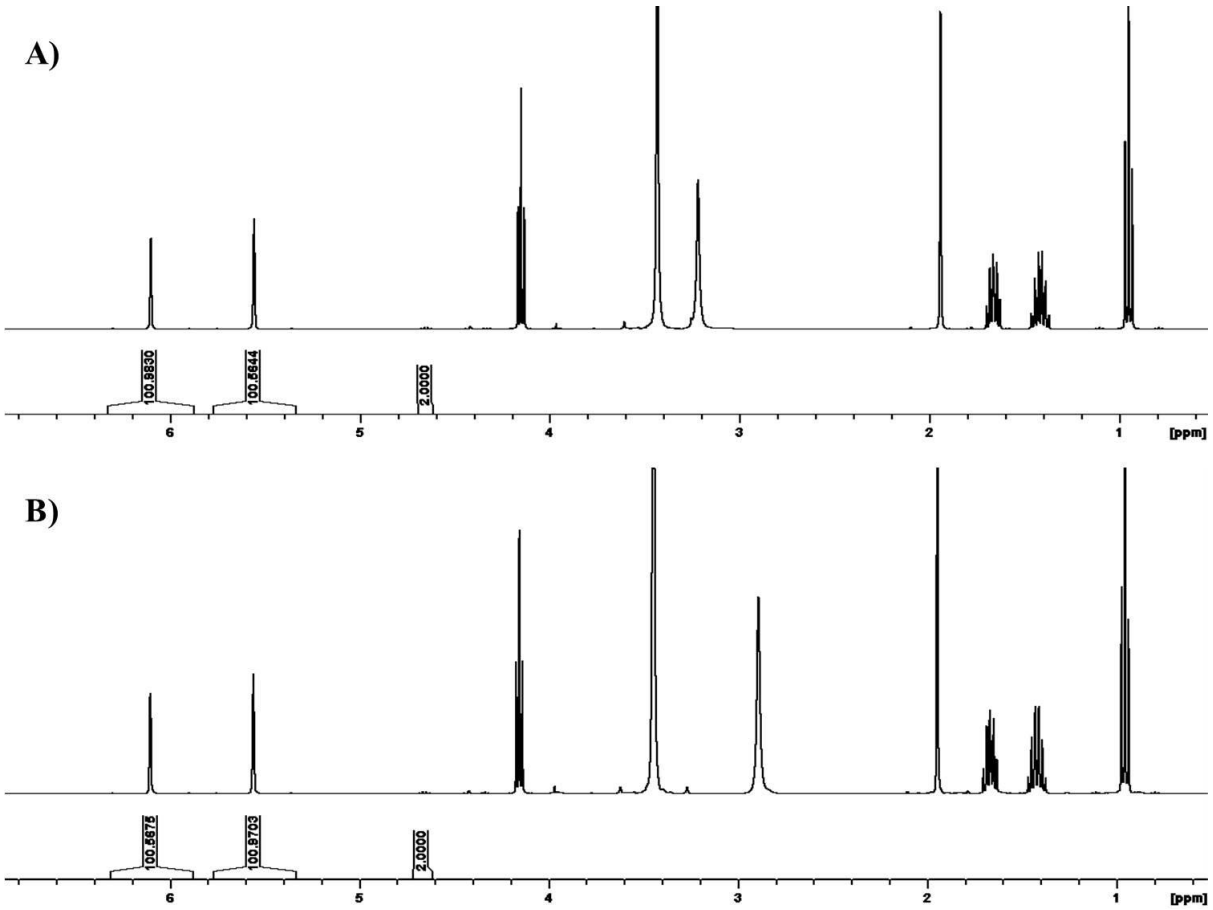

Figure S2.56 ^{1}H NMR (400 MHz, $CDCl_3$) of **[Xan_1-G_0-BiB]** initiated polymerisation of nBMA (DP_{100}) with **no CuCl present**; A) t = 0, and B) t = 24 hrs.

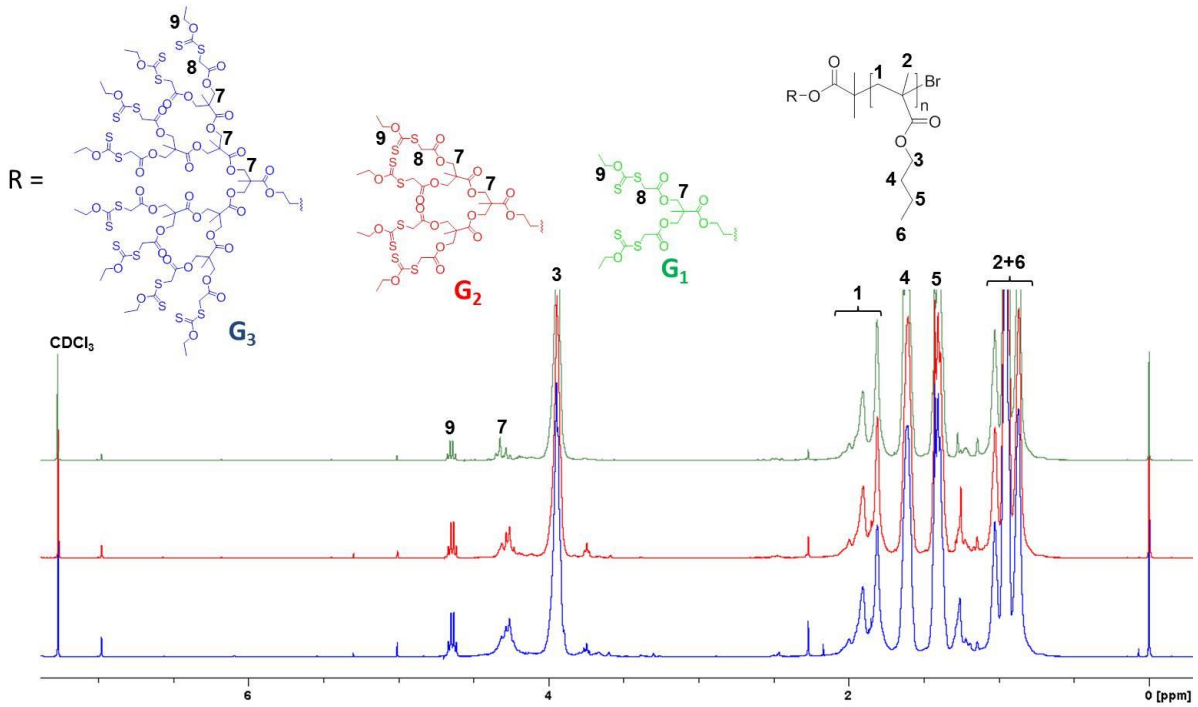

Fig. S2.57 ^{1}H NMR (400 MHz, $CDCl_3$) spectra overlay of **p[(Xan_2-G_1)-nBMA$_{50}$];[29]** (green), **p[(Xan_4-G_2)-nBMA$_{50}$];[30]** (red) and **p[(Xan_8-G_3)-nBMA$_{50}$];[31]** (blue) with major peaks assigned

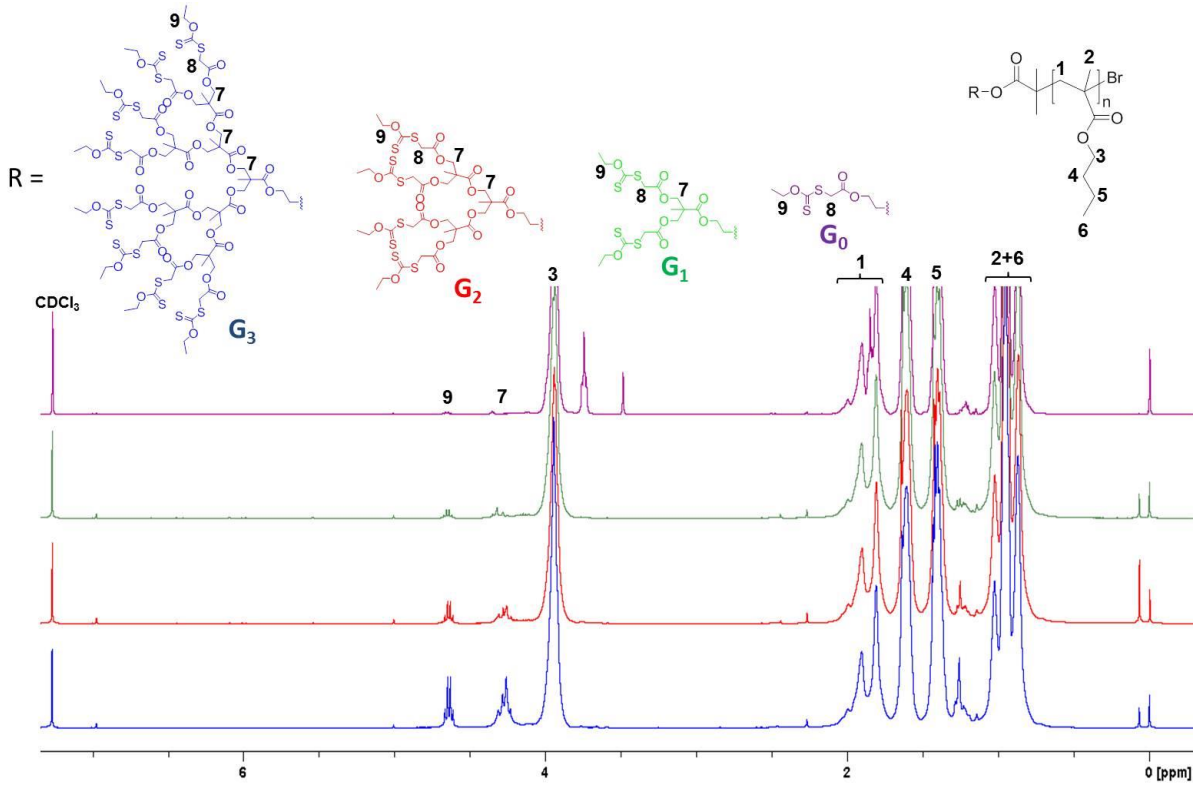

Fig. S2.58 ^{1}H NMR (400 MHz, $CDCl_3$) spectra overlay of **p[(Xan$_1$-G$_0$)-nBMA$_{100}$];[32]** (purple), **p[(Xan$_2$-G$_1$)-nBMA$_{100}$];[33]** (green), **p[(Xan$_4$-G$_2$)-nBMA$_{100}$];[34]** (red) and **p[(Xan$_8$-G$_3$)-nBMA$_{100}$];[35]** (blue) with major peaks assigned

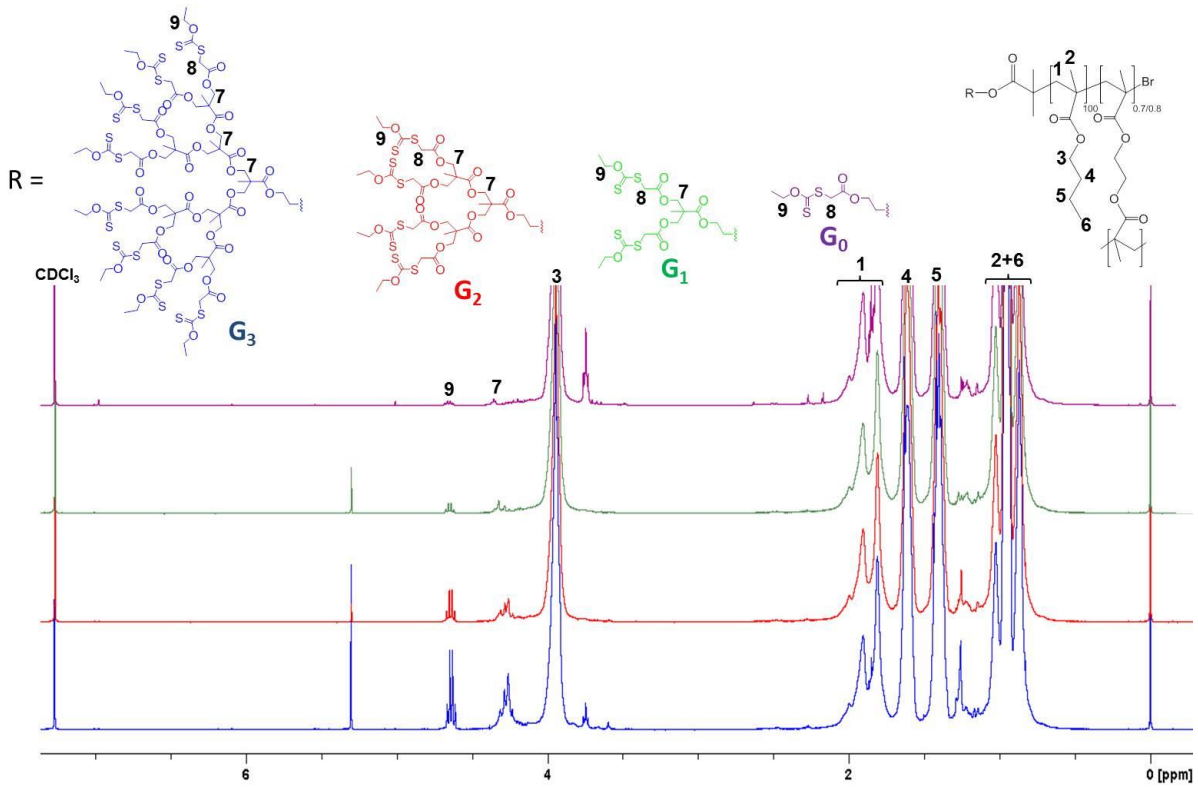

Fig. S2.59 ^{1}H NMR (400 MHz, $CDCl_3$) spectra overlay of **p[(Xan$_1$-G$_0$)-nBMA$_{100}$-*co*-EGDMA$_{0.7}$];[36]** (purple), **p[(Xan$_2$-G$_1$)-nBMA$_{100}$-*co*-EGDMA$_{0.8}$];[37]** (green), **p[(Xan$_4$-G$_2$)-nBMA$_{100}$-*co*-EGDMA$_{0.8}$];[38]** (red) and **p[(Xan$_8$-G$_3$)-nBMA$_{100}$-*co*-EGDMA$_{0.8}$];[39]** (blue) with major peaks assigned

CHAPTER 3

Xanthate-mediated thiol-acrylate Michael addition: Sequential and Simultaneous strategies for multifunctionalisation

Publication arising from this Chapter:

"Model studies of the sequential and simultaneous statistical modification of dendritic functional groups and their implications within complex polymer architecture synthesis."

F. Y. Hern, S. E. R. Auty, O. C. J. Andrén, M. Malkoch and S. P. Rannard, *Polym. Chem.*, 2017, **8**, 1644-1653.

Individual contributions: S. E. R. Auty – Initial studies to establish xanthate chemistry;

O. C. J. Andrén – recorded MALDI-TOF spectra; M. Malkoch and S. P. Rannard – supervisors.

3.1 Introduction

Multivalency, also known as polyvalency, is a naturally occurring phenomenon where non-covalent bonds form between multiple ligands and multiple receptors; the cumulative effect enables strong bonds to be made between molecules or molecules and substrates/surfaces.[1] Interactions between materials and biological systems often relies on the simultaneous binding of multiple different chemistries, rather than one single chemistry performing multiple tasks; the cooperative/synergistic nature of the multiple lower energy interactions often leads to higher binding strength.[2] Although dendrimers, with their high density of spatially well-defined surface functionality, would be well suited to providing this multivalency of biologically relevant functionality, key challenges such as limited payload and complex synthetic procedures have limited their application within drug delivery and nanomedicine (see Chapter 1.1.1). The size and shape of nanomaterials is also known to impact their fate *in vivo*; affecting accumulation, residence time and biodistribution.[3,4] Opsonisation and subsequent recognition of nanomaterials by macrophages has been shown to correlate strongly with size and surface functionality,[5,6] whilst biodistribution and pharmacokinetics may be tuned by carefully controlling dendrimer size or synthesising dendritic hybrid materials.[7,8] Incorporation of dendrons and their multiple surface functional groups into polymer hybrids may allow integration of multivalent regions of functionality.

Post-polymerisation modification is based on polymerisations involving initiators or monomers bearing chemoselective handles, tolerant to polymerisation conditions, that are able to undergo subsequent quantitative conversion into a range of functional groups.[9] This method of functionalisation allows the incorporation of functionality that is incompatible with polymerisation techniques. Post-modification of a single, well-defined precursor is particularly attractive for synthesising multifunctional and multi-responsive (co)polymers for

advanced applications since it facilitates the incorporation of a wide range of functional groups for different target applications.[10]

Deprotection and surface functionalisation via thiol-acrylate Michael addition to introduce a range of functionality at the dendron periphery has previously been reported[11], as outlined in Fig. 3.1, illustrated using a G_3 dendron. From three generations of xanthate peripheral polyester dendrimers, a library of materials with hydrophilic, hydrophobic and polymeric surface groups were readily generated through ambient temperature one-pot reactions.

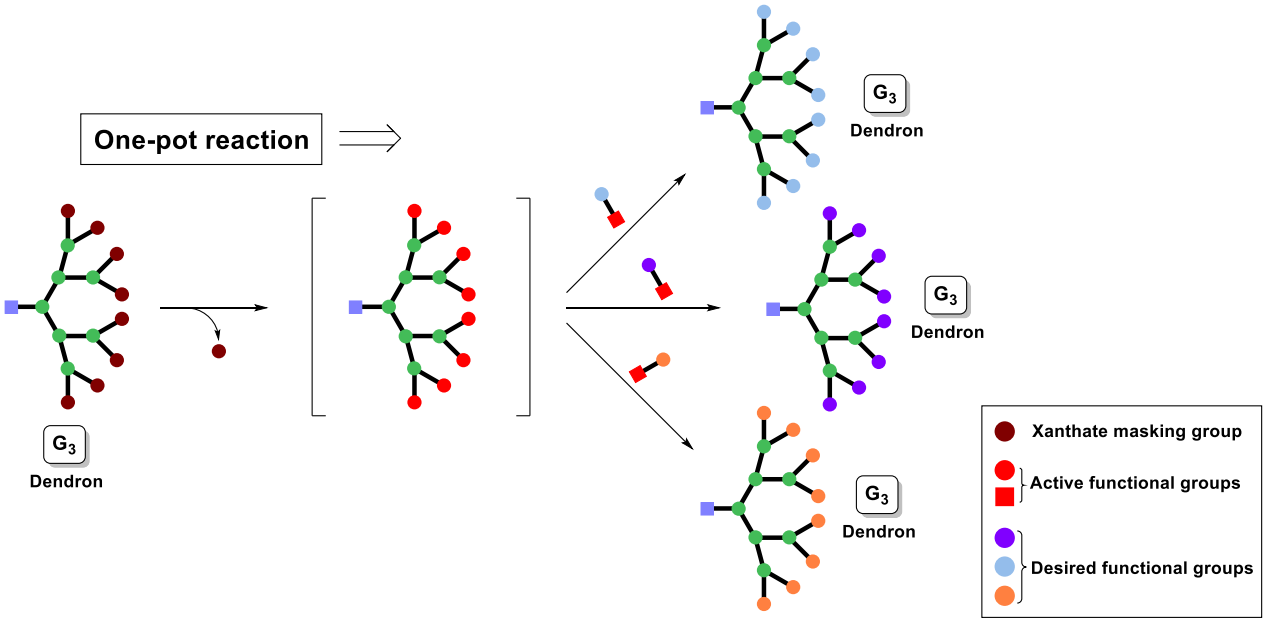

Fig. 3.1 Schematic representation of the one-pot xanthate deprotection/thiol-acrylate functionalisation strategy, illustrated using a G_3 dendron.[11]

This method of post-synthetic modification was extended to linear dendritic hybrids (LDHs)[12], with a library of twenty different surface functional LDHs readily generated through individual one-pot reactions from just four initial polymers.

To further expand the scope of post-polymerisation modification of xanthate functional materials, the work within this chapter is focussed on the efficient, orthogonal multifunctionalisation of a range of dendritic polymer architectures via sequential and

simultaneous methodologies. This allows for the accurate statistical placement of functional groups to allow comparisons with spatially-directed functionalisation and assessment of different polymer performance.

Following on from the success of the thiol-acrylate Michael addition for full functional modification of xanthate-derived thiols,[11,12] this chapter will explore the partial- and multi-functionalisation of four generations of xanthate peripheral dendrons (G_0, G_1, G_2, G_3), linear dendritic hybrids (LDHs) and hyperbranched polydendrons (HPDs), with full characterisation, Fig. 3.2.

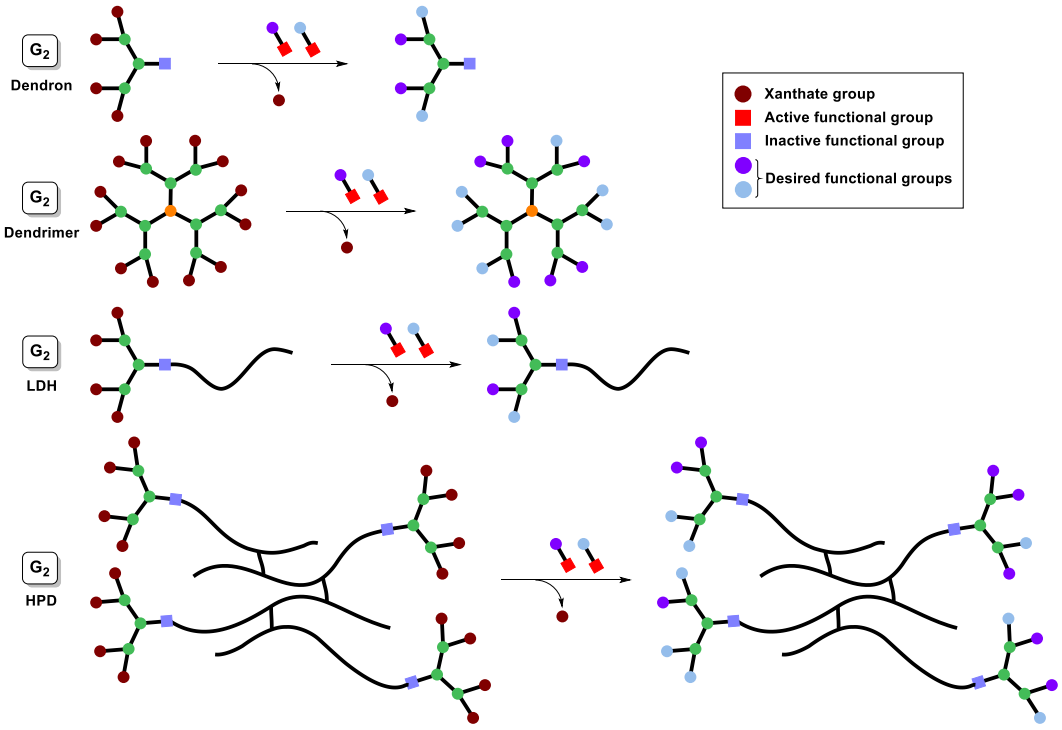

Fig. 3.2 Schematic representation of the aims within this chapter: Statistical multifunctionalisation of dendrons, dendrimers, linear dendritic hybrids (LDH) and hyperbranched polydendrons (HPD), shown here for G_2

Two methods of statistical multifunctionalisation will be considered: Sequential modification involves partial deprotection of the xanthate peripheral groups, followed by thiol Michael addition with a functional acrylate and repetition of these steps to incorporate multiple functionalities (Fig. 3.3A); Simultaneous modification involves the complete deprotection of

xanthate groups followed by reaction with a stoichiometric mixture of functional acrylates (Fig. 3.3B).

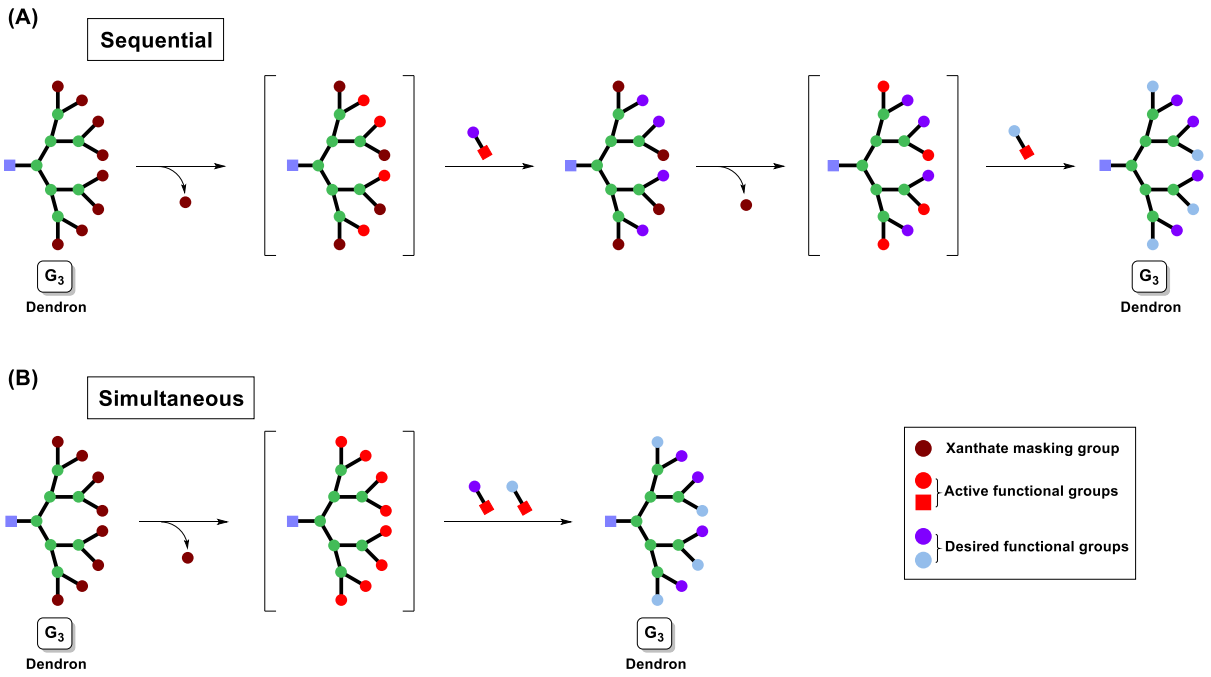

Fig. 3.3 Schematic representation of G_3 dendron undergoing: (A) Sequential partial one-pot xanthate deprotection/thiol-acrylate functionalisation strategy, followed by deprotection of remaining xanthate groups/ thiol-acrylate functionalisation; (B) Simultaneous full xanthate deprotection/thiol-acrylate multifunctionalisation

These methods offer respective advantages; sequential modification may allow incorporation of sensitive or highly reactive functionalities in the last step, whereas simultaneous modification reduces the number of reactive steps required for multifunctionalisation. It is unclear which of these strategies will be ideal for the main aims of this research, and a detailed examination is therefore required.

3.2 Statistical multifunctionalisation of xanthate functional dendrons

Sequential and simultaneous multifunctionalisation strategies were evaluated using focal point protected xanthate peripheral G_1-G_3 dendrons **[Xan$_2$-G$_1$-TSe];[12]**, **[Xan$_4$-G$_2$-TSe];[13]** and **[Xan$_8$-G$_3$-TSe];[14]**. Following reported procedures, deprotection by aminolysis using *n*-butylamine and subsequent one-pot thiol-acrylate Michael addition were studied in tetrahydrofuran (THF).[11,12]

3.2.1 Sequential modification

3.2.1.1 Controlled deprotection of xanthate peripheral groups

Xanthate peripheral dendrons **[12]**, **[13]** and **[14]** (Fig. 3.4) were deprotected at ambient temperature in THF with varying equivalents of *n*-butylamine for 1.5 hours.

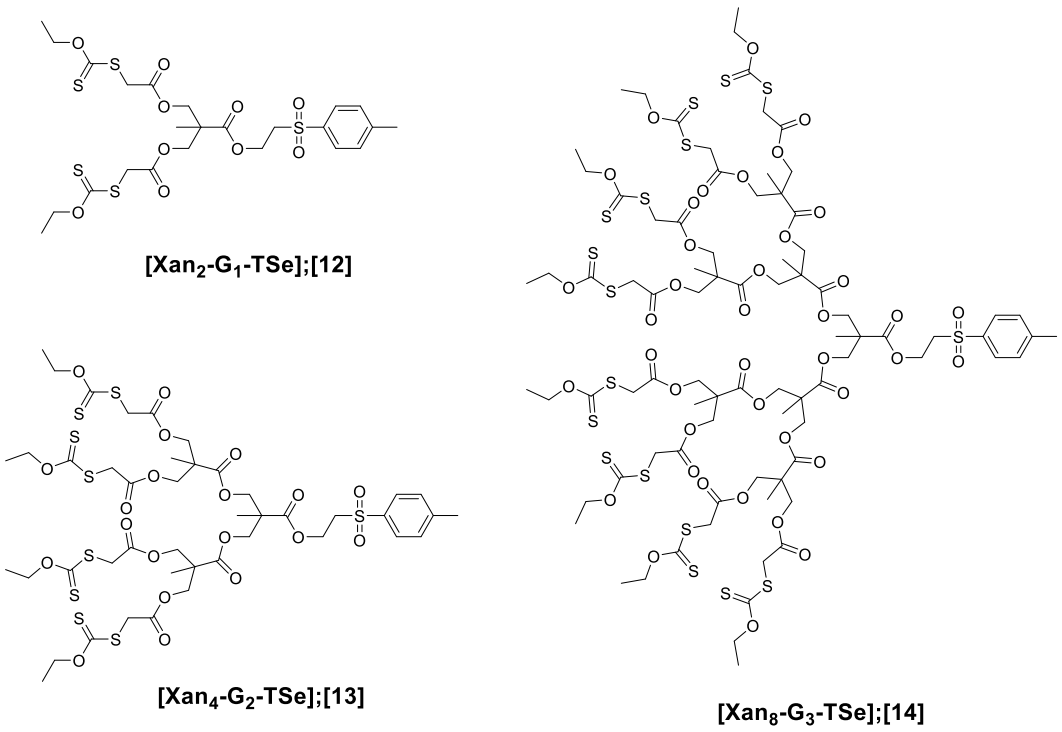

Fig. 3.4 Xanthate peripheral dendrons **[Xan$_2$-G$_1$-TSe];[12]**, **[Xan$_4$-G$_2$-TSe];[13]** and **[Xan$_8$-G$_3$-TSe];[14]**

After this time, the partially deprotected dendrons were analysed by ^{1}H NMR spectroscopy, shown here for G_3 dendron **[14]** with 1-8 equivalents of *n*-butylamine, Fig. 3.5. The characteristic xanthate CH_2 resonance at δ = 4.64 ppm decreases with increasing equivalents of *n*-butylamine used. Following xanthate deprotection, the CH_2 neighbouring the backbone thiol at δ ≈ 3.95 ppm shifts to δ ≈ 3.29 ppm. This is likely to be due to loss of the electron withdrawing xanthate group.

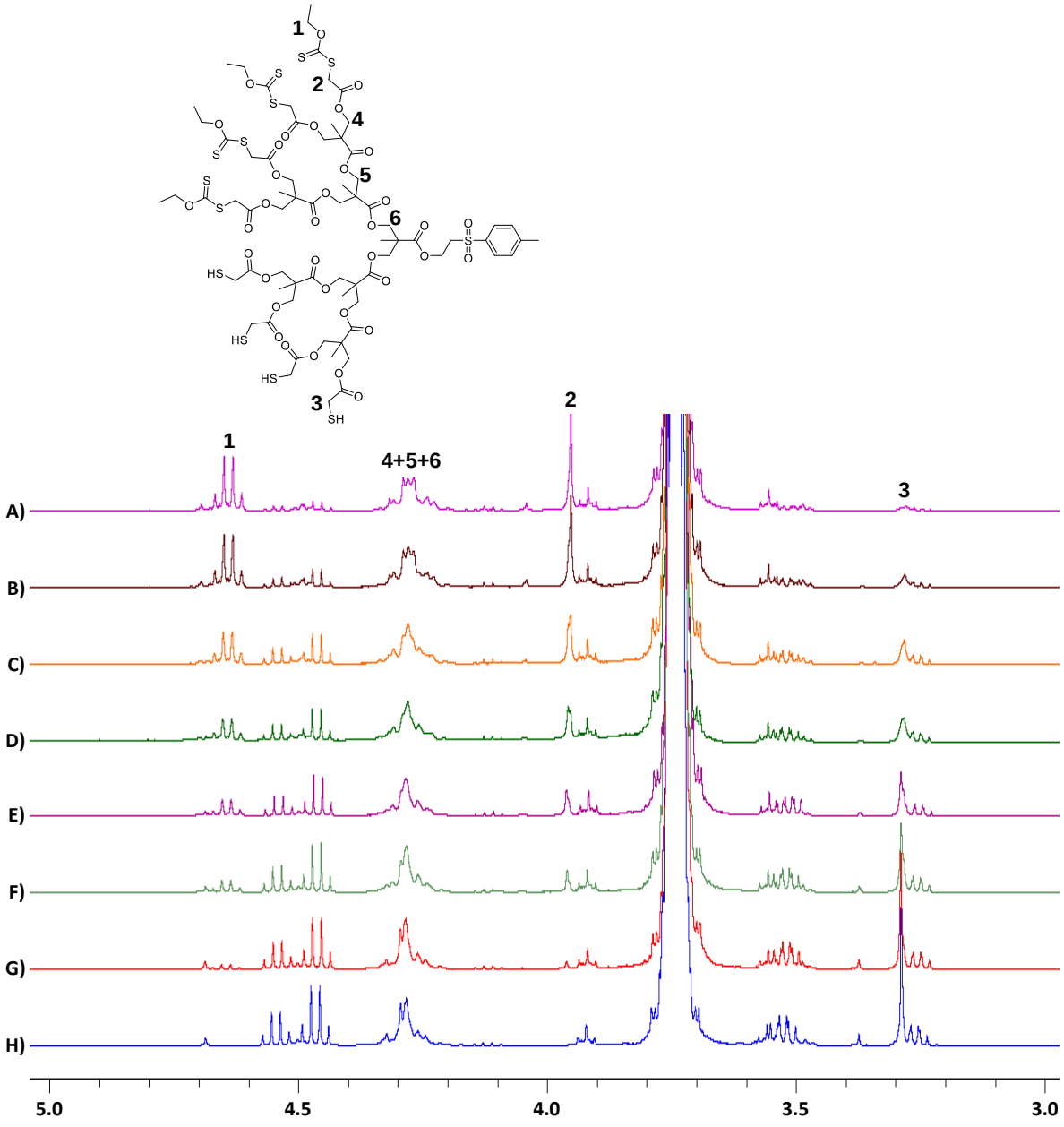

Fig. 3.5 Stacked ^{1}H NMR (400 MHz, $CDCl_3$) spectra of partially deprotected xanthate peripheral G_3 dendron **[14]**. Equivalents of *n*-butylamine added: A) 1, B) 2, C) 3, D) 4, E) 5, F) 6, G) 7 and H) 8.

Addition of 1 molar equivalent of *n*-butylamine per dendron resulted in deprotection of 48% of the xanthate groups for G_1 dendron **[12]**, 21% of the xanthate groups of the G_2 dendron **[13]**, and 12% of the xanthate groups of the G_3 dendron **[14]**. Within experimental and expected NMR error[13], these figures represent an average deprotection of 1 xanthate group per dendron for each generation. Incremental increases in the amount of *n*-butylamine added (up to a maximum of 2 equivalents for the G_1 dendron, 4 equivalents for the G_2 dendron and 8 equivalents for the G_3 dendron) resulted in a controlled and linear average number of xanthate groups deprotected for each dendron generation (calculated by ^{1}H NMR), suggesting good synthetic control, Fig. 3.6. Disulphide formation was not seen under these conditions.

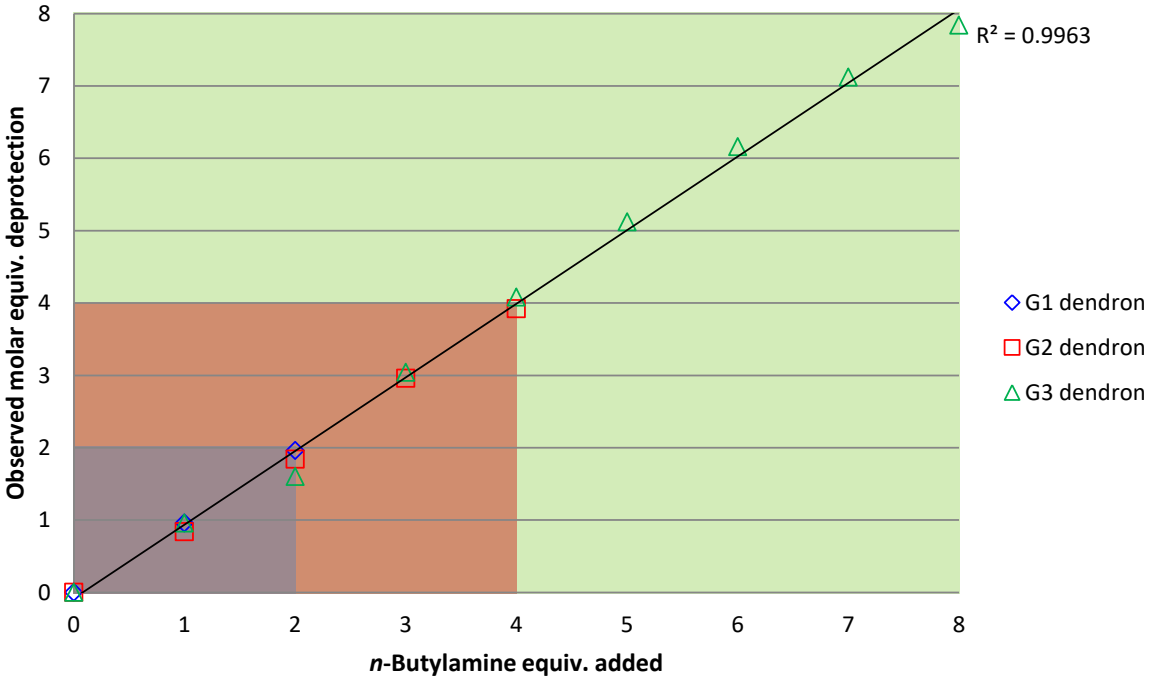

Fig. 3.6 Partial deprotection of xanthate peripheral groups of G_1-G_3 xanthate functional dendrons (**[12]-[14]**)

The degree to which the xanthate groups, i.e., the thiol protecting groups, are removed is preferably controllable for targeted sequential multifunctionalisation. Reaction of xanthate groups with *n*-butylamine is expected to be a statistical process and therefore, non-uniform; the ^{1}H NMR-determined correlation shown in Fig. 3.6 represents the averaged value across all dendrons within each sample. Direct analysis of the partially deprotected materials using

mass spectroscopic techniques is hampered by the formation of disulphide bonds between the highly thiol-functional structures during sample preparation, as previously reported.[11] Therefore, partial modification of xanthate peripheral groups by reaction of deprotected thiols with a functional acrylate may assist the determination of the distribution of materials formed during statistical deprotection.

3.2.1.2 Partial modification of xanthate functional dendrons

It is possible to selectively deprotect desired numbers of xanthate peripheral groups of G_1-G_3 dendrons **[Xan$_2$-G$_1$-TSe];[12]**, **[Xan$_4$-G$_2$-TSe];[13]** and **[Xan$_8$-G$_3$-TSe];[14]**, therefore, it may be possible to partially functionalise these materials by thiol-acrylate Michael addition with an excess of functional acrylate. Previous studies have revealed enhanced uptake of materials possessing secondary amine groups into monocyte-derived macrophages (ATHP-1) and epithelial cells (Caco-2)[14], therefore, 2-(dimethylamino)ethyl acrylate (DMAEA, Am) was identified as a target functionality to incorporate into these materials. Benzyl acrylate (Bz) was chosen as opsonins attach more easily to hydrophobic surfaces than hydrophilic surfaces, thus increasing phagocytosis of nanoparticles with more hydrophobic surfaces.[15,16] The benzyl groups are also useful as they can be easily distinguished via ^{1}H NMR spectroscopy as the chemical shifts of the aromatic protons are significantly different to others present in the target structures. These acrylates allow ready quantitative spectroscopic analysis and provide suitable mass differences for spectrometric assignment of products with varying distributions of functional groups.

As outlined in literature[11], full one-pot deprotection and thiol-acrylate Michael addition was carried out with an excess of *n*-butylamine and dimethylamino- and benzyl-functional acrylates, Am and Bz. The resulting materials, **[Am$_8$-G$_3$-TSe];[44]** and **[Bz$_8$-G$_3$-TSe];[45]** were analysed by ^{1}H NMR, Fig. 3.7A and 3.7B, respectively, and ^{13}C NMR, Fig. S3.1.

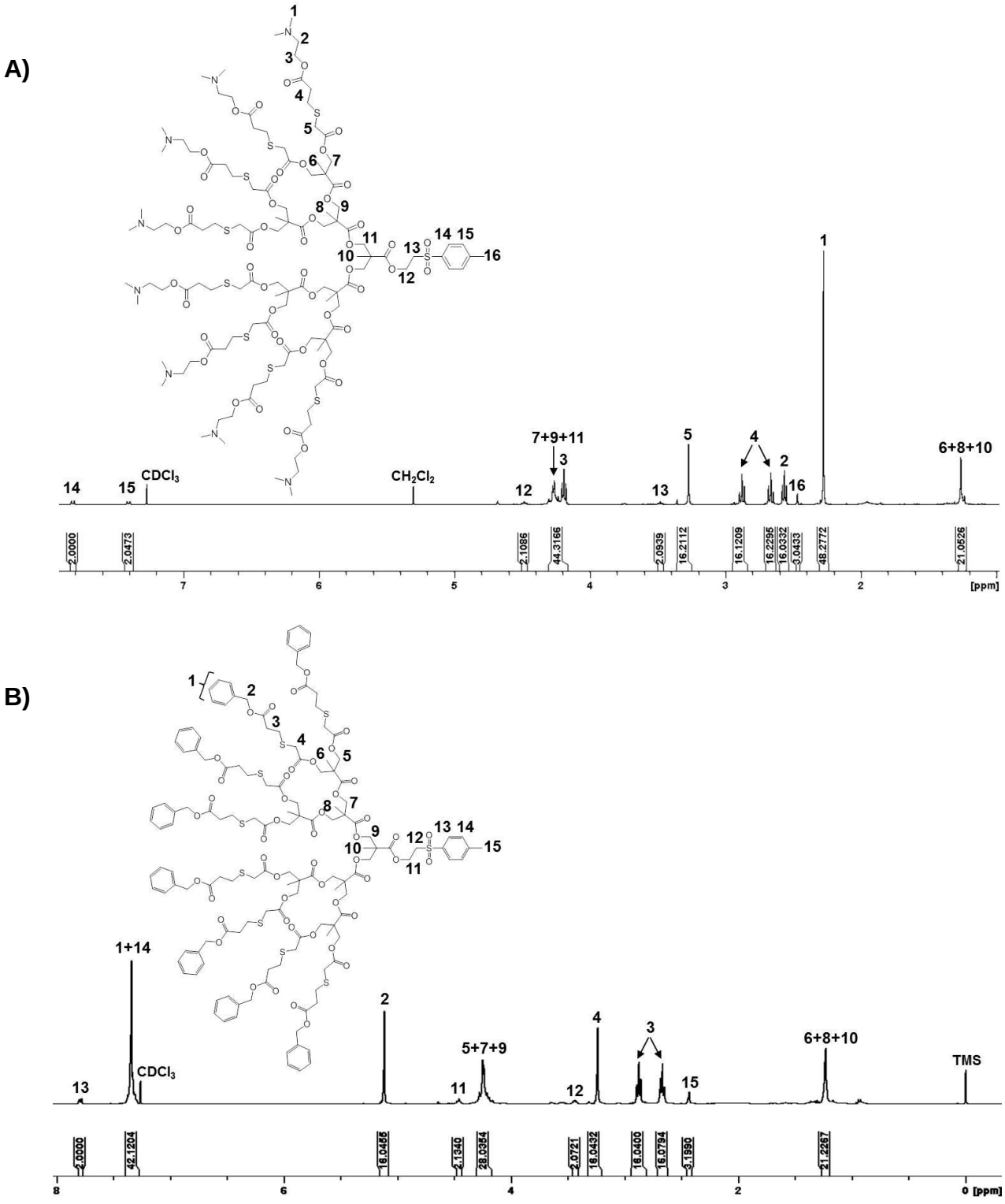

Fig. 3.7 ^{1}H NMR (400 MHz, $CDCl_3$) spectra of A) **[Am_8-G_3-TSe];[44]** and B) **[Bz_8-G_3-TSe];[45]**

For partially functionalised materials, G_3 xanthate peripheral dendron **[14]** was deprotected with 1-8 equivalents of *n*-butylamine at ambient temperature for 1.5 hours, to generate thiols *in situ*. After this time, 1.5 equivalents of DMAEA (Am) per deprotected xanthate group was

added and the reaction left to stir overnight. The resulting materials were analysed by ^{1}H NMR spectroscopy and MALDI-TOF mass spectrometry. Decreasing xanthate functionality and increasing Am functionality could be seen by ^{1}H NMR analysis, Fig. 3.8.

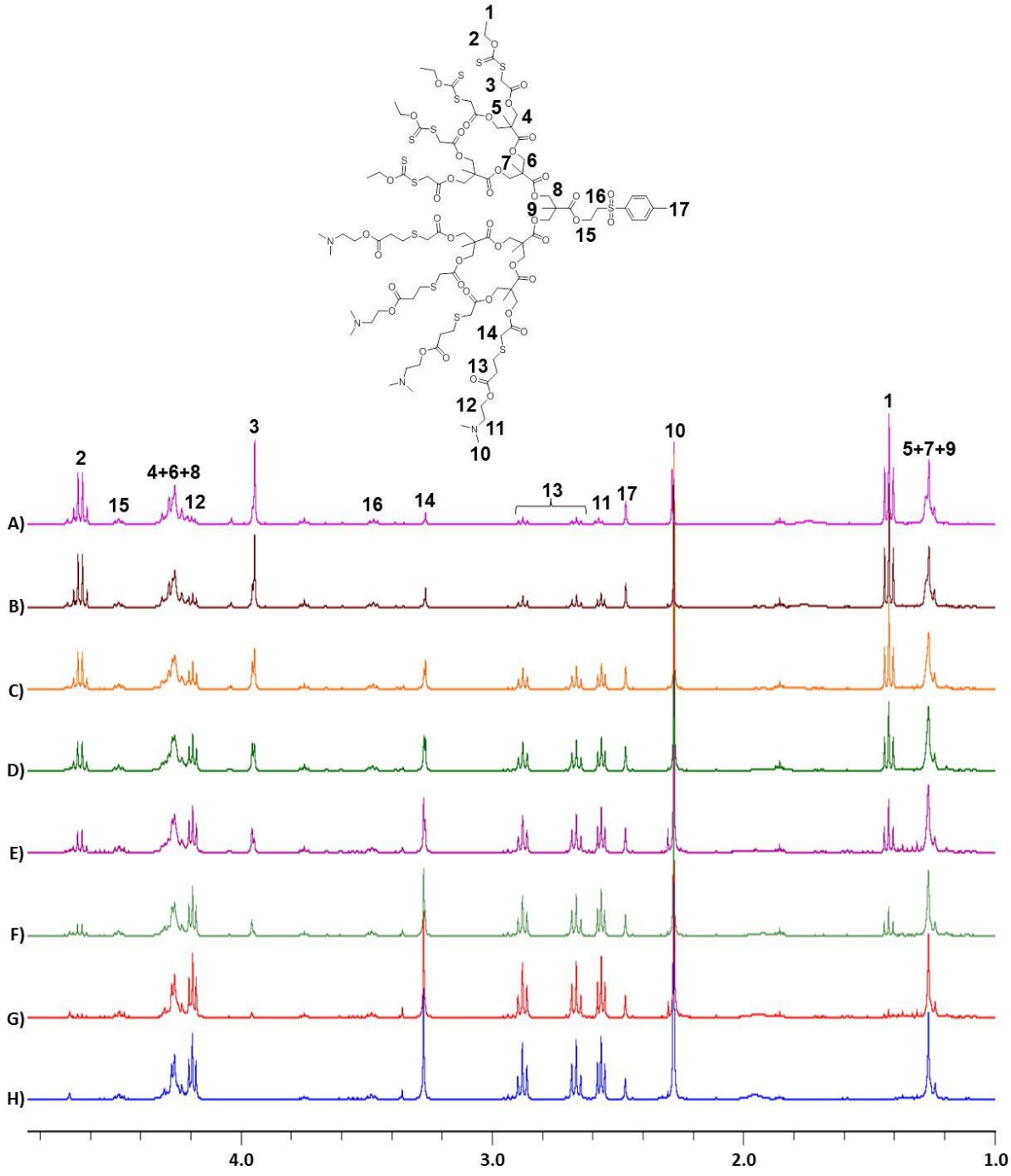

Fig. 3.8 Stacked ^{1}H NMR (400 MHz, $CDCl_3$) spectra of partially DMAEA (Am) functionalised **[Xan$_8$-G$_3$-TSe];[14]**: A) **[Xan$_7$-Am$_1$-G$_3$-TSe];[50]**; B) **[Xan$_6$-Am$_2$-G$_3$-TSe];[51]**; C) **[Xan$_5$-Am$_3$-G$_3$-TSe];[52]**; D) **[Xan$_4$-Am$_4$-G$_3$-TSe];[53]**; E) **[Xan$_3$-Am$_5$-G$_3$-TSe];[54]**; F) **[Xan$_2$-Am$_6$-G$_3$-TSe];[55]**; G) **[Xan$_1$-Am$_7$-G$_3$-TSe];[56]**; H) **[Am$_8$-G$_3$-TSe];[44]**

The gradual disappearance of characteristic xanthate resonances (CH_2 quartet at δ ≈ 4.64 ppm and CH_3 triplet at δ ≈ 1.42 ppm) and appearance of new resonances at δ ≈ 2.66 and 2.88 ppm in the ^{1}H NMR spectra confirm partial deprotection and C-C bond formation via thiol-Michael addition during the one-pot reaction. At high levels of Am functionalisation, an extra resonance at δ = 2.91-2.96 ppm appears in the ^{1}H NMR spectra; this could be as a result of restricted rotation within the dendron structure, or the generation of different conformations with increasing Am incorporation. New resonances corresponding to Am at δ ≈ 2.28 ppm (terminal CH_3 groups), δ ≈ 2.57 ppm (CH_2 adjacent to amine) and δ ≈ 4.19 ppm (CH_2 adjacent to carbonyl) were also present in the ^{1}H NMR spectra; their relative integrals relate to the number of xanthate groups deprotected in the first step.

3.2.1.2.1 Analysis by mass spectrometry

^{1}H NMR spectroscopy of the systematically varying xanthate (Xan) and DMAEA (Am) functional Michael adducts showed that it is possible to direct an overall molar average functionalisation, but gives little information about the structural variation within the sample. MALDI-TOF mass spectrometry was therefore applied to elucidate the distribution of structures formed during statistical partial functionalisation. As previously reported, sulphur has over 20 known isotopes of which ^{32}S, ^{33}S, ^{34}S and ^{36}S are stable with varying abundance. Sulphur is also prone to oxidation during mass spectrometric analysis, making definitive analysis difficult[12,17]; oxidation of thio-ethers will add multiples of 16 Da to the expected mass ion, which may be confused with the difference between sodium and potassium adducts.

The MALDI-TOF spectra of the targeted materials (**[Xan$_7$-Am$_1$-G$_3$-TSe];[50]**, **[Xan$_6$-Am$_2$-G$_3$-TSe];[51]**, **[Xan$_5$-Am$_3$-G$_3$-TSe];[52]**, **[Xan$_4$-Am$_4$-G$_3$-TSe];[53]**, **[Xan$_3$-Am$_5$-G$_3$-TSe];[54]**, **[Xan$_2$-Am$_6$-G$_3$-TSe];[55]**, **[Xan$_1$-Am$_7$-G$_3$-TSe];[56]** and **[Am$_8$-G$_3$-TSe];[44]**) displayed a broad distribution of products, becoming more defined at higher Am incorporation (**[Xan$_x$-Am$_y$-G$_3$-TSe]**, x≤2, y≥6, x+y = 8), Fig. 3.9.

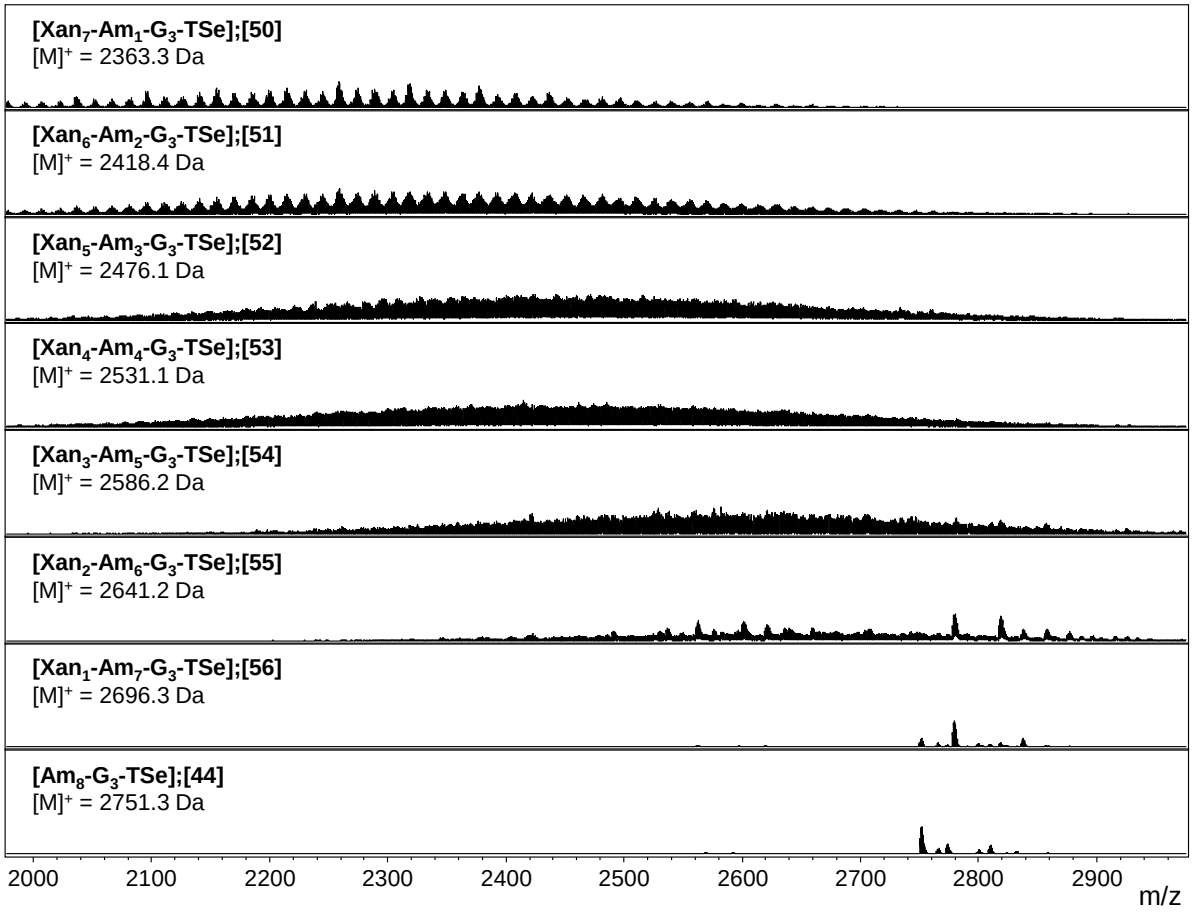

Fig. 3.9 Stacked MALDI-TOF (DCTB) mass spectra of partially DMAEA (Am) functionalised **[Xan$_8$-G$_3$-TSe];[14]**

The MALDI-TOF spectrum of the partially functionalised G_3 dendron with 6 Am units, nominally **[Xan$_2$-Am$_6$-G$_3$-TSe];[55]** (Fig. 3.10, Table S3.1), was tentatively assigned assuming each observed species was either a protonated or potassium adduct; structures ranging from **[Xan$_5$-Am$_3$-G$_3$-TSe];[52]** to **[Am$_8$-G$_3$-TSe];[44]** were clearly present. The repeating mass unit of 55 Da corresponds to the mass difference expected from removal of one xanthate and addition of one Am unit.

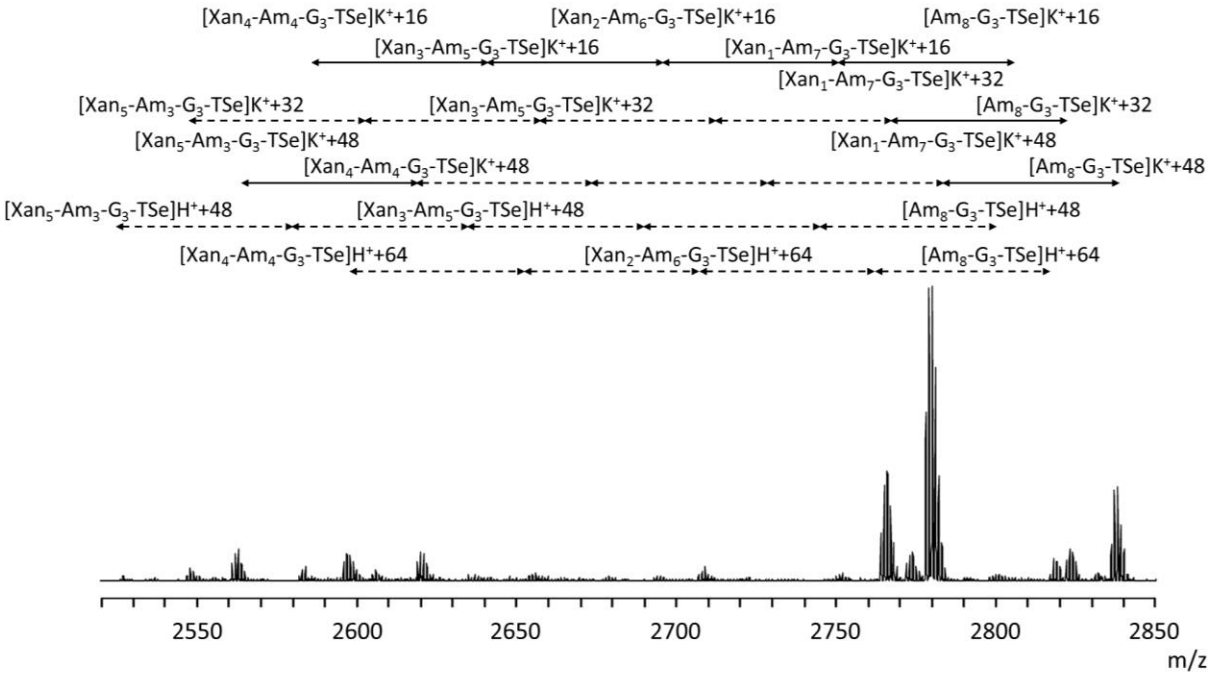

Fig. 3.10 MALDI-TOF analysis (HABA) of the Michael adduct **[Xan_2-Am_6-G_3-TSe];[55]**.

Double-headed arrows indicate mass differences of 55 Da

(dotted arrows indicate missing peaks; solid arrows indicate identified peaks)[18]

As can be seen from Fig. 3.10, a considerable range of structures was present within the nominal **[Xan_2-Am_6-G_3-TSe];[55]** product, spanning structures up to the complete deprotection and amine functionalisation, ie **[Am_8-G_3-TSe];[44]**. The technique can accurately determine the masses of individual structures, confirming MALDI-TOF is a useful tool for end-group analysis as well as product confirmation. Within the individual species identified, considerable isomeric variation is expected, Fig. 3.11, although no further analysis techniques (e.g. advanced NMR) were developed for this project to establish the presence of these structures.

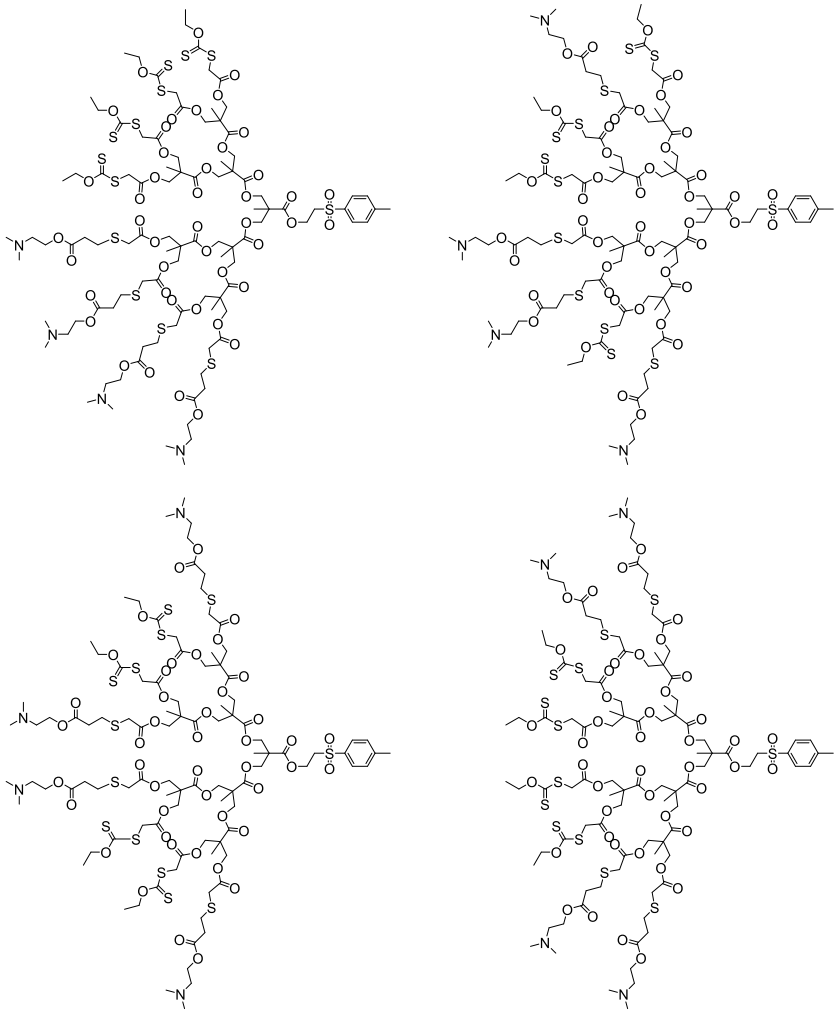

Fig. 3.11 Probable isomeric distribution of **[Xan$_4$-Am$_4$-G$_3$-TSe];[53]** formed as a result of statistical deprotection of four xanthate groups followed by Michael addition with an excess of DMAEA (Am)

3.2.1.3 Sequential multifunctionalisation

The sequential deprotection/functionalisation strategy requires initial partial deprotection of available peripheral xanthate groups, followed by reaction with a slight molar excess (1.5 molar equiv. per thiol) of functional acrylate with respect to deprotected thiols; the remaining xanthate groups are subsequently deprotected, followed by addition of a second functional acrylate in excess, Fig. 3.3(A).

A series of sequential reactions were conducted with xanthate peripheral G_1-G_3 dendrons **[12]-[14]**, to target statistically multifunctionalised materials with benzyl (Bz) and dimethylamino (Am) functional groups, shown here for the 50/50 multifunctionalisation of G_3 dendron **[Xan$_8$-G$_3$-TSe];[14]**, Fig. 3.12.

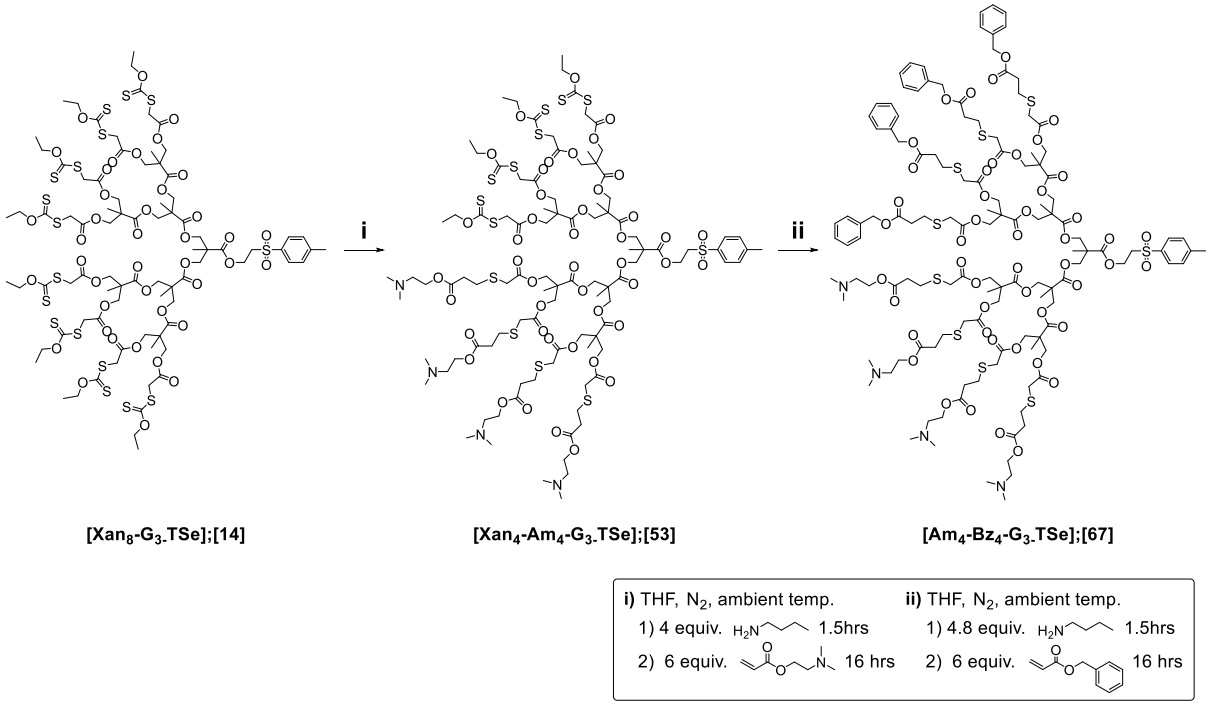

Fig. 3.12 Sequential multifunctionalisation of G_3 dendron **[Xan$_8$-G$_3$-TSe];[14]**, targeting an average 50/50 functionalisation to obtain **[Am$_4$-Bz$_4$-G$_3$-TSe];[67]** (representative structure)

Targeting a 1:1 molar ratio of Am:Bz functionality with G_1 dendron **[12]** involved initial deprotection of the available xanthate groups with 1 molar equivalent of *n*-butylamine at

ambient temperature, and subsequent addition of a slight excess (1.5 molar equivalents) of DMAEA with respect to the exposed thiol groups, followed by purification and ^{1}H NMR spectroscopic analysis. The remaining xanthate groups were then deprotected and a 1.5 molar excess of benzyl acrylate per thiol was added. The resulting product was analysed by ^{1}H NMR spectroscopy (Fig. S3.2) and MALDI-TOF MS following purification, confirming the expected average 50/50 functionalisation and the presence of targeted compound (**[Am_1-Bz_1-G_1-TSe];[60]**, calculated $[MH]^+$ = 770.96 Da). Signals were also observed in the mass spectrum corresponding to the symmetrical **[Am_2-G_1-TSe];[40]** (calculated $[MH]^+$ = 751.95 Da); signals indicating the presence of **[Bz_2-G_1-TSe];[41]** were not observed (Fig. S3.4), suggesting variable ionisation. The oxidised **[Am_1-Bz_1-G_1-TSe];[60]** products were seen as a series of peaks separated by 16 Da.

This sequential multifunctionalisation methodology was applied to G_2 dendron **[13]** to generate, **[Bz_4-G_2-TSe];[43]**, **[Am_1-Bz_3-G_2-TSe];[61]**, **[Am_2-Bz_2-G_2-TSe];[62]**, **[Am_3-Bz_1-G_2-TSe];[63]** and **[Am_4-G_2-TSe];[42]**. The MALDI-TOF mass spectra of these materials showed significant complexity, despite an excellent correlation between expected average structures and ^{1}H NMR analysis in each case (Fig S3.5, S3.7-S3.9). The MALDI-TOF analysis for the targeted mixed functional dendron **[Am_3-Bz_1-G_2-TSe];[63]**, for example, exhibited species ranging from no benzyl functional groups present (**[Am_4-G_2-TSe];[42]**), through to species with 100% benzyl functionality (**[Bz_4-G_2-TSe];[43]**) (Fig. 3.13), confirming the statistical nature of the functionalisation strategy.

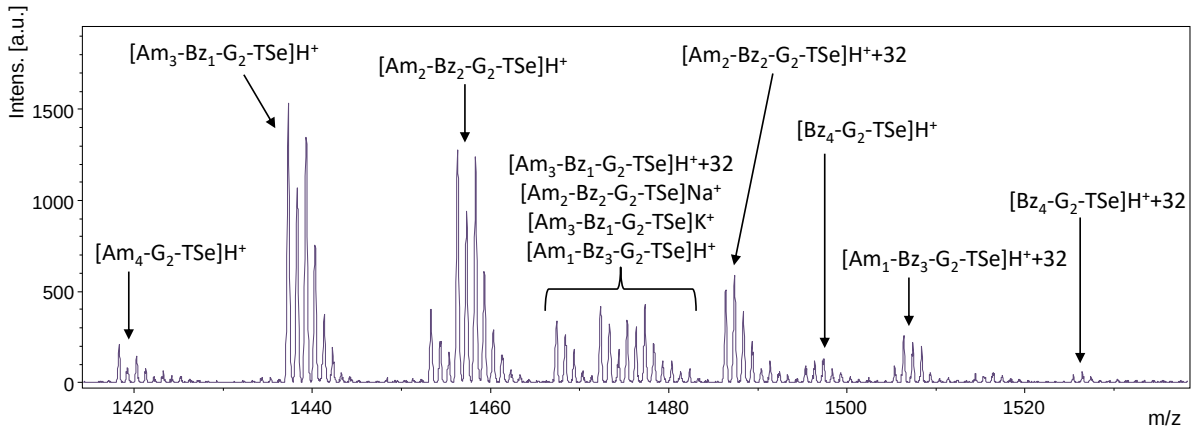

Fig. 3.13 Expansion of the MALDI-TOF (9-nitroanthracene) mass spectrum of targeted material **[Am_3-Bz_1-G_2-TSe];[63]** by sequential multifunctionalisation

It should be noted that variation of relative peak intensities within each isotopic distribution was observed with each different matrix material used during optimisation of the analytical procedures (*trans*-2-[3-(4-*tert*-butylphenyl)-2-methyl-2-propenylidene]malononitrile (DCTB), 9-nitroanthracene (9A), 2-(4'-hydroxybenzeneazo)benzoic acid (HABA), 2,5-dihydroxybenzoic acid (DHB), dithranol), indicating differences in ionisation and therefore indicating that the relative abundance of each species should not be inferred from these analyses.

A good agreement between ^{1}H NMR analysis and expected average structures was seen for products resulting from the sequential multifunctionalisation of G_3 dendron **[14]**, targeting **[Am_x-Bz_y-G_3-TSe]** (x = 0-8, y = 0-8; x+y = 8) (Fig. S3.10), shown here for **[Am_4-Bz_4-G_3-TSe];[67],** Fig. 3.14; although MALDI-TOF spectra of the resulting materials displayed three distinct populations, in many cases (Fig. S3.12-S3.19).

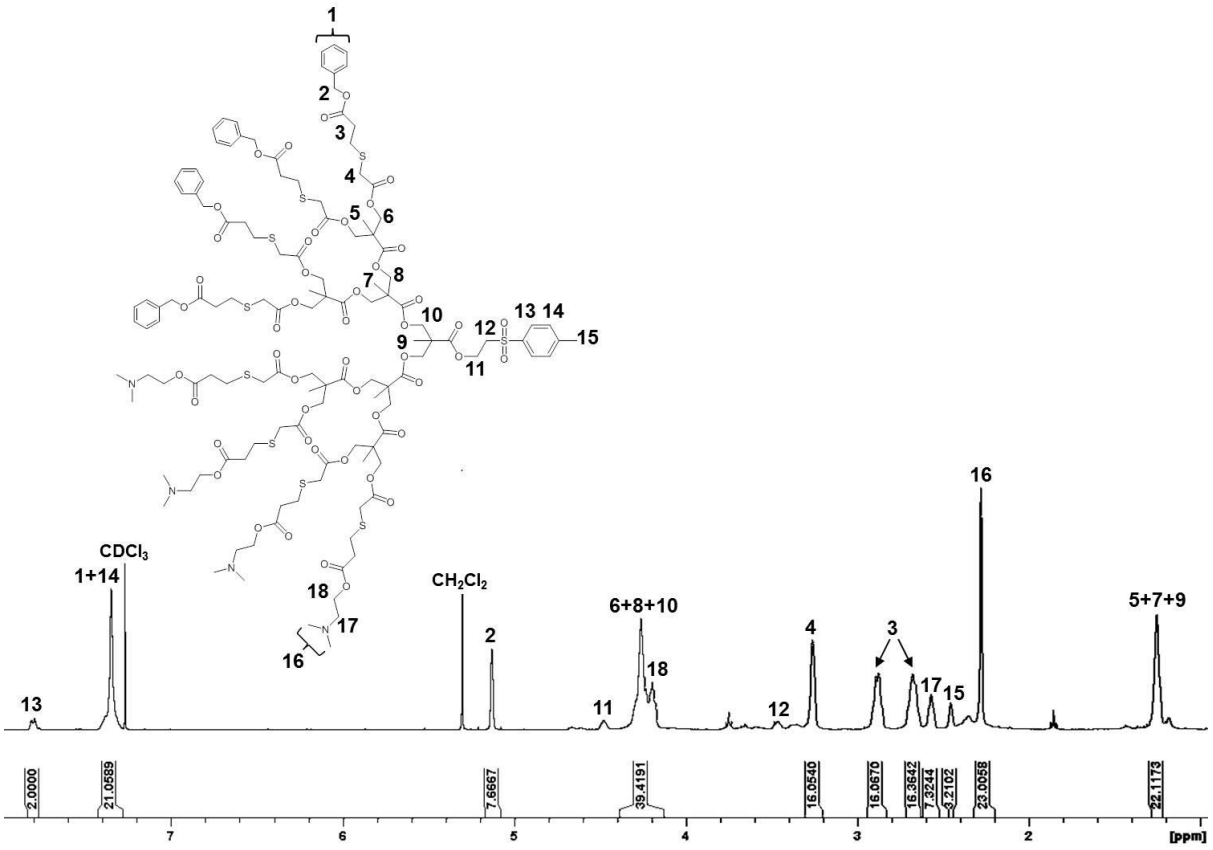

Fig. 3.14 ^{1}H NMR (400 MHz, $CDCl_3$) of **[Am$_4$-Bz$_4$-G$_3$-TSe];[67]** by sequential multifunctionalisation of **[Xan$_8$-G$_3$-TSe];[14]**

For example, MALDI-TOF analysis of the targeted **[Am$_4$-Bz$_4$-G$_3$-TSe];[67]** displayed a group of peaks that were readily assigned to chemical species as a direct result of the statistical nature of the sequential deprotection/functionalisation strategy, Fig. 3.15 and Table 3.1, peaks 16-29. Two further populations of peaks at lower molecular weight can be assigned to materials containing either one (Fig. 3.15, Table 3.1 peaks 8-15) or two (Fig. 3.15, Table 3.1 peaks 1-7) unreacted thiol functional groups. These thiols are thought to remain unreacted as a result of steric crowding and isolation during the sequential deprotection and thiol-acrylate Michael addition strategy.

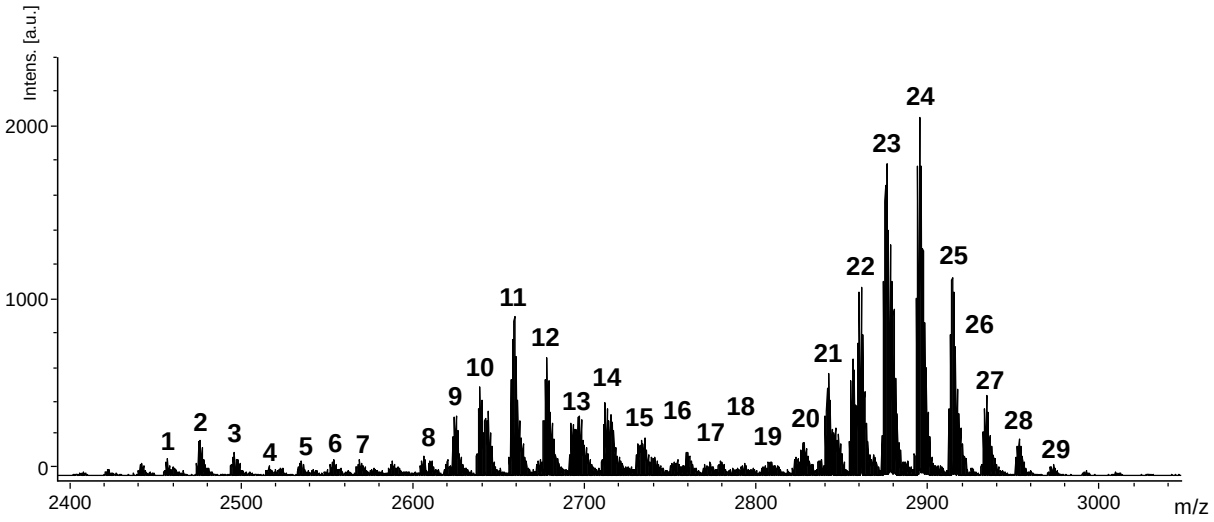

Fig. 3.15 MALDI-TOF analysis (DCTB) of the product targeting **[Am_4-Bz_4-G_3-TSe];[67]** via sequential multifunctionalisation

The observation of species assigned as **[Am_6-$(SH)_2$-G_3-TSe];[81]** and **[Am_7-$(SH)_1$-G_3-TSe];[88]**, peaks 1 and 8 respectively (Fig. 3.15), supports thiol isolation as excess benzyl acrylate addition in the second reactive step would be expected to react all exposed thiols. Although more noticeable within the G_3 dendron series (Fig. S3.12-S3.18), thiol isolation was also observed within several G_2 dendron sequential multifunctionalisation reactions (Fig. S3.7-S3.9). Thiol trapping within higher generation dendrons may be as a result of backfolding[19,20] or steric crowding around functional groups from the first step of sequential multifunctionalisation and may render this approach impractical for systems that require accurate statistical functionalisation.

Table 3.1 Peaks identified and assigned within the MALDI-TOF mass spectrum of the targeted **[Am_4-Bz_4-G_3-TSe];[67]** via sequential multifunctionalisation – see Fig. 3.15

Peak	Species assignment	Theoretical *m/z*+1 (Da)	Observed *m/z* (Da)
1	[Am_6-$(SH)_2$-G_3-TSe];**[81]**	MH^+ = 2463	2462.99
2	[Am_5-Bz_1-$(SH)_2$-G_3-TSe];**[82]**	MH^+ = 2482	2481.97
3	[Am_4-Bz_2-$(SH)_2$-G_3-TSe];**[83]**	MH^+ = 2501	2500.97
4	[Am_3-Bz_3-$(SH)_2$-G_3-TSe];**[84]**	MH^+ = 2520	2519.97
5	[Am_2-Bz_4-$(SH)_2$-G_3-TSe];**[85]**	MH^+ = 2539	2539.02
6	[Am_1-Bz_5-$(SH)_2$-G_3-TSe];**[86]**	MH^+ = 2558	2558.06
7	[Bz_6-$(SH)_2$-G_3-TSe];**[87]**	MH^+ = 2577	2577.05
8	[Am_7-$(SH)_1$-G_3-TSe];**[88]**	MH^+ = 2606	2606.14
9	[Am_6-Bz_1-$(SH)_1$-G_3-TSe];**[89]**	MH^+ = 2625	2625.12
10	[Am_5-Bz_2-$(SH)_1$-G_3-TSe];**[90]**	MH^+ = 2644	2644.11
11	[Am_4-Bz_3-$(SH)_1$-G_3-TSe];**[91]**	MH^+ = 2663	2663.12
12	[Am_3-Bz_4-$(SH)_1$-G_3-TSe];**[92]**	MH^+ = 2682	2682.14
13	[Am_2-Bz_5-$(SH)_1$-G_3-TSe];**[93]**	MH^+ = 2701	2701.14
14	[Am_1-Bz_6-$(SH)_1$-G_3-TSe];**[94]**	MH^+ = 2720	2720.15
15	[Bz_7-$(SH)_1$-G_3-TSe];**[95]**	MH^+ = 2739	2739.19
16	[Am_8-G_3-TSe];**[44]**	MH^+ = 2750	2750.21
17	[Am_7-Bz_1-G_3-TSe];**[70]**	MH^+ = 2768	2768.26
18	[Am_6-Bz_2-G_3-TSe];**[69]**	MH^+ = 2787	2787.21
19	[Am_5-Bz_3-G_3-TSe];**[68]**	MH^+ = 2806	2806.20
20	**[Am_4-Bz_4-G_3-TSe];[67]**	**MH^+ = 2825**	**2825.26**
21	[Am_3-Bz_5-G_3-TSe];**[66]**	MH^+ = 2844	2844.30
22	[Am_2-Bz_6-G_3-TSe];**[65]**	MH^+ = 2863	2863.29
23	[Am_1-Bz_7-G_3-TSe];**[64]**	MH^+ = 2882	2882.28
24	[Bz_8-G_3-TSe];**[45]**	MH^+ = 2901	2901.32
25	[Bz_8-G_3-TSe]H^+ + 16	MH^+ = 2901	2917.29
26	[Bz_8-G_3-TSe]K^+	MH^+ = 2901	2939.32
27	[Bz_8-G_3-TSe]K^+ + 16	MH^+ = 2901	2955.32
28	[Bz_8-G_3-TSe]K^+ + 32	MH^+ = 2901	2971.32
29	[Bz_8-G_3-TSe]K^+ + 48	MH^+ = 2901	2987.26

3.2.2 Simultaneous multifunctionalisation

An alternative method of statistical multifunctionalisation to consider is the complete deprotection of xanthate functional groups and simultaneous reaction of exposed thiols with a stoichiometric mixture of functional acrylates, at the desired molar ratio, Fig. 3.3(B). A series of multifunctional materials were therefore targeted using G_1-G_3 dendrons **[12]-[14]**, by full deprotection and reaction with a mixture of benzyl acrylate (Bz) and DMAEA (Am) to match the materials formed by sequential multifunctionalisation. As seen previously, ^{1}H NMR analysis of the resulting products confirmed formation of the targeted materials, on average, shown here for **[Am$_4$-Bz$_4$-G$_3$-TSe];[67]**, Fig. 3.16 (see Fig. 3.14 for corresponding material formed via sequential modification).

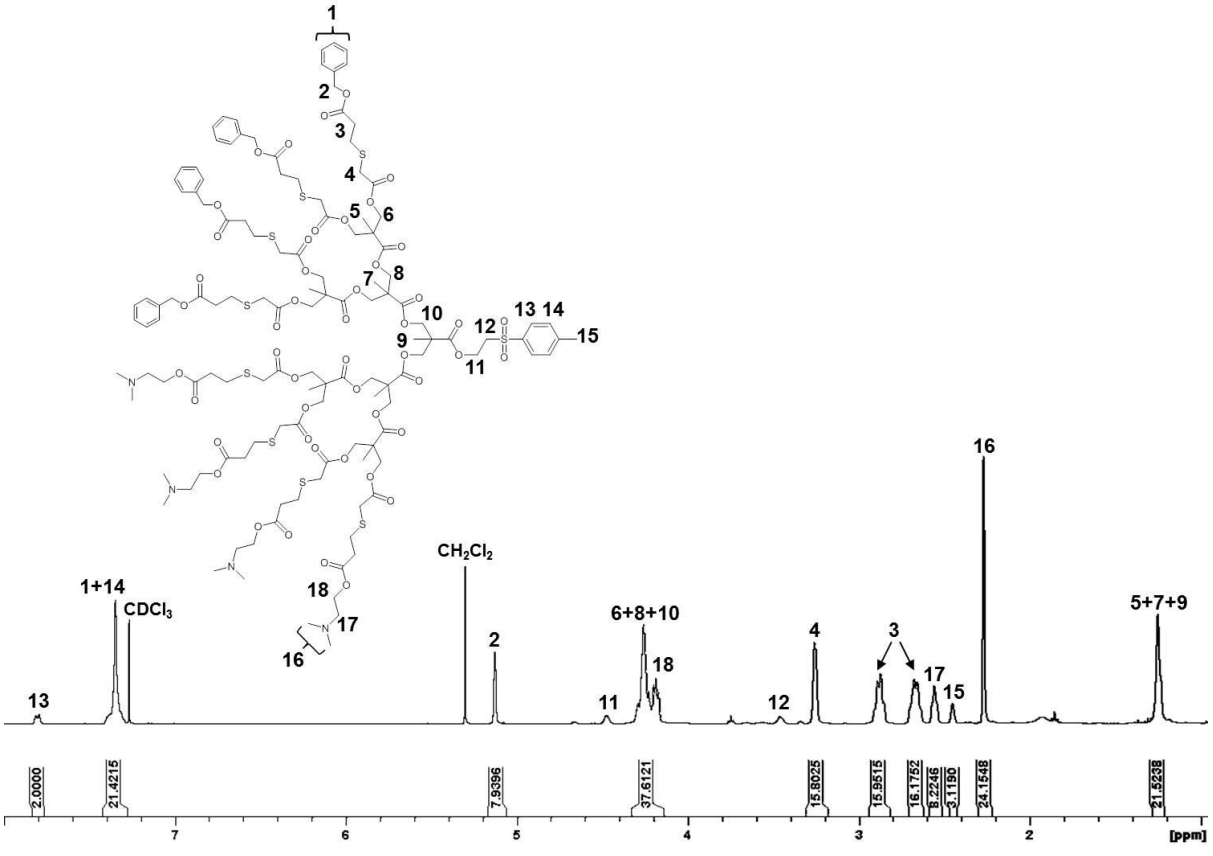

Fig. 3.16 ^{1}H NMR (400 MHz, $CDCl_3$) of **[Am$_4$-Bz$_4$-G$_3$-TSe];[67]** by simultaneous multifunctionalisation of **[Xan$_8$-G$_3$-TSe];[14]**

MALDI-TOF analysis, conducted under the same analytical conditions as for samples generated via the sequential multifunctionalisation strategy, showed a markedly different distribution of species when conducting the simultaneous mixed acrylate functionalisation. A single reaction with a mixture of acrylates yielded structures with far fewer isolated thiols in all studied reactions. In some cases, the formation of species with two unreacted thiols was almost undetectable. In comparison with previous results, MALDI-TOF analysis of **[Am_4-Bz_4-G_3-TSe];[67]**, synthesised via the simultaneous multifunctionalisation strategy, exhibited almost the entire peak distribution listed in Table 3.1, but the relative intensities of the main distribution of ions (Fig. 3.15 and Table 3.1 peaks 16-29) was significantly higher in comparison to the peaks indicating the presence of isolated thiols (Fig. 3.15 and Table 3.1 peaks 1-15), Fig. 3.17; in this case comparative concentrations are inferred between the same species in different samples as the materials are chemically highly related and the conditions of the MALDI-TOF analysis is identical. Almost no species containing isolated thiols were observed in some cases, such as targeting of **[Am_1-Bz_7-G_3-TSe];[64]** and **[Am_2-Bz_6-G_3-TSe];[65]** (Fig. S3.12, S3.13), when using the simultaneous multifunctionalisation strategy.

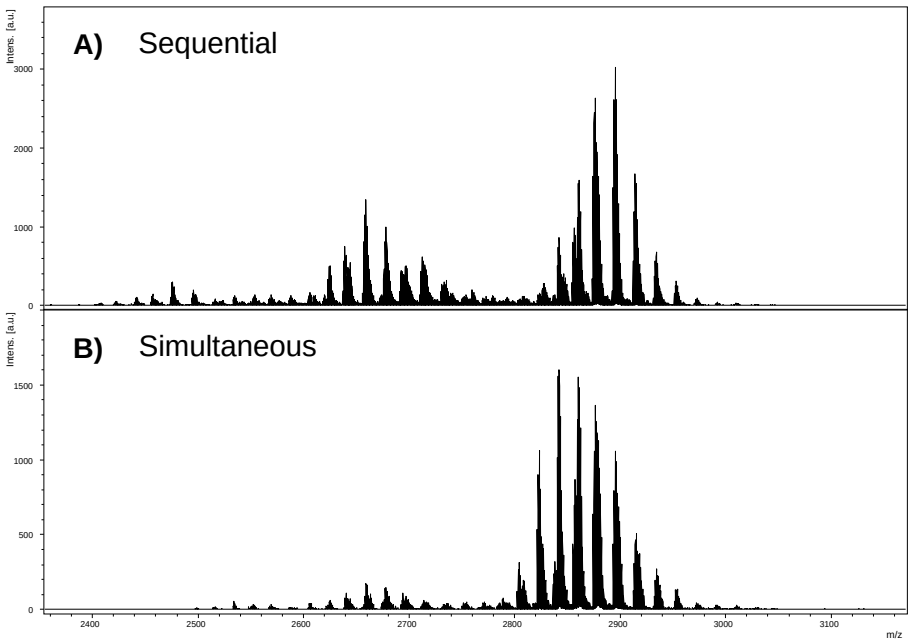

Fig. 3.17 MALDI-TOF analysis (DCTB) of the product targeting **[Am_4-Bz_4-G_3-TSe];[67]** via: A) Sequential multifunctionalisation; and B) Simultaneous multifunctionalisation

3.2.3 SEC analysis of multifunctional dendrons

Triple detection SEC analysis of the multifunctional materials shows an incremental decrease in retention time with increasing Bz functionality from **[Am_4-G_2-TSe];[42]** to **[Bz_4-G_2-TSe];[43]** for the G_2 dendron series, which may be correlated to an increase in molecular weight and molecular size in solution (Fig. 3.18). The observed size increase is surprising when just one Am functional group is replaced with a Bz group each time.

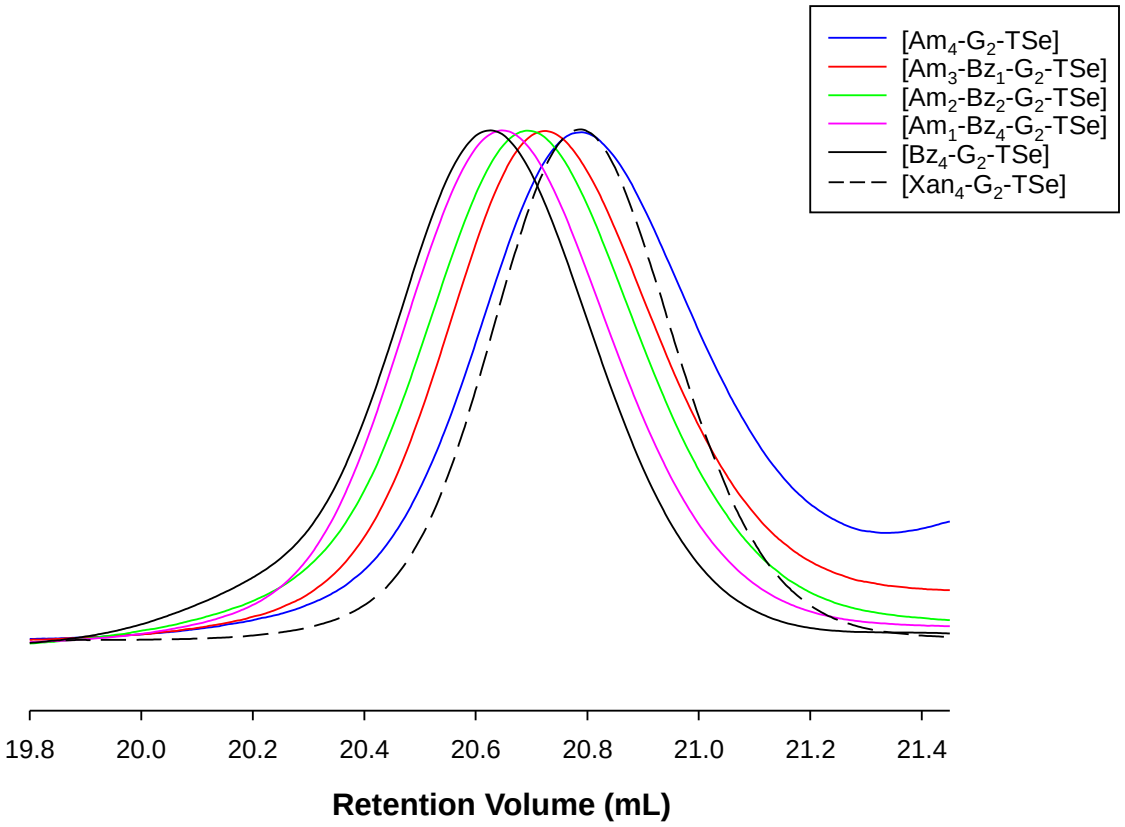

Fig. 3.18 SEC chromatogram overlay of RI traces for **[Xan_4-G_2-TSe];[13]** (dashed black line), **[Am_4-G_2-TSe];[42]** (blue line), **[Am_3-Bz_1-G_2-TSe];[63]** (red line), **[Am_2-Bz_2-G_2-TSe];[62]** (green line), **[Am_1-Bz_3-G_2-TSe];[61]** (pink line) and **[Bz_4-G_2-TSe];[43]** (solid black line)

The materials maintained a narrow dispersity (Đ) and a monomodal distribution (Table S3.2), despite the distribution of materials observed by MALDI-TOF analysis.

3.3 Statistical multifunctionalisation of xanthate functional dendrimers

So far, the multifunctionalisation of increasingly complex model dendrons via sequential and simultaneous strategies has been explored. The overall aim of this research is the multifunctionalisation of HPDs, which possess large numbers of dendron chain ends, and hence, xanthate peripheral groups. Therefore, the sequential and simultaneous multifunctionalisation of a G_2 model dendrimer, which presents a high concentration of xanthate functional groups in close proximity, would provide an insight into the multifunctionalisation of more complex polymers containing multiple xanthate functional dendrons, studied later, Fig. 3.19.

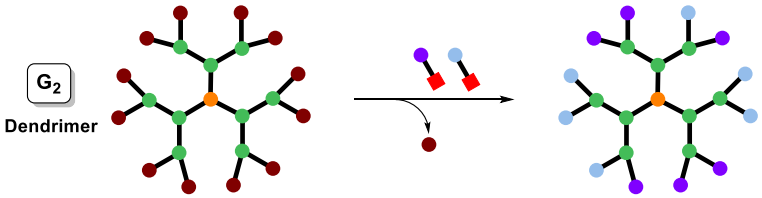

Fig. 3.19 Schematic representation of the multifunctionalisation of a xanthate peripheral G_2 dendrimer

3.3.1 Sequential multifunctionalisation

As outlined in section 3.2.1.3, the xanthate functional G_2 dendrimer **[Xan$_{12}$-G$_2$-THPE];[18]** was subjected to varying molar equivalents of *n*-butylamine, targeting 25%, 50% and 75% of xanthate groups deprotected. Xanthate groups of the dendrimer were deprotected in a controlled manner, as seen previously for the model dendrons (Fig. S3.23). A slight molar excess of DMAEA was added with respect to the exposed thiols. Remaining xanthate groups were then deprotected and benzyl acrylate added in excess. The resulting materials were analysed by ^{1}H NMR spectroscopy, Fig. 3.20.

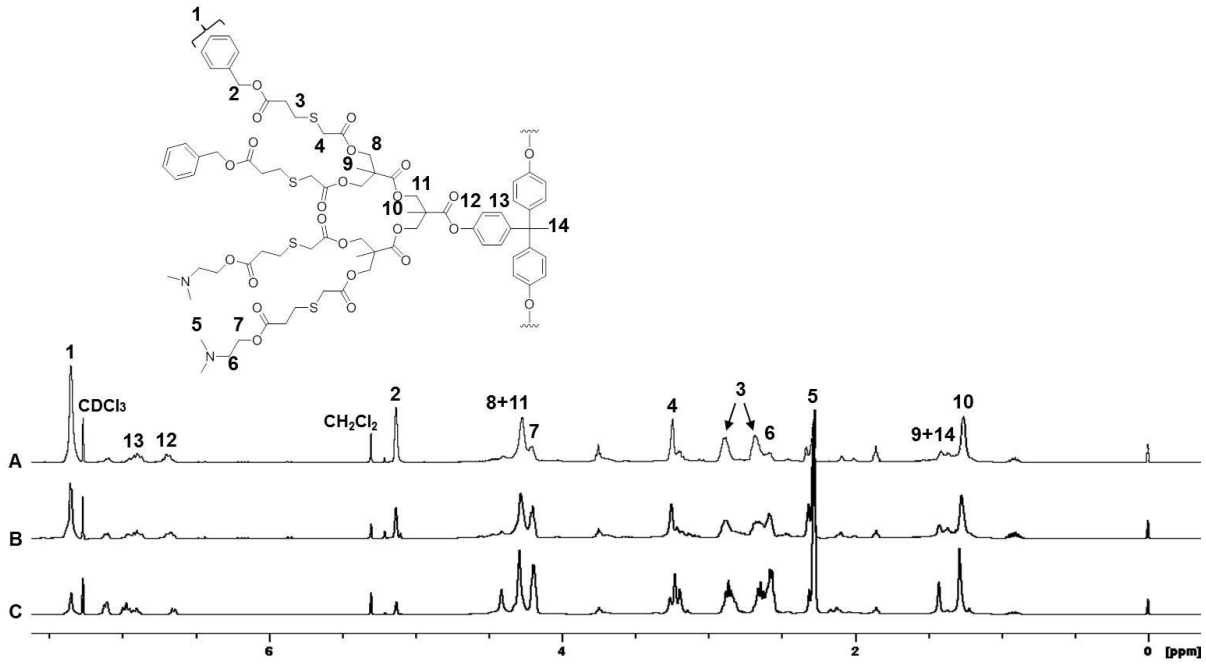

Fig. 3.20 Stacked ^{1}H NMR (400 MHz, $CDCl_3$) spectra of Am and Bz functionalised **[Xan_{12}-G_2-THPE];[18]** *via* the sequential strategy: A) **[Am_3-Bz_9-G_2-THPE];[96]**; B) **[Am_6-Bz_6-G_2-THPE];[97]**; C) **[Am_9-Bz_3-G_2-THPE];[98]**

As an example, targeting **[Am_6-Bz_6-G_2-THPE];[97]**, 50% of xanthate groups were initially deprotected by addition of 6 equivalents of *n*-butylamine, followed by addition of 9 molar equivalents of Am acrylate. The product was purified, analysed by ^{1}H NMR (Fig. S3.24), and the remaining xanthate groups deprotected and reacted with a 1.5 molar excess of Bz acrylate per exposed thiol. The resulting product was analysed by ^{1}H NMR after purification, confirming the average 50/50 functionalisation targeted (Fig. S3.25). ^{1}H NMR analysis of the targeted materials revealed ratios of 25:73, 50:46 and 85:15 of Am:Bz functionality incorporated (Fig. 3.20). Restricted rotation and slow molecular tumbling results in fairly broad resonances in the ^{1}H NMR spectra of the functionalised dendrimer materials, despite their highly symmetric structures.

3.3.2 Simultaneous multifunctionalisation

As described previously, in the simultaneous methodology, all xanthate groups are deprotected with an excess of *n*-butylamine and a stoichiometric mixture of functional acrylates added to simultaneously react with exposed thiols in a one-pot reaction. Multifunctionalisation with Am and Bz acrylates was targeted at 25:75, 50:50 and 75:25 ratios by varying the molar equivalents of each acrylate added following deprotection. Materials analysed by ^{1}H NMR spectroscopy showed good control over multifunctionalisation, with ratios of 26:73, 60:40 and 78:22 of Am:Bz functionality achieved, Fig. 3.21.

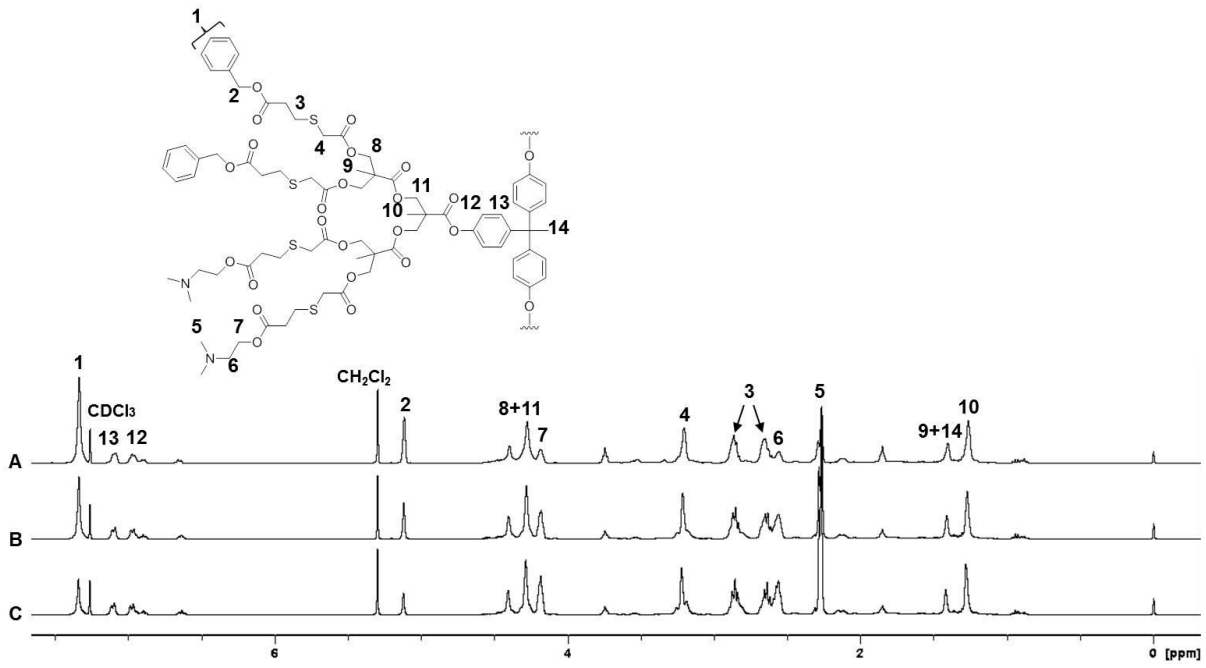

Fig. 3.21 Stacked ^{1}H NMR (400 MHz, $CDCl_3$) spectra of Am and Bz functionalised **[Xan$_{12}$-G$_2$-THPE];[18]** *via* the simultaneous strategy: A) **[Am$_3$-Bz$_9$-G$_2$-THPE];[96]**; B) **[Am$_6$-Bz$_6$-G$_2$-THPE];[97]**; C) **[Am$_9$- Bz$_3$-G$_2$-THPE];[98]**

Simultaneous multifunctionalisation, targeting **[Am$_6$-Bz$_6$-G$_2$-THPE];[97]**, involved complete deprotection of all xanthate groups under mild basic conditions at ambient temperature, followed by addition of a 50/50 stoichiometric mixture of Am and Bz acrylates, and the

reaction left to stir overnight. The resulting mixture was purified by precipitation and analysed by ^{1}H NMR spectroscopy, Fig. 3.22.

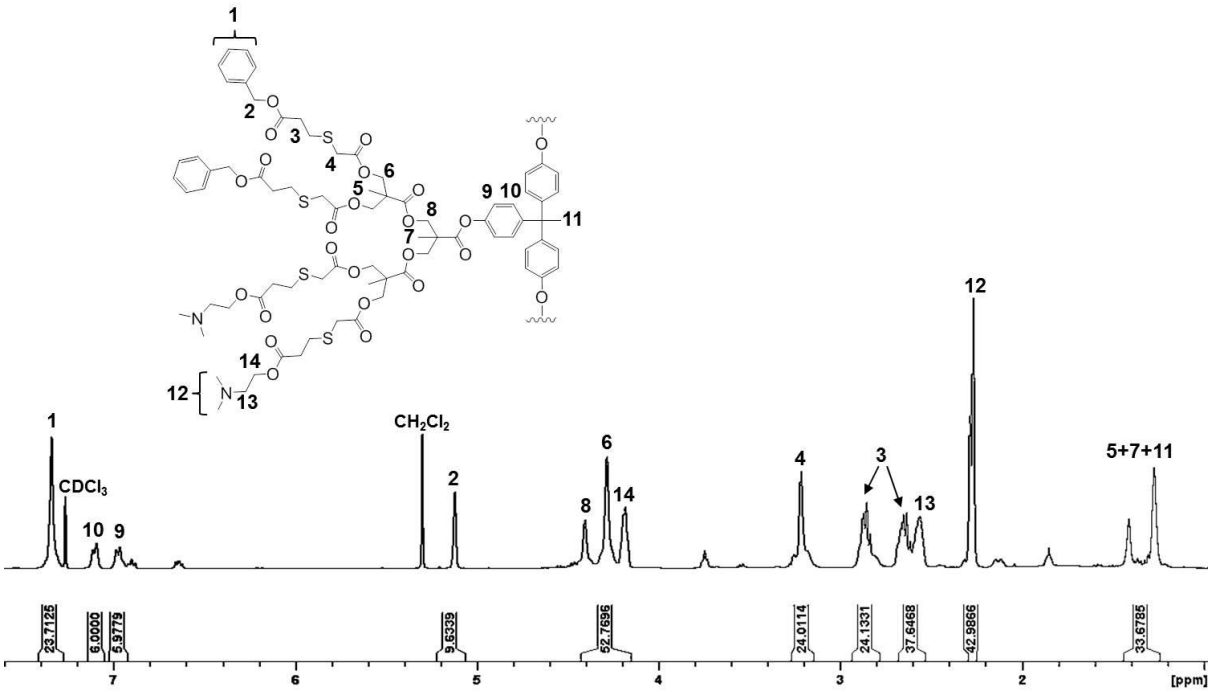

Fig. 3.22 ^{1}H NMR (400 MHz, $CDCl_3$) of **[Am$_6$-Bz$_6$-G$_2$-THPE];[97]** by simultaneous multifunctionalisation

According to ^{1}H NMR analysis, both methods achieved a good degree of control over multifunctionalisation of the xanthate functional G_2 dendrimer **[18]**, however, mass spectrometry data obtained for the model dendrons (sections 3.2.1.3 and 3.2.2) suggests there is likely to be a broad distribution of materials obtained for each target structure. MALDI TOF mass spectrometry was not conducted on these functionalised dendrimer materials, but this served as proof of principal for later studies of complex polymers containing multiple dendrons that would not be able to be studied by mass spectrometry.

3.4 Post-polymerisation modification of xanthate functional polymeric materials with complex architectures

Post-polymerisation modification of a single, well-defined macromolecular precursor allows the opportunity to control end group functionality without the potential for significant changes in chain length distribution that may result from multiple polymer sample syntheses. Due to the nature of polymerisation, HPDs are fundamentally polydisperse; the distribution can be maintained if post-polymerisation modification is applied. The synthesis of multiple samples with different molecular weight distributions and different functional group distributions would make it much more difficult to establish differences in behaviour and correlate surface group variation between samples. This method of functional material synthesis involves polymerisation of monomers or initiators with functional groups which are inert to polymerisation conditions, but allow quantitative conversion in a subsequent reaction step to incorporate a wide range of functionalities. Libraries of functional polymers with identical number average degrees of polymerisation (DP_n) but with variable side chain functionality may be easily generated from a single sample of polymer.[21] Detailed analysis of these materials is very difficult to achieve without lengthy separation of individual components of complex distributions and analysis using multiple techniques. The model studies of G_1-G_3 dendrons presented above (section 3.2) offers new insights into outcomes that would result from post-polymerisation modification of novel complex polymer architectures bearing dendron subunits, e.g. Janus-dendrimers, hyperbranched polymers, linear dendritic hybrids, dendron modified surfaces, dendron-bearing networks, dendronised polymers and hyperbranched polydendrons.

The orthogonal nature of the dendron periphery and focal point protection chemistries used in these studies allows selective deprotection and introduction of ATRP initiating functional

groups at the focal point of the model dendrons. The syntheses of xanthate functional dendron macroinitiators (G_0-G_3) and subsequent polymerisations with nBMA and tBMA monomers is described in Chapter 2 (sections 2.7 and 2.8), to form linear dendritic hybrid (LDH) species, and corresponding hyperbranched polydendrons (HPDs) by inclusion of bifunctional monomer EGDMA. The potential of the sequential and simultaneous multifunctionalisation strategies are evaluated for the controlled introduction of mixed functionality to the dendron periphery of both LDH and HPD species, Fig. 3.23.

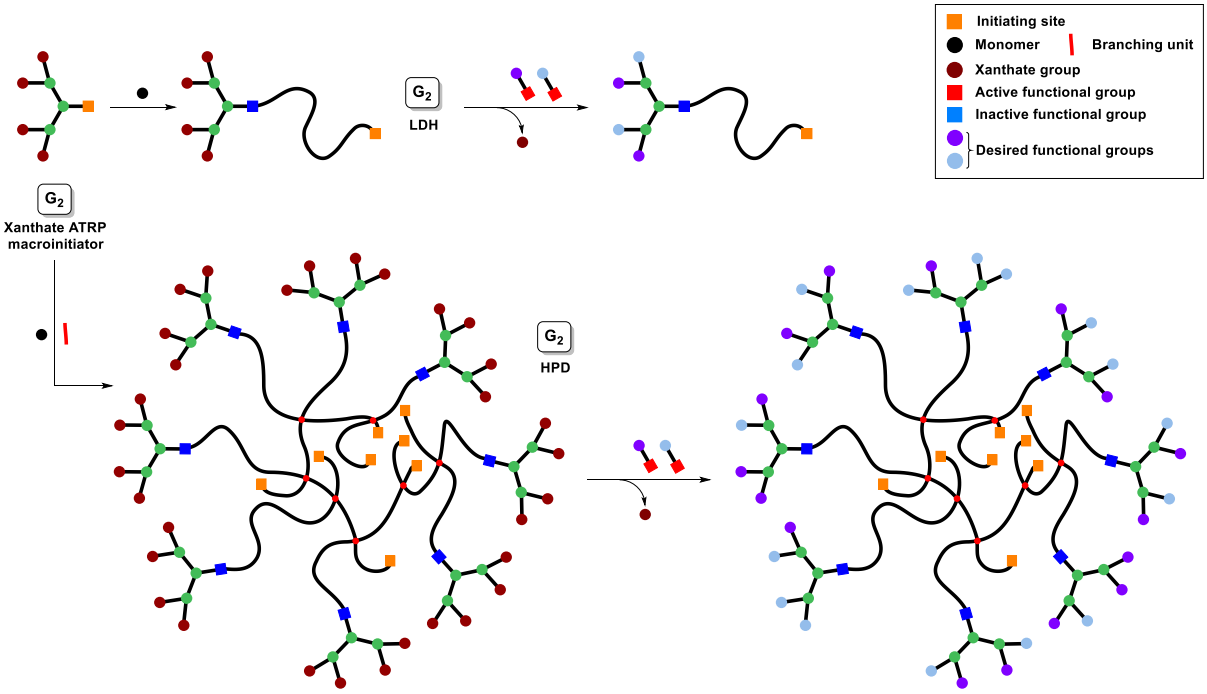

Fig. 3.23 Synthesis and post-polymerisation modification of G_2 LDH and corresponding HPD materials

3.4.1 Statistical multifunctionalisation of xanthate functional LDHs and HPDs

3.4.1.1 tBMA

Xanthate peripheral G_1 and G_2 dendron initiated *tert*-butylmethacrylate (tBMA) LDHs and HPDs (**[25]-[28]**), synthesised in Chapter 2 (sections 2.8.4.1 and 2.8.5.1, respectively), were investigated for their ability to undergo sequential and simultaneous multifunctionalisation with Bz and Am acrylate. The ability to access the chain-ends of these complex polymer architectures to controllably deprotect and functionalise peripheral groups has been investigated. The triple detection SEC-derived molecular weight distributions of the G_1 and G_2 dendron initiated LDH and HPD materials, and G_2 materials following simultaneous multifunctionalisation are summarised in Table 3.2.

Table 3.2 Triple detection SEC[a] analysis of G_1 and G_2 dendron initiated polymer materials

Polymer	Type[b]	Monomer conv. (%)	SEC (THF)[a] M_n (g mol^{-1})	SEC (THF)[a] M_w (g mol^{-1})	Đ
p[(Xan$_2$-G$_1$)-tBMA$_{50}$];[25]	LDH	>99	13 700	17 000	1.24
p[(Xan$_2$-G$_1$)-tBMA$_{50}$-*co*-EGDMA$_{0.8}$];[27]	HPD	>99	59 600	935 800	15.69
p[(Xan$_4$-G$_2$)-tBMA$_{50}$];[26]	LDH	>99	12 900	15 200	1.19
p[(Am$_2$-Bz$_2$-G$_2$)-tBMA$_{50}$];[118]	LDH	-	16 300	19 100	1.18
p[(Xan$_4$-G$_2$)-tBMA$_{50}$-*co*-EGDMA$_{0.8}$];[28]	HPD	>99	46 500	340 700	7.29
p[(Am$_2$-Bz$_2$-G$_2$)-tBMA$_{50}$-*co*-EGDMA$_{0.8}$];[121]	HPD	-	51 200	312 400	6.10

[a]SEC values (M_n, M_w and $Đ$) determined using THF eluent containing 2% TEA (v/v), 1 ml min^{-1} flow rate. [b]LDH = linear dendritic hybrid; HPD = hyperbranched polydendron

3.4.1.1.1 Sequential modification

G_1 and G_2 LDHs; **p[(Xan$_2$-G$_1$)-tBMA$_{50}$];[25]** and **p[(Xan$_4$-G$_2$)-tBMA$_{50}$];[26],** and HPDs; **p[(Xan$_2$-G$_1$)-tBMA$_{50}$-*co*-EGDMA$_{0.8}$];[27]** and **p[(Xan$_4$-G$_2$)-tBMA$_{50}$-*co*-EGDMA$_{0.8}$];[28]**, were subjected to the same sequential xanthate deprotection strategy as outlined for the model dendrons in section 3.2.1.1; increasing molar equivalents of *n*-butylamine were added to yield increasing numbers of exposed thiols. The polymer compositions are less well-defined than the model dendrons, thus complicating the direct targeting of thiol-functionality, therefore, *pseudo*-calibration curves for xanthate deprotection were generated for each material. The *pseudo*-calibration curves relate the number of equivalents of *n*-butylamine used for deprotection with the percentage of thiols deprotected, as calculated by ^{1}H NMR spectroscopy by integrating the characteristic xanthate resonance at $\delta = 4.64$ ppm, relative to the polymer backbone ($\delta \approx 0.8$-1.1 ppm), which remains unchanged after deprotection. These curves are individually constructed for each polymer due to the distribution of species present; accurate calculation of molecular weight of primary polymer chains, and hence the number of xanthates per mole, is difficult and lengthy, particularly for branched polymer species which possess a broad dispersity of structures. The curves generated for the model dendrons (Fig. 3.6) are therefore inapplicable to polymeric species. The *pseudo*-calibration curves can be used to calculate the number of moles of *n*-butylamine required to target different degrees of deprotection during the first step of sequential multifunctionalisation when targeting different ratios of functional groups. The data can also be used to calculate the number of moles of each functional acrylate required to react with exposed thiols when targeting desired ratios of functionality during simultaneous multifunctionalisation.

The *pseudo*-calibration curves were generated by: (1) estimation of number average degree of polymerisation (DP_n) of the primary polymer chains using ^{1}H NMR end-group analysis; (2) calculation of the average number of moles of xanthate groups in each sample; (3) addition of

varying equivalents of *n*-butylamine; and (4) determination of the average number of xanthates deprotected using ^{1}H NMR analysis. It was evident from the resultant deprotection curves that the G_1 dendron initiated LDH and HPD polymer materials required considerably more *n*-butylamine for deprotection than the model dendron (**[Xan$_2$-G$_1$-TSe];[12]**) to achieve the desired level of deprotection (Fig. 3.24A; LDH Fig. S3.26, HPD Fig. S3.29). Within experimental error, the G_2 dendron initiated LDH and HPD closely resembled the behaviour of the model G_2 dendron (**[Xan$_4$-G$_2$-TSe];[13]**), requiring approximately 1 molar equivalent of *n*-butylamine per xanthate to liberate the required number of thiols (Fig. 3.24B; LDH Fig. S3.32, HPD Fig. S3.35).

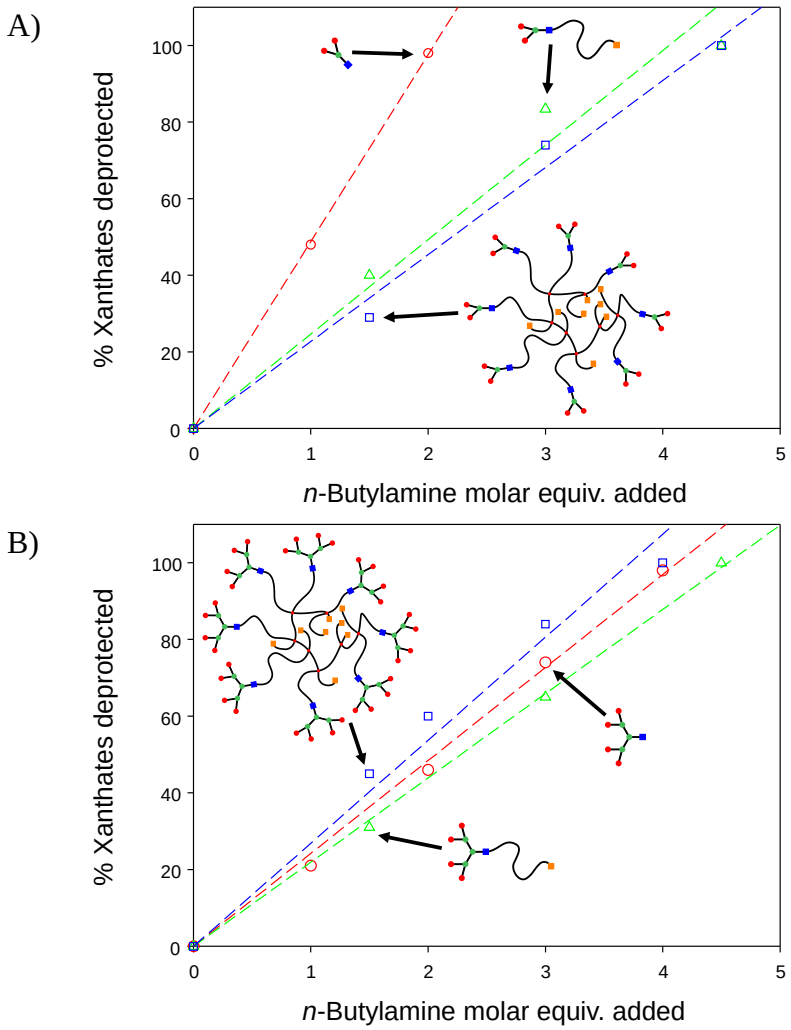

Fig. 3.24 *Pseudo*-calibration curves for xanthate deprotection of; A) structures derived from **G$_1$** dendrons, and B) structures derived from **G$_2$** dendrons. Model dendrons (open red circles), LDHs (open green triangles) and HPDs (open blue squares). All data was determined using ^{1}H NMR spectroscopy and linear regression is shown.

To investigate this further, the deprotected materials were treated with Bz acrylate and the percentage of Michael adduct was determined by ^{1}H NMR after purification (G_1 LDH Fig. S3.27, HPD Fig. S3.30; G_2 Fig. S3.33, HPD Fig. S3.36), shown here for **p[(Xan$_2$-Bz$_2$-G$_2$)-tBMA$_{50}$-*co*-EGDMA$_{0.8}$];[113]**, Fig. 3.25; 5 equivalents of Bz acrylate per thiol were added to ensure full reaction.

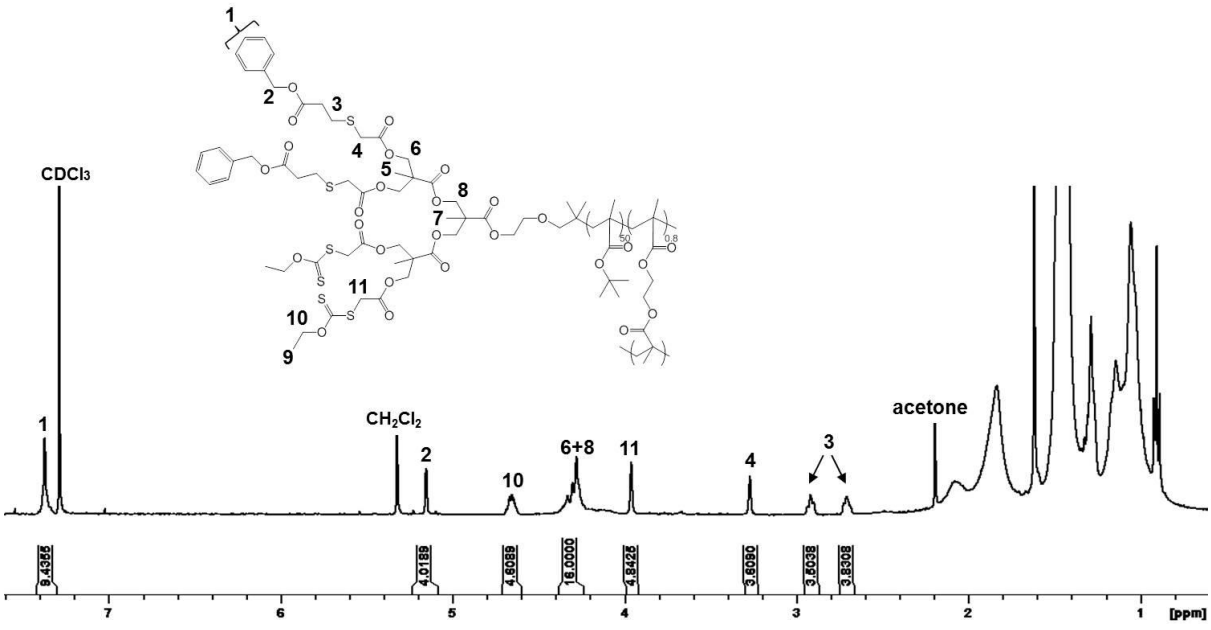

Fig. 3.25 ^{1}H NMR (400MHz, $CDCl_3$) of **p[(Xan$_2$-Bz$_2$-G$_2$)-tBMA$_{50}$-*co*-EGDMA$_{0.8}$];[113]** by sequential modification of **p[(Xan$_4$-G$_2$)-tBMA$_{50}$-*co*-EGDMA$_{0.8}$];[28]**

The number of thiol-acrylate Michael adducts formed in each sequential deprotection-functionalisation confirmed the observations seen within the *pseudo*-calibration curves; a significant molar excess of *n*-butylamine was required to efficiently deprotect the xanthates within both G_1 dendron initiated LDH and HPD polymer samples. In all cases the ability to target the deprotection of a bespoke number of thiols, and a near-linear relationship with subsequent thiol-acrylate Michael addition, was seen, Fig. 3.26.

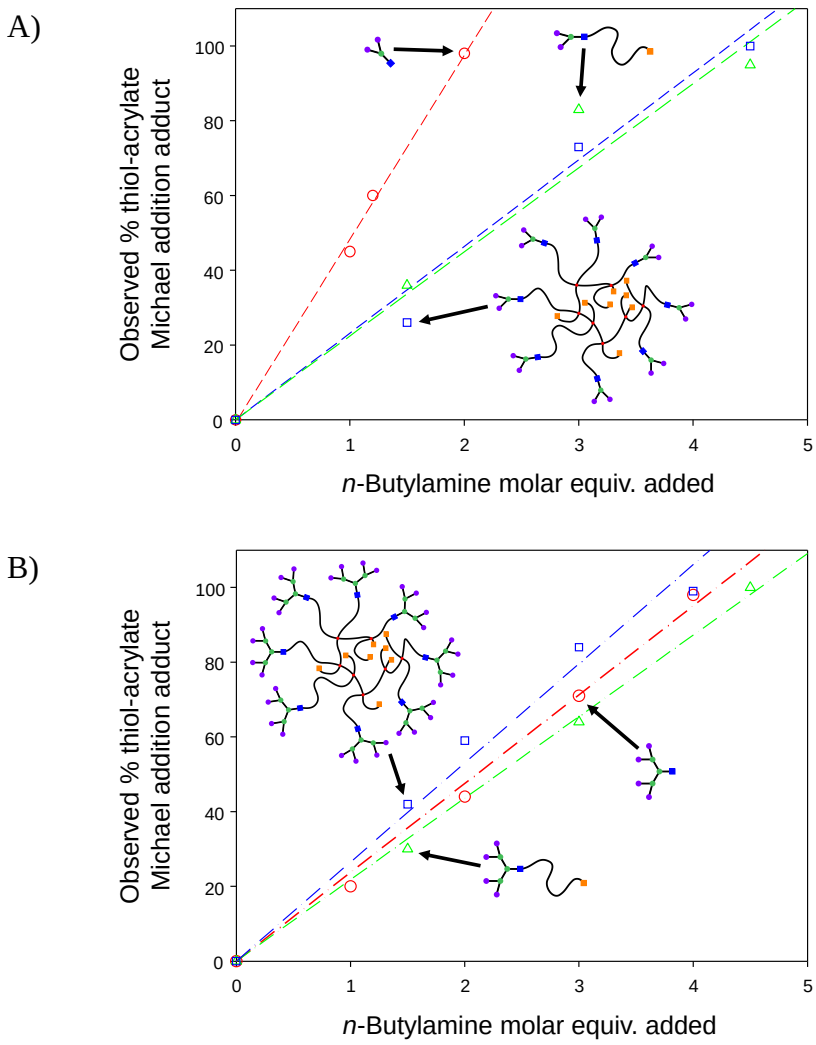

Fig. 3.26 Relationship between moles of *n*-butylamine required for sequential xanthate deprotection and subsequent benzyl acrylate Michael adducts. A) Structures derived from G_1 dendrons, and B) structures derived from G_2 dendrons. Model dendrons (open red circles), LDHs (open green triangles) and HPDs (open blue squares). All data was determined using ^{1}H NMR spectroscopy and linear regression is shown.

The difference in behaviour between the model G_1 dendron and the polymers derived from the G_1 dendron initiator may suggest a difficulty in accessing peripheral xanthates for deprotection and subsequent thiol-acrylate Michael addition. The G_2 dendron initiated samples appear, conversely, to be accessible; suggesting that even at relatively low dendron generation, a different coiling of chains in solution may be present.

Further functionalisation was achieved by deprotection of the remaining xanthate groups in the partially Bz functional materials with a 5-fold molar excess of *n*-butylamine and

subsequent addition of an excess of Am acrylate. Resulting materials were analysed by ^{1}H NMR following purification, confirming the formation of mixed Bz and Am functional **p[(Am$_x$-Bz$_y$-G$_2$)-tBMA$_{50}$-*co*-EGDMA$_{0.8}$]** (x = 0-4, y = 0-4, x+y = 4) (G_1 LDH Fig. S3.28, HPD Fig. S3.31; G_2 LDH Fig. S3.34, HPD Fig. S3.37).

3.4.1.1.2 Simultaneous modification

Simultaneous statistical multifunctionalisation was investigated using the G_2 dendron initiated LDH **p[(Xan$_4$-G$_2$)-tBMA$_{50}$];[26]** and HPD **p[(Xan$_4$-G$_2$)-tBMA$_{50}$-*co*-EGDMA$_{0.8}$];[28]**. The complete deprotection of chain-end xanthate functionality (1.2 molar equivalents of *n*-butylamine per xanthate) and addition of a 1:1 molar ratio of Bz and Am acrylates (1 molar equivalent per thiol) resulted in the functionalised LDH **p[(Am$_2$-Bz$_2$-G$_2$)-tBMA$_{50}$];[118]** and HPD **p[(Am$_2$-Bz$_2$-G$_2$)-tBMA$_{50}$-*co*-EGDMA$_{0.8}$];[121]** as confirmed by ^{1}H NMR spectroscopy (Fig. S3.38 and Fig. 3.27, respectively) and SEC (Fig. 3.28; Table 3.2).

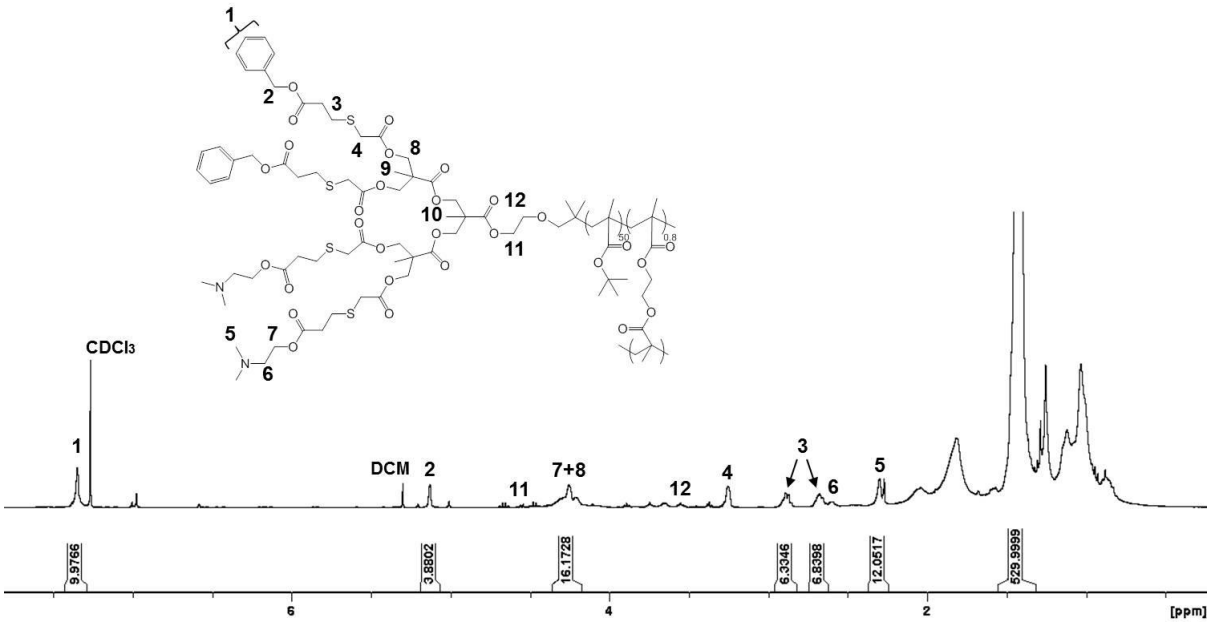

Fig. 3.27 ^{1}H NMR (400MHz, $CDCl_3$) of **p[(Am$_2$-Bz$_2$-G$_2$)-tBMA$_{50}$-*co*-EGDMA$_{0.8}$];[121]** by simultaneous multifunctionalisation of **p[(Xan$_4$-G$_2$)-tBMA$_{50}$-*co*-EGDMA$_{0.8}$];[28]**

^{1}H NMR analysis confirmed a 1:1 ratio of Bz and Am functionality within both products, however, integrals for the methylene resonances (δ ≈ 2.68 and 2.89 ppm; Fig. 3.27 peak 3) of the targeted Michael adduct **p[(Am$_2$-Bz$_2$-G$_2$)-tBMA$_{50}$-*co*-EGDMA$_{0.8}$];[121]** were lower than expected when compared to the polymer backbone C*H*$_3$ resonance at δ ≈ 1.32–1.55 ppm; this is thought to be due to restricted movement of protons within the structure.

SEC analysis of the linear-dendritic hybrid before and after the full deprotection and subsequent thiol-acrylate Michael addition showed a slight shift to lower retention times (Fig. 3.28A) and subsequent increase in the determined values for M_n and M_w (Table 3.2). Interestingly, the shape of the molecular weight distributions of the LDHs, and subsequent Đ values, were nearly identical with no obvious broadening or bimodality. This would suggest an absence of intermolecular coupling after deprotection and exposure of a large number of thiol functional groups. To establish the storage stability of the xanthate-protected **p[(Xan$_4$-G$_2$)-tBMA$_{50}$];[26]**, a sample was stored for approximately 2 years and showed no meaningful change in the molecular weight distribution (Fig. 3.28A). The same simultaneous deprotection/thiol-Michael addition strategy also formed the mixed-functionality HPD **p[(Am$_2$-Bz$_2$-G$_2$)-tBMA$_{50}$-*co*-EGDMA$_{0.8}$];[121]** without obvious intermolecular coupling, as confirmed by SEC analysis (Fig. 3.28B); additionally, xanthate-functional HPD storage stability was confirmed by analysis of a sample approximately two years after initial synthesis (Fig. 3.28B).

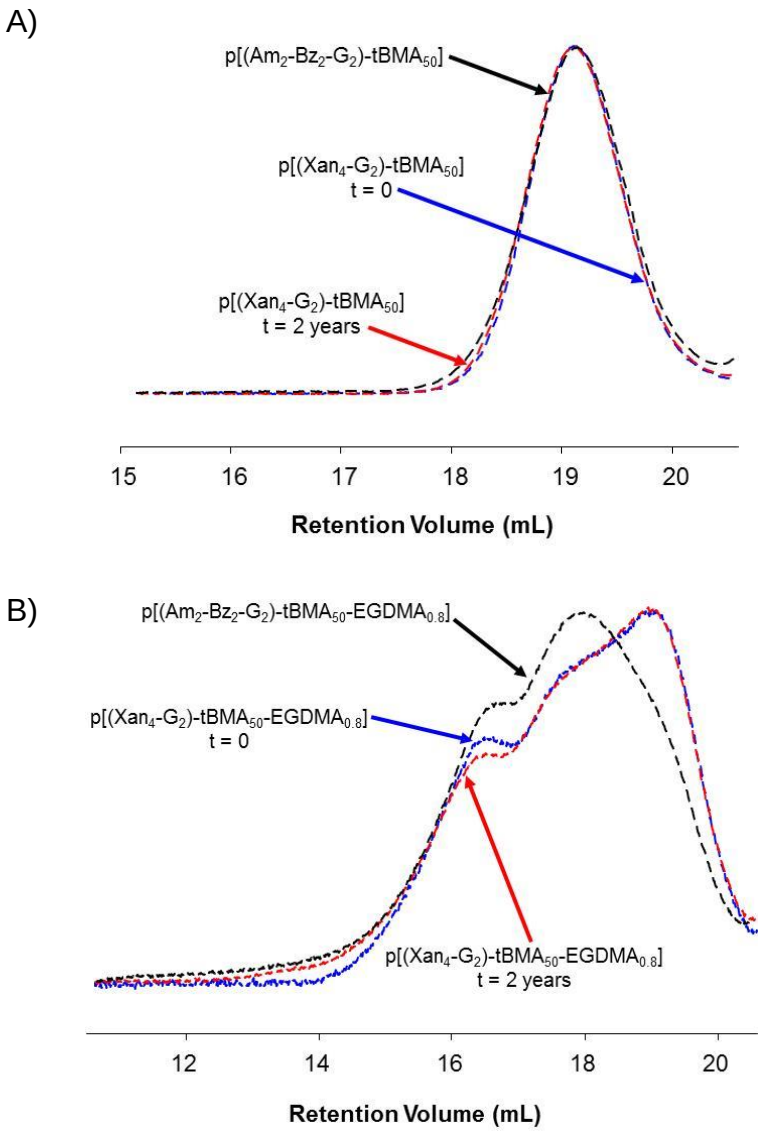

Fig. 3.28 SEC chromatogram overlays of RI of (A) LDH materials and (B) HPD materials. Molecular weight distributions for xanthate-functional materials as prepared (blue lines), stored for 2 years (red lines) and after full xanthate deprotection and subsequent simultaneous Michael addition reaction with 1:1 molar ratio of Bz and Am (black lines).

3.4.1.2 nBMA

The polymer was changed from tBMA (T_g = 118°C) to nBMA (T_g = 20°C)[22] for this study as the aim of this research is to generate multifunctional nanoparticles for drug delivery; a lower T_g material would present cells with a more pliable particle, rather than a hard sphere, which may influence uptake.[3-6] Xanthate peripheral G_0-G_3 dendron initiated *n*-butylmethacrylate (nBMA) HPDs (**[36]-[39]**) were investigated for their ability to undergo sequential and simultaneous statistical post-polymerisation modification, shown here for G_3 initiated HPD, Fig. 3.29.

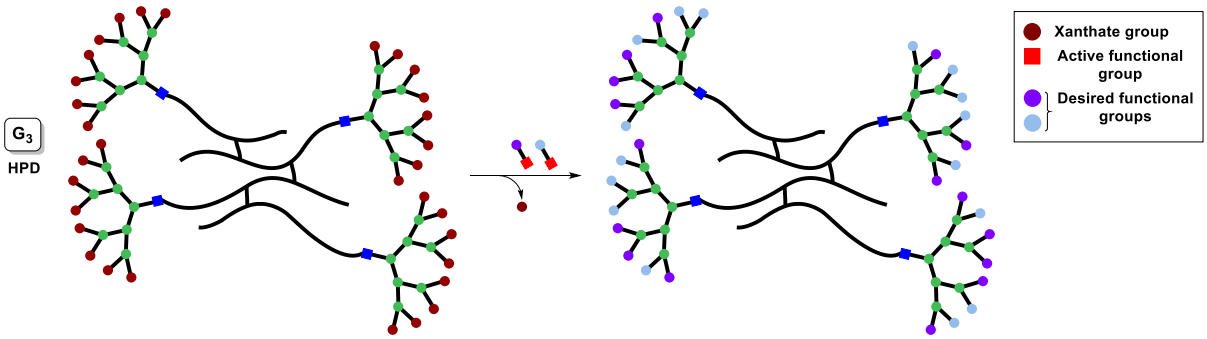

Fig. 3.29 Statistical multifunctionalisation of xanthate functional G_3 dendron initiated HPD

G_0-G_3 nBMA HPDs; **p[(Xan$_1$-G$_0$)-nBMA$_{100}$-*co*-EGDMA$_{0.7}$];[36]**, **p[(Xan$_2$-G$_1$)-nBMA$_{100}$-*co*-EGDMA$_{0.8}$];[37]**, **p[(Xan$_4$-G$_2$)-nBMA$_{100}$-*co*-EGDMA$_{0.8}$];[38]** and **p[(Xan$_8$-G$_3$)-nBMA$_{100}$-*co*-EGDMA$_{0.8}$];[39]**, were subjected to sequential deprotection to construct *pseudo*-calibration curves for each material. Increasing molar equivalents of *n*-butylamine resulted in increasing deprotection of peripheral xanthate groups, giving rise to a near-linear correlation, independent of the dendron generation of the HPD structures, Fig. 3.30.

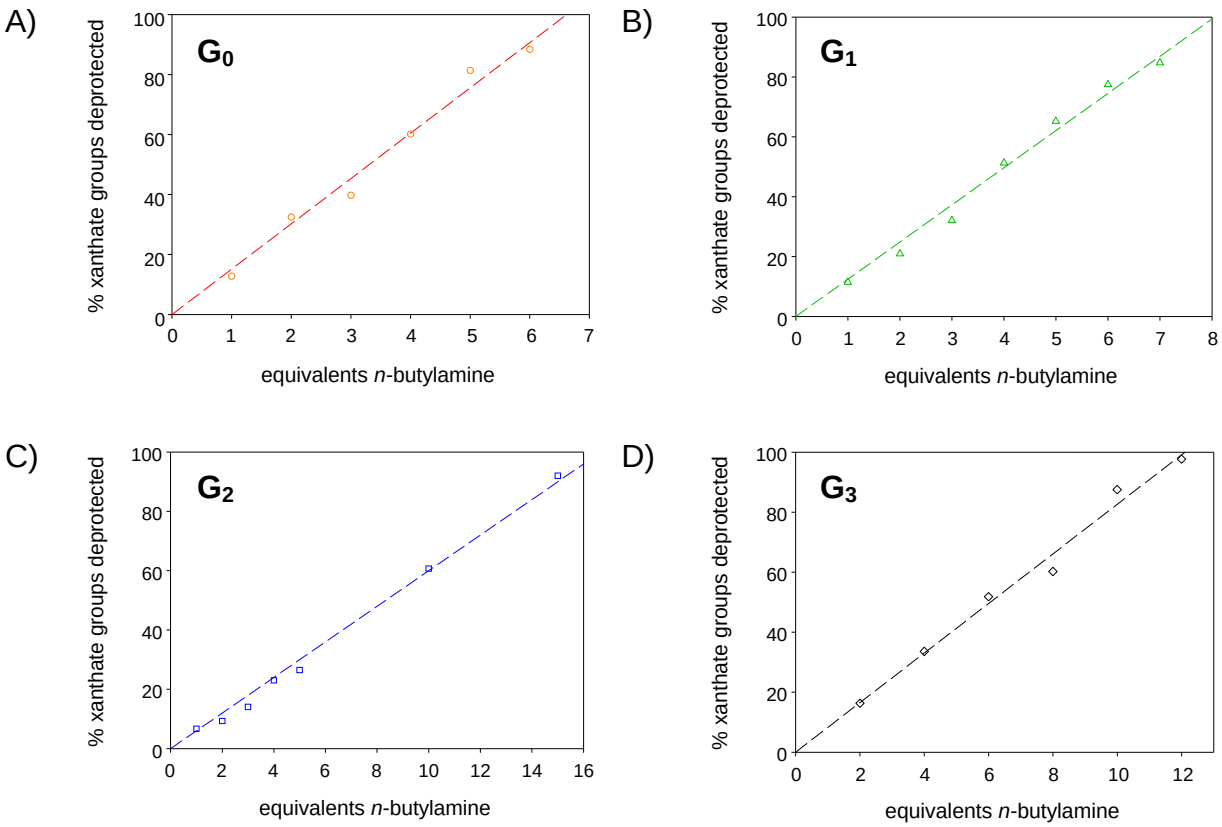

Fig. 3.30 *Pseudo*-calibration curves for the sequential deprotection of xanthate groups of branched *n*-butylmethacrylate HPDs; A) **p[(Xan$_1$-G$_0$)-nBMA$_{100}$-*co*-EGDMA$_{0.7}$];[36]**, B) **p[(Xan$_2$-G$_1$)-nBMA$_{100}$-*co*-EGDMA$_{0.8}$];[37]**, C) **p[(Xan$_4$-G$_2$)-nBMA$_{100}$-*co*-EGDMA$_{0.8}$];[38]** and D) **p[(Xan$_8$-G$_3$)-nBMA$_{100}$-*co*-EGDMA$_{0.8}$];[39]**

The G$_2$ dendron initiated HPD required more molar equivalents of *n*-butylamine for xanthate deprotection than expected. This is likely to be due to a population of very high molecular weight species in the polymer distribution, which can be easily seen in the SEC RALS trace for the G$_2$ dendron initiated HPD material (Fig. 2.24C). This is thought to have led to a poor estimation of primary polymer chain length, and hence, the number of xanthates per mole of polymer. It may also be a diffusion control effect of the very high molecular weight polymers, restricting penetration of *n*-butylamine into the dense polymer structures. This further highlights the need to generate *pseudo*-calibration curves for each polymer sample for targeted statistical multifunctionalisation of these complex architectures.

Overall, the nBMA HPDs required much more equivalents of *n*-butylamine for xanthate deprotection than the equivalent tBMA HPDs. This may suggest differences in amine penetration, or coiling of polymer chains in solution between the polymers.

3.4.1.2.1 Simultaneous modification

Simultaneous multifunctionalisation was carried out by deprotection of all xanthate peripheral groups with an excess of *n*-butylamine and reaction with a stoichiometric mixture of the chosen acrylates at various ratios (Am:Bz 25:75, 50:50 and 75:25), as calculated using the *pseudo*-calibration curves (Fig. 3.30) (^{1}H NMRs G_0-G_3 Fig. S3.42-S3.45).

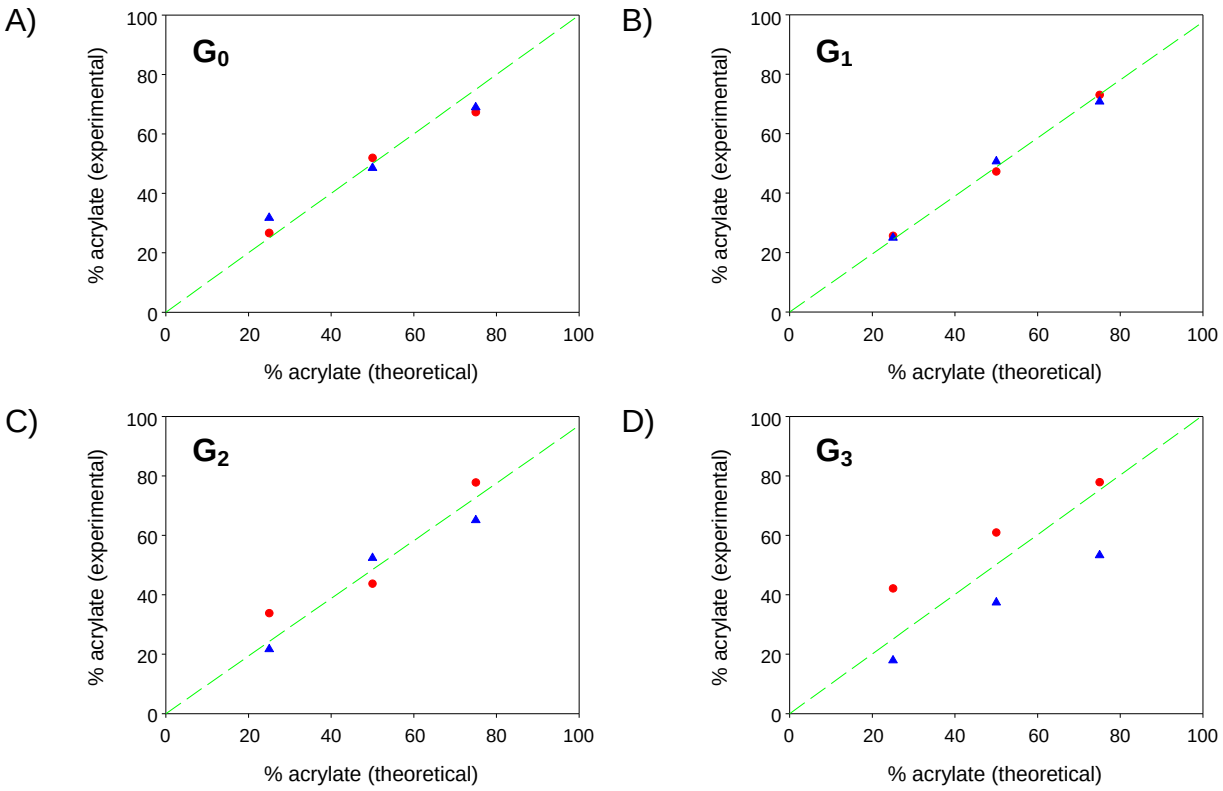

Fig. 3.31 Results of simultaneous multifunctionalisation of HPDs targeting Am:Bz ratios of 25:75, 50:50 and 75:25 for: A) **p[(Xan$_1$-G$_0$)-nBMA$_{100}$-*co*-EGDMA$_{0.7}$];[36]**; B) **p[(Xan$_2$-G$_1$)-nBMA$_{100}$-*co*-EGDMA$_{0.8}$];[37]**; C) **p[(Xan$_4$-G$_2$)-nBMA$_{100}$-*co*-EGDMA$_{0.8}$];[38]**; and D) **p[(Xan$_8$-G$_3$)-nBMA$_{100}$-*co*-EGDMA$_{0.8}$];[39]**. Bz (red closed circles) and Am (blue closed triangles), *pseudo*-calibration curves for G_0-G_3 dendrons shown (green dashed line)

There is a good agreement between targeted % functionalisation for G_0-G_2 dendron initiated HPDs, showing good control when applying the simultaneous strategy to these highly complex structures, despite the structural complexity and variation between the samples (Table S3.3). However, there is a disparity between theoretical and experimental values of % acrylate incorporated (analysed *via* ^{1}H NMR) for the G_3 dendron initiated HPDs, suggesting less control. This inconsistency in multifunctionalisation at higher dendron generations could be as a result of a steric effect; access to thiols may be difficult for acrylates in highly hydrophobic polymers. The problems seen with steric "trapping" of thiols in G_3 dendrons is magnified in these much larger, branched polymer systems. Statistical multifunctionalisation of HPDs appears to be more successful for lower generation dendrons.

3.5 Conclusion

Although significant progress has been made in recent years, the precise control over the distribution of surface functional groups on large, multifunctional materials, and their characterisation, remains a challenge. Many analytical techniques that are commonly used in multifunctional material characterisation (NMR spectroscopy, elemental analysis, UV-Vis spectrophotometry) can only be used to identify the mean functional group ratio. Results generated from these types of analytical techniques are clearly not sufficient to ensure clinical translation of multifunctional materials.

A rigorous model study of two strategies (sequential and simultaneous) to introduce mixed functionality onto masked-thiol dendrons has been conducted. These model studies allow detailed evaluation and comparison of the strategies, which would not be possible through analysis of the linear-dendritic hybrid (LDH) and hyperbranched polydendron (HPD) architectures alone, due to their inherent distribution of molecular weights. A distribution of

outcomes from statistical multifunctionalisation was expected (Fig. 3.32); however, the dendron studies shown here provide an insight into the complexity of the diverse structures and isolation of unreacted groups. NMR spectroscopy was the primary characterisation technique used to analyse the multifunctional dendritic materials within this study, however, MALDI-TOF mass spectrometry was required to resolve structure distributions within the sample. Interestingly, the simultaneous reaction of the chosen acrylates with thiol-functional dendrons generally led to fewer isolated thiols in the final materials. Coupling of exposed thiols during reactions was not observed.

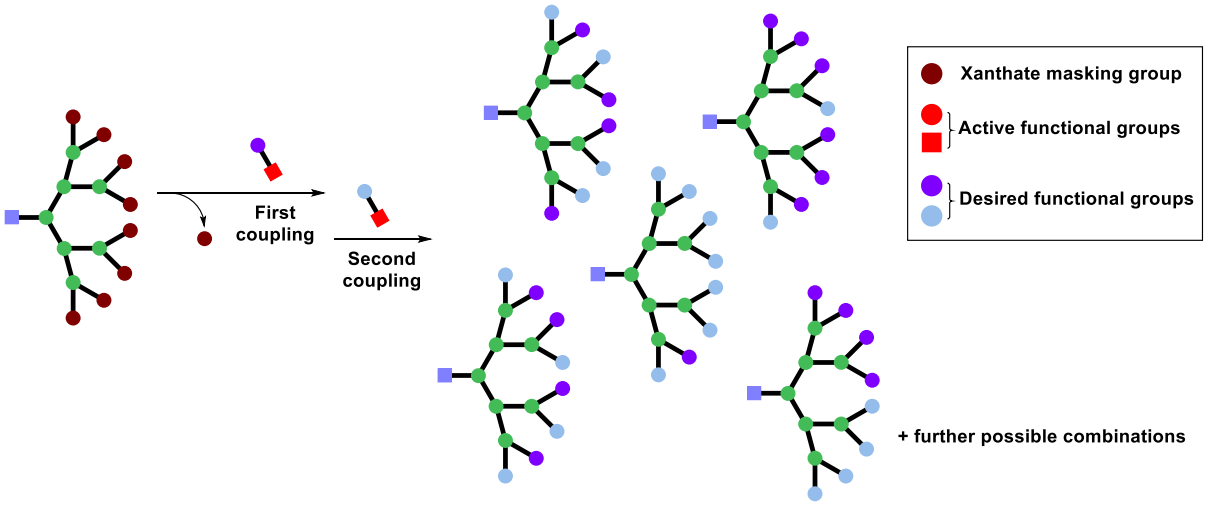

Fig. 3.32 Schematic representation of the distribution of possible outcomes from statistical multifunctionalisation of G_3 dendron **[Xan$_8$-G$_3$-TSe];[14]**

Although it is apparent that LDH materials, and their more complex HPD analogues, can be successfully manipulated through both functionalisation approaches, it is also clear that neither statistical functionalisation approach would lead to outcomes substantially resembling the nominal chosen product, and a large range of structures including full functionalisation with a single functional group will be formed on individual dendrons. The statistical introduction of two functional groups will potentially generate a considerable chemical diversity within the final sample leading to incorrect conclusions being drawn from the study

of molecular behaviour that is interpreted through an ill-informed view of the composition of the material under investigation.

The implications for partial or mixed post-synthesis surface group modification of any material are clear. These are more substantial when attempting to modify the functional groups of dendron-bearing materials. For example, LDHs bear a single dendron at the end of each chain and when subjected to partial or mixed-functionalisation, would be expected to generate end-groups representing the full spectrum of chemical compositions and very little of the targeted chemistry. In the example studied here, compositions ranging from 100% amine-containing through to 100% benzyl-terminated species would be present, leading to significant impact on the physical behaviour of the product. Although this was not studied here, highly heterogeneous and non-uniform behaviour to environmental conditions of varying pH[23] or temperature would be expected, as shown previously for subtle changes in the single functionality at the chain-ends of linear polymers.[24,25] Through the formation of HPDs, however, the distribution of outcomes is widely averaged across the large number of conjoined chain-ends, allowing the inclusion of the intended ratio of functional groups to be more closely achieved within individual highly branched molecules (Fig. 3.33) rather than at the single chain-end of LDHs. Such a result would also be expected for materials such as dendronised polymers, but the distribution of diverse compositions, even in LDHs and linear polymers, does potentially lead to other implications such as the formation of concentrated areas of specific functional groups which may influence the behaviour of the materials under specific conditions (e.g. biological interactions).[26-28] It would be incorrect to assume that localised domains of grouped functionality are not present within statistically modified mixed functionality materials (Fig. 3.33), therefore we are not confident that this is the most appropriate strategy to undertake the detailed studies of patchy vs. statistical functionality

detailed in Chapter 1 and highlighted again at the beginning of this chapter. Another strategy (see Chapter 4) to allow such studies was therefore adopted.

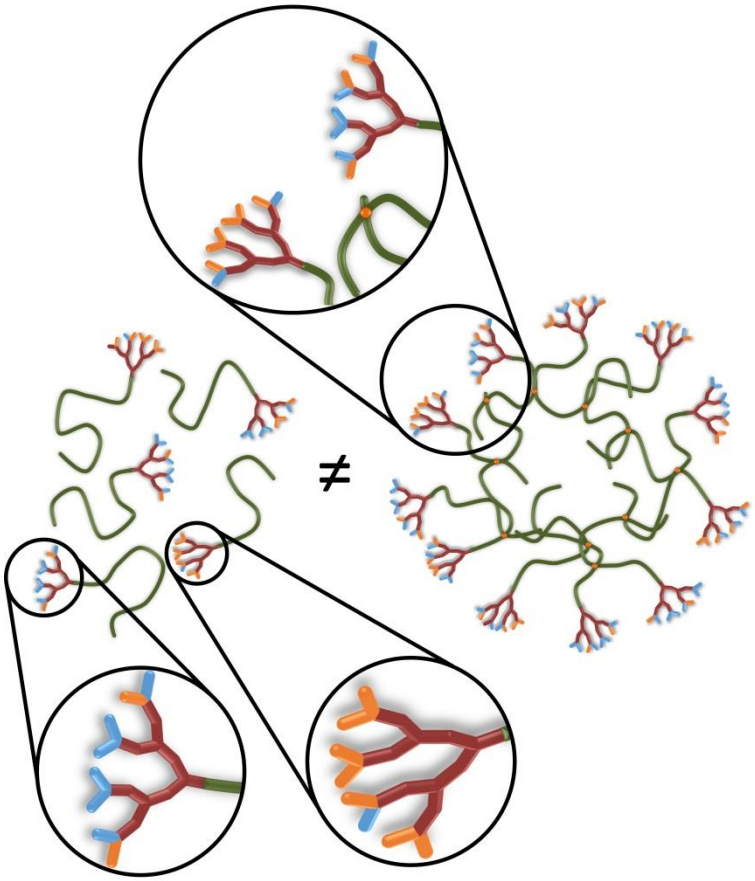

Fig. 3.33 Schematic representation of the outcome of statistical chain-end modification of LDHs and HPDs

These multifunctionalisation strategies provide an opportunity to build systematically varying complex architectures which may overcome many of the limitations of analogous macromolecules with more iterative and lengthy syntheses. These materials have tremendous potential in applications involving multifunctional nanoparticulate systems combining targeting, imaging, diagnostics and therapy.

3.6 References

1. J. Huskens, *Curr. Opin. Chem. Biol.*, 2006, **10**, 537–543.
2. M. Mammen, S. K. Choi, and G. M. Whitesides, *Angew. Chemie - Int. Ed.*, 1998, 37, 2754–2794.
3. H. Carrstensen, R. H. Müller, and B. W. Müller, *Clin. Nutr.*, 1992, **11**, 289–297.
4. S. D. Li and L. Huang, *Mol. Pharm.*, 2008, **5**, 496–504.
5. C. He, Y. Hu, L. Yin, C. Tang, and C. Yin, *Biomaterials*, 2010, **31**, 3657–66.
6. S. E. A. Gratton, P. A. Ropp, P. D. Pohlhaus, J. C. Luft, V. J. Madden, M. E. Napier, and J. M. DeSimone, *Proc. Natl. Acad. Sci.*, 2008, **105**, 11613–11618.
7. C. C. Lee, J. A. MacKay, J. M. J. Frechet, and F. C. Szoka, *Nat Biotech*, 2005, **23**, 1517–1526.
8. F. L. Hatton, L. M. Tatham, L. R. Tidbury, P. Chambon, T. He, A. Owen, and S. P. Rannard, *Chem. Sci.*, 2015, **6**, 326–334.
9. M. A. Gauthier, M. I. Gibson, and H. A. Klok, *Angew. Chemie Int. Ed.*, 2009, **48**, 48–58.
10. S. Nayak and L. Andrew Lyon, *Angew. Chemie - Int. Ed.*, 2005, **44**, 7686–7708.
11. S. E. R. Auty, O. Andren, M. Malkoch, and S. P. Rannard, *Chem. Commun.*, 2014, **50**, 6574–6577.
12. S. E. R. Auty, O. C. J. Andrén, F. Y. Hern, M. Malkoch, and S. P. Rannard, *Polym. Chem.*, 2014, **6**, 573–582.
13. K. McLeod and M. B. Comisarow, *J. Magn. Reson.*, 1969, **84**, 490–500.
14. H. E. Rogers (2016), *Exploring Hyperbranched-Polydendron Chemistry and Architecture for Nanomedicine Applications.* PhD thesis, University of Liverpool.
15. H. M. Patel, *Crit. Rev. Ther. Drug Carrier Syst.*, 1992, **9**, 39–90.
16. D. E. Owens and N. A. Peppas, *Int. J. Pharm.*, 2006, **307**, 93–102.

17. Y. Wang, J. Li, and L. Chengdu Yuan Dong Pharmaceutical Co. Ltd., Novel chiral sulfoxide compound and method for preparing esomeprazole by using novel chiral sulfoxide compound, Chinese Pat, CN102603621A, 2012.

18. F. Y. Hern, S. E. R. Auty, O. C. J. Andren, M. Malkoch, and S. P. Rannard, *Polym. Chem.*, 2017, **8**, 1644–1653.

19. D. Boris and M. Rubinstein, *Macromolecules*, 1996.

20. R. L. Lescanec and M. Muthukumar, *Macromolecules*, 1990.

21. P. Theato and H. A. Klok, *Functional Polymers by Post-Polymerization Modification: Concepts, Guidelines, and Applications*, WILEY-VCH Verlag GmbH, 2013.

22. https://www.sigmaaldrich.com/content/dam/sigma-aldrich/docs/Aldrich/General_Information/thermal_transitions_of_homopolymers.pdf

23. H. E. Rogers, P. Chambon, S. E. R. Auty, F. Y. Hern, A. Owen, and S. P. Rannard, *Soft Matter*, 2015, **11**, 7005–15.

24. M. Long, D. W. Thornthwaite, S. H. Rogers, F. R. Livens, and S. P. Rannard, *Polym. Chem.*, 2012, **3**, 154–161.

25. S. Jana, S. P. Rannard, and A. I. Cooper, *Chem. Commun.*, 2007, 2962–2964.

26. S. L. Mangold, R. T. Carpenter, and L. L. Kiessling, *Org. Lett.*, 2008, **10**, 2997–3000.

27. N. R. Bennett, D. B. Zwick, A. H. Courtney, and L. L. Kiessling, *ACS Chem. Biol.*, 2015, **10**, 1817–1824.

28. S. Szunerits, A. Barras, M. Khanal, Q. Pagneux, and R. Boukherroub, *Molecules*, 2015, **20**, 14051–14081.

3.7 Appendix

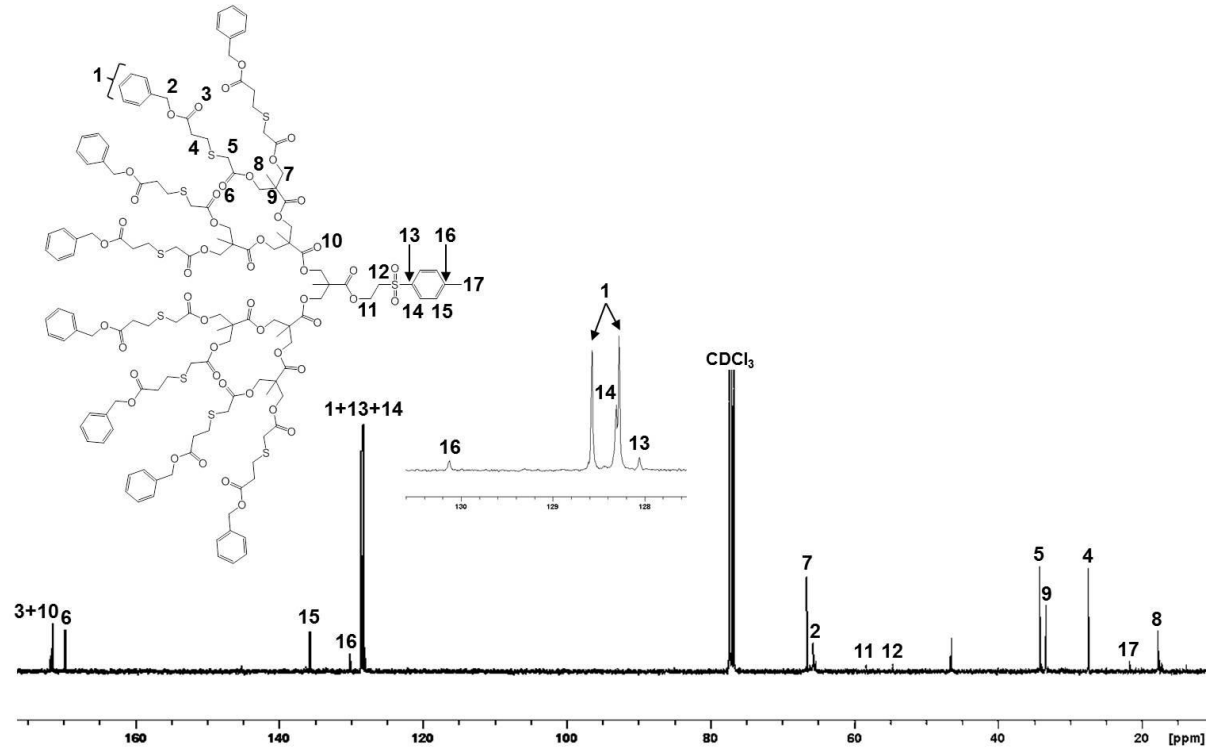

Fig. S3.1 ^{13}C NMR (100 MHz, $CDCl_3$) of **[Bz_8-G_3-TSe];[45]**

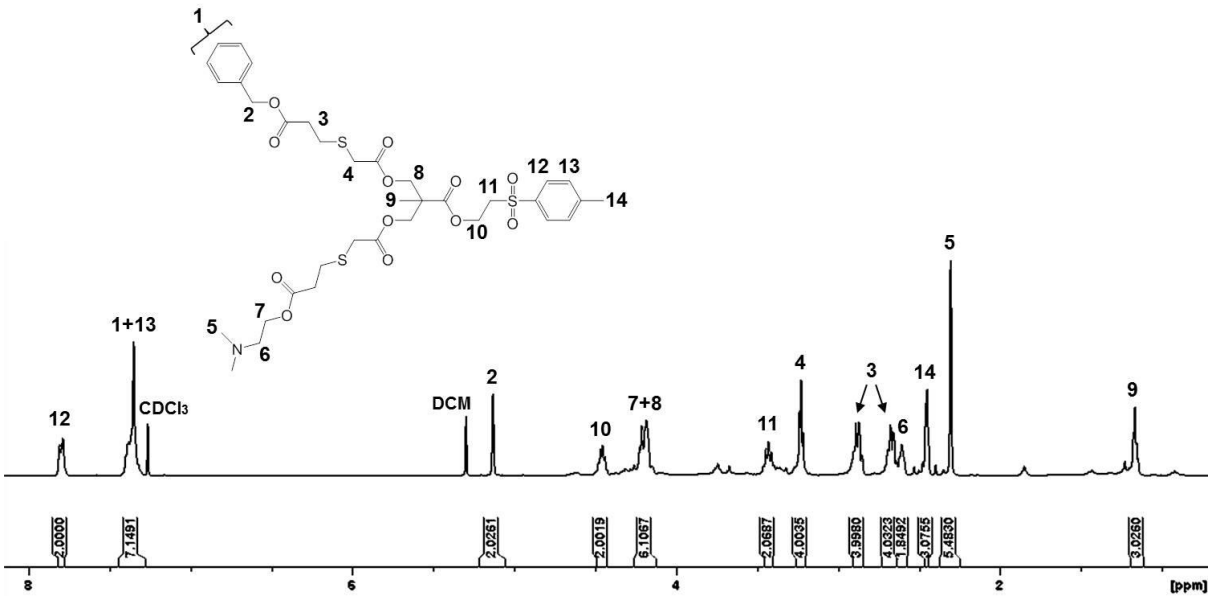

Fig. S3.2 ^{1}H NMR (400 MHz, $CDCl_3$) of Sequential **[Am_1-Bz_1-G_1-TSe];[60]**

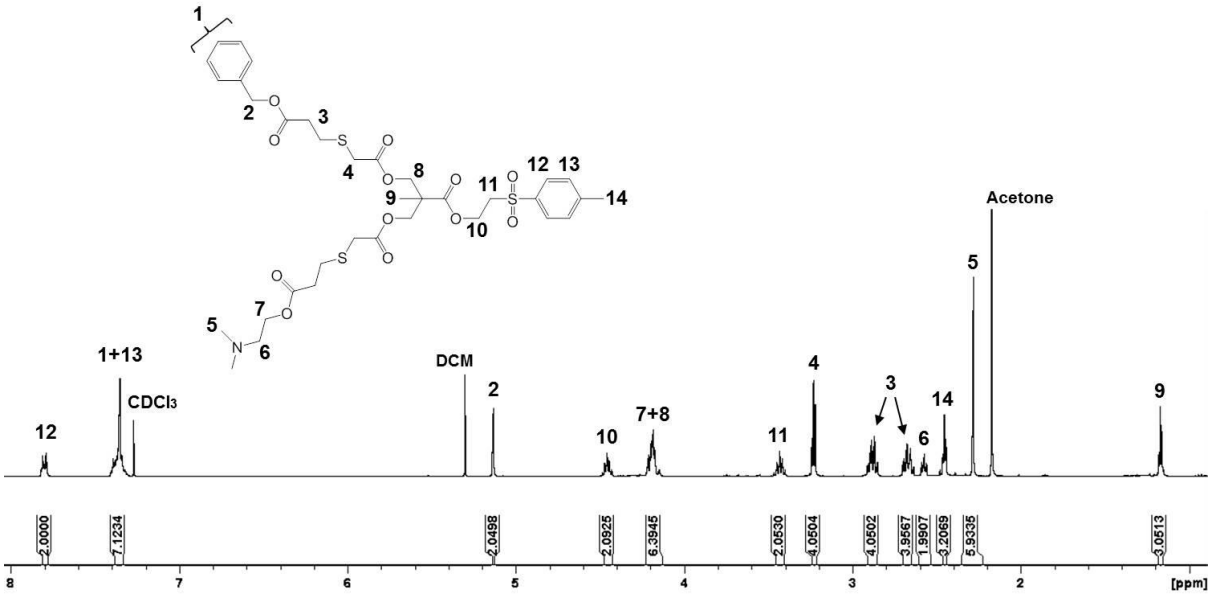

Fig. S3.3 ^{1}H NMR (400 MHz, $CDCl_3$) of Simultaneous **[Am_1-Bz_1-G_1-TSe];[60]**

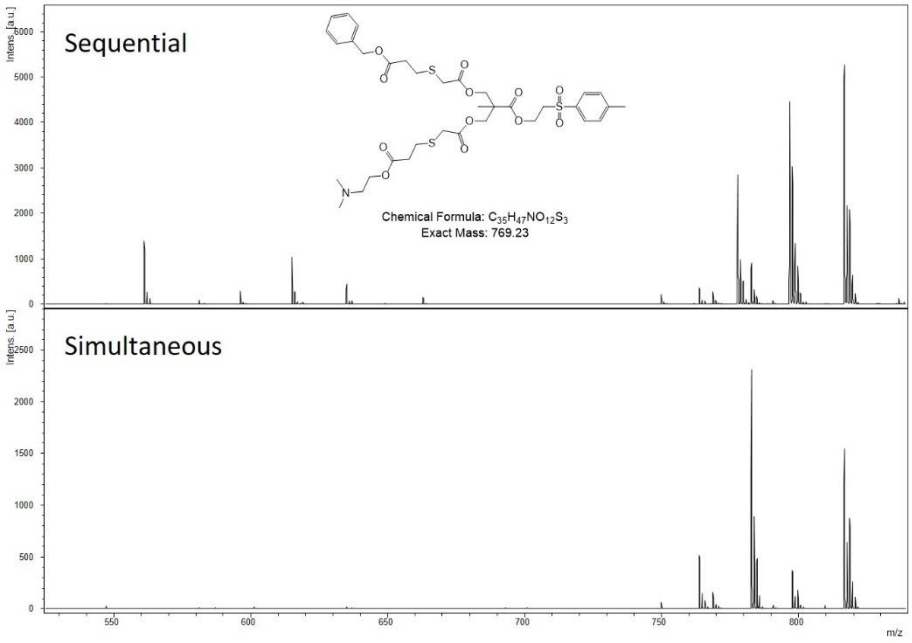

Fig. S3.4 MALDI-TOF MS (Dith, THF) comparison of Sequential vs. Simultaneous **[Am_1-Bz_1-G_1-TSe];[60]**

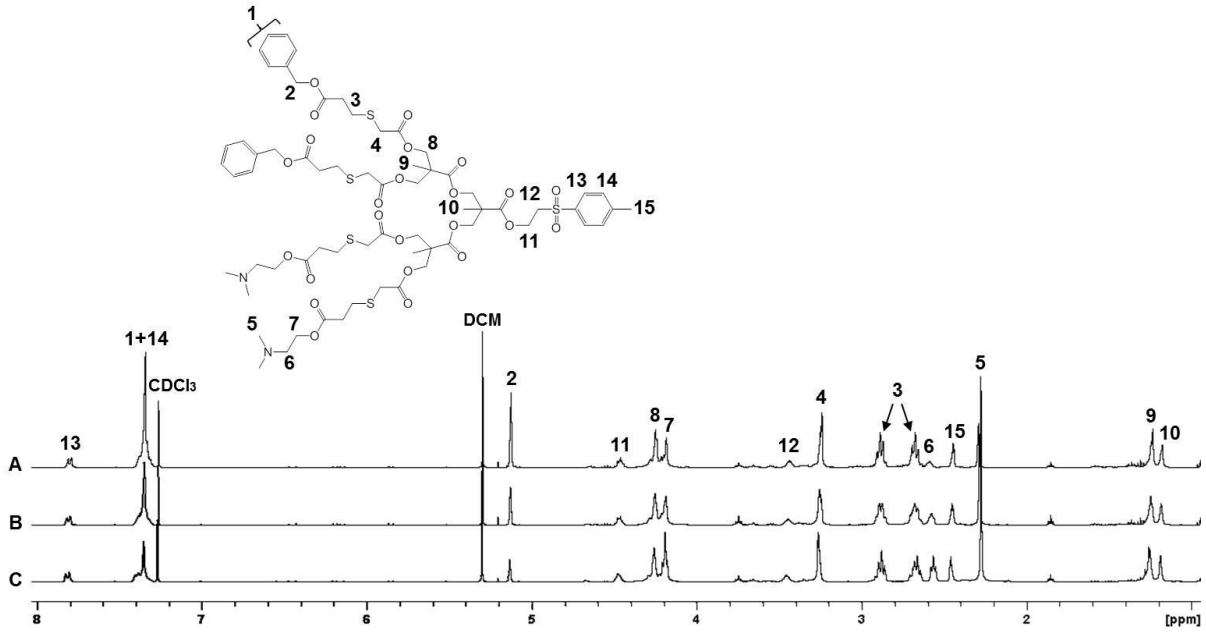

Fig. S3.5 ^{1}H NMR (400 MHz, $CDCl_3$) of Sequential **[$Am_{1\text{-}4}$-$Bz_{1\text{-}4}$-G_2-TSe]**: (A) **[Am_1-Bz_3-G_2-TSe];[61]**; (B) **[Am_2-Bz_2-G_2-TSe];[62]**; (C) **[Am_3-Bz_1-G_2-TSe];[63]**.

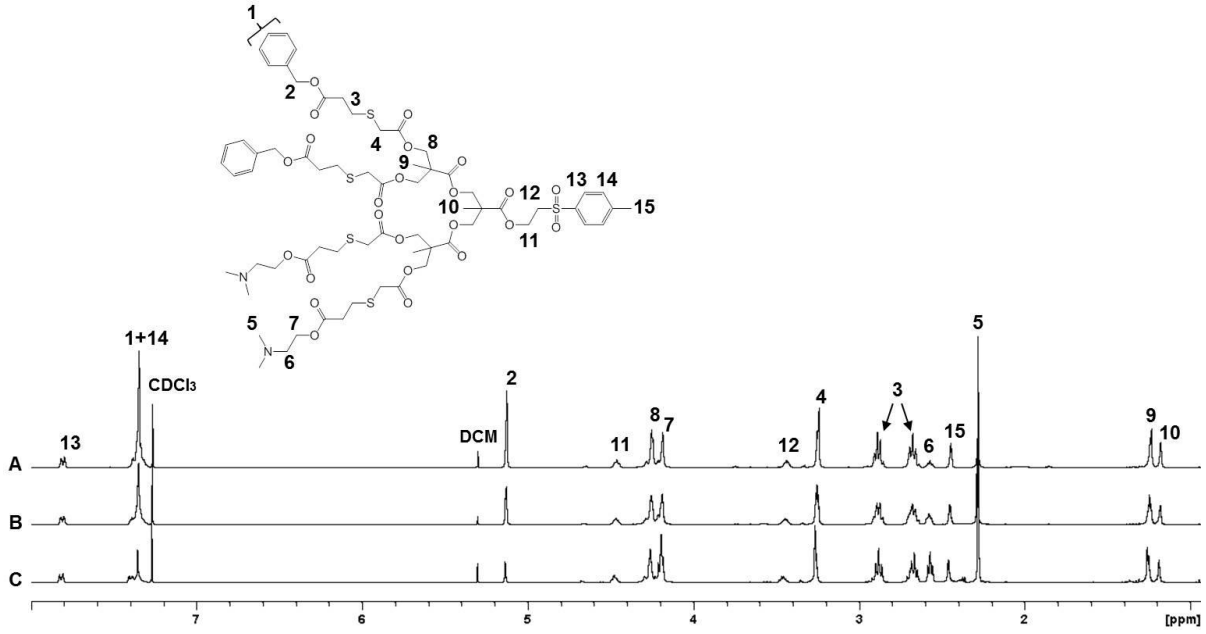

Fig. S3.6 ^{1}H NMR (400 MHz, $CDCl_3$) of Simultaneous **[$Am_{1\text{-}4}$-$Bz_{1\text{-}4}$-G_2-TSe]**: (A) **[Am_1-Bz_3-G_2-TSe];[61]**; (B) **[Am_2-Bz_2-G_2-TSe];[62]**; (C) **[Am_3-Bz_1-G_2-TSe];[63]**.

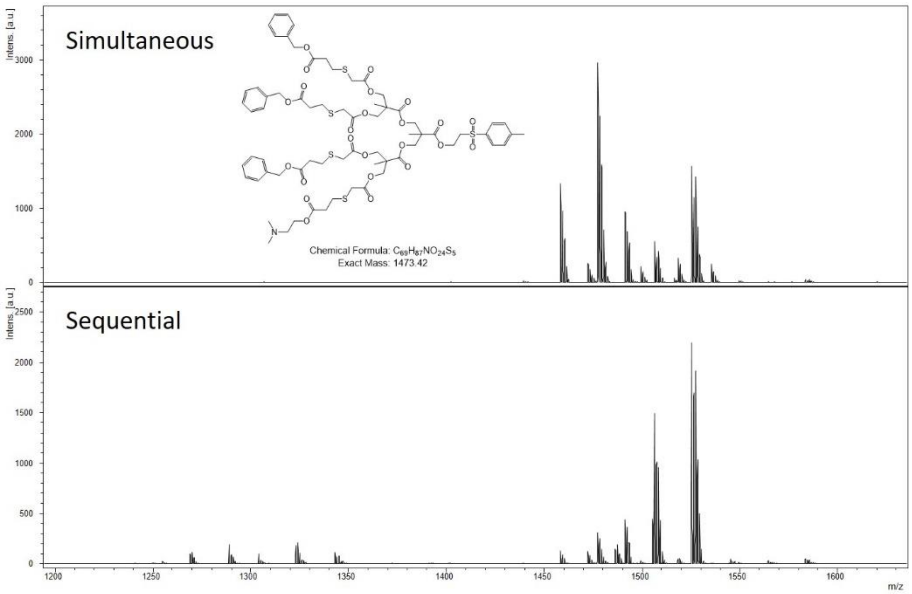

Fig. S3.7 MALDI-TOF MS (Dith, THF) comparison of Sequential vs. Simultaneous **[Am_1-Bz_3-G_2-TSe];[61]**

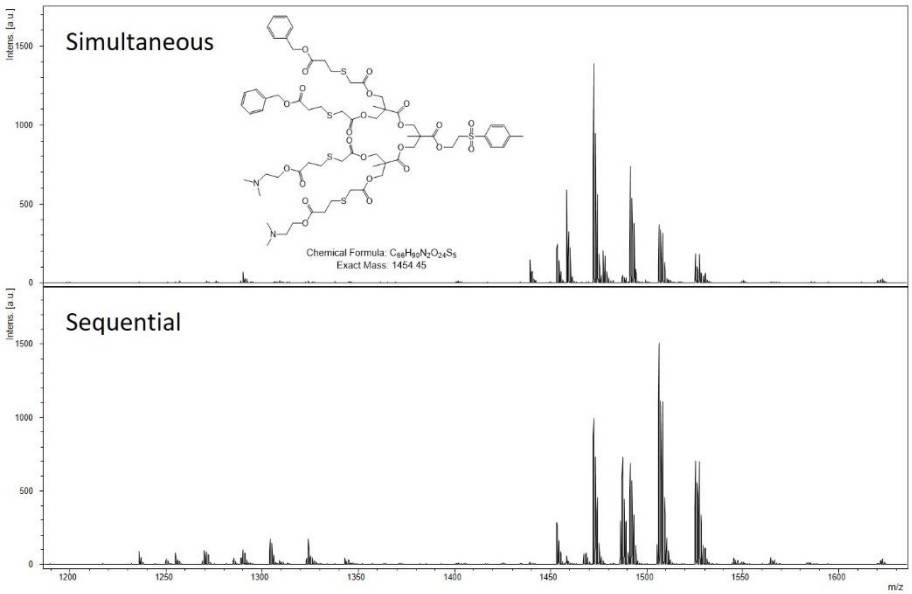

Fig. S3.8 MALDI-TOF MS (Dith, THF) comparison of Sequential vs. Simultaneous **[Am_2-Bz_2-G_2-TSe];[62]**

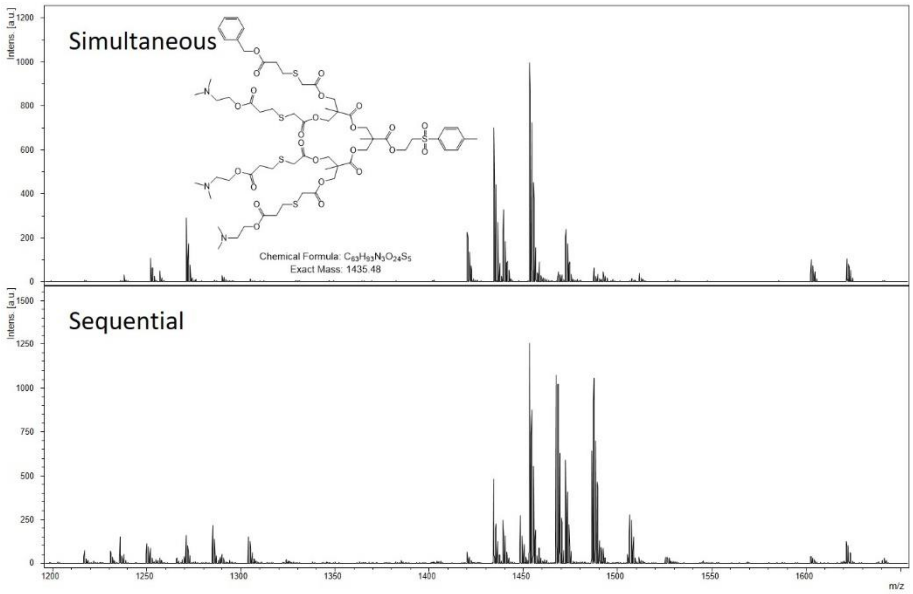

Fig. S3.9 MALDI-TOF MS (Dith, THF) comparison of Sequential vs. Simultaneous **[Am_3-Bz_1-G_2-TSe];[63]**

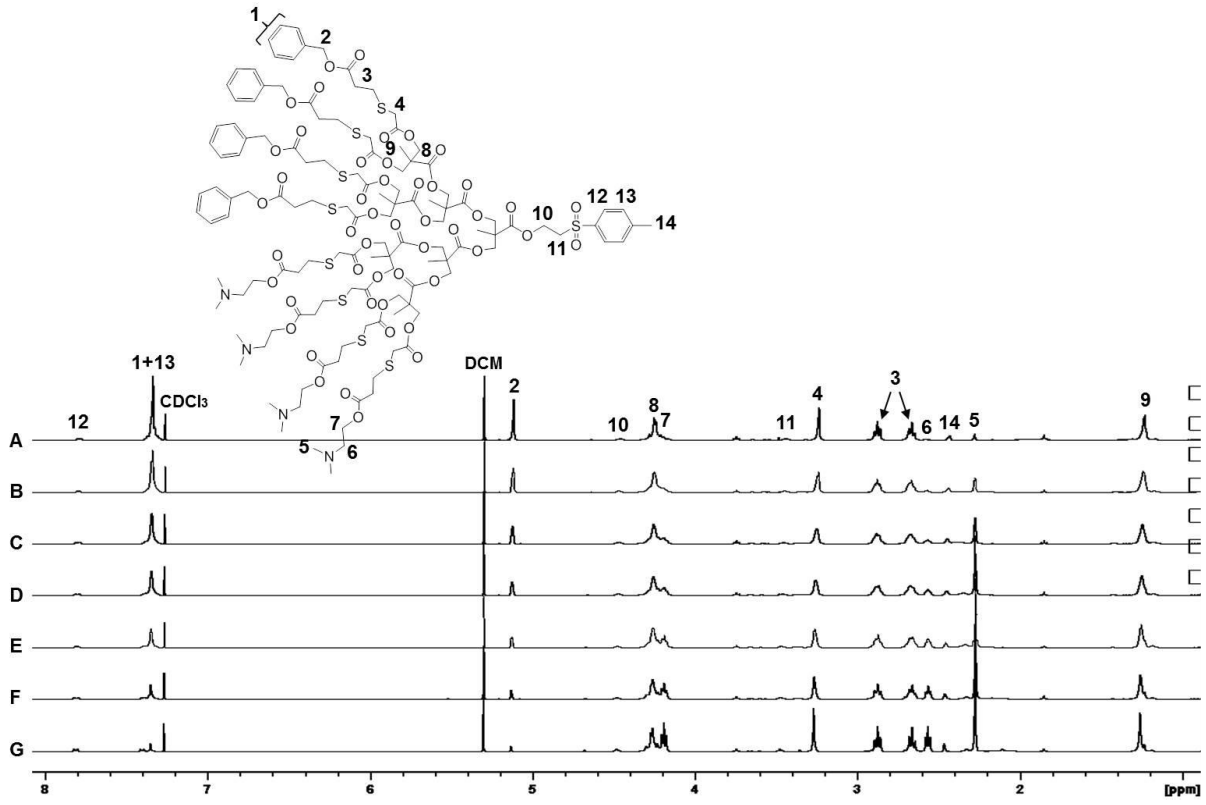

Fig. S3.10 ^{1}H NMR (400 MHz, $CDCl_3$) of Sequential **[$Am_{1\text{-}8}$-$Bz_{1\text{-}8}$-G_3-TSe]**: (A) **[Am_1-Bz_7-G_3-TSe];[64]**; (B) **[Am_2-Bz_6-G_3-TSe];[65]**; (C) **[Am_3-Bz_5-G_3-TSe];[66]**; (D) **[Am_4-Bz_4-G_3-TSe];[67]**; (E) **[Am_5-Bz_3-G_3-TSe];[68]**; (F) **[Am_6- Bz_2-G_3-TSe];[69]**; (G) **[Am_7- Bz_1-G_3-TSe];[70]**

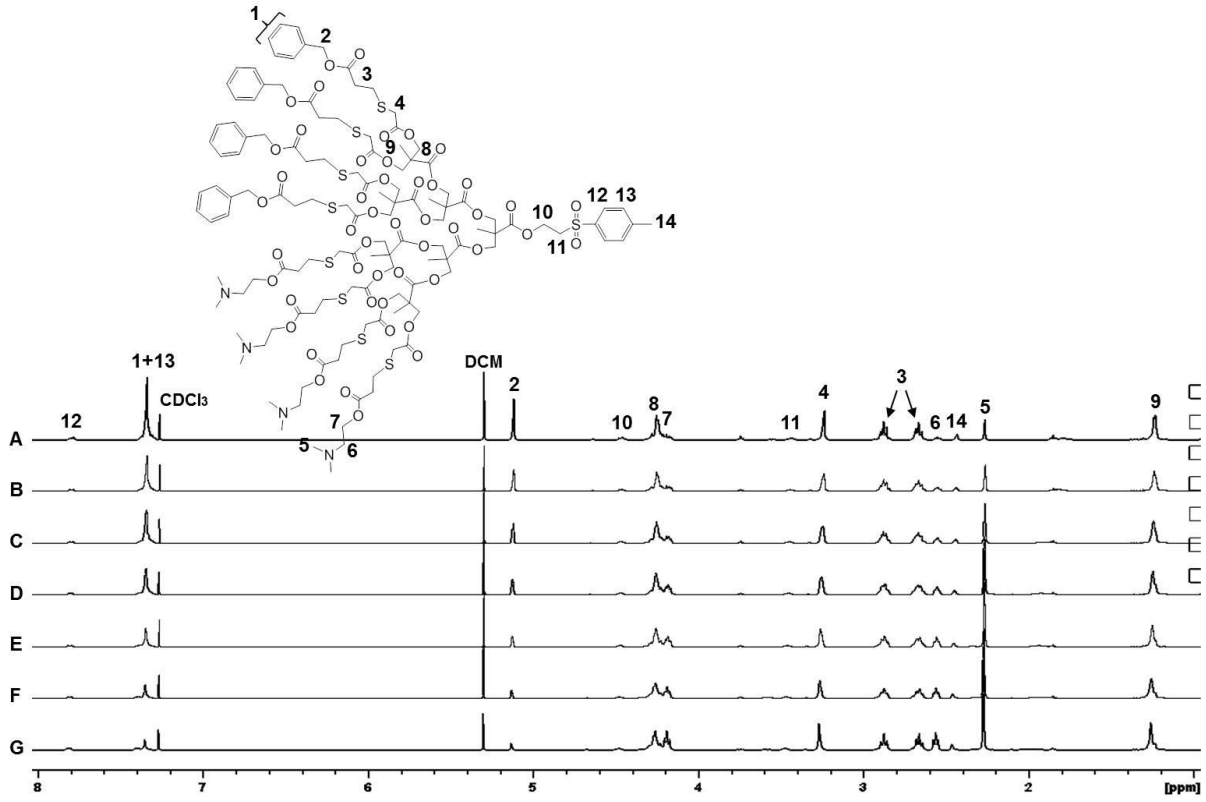

Fig. S3.11 ^{1}H NMR (400 MHz, $CDCl_3$) of Simultaneous **[$Am_{1\text{-}8}$-$Bz_{1\text{-}8}$-G_3-TSe]**: (A) **[Am_1-Bz_7-G_3-TSe];[64]**; (B) **[Am_2-Bz_6-G_3-TSe];[65]**; (C) **[Am_3-Bz_5-G_3-TSe];[66]**; (D) **[Am_4-Bz_4-G_3-TSe];[67]**; (E) **[Am_5-Bz_3-G_3-TSe];[68]**; (F) **[Am_6- Bz_2-G_3-TSe];[69]**; (G) **[Am_7- Bz_1-G_3-TSe];[70]**

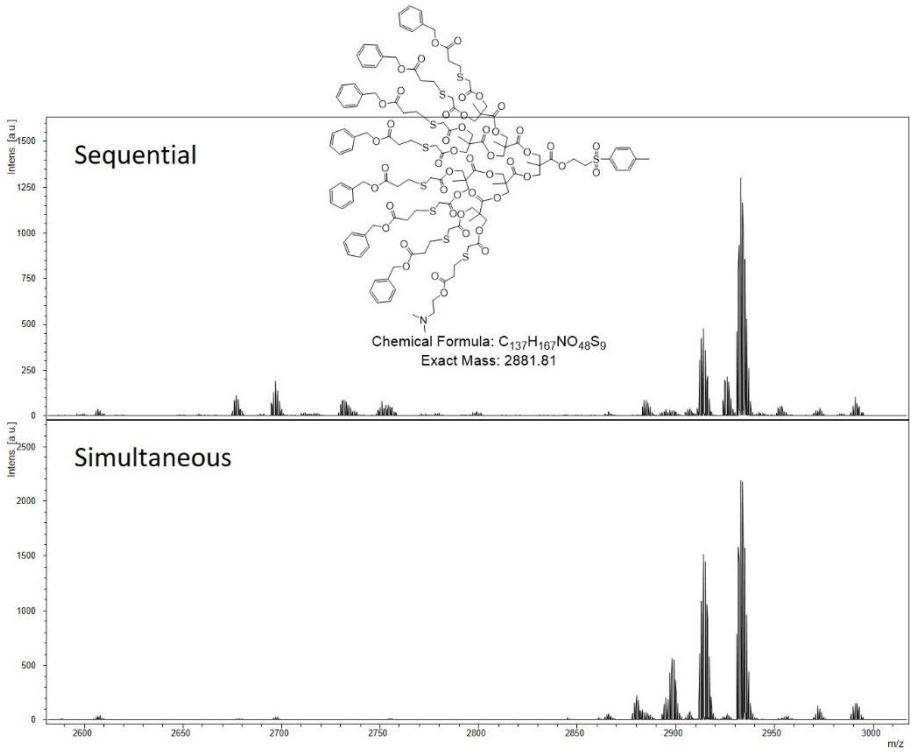

Fig. S3.12 MALDI-TOF MS (Dith, THF) comparison of Sequential vs. Simultaneous **[Am_1-Bz_7-G_3-TSe];[64]**

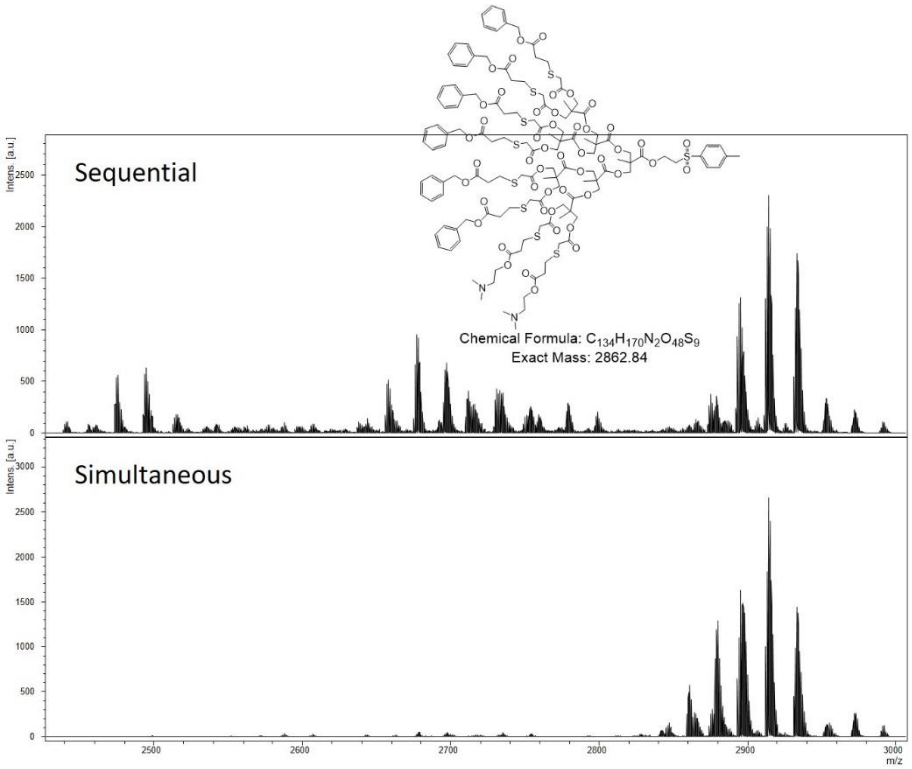

Fig. S3.13 MALDI-TOF MS (Dith, THF) comparison of Sequential vs. Simultaneous **[Am_2-Bz_6-G_3-TSe];[65]**

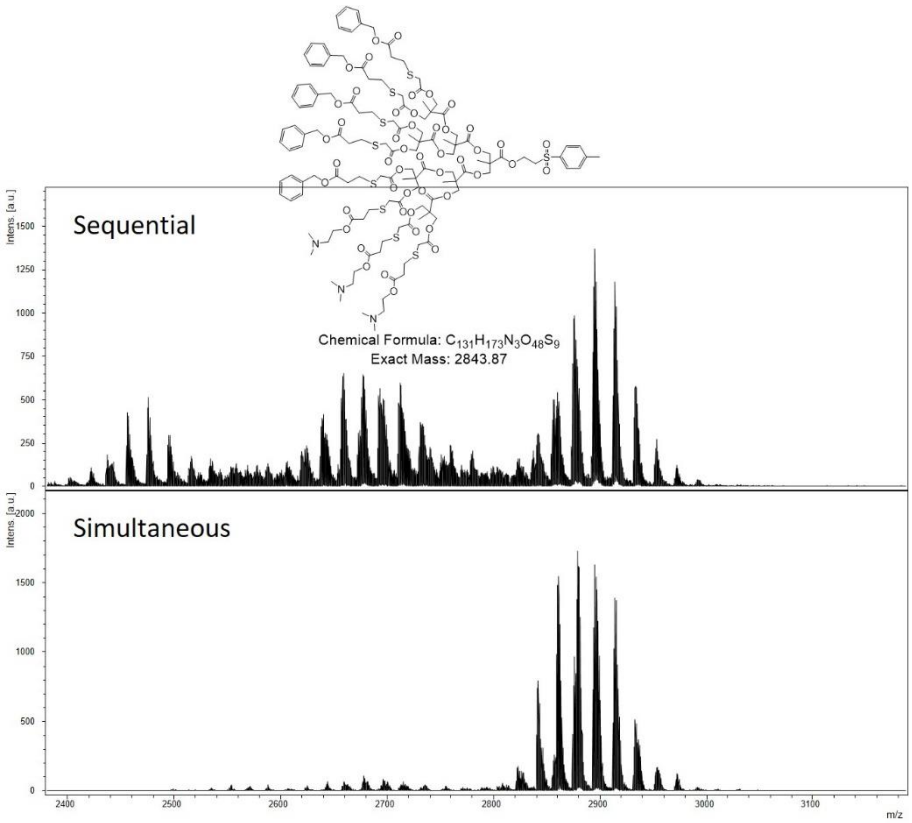

Fig. S3.14 MALDI-TOF MS (Dith, THF) comparison of Sequential vs. Simultaneous **[Am_3-Bz_5-G_3-TSe];[66]**

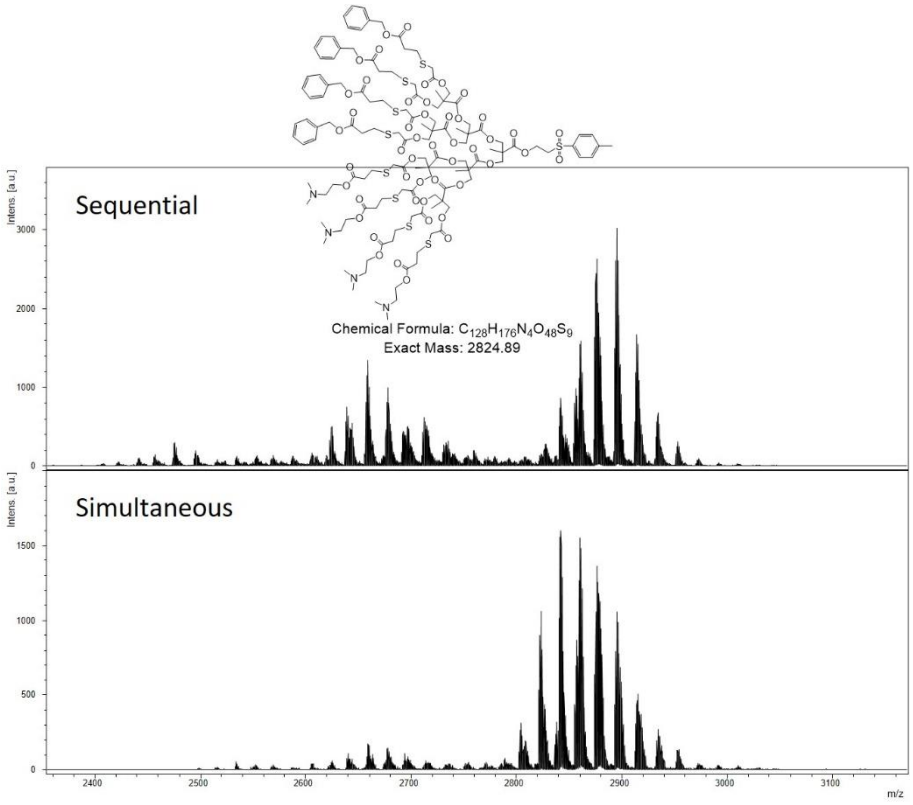

Fig. S3.15 MALDI-TOF MS (Dith, THF) comparison of Sequential vs. Simultaneous **[Am_4-Bz_4-G_3-TSe];[67]**

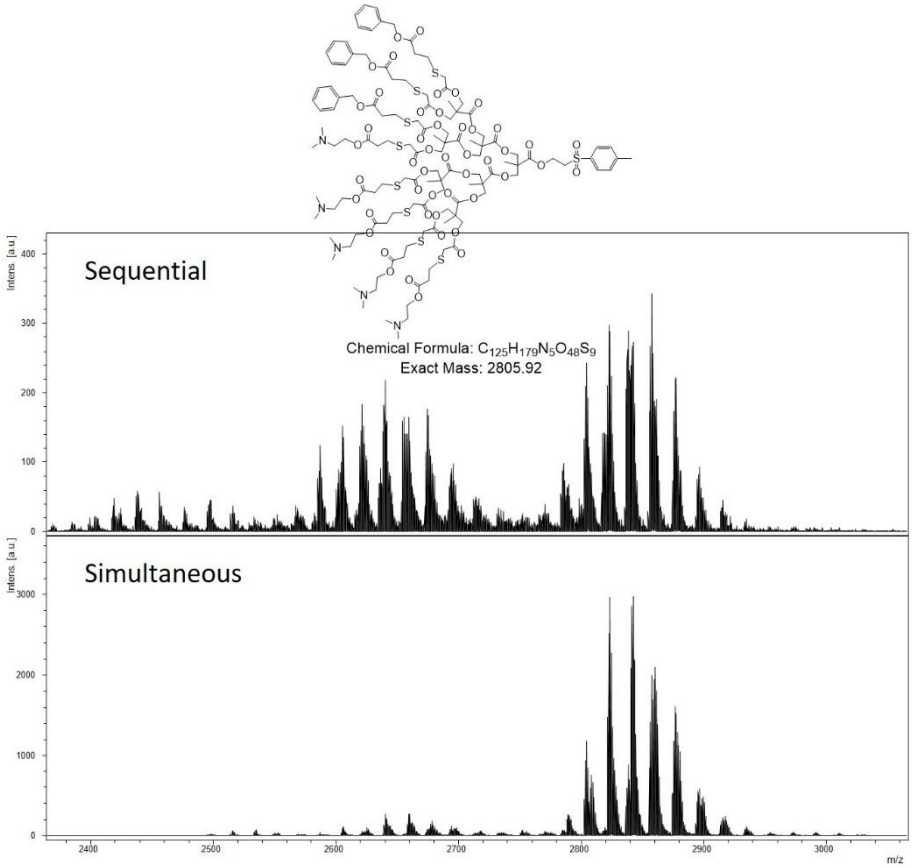

Fig. S3.16 MALDI-TOF MS (Dith, THF) comparison of Sequential vs. Simultaneous **[Am_5-Bz_3-G_3-TSe];[68]**

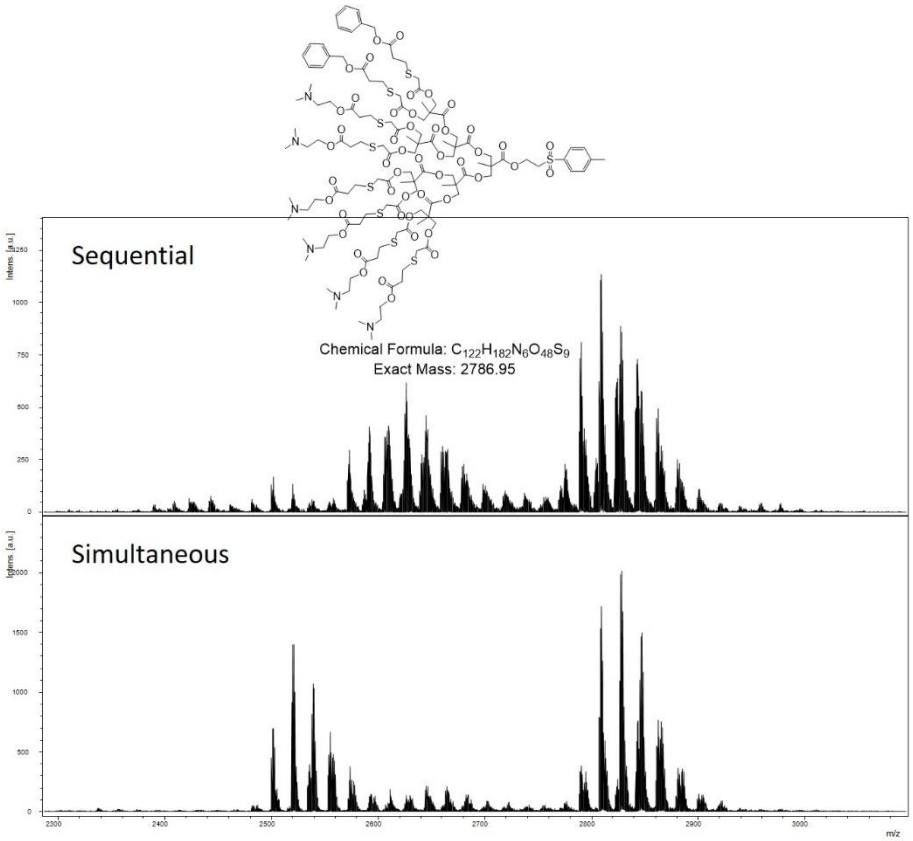

Fig. S3.17 MALDI-TOF MS (Dith, THF) comparison of Sequential vs. Simultaneous **[Am_6-Bz_2-G_3-TSe];[69]**

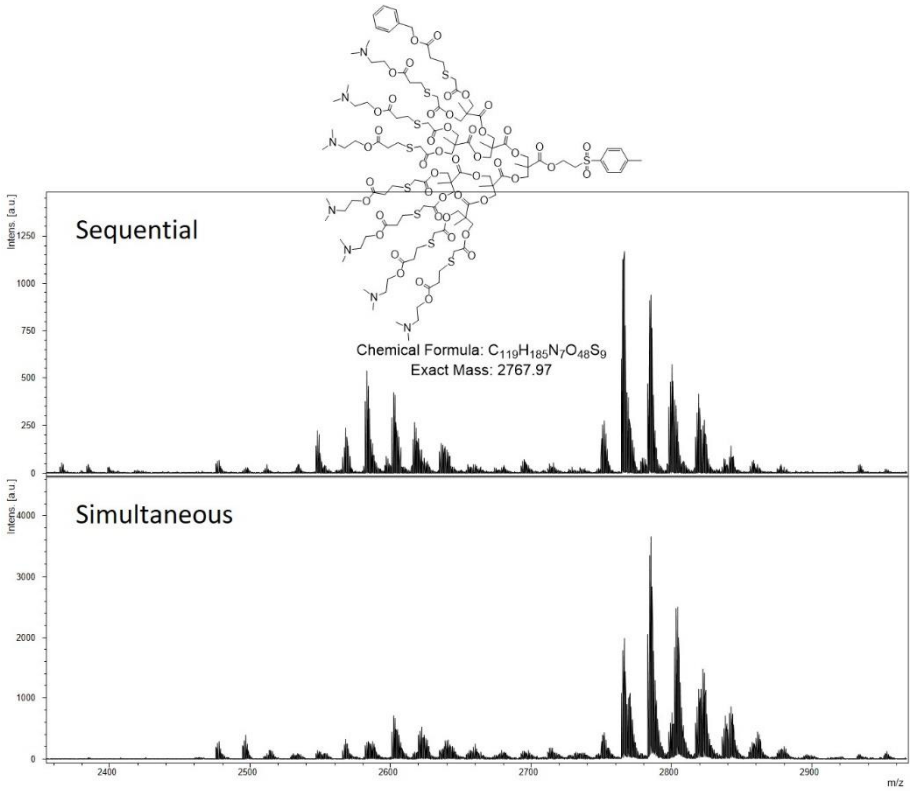

Fig. S3.18 MALDI-TOF MS (Dith, THF) comparison of Sequential vs. Simultaneous **[Am_7-Bz_1-G_3-TSe];[70]**

Table S3.1. Peaks identified and assigned within the MALDI-TOF spectrum of **[Xan_2-Am_6-G_3-TSe];[55]** – see Fig. 3.10

Peak	Species assignment	Theoretical Exact mass m/z+1 (Da)	Peak identified m/z (Da)
1	$[Xan_5\text{-}Am_3\text{-}G_3\text{-}TSe]H^+ + 48$	2525	2526.9
2	$[Xan_5\text{-}Am_3\text{-}G_3\text{-}TSe]K^+ + 32$	2547	2546.9
3	$[Xan_5\text{-}Am_3\text{-}G_3\text{-}TSe]K^+ + 48$	2563	2561.0
4	$[Xan_4\text{-}Am_4\text{-}G_3\text{-}TSe]K^+ + 16$	2586	2582.0
5	$[Xan_4\text{-}Am_4\text{-}G_3\text{-}TSe]H^+ + 64$	2596	2596.0
6	$[Xan_4\text{-}Am_4\text{-}G_3\text{-}TSe]K^+ + 48$	2618	2618.9
7	$[Xan_3\text{-}Am_5\text{-}G_3\text{-}TSe]H^+ + 48$	2635	2635.6
8	$[Xan_3\text{-}Am_5\text{-}G_3\text{-}TSe]K^+ + 16$	2641	2641.1
9	$[Xan_3\text{-}Am_5\text{-}G_3\text{-}TSe]K^+ + 32$	2657	2656.1
10	$[Xan_2\text{-}Am_6\text{-}G_3\text{-}TSe]K^+ + 16$	2696	2694.6
11	$[Xan_2\text{-}Am_6\text{-}G_3\text{-}TSe]H^+ + 64$	2706	2708.6
12	$[Xan_1\text{-}Am_7\text{-}G_3\text{-}TSe]K^+ + 16$	2751	2750.0
13	$[Xan_1\text{-}Am_7\text{-}G_3\text{-}TSe]K^+ + 32$	2767	2764.1
14	$[Xan_1\text{-}Am_7\text{-}G_3\text{-}TSe]K^+ + 48$	2783	2781.2
15	$[Am_8\text{-}G_3\text{-}TSe]H^+ + 48$	2800	2800.1
16	$[Am_8\text{-}G_3\text{-}TSe]K^+ + 16$	2806	2805.9
17	$[Am_8\text{-}G_3\text{-}TSe]H^+ + 64$	2816	2817.1
18	$[Am_8\text{-}G_3\text{-}TSe]K^+ + 32$	2822	2822.1
19	$[Am_8\text{-}G_3\text{-}TSe]K^+ + 48$	2838	2836.2

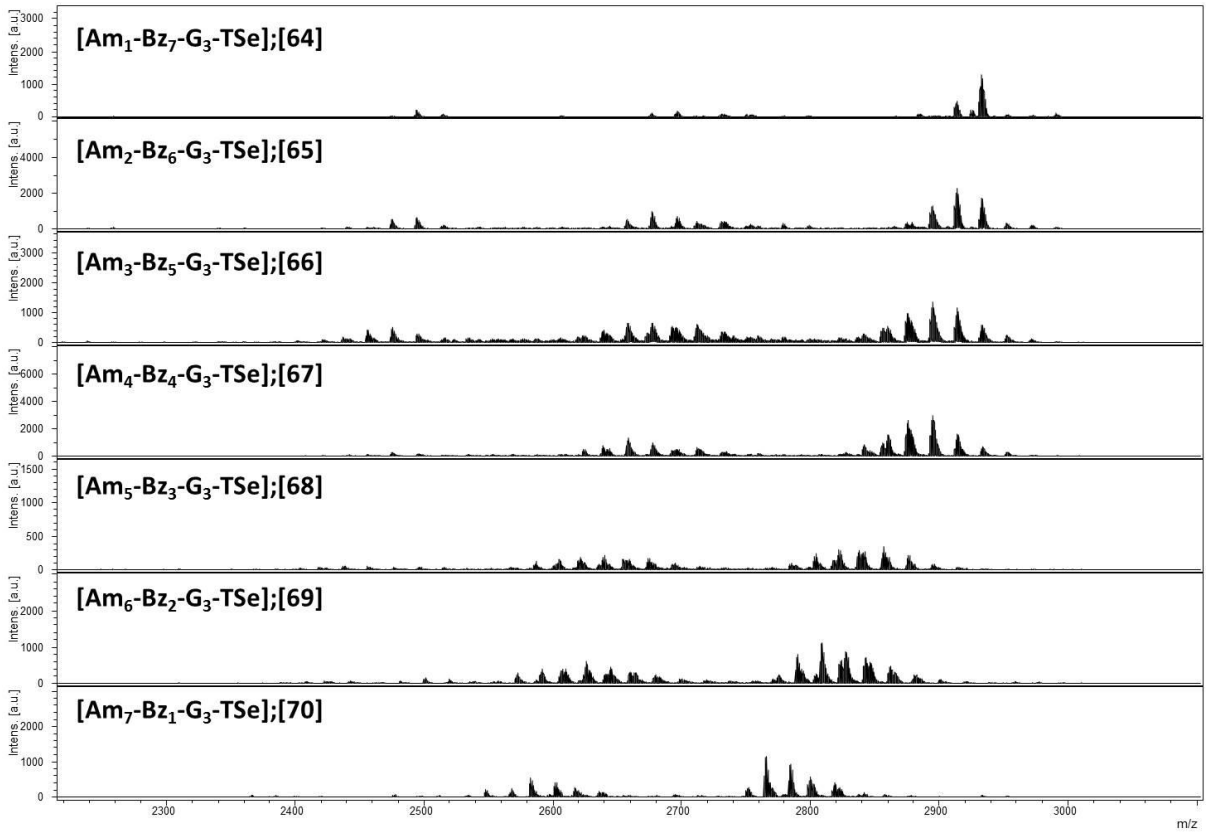

Fig. S3.19 MALDI-TOF MS (Dith, THF) comparison of Sequential **[Am_{1-8}-Bz_{1-8}-G_3-TSe];[64]-[70]**

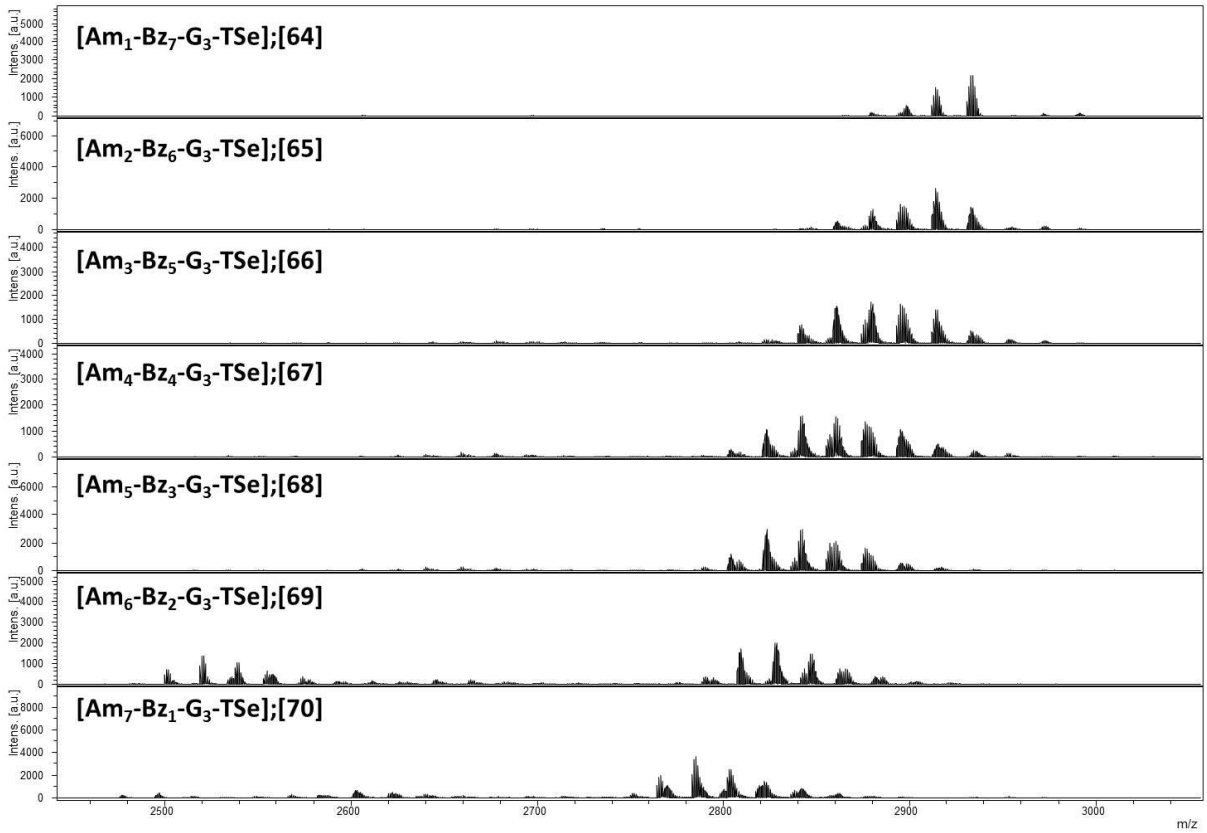

Fig. S3.20 MALDI-TOF MS (Dith, THF) comparison of Simultaneous **[Am_{1-8}-Bz_{1-8}-G_3-TSe];[64]-[70]**

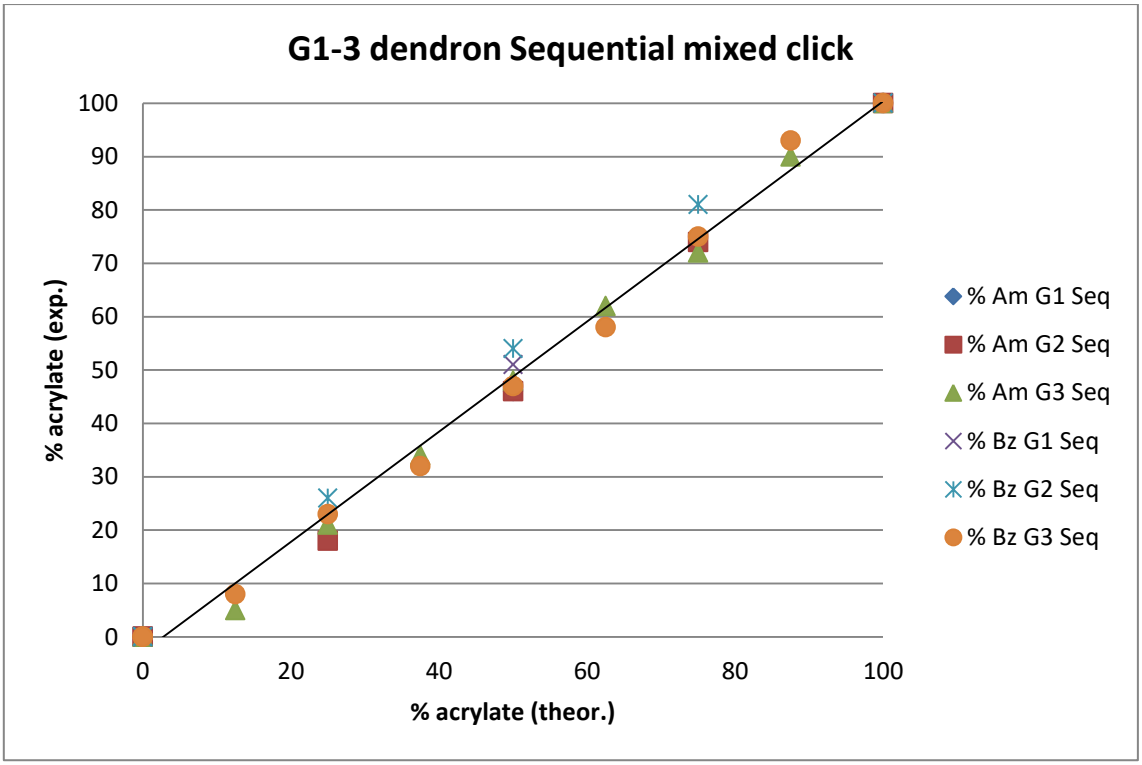

Fig. S3.21 Experimental vs. theoretical % acrylate for Sequentially multifunctionalised G_1-G_3 dendrons **[12]-[14]**

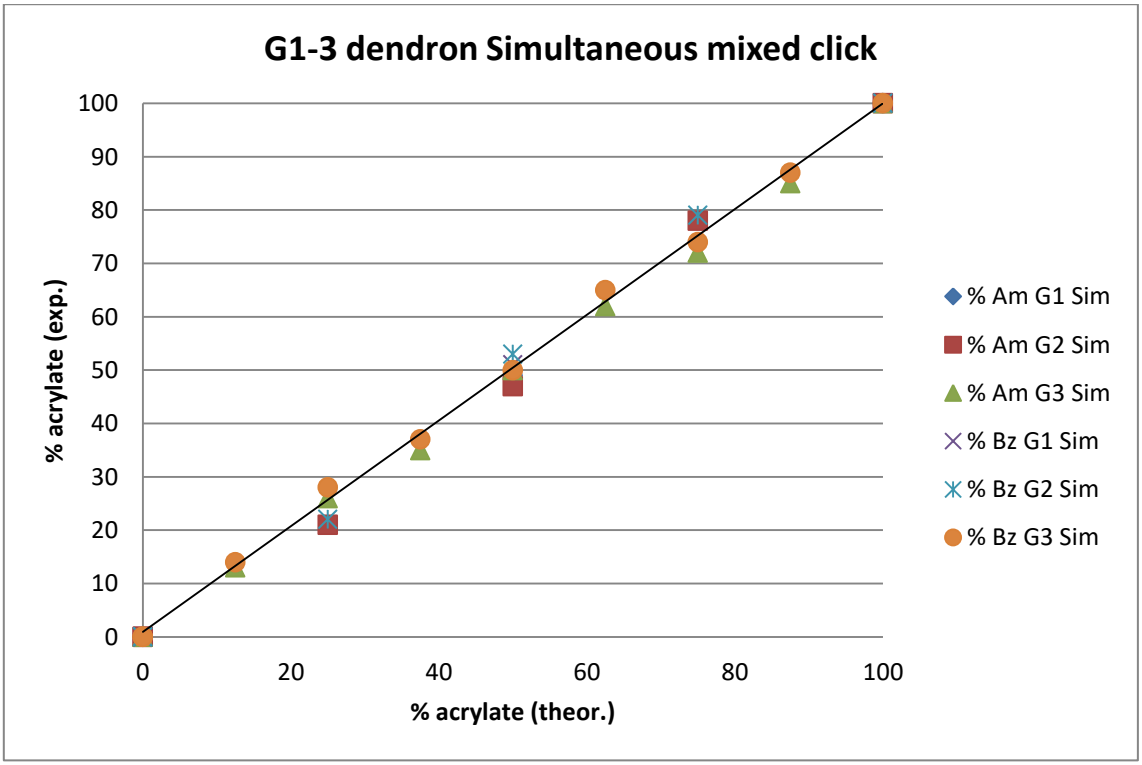

Fig. S3.22 Experimental vs. theoretical % acrylate for Simultaneously multifunctionalised G_1-G_3 dendrons **[12]-[14]**

Table S3.2 Triple detection SEC analysis of simultaneously multifunctionalised G_2 dendron **[Xan$_4$-G$_2$-TSe];[13]**; **[Am$_4$-G$_2$-TSe];[42]**, **[Am$_3$-Bz$_1$-G$_2$-TSe];[63]**, **[Am$_2$-Bz$_2$-G$_2$-TSe];[62]**, **[Am$_1$-Bz$_3$-G$_2$-TSe];[61]** and **[Bz$_4$-G$_2$-TSe];[43]**

		MS $[MNa]^+$	SEC (THF)[a]		
Dendron	M_{Calc} (Da)	M_{Obs} (Da)	M_n	M_w	Đ
[Xan$_4$-G$_2$-TSe];[13]	1196.1	1219.1	1193	1413	1.19
[Am$_4$-G$_2$-TSe];[42]	1416.5	-	1432	1704	1.19
[Am$_3$-Bz$_1$-G$_2$-TSe];[63]	1435.5	-	1450	1726	1.19
[Am$_2$-Bz$_2$-G$_2$-TSe];[62]	1454.5	-	1449	1666	1.15
[Am$_1$-Bz$_3$-G$_2$-TSe];[61]	1473.4	-	1470	1735	1.18
[Bz$_4$-G$_2$-TSe];[43]	1492.4	-	1493	1747	1.17

[a]THF containing 2% TEA (v/v) at 35°C, 1mL min^{-1} flow rate.
M_n – number average molecular weight; M_w – weight average molecular weight

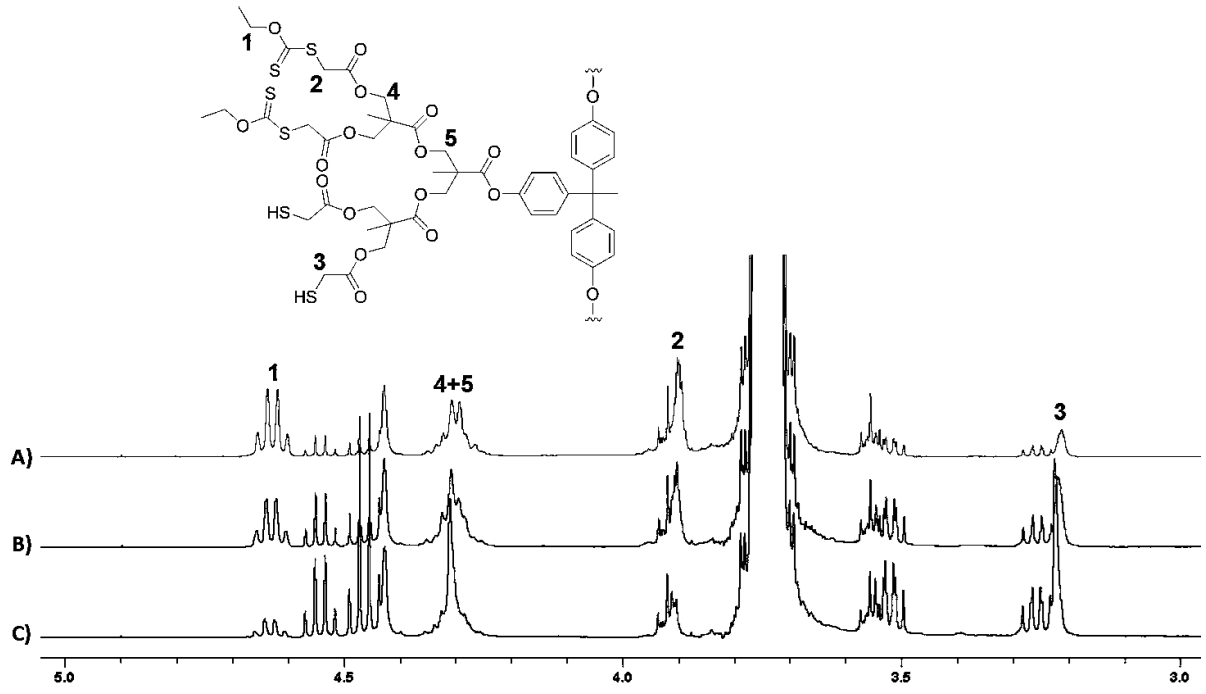

Fig. S3.23 Stacked ^{1}H NMR (400 MHz, $CDCl_3$) spectra of partially deprotected xanthate peripheral G_2 dendrimer **[18]**. Equivalents of *n*-butylamine added: A) 3, B) 6 and C) 9

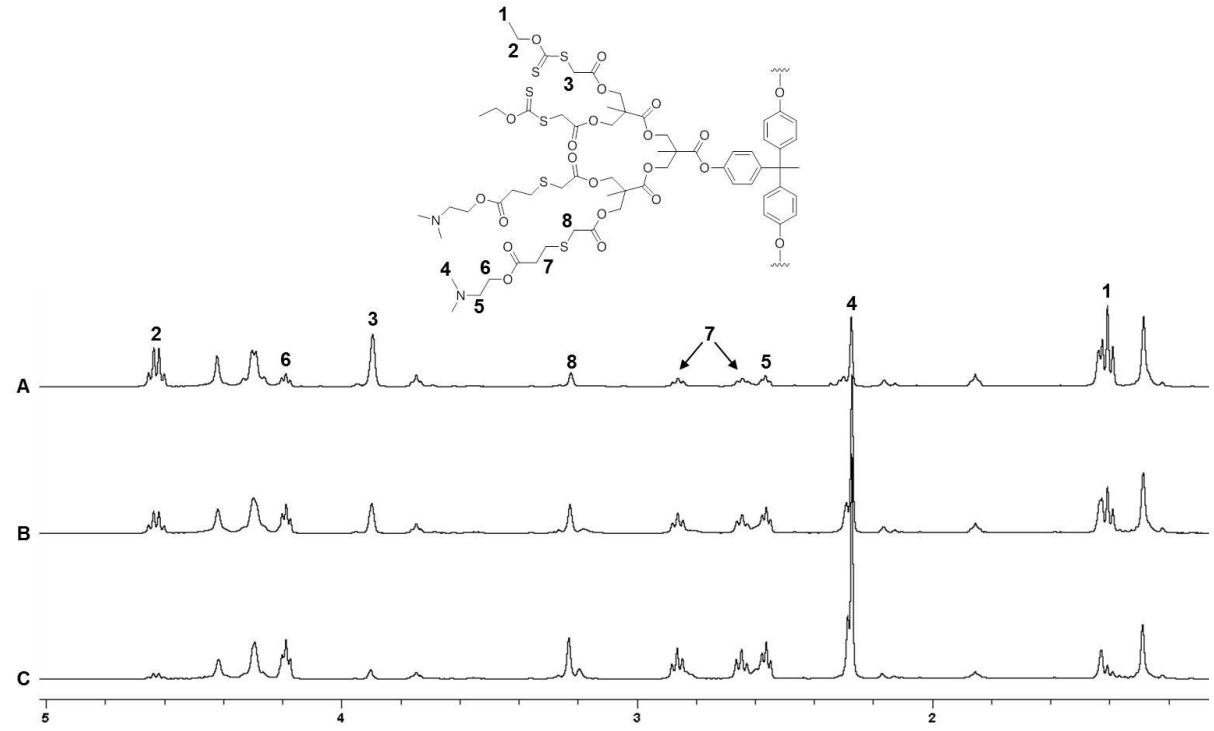

Fig. S3.24 Stacked ^{1}H NMR (400 MHz, $CDCl_3$) spectra of partially Am functionalised G_2 dendrimer **[18]**; A) **[Am_3-Xan_9-G_2-THPE];[57]**, B) **[Am_6-Xan_6-G_2-THPE];[58]** and C) **[Am_9-Xan_3-G_2-THPE];[59]**.

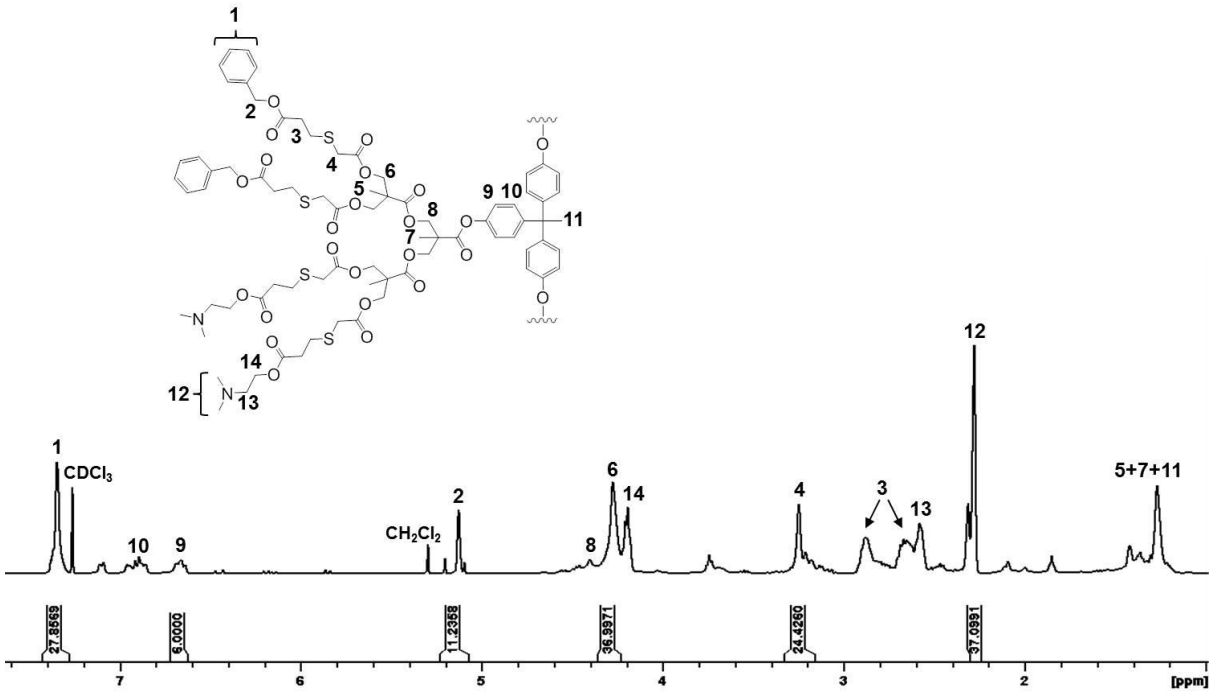

Fig. S3.25 ^{1}H NMR (400 MHz, $CDCl_3$) of **[Am_6-Bz_6-G_2-THPE];[97]** by sequential multifunctionalisation

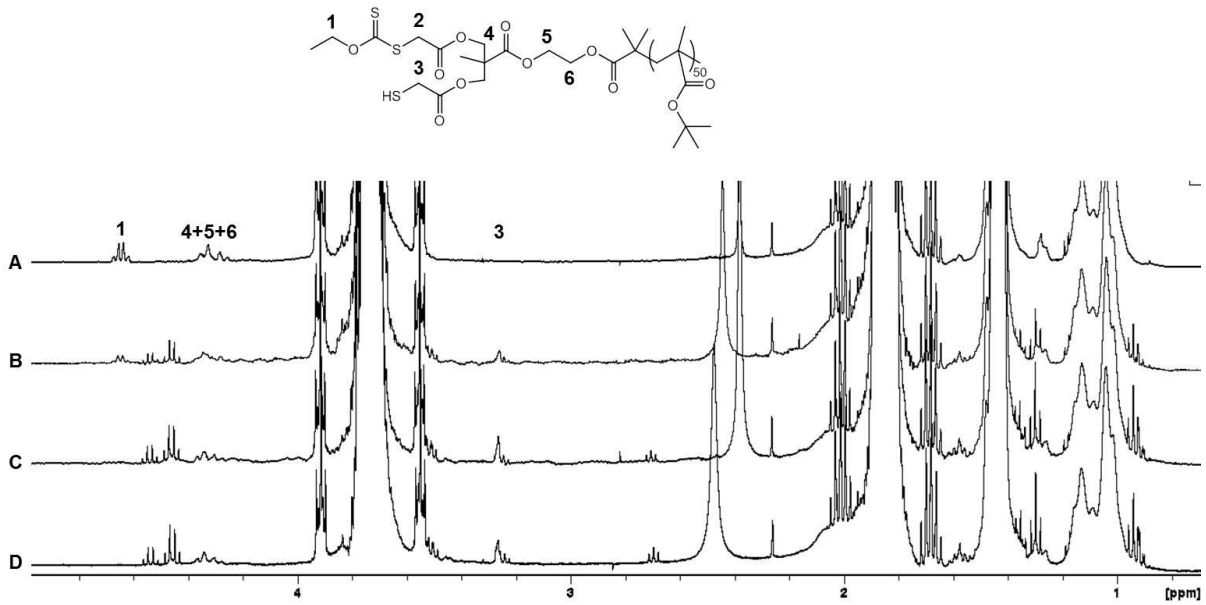

Fig. S3.26 Stacked ^{1}H NMR (400 MHz, $CDCl_3$) spectra of partially deprotected **p[(Xan$_2$-G$_1$)-tBMA$_{50}$];[25]**.

Equivalents of *n*-butylamine added: A) 0, B) 1.5, C) 3, D) 4.5.

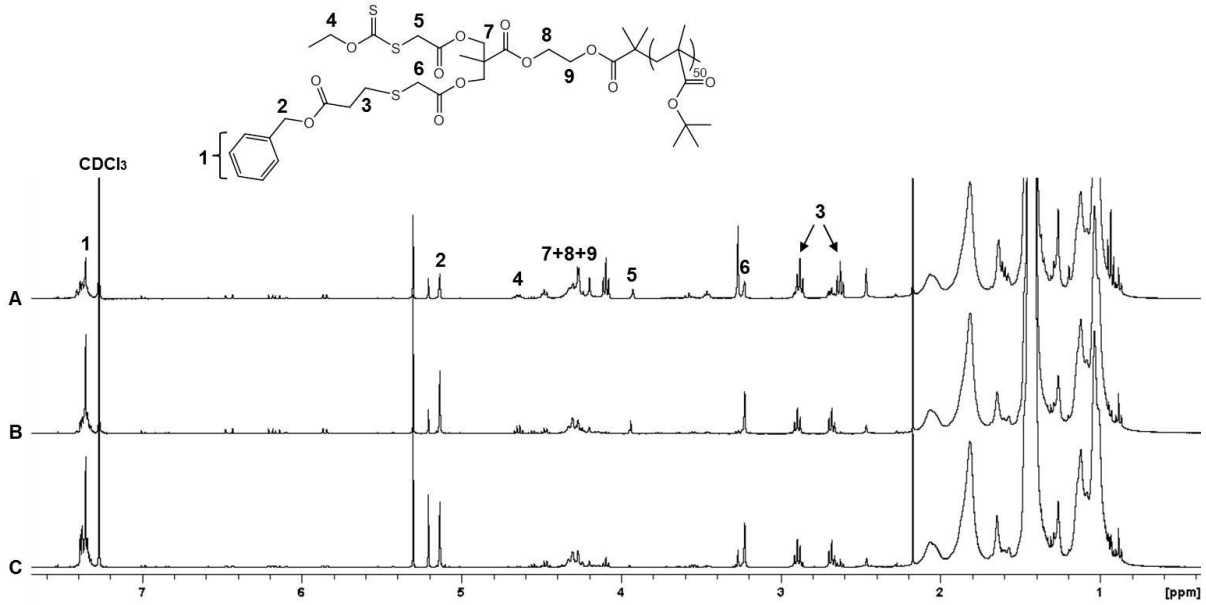

Fig. S3.27 Stacked ^{1}H NMR (400 MHz, $CDCl_3$) spectra of partially Bz functionalised **p[(Xan$_2$-G$_1$)-tBMA$_{50}$];[25]**. Equivalents of *n*-butylamine added: A) 1.5, B) 3, C) 4.5.

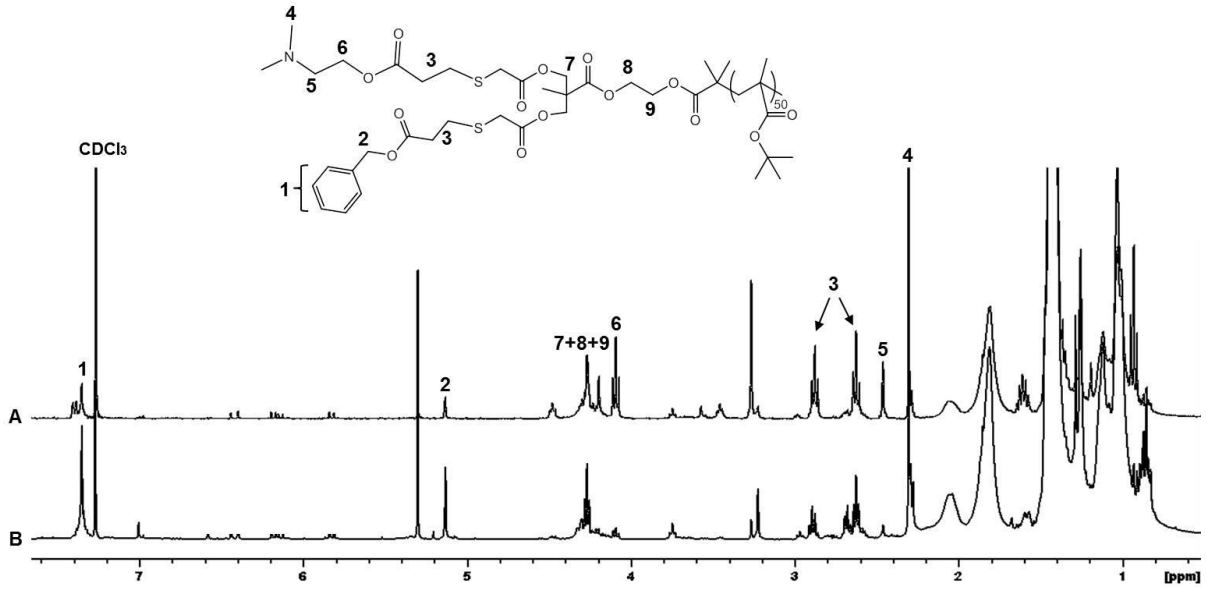

Fig. S3.28 Stacked ^{1}H NMR (400 MHz, $CDCl_3$) spectra of sequentially multifunctionalised **p[(Xan$_2$-G$_1$)-tBMA$_{50}$];[25]**. Equivalents of *n*-butylamine added for deprotection in first step: A) 1.5, B) 3.

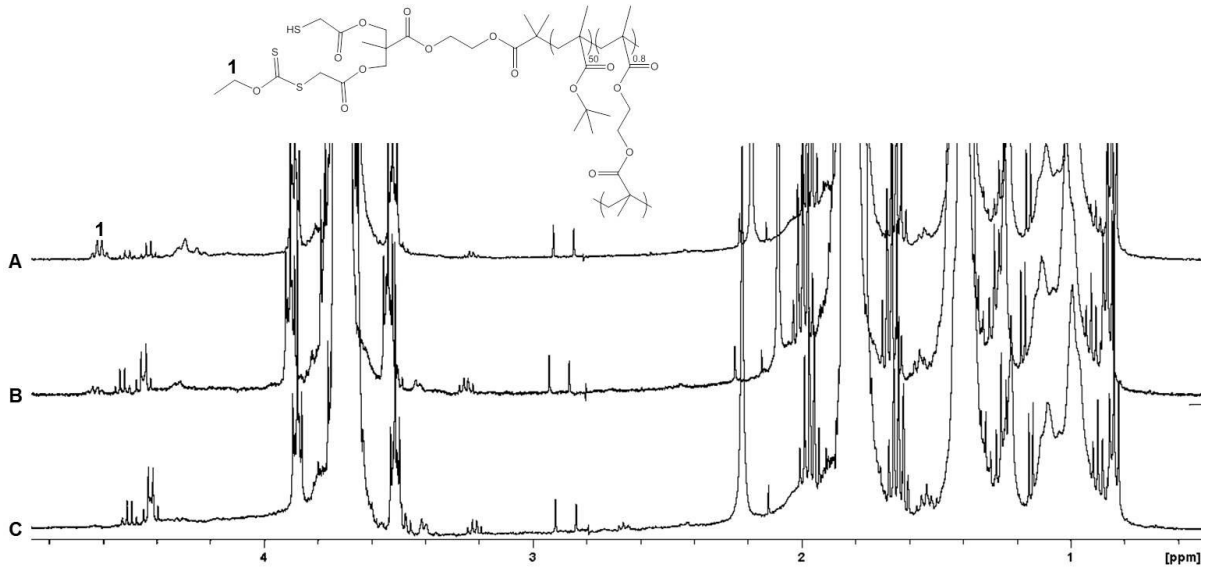

Fig. S3.29 Stacked ^{1}H NMR (400 MHz, $CDCl_3$) spectra of partially deprotected **p[(Xan$_2$-G$_1$)-tBMA$_{50}$-*co*-EGDMA$_{0.8}$];[27]**. Equivalents of *n*-butylamine added: A) 1.5, B) 3, C) 4.5.

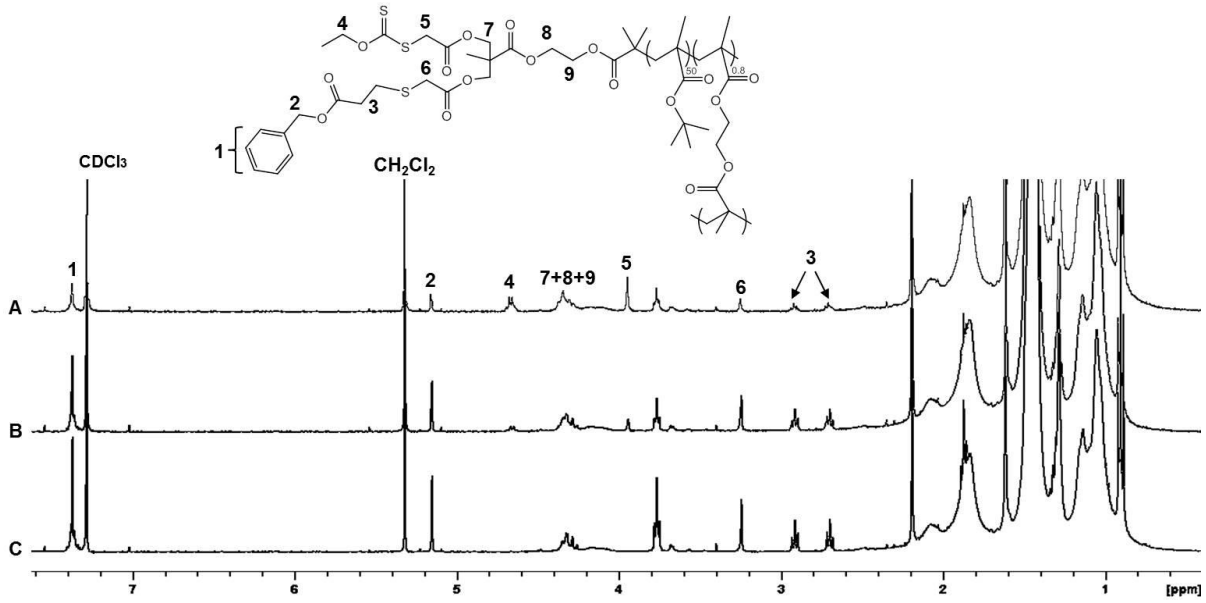

Fig. S3.30 Stacked ^{1}H NMR (400 MHz, $CDCl_3$) spectra of partially Bz functionalised **p[(Xan$_2$-G$_1$)-tBMA$_{50}$-*co*-EGDMA$_{0.8}$];[27]**. Equivalents of *n*-butylamine added: A) 1.5, B) 3, C) 4.5.

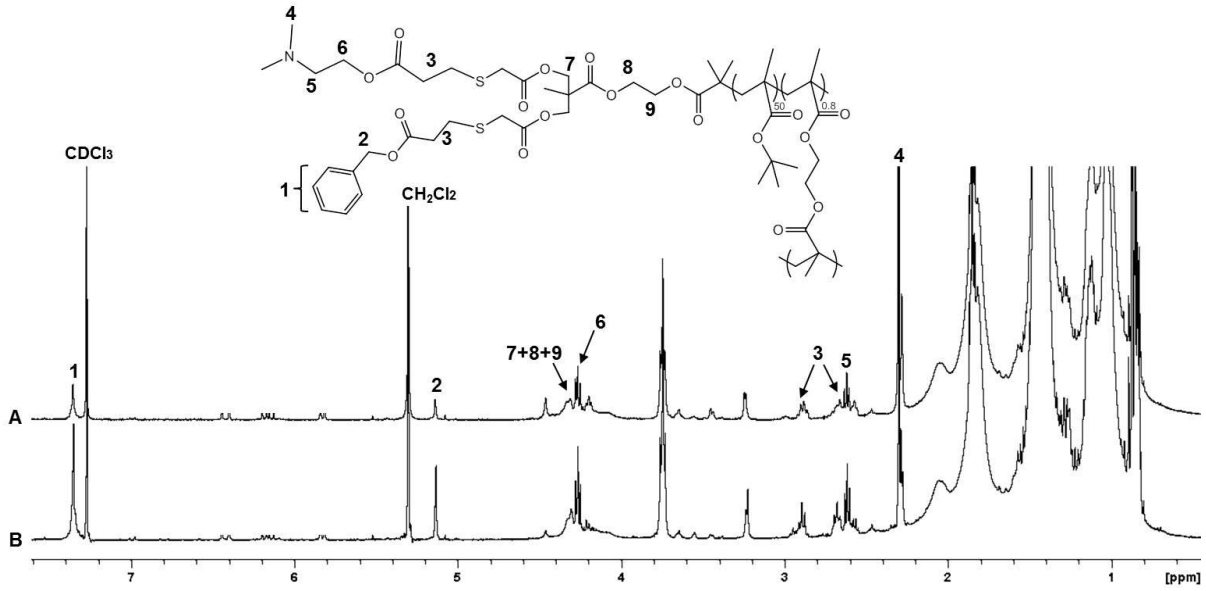

Fig. S3.31 Stacked ^{1}H NMR (400 MHz, $CDCl_3$) spectra of <u>sequentially</u> multifunctionalised **p[(Xan$_2$-G$_1$)-tBMA$_{50}$-*co*-EGDMA$_{0.8}$];[27]**. Equivalents of *n*-butylamine added for deprotection in first step: A) 1.5, B) 3.

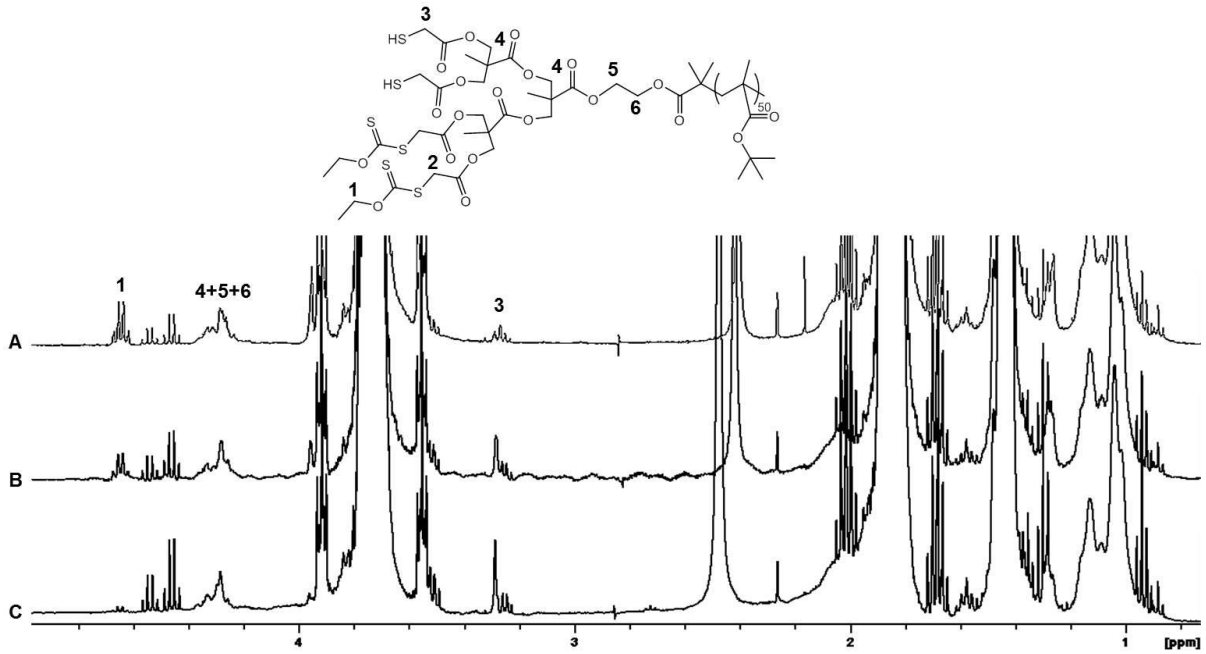

Fig. S3.32 Stacked ^{1}H NMR (400 MHz, $CDCl_3$) spectra of partially deprotected **p[(Xan$_4$-G$_2$)-tBMA$_{50}$];[26]**.

Equivalents of *n*-butylamine added: A) 1.5, B) 3, C) 4.5.

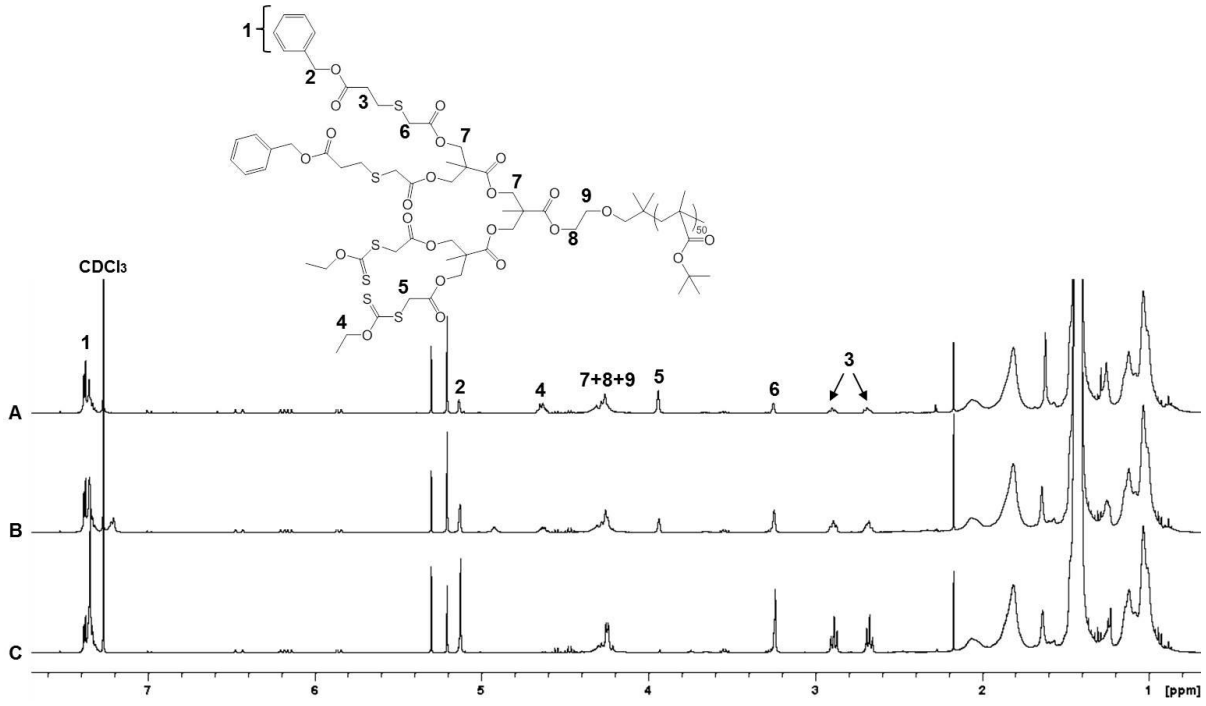

Fig. S3.33 Stacked ^{1}H NMR (400 MHz, $CDCl_3$) spectra of partially Bz functionalised **p[(Xan$_4$-G$_2$)-tBMA$_{50}$];[26]**. Equivalents of *n*-butylamine added: A) 1.5, B) 3, C) 4.5.

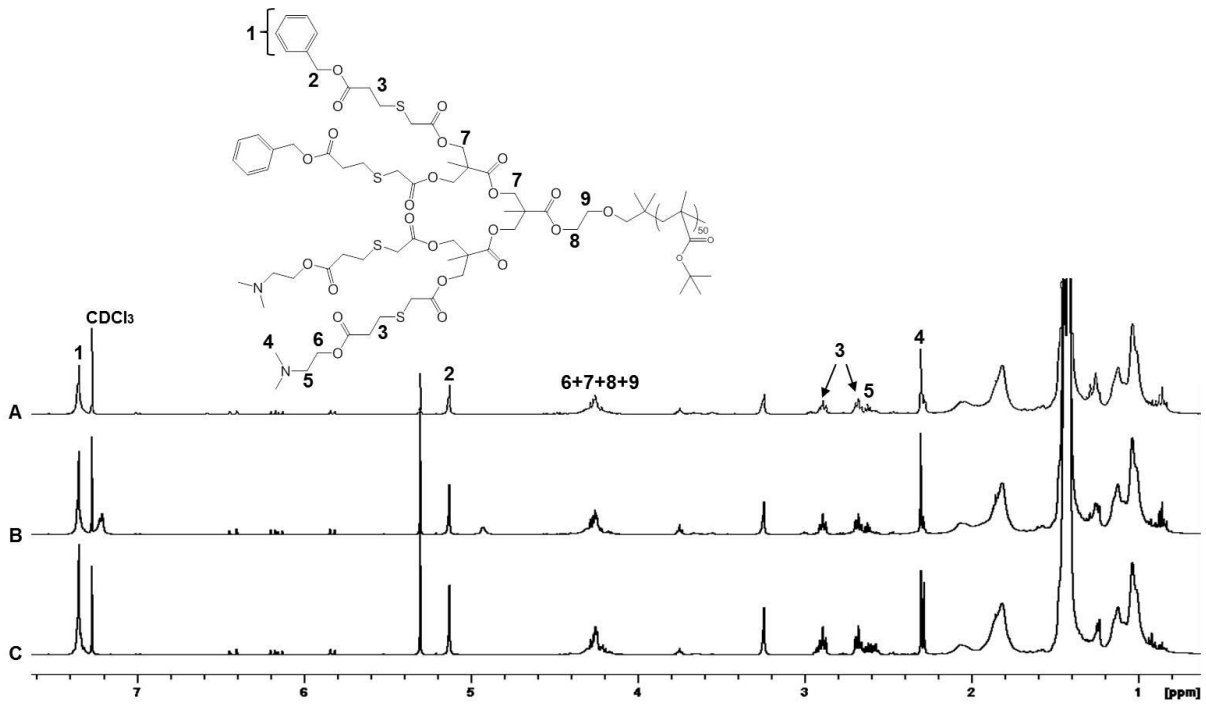

Fig. S3.34 Stacked ^{1}H NMR (400 MHz, $CDCl_3$) spectra of sequentially multifunctionalised **p[(Xan$_4$-G$_2$)-tBMA$_{50}$];[26]**. Equivalents of *n*-butylamine added for deprotection in first step: A) 1.5, B) 3.

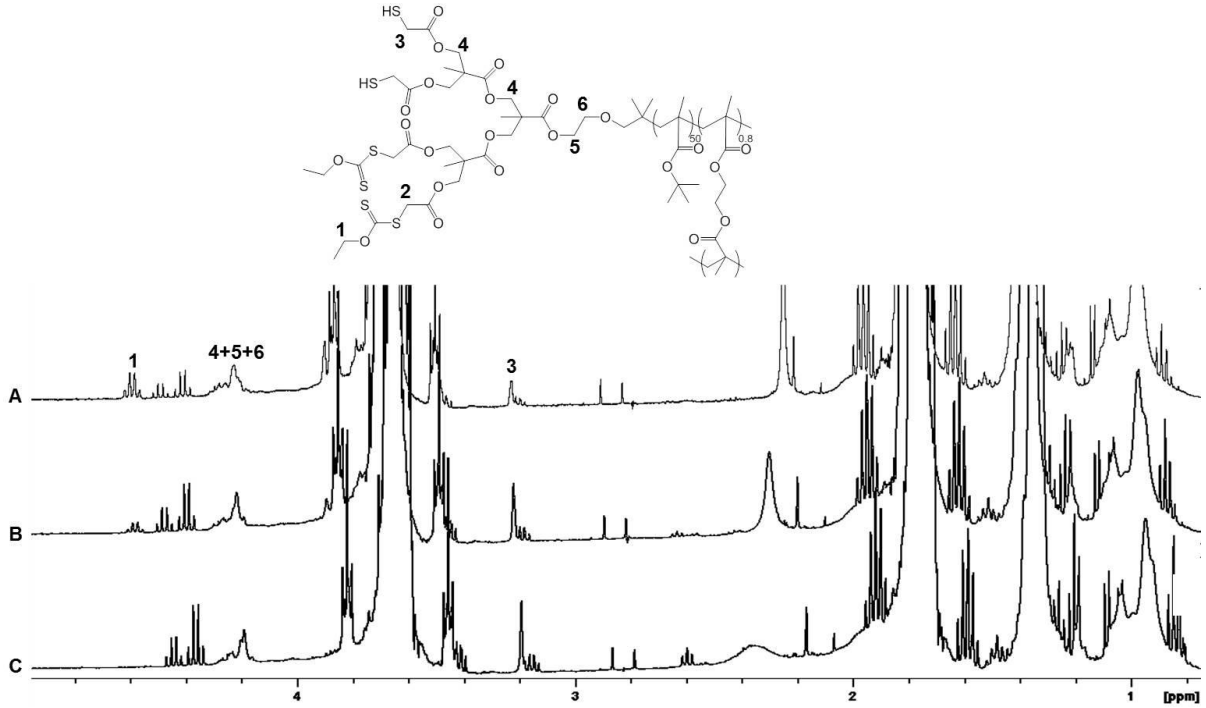

Fig. S3.35 Stacked ^{1}H NMR (400 MHz, $CDCl_3$) spectra of partially deprotected **p[(Xan$_4$-G$_2$)-tBMA$_{50}$-*co*-EGDMA$_{0.8}$];[28]**. Equivalents of *n*-butylamine added: A) 1.5, B) 3, C) 4.5.

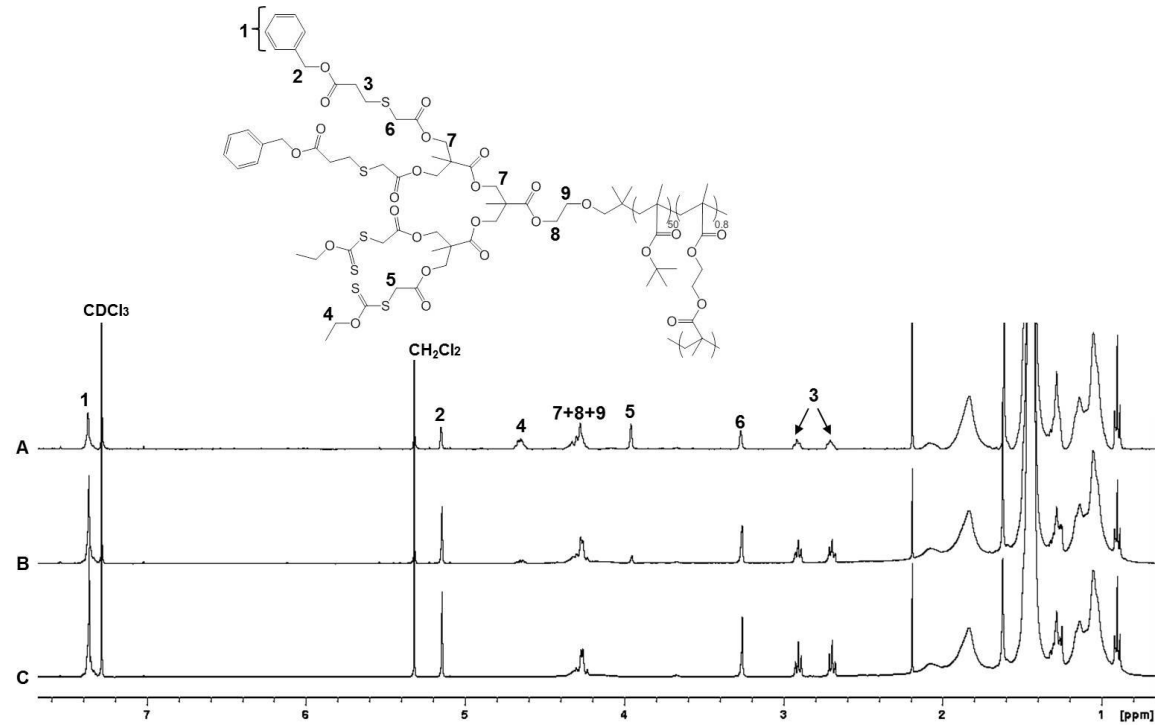

Fig. S3.36 Stacked ^{1}H NMR (400 MHz, $CDCl_3$) spectra of partially Bz functionalised **p[(Xan$_4$-G$_2$)-tBMA$_{50}$-*co*-EGDMA$_{0.8}$];[28]**. Equivalents of *n*-butylamine added: A) 1.5, B) 3, C) 4.5.

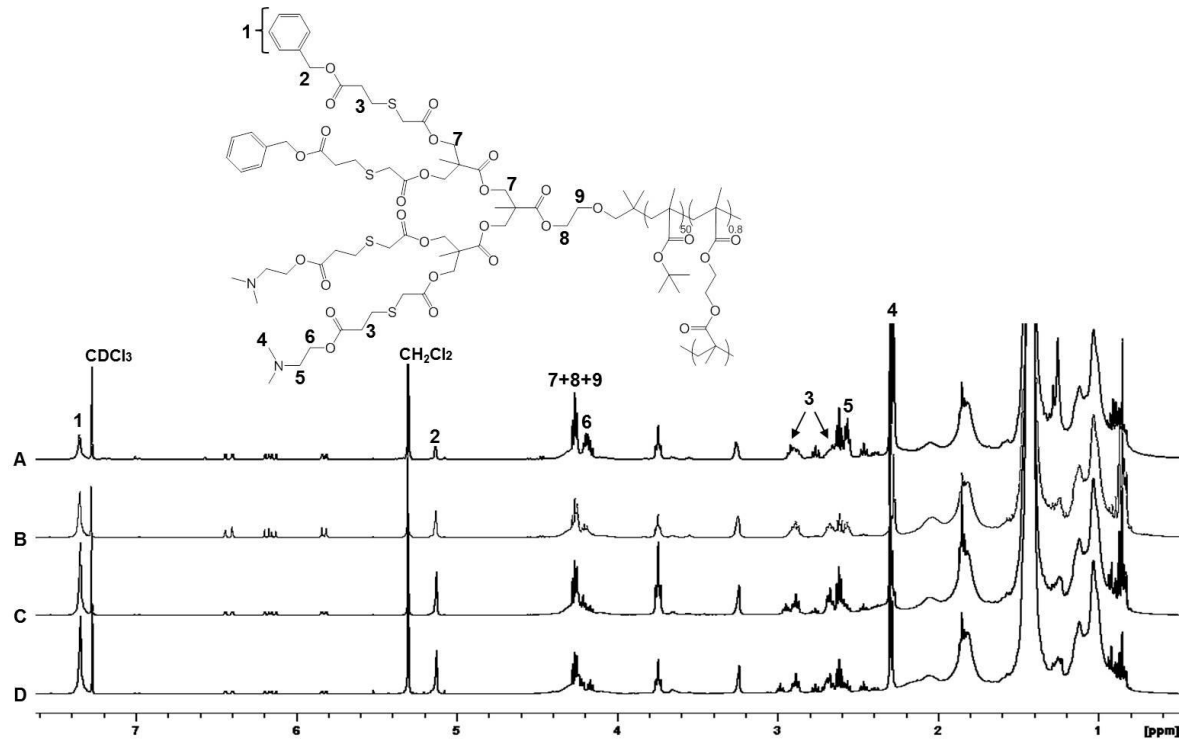

Fig. S3.37 Stacked ^{1}H NMR (400 MHz, $CDCl_3$) spectra of sequentially multifunctionalised **p[(Xan$_4$-G$_2$)-tBMA$_{50}$-*co*-EGDMA$_{0.8}$];[28]**. Equivalents of *n*-butylamine added for deprotection in first step: A) 1.5, B) 2, C) 3, D) 4.

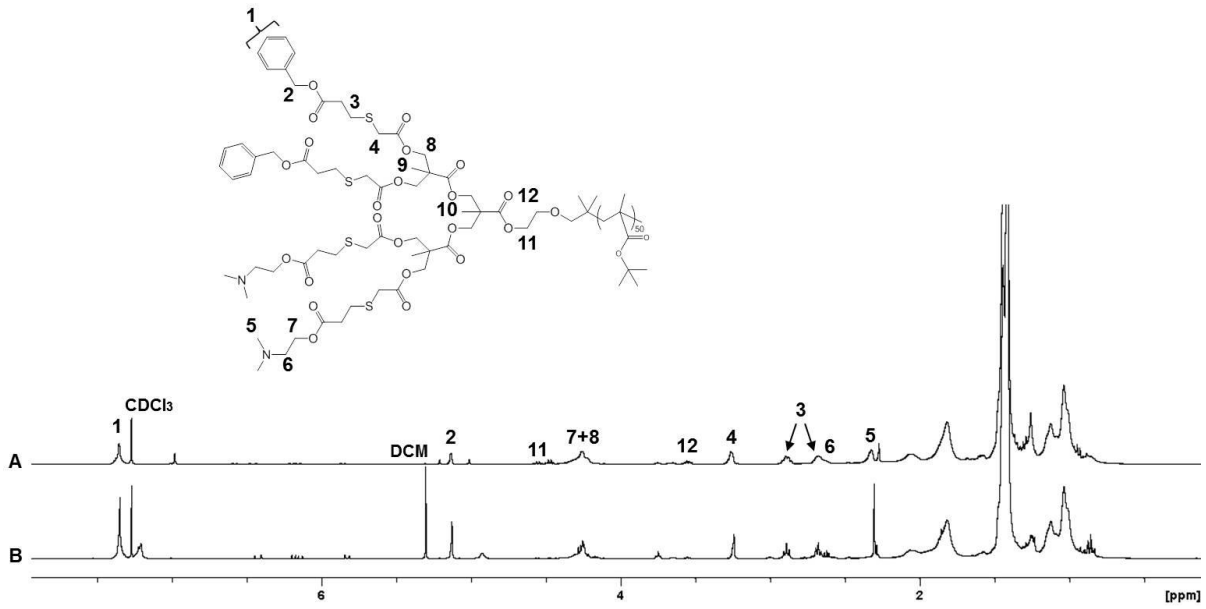

Fig. S3.38 ^{1}H NMR (400 MHz, $CDCl_3$) of **p[(Am_2-Bz_2-G_2)-tBMA$_{50}$];[118]**: (A) Simultaneous (B) Sequential

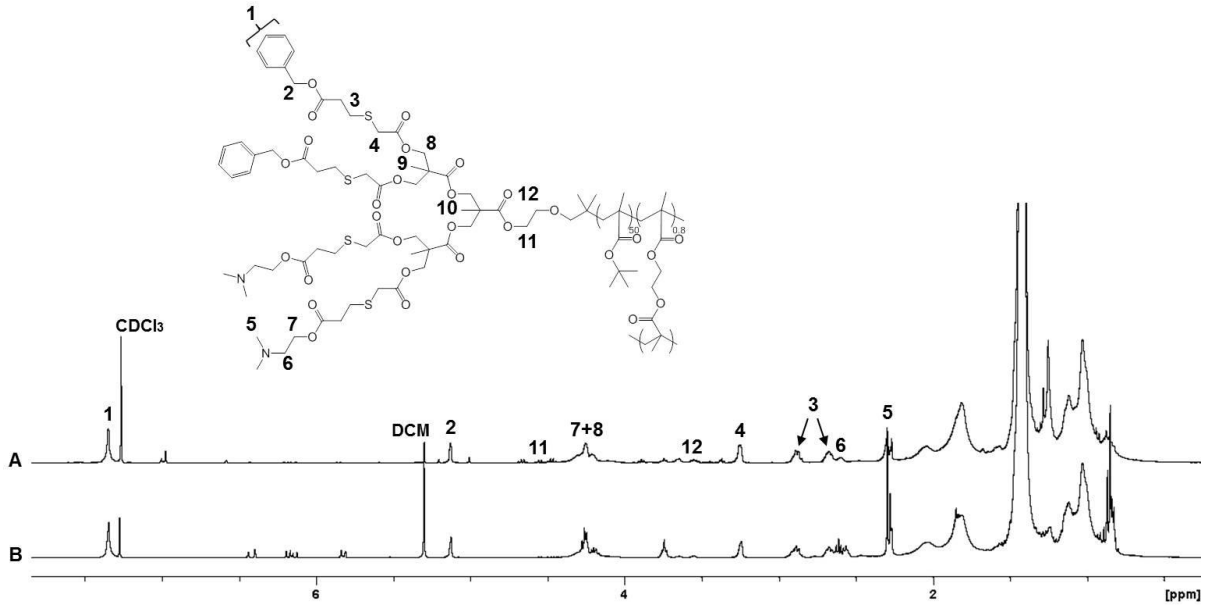

Fig. S3.39 ^{1}H NMR (400 MHz, $CDCl_3$) of **p[(Am_2-Bz_2-G_2)-tBMA$_{50}$-*co*-EGDMA$_{0.8}$];[121]**: (A) Simultaneous (B) Sequential

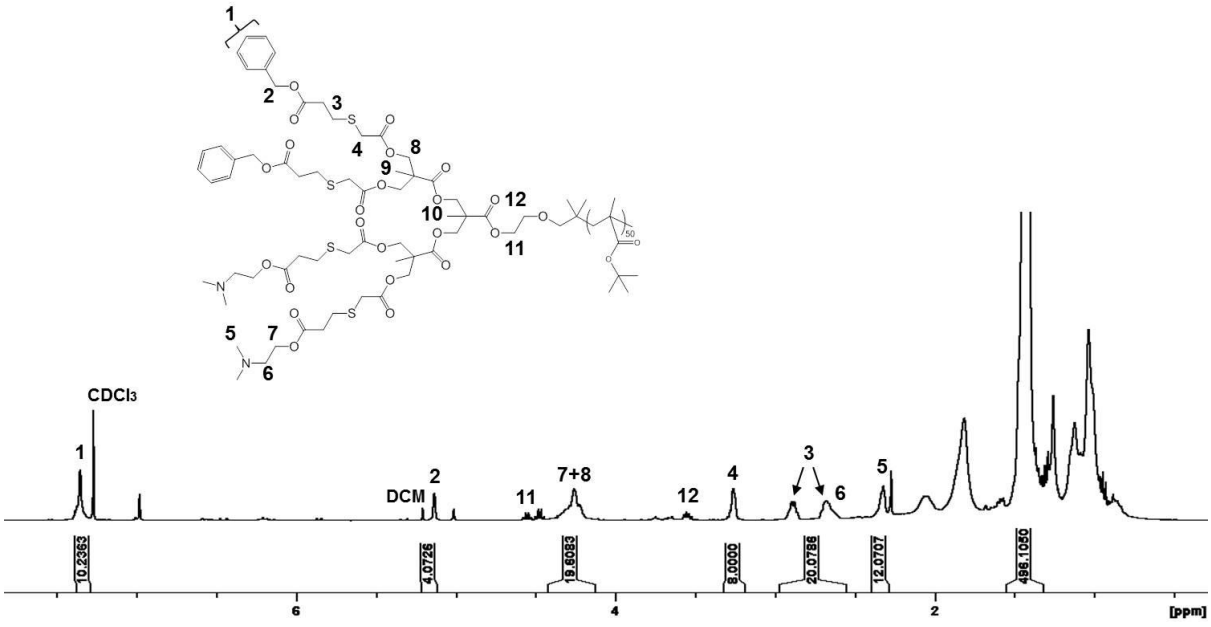

Fig. S3.40 ^{1}H NMR (400 MHz, $CDCl_3$) of Simultaneous **p[(Am_2-Bz_2-G_2)-$tBMA_{50}$];[118]**

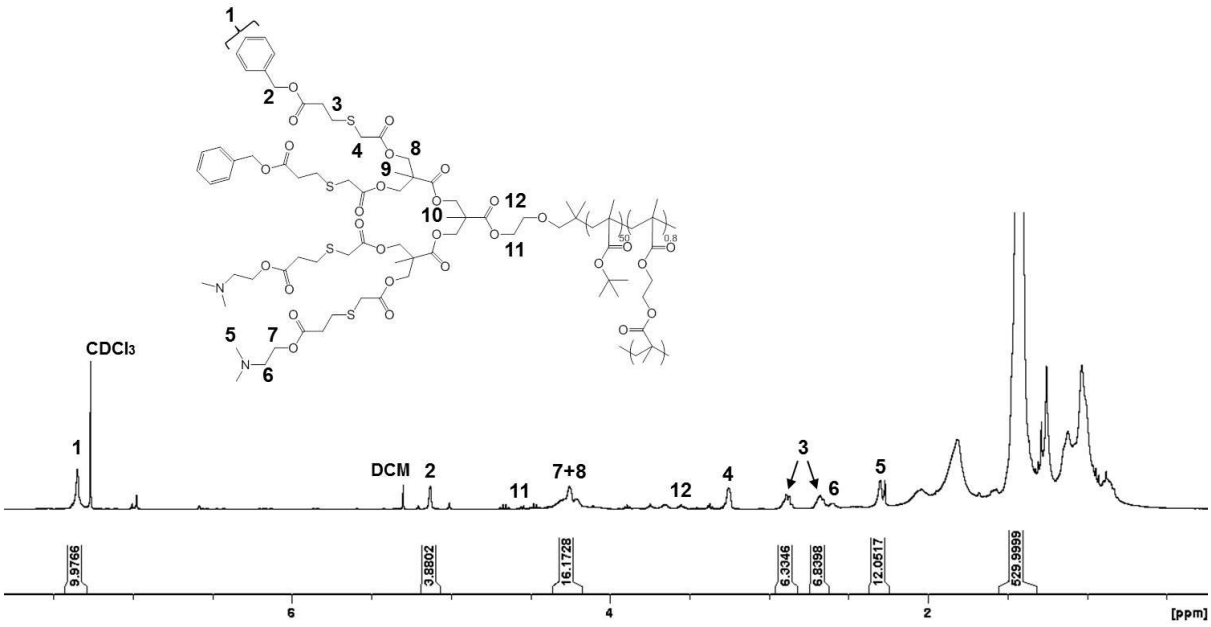

Fig. S3.41 ^{1}H NMR (400 MHz, $CDCl_3$) of Simultaneous **p[(Am_2-Bz_2-G_2)-$tBMA_{50}$-*co*-$EGDMA_{0.8}$];[121]**

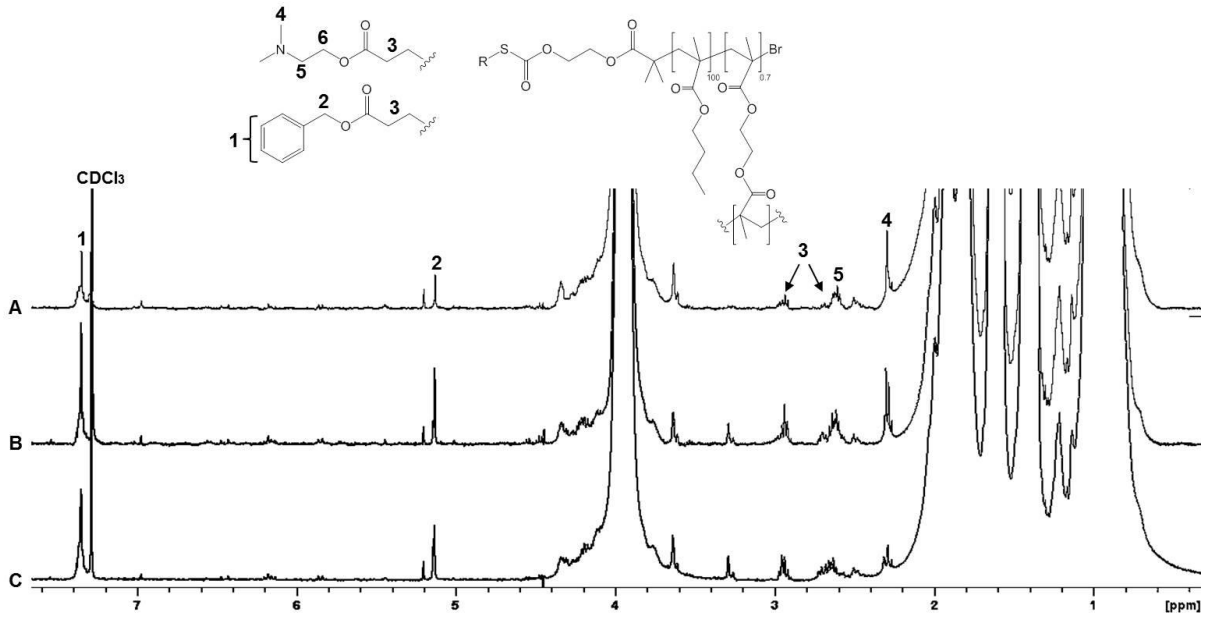

Fig. S3.42 Stacked ^{1}H NMR (400 MHz, $CDCl_3$) spectra of simultaneously multifunctionalised **p[(Xan$_1$-G$_0$)-nBMA$_{100}$-*co*-EGDMA$_{0.7}$];[36]**, **p[(Am$_x$-Bz$_y$-G$_0$)-nBMA$_{100}$-*co*-EGDMA$_{0.7}$];[127]** (x = 0-1, y = 0-1, x+y = 1) targeting; A) 75:25, B) 50:50 and C) 25:75 Am:Bz functionality.

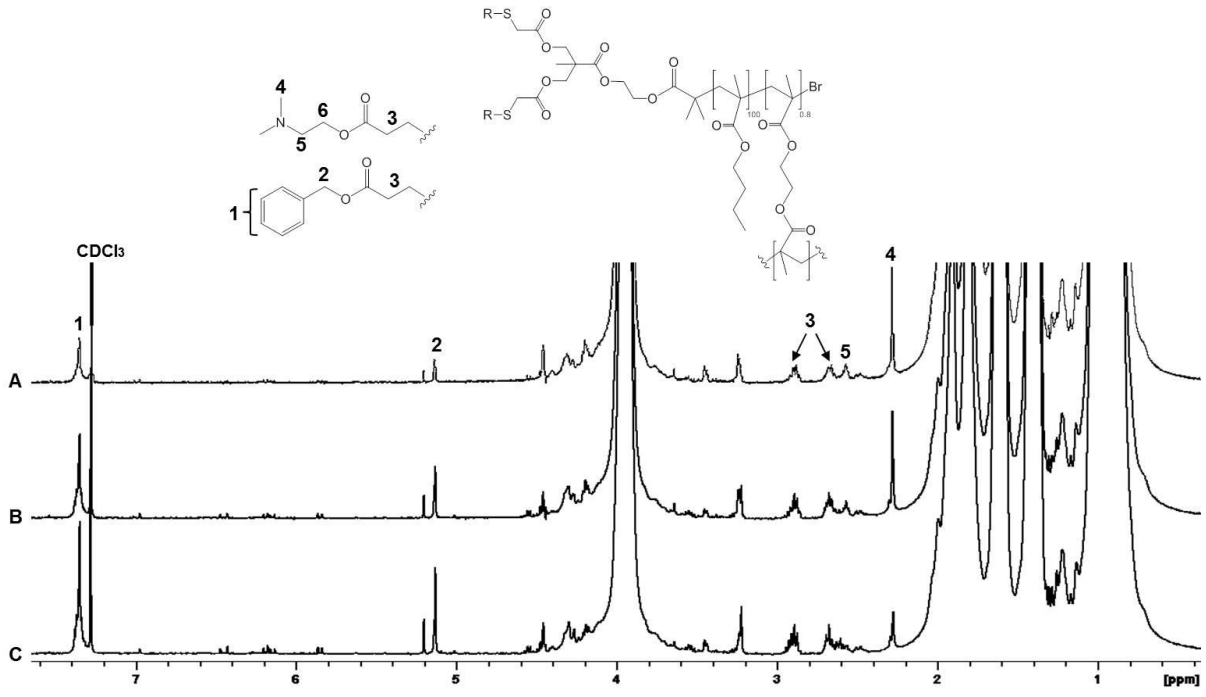

Fig. S3.43 Stacked ^{1}H NMR (400 MHz, $CDCl_3$) spectra of simultaneously multifunctionalised **p[(Xan$_2$-G$_1$)-nBMA$_{100}$-*co*-EGDMA$_{0.8}$];[37]**, **p[(Am$_x$-Bz$_y$-G$_1$)-nBMA$_{100}$-*co*-EGDMA$_{0.8}$];[128]** (x = 0-2, y = 0-2, x+y = 2) targeting; A) 75:25, B) 50:50 and C) 25:75 Am:Bz functionality.

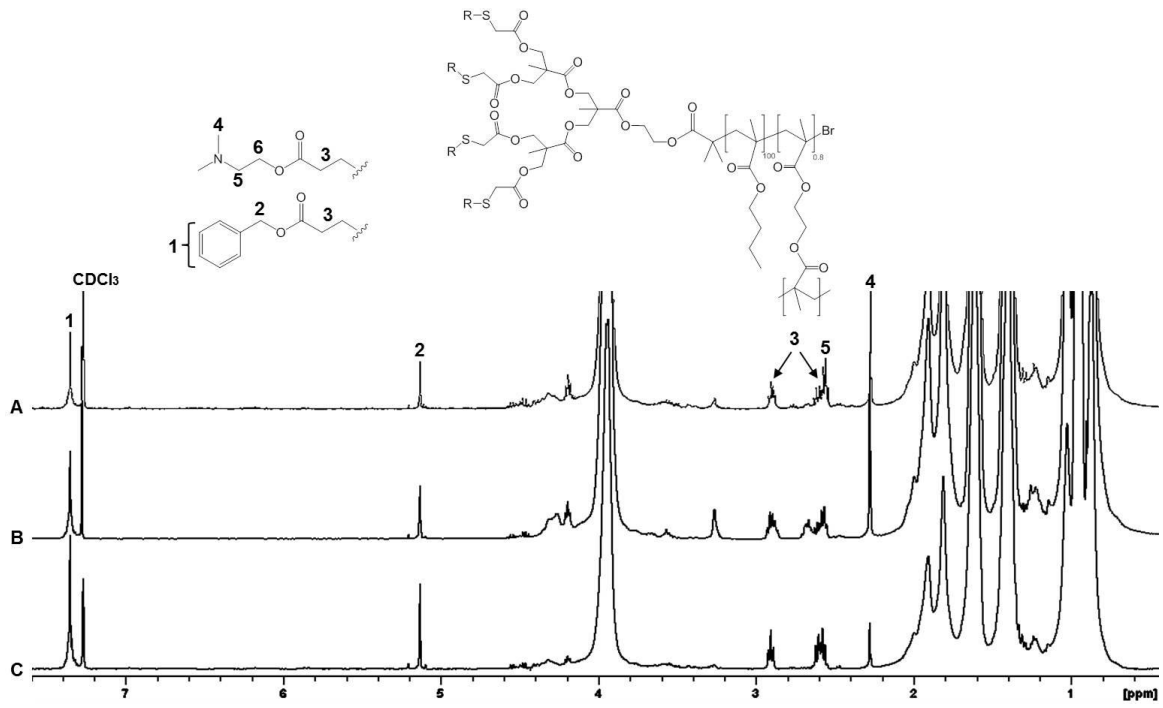

Fig. S3.44 Stacked ^{1}H NMR (400 MHz, $CDCl_3$) spectra of simultaneously multifunctionalised **p[(Xan_4-G_2)-nBMA$_{100}$-*co*-EGDMA$_{0.8}$];[38]**, **p[(Am_x-Bz_y-G_2)-nBMA$_{100}$-*co*-EGDMA$_{0.8}$];[129]** (x = 0-4, y = 0-4, x+y = 4) targeting; A) 75:25, B) 50:50 and C) 25:75 Am:Bz functionality.

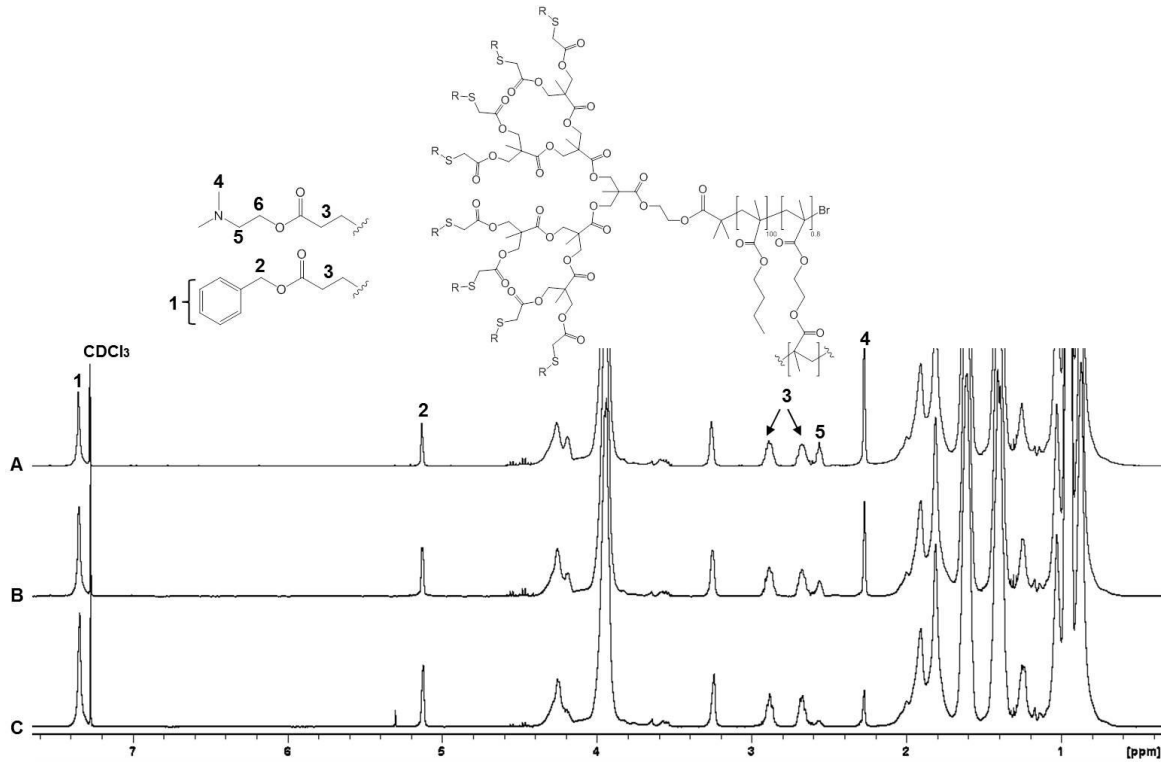

Fig. S3.45 Stacked ^{1}H NMR (400 MHz, $CDCl_3$) spectra of simultaneously multifunctionalised **p[(Xan_8-G_3)-nBMA$_{100}$-*co*-EGDMA$_{0.8}$];[39]**, **p[(Am_x-Bz_y-G_3)-nBMA$_{100}$-*co*-EGDMA$_{0.8}$];[130]** (x = 0-8, y = 0-8, x+y = 8) targeting; A) 75:25, B) 50:50 and C) 25:75 Am:Bz functionality.

Table S3.3 % Am and Bz functional group incorporation following simultaneous multifunctionalisation of G_0-G_3 nBMA HPDs **[36]-[39]**.

Polymer	Targeted (%)		Experimental (%)[a]	
	Am	Bz	Am	Bz
p[(Xan_1-G_0)-$nBMA_{100}$-*co*-$EGDMA_{0.7}$];[36]	25	75	31.8	67.3
	50	50	48.5	51.9
	75	25	68.9	26.6
p[(Xan_2-G_1)-$nBMA_{100}$-*co*-$EGDMA_{0.8}$];[37]	25	75	25.0	73.1
	50	50	50.7	47.3
	75	25	70.8	25.6
p[(Xan_4-G_2)-$nBMA_{100}$-*co*-$EGDMA_{0.8}$];[38]	25	75	21.7	77.8
	50	50	52.4	43.7
	75	25	65.1	33.8
p[(Xan_8-G_3)-$nBMA_{100}$-*co*-$EGDMA_{0.8}$];[39]	25	75	17.9	77.9
	50	50	37.4	60.9
	75	25	50.3	48.1

[a]Determined by ^{1}H NMR in $CDCl_3$

CHAPTER 4

Controlling the distribution of surface functional groups of dendritic polymer nanoparticles

Publication arising from this Chapter:

"Co-initiated hyperbranched-polydendron building blocks for the direct nanoprecipitation of dendron-directed patchy particles with heterogeneous surface functionality."

F. Y. Hern, A. Hill, A. Owen and S. P. Rannard (*Chem. Commun.*, 2018, manuscript under review).

Individual contributions: A. Hill – GNP synthesis; A. Owen and S. P. Rannard – supervisors.

4.1 Introduction

Performing multiple reactions on a single substrate or inducing multiple interactions in complex biological environments presents a significant challenge for chemistry and materials science. Naturally occurring multivalent interactions provide inspiration as biological systems are able to perform multiple simultaneous reactions with excellent regio/stereospecificity in complex environments under mild conditions, and dramatically enhance substrate-substrate interactions and recognition.[1] Surface heterogeneity (denoted as "patchiness") may induce a multivalency effect, reminiscent of interactions widely occurring in biological systems. Patchy particles have an anisotropic distribution of surface functional groups which may be useful in the medical field due to their ability to simultaneously present multiple different surface chemistries on the same construct (see section 1.6).[2]

Building on the previous chapter, we aim to synthesise nanoparticles with statistical and patchy distributions of surface functional groups. The initial aim of generating statistically distributed functional groups through one-pot deprotection/thiol-mixed acrylate reactions led to measureable thiol isolation within model xanthate functional G_3 dendron studies and considerably reduced confidence in this approach to accurately generate hyperbranched polydendrons (HPDs) with comparable statistical and patchy chemistry. The G_0 initiator **[Xan_1-G_0-BiB];[20]** provides an opportunity to deliver spatially distributed individual functional groups that are considerably different to the arrangement of functionality within the modified G_3 dendrons; subsequent post-polymerisation modification of the G_0-xanthate functional HPD utilising a mixed acrylate feedstock for the synthesis of statistically multifunctionalised materials is expected to significantly overcome or minimise thiol isolation in the resulting structures, Fig. 4.1A. The formation of patches of functionality is hypothesised from co-initiation of HPDs using two mono-functional G_3 dendron

macroinitiators, resulting in the formation of "zones" of functionality on the resulting anisotropic polymeric particle periphery after nanoprecipitation (a single-step process that does not require the use of surfactants and yields nanoparticles with narrow size distributions (see section 1.6.2)), Fig. 4.1B. Tailoring of initiator feeds is also hypothesised to nominally maintain the same molar ratio of the different functional groups in both statistical and patchy materials, allowing for direct comparison of nanoprecipitate behaviour.

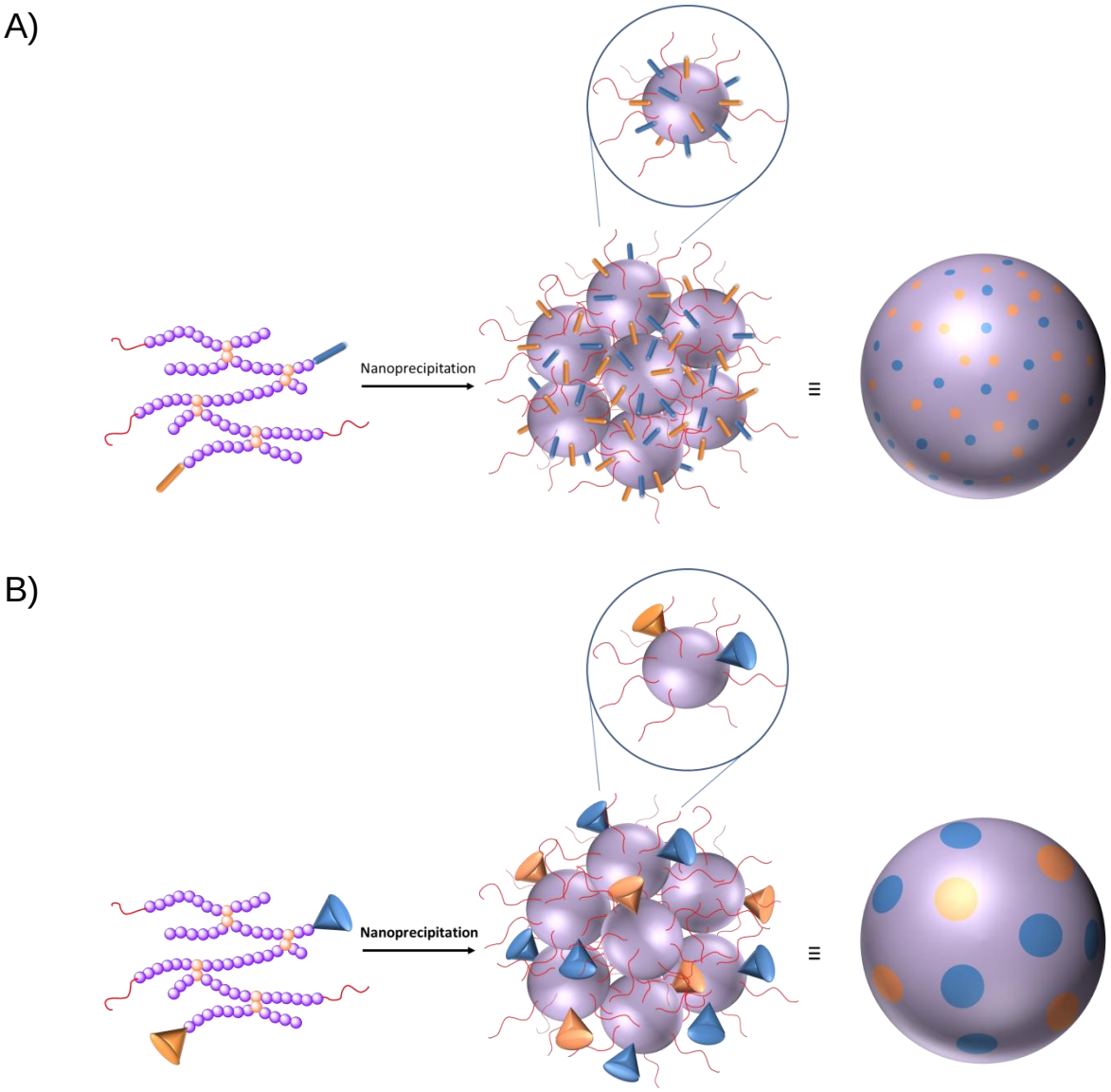

Fig. 4.1 Overall target materials; A) statistically and B) patchy multifunctionalised nanomaterials

In the late 1970s, Abuchowski *et al.* pioneered the covalent attachment of poly(ethylene glycol) (PEG) to proteins (commonly known as "PEGylation") to form polymer-protein bioconjugates; resulting in enhanced solubility, electrophoretic mobility, reduced immunogenicity and prolonged residence time.[3,4] Since then, PEGylation has been applied to a range of bioconjugate systems to improve biocompatibility and can be found in a range of FDA-approved drug formulations.[5-13] In order to sustain nanoparticle stability in aqueous environments for the envisioned nanoprecipitates and to mediate, but not eliminate, interactions between these materials and components of the mononuclear phagocyte system (MPS) in future applications, the incorporation of PEG chains into branched polymer structures by either post-polymerisation modification of the xanthate groups via Michael addition with a PEG acrylate, or co/ter-initiation of dendron macroinitiators and a PEG-derived macroinitiator will be studied; this has previously been shown to be an effective approach and an advantage of the HPD platform.[14] Patchiness may benefit from varying the PEG:dendron initiator ratio in co/ter-initiated HPD synthesis, leading to isolation of dendron peripheral groups. Different generations of dendron initiators could also potentially lead to patches of different numbers of functional groups, which may alter interaction with biological systems.

4.1.1 Confirmation of patchy and statistical particle formation

The aim of this chapter is, therefore, to synthesise materials and nanoparticles with different spatial arrangements of functional groups at the periphery of primary chains, and ultimately, spherical nanoparticles. A key factor within the formation of patchy nanoparticles is the generation of clear indications that patchiness has actually been achieved. Analytical techniques for measuring the distribution of different functional groups at the atomic scale are not available to the project; therefore a direct imaging approach was hypothesised and studied to establish whether evidence of patchy nanoparticle surfaces could be determined.

As stated above, xanthate functional G_0 and G_3 initiators will be used in the copolymerisation of branched nBMA with the bifunctional monomer EGDMA. Co-initiation of a PEG-derived macroinitiator with either xanthate functional G_0 or G_3 dendron macroinitiators is expected to result in branched polymers with mixed end groups that will nanoprecipitate to form particles with a statistical distribution (Fig. 4.2A) or patches (Fig. 4.2B) of xanthate groups at the periphery. A large proportion of PEG groups are required at the surface in order to induce functional group isolation in materials with both grouped and statistically distributed functionality. The incorporation of PEG groups at the periphery may also enable nanoprecipitation of the polymers, without the need of a surfactant. Molar equivalents of peripheral xanthate groups will be maintained between the patchy and statistical structures, as outlined in Fig. 4.2.

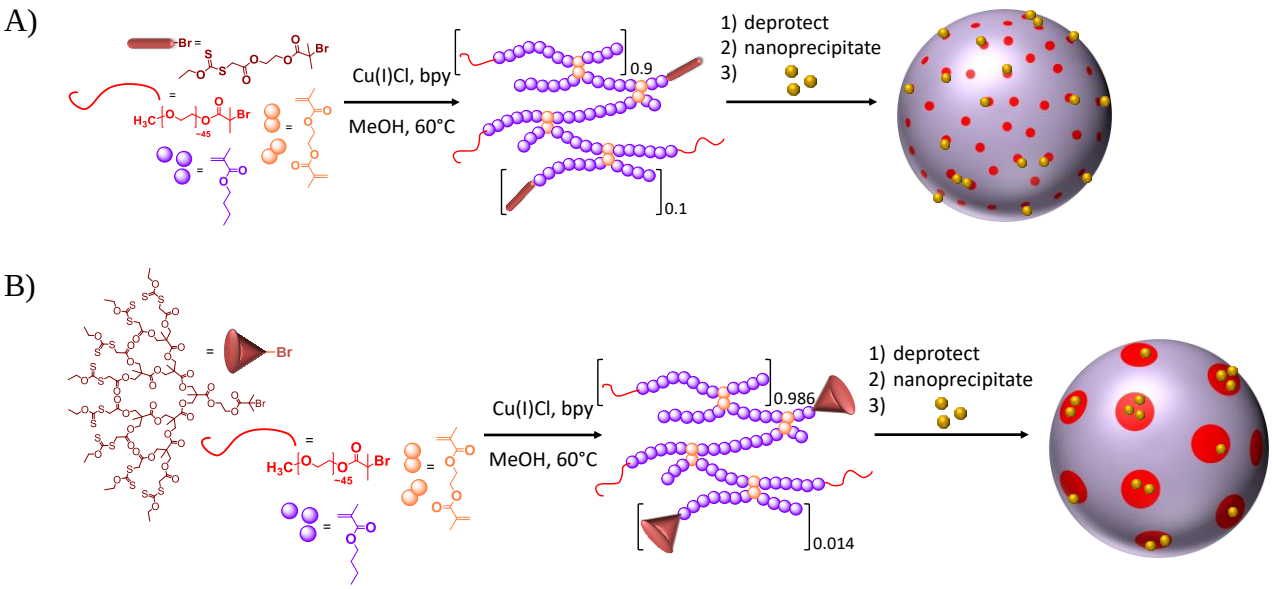

Fig. 4.2 Probing the distribution of; A) statistical and B) patchy distributions of surface functional groups

As demonstrated in Chapter 3, thiols can be readily generated from xanthate groups under mild basic conditions. It is hypothesised that visualisation of the distribution of accessible functional groups at the surface of the nanoprecipitates may be achieved by deprotection of the xanthate functional HPDs to expose thiols, followed by nanoprecipitation and coordination of small gold nanoparticles (GNPs). Due to the binding affinity of gold for thiols, the GNPs should bind with accessible thiols on the surface of the nanomaterials. The electron density of gold would enable the application of transmission electron microscopy (TEM) to visualise the distribution of coordinated GNPs and provide a clear indication of either isolated GNPs or grouped GNPs which will be interpreted as providing evidence for differing distributions of functional groups at the nanoparticle surface as either patchy or statistical; see Fig. 4.2.

4.2 Nanoparticle formation

4.2.1 Aqueous nanoprecipitation of xanthate functional LDHs and HPDs

Initial studies of the nanoprecipitation of xanthate-functional linear and branched polymers were carried out to ascertain ideal conditions for nanoparticle formation and establish differences between simple and complex architectures. G_0-G_3 xanthate functional LDHs (**p[(Xan$_1$-G$_0$)-nBMA$_{100}$];[32]**, **p[(Xan$_2$-G$_1$)-nBMA$_{100}$];[33]**, **p[(Xan$_4$-G$_2$)-nBMA$_{100}$];[34]** and **p[(Xan$_8$-G$_3$)-nBMA$_{100}$];[35]**) and HPDs (**p[(Xan$_1$-G$_0$)-nBMA$_{100}$-*co*-EGDMA$_{0.7}$];[36]**, **p[(Xan$_2$-G$_1$)-nBMA$_{100}$-*co*-EGDMA$_{0.8}$];[37]**, **p[(Xan$_4$-G$_2$)-nBMA$_{100}$-*co*-EGDMA$_{0.8}$];[38]** and **p[(Xan$_8$-G$_3$)-nBMA$_{100}$-*co*-EGDMA$_{0.8}$];[39]**) were dissolved in acetone ("good" solvent) at an initial concentration of 5 mg/mL, then rapidly added to water (miscible anti-solvent) with stirring. The acetone was allowed to evaporate overnight resulting in nanoparticle dispersions with a final concentration of 1 mg/mL of polymer in water, Fig. 4.3.

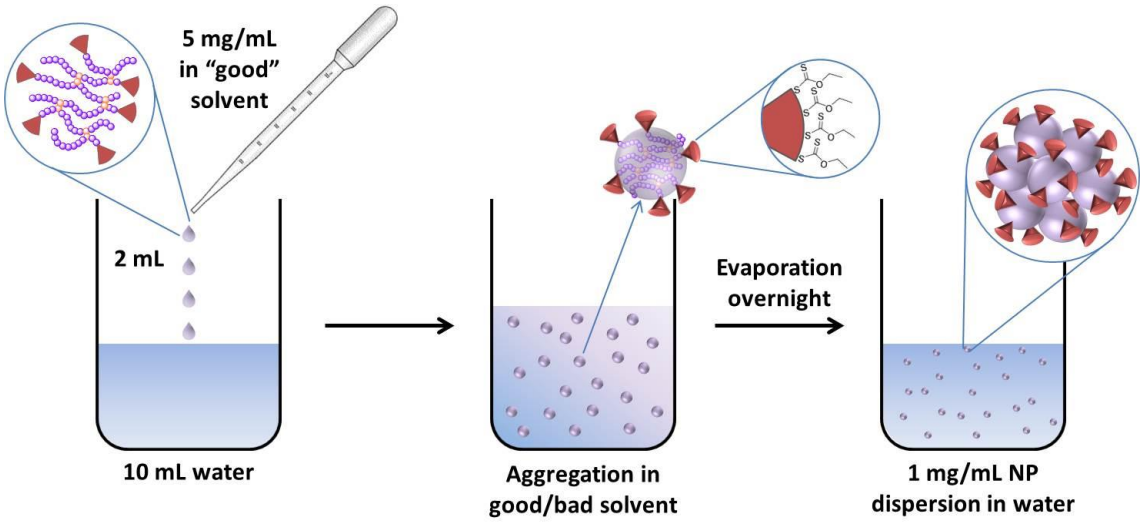

Fig. 4.3 Aqueous nanoprecipitation of xanthate functional HPDs

The nanoparticles were analysed primarily by dynamic light scattering (DLS), as summarised in Table 4.1 below, with size by intensity distributions shown in Fig. 4.4. The hydrodynamic diameter, also known as the Z-average diameter (D_z), of the HPD nanoprecipitates decreases with increasing dendron generation number, and hence number of peripheral xanthate groups. A narrow polydispersity index (PdI) (< 0.2) indicates size consistency across each sample.

Table 4.1 DLS measurement data for G_0-G_3 xanthate functional DP_{100} LDH and HPD polymers

Polymer	acetone		
	D_z (nm)	PdI	ζ (mV)
p[(Xan_1-G_0)-$nBMA_{100}$];[32]	161	0.052	-19.1
p[(Xan_2-G_1)-$nBMA_{100}$];[33]	123	0.037	-19.6
p[(Xan_4-G_2)-$nBMA_{100}$];[34]	102	0.040	-20.8
p[(Xan_8-G_3)-$nBMA_{100}$];[35]	60	0.094	-28.3
p[(Xan_1-G_0)-$nBMA_{100}$-*co*-$EGDMA_{0.7}$];[36]	125	0.028	-18.4
p[(Xan_2-G_1)-$nBMA_{100}$-*co*-$EGDMA_{0.8}$];[37]	104	0.066	-20.6
p[(Xan_4-G_2)-$nBMA_{100}$-*co*-$EGDMA_{0.8}$];[38]	78	0.039	-20.1
p[(Xan_8-G_3)-$nBMA_{100}$-*co*-$EGDMA_{0.8}$];[39]	53	0.107	-26.8

The nanoprecipitates formed from the equivalent LDH materials to the previously discussed HPDs were generally larger in size. For example, linear polymer **p[(Xan_1-G_0)-$nBMA_{100}$];[32]** nanoprecipitates had a D_z of 161 nm, whilst branched polymer **p[(Xan_1-G_0)-$nBMA_{100}$-*co*-$EGDMA_{0.7}$];[36]** nanoparticles were 125 nm in diameter. The trend follows with increasing dendron generation producing smaller nanoparticles: **p[(Xan_2-G_1)-$nBMA_{100}$];[33]** produces 123 nm diameter nanoparticles, whilst **p[(Xan_2-G_1)-$nBMA_{100}$-*co*-$EGDMA_{0.8}$];[37]** generates 104 nm particles; **p[(Xan_4-G_2)-$nBMA_{100}$];[34]** nanoparticles were 102 nm in diameter, whilst **p[(Xan_4-G_2)-$nBMA_{100}$-*co*-$EGDMA_{0.8}$];[38]** nanoparticles were 78 nm in diameter; and **p[(Xan_8-G_3)-$nBMA_{100}$];[35]** produces 60 nm diameter nanoparticles, whilst **p[(Xan_8-G_3)-$nBMA_{100}$-*co*-$EGDMA_{0.8}$];[39]** nanoprecipitates were 53 nm in diameter.

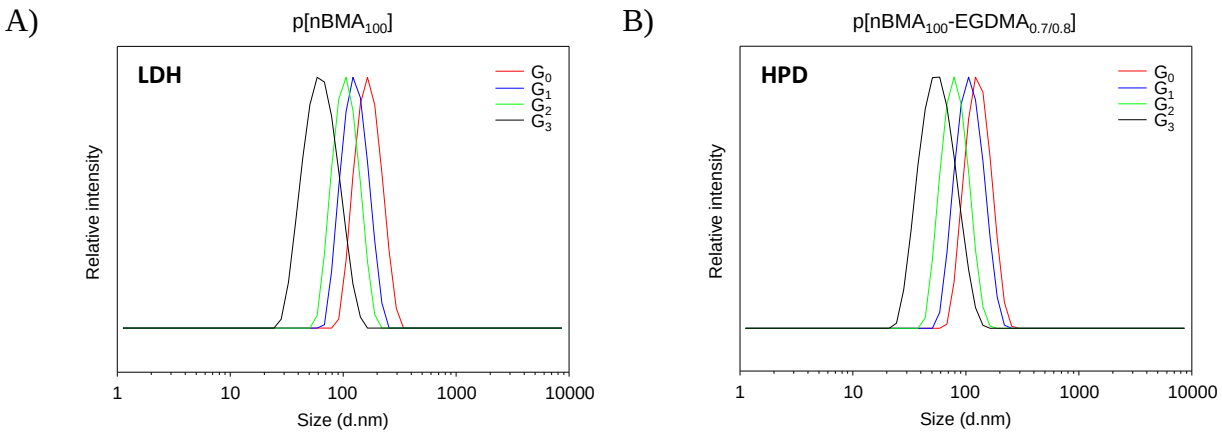

Fig. 4.4 DLS size distribution by intensity traces of aqueous nanoparticle dispersions of; A) LDHs **p[(Xan$_1$-G$_0$)-nBMA$_{100}$];[32]**, **p[(Xan$_2$-G$_1$)-nBMA$_{100}$];[33]**, **p[(Xan$_4$-G$_2$)-nBMA$_{100}$];[34]** and **p[(Xan$_8$-G$_3$)-nBMA$_{100}$];[35]**, and B) HPDs **p[(Xan$_1$-G$_0$)-nBMA$_{100}$-*co*-EGDMA$_{0.7}$];[36]**, **p[(Xan$_2$-G$_1$)-nBMA$_{100}$-*co*-EGDMA$_{0.8}$];[37]**, **p[(Xan$_4$-G$_2$)-nBMA$_{100}$-*co*-EGDMA$_{0.8}$];[38]** and **p[(Xan$_8$-G$_3$)-nBMA$_{100}$-*co*-EGDMA$_{0.8}$];[39]** (correlograms Fig. S4.4)

The nanoprecipitates were not expected to be stable when dispersed in water due to the hydrophobic nature of the polymers. The zeta potential (ζ) measured for each sample was slightly negative (approx. -20 mV), indicating that there may be an inherent charge stability. The negative ζ value is consistent with previous reports of hydrophobic nanoparticles formed by nanoprecipitation[14-16] and other hydrophobic polymer surfaces[17]. Although the origin of the negative charge in such systems is somewhat disputed, localised concentrations of negative charge are thought to originate from adsorbed hydroxide ions at the polymer/water interface as a result of water auto-dissociation and hydrogen bonding with surface functional groups.[18] Here, the polarity within the xanthate functional groups appears to provide sufficient hydrogen bonding capability to interact with multiple hydroxide ions; the increasing density of xanthates within the increasing dendron generations results in both smaller nanoprecipitates (due to the more rapid establishment of colloidal stability during nanoparticle growth) and higher negative ζ values.

The negative charge on the nanoparticle surface indicates a degree of electrostatic repulsion between similarly charged particles in the dispersion, which when high enough (≥ ±40 mV), may prevent aggregation or flocculation, which can lead to sedimentation and precipitation. Charge stabilised colloids can be easily destabilised by screening of surface charges via the addition of electrolytes.[19] The screening of surface charge blocks the repulsion between particles in suspension, which may aggregate and ultimately precipitate. The desire is therefore to produce sterically stabilised nanoparticles for use in biological systems due to the presence of various salts within the body; a PEG will therefore be used in later syntheses.

4.2.2 Probing accessible xanthate groups of HPD nanoprecipitates

The formation of nanoprecipitates will result in the full encapsulation of some polymer chains within the final nanoparticle and the "burying" of dendron end-groups, as shown in earlier reports of similar systems.[14] It is therefore possible that the formation of nanoprecipitates only allows the displaying of a small fraction of the available dendrons at the particle surface. The variation in negative ζ clearly suggests that some xanthate functional groups are present at the particle periphery, but in order to probe the number of accessible groups at the periphery of xanthate functional HPD nanoprecipitates, an excess of *n*-butylamine (50 equiv.) was added to each nanoparticle dispersion (G_0-G_3) and the resultant mixtures were left to stir overnight. Nanoparticles formed from HPDs containing higher generation dendrons (G_2 and G_3) were destabilised soon after addition of excess *n*-butylamine, strongly suggesting larger numbers of xanthate groups are accessible at the periphery of these nanoparticles as the amine removes the proposed hydrogen bonding site (xanthate carbonyl) for the adsorbed hydroxide ions, reducing the possibility of charge stabilisation and causing the particles to destabilise and precipitate.

The nanoparticle suspensions were rapidly frozen in liquid nitrogen and lyophilised for 72 hours to remove the water and excess *n*-butylamine. The resulting polymer monolith was dissolved in deuterated chloroform ($CDCl_3$) and analysed by ^{1}H NMR spectroscopy. The percentage of remaining xanthate groups was calculated using the characteristic CH_2 resonance at $\delta = 4.64$ ppm, calibrated against the polymer signal at $\delta \approx 0.8$-1.1 ppm, which remains unchanged after deprotection of the xanthate groups. The percentage of xanthate groups deprotected in the aqueous nanoparticle suspensions were as follows: $G_0 = 42.5\%$; $G_1 = 71.5\%$; $G_2 = 84.7\%$; and $G_3 = 89.7\%$ (^{1}H NMRs Fig. 4.5 and S4.1-4.3).

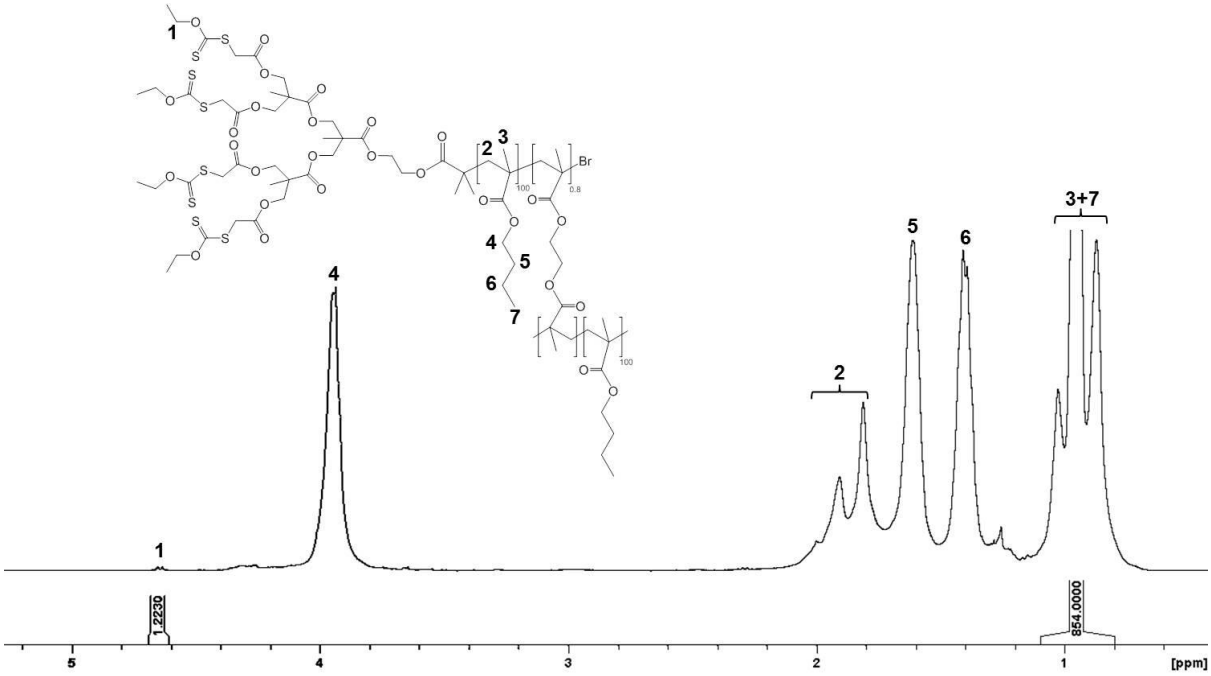

Fig. 4.5 ^{1}H NMR (400MHz, $CDCl_3$) of **p[(Xan$_4$-G$_2$)-nBMA$_{100}$-*co*-EGDMA$_{0.8}$];[38]** lyophilised deprotected nanoparticle dispersion

This correlates well with the variation in ζ measured for the nanoparticles, Fig. 4.6, although it is unclear whether some hydroxide binding would be expected in the absence of xanthate functional groups and whether some penetration of the *n*-butylamine into the nanoparticle occurred prior to freeze-drying.

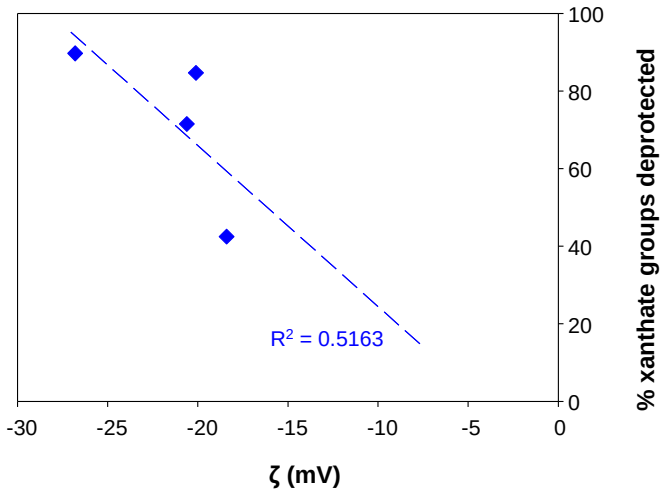

Fig. 4.6 Correlation between % of xanthate groups deprotected and zeta potential of nanoprecipitate suspensions

4.3 Post-polymerisation modification of p[(Xan$_1$-G$_0$)-nBMA$_{100}$-*co*-EGDMA$_{0.7}$] with PEG(2K) acrylate

In order to increase the steric stability of nanoparticles in water following deprotection of the xanthate peripheral groups, a PEG functional group may be added at the periphery of the polymer samples. PEG groups sterically stabilise nanoparticles in water when formed by rapid nanoprecipitation. In order to investigate the impact of PEG chains at the nanoparticle surface, branched G_0 initiated HPD **p[(Xan$_1$-G$_0$)-nBMA$_{100}$-*co*-EGDMA$_{0.7}$];[36]** was subjected to partial post-polymerisation modification with PEG(2K) acrylate, applying 1 equivalent of *n*-butylamine per xanthate group for deprotection, as calculated in Chapter 3 from the *pseudo*-calibration curve (Fig. 3.30A), followed by addition of a slight excess of PEG(2K) acrylate (1.5 equiv.) per deprotected xanthate, Scheme 4.1. A PEG(2K) content of 25%, 50%, 75% and 100% was targeted during the post-polymerisation modification of G_0 xanthate functional HPD **[36]**.

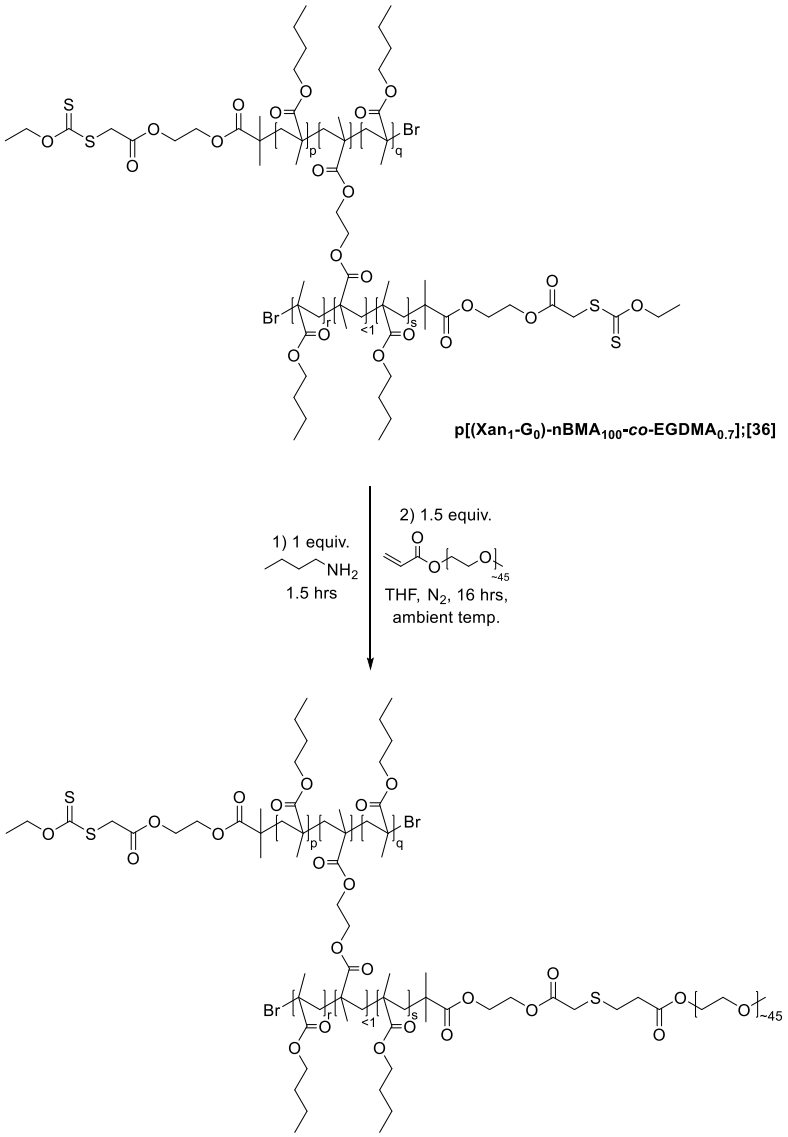

Scheme 4.1 Post-polymerisation modification of **p[(Xan$_1$-G$_0$)-nBMA$_{100}$-*co*-EGDMA$_{0.7}$];[36]** with PEG(2K) acrylate

The resulting polymers contained 22%, 49%, 70% and >99% of PEG(2K) groups at the periphery respectively, as calculated via ^{1}H NMR end group analysis using the characteristic C*H*$_3$ end group resonance at δ = 3.38 ppm and the backbone resonance at δ = 3.63-3.66 ppm of the PEG(2K) groups, calibrated against the nBMA polymer signal at δ ≈ 0.8-1.1 ppm, which remains unchanged after post-polymerisation modification (Fig. 4.7 and Fig. S4.5-S4.7).

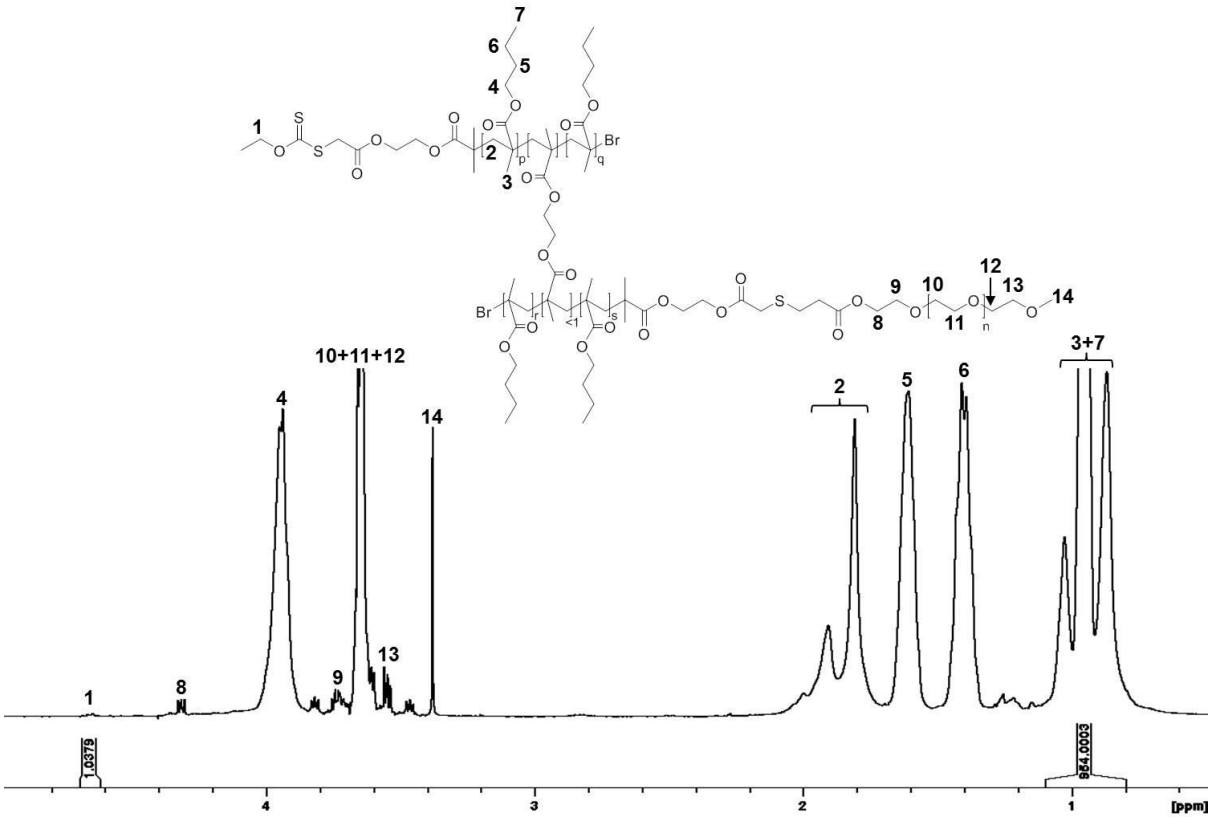

Fig. 4.7 ^{1}H NMR (400MHz, $CDCl_3$) of **p[(Xan$_1$-G$_0$)-nBMA$_{100}$-*co*-EGDMA$_{0.7}$];[36]** following partial modification with 49% of PEG(2K) groups

4.3.1 Aqueous nanoprecipitation studies of branched polymers with varying PEG functionality

A nanoprecipitation approach was utilised to assess the ability of these PEG(2K) post-polymerisation functionalised HPDs to form stable nanoparticles in water. The polymers were dissolved in acetone or THF at an initial concentration of 5 mg/mL, then rapidly added to water, with stirring. The solvent was allowed to evaporate overnight resulting in nanoparticle dispersions with a final concentration of 1 mg/mL of polymer in water. The nanoparticles were analysed primarily by DLS, as summarised in Table 4.2, below.

Table 4.2 DLS measurement data for partially PEG(2K) functionalised G_0 HPD polymers

PEG(2K) end groups (mol%)	Solvent			
	acetone		THF	
	D_z (nm)	PdI	D_z (nm)	PdI
22	135	0.058	184	0.023
49	108	0.042	145	0.042
70	86	0.054	114	0.056
>99	66	0.077	89	0.085

The data in Table 4.2 shows that increasing the molar percentage of PEG end-groups results in an overall decrease in D_z of the resulting nanoparticles. This effect can be clearly seen when comparing the size distribution by intensity traces of each sample, Fig. 4.8 and results from the rapid attainment of steric stability during the growth of the nanoprecipitates. When steric stability is achieved, the growth of the individual nanoparticles ceases; the higher the density of PEG chains, the earlier in the growth stage this is achieved. Additionally, a difference in the final nanoparticle size was observed when using the different solvents; an observation which has been reported previously.[20] This is not widely understood but it is believed to result from the different rates of diffusion and mixing of the water-miscible solvents, and the ability of the solvent/water mixture to swell the particles and modify the particle formation process.

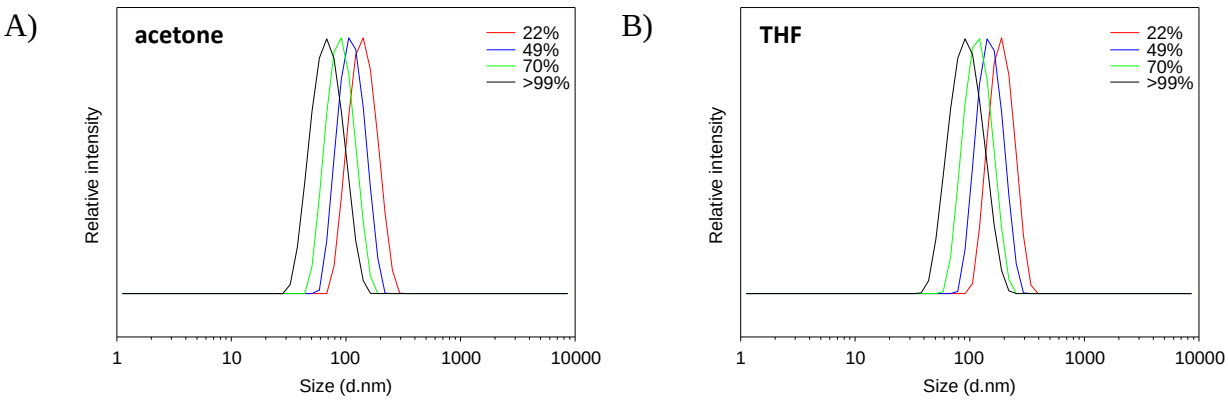

Fig. 4.8 DLS size distribution by intensity traces of aqueous nanoparticle dispersions of **p[(Xan_1-G_0)-$nBMA_{100}$-*co*-$EGDMA_{0.7}$];[36]** post-functionalised with PEG(2K) acrylate, containing 22%, 49%, 70% and >99% of PEG(2K) groups, nanoprecipitated from; A) acetone and B) THF (correlograms Fig. S4.8)

4.3.2 Probing accessible xanthate groups of PEG-functionalised HPDs

The PEG stabilised xanthate functional HPDs, synthesised by post-polymerisation modification of **p[(Xan$_1$-G$_0$)-nBMA$_{100}$-*co*-EGDMA$_{0.7}$];[36]** with varying degrees of PEG(2K) acrylate, were nanoprecipitated into water from acetone and the solvent left to evaporate with stirring overnight at ambient temperature. After this time, an excess of *n*-butylamine (50 mol. equiv.) was added to the nanoparticle dispersions, and then left to stir for 24 hours. The nanoparticle suspensions were rapidly frozen in liquid nitrogen and lyophilised for 72 hours to remove the water and excess *n*-butylamine. The resulting polymer monoliths were dissolved in deuterated chloroform ($CDCl_3$) and analysed by ^{1}H NMR spectroscopy. The percentage of remaining xanthate groups was calculated using the characteristic C*H*$_2$ resonance at 4.64 ppm, calibrated against the polymer signal at $\delta \approx 0.8$-1.1 ppm, which remains unchanged after deprotection of the xanthate groups, Fig. 4.9 (Fig. S4.9 and S4.10).

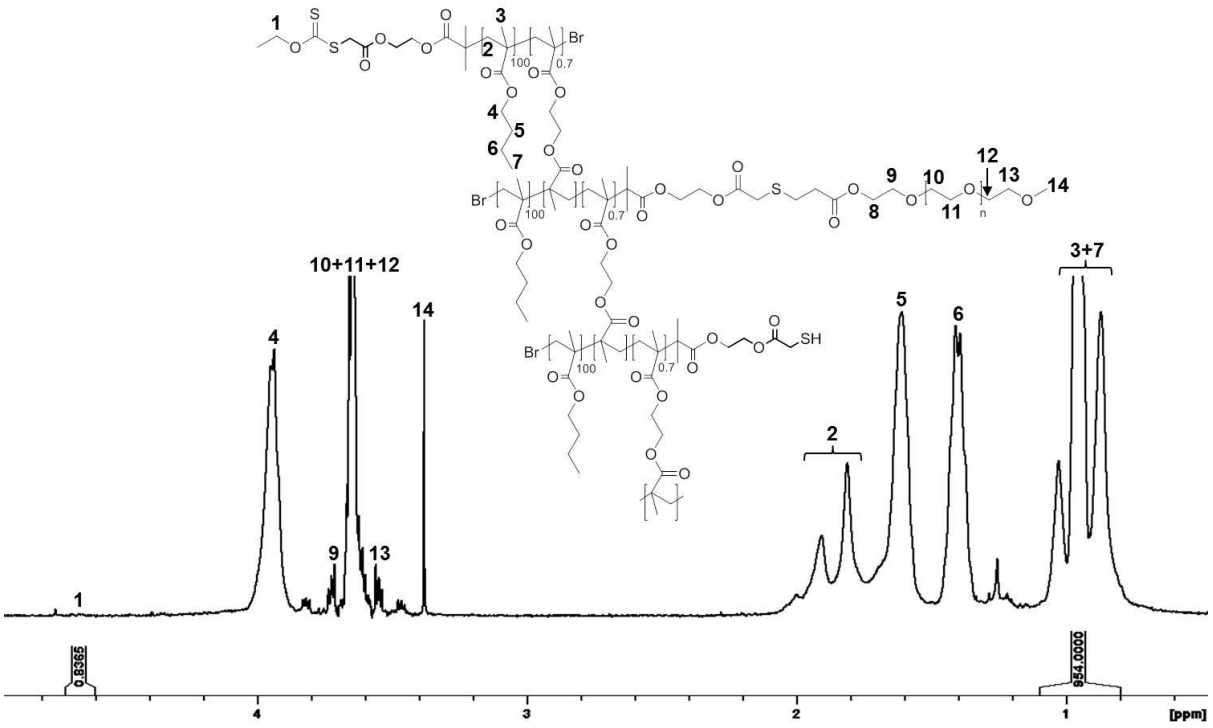

Fig. 4.9 ^{1}H NMR (400MHz, $CDCl_3$) of **p[(Xan$_1$-G$_0$)-nBMA$_{100}$-*co*-EGDMA$_{0.7}$];[36]**, partially post-modified with 49% of PEG(2K) groups, lyophilised deprotected nanoparticle dispersion

The data for the number of xanthate groups (mol%) deprotected in the aqueous nanoparticle suspensions are summarised in Table 4.3, below.

Table 4.3 Xanthate groups deprotected in aqueous suspension[a]

PEG(2K) end groups (mol%)	Initial xanthate end groups (mol%)	Final xanthate end groups (mol%)	Xanthate groups deprotected (% of initial)
22	78	49	38
49	51	42	18
70	30	28	8

[a]Determined by ^{1}H NMR spectroscopy (400 MHz) in $CDCl_3$

Increasing numbers of PEG(2K) end groups results in decreasing numbers of xanthate groups accessible to deprotection by excess *n*-butylamine in aqueous nanoparticle suspension. This could be due to the interior of the particles being less permeable to *n*-butylamine as the internal PEG concentration increases.[14] It may also be due to less xanthate groups being expressed on the surface of the particles, and are therefore inaccessible to deprotection. There may also be a decrease in reaction rates between *n*-butylamine and surface xanthates in the presence of increasing numbers of PEG groups.

Although nanoparticles containing the least amount (22 mol%) of PEG(2K) end groups remained stable, a higher percentage of PEG groups are expected to be required at the surface for functional group isolation to obtain the desired “patchy” and “statistical” distributions of surface groups.

4.4 Utilisation of co-initiation to generate mixed functionality polymers

The co-initiation of dendron and PEG-derived macroinitiators to form highly branched macromolecular architectures with tuneable surface chemistry has recently been reported by Hatton *et al*.[14] Varying the ratio of the initiator feeds results in polymers which form highly uniform nanoparticles by nanoprecipitation, with varying surface and internal chemistry. These early studies highlight the potential for moderating permeation of nanoparticles through a model human gut epithelium. Understanding the mechanisms involved in multifunctional material synthesis and subsequent nanoparticle formation allows us to have better control over physicochemical properties and interaction behaviour with biological targets within the body.

We hypothesise that co-initiation of PEG and dendron macroinitiators of varying generations may also result in functional group isolation or the formation of "patches" of functionality within nanoprecipitates and may offer a simpler route to control the chain end composition of HPDs. In order to induce functional group isolation, and hence, patchiness on the surface of resulting nanomaterials, a large proportion of PEG groups is expected to be required at the periphery. This may be achieved by tailoring the initiator feed during co-initiated HPD synthesis, with a large mole percentage of chain ends as PEG chains.

4.4.1 PEG(2K) macroinitiator synthesis

Monomethoxy PEG (M_n ~ 2000 g mol^{-1}) was converted into an ATRP macroinitiator via esterification with α-bromoisobutyryl bromide, Scheme 4.2.[21] The use of monomethoxy PEG circumvents crosslinking and allows selective activation and reaction of one end of the PEG chain.

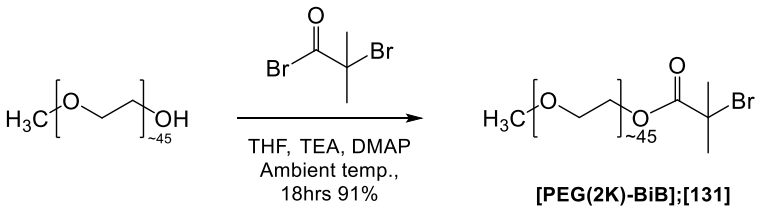

Scheme 4.2 PEG(2K) macroinitiator synthesis

Initiator formation was confirmed by ^{1}H NMR spectroscopy, with integrals of the terminal methyl environment (δ ≈ 3.33 ppm) and the two symmetrical methyl environments of the bromoisobutyrate moiety (δ ≈ 1.91 ppm) in a 3:6 ratio, as expected, Fig. 4.10 (^{13}C NMR analysis Fig. S4.11).

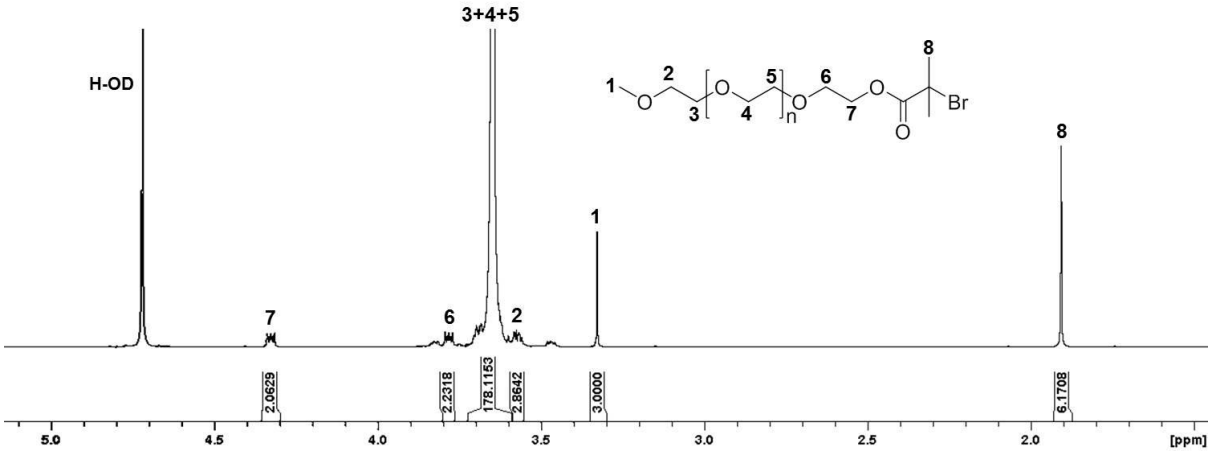

Fig. 4.10 ^{1}H NMR (400 MHz, D_2O) of **[PEG(2K)-BiB];[131]**

4.4.2 Linear polymer synthesis

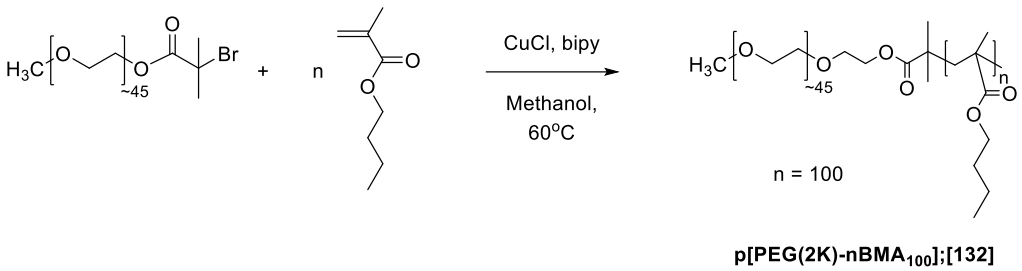

Scheme 4.3 Linear polymerisation with **[PEG(2K)-BiB];[131]** macroinitiator

The **[PEG(2K)-BiB];[131]** initiator was used to polymerise nBMA in a linear polymerisation to establish confidence in the conditions used for HPD co-initiated polymerisations, initially targeting a DP_n of 100 monomer units, **p[(PEG(2K))-nBMA$_{100}$];[132]**. The polymerisation was carried out at 60°C in methanol with a CuCl:bpy (1:2) catalyst system and a monomer concentration of 50 v/v% with respect to solvent. Polymerisation kinetics studies were carried out by sampling the reaction (approx. 0.2 mL) at regular intervals and diluting in $CDCl_3$ for ^{1}H NMR studies and DMF for SEC analysis.

The semi-logarithmic plot ($\ln([M_0]/[M])$) for **p[(PEG(2K))-nBMA$_{100}$];[132]** reveals a slight deviation from the expected linear time dependency, indicating a variation in radical concentration during the polymerisation, Fig. 4.11A. This is indicative of the persistent radical effect (PRE); the radical initiation rate of another species, e.g. the monomer itself, is much lower than the dissociation rate of the transition metal catalyst, and the polymerisation is therefore self-regulating.[22] Termination early in the polymerisation leads to a build-up of deactivated species. The polymerisation equilibrium is therefore shifted towards the dormant species and the radical concentration is lowered. Despite this, high conversion (>80%) was achieved within 7 hours, and the polymerisation was terminated at 28 hours (94% conversion).

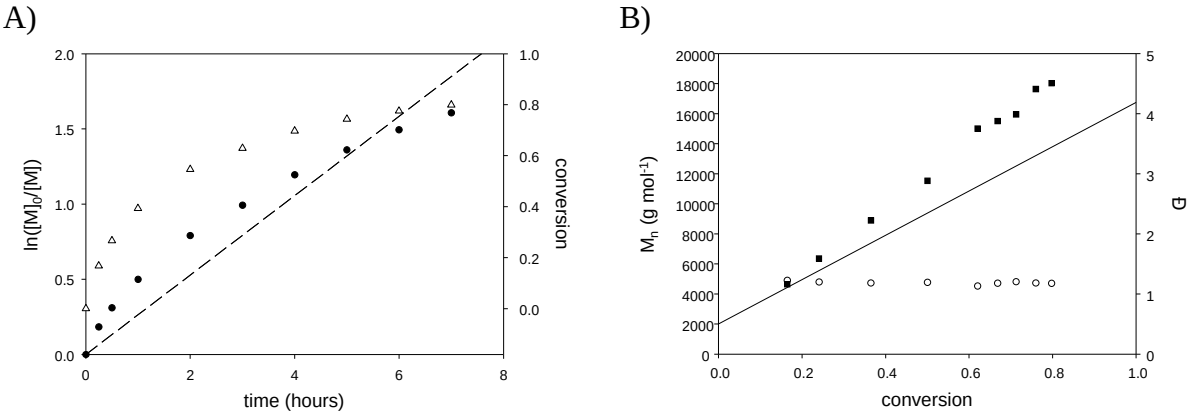

Fig. 4.11 Kinetic studies of the ATRP of nBMA **p[(PEG(2K))-nBMA$_{100}$];[132]**: A) Conversion *vs.* time (open triangles) with corresponding semi-logarithmic plots (closed black circles); dashed line represents linear regression of semi-logarithmic plot; B) M_n *vs.* conversion (closed black squares) with theoretical M_n *vs.* conversion (solid line) and Đ (open circles).

The refractive index increment (dn/dc) quantifies the change in refractive index of a solution with concentration of the analyte. Due to the difference in dn/dc values of PEG and p(nBMA), the evolution of dn/dc of the block copolymer was studied as the polymerisation progressed. The fraction of each monomer in a copolymer system can be estimated if the dn/dc values of the two monomers vary significantly; above a certain molecular weight, the effect of end groups is negligible and the dn/dc of the homopolymer is constant.

$$\left(\frac{dn}{dc}\right)_{copolymer} = \left(W_{PEG} \times \left(\frac{dn}{dc}\right)_{PEG}\right) + \left((1 - W_{PEG}) \times \left(\frac{dn}{dc}\right)_{p(nBMA)}\right) \qquad \text{(Eq. 4.1)}$$

For each kinetic time point, the weight fraction of PEG, W_{PEG}, was calculated using the theoretical M_n by ^{1}H NMR analysis. A theoretical $(dn/dc)_{copolymer}$ was then calculated using Eq 4.1 for each kinetic time point (average $(dn/dc)_{PEG}$ and $(dn/dc)_{p(nBMA)}$ obtained from published literature[23]). The value of dn/dc is expected to vary systematically as the p(nBMA) portion of the copolymer chain increases throughout the polymerisation. The calculated $(dn/dc)_{copolymer}$ value for each time point was then input into the SEC analysis software by editing the method to obtain more accurate values for M_n and M_w, and the corrected values of

M_n plotted against conversion, Fig. 4.11B, to produce a corrected kinetic plot for molecular weight evolution.[24] Molecular weight (M_n) evolves linearly with conversion, as expected, and Đ remains low (<1.23) throughout the polymerisation, despite a non-linear semi-logarithmic plot, suggesting very little impact on the control of the polymerisation from the varying radical concentration indicated.

A linear polymerisation combining both PEG(2K) and xanthate functional G_3 macroinitiators, at a xanthate:PEG functional group molar ratio of 1:1 (initiator molar ratio G_3 dendron:PEG of 0.125:0.875) was studied to ascertain whether the mixed initiator functionality would affect the polymerisation adversely. The resulting mixed polymer sample contained linear polymers bearing either PEG(2K) or G_3 dendron functionalities at one chain-end. During branched ATRP, the different chain-end functionalities are expected to be statistically incorporated into the growing branched macromolecules at the nominal molar ratio of initiators used. A difference in initiation or polymerisation during ATRP in the presence of both initiators would be evidenced by two distinct populations in the SEC chromatogram of the resulting polymer or a marked broadening of the molecular weight distribution. Data obtained from polymerisations containing 100:0, 12.5:87.5 and 0:100 G_3 dendron:PEG(2K) initiators are summarised in Table 4.4 and the RI traces shown in Fig. 4.12.

Table 4.4 Triple detection SEC data for linear polymers with **[Xan_8-G_3-BiB];[23]** and **[PEG(2K)-BiB];[131]** macroinitiators

Sample name	Initiator (mol%)		Conv. (%)[a]	SEC		Đ
	G_3 dendron	**PEG(2K)**		M_n (g mol^{-1})	M_w (g mol^{-1})	
p[(Xan_8-G_3)-nBMA_{100}];[35]	100	0	84	26 600[b]	31 800[b]	1.19[b]
p[(PEG(2K))$_{0.875}$-(Xan_8-G_3)$_{0.125}$-nBMA_{100}];[133]	12.5	87.5	95	17 600[c]	22 600[c]	1.28[c]
p[(PEG(2K))-nBMA_{100}];[132]	0	100	94	13 400[b]	14 500[b]	1.08[b]

[a] Determined by ^{1}H NMR analysis in $CDCl_3$ [b]Sample analysed in DMF containing 0.01 M LiBr at 60°C, 1mL min^{-1} flow rate. [c]Sample analysed in THF containing 2% TEA (v/v) at 35°C, 1 mL min^{-1} flow rate.

The molecular weights of these linear polymers appear to increase with increasing G_3 initiator content. This would suggest that **[PEG(2K)-BiB];[131]** has a much better initiator efficiency than **[Xan$_8$-G$_3$-BiB];[23]**, thus decreasing the number average molecular weight of the resulting polymer sample. Decreased initiator efficiency, conversely, results in less polymer chains in the sample, with a higher number average molecular weight. The linear polymerisation conducted with mixed initiators has a molecular weight between the two single initiator polymerisations, which can be easily seen in the SEC chromatogram overlay in Fig. 4.12. Additionally, indications of a residual dendron initiator are also present in the SEC chromatogram of **p[(Xan$_8$-G$_3$)-nBMA$_{100}$];[35]**, also supporting the possibility of reduced initiator efficiency in this case.

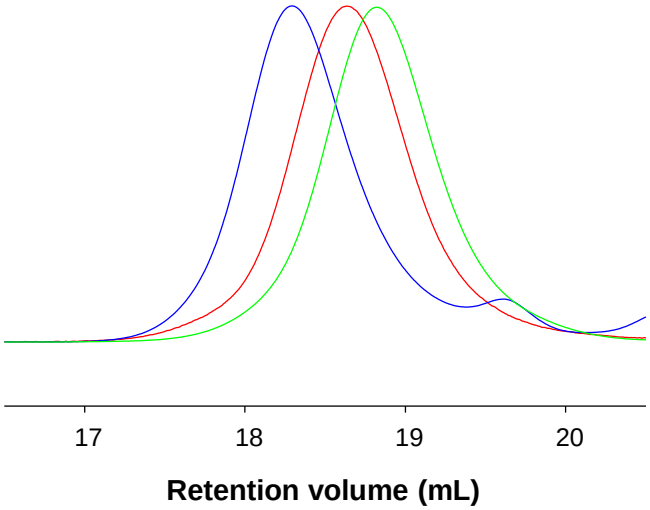

Fig. 4.12 SEC chromatogram overlay (refractive index) of **p[(Xan$_8$-G$_3$)-nBMA$_{100}$];[35]** (blue), **p[(PEG(2K))-nBMA$_{100}$];[132]** (red) and **p[(PEG(2K))$_{0.875}$-(Xan$_8$-G$_3$)$_{0.125}$-nBMA$_{100}$];[133]** (green)

The ^{1}H NMR spectrum of **p[(Xan$_8$-G$_3$)-nBMA$_{100}$];[35]** LDH is shown in Chapter 2, Fig. S2.58, with major peaks assigned. The ^{1}H NMR spectrum of **p[(PEG(2K))$_{0.875}$-(Xan$_8$-G$_3$)$_{0.125}$-nBMA$_{100}$];[133]** co-initiated linear polymers is shown in Fig. 4.13. Integrals corresponding to the xanthate functional group (CH_2 $\delta \approx 4.64$ ppm, peak 7 Fig. 4.13) and the PEG chain end (terminal methyl $\delta \approx 3.33$ ppm, peak 8 Fig. 4.13) confirm a nominal chain-end functional group molar ratio of 0.125:0.875 of G_3 dendron:PEG(2K), as targeted.

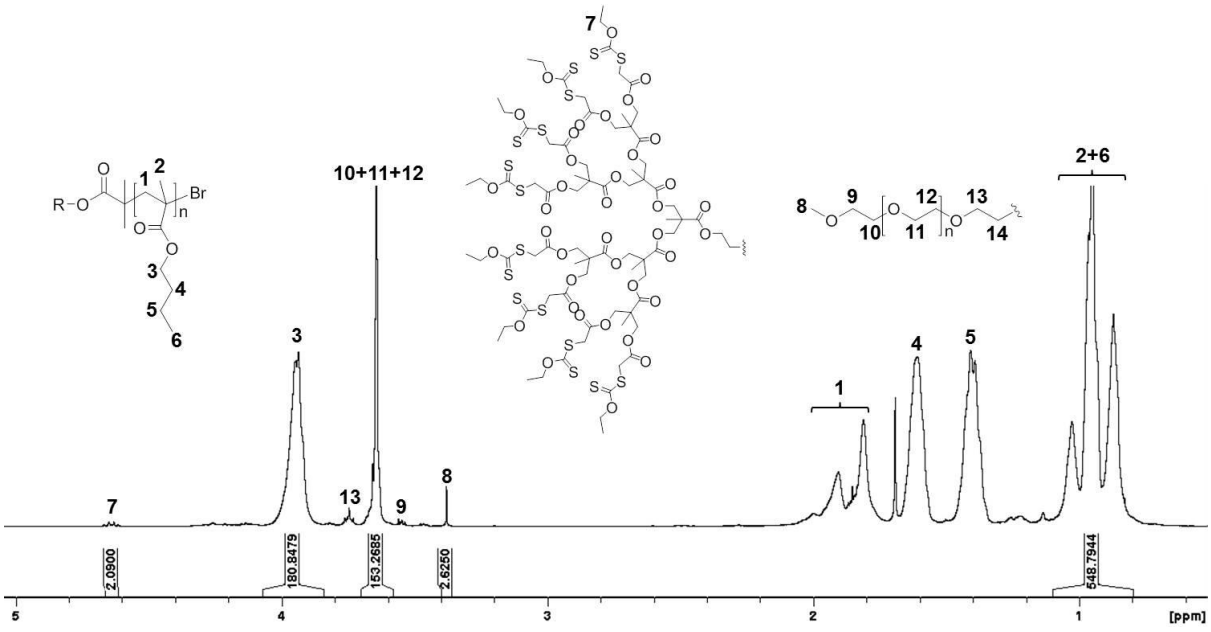

Fig. 4.13 ^{1}H NMR (400 MHz, $CDCl_3$) of **p[(PEG(2K))$_{0.875}$-(Xan$_8$-G$_3$)$_{0.125}$-nBMA$_{100}$];[133]**

4.4.3 Branched polymer synthesis

The co-initiated branched copolymerisation of nBMA and EGDMA with xanthate functional G_0 or G_3 dendron initiators (**[Xan$_1$-G$_0$-BiB];[20]** and **[Xan$_8$-G$_3$-BiB];[23]**) and PEG(2K) macroinitiator (**[PEG(2K)-BiB];[131]**) was carried out, targeting a range of functional chain-end molar ratios. The targeted DP_n of the primary polymer chains was maintained at 100 monomer units, with an initiator:brancher ratio of 1:0.8.

4.4.3.1 G_0 dendron and PEG(2K) co-initiated HPDs

G_0 and PEG macroinitiator ratios of 1:99, 7.5:92.5 and 10:90 were targeted for the co-initiated copolymerisation of nBMA and EGDMA. Methanolic ATRP was carried out as previously described (see section 2.8.5.2) with a CuCl:bpy (1:2) catalyst system, at a concentration of 50 v/v% relative to the monomer. The targeted DP_n of nBMA was kept

constant (DP_n = 100 monomer units), as was the initiator:brancher ratio (1:0.8). The molecular weights of the resulting polymers are summarised in Table 4.5. Inclusion of bifunctional monomer EGDMA resulted in branched polymers with high molecular weights and a broad Đ, as previously reported in the published literature[14,15,20,25] and in Chapter 2. Due to the incorporation of a long chain PEG initiator, the resulting polymers were analysed by SEC in a dimethylformamide (DMF) eluent system at 60°C with 0.01 M LiBr (to minimise any polyelectrolyte effects), utilising triple detection.

Table 4.5 Triple detection SEC data of G_0/PEG co-initiated HPDs, with corresponding linear polymers

Entry no.	Initiator (mol%)		Target polymer composition	Conv. (%)[a]	SEC (DMF)[b]		
	G_0 dendron	**PEG(2K)**			M_n (g mol^{-1})	M_w (g mol^{-1})	Đ
1	100	0	$p(nBMA)_{100}$	95	21 700	26 400	1.21
2	0	100	$p(nBMA)_{100}$	94	13 400	14 500	1.08
3	1	99	$p(nBMA)_{100}$-*co*-$EGDMA_{0.8}$	99	43 100	283 000	6.56
4	7.5	92.5	$p(nBMA)_{100}$-*co*-$EGDMA_{0.8}$	94	36 400	216 200	5.94
5	10	90	$p(nBMA)_{100}$-*co*-$EGDMA_{0.8}$	98	41 600[c]	149 600[c]	3.60[c]

[a]Determined by ^{1}H NMR analysis in $CDCl_3$ [b]DMF containing 0.01 M LiBr at 60°C, 1mL min^{-1} flow rate. [c]Sample analysed in THF containing 2% TEA (v/v) at 35°C, 1mL min^{-1} flow rate.

Despite the differing chain-end molar ratios, the G_0/PEG(2K) co-initiated HPDs had relatively similar molecular weights, presumably as the polymerisation is dominated by the PEG(2K) initiator, **[131]**; the major component in the co-initiation mixture in all cases. An approximation of the average number of conjoined chains was determined by utilising the PEG(2K) initiated linear polymers and dividing the M_n and M_w values into the values determined for the branched polymer materials. As the mole percentage of G_0 dendrons increases, the number average number of conjoined chains remains approximately 3-3.5 primary chains, whilst the weight average number of chains varies progressively from 19.5 primary chains to 15 primary chains and finally 10.5 chains.

4.4.3.2 G_3 dendron and PEG(2K) co-initiated HPDs

A series of branched p(nBMA) polymers with G_3 dendron and PEG(2K) initiator molar ratios of 1:99, 1.4:98.6 and 5:95 (with relative xanthate:PEG functional group molar ratios of approximately 7.5:92.5, 10:90 and 30:70) were synthesised. A targeted DP_{100} for the p(nBMA) primary chains was maintained, as was the initiator:brancher ratio (1:0.8). The molecular weights of the resulting polymers are summarised in Table 4.6.

Table 4.6 Triple detection SEC data of G_3/PEG co-initiated HPDs, with corresponding linear polymers

Entry no.	Initiator (%)		Target polymer composition	Conv. (%)[a]	SEC (DMF)[b]		
	G_3 dendron	**PEG(2K)**			M_n (g mol^{-1})	M_w (g mol^{-1})	Đ
1	100	0	$p(nBMA)_{100}$	84	26 600	31 800	1.19
2	12.5	87.5	$p(nBMA)_{100}$	95	17 600[c]	22 600[c]	1.28[c]
3	0	100	$p(nBMA)_{100}$	94	13 400	14 500	1.08
4	1	99	$p(nBMA)_{100}$-*co*-$EGDMA_{0.8}$	97	39 200	235 700	6.01
5	1.4	98.6	$p(nBMA)_{100}$-*co*-$EGDMA_{0.8}$	99	39 900[c]	185 700[c]	4.66[c]
6	5	95	$p(nBMA)_{100}$-*co*-$EGDMA_{0.8}$	98	37 200	190 400	5.12

[a]Determined by ^{1}H NMR analysis in $CDCl_3$ [b]DMF containing 0.01 M LiBr at 60°C, 1mL min^{-1} flow rate. [c]Sample analysed in THF containing 2% TEA (v/v) at 35°C, 1mL min^{-1} flow rate.

As seen previously, the G_3/PEG(2K) co-initiated polymerisations appear to be dominated by the PEG(2K) initiator, resulting in similar molecular weights in all cases, and closely resembled the molecular weights achieved for the G_0 co-initiated materials (Table 4.5). The resulting branched polymers, although tailored to maintain the same xanthate functional group molar ratios as the G_0 initiated polymers (xanthate:PEG 7.5:92.5 and 10:90, section 4.4.3.1), contain a larger molar proportion of PEG chain-ends; this is due to each G_3 dendron initiator possessing eight xanthate functional groups at the periphery. In this case, the number average number of conjoined primary chains was again maintained at approximately 3 chains, but due to the lower mole percentage of the G_3 dendron macroinitiator used, the weight average number of conjoined chains only varied from 16 to 13 over these materials.

4.5 Probing the distribution of functional groups at the surface

Taking advantage of the ability to easily generate thiols on the surface of co-initiated HPDs by deprotection of xanthate groups, it may be possible to coordinate GNPs on the surface of thiol-functional nanoprecipitates due to their high binding affinity. Altered distributions of GNPs would indicate the patchy nature of the surface functional groups. In order to probe the distribution of thiols, small GNPs are required to diffuse through the peripheral PEG chains and bind with free thiols at the surface of the nanoparticles. The size range of the GNPs also needs to be on a scale to allow multiple GNPs to group around a single G_3 dendron site to allow visualisation of the patches of multiple thiol functional groups.

4.5.1 Modelling of dendron initiators

Computational estimates were used to determine the optimum size of GNPs required to diffuse through peripheral PEG chains of the polymer nanoparticle, and bind with free thiols at the surface. The surface area of a thiol functional G_3 dendron at the chain-end of a short p(nBMA) chain (DP_9) was calculated using Avogadro v1.2.0 molecular modelling software, Fig. 4.14.[26]

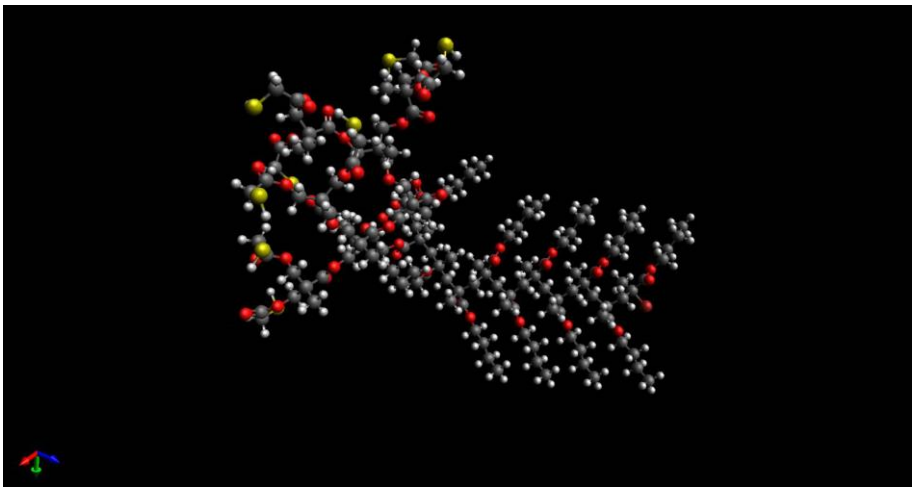

Fig. 4.14 Molecular modelling of p($nBMA_9$) with thiol-functional G_3 dendron chain-end

It was found that the span of the thiol-functional G_3 dendron site in vacuum measured 23 Å in total, Fig. 4.15. This is may be an over-estimation of the G_3 dendron site span in the co-initiated HPD structures, which present a high density of functional groups at the surface; this is likely to result in a contraction of the dendron sites located between large, hydrated PEG chain-ends in aqueous nanoprecipitates.

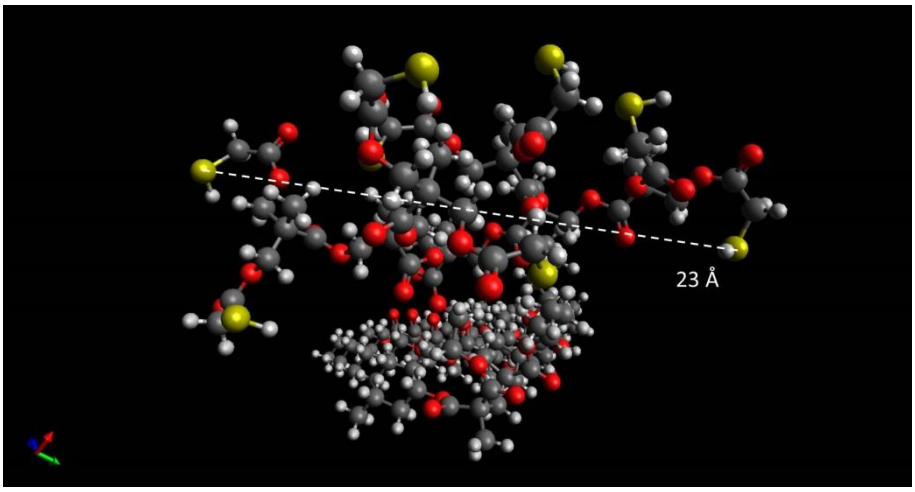

Fig. 4.15 Molecular modelling of G_3 dendron site on p($nBMA_9$), marking the maximum distance between thiol functional groups at the periphery (23 Å)

The distance between neighbouring branches in the G_3 dendron chain-end was measured at 13 Å, Fig. 4.16.

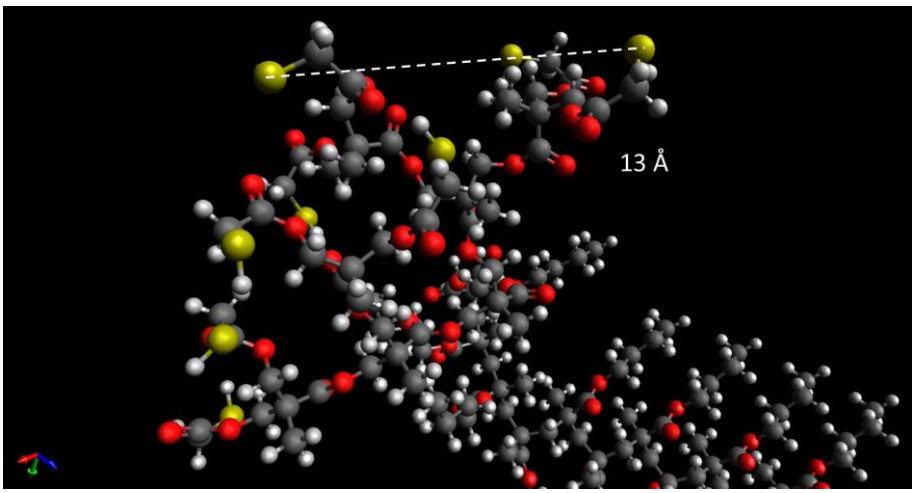

Fig. 4.16 Molecular modelling of G_3 dendron site on p($nBMA_9$), marking the distance between thiol functional groups on adjacent branches at the periphery (13 Å)

From the measurements obtained from the molecular modelling projections, it was decided that GNPs on the scale of <5 nm were required to penetrate the PEG corona of the nanoprecipitates and bind with free thiols on the surface. The relative size of 3 nm GNPs, the total span of the modelled G_3 dendron site, and distance between adjacent branches were compared to see whether binding of multiple GNPs was possible, Fig. 4.17.

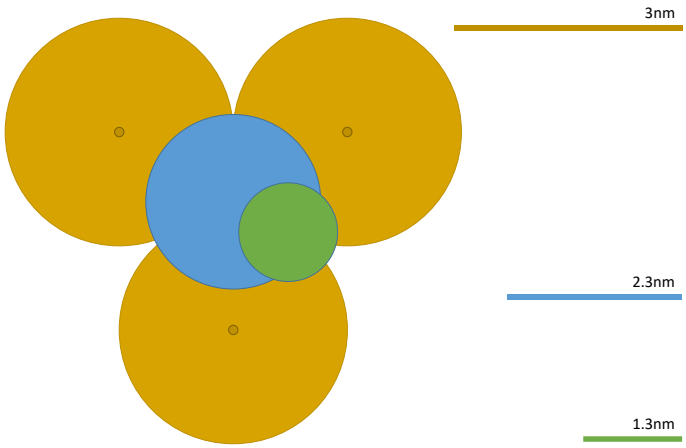

Fig. 4.17 Relative size of 3 nm GNPs (gold) and G_3 dendron site of p(nBMA); maximum span (blue) of 2.3 nm and adjacent branches (green) of 1.3 nm

The relative size of 3 nm GNPs, overlaid with the molecular modelling projection of the G_3 dendron site (oriented end-on), gives an idea of how many thiols may simultaneously bind with the individual GNPs, Fig. 4.18.

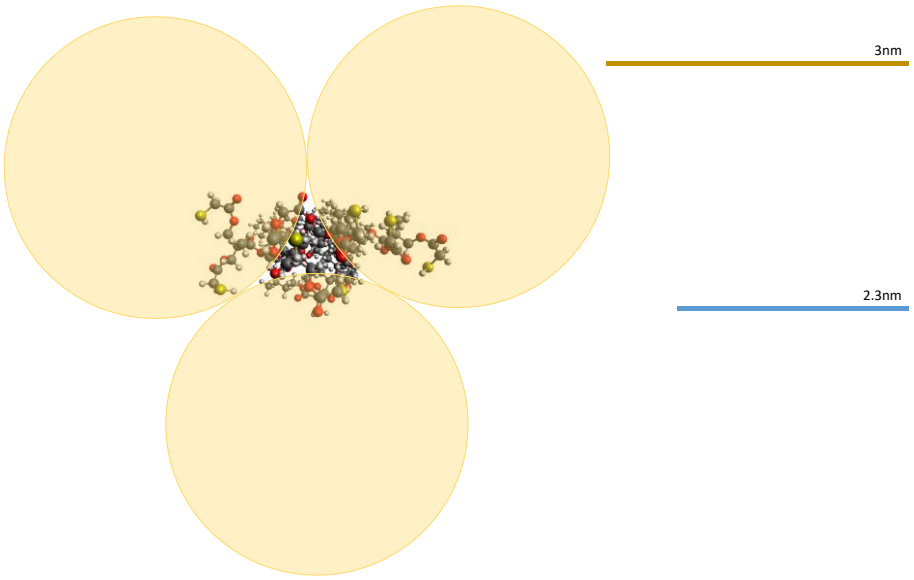

Fig. 4.18 Molecular modelling of G_3 dendron site of p(nBMA), overlaid with relative size of 3 nm GNPs

From the molecular modelling projections, it appears that it may be possible to cluster up to three GNPs on a single thiol-functional G_3 dendron site. We would expect to see only one GNP bound per thiol-functional G_0 dendron site, however, due to the statistical distribution of G_0 chain-ends on the surface of resulting nanoprecipitates, groups of two or even three GNPs may be possible. For a G_3 dendron, we could see one GNP bound as the nanoparticle could dominate the dendron; two bound particles would be possible, and even up to three from a single dendron; four and above bound GNPs may be possible for G_3 dendrons in statistically close proximity on the surface. Higher than four or five bound GNPs would be unlikely, however.

Molecular modelling has been applied to study the packing of small GNPs around a G_3 dendron site; the relative size of an average polymer nanoparticle (65 nm), a G_3 dendron site (2.3 nm) and a 3 nm GNP has been represented here to assess the ability to visualise the different arrangements of GNPs on the polymer nanoparticle surfaces with differing spatial arrangements of functional groups by TEM, Fig. 4.19.

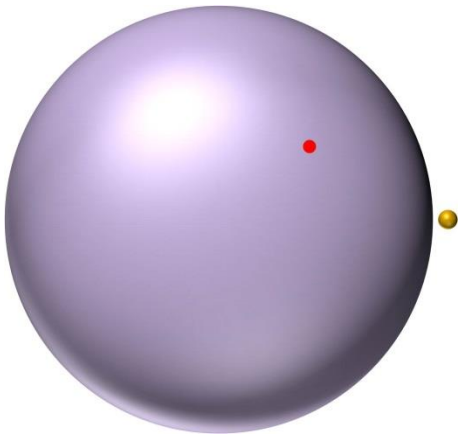

Fig. 4.19 Relative size of 65 nm polymer nanoparticle (purple), 2.3 nm G_3 dendron site (red) and 3 nm GNP (gold)

4.5.2 Coordination of GNPs to thiol-functional co-initiated HPDs

Small GNPs (approximately 3 nm) were coordinated to the surface of thiol-functional nanoprecipitated HPDs by stirring in solution for 24 hrs. The electron density of the GNPs allowed the application of TEM to image the resulting nanomaterials.

4.5.2.1 3 nm GNP synthesis

Combined citrate and tannic acid stabilised GNPs, approximately 3 nm in diameter, were synthesised via the Inverse Turkevich method[27], as outlined in literature[28] by Mr Alex Hill of the Brust research group at the University of Liverpool. The resulting particles were analysed by UV-Vis spectroscopy and TEM to determine their size. A summary of the GNP characterisation is included in the appendix (Fig. S4.12 and S4.13).

4.5.2.2 Confirming availability of thiols at the surface

In order to confirm thiol groups are available on the surface, the co-nanoprecipitation of 100% thiol-functional and 99:1 PEG:thiol functional branched polymers was carried out. Xanthate functional polymers **p[(Xan$_1$-G$_0$)-nBMA$_{100}$-*co*-EGDMA$_{0.7}$];[36]** and **p[(PEG(2K))$_{0.99}$-(Xan$_1$-G$_0$)$_{0.01}$-nBMA$_{100}$-*co*-EGDMA$_{0.8}$];[134]** were deprotected with excess *n*-butylamine (20 equiv.) at room temperature for 1.5 hours, to generate thiols *in situ*. The thiol-functional polymers were then co-nanoprecipitated from acetone at a combined initial concentration of 5 mg/mL (1:1 ratio of **[36]**:**[134]**) into water at ambient temperature with stirring. The acetone was allowed to evaporate overnight and the resulting nanoparticle suspension (1 mg/mL) analysed initially by DLS (Entry 2 Table 4.7). 3 nm GNPs were added to the polymer nanoparticle suspension at a 1:9 ratio (v/v) of polymer:GNP, and left to stir for

24 hours. The resulting nanomaterials were analysed by DLS, summarised in Table 4.7 and TEM, Fig. 4.20, below.

Table 4.7 DLS measurement data for co-nanoprecipitated 100% thiol- and 99:1 PEG:thiol-functional polymers

Entry	Polymer	D_z (nm)	PdI
1	**p[(Xan_1-G_0)-$nBMA_{100}$-*co*-$EGDMA_{0.7}$]/ p[$(PEG(2K))_{0.99}$-(Xan_1-G_0)$_{0.01}$-$nBMA_{100}$-*co*-$EGDMA_{0.8}$]**	95	0.072
2	**p[$(SH)_1$-G_0)-$nBMA_{100}$-*co*-$EGDMA_{0.7}$]/ p[$(PEG(2K))_{0.99}$-($(SH)_1$-G_0)$_{0.01}$-$nBMA_{100}$-*co*-$EGDMA_{0.8}$]**	75	0.073
3	**p[($(SH)_1$-G_0)-$nBMA_{100}$-*co*-$EGDMA_{0.7}$]/ p[$(PEG(2K))_{0.99}$-($(SH)_1$-G_0)$_{0.01}$-$nBMA_{100}$-*co*-$EGDMA_{0.8}$]** + 3 nm GNPs	79	0.094

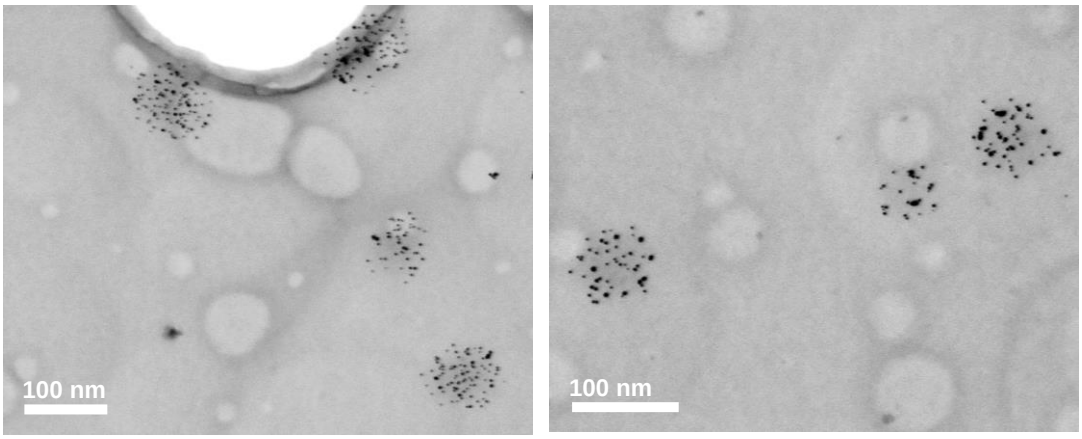

Fig. 4.20 TEM images (3 mm Cu(holey carbon) grids) of co-nanoprecipitated thiol-functional polymers **p[($(SH)_1$-G_0)-$nBMA_{100}$-*co*-$EGDMA_{0.7}$]** and **p[$(PEG(2K))_{0.99}$-($(SH)_1$-G_0)$_{0.01}$-$nBMA_{100}$-*co*-$EGDMA_{0.8}$]**, with coordinated 3 nm GNPs

It is evident from the TEM images (Fig. 4.20) that thiols of the co-nanoprecipitated polymers are available at the surface to bind with GNPs in aqueous suspension. This can be seen from clusters of GNPs (dark spots in images) across the surface of what is assumed to be the polymer nanoparticles. The sizes of polymer nanoparticles in the images correspond well with the nanoparticle diameter obtained via DLS, providing more confidence that these slightly darker regions on the TEM grids are polymer nanoparticles. Staining was not used to image the polymer nanoparticles as the resolution of the individual gold nanoparticles was the aim of this study.

4.5.2.3 Probing nanoprecipitates formed from co-initiated HPDs with a statistical distribution of xanthate functional groups

Co-initiated HPDs with a statistical distribution of xanthate functional groups, **p[(PEG(2K))$_{0.99}$-(Xan$_1$-G$_0$)$_{0.01}$-nBMA$_{100}$-*co*-EGDMA$_{0.8}$];[134]**, **p[(PEG(2K))$_{0.925}$-(Xan$_1$-G$_0$)$_{0.075}$-nBMA$_{100}$-*co*-EGDMA$_{0.8}$];[135]** and **p[(PEG(2K))$_{0.9}$-(Xan$_1$-G$_0$)$_{0.1}$-nBMA$_{100}$-*co*-EGDMA$_{0.8}$];[136]**, were deprotected with excess *n*-butylamine, and nanoprecipitated from acetone into water to give nanoparticles with a final concentration of 1 mg/mL. The resulting nanoparticles were analysed by DLS, summarised in Table 4.8. 3 nm GNPs were added at a 1:9 ratio (v/v) of polymer:GNP suspensions, and the mixture left to stir for 24 hrs. The nanoparticles were analysed by DLS, Table 4.8, and TEM, Fig 4.21.

Table 4.8 DLS measurement data for nanoprecipitated deprotected statistical polymers **[134]**, **[135]** and **[136]**, + with coordinated 3 nm GNPs

Polymer	D_z (nm)	PdI
p[(PEG(2K))$_{0.99}$-((SH)$_1$-G$_0$)$_{0.01}$-nBMA$_{100}$-*co*-EGDMA$_{0.8}$]	53	0.128
p[(PEG(2K))$_{0.925}$-((SH)$_1$-G$_0$)$_{0.075}$-nBMA$_{100}$-*co*-EGDMA$_{0.8}$]	52	0.083
p[(PEG(2K))$_{0.9}$-((SH)$_1$-G$_0$)$_{0.1}$-nBMA$_{100}$-*co*-EGDMA$_{0.8}$]	65	0.097
p[(PEG(2K))$_{0.99}$-((SH)$_1$-G$_0$)$_{0.01}$-nBMA$_{100}$-*co*-EGDMA$_{0.8}$] + 3 nm GNPs	60	0.230
p[(PEG(2K))$_{0.925}$-((SH)$_1$-G$_0$)$_{0.075}$-nBMA$_{100}$-*co*-EGDMA$_{0.8}$] + 3 nm GNPs	64	0.224
p[(PEG(2K))$_{0.9}$-((SH)$_1$-G$_0$)$_{0.1}$-nBMA$_{100}$-*co*-EGDMA$_{0.8}$] + 3 nm GNPs	74	0.235

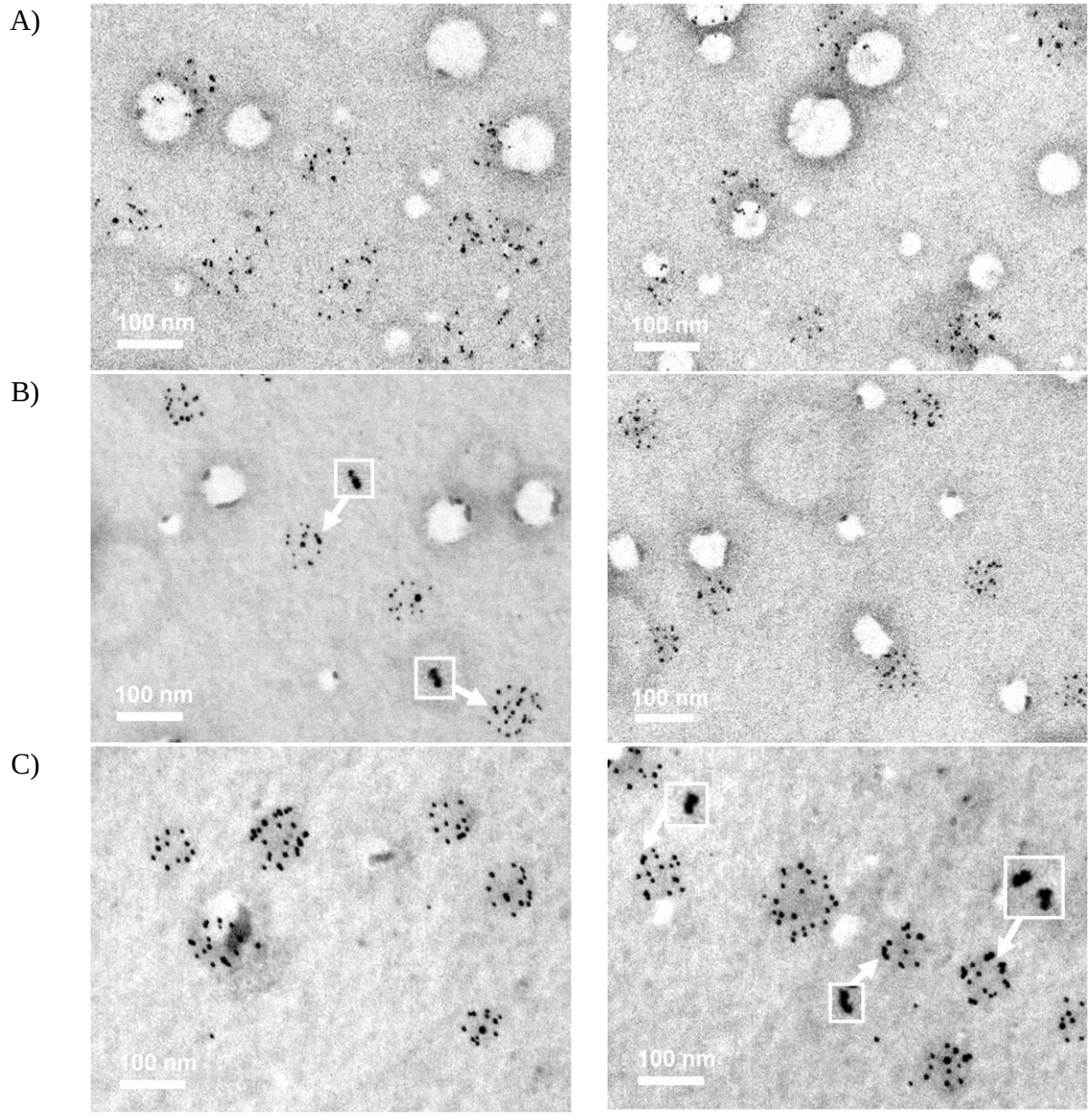

Fig. 4.21 TEM images of HPD nanomaterials with a statistical distribution of thiols, with coordinated 3 nm GNPs, with thiol:PEG functional group molar ratios of; A) 1:99, B) 7.5:92.5 and C) 10:90.

The GNPs appear to be generally evenly distributed across the surface of the polymer nanoparticles, with some cases of grouping seen where it is assumed that G_0 sites are located in close proximity due to their statistical distribution (Fig. 4.21). This is seen more prominently for nanoparticles with a higher thiol content (10:90 thiol:PEG, Fig. 4.21C), as there is greater probability of G_0 sites being located close together. The GNPs may also have bound on the "top" or "bottom" of the particle, relative to the TEM grid, and appear close together due to the transmission of the electron beam through the sample.

4.5.2.4 Probing nanoprecipitates formed from co-initiated HPDs with a patchy distribution of xanthate functional groups

Co-initiated HPDs with a patchy distribution of xanthate functional groups, **p[(PEG(2K))$_{0.99}$-(Xan$_8$-G$_3$)$_{0.01}$-nBMA$_{100}$-*co*-EGDMA$_{0.8}$];[137]**, **p[(PEG(2K))$_{0.986}$-(Xan$_8$-G$_3$)$_{0.014}$-nBMA$_{100}$-*co*-EGDMA$_{0.8}$];[138]** and **p[(PEG(2K))$_{0.95}$-(Xan$_8$-G$_3$)$_{0.05}$-nBMA$_{100}$-*co*-EGDMA$_{0.8}$];[139]**, were deprotected with excess *n*-butylamine, and nanoprecipitated from acetone into water to give nanoparticles with a final concentration of 1 mg/mL. The resulting nanoparticles were analysed by DLS, summarised in Table 4.9. 3 nm GNPs were added at a 1:9 ratio (v/v) of polymer:GNP suspensions, and the mixture left to stir for 24 hrs. The nanoparticles were analysed by DLS, Table 4.9, and TEM, Fig 4.22.

Table 4.9 DLS measurement data for nanoprecipitated deprotected patchy polymers **[137]**, **[138]** and **[139]**, + with coordinated 3 nm GNPs

Polymer	D_z (nm)	PdI
p[(PEG(2K))$_{0.99}$-((SH)$_8$-G$_3$)$_{0.01}$-nBMA$_{100}$-*co*-EGDMA$_{0.8}$]	51	0.105
p[(PEG(2K))$_{0.986}$-((SH)$_8$-G$_3$)$_{0.014}$-nBMA$_{100}$-*co*-EGDMA$_{0.8}$]	61	0.141
p[(PEG(2K))$_{0.95}$-((SH)$_8$-G$_3$)$_{0.05}$-nBMA$_{100}$-*co*-EGDMA$_{0.8}$]	52	0.101
p[(PEG(2K))$_{0.99}$-((SH)$_8$-G$_3$)$_{0.01}$-nBMA$_{100}$-*co*-EGDMA$_{0.8}$] + 3 nm GNPs	54	0.124
p[(PEG(2K))$_{0.986}$-((SH)$_8$-G$_3$)$_{0.014}$-nBMA$_{100}$-*co*-EGDMA$_{0.8}$] + 3 nm GNPs	66	0.190
p[(PEG(2K))$_{0.95}$-((SH)$_8$-G$_3$)$_{0.05}$-nBMA$_{100}$-*co*-EGDMA$_{0.8}$] + 3 nm GNPs	56	0.101

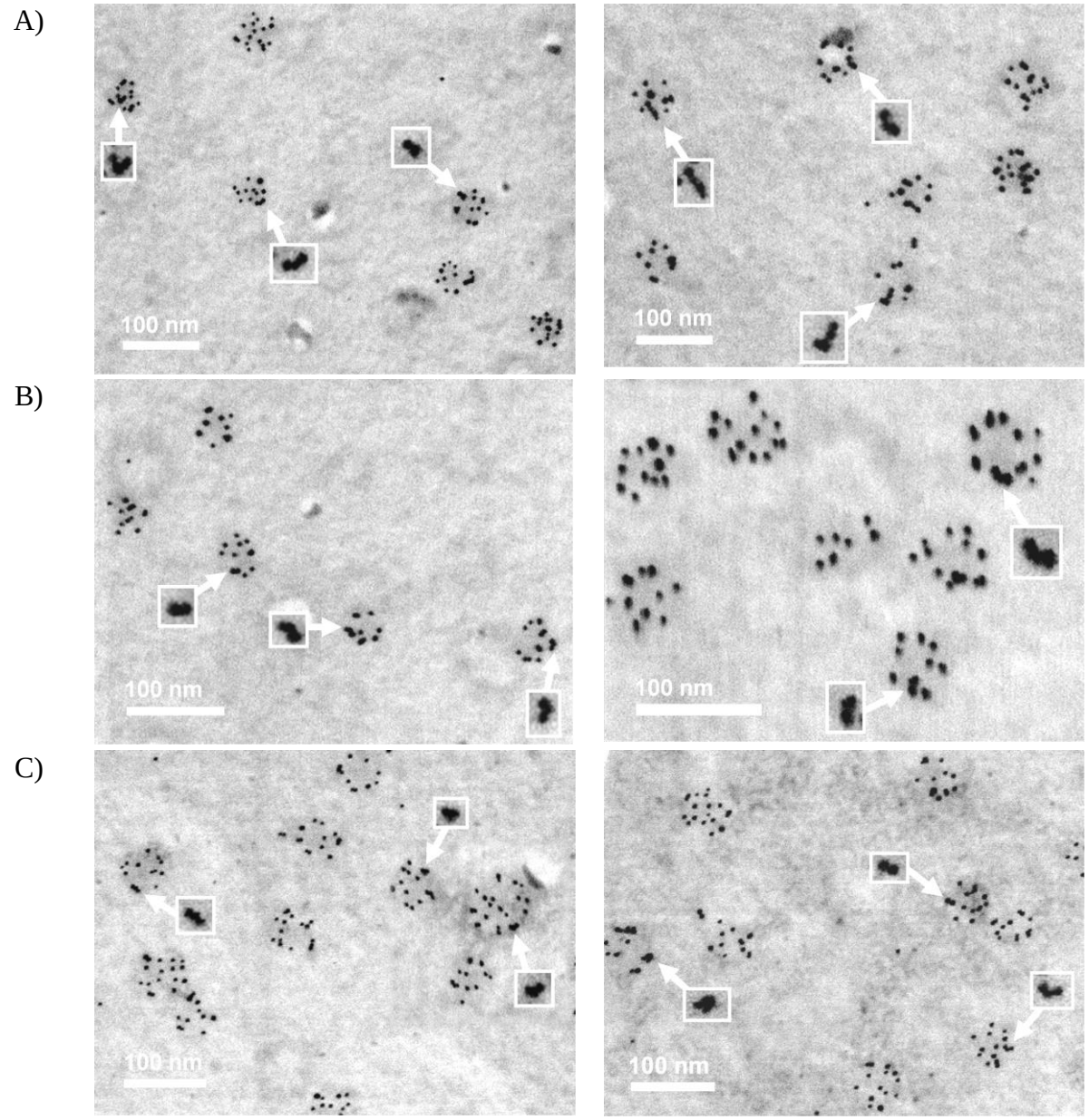

Fig. 4.22 TEM images of HPD nanomaterials with a patchy distribution of thiols, with coordinated 3 nm GNPs, with thiol:PEG functional group molar ratios of; A) 7.5:92.5, B) 10:90 and C) 30:70.

In the case of particles possessing a thiol:PEG ratio of 7.5:92.5 and 10:90 (Fig. 4.22A and 4.22B), the GNPs appear to be clustered on the surface of the polymer nanoparticles. This effect is less prominent for particles with a higher thiol:PEG ratio of 30:70 (Fig. 4.22C), where GNPs appear to be statistically distributed across the surface, with some evidence of clustering. The clusters of GNPs suggest multiple particles binding to an area with a higher concentration of thiol functional groups, likely to be originating from G_3 dendron sites.

TEM studies of GNP binding on HPD nanoprecipitates with statistical (G_0 chain-ends, Fig. 4.21) and patchy (G_3 chain-ends, Fig. 4.22) distributions of thiol groups demonstrated observable differences in the spatial arrangement of surface functional groups. Comparing the clustering of GNPs on the surface of particles derived from **p[(PEG(2K))$_{0.9}$-((SH)$_1$-G$_0$)$_{0.1}$-nBMA$_{100}$-*co*-EGDMA$_{0.8}$]** and **p[(PEG(2K))$_{0.986}$-((SH)$_8$-G$_3$)$_{0.014}$-nBMA$_{100}$-*co*-EGDMA$_{0.8}$]** comprising a nominal 10 mole % thiol functionality relative to total chain-ends (Fig. 4.21C and 4.22B, respectively) allowed quantification of the different sized clusters; GNPs were considered clustered when ≥two particles were visibly touching. In all samples, isolated single GNPs were the most common species, however higher order clusters (≥two GNPs) were frequently seen. Quantification of the number of clusters, containing one to ≥four GNPs showed a considerable bias towards clusters of ≥two GNPs within G_3-initiated materials (Fig. 4.23 and 4.24).

For the G_0-initiated samples, 1193 individual GNPs were observed as either single isolated GNPs (820; 68.7%) or clusters containing two (258 total; 21.6%), three (99 total; 8.3%) or ≥four (16 total; 1.3%) GNPs, Fig. 4.23. Similar observation of 572 individual GNPs within the G_3-initiated samples shows a markedly different distribution, observed as single isolated GNPs (231; 40.4%), or clusters containing two (220 total; 38.5%), three (93 total; 16.3%) and ≥four (28 total; 4.9%) GNPs, Fig. 4.23. This strongly suggests that GNPs were nearly equally likely to be part of a clustered pair on G_3-containing nanoprecipitates as they were to be isolated as single GNPs; in comparison, GNPs on G_0-containing nanoprecipitates are less than a third as likely to be in clustered pairs than isolated on the surface. GNPs were nearly twice as likely to be present in clusters of three, and >3.5 times as likely to be in clusters of ≥four GNPs within the G_3-containing samples than the comparative G_0-containing nanoprecipitates.

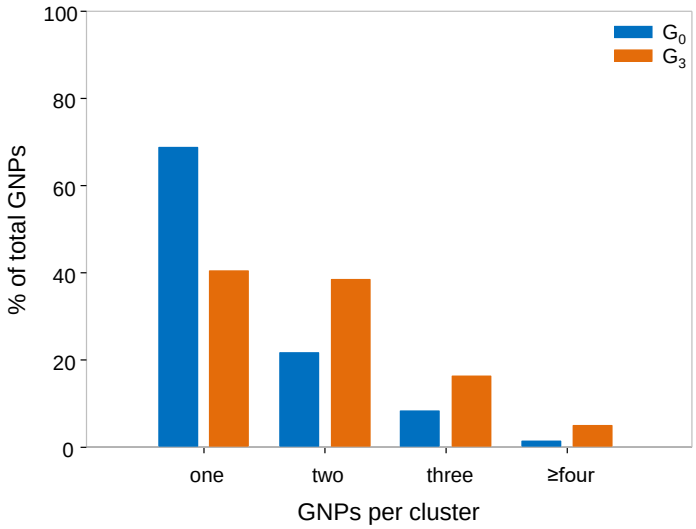

Fig. 4.23 GNP clustering on co-initiated HPD nanoprecipitates containing statistical (G_0, blue) and patchy (G_3, orange) distributions of surface functional groups; GNPs per cluster as a % of total GNPs observed

An alternative quantification approach treats each cluster as a single entity, normalising the percentage of single GNPs and cluster type in each sample, Fig. 4.24. Using this approach, a total of 986 GNP-derived entities were observed in the G_0 materials, and 379 entities in the G_3 materials. G_0-containing samples showed isolated single GNPs (820; 83.2%), and clusters containing two (129; 13.1%), three (33, 3.3%) and ≥four (4; 0.4%) GNPs; corresponding G_3-containing samples showed isolated single GNPs (231; 60.9%), and clusters containing two (110; 29%), three (31; 8.2%) and ≥four (7; 1.8%) GNPs, Fig. 4.24.

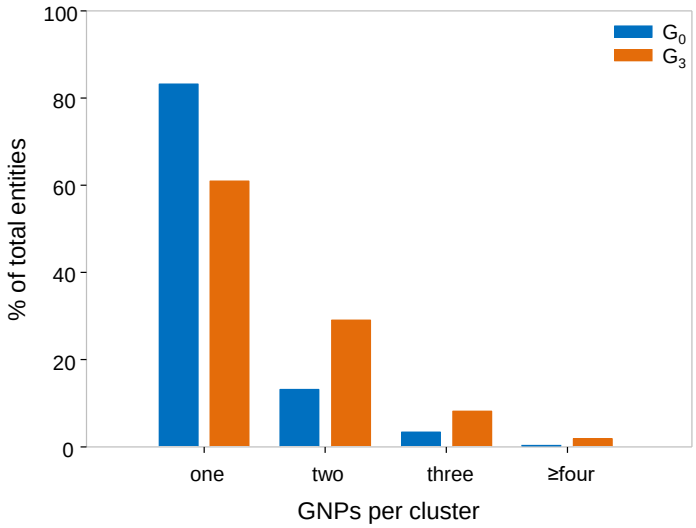

Fig. 4.24 GNP clustering on co-initiated HPD nanoprecipitates containing statistical (G_0, blue) and patchy (G_3, orange) distributions of surface functional groups; GNPs per cluster as a % of total entities observed

The patchy and statistical materials contain the same molar ratio of thiol and PEG chain-ends (10:90), therefore, despite larger numbers of thiol-bearing chain-ends in the G_0-initiated HPD nanoprecipitates, the G_3 dendrons appear to significantly impact GNP clustering; this is thought to be due to the additional dendron-directed anisotropic spatial distribution of thiol functionality. These observations provide compelling evidence to suggest that it is possible to design and synthesise stable nanomaterials with predetermined spatial arrangements of functional groups by simple nanoprecipitation.

The nanoprecipitates and corresponding GNP-coordinated nanoparticle suspensions were re-analysed by DLS after 1 year storage under ambient conditions, Table 4.10. There were no significant changes in D_z or PdI of the nanoparticle suspensions, indicating that they remain remarkably stable. The GNPs bound on the surface of the polymer nanoparticles appeared to remain stable much longer than the GNP suspension alone; retaining a characteristic red colour long after the citrate/tannic acid GNP suspension had aggregated and turned grey, as can be seen from the images in the final column of Table 4.10, next to the deprotected G_0/G_3 and PEG(2K) co-initiated HPD nanoprecipitates (**[134]-[139]**). This is, again, remarkable as the GNPs are coordinated onto the HPD nanoprecipitate surface which prevents further aggregation due to their immobilisation as long as the nanoprecipitates maintain stability.

Table 4.10 DLS data for: **p[(PEG(2K))$_x$-(Xan$_1$-G$_0$)$_y$-nBMA$_{100}$-*co*-EGDMA$_{0.8}$];[134]** (x = 0.99, y = 0.01)**;[135]** (x = 0.925, y = 0.075)**;[136]** (x = 0.9, y = 0.1); and **p[(PEG(2K))$_x$-(Xan$_8$-G$_3$)$_y$-nBMA$_{100}$-*co*-EGDMA$_{0.8}$];[137]** (x = 0.99, y = 0.01)**;[138]** (x = 0.986, y = 0.014)**;[139]** (x = 0.95, y = 0.05) nanoprecipitates 1 year stability studies at ambient temperature with coordinated 3 nm GNPs

Material	Initiator (%)			GNPs	Original		1 year			
	G_0	G_3	PEG(2K)		D_z	PdI	D_z	PdI	polymer nanoparticle suspension	polymer nanoparticle suspension + 3 nm GNPs
[134]	1	0	99	-	53	0.128	56	0.101		
[134]	1	0	99	✓	60	0.230	55	0.078		
[135]	7.5	0	92.5	-	52	0.083	56	0.063		
[135]	7.5	0	92.5	✓	64	0.224	54	0.082		
[136]	10	0	90	-	65	0.097	65	0.100		
[136]	10	0	90	✓	74	0.235	61	0.134		
[137]	0	1	99	-	51	0.105	53	0.094		
[137]	0	1	99	✓	54	0.124	60	0.102		
[138]	0	1.4	98.6	-	61	0.141	62	0.107		
[138]	0	1.4	98.6	✓	66	0.190	78	0.167		
[139]	0	5	95	-	52	0.101	55	0.065		
[139]	0	5	95	✓	56	0.101	56	0.083		

4.6 Conclusion

In this chapter, we aimed to synthesise and visualise stable nanoparticulates with differing spatial arrangements of functional groups on the surface; patchy and statistical. Compelling evidence for achieving these predeterminate and different structures was obtained via coordination of small GNPs to thiol functional groups, readily liberated by deprotection of xanthate groups under mild basic conditions, and subsequent TEM imaging. Clustering of GNPs was seen for nanoparticles possessing a patchy distribution of surface functional groups, whereas materials with a statistical distribution of thiols on the surface appeared to coordinate 3 nm GNPs statistically across the surface.

4.7 References

1. M. Mammen, S. K. Choi and G. M. Whitesides, *Angew. Chemie - Int. Ed.*, 1998, 37, 2754–2794.
2. N. Rasheed, A. A. Khorasani, J. Cebral, F. Mut, R. Löhner, and C. Salvador-Morales, *Langmuir*, 2015, **31**, 6639–6648.
3. A. Abuchowski, J. R. McCoy, N. C. Palczuk, T. van Es, and F. F. Davis, *J. Biol. Chem.*, 1977, **252**, 3582–3586.
4. A. Abuchowski, T. van Es, N. C. Palczuk, and F. F. Davis, *J. Biol. Chem.*, 1977, **252**, 3578–3581.
5. F. Fuertges and A. Abuchowski, *J. Control. Release*, 1990, **680**, 139–148.
6. F. M. Veronese, *Biomaterials*, 2001, **22**, 405–417.
7. M. J. Roberts, M. D. Bentley, and J. M. Harris, *Adv. Drug Deliv. Rev.*, 2002, **54**, 459–476.
8. P. Caliceti and F. M. Veronese, *Adv. Drug Deliv. Rev.*, 2003, **55**, 1261–1277.

9. J. M. Harris and R. B. Chess, *Nat. Rev. Drug Discov.*, 2003, **2**, 214–221.

10. F. M. Veronese and G. Pasut, *Drug Discov. Today*, 2005, **10**, 1451–1458.

11. M. J. Joralemon, S. McRae, and T. Emrick, *Chem. Commun.*, 2010, **46**, 1377–1393.

12. K. Knop, R. Hoogenboom, D. Fischer, and U. S. Schubert, *Angew. Chemie - Int. Ed.*, 2010, **49**, 6288–6308.

13. S. N. S. Alconcel, A. S. Baas, and H. D. Maynard, *Polym. Chem.*, 2011, **2**, 1442–1448.

14. F. L. Hatton, L. M. Tatham, L. R. Tidbury, P. Chambon, T. He, A. Owen, and S. P. Rannard, *Chem. Sci.*, 2015, **6**, 326–334.

15. R. A. Slater, T. O. McDonald, D. J. Adams, E. R. Draper, J. V. M. Weaver, and S. P. Rannard, *Soft Matter*, 2012, **8**, 9816–9827.

16. H. E. Rogers, P. Chambon, S. E. R. Auty, F. Y. Hern, A. Owen, and S. P. Rannard, *Soft Matter*, 2015, **11**, 7005–15.

17. R. Zangi and J. B. F. N. Engberts, *J. Am. Chem. Soc.*, 2005, **127**, 2272–2276.

18. K. N. Kudin and R. Car, *J. Am. Chem. Soc.*, 2008, **113**, 3915–3919.

19. J. W. Goodwin, *Colloids and Interfaces with Surfactants and Polymers*, 2nd edition, John Wiley & Sons Ltd., UK, 2009, ISBN: 978-0-470-51880-9.

20. F. L. Hatton, P. Chambon, T. O. McDonald, A. Owen, and S. P. Rannard, *Chem. Sci.*, 2014, **5**, 1844–1853.

21. K. Jankova, X. Chen, J. Kops, and W. Batsberg, *Macromolecules*, 1998, **31**, 538–541.

22. H. Fischer, *J. Polym. Sci. Part A Polym. Chem.*, 1999, **37**, 1885–1901.

23. A. B. Dwyer, P. Chambon, A. Town, F. L. Hatton, J. Ford, and S. P. Rannard, *Polym. Chem.*, 2015, **6**, 7286–7296.

24. N. Hadjichristidis, S. Pispas and G. Floudas, *Block Copolymers: Synthetic Strategies, Physical Properties, and Applications*, John Wiley & Sons, Inc., New Jersey, 2003, ISBN: 978-0471394365.

25. I. Bannister, N. C. Billingham, S. P. Armes, S. P. Rannard, and P. Findlay, *Macromolecules*, 2006, **39**, 7483–7492.

26. M. D. Hanwell, D. E. Curtis, D. C. Lonie, T. Vandermeersch, E. Zurek and G. R. Hutchison, *J. Cheminform.*, 2012, **4**, 17.

27. N. G. Bastús, J. Comenge, and V. Puntes, *Langmuir*, 2011, **27**, 11098–11105.

28. J. Piella, N. G. Bastús, and V. Puntes, *Chem. Mater.*, 2016, **28**, 1066–1075.

4.8 Appendix

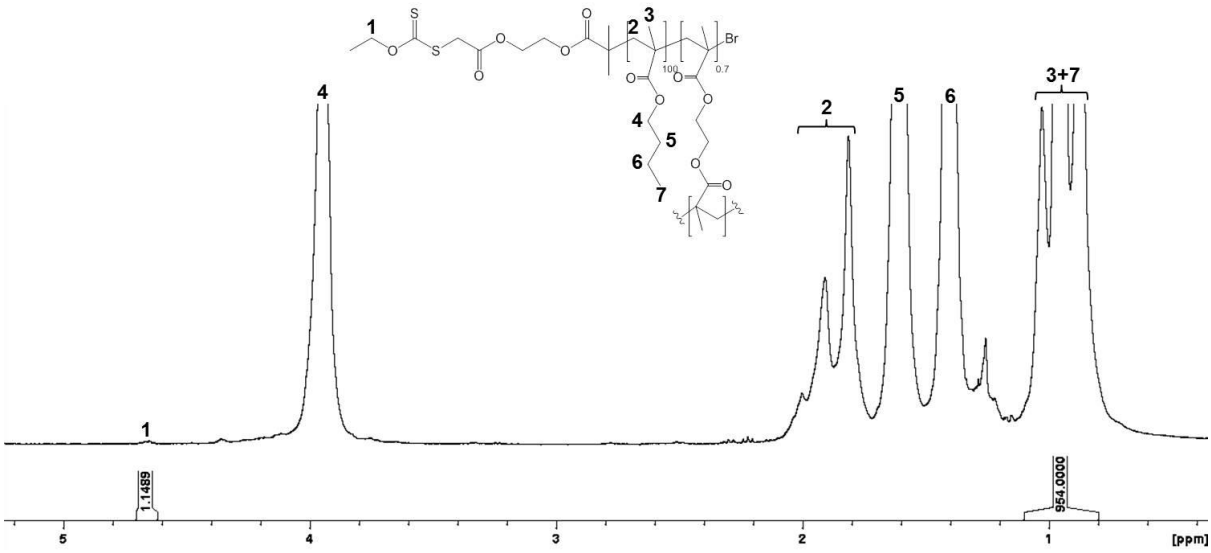

Fig. S4.1 ^{1}H NMR (400MHz, $CDCl_3$) of **p[(Xan_1-G_0)-nBMA_{100}-*co*-$EGDMA_{0.7}$];[36]** lyophilised deprotected nanoparticle dispersion

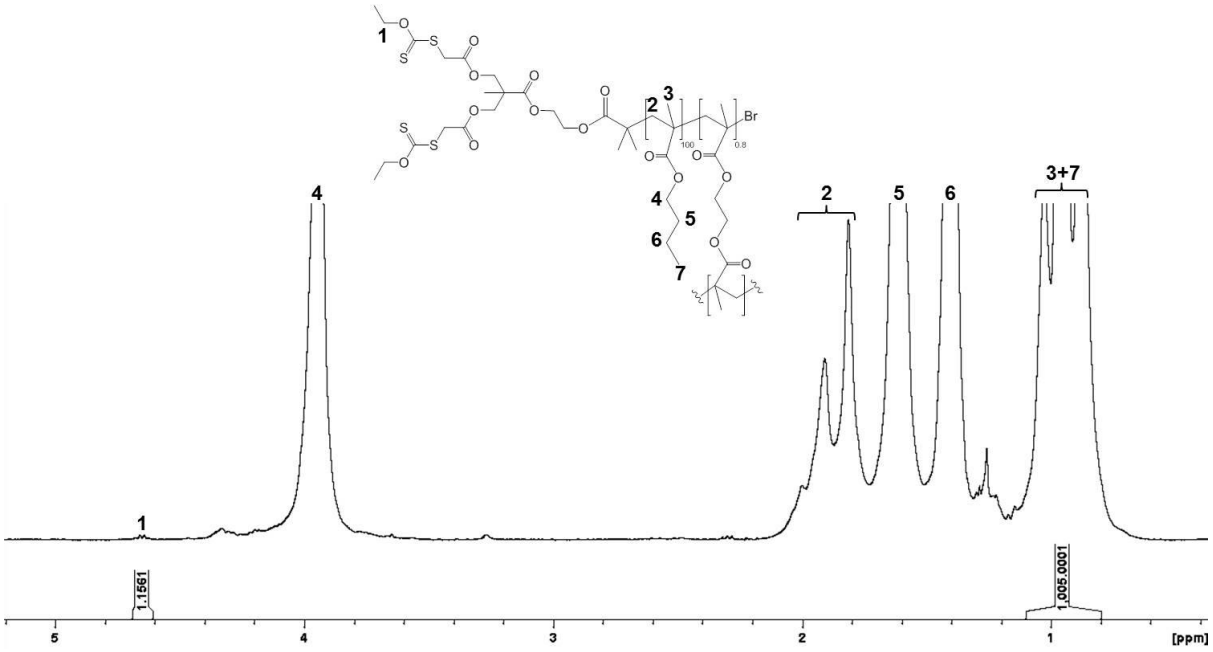

Fig. S4.2 ^{1}H NMR (400MHz, $CDCl_3$) of **p[(Xan_2-G_1)-nBMA$_{100}$-*co*-EGDMA$_{0.8}$];[37]** lyophilised deprotected nanoparticle dispersion

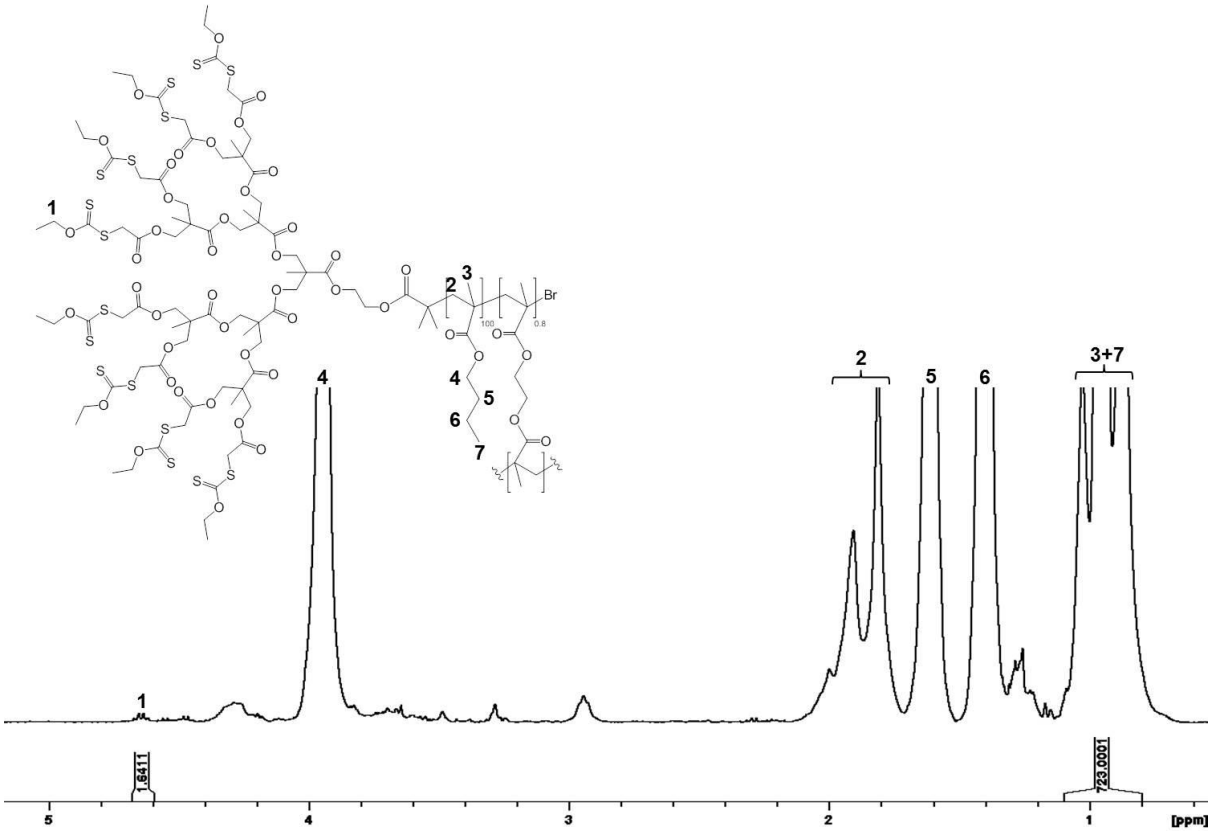

Fig. S4.3 ^{1}H NMR (400MHz, $CDCl_3$) of **p[(Xan_8-G_3)-nBMA$_{100}$-*co*-EGDMA$_{0.8}$];[39]** lyophilised deprotected nanoparticle dispersion

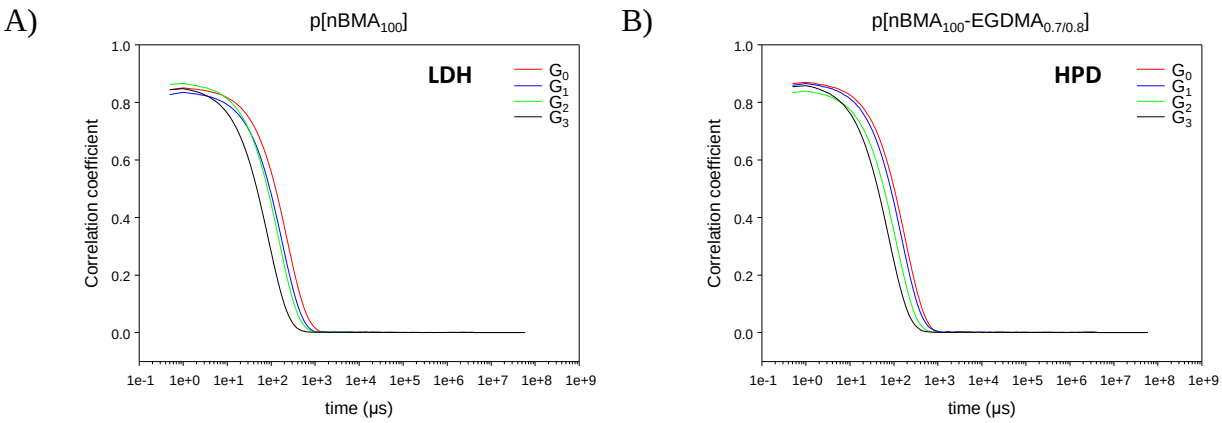

Fig. S4.4 DLS correlograms of aqueous nanoparticle dispersions of; A) LDHs **p[(Xan$_1$-G$_0$)-nBMA$_{100}$];[32]**, **p[(Xan$_2$-G$_1$)-nBMA$_{100}$];[33]**, **p[(Xan$_4$-G$_2$)-nBMA$_{100}$];[34]** and **p[(Xan$_8$-G$_3$)-nBMA$_{100}$];[35]**, and B) HPDs **p[(Xan$_1$-G$_0$)-nBMA$_{100}$-*co*-EGDMA$_{0.7}$];[36]**, **p[(Xan$_2$-G$_1$)-nBMA$_{100}$-*co*-EGDMA$_{0.8}$];[37]**, **p[(Xan$_4$-G$_2$)-nBMA$_{100}$-*co*-EGDMA$_{0.8}$];[38]** and **p[(Xan$_8$-G$_3$)-nBMA$_{100}$-*co*-EGDMA$_{0.8}$];[39]**.

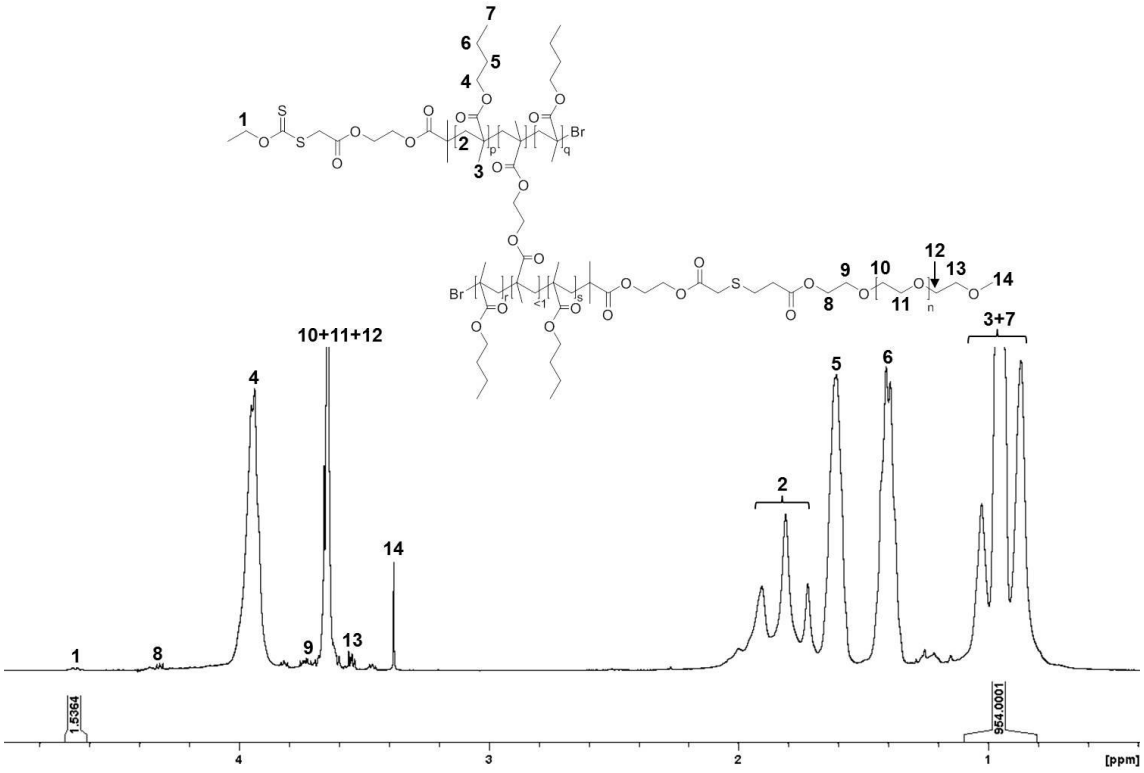

Fig. S4.5 ^{1}H NMR (400MHz, $CDCl_3$) of **p[(Xan$_1$-G$_0$)-nBMA$_{100}$-*co*-EGDMA$_{0.7}$];[36]** following partial modification with 22% of PEG(2K) groups

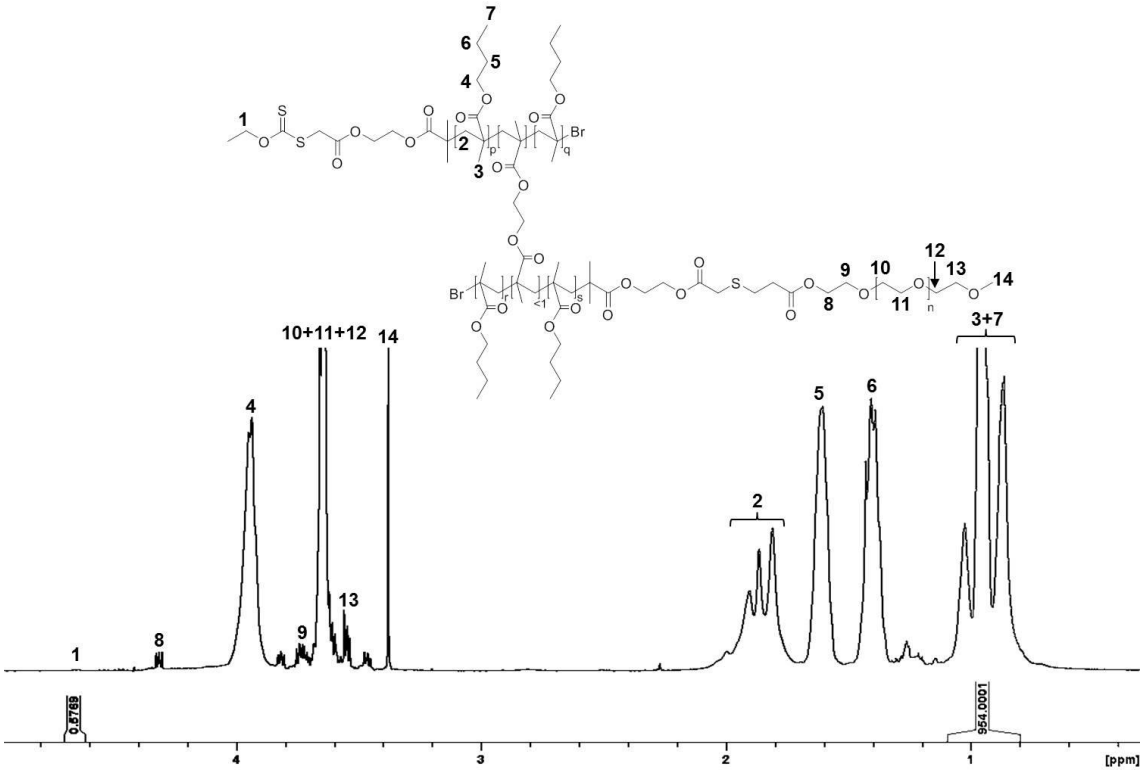

Fig. S4.6 ^{1}H NMR (400MHz, $CDCl_3$) of **p[(Xan_1-G_0)-nBMA$_{100}$-*co*-EGDMA$_{0.7}$];[36]** following partial modification with 70% of PEG(2K) groups

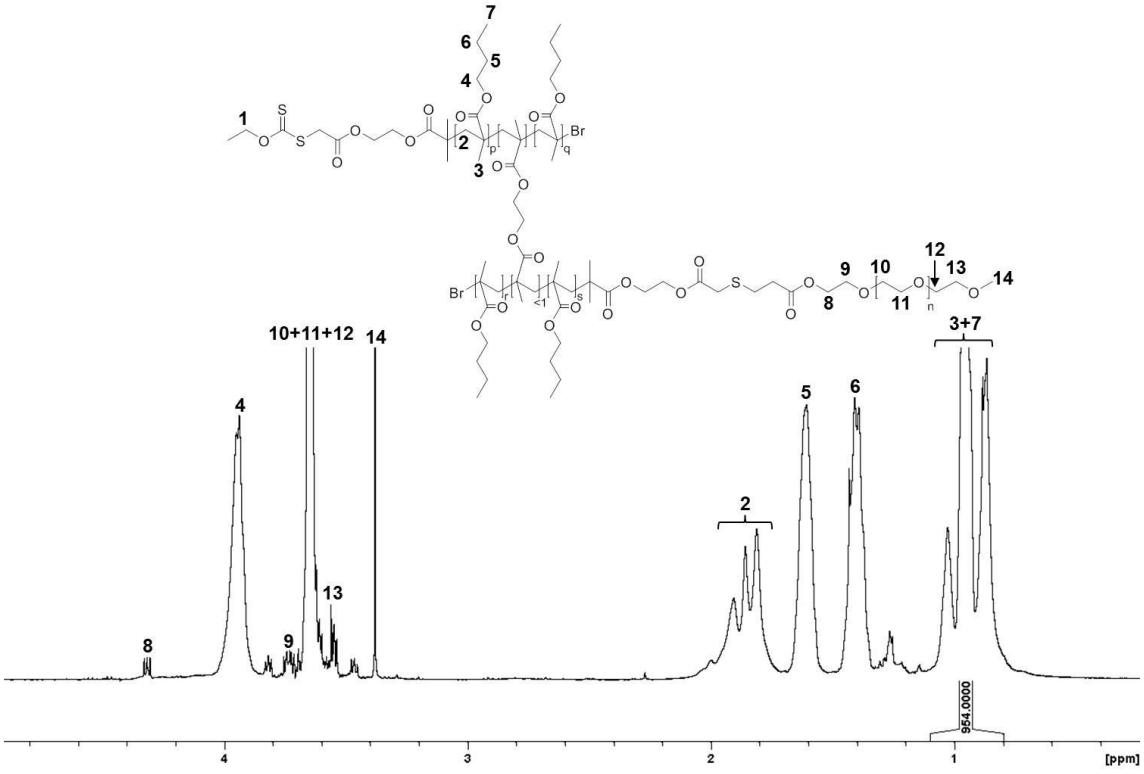

Fig. S4.7 ^{1}H NMR (400MHz, $CDCl_3$) of **p[(Xan_1-G_0)-nBMA$_{100}$-*co*-EGDMA$_{0.7}$];[36]** following partial modification with >99% of PEG(2K) groups

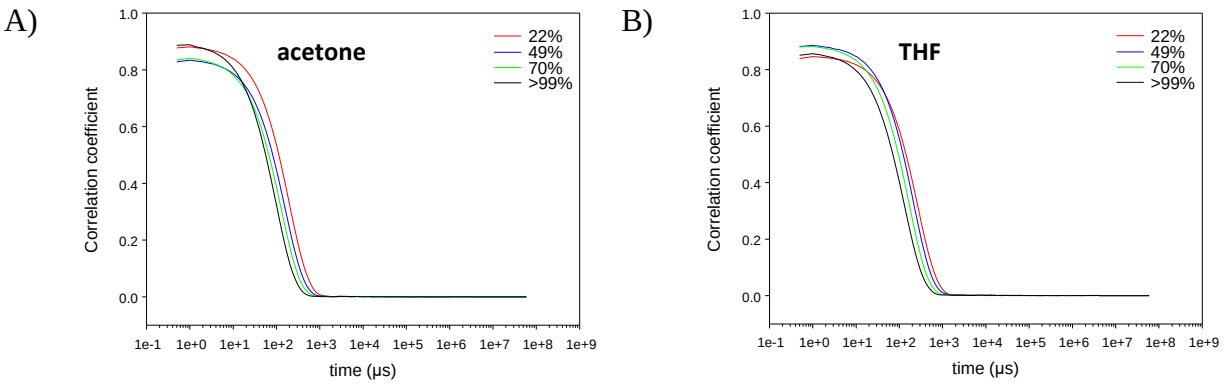

Fig. S4.8 DLS correlograms of aqueous nanoparticle dispersions of **p[(Xan$_1$-G$_0$)-nBMA$_{100}$-*co*-EGDMA$_{0.7}$];[36]** post-functionalised with PEG(2K) acrylate, containing 22%, 49%, 70% and >99% of PEG(2K) groups, nanoprecipitated from; A) acetone and B) THF

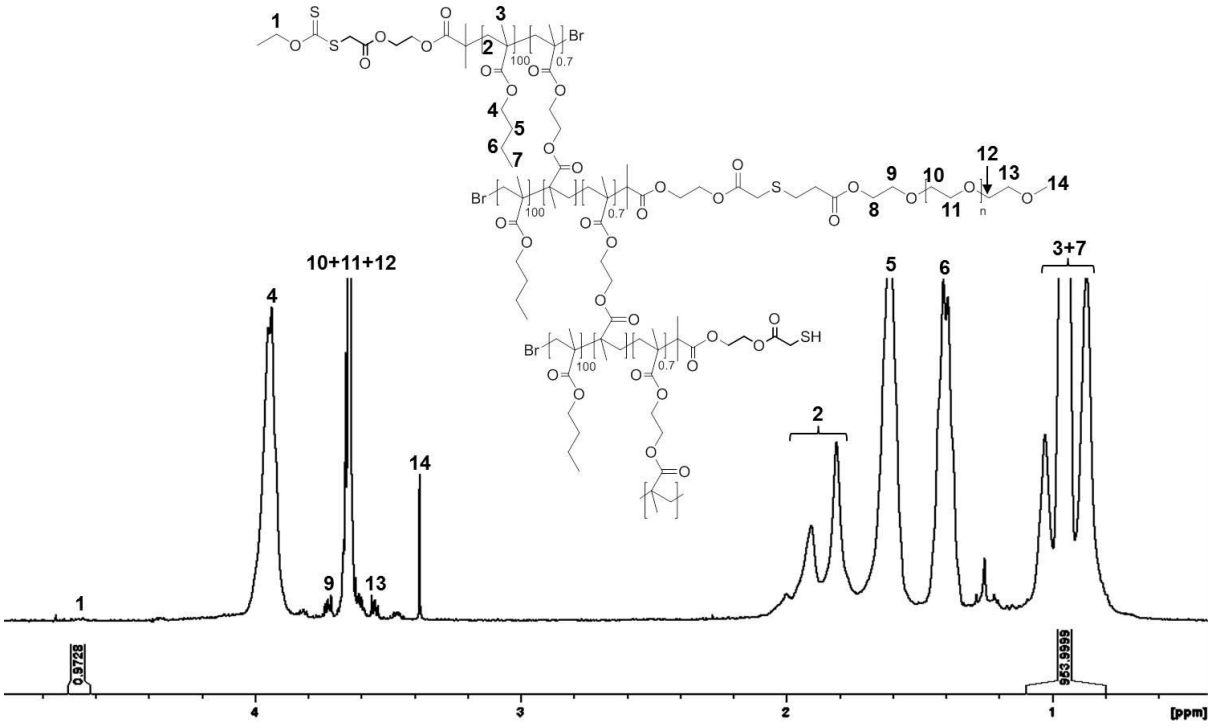

Fig. S4.9 ^{1}H NMR (400MHz, $CDCl_3$) of **p[(Xan$_1$-G$_0$)-nBMA$_{100}$-*co*-EGDMA$_{0.7}$];[36]**, partially post-modified with 22% of PEG(2K) groups, lyophilised deprotected nanoparticle dispersion

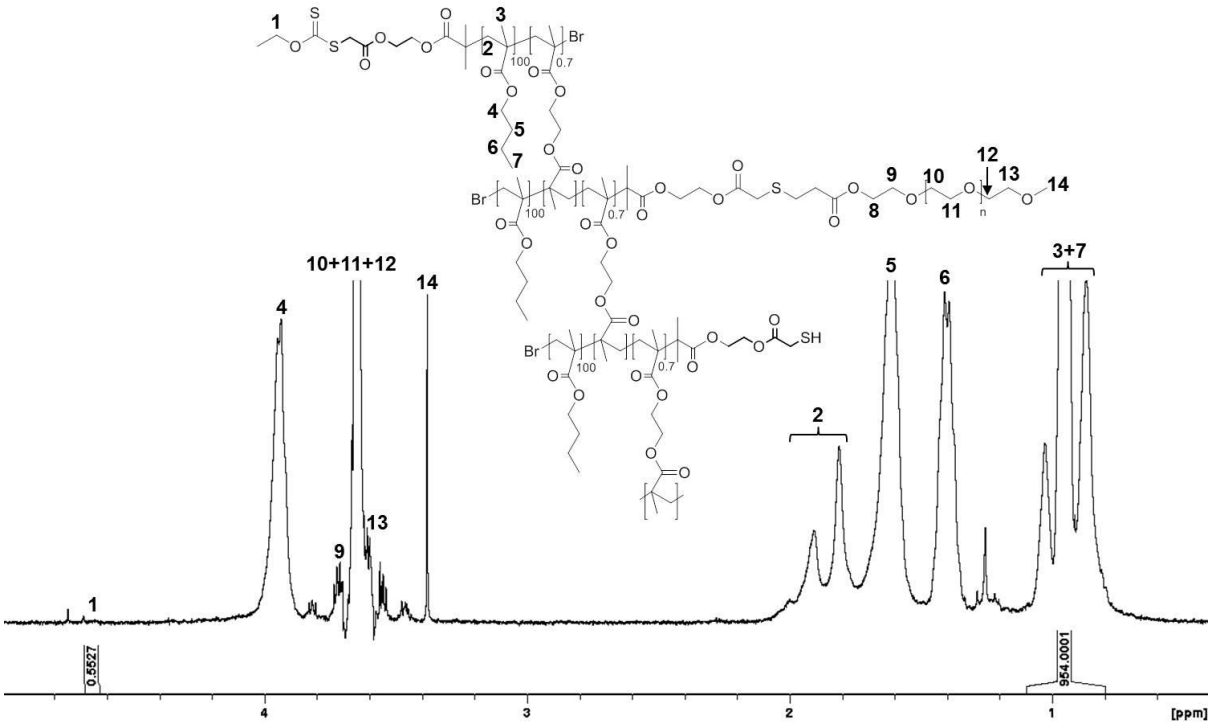

Fig. S4.10 ^{1}H NMR (400MHz, $CDCl_3$) of **p[(Xan$_1$-G$_0$)-nBMA$_{100}$-*co*-EGDMA$_{0.7}$];[36]**, partially post-modified with 70% of PEG(2K) groups, lyophilised deprotected nanoparticle dispersion

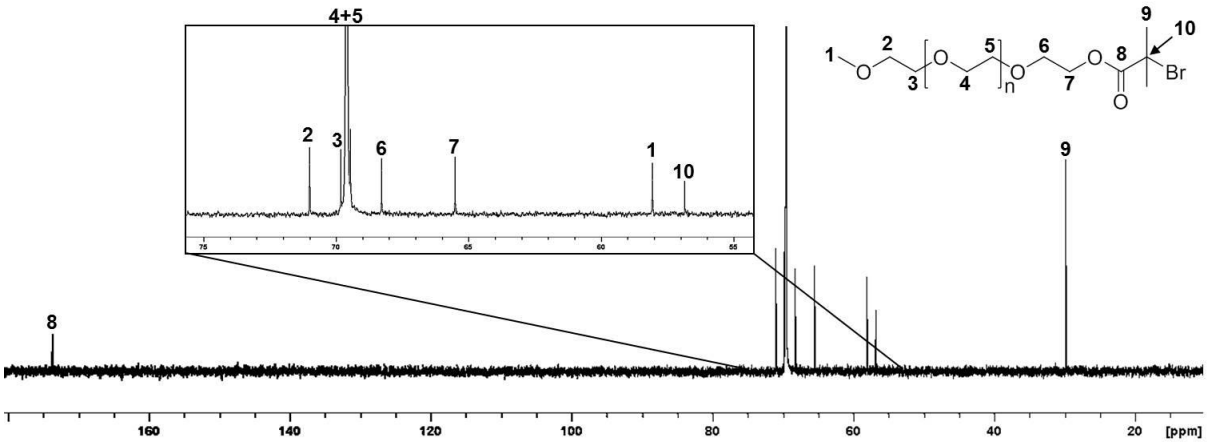

Fig. S4.11 ^{13}C NMR (100 MHz, $CDCl_3$) of **[PEG(2K)-BiB];[131]**

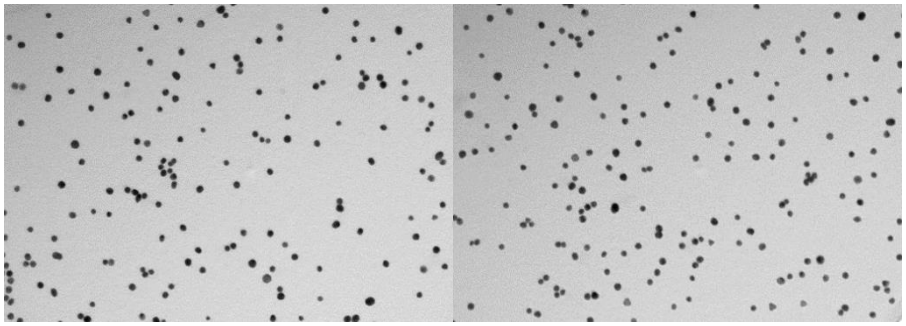

Fig. S4.12 TEM images of 3 nm GNPs synthesised by the Inverse Turkevich method

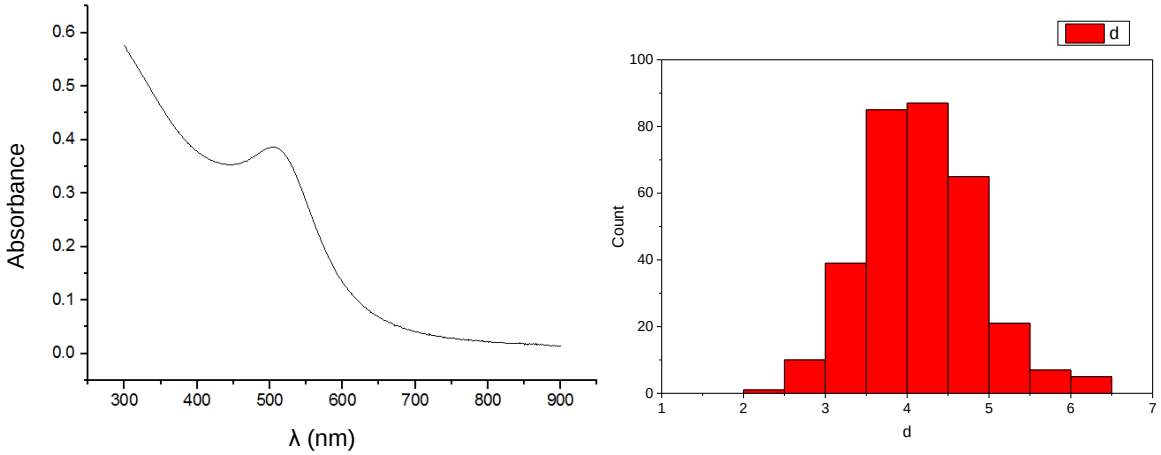

	N total	Mean	Standard Deviation	Sum	Minimum	Median	Maximum
d	323	4.13583	0.77112	1335.87358	0.51586	4.07093	6.30369

Fig. S4.13 Size determination of GNPs by UV-Vis spectroscopy

CHAPTER 5

Nanoparticle design, radiolabelling and pharmacology

5.1 Introduction

When a freely dissolved drug is administered, various metabolic processes leading to non-specific distribution and renal clearance occur, resulting in reduced efficacy and undesirable side-effects. These problems can be limited by designing drug carriers that perform multiple tasks such as encapsulation, controlled release, minimising immune clearance, penetration of biological barriers and site-specific targeting.[1] Surface properties of drug carriers such as hydrophobicity, charge and chemical composition play an important role in determining the nature of particle-cell interaction, and hence their fate *in vivo*, *in vitro* and in the environment.[2] Tailoring nanoparticle surface properties to mediate non-specific protein deposition will facilitate the design of new delivery systems with desirable macrophage uptake whilst avoiding adverse toxicological effects.[3]

The application of co-initiated HPD synthesis to generate materials with patchy and statistical distributions of functional groups was demonstrated in Chapter 4. In this chapter, we aim to synthesise multifunctional nanomaterials containing dimethylamino (Am) and benzyl (Bz) functionality, varying only in the spatial arrangement of functional groups at the periphery. Post-polymerisation modification of xanthate-functional co-initiated HPDs will be applied to generate statistically multifunctionalised materials in a simultaneous, one-pot strategy; whilst co-initiation of two different functional G_3 dendron macroinitiators with a PEG(2K) macroinitiator is hypothesised to generate materials with patches of the two different functionalities, Fig. 5.1.

A) B)

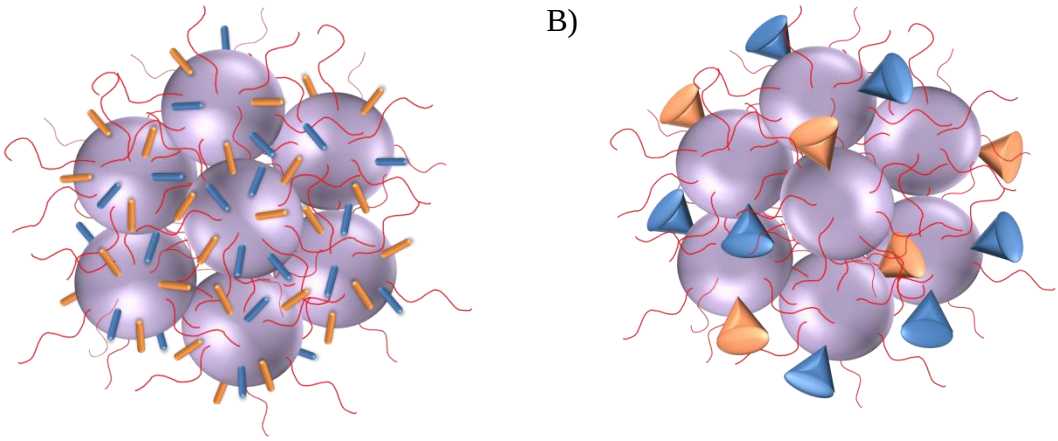

Fig. 5.1 Overall target materials; A) statistically multifunctionalised nanomaterials via post-polymerisation modification and B) patchy multifunctionalised nanomaterials by co-initiated HPD synthesis

5.2 Statistical and Patchy material synthesis

As demonstrated in Chapter 4, the formation of materials with differing spatial arrangements of functional groups at the periphery is possible by varying the dendron generation (G_0 and G_3), and hence the number of functional groups per "patch", during co-initiated HPD synthesis with a PEG(2K) macroinitiator. The availability and distribution of functional groups at the surface was probed by deprotection of the xanthate groups and coordination of 3 nm GNPs. For the study of biological interactions, a functional group ratio of 10:90 xanthate:PEG groups was chosen, as these structures (**p[(PEG(2K))$_{0.9}$-(Xan$_1$-G$_0$)$_{0.1}$-nBMA$_{100}$-*co*-EGDMA$_{0.8}$];[136]** and **p[(PEG(2K))$_{0.986}$-(Xan$_8$-G$_3$)$_{0.014}$-nBMA$_{100}$-*co*-EGDMA$_{0.8}$];[138]**) displayed clear differences in functional group distribution when probed with GNPs and imaged using TEM.

5.2.1 Statistical multifunctional polymer synthesis

Synthesis of the G_0 dendron and PEG(2K) coinitiated HPD **p[(PEG(2K))$_{0.9}$-(Xan$_1$-G$_0$)$_{0.1}$-nBMA$_{100}$-*co*-EGDMA$_{0.8}$];[136]** is outlined in Chapter 4 (section 4.4.3.1), Fig. 5.2.

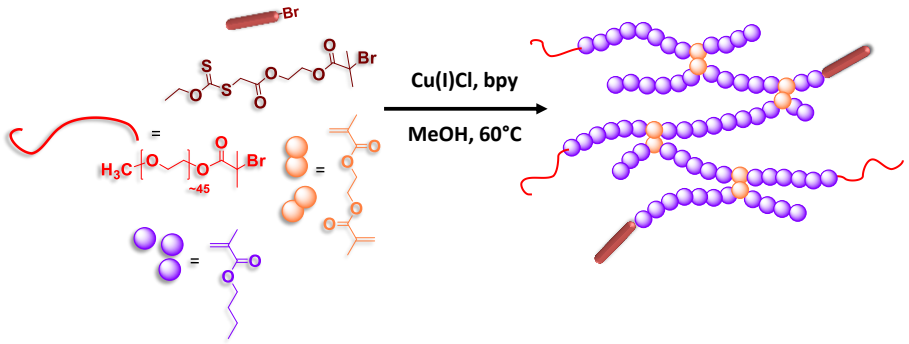

Fig. 5.2 Synthesis of G_0 and PEG(2K) co-initiated HPD

A *pseudo*-calibration curve for sequential xanthate deprotection was generated for this co-initiated HPD, based on the estimated DP_n of the primary chains by ^{1}H NMR end-group analysis (see section 3.4.1.1.1), Fig. 5.3.

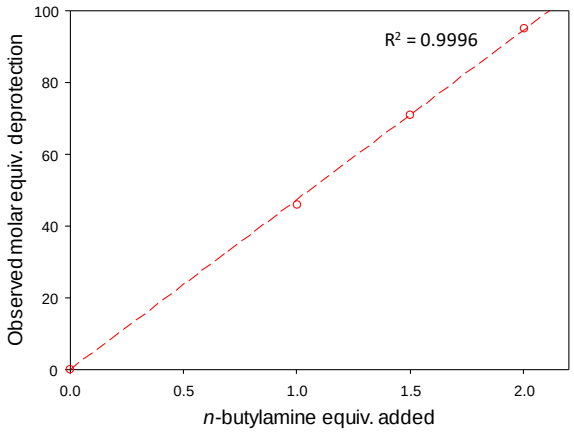

Fig. 5.3 Calibration curve for partial deprotection of xanthate peripheral groups of **p[(PEG(2K))$_{0.9}$-(Xan$_1$-G$_0$)$_{0.1}$-nBMA$_{100}$-*co*-EGDMA$_{0.8}$];[136]**

From the calibration curve, it was found that 1.1 molar equivalents of *n*-butylamine were required for deprotection of 50% of the xanthate peripheral groups, therefore, 1.1 molar equivalents of each functional acrylate (Am and Bz) was applied for the simultaneous 50:50 functionalisation of the G_0 and PEG co-initiated HPD **[136]**, following full deprotection, Fig. 5.4.

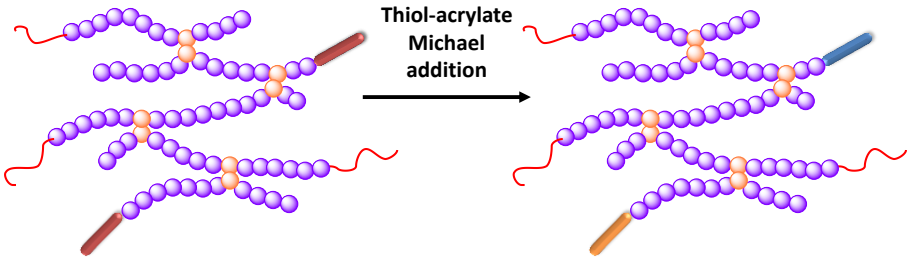

Fig. 5.4 Simultaneous thiol-acrylate Michael addition for statistical multifunctionalisation of G_0 and PEG(2K) co-initiated HPD

The complete deprotection of xanthate chain-end functionality (4.5 molar equivalents of *n*-butylamine per xanthate) and addition of a 1:1 molar ratio of Bz and Am acrylates (1.1 molar equivalents per thiol) resulted in the multifunctionalised co-initiated HPD **p[(PEG(2K))$_{0.9}$-(Am$_{0.5}$-Bz$_{0.5}$-G$_0$)$_{0.1}$-nBMA$_{100}$-*co*-EGDMA$_{0.8}$];[140]**, as confirmed by ^{1}H NMR spectroscopy (Fig. 5.5).

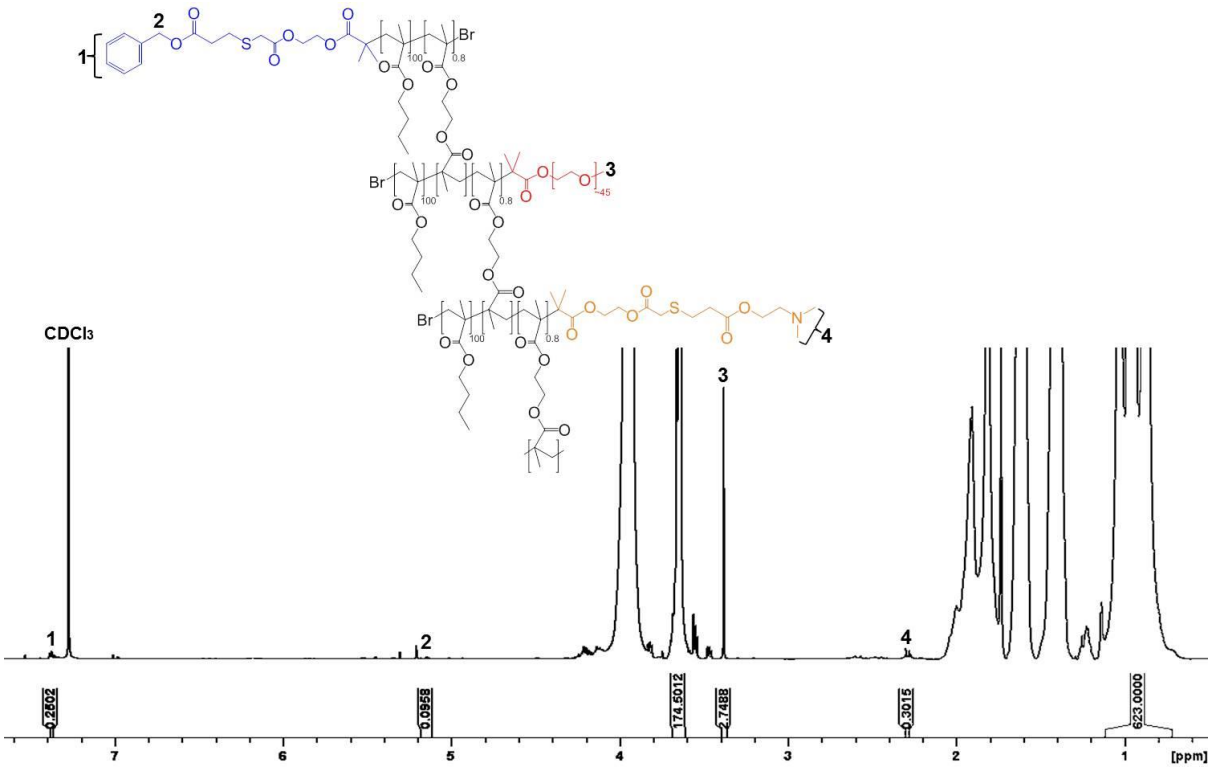

Fig. 5.5 ^{1}H NMR (400 MHz, $CDCl_3$) of **p[(Am$_{0.5}$-Bz$_{0.5}$-G$_0$)$_{0.1}$-(PEG(2K))$_{0.9}$-nBMA$_{100}$-*co*-EGDMA$_{0.8}$];[140]** by simultaneous multifunctionalisation of **p[(Xan$_1$-G$_0$)$_{0.1}$-(PEG(2K))$_{0.9}$-nBMA$_{100}$-*co*-EGDMA$_{0.8}$];[136]**

Peaks corresponding to Bz (peaks 1 and 2, Fig. 5.5) and Am (peak 4, Fig. 5.5) functionalities are present in the resulting ^{1}H NMR spectrum, at a 1:1 ratio, relative to the polymer backbone

resonance at δ ≈ 0.8-1.1 ppm, which remains unchanged following multifunctionalisation. At these very low levels of functional group incorporation the confirmatory signals within the NMR spectra are very small and expansion of the baseline was required to establish their presence and carry out integration. Peaks in the ^{1}H NMR spectrum corresponding to the Bz functionality at δ = 7.17 ppm (aromatic, $\int_{7.17\ ppm}$ = 0.2502/5 = 5%) and δ = 5.15 ppm (CH_2, $\int_{5.15\ ppm}$ = 0.0958/2 = 5%) confirm an incorporation of 5% benzyl functionality; a peak corresponding to the Am functionality at δ = 2.30 ppm ($2CH_3$, $\int_{2.30\ ppm}$ = 0.3015/6 = 5%) confirms incorporation of 5% dimethylamino functionality, relative to the polymer backbone.

5.2.2 Patchy multifunctional polymer synthesis

Specific, directed cell binding interactions may be triggered by materials with spatially-directed functionalisation at the nanoparticle periphery.[4] It was shown in Chapter 4 that patchy particles can be generated by aqueous nanoprecipitation of co-initiated hyperbranched polydendrons possessing G_3 dendrons at the periphery. Here, it was hypothesised that co-initiation of a PEG(2K) macroinitiator and two different mono-functional G_3 dendron macroinitiators may generate co-initiated HPDs with patches of different functional groups to generate multifunctional patchy particles, Fig. 5.6.

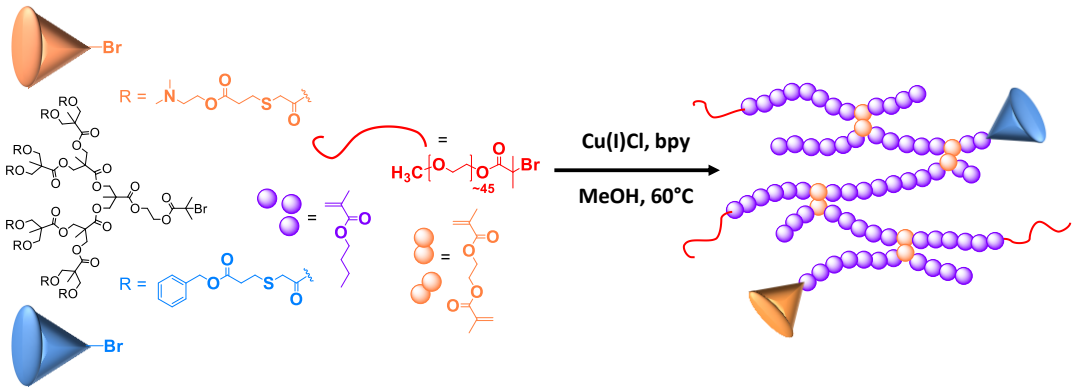

Fig. 5.6 Synthesis of benzyl- and dimethylamino-functional G_3 dendron and PEG(2K) co-initiated HPD

The synthesis of mono-functional G_3 macroinitiators was targeted by full one-pot deprotection and thiol-acrylate Michael addition of xanthate functional G_3 dendron **[Xan$_8$-G$_3$-TSe];[14]** with Bz and Am acrylate, followed by focal point manipulation to incorporate the tertiary alkyl bromide ATRP initiation site. Modification of the xanthate functional G_3 dendron macroinitiator **[Xan$_8$-G$_3$-BiB];[23]** was not attempted as previous studies have seen complications thought to be due to the *in situ* generation of thiols leading to competing thiol-bromo click reactions.[5,6] Tailoring the initiator feed ratio of the G_3 dendron and PEG macroinitiators is hypothesised to nominally maintain the same molar ratio of functional groups as targeted for the statistically multifunctional materials (5:5:90 Am:Bz:PEG, section 5.2.1).

5.2.2.1 Benzyl functional G_3 dendron initiator synthesis

As outlined in literature[7], and as described in Chapter 3 (section 3.2.1.2), full one-pot deprotection of xanthate functional G_3 dendron **[Xan$_8$-G$_3$-TSe];[14]**, and subsequent thiol-acrylate Michael addition, was carried out with an excess of *n*-butylamine and Bz acrylate to generate **[Bz$_8$-G$_3$-TSe];[45]**. The resulting Bz functional G_3 dendron was analysed by ^{1}H and ^{13}C NMR (Fig. 3.7B and S3.1, respectively).

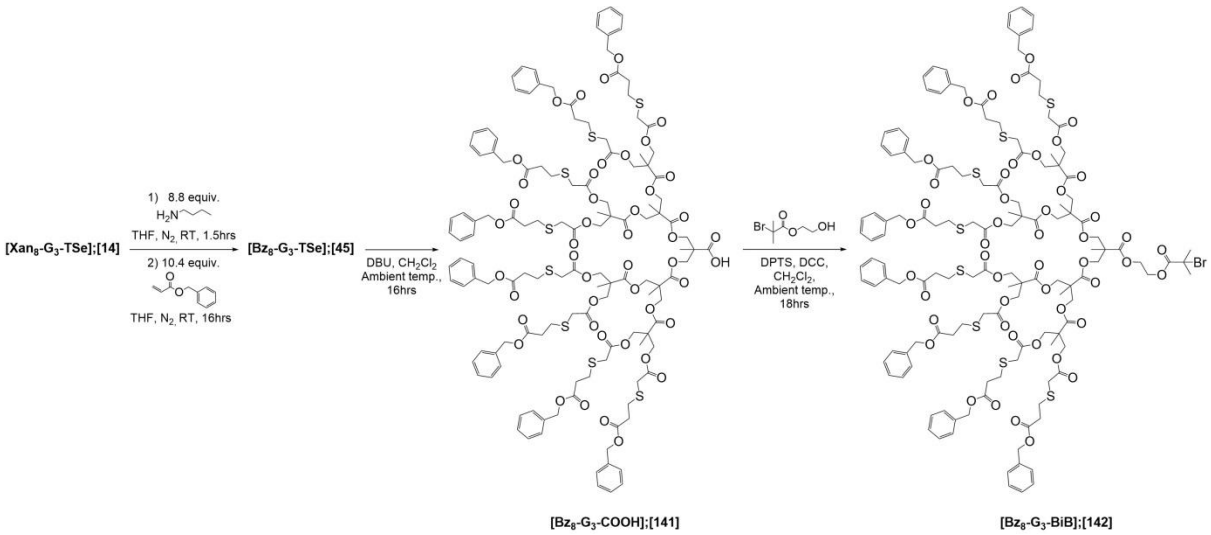

Scheme 5.1 Synthesis of benzyl functional G_3 macroinitiator, **[Bz$_8$-G$_3$-BiB];[142]**

Complete removal of focal point protecting group *p*-toluenesulfonyl ethyl (TSe) was carried out as described in Chapter 2 (section 2.5), with an excess (1.3 molar equivalents) of 1,8-diazabicyclo[5.4.0]undec-7-ene (DBU) and stirring at ambient temperature for 16 hours, Scheme 5.1. ^{1}H NMR analysis of the resulting focal point acid functional material **[Bz_8-G_3-COOH];[141]** confirmed the loss of CH_2 resonances at δ = 4.46 ppm and 3.45 ppm and aromatic resonance at δ = 7.79 ppm, corresponding to the loss of the TSe protecting group, Fig. 5.7. Some evidence of the vinyl sulfone by-product generated during deprotection was indicated at δ = 7.53 ppm and 7.15 ppm (aromatic resonances) and δ = 6.45, 6.18 and 5.86 ppm (vinyl resonances), although no further purification was carried out as the by-products would not lead to side reactions and would be removed by liquid chromatography in the next step. Confirmation by ^{13}C NMR revealed a characteristic carbonyl resonance at δ = 172 ppm, corresponding to the newly formed acid functionality, Fig. S5.1.

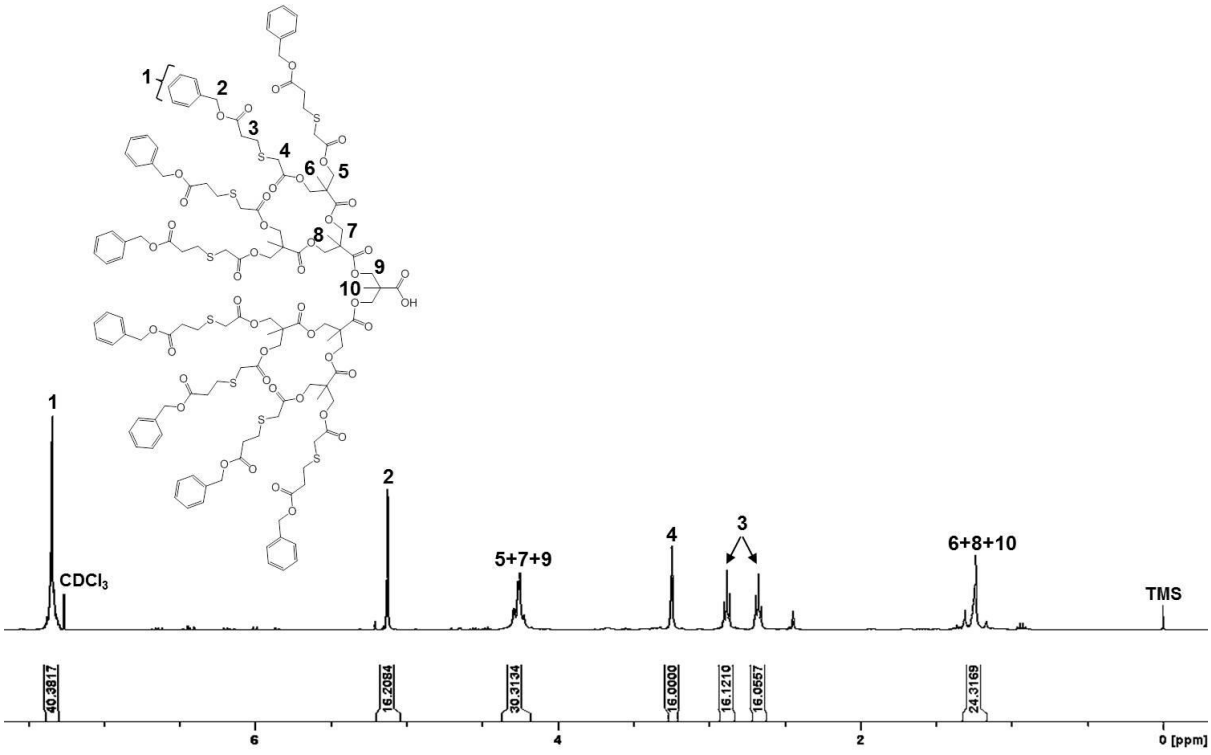

Fig. 5.7 ^{1}H NMR (400 MHz, $CDCl_3$) of **[Bz_8-G_3-COOH];[141]**

[HEBiB];[19] was used to react with focal point acid functional dendron **[Bz_8-G_3-COOH];[141]** using DCC/DPTS chemistry to generate benzyl functional G_3 macroinitiator **[Bz_8-G_3-BiB];[142]** in 74% yield. ^{1}H NMR analysis revealed the formation of a broad singlet at δ ≈ 1.92 ppm corresponding to the two symmetrical methyl environments on the bromoisobutyrate moiety, Fig. 5.8. A broad resonance is also observed at δ ≈ 4.36 ppm, overlapping with backbone CH_2 resonances, corresponding to the two OCH_2 environments from the HEBiB unit (peaks 11 and 12, Fig. 5.8).

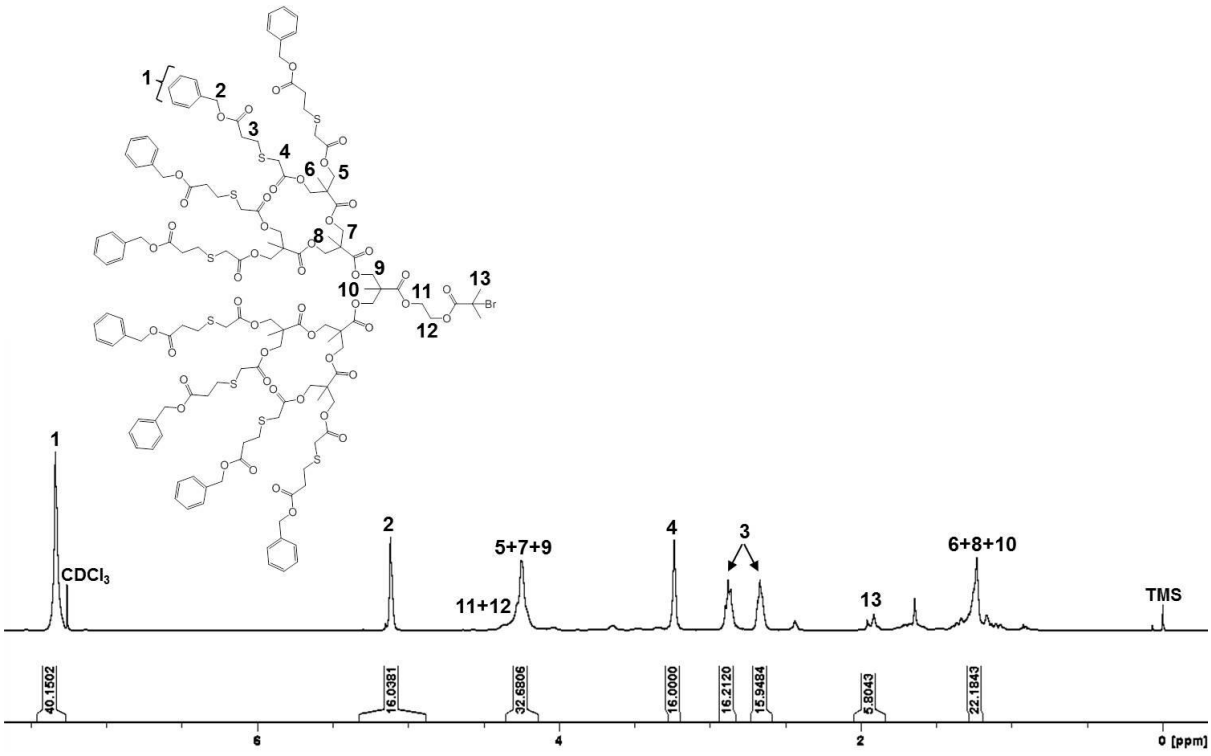

Fig. 5.8 ^{1}H NMR (400 MHz, $CDCl_3$) of **[Bz_8-G_3-BiB];[142]**

^{13}C NMR analysis indicated the presence of new resonances at δ = 21.7, 30.7 and 49.2 ppm corresponding to the HEBiB unit, the loss of acid carbonyl resonance at approximately δ = 172 ppm and the subsequent formation of a new ester carbonyl at δ = 171 ppm; confirming incorporation of the bromoinitiator functionality, Fig. S5.2.

5.2.2.2 LDH synthesis with benzyl functional initiator, Bz_8-G_3-BiB

The polymerisation of nBMA with a targeted DP_n of 100 monomer units was carried out with benzyl functional G_3 dendron macroinitiator **[Bz_8-G_3-BiB];[142]** at 60°C in methanol with a CuCl:bpy (1:2) catalyst system, Scheme 5.2, to establish the efficiency of the initiator within the proposed polymerisations.

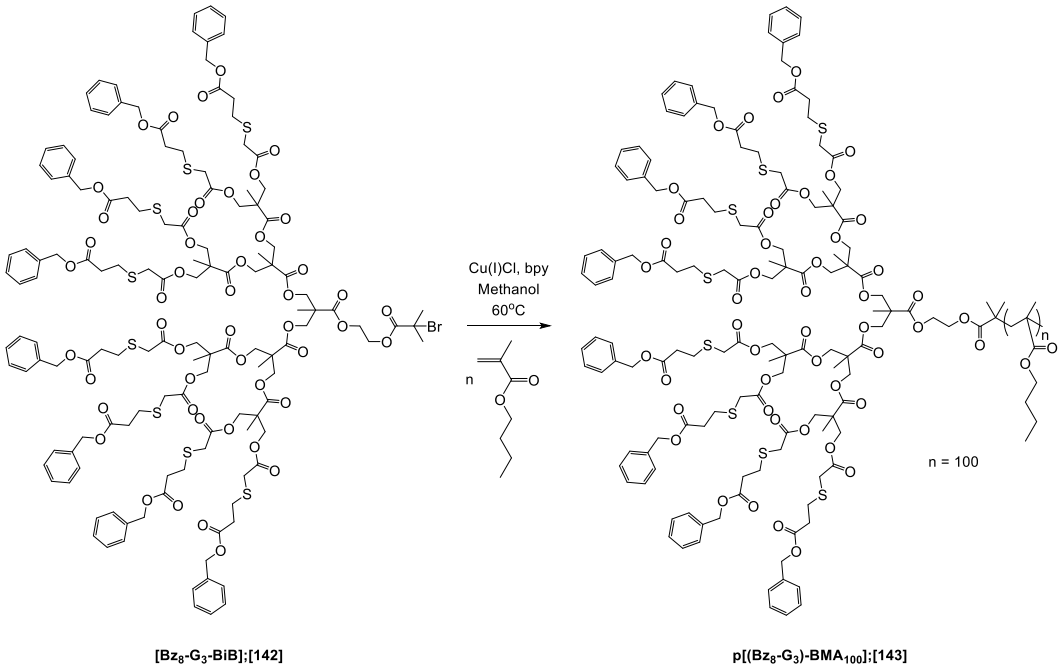

Scheme 5.2 Synthesis of LDH using benzyl functional G_3 initiator **[Bz_8-G_3-BiB];[142]**

The polymerisation was terminated by exposure to oxygen when conversion reached >95%, as calculated by ^{1}H NMR spectroscopy. The SEC and ^{1}H NMR analysis is summarised in Table 5.1.

Table 5.1 ^{1}H NMR and SEC data for **p[(Bz_8-G_3)-$nBMA_{100}$];[143]**

Polymer	Monomer conv. (%)	SEC (THF)[a] M_n (g mol^{-1})	M_w (g mol^{-1})	Đ	DP_n	^{1}H NMR[b] DP_n
P[(Bz_8-G_3)-$nBMA_{100}$]	95	28,100	34,700	1.24	177	174

[a]THF containing 2% TEA (v/v) at 35°C, 1 mL min^{-1} flow rate. [b]Determined by ^{1}H NMR analysis in $CDCl_3$

The benzyl-functional LDH eluted at lower retention volumes than seen previously for xanthate functional dendron initiated LDHs (section 2.8.4.2), Fig. 5.9, indicating higher than expected chain lengths being formed. This could be due to <100% initiator efficiency as a result of poor solubility in methanol and steric hindrance around the initiating site due to the bulky, hydrophobic benzyl peripheral groups. This generates fewer initiated chains, and hence, higher than expected molecular weight of the resulting polymer; some evidence of residual initiator is indicated by a small peak in the RI detector trace at an elution volume of ~19-20 mL. A slight shoulder is also seen at lower retention volumes, which could be due to coupling of chains at high conversion.[8]

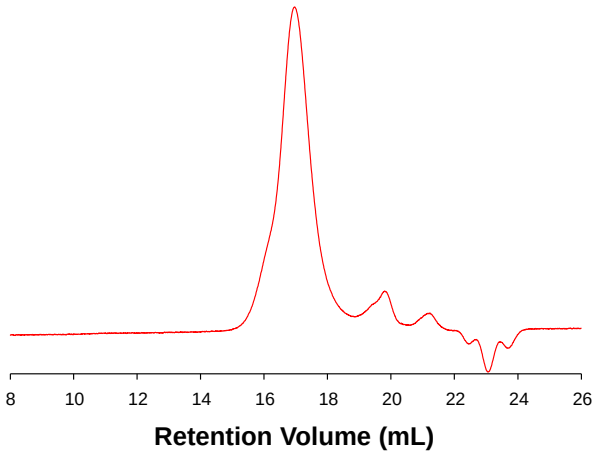

Fig. 5.9 SEC RI chromatogram trace of **p[(Bz_8-G_3)-nBMA$_{100}$];[143]**

The polymerisation did, however, achieve high conversion and relatively low dispersity (<1.3), and it was clear that the incorporation of benzyl-functional G_3 chain ends via methanolic ATRP of nBMA was successful.

5.2.2.3 Patchy co-initiated HPD synthesis

Synthesis of the Am-functional G_3 dendron macroinitiator was not successful as focal point protecting group removal of **[Am$_8$-G$_3$-TSe];[44]** (synthesised by full one-pot deprotection/thiol-acrylate Michael addition of **[Xan$_8$-G$_3$-TSe];[14]** with Am acrylate, see section 3.2.1.2) with DBU cleaved the Am functionality at the periphery. The strategy was therefore modified to allow co-initiation with xanthate-functional G_3 macroinitiator, **[Xan$_8$-G$_3$-BiB];[23]**, and subsequent post-polymerisation modification with Am acrylate, Fig. 5.10.

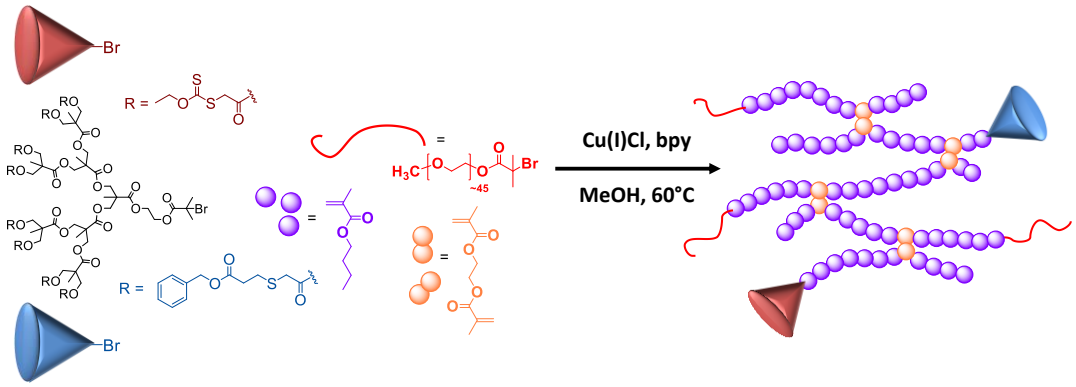

Fig. 5.10 Synthesis of benzyl- and xanthate-functional G_3 dendron and PEG(2K) co-initiated HPD

The co-initiated branched copolymerisation of nBMA and EGDMA with benzyl- and xanthate-functional G_3 dendron macroinitiators (**[Bz$_8$-G$_3$-BiB];[142]** and **[Xan$_8$-G$_3$-BiB];[23]**) and PEG(2K) macroinitiator (**[PEG(2K)-BiB];[131]**) was carried out, targeting a 5:5:90 molar ratio of xanthate:benzyl:PEG chain-ends. The DP_n of primary polymer chains was targeted at 100 monomer units, with an initiator:brancher ratio of 1:0.8. Triple detection SEC analysis of the co-initiated HPD and corresponding linear polymers are summarised in Table 5.2.

Table 5.2 Triple detection SEC data of benzyl- and xanthate-functional G_3 dendron/PEG(2K) co-initiated HPDs, with corresponding linear polymers

Entry no.	Initiator (mol%)			Target polymer composition	Conv. (%)[a]	SEC		
	xanthate G_3 dendron	**benzyl G_3 dendron**	**PEG(2K)**			M_n (g mol^{-1})	M_w (g mol^{-1})	Đ
1	100	0	0	$p(nBMA)_{100}$	84	26 600[b]	31 800[b]	1.19[b]
2	0	100	0	$p(nBMA)_{100}$	95	28,100[c]	34,700[c]	1.24[c]
3	0	0	100	$p(nBMA)_{100}$	94	13 400[b]	14 500[b]	1.08[b]
4	0.7	0.7	98.6	$p(nBMA)_{100}$-*co*-$EGDMA_{0.8}$	99	37,700[c]	148,300[c]	3.94[c]

[a]Determined by ^{1}H NMR analysis in $CDCl_3$ [b]DMF containing 0.01 M LiBr at 60°C, 1mL min^{-1} flow rate. [c]Sample analysed in THF containing 2% TEA (v/v) at 35°C, 1mL min^{-1} flow rate.

As seen previously, the benzyl- and xanthate-functional G_3 dendron/PEG(2K) co-initiated polymerisation appears to be dominated by the PEG(2K) initiator, the major component in the initiator mixture, resulting in molecular weights that closely resembled those previously achieved for the xanthate-functional G_0/G_3 dendron and PEG(2K) co-initiated materials (sections 4.4.3.1 and 4.4.3.2), Fig. 5.11.

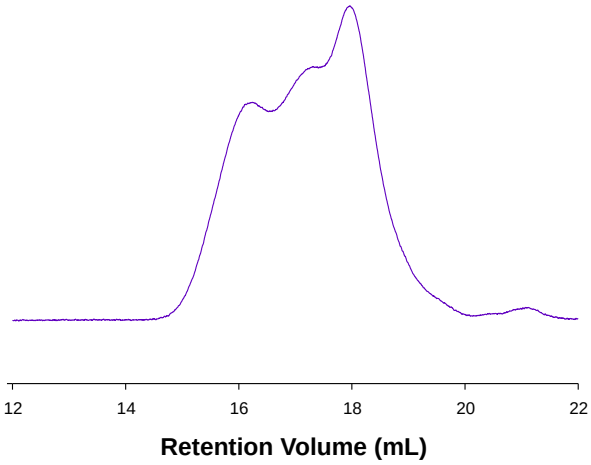

Fig. 5.11 SEC RI chromatogram trace of **p[(PEG(2K))$_{0.986}$-(Xan$_8$-G$_3$)$_{0.007}$-(Bz$_8$-G$_3$)$_{0.007}$-nBMA$_{100}$-*co*-EGDMA$_{0.8}$];[144]**

During singly-initiated linear polymerisations, the xanthate- and benzyl-functional G_3 dendron macroinitiators seem to have very similar initiator efficiency (see sections 2.8.4.2 and 5.2.2.2), and should therefore be incorporated equally during co-initiated polymerisation.

Complete deprotection of the incorporated xanthate functional G_3 dendrons of co-initiated HPD **p[(PEG(2K))$_{0.986}$-(Xan$_8$-G$_3$)$_{0.007}$-(Bz$_8$-G$_3$)$_{0.007}$-nBMA$_{100}$-*co*-EGDMA$_{0.8}$];[144]**, followed by functionalisation with Am acrylate was applied to achieve 50:50 functionalisation, following chemical procedures described and optimised in Chapter 3, Fig. 5.12.

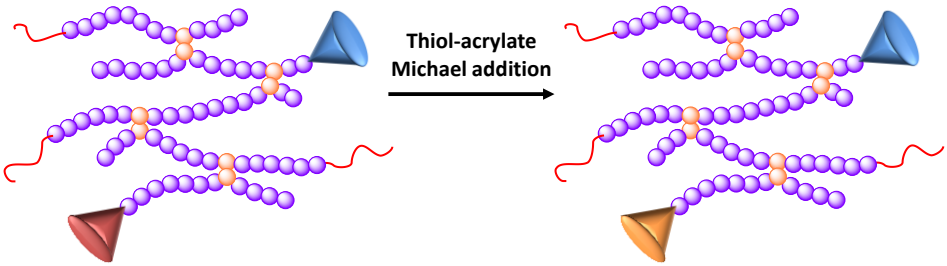

Fig. 5.12 Schematic representation of the complete deprotection and thiol-acrylate Michael addition for patchy multifunctionalisation of G_3 and PEG(2K) co-initiated HPD

The complete deprotection of xanthate chain-end functionality with an excess of *n*-butylamine (10 molar equivalents), followed by thiol-Michael addition with Am acrylate (15 molar equivalents), resulted in the multifunctionalised co-initiated HPD **p[(PEG(2K))$_{0.986}$-(Am$_8$-G$_3$)$_{0.007}$-(Bz$_8$-G$_3$)$_{0.007}$-nBMA$_{100}$-*co*-EGDMA$_{0.8}$];[145]**, as confirmed by ^{1}H NMR spectroscopy (Fig. 5.13).

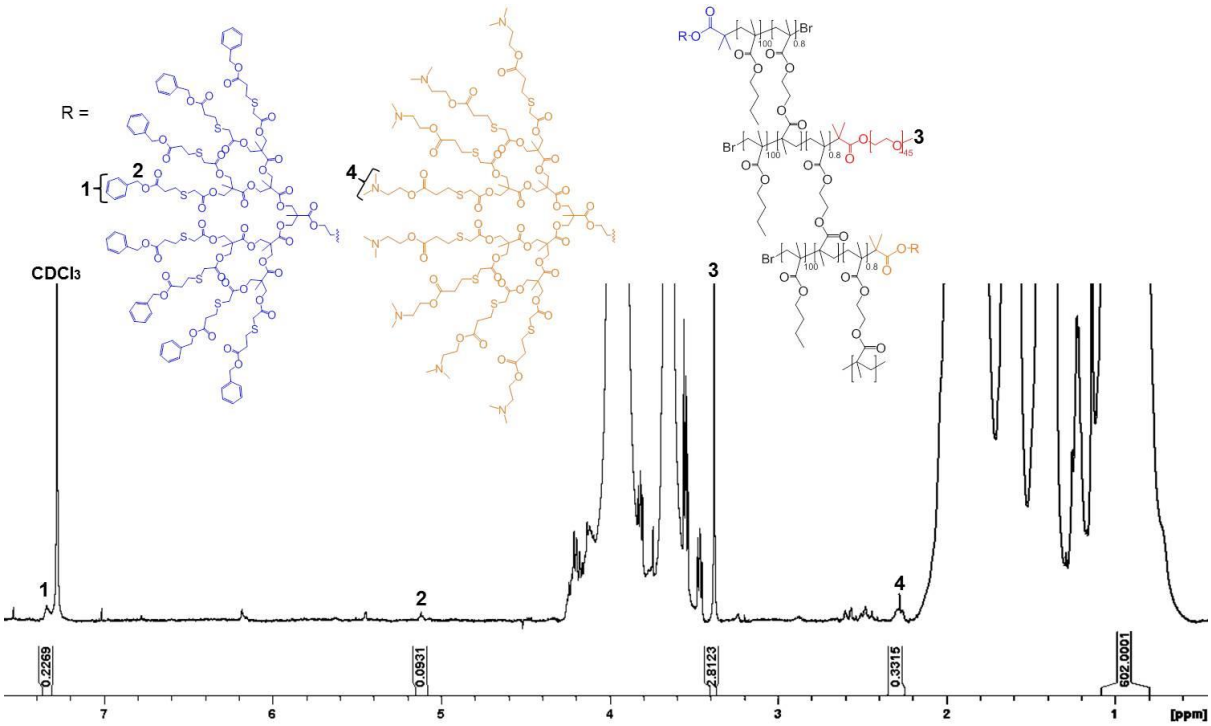

Fig. 5.13 ^{1}H NMR (400 MHz, $CDCl_3$) of **p[(PEG(2K))$_{0.986}$-(Am$_8$-G$_3$)$_{0.007}$-(Bz$_8$-G$_3$)$_{0.007}$-nBMA$_{100}$-*co*-EGDMA$_{0.8}$];[145]**, by post-polymerisation modification of **p[(PEG(2K))$_{0.986}$-(Xan$_8$-G$_3$)$_{0.007}$-(Bz$_8$-G$_3$)$_{0.007}$-nBMA$_{100}$-*co*-EGDMA$_{0.8}$];[144]**

Peaks corresponding to Bz (peaks 1 and 2, Fig. 5.13) and Am (peak 4, Fig. 5.13) functionalities are present in the resulting ^{1}H NMR spectrum, in an approximately 1:1 ratio, relative to the polymer backbone resonance at $\delta \approx 0.8$-1.1 ppm, which remains unchanged following functionalisation. Again, the very low incorporation of the dimethylamino and benzyl functionality resulted in restricted analysis by NMR and the resonances relating to these functional groups were only identified after considerable expansion of the baseline. Peaks in the ^{1}H NMR spectrum corresponding to the Bz functionality at δ = 7.34 ppm (aromatic, $\int_{7.34\ ppm}$ = 0.2269/40 = 0.6%) and δ = 5.12 ppm (CH_2, $\int_{5.12\ ppm}$ = 0.0931/16 = 0.6%) confirm an incorporation of 0.6% benzyl functional G_3 dendrons, which equates to 4.5% benzyl functionality overall (0.6*8 peripheral groups per G_3 dendron), relative to the polymer backbone; a peak corresponding to the Am functionality at δ = 2.28 ppm ($2CH_3$, $\int_{2.28\ ppm}$ = 0.3315/48 = 0.7%) confirms incorporation of 0.7% dimethylamino functional G_3 dendrons,

which equates to 5.5% dimethylamino functionality overall (0.7*8 peripheral groups per G_3 dendron), relative to the polymer backbone.

5.2.3 Aqueous nanoprecipitation studies of branched polymers with patchy and statistical functional group distributions

Aqueous nanoprecipitation of multifunctionalised co-initiated HPDs, with statistical and patchy distributions of functional groups (statistical **p[(PEG(2K))$_{0.9}$-(Am$_{0.5}$-Bz$_{0.5}$-G$_0$)$_{0.1}$-nBMA$_{100}$-*co*-EGDMA$_{0.8}$];[140]**, Fig. 5.14A; patchy **p[(PEG(2K))$_{0.986}$-(Am$_8$-G$_3$)$_{0.007}$-(Bz$_8$-G$_3$)$_{0.007}$-nBMA$_{100}$-*co*-EGDMA$_{0.8}$];[145]**, Fig. 5.14B) was carried out from an initial concentration of 5 mg/mL in acetone.

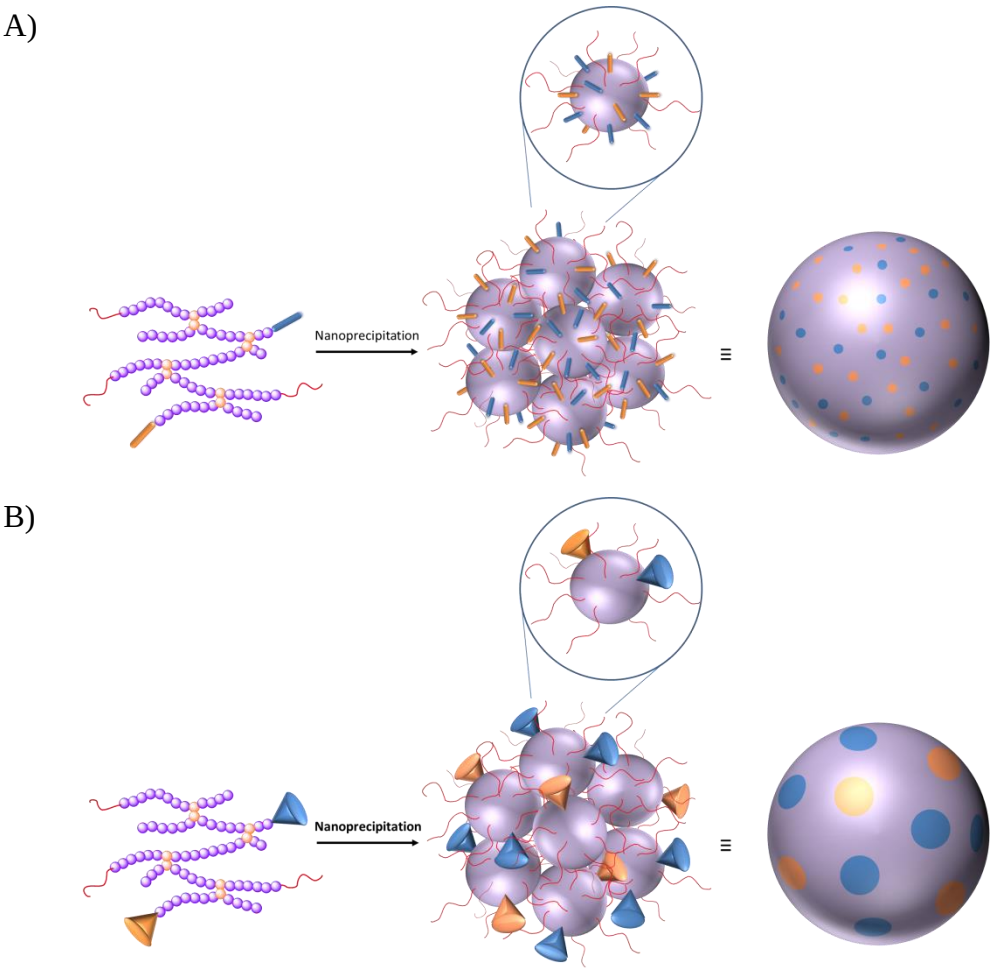

Fig. 5.14 Graphical representation of nanoparticles with; A) statistical and B) patchy distributions of surface functional groups, formed by nanoprecipitation

The dissolved polymer was rapidly added to water with stirring at ambient temperature. The solvent was allowed to evaporate overnight in a high velocity fume cupboard, and the resulting nanoparticle suspension (1 mg/mL) analysed by DLS, as summarised in Table 5.3 below, with average size by intensity distributions shown in Fig. 5.15.

Table 5.3 DLS measurement data for multifunctional co-initiated HPDs with statistical (**[140]**) and patchy (**[145]**) functional group distributions

Polymer	D_z (nm)	PdI	pH7 ζ (mV)	pH5 ζ (mV)
p[(PEG(2K))$_{0.9}$-(Am$_{0.5}$-Bz$_{0.5}$-G$_0$)$_{0.1}$-nBMA$_{100}$-*co*-EGDMA$_{0.8}$];[140]	66	0.203	-23.0	-7.5
p[(PEG(2K))$_{0.986}$-(Am$_8$-G$_3$)$_{0.007}$-(Bz$_8$-G$_3$)$_{0.007}$-nBMA$_{100}$-*co*-EGDMA$_{0.8}$];[145]	68	0.189	-8.4	-7.7

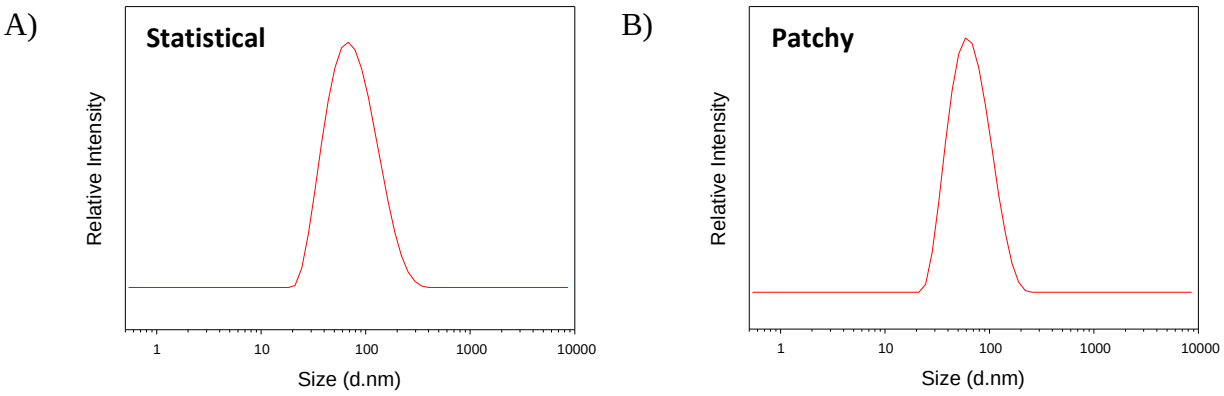

Fig. 5.15 Average DLS size distribution by intensity traces of aqueous nanoparticle dispersions of; A) statistical **p[(PEG(2K))$_{0.9}$-(Am$_{0.5}$-Bz$_{0.5}$-G$_0$)$_{0.1}$-nBMA$_{100}$-*co*-EGDMA$_{0.8}$];[140]** and B) patchy **p[(PEG(2K))$_{0.986}$-(Am$_8$-G$_3$)$_{0.007}$-(Bz$_8$-G$_3$)$_{0.007}$-nBMA$_{100}$-*co*-EGDMA$_{0.8}$];[145]** nanoprecipitates (correlograms Fig. S5.4)

The Z-average diameter (D_z) and PdI of the nanoprecipitates were approximately the same for both materials with differing spatial arrangements of functional groups, despite the different molar ratio of PEG:dendron chain-ends. A clearer representation of the relative molar ratio of macroinitiators required to maintain the same Am/Bz:PEG functional group ratio between the materials is shown in Fig. 5.16.

A)

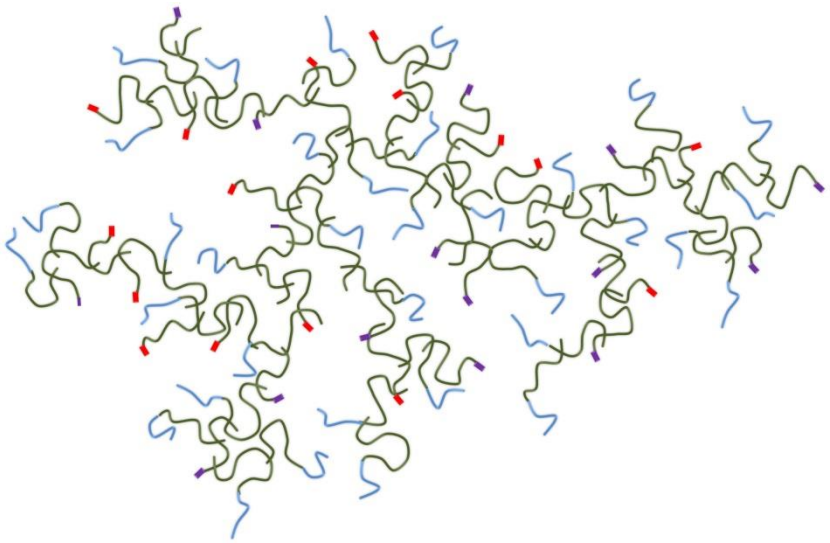

B)

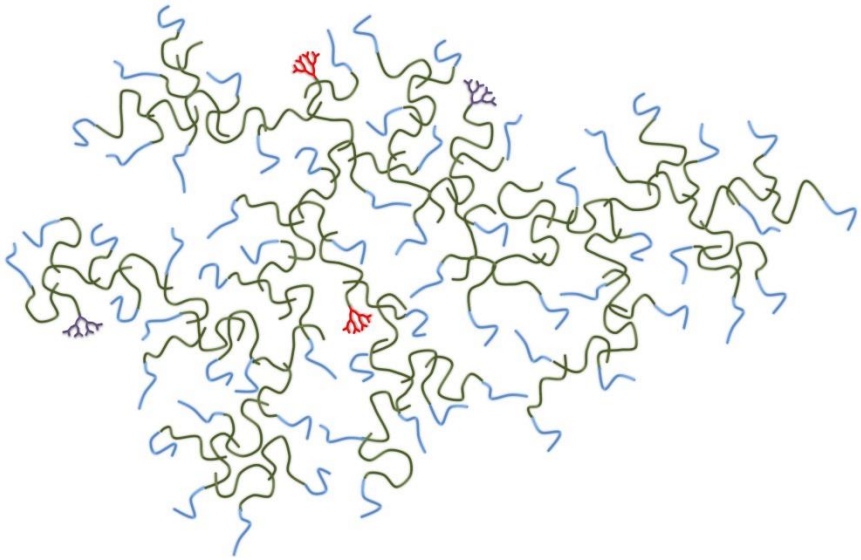

Fig. 5.16 A graphical representation of the chain-end distribution in; A) statistical and B) patchy multifunctionalised co-initiated HPDs to maintain a 5:5:90 Am:Bz:PEG ratio (green = polymer backbone; blue = PEG chain-ends; red = Am functional G_3 dendron chain-ends; purple = Bz functional G_3 dendron chain-ends)

A much lower concentration of G_3 dendron chain-ends are required to maintain a 5:5:90 Am:Bz:PEG functional group ratio than co-initiated HPDs containing G_0 dendrons, as G_3 dendrons have 8 peripheral groups whereas G_0 dendrons have 1; this clearly adds considerable spatial inhomogeneity and ensures the isolation of the functional groups within defined zones of the branched polymer.

Materials with a statistical distribution of Am groups are expected to charge differently to those co-localised on a G_3 dendron in the patchy materials. Neighbouring protonated Am groups on the G_3 dendron periphery are expected to repel each other, meaning multiple charges on the same dendron are less likely, leading to a lower average charge on the structure. It is hypothesised that protonation of Am groups which are statistically distributed lead to somewhat isolated charges across the polymer periphery, increasing the average positive charge on the particle. Evidence for this was obtained when the pH of the nanoparticle suspensions was lowered from neutral (pH7) to slightly acidic (pH5) via the addition of HCl. Zeta potential (ζ) values of statistical materials increased from -23.0 mV to -7.5 mV, indicating amine protonation, whereas ζ values obtained for the patchy material (ζ = -8.4 mV at pH7, increased to ζ = -7.7 mV at pH5) suggest the average charge remains approximately constant after addition of acid.

5.3 Radiolabelling

For the statistically multifunctionalised materials, isotropy in the surface functional group distribution and hence interaction behaviour with biological systems is an idealisation; even on the molecular scale anisotropy is encountered, leading to theories of molecular liquids[9] and anisotropic fluids[10]. This was seen in Chapter 4 where multiple GNP binding was seen for materials with functional groups in statistically close proximity (Fig. 4.21). Therefore, it is important to monitor these nanoparticulate delivery systems with differing spatial arrangements of functional groups on the surface (patchy and statistical) by non-invasive means, such as radiolabelling. Radiolabelling of the synthesised polymers with ^{3}[H] ensures a high degree of radioactivity due to rapid exchange of labile protons throughout the structure. This allows direct monitoring of the delivery vehicle in cell studies, rather than encapsulation

of a radiolabelled compound which may leach out. Also, the simple exchange of labile protons with tritium prevents additional manipulation of the polymers and the unnecessary introduction of functional groups that would perturb the target chemistry. It is possible to induce specific behaviour by other labelling techniques such as methylation using $^{14}CH_3I$, which would generate permanent positive charge, or fluorescent labelling, which would create large areas of considerable hydrophobicity.

5.3.1 Radio analysis

The radiolabelled polymer sample was generated with >3 mCi of activity by treatment with tritium gas by a contract research organisation (RC Trictec AG, Teufen, Switzerland) on a scale too small to fully analyse the distribution of radioactivity throughout the sample (patchy = 20.68 μg, statistical = 22.38 μg), however, it has previously been reported that the broad distribution of polymers formed via statistical branching during ATRP (linear to highly branched species) nanoprecipitate to give rise to uniform nanoprecipitates.[11] The addition of a small quantity of the radiolabelled polymer to the conventional sample is not expected to modify any behaviour of the branched material. Therefore, the radiolabelled polymers are still likely to be incorporated into resulting nanoprecipitates when mixed with the "cold" (unlabelled) sample, leading to nanoprecipitates that may be studied quantitatively.

5.3.2 Aqueous nanoprecipitation of radiolabelled materials

In a 5 mL scale nanoprecipitation with a targeted final concentration of 1 mg/mL, the total activity of the statistical material used was 53.71 μCi, meaning a specific activity of 10.74 μCi/mg; and for the patchy material, the total activity used was 64.09 μCi, meaning a specific activity of 12.82 μCi/mg. The radiolabelled polymers were nanoprecipitated from acetone, as described previously (section 5.2.3), and the solvent left to evaporate overnight in

a high velocity fume cupboard. It was found that the volume of water in the resulting nanoprecipitates was lower than expected, and hence the concentration of the sample had increased. The nanoprecipitates were diluted with water back to the initially targeted concentration of 1 mg/mL of polymer in water and analysed by DLS, as summarised in Table 5.4 below, with average size by number (D_n) distributions shown in Fig. 5.17.

Table 5.4 DLS measurement data for nanoprecipitated cold (Entry 1 and 2) and radiolabelled (Entry 3 and 4) statistical and patchy co-initiated HPDs

Entry	Polymer	D_n (nm)
1	**p[(PEG(2K))$_{0.9}$-(Am$_{0.5}$-Bz$_{0.5}$-G$_0$)$_{0.1}$-nBMA$_{100}$-*co*-EGDMA$_{0.8}$]**	33
2	**p[(PEG(2K))$_{0.986}$-(Am$_8$-G$_3$)$_{0.007}$-(Bz$_8$-G$_3$)$_{0.007}$-nBMA$_{100}$-*co*-EGDMA$_{0.8}$]**	36
3	**p[(PEG(2K))$_{0.9}$-(Am$_{0.5}$-Bz$_{0.5}$-G$_0$)$_{0.1}$-nBMA$_{100}$-*co*-EGDMA$_{0.8}$] +^{3}[H]**	51
4	**p[(PEG(2K))$_{0.986}$-(Am$_8$-G$_3$)$_{0.007}$-(Bz$_8$-G$_3$)$_{0.007}$-nBMA$_{100}$-*co*-EGDMA$_{0.8}$] +^{3}[H]**	38

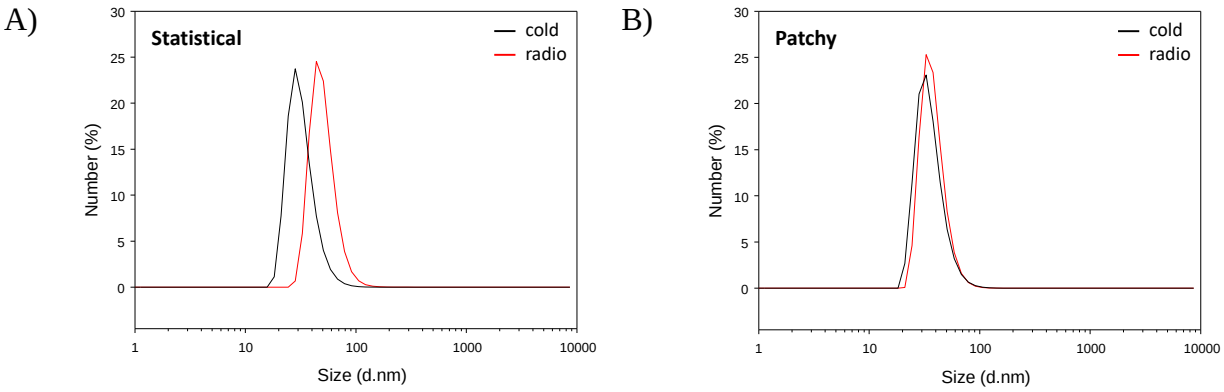

Fig. 5.17 Average DLS size distribution by number traces of aqueous nanoparticle dispersions of radiolabelled; A) statistical **p[(PEG(2K))$_{0.9}$-(Am$_{0.5}$-Bz$_{0.5}$-G$_0$)$_{0.1}$-nBMA$_{100}$-*co*-EGDMA$_{0.8}$];[140]** and B) patchy **p[(PEG(2K))$_{0.986}$-(Am$_8$-G$_3$)$_{0.007}$-(Bz$_8$-G$_3$)$_{0.007}$-nBMA$_{100}$-*co*-EGDMA$_{0.8}$];[145]** nanoprecipitates

Although some aggregates could be seen in the radiolabelled nanoprecipitates due to excessive water evaporation, the D_n values obtained by DLS were comparable with the corresponding cold samples (section 5.2.3, Table 5.3). The samples were therefore taken forward to be used in pharmacological studies.

5.4 Pharmacology

Studies on cellular accumulation of the radiolabelled multifunctional nanoprecipitates were carried out in the Department of Molecular and Clinical Pharmacology at the University of Liverpool by Dr Lee Tatham under the supervision of Prof. Andrew Owen.

5.4.1 Cellular accumulation studies

We hypothesised that the binding of opsonins on hydrophobic regions of patchy materials may introduce a distinct biological "handle" that components of the MPS can recognise; this may lead to enhanced uptake compared to the statistically multifunctionalised materials where a more even adsorption of opsonins, or possibly a reduced strength of adsorption, would be expected. Directed interactions may occur between patches of surface functional groups and receptor clusters on the macrophage. Enhanced uptake has been seen previously for non-spherical, flexible particles.[12]

5.4.1.1 ATHP-1 cells

The cellular accumulation ratio (CAR) of the radiolabelled statistical (**[140]**) and patchy (**[145]**) co-initiated HPD nanoprecipitates was investigated in ATHP-1 cells. ATHP-1 cells are *in vitro*-differentiated monocyte-derived macrophages used as a model to monitor accumulation in macrophages, and can be used to evaluate mechanisms of phagocytosis. Accumulation in macrophages is advantageous for the treatment of HIV as they behave as cellular sanctuary sites in systemic circulation for the virus.[13] The CAR of the nanoprecipitates with different spatial arrangements of surface functional groups in ATHP-1 cells was compared directly at 1 and 6 hours incubation time, Fig. 5.18.

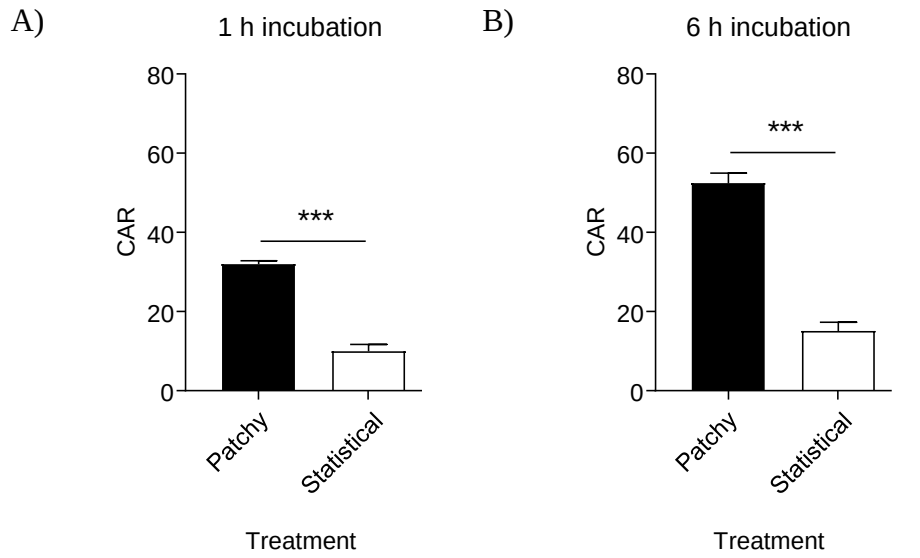

Fig. 5.18 Cellular accumulation ratios (CAR) for patchy (black bar) and statistically (white bar) multifunctional nanoprecipitates at; A) 1 hour incubation, and B) 6 hours incubation with ATHP-1 cells

Enhanced cellular accumulation is seen for materials with a patchy distribution of surface functional groups, compared to statistically multifunctionalised materials, as postulated in Chapter 1 (1.8.3, Fig. 1.18). The patchy material appears to accumulate 3.2-fold more in ATHP-1 cells following 1 hour exposure and 3.4-fold more following 6 hours of exposure compared to the statistically multifunctional material. The enhanced CAR of materials with a patchy distribution of surface functional groups may be because the structure contains inhomogeneous surface characteristics which trigger an enhanced response within the macrophages. Surface charge anisotropy originating from the patches of Am functional groups may affect uptake, as has been seen previously for protein-protein interactions.[14] Anisotropic interactions dominate if entropic penalties are overcome, which cannot occur if patches are too small, as in the case of statistically multifunctional nanoparticles.[15]

5.4.1.2 THP-1 cells

Undifferentiated THP-1 cells (human monocytic cells) were incubated with the patchy and statistical materials and their CAR assessed, Fig. 5.19.

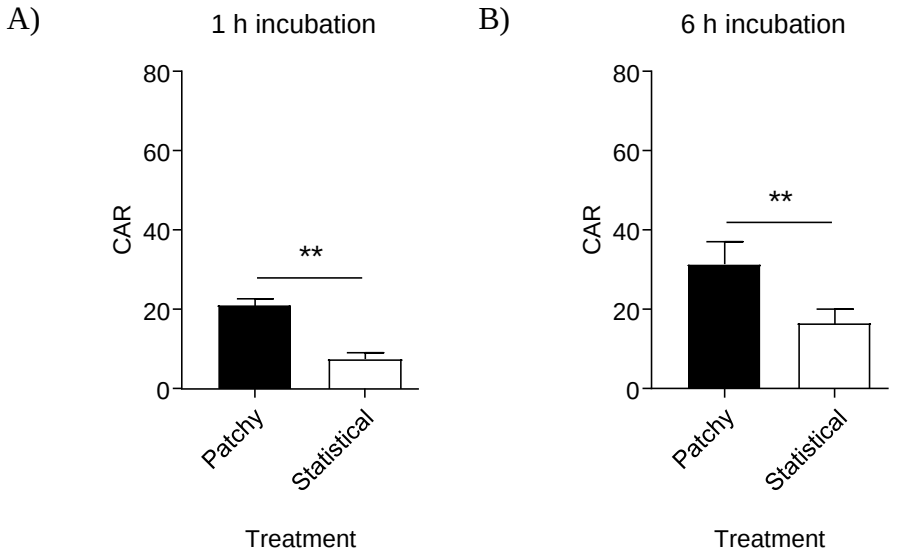

Fig. 5.19 Cellular accumulation ratios (CAR) for patchy (black bar) and statistically (white bar) multifunctional nanoprecipitates at; A) 1 hour incubation, and B) 6 hours incubation with undifferentiated THP-1 cells

Reduced accumulation of nanomaterials was observed for THP-1 cells compared to ATHP-1 cells at 1 hour and 6 hours incubation; however, similar trends were seen with patchy nanoprecipitates appearing to accumulate more than statistically multifunctionalised materials, although the difference between the materials is reduced compared to ATHP-1 cells.

5.4.1.3 Cell-free particle adhesion

ATHP-1 and THP-1 are not adherent cell lines, therefore, the previous studies were conducted using collagen-coated plastic well plates to promote adhesion of cells and facilitate the washing steps required to aid the cell accumulation quantification. In order to rule out the impact of spatially-derived adhesion to collagen and/or the plastic plates as the cause of the observed differences in CAR, cell-free experiments were carried out to monitor particle adhesion to collagen and plastic, in the same way as detailed for the cell-based experiments, Fig. 5.20.

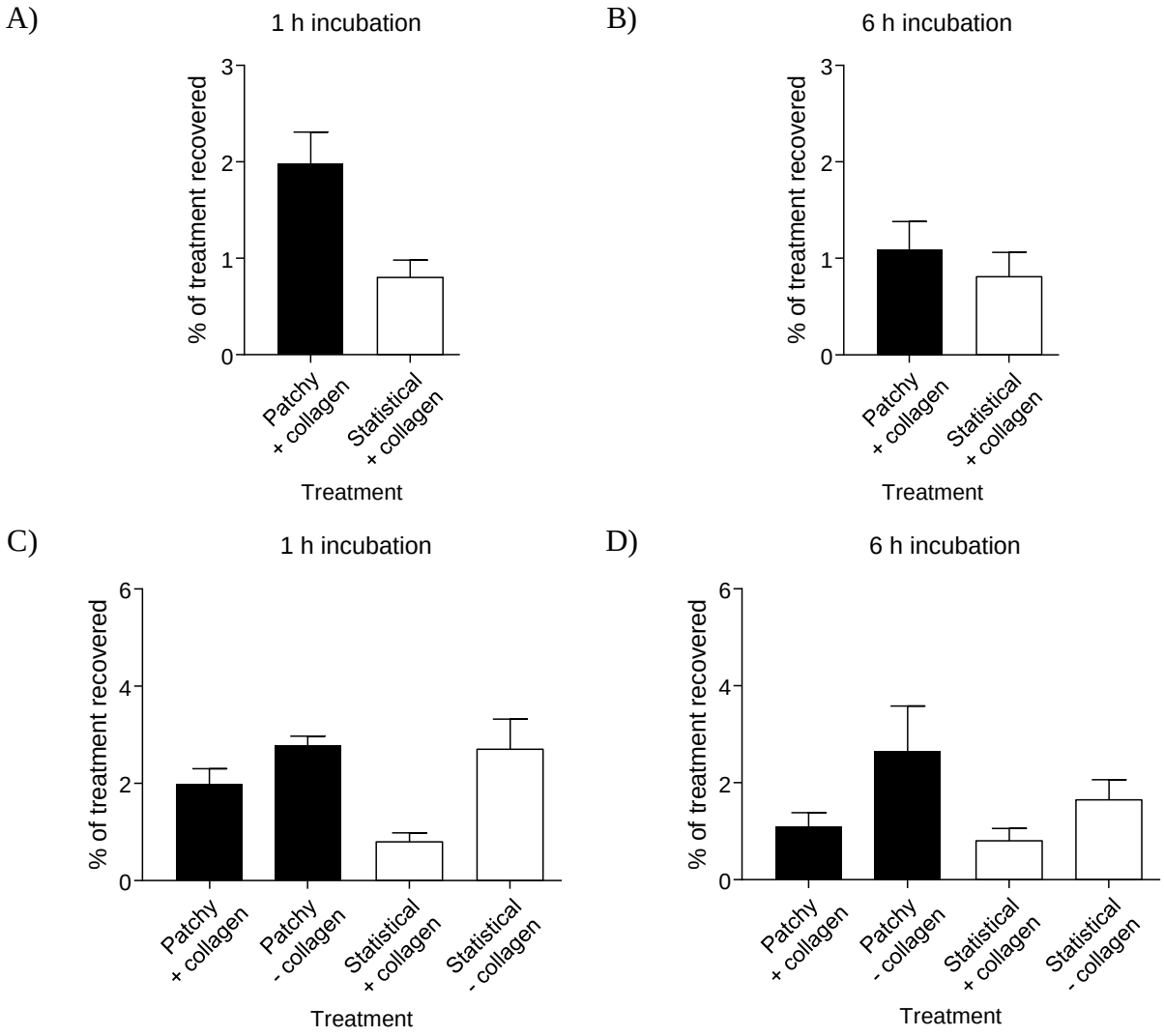

Fig. 5.20 % of treatment recovered for cell-free studies with patchy and statistically multifunctional nanoprecipitates at; A) 1 hour incubation, and B) 6 hours incubation with collagen; and C) 1 hour incubation, and D) 6 hours incubation with and without collagen

Modified nanoparticle adhesion was again seen in the presence of collagen for both radiolabelled patchy and statistical nanoparticles, although a lower overall % recovery was achieved for both materials, essentially removing this potential error as the cause of the differences seen in CAR experiments in the presence of cells. Interestingly, the patchy particles appear to have a greater rate of adsorption to collagen than the statistically multifunctional nanoparticles but overall there were no statistical differences between the materials after 6 hours incubation in the presence or absence of collagen.

5.5 Conclusion

The formation of patchy and statistically multifunctionalised nanomaterials was achieved by co-initiation of dendron and PEG(2K) macroinitiators, followed by one-pot thiol-acrylate Michael addition to introduce multifunctionality at the periphery, and nanoprecipitation to form stable nanoparticles in water. The polymers were radiolabelled by tritiation and the accumulation of the resulting nanoprecipitates in ATHP-1 cells assessed. It was found that nanomaterials with a patchy distribution of functional groups at the periphery favourably accumulate in ATHP-1 cells; 3.2-fold more than statistically multifunctional materials after 1 hour incubation, and 3.4-fold more after 6 hours. The results were confirmed by repeating the cell studies with undifferentiated THP-1 cells and investigating cell-free particle adhesion. The THP-1 cell studies suggest this difference isn’t simply due to enhanced phagocytosis and the cell-free control suggests that there may be adhesion differences, but these are not driving the results seen.

5.6 References

1. E. Blanco, H. Shen, and M. Ferrari, *Nat. Biotechnol.*, 2015, **33**, 941–951.
2. S. T. Kim, K. Saha, C. Kim, and V. M. Rotello, *Acc. Chem. Res.*, 2013, **46**, 681–691.
3. D. E. Owens and N. A. Peppas, *Int. J. Pharm.*, 2006, **307**, 93–102.
4. Z. Poon, S. Chen, A. C. Engler, H. Lee, E. Atas, G. von Maltzahn, S. N. Bhatia and P. T. Hammond, *Angew. Chemie Int. Ed.*, 2010, **49**, 7266–7270.
5. S. E. R. Auty (2014), *Utilising novel thiol-acrylate click reactions to synthesise controlled branched polymer emulsifiers.*, PhD thesis, University of Liverpool.
6. J. Xu, L. Tao, C. Boyer, A. B. Lowe, and T. P. Davis, *Macromolecules*, 2010, **43**, 20–24.
7. S. E. R. Auty, O. Andren, M. Malkoch, and S. P. Rannard, *Chem. Commun.*, 2014, **50**, 6574–6577.
8. K. Matyjaszewski, *Prog. Polym. Sci.*, 2005, **30**, 858–875.
9. G. C. Gray and K. E. Gubbins, *Theory of Molecular Fluids, Vol 1: Fundamentals*, Clarendon Press, Oxford, UK, 1984, ISBN: 0-19-855602-0.
10. J. M. Caillol, J. J. Weis, and G. N. Patey, *Phys. Rev. A*, 1988, **38**, 4772–4788.
11. F. L. Hatton, P. Chambon, A. C. Savage, and S. P. Rannard, *Chem. Commun.*, 2016, **52**, 3915–3918.
12. S. E. A. Gratton, P. A. Ropp, P. D. Pohlhaus, J. C. Luft, V. J. Madden, M. E. Napier, and J. M. DeSimone, *Proc. Natl. Acad. Sci.*, 2008, **105**, 11613–11618.
13. A. Owen and S. Rannard, *Nanomedicine*, 2015, **10**, 3103–3107.
14. L. J. Quang, S. I. Sandler, and A. M. Lenhoff, *J. Chem. Theory Comput.*, 2014, **10**, 835–845.
15. C. J. Roberts and M. A. Blanco, *J. Phys. Chem. B*, 2014, **118**, 12599–12611.

5.7 Appendix

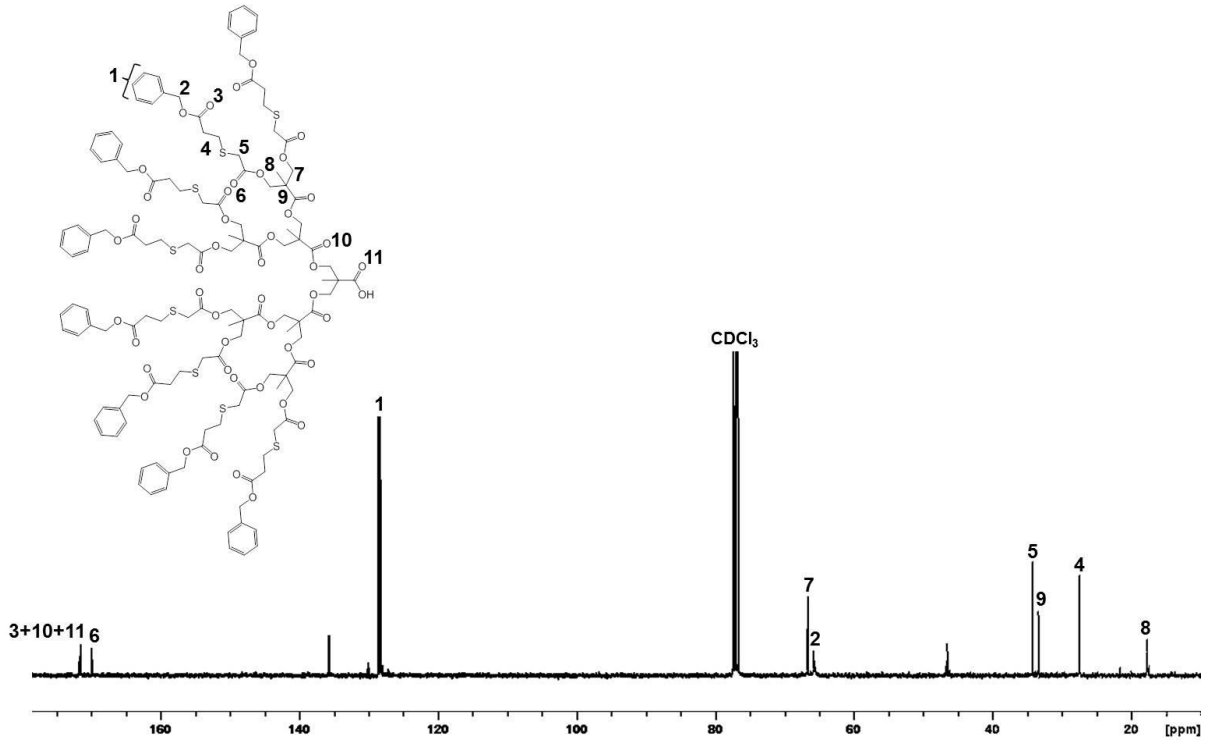

Fig. S5.1 ^{13}C NMR (100 MHz, $CDCl_3$) of **[Bz_8-G_3-COOH];[141]**

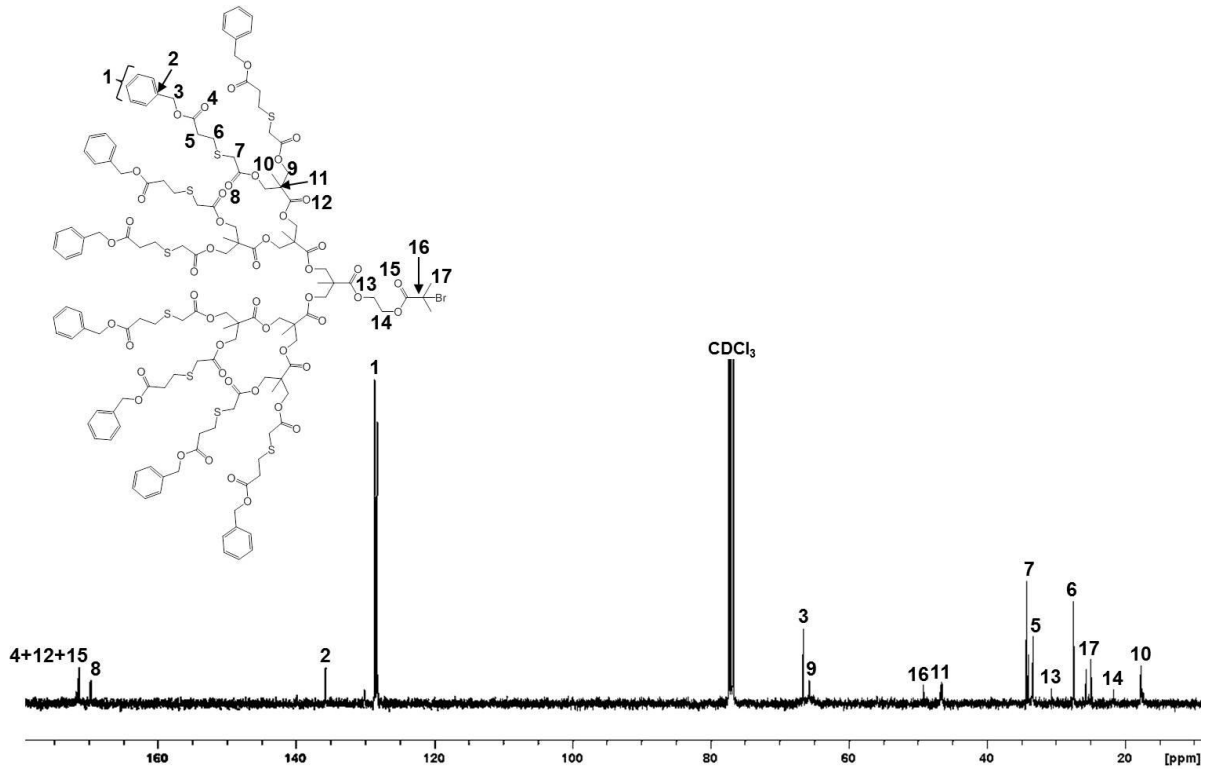

Fig. S5.2 ^{13}C NMR (100 MHz, $CDCl_3$) of **[Bz_8-G_3-BiB];[142]**

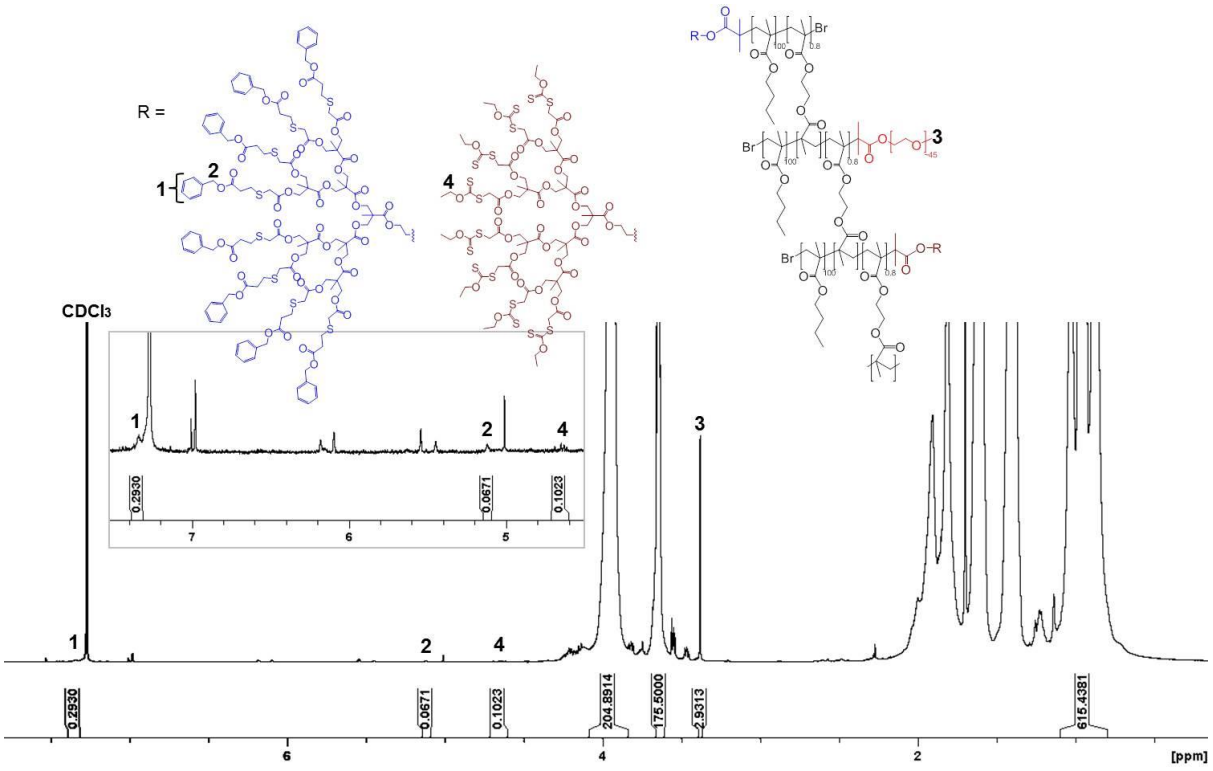

Fig. S5.3 ^{1}H NMR (400 MHz, $CDCl_3$) of **p[(PEG(2K))$_{0.986}$-(Xan$_8$-G$_3$)$_{0.007}$-(Bz$_8$-G$_3$)$_{0.007}$-nBMA$_{100}$-*co*-EGDMA$_{0.8}$];[144]**

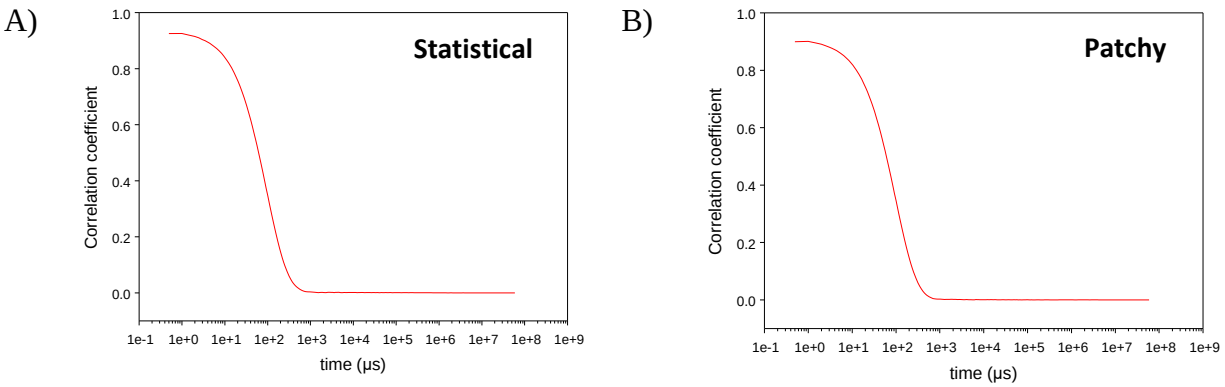

Fig. S5.4 DLS correlograms of aqueous nanoparticle dispersions of; A) statistical **p[(PEG(2K))$_{0.9}$-(Am$_{0.5}$-Bz$_{0.5}$-G$_0$)$_{0.1}$-nBMA$_{100}$-*co*-EGDMA$_{0.8}$];[140]** and B) patchy **p[(PEG(2K))$_{0.986}$-(Am$_8$-G$_3$)$_{0.007}$-(Bz$_8$-G$_3$)$_{0.007}$-nBMA$_{100}$-*co*-EGDMA$_{0.8}$];[145]** nanoprecipitates

CHAPTER 6

Conclusions and Further work

6.1 Synthesis

The chosen strategy for the direct synthesis of patterned nanoparticles for tailored biological interactions required the formation of dendrons to allow the spatial control of functionality within complex polymer architectures, and the formation of nanoparticles with patchy surface distributions. The divergent synthesis of polyester dendrons up to the third generation was achieved by anhydride coupling of acetonide-protected bis-MPA. Although this highly efficient dendron synthesis route has been widely explored and applied[1-5], this strategy is limited by tedious purification steps and toxic reagents, and is highly mass inefficient as each functionalisation/growth step only uses half of the symmetrical anhydride. Recovery of the unreacted portion of the anhydride may be possible in optimised syntheses. A recently developed alternative involves the use of 1,1'-carbonyldiimidazole (CDI) as a coupling reagent and caesium fluoride (CsF) as a catalyst.[6,7] Dendritic scaffolds based on bis-MPA were reportedly synthesised by fluoride-promoted esterification (FPE) on a multigram scale in high yields (>90%) using simple purification, under sustainable conditions. This synthetic strategy may alleviate problems associated with poor mass efficiency of the anhydride route, and overcome scaling issues. Focal point manipulation allowed the formation of ATRP bromoinitiators which were used in the methanolic copolymerisation of nBMA and bifunctional monomer EGDMA to generate hyperbranched polydendrons (HPDs), bearing the dendron functionality at every primary chain-end. Carefully controlling the brancher:initiator ratio to avoid cross-linking of the polymer core, and to compensate for varying initiator efficiency of the dendron macroinitiators, yielded high molecular weight, soluble branched polymers (up to M_w = 3.7 x 10^6 g mol^{-1}). ATRP was applied for polymer synthesis due to its versatility towards monomers and its tolerance to various functional groups and solvents. Cytotoxicity assays of polymers made via ATRP previously within the research group[8] have not revealed any toxicity with Caco-2 cells (human epithelial colorectal

adenocarcinoma cell line) across a range of nanoparticle concentrations and hence it is not believed that the residual copper catalyst renders the materials unusable for biological studies, as reported in many publications. However, scale-up of ATRP procedures may be difficult; therefore, more conventional chemistries would facilitate the application of materials demonstrated in this study.

6.2 Post-polymerisation modification

With the successful formation of a range of materials that were targeted to address the chosen strategy for controlling the placement of surface functionality, post-polymerisation modification was utilised through the xanthate chemistry. Manipulation of peripheral xanthate groups of G_0-G_3 dendrons avoided the direct handling of thiols, which were shown to be controllably generated *in situ* under mild basic conditions. Thiol-acrylate Michael addition allows the incorporation of a wide range of functional groups at the periphery of dendritic materials in a simple, one-pot reaction. Statistical modification of xanthate functional materials, via either the sequential or simultaneous strategy, allowed control over the molar average of functional groups introduced. Sequential and simultaneous Michael addition offer respective advantages; sequential thiol Michael addition allows incorporation of sensitive or highly reactive functionality at a late stage in the synthesis, whereas simultaneous Michael addition reduces thiol isolation seen for sequential multifunctionalisation of higher generation dendrons, and reduces the number of reaction and purification steps. The functional acrylates used in this research were chosen as hydrophobic benzyl (Bz) groups may induce opsonin adsorption, which may promote immune recognition and uptake by macrophages; whereas dimethyl amino (Am) groups have been previously shown[9] to lead to enhanced uptake in ATHP-1 and Caco-2 cell studies. Detailed analysis of

the resulting multifunctional dendrons showed that statistical modification of HPDs has the potential to lead to materials with significant homogeneity, not unlike the targeted patchy materials. This is not completely unexpected, but the level of homogeneity formed was surprising and shown very clearly by MALDI-TOF analysis of the model dendron studies; this may actually provide an easier route to patchy materials with benefits not unlike those seen from our more detailed and precise proof-of-concept. Other approaches to generate truly statistically multifunctionalised materials may be available, but xanthates were maintained and a new approach was taken to create the more clear segregation of chemistry required for the proof-of-concept demonstration.

6.3 Particle formation and patchiness

Co-initiated HPD synthesis with G_0 and G_3 dendron initiators and a PEG(2K) macroinitiator was chosen as the route to achieve statistical and patchy distributions of surface functional groups on resulting nanomaterials. Nanoprecipitation for the formation of nanoparticles was successfully applied to these systems and long-term stability (>1 year) was also seen. The formation of patchy particles is somewhat controversial; imaging of the patchiness was shown via electron microscopy of thiol-functional polymer nanoparticles with coordinated gold nanoparticles (GNPs). However, even this approach showed that despite the statistics of patchiness being biased towards the G_3-containing materials, significant patchiness was also presented on the structures possessing G_0 dendrons. The imaging of thiol-containing materials was highly successful and directly extrapolated to the Am/Bz-containing materials, however the author is aware that direct imaging of patchiness in these materials was not achieved and is postulated without direct evidence. G_0 and G_3 individually co-initiated HPDs with PEG-initiators allowed the direct biological comparison of materials with statistical and

patchy multifunctionality at the surface, however, other materials would be required to allow a full and fair demonstration of the effects of functional group distribution on cellular accumulation; for example G_3-(Am/Bz)/PEG, G_3-Bz/PEG, G_3-Am/PEG, G_0-Bz/PEG and G_0-Am/PEG, Fig. 6.1.

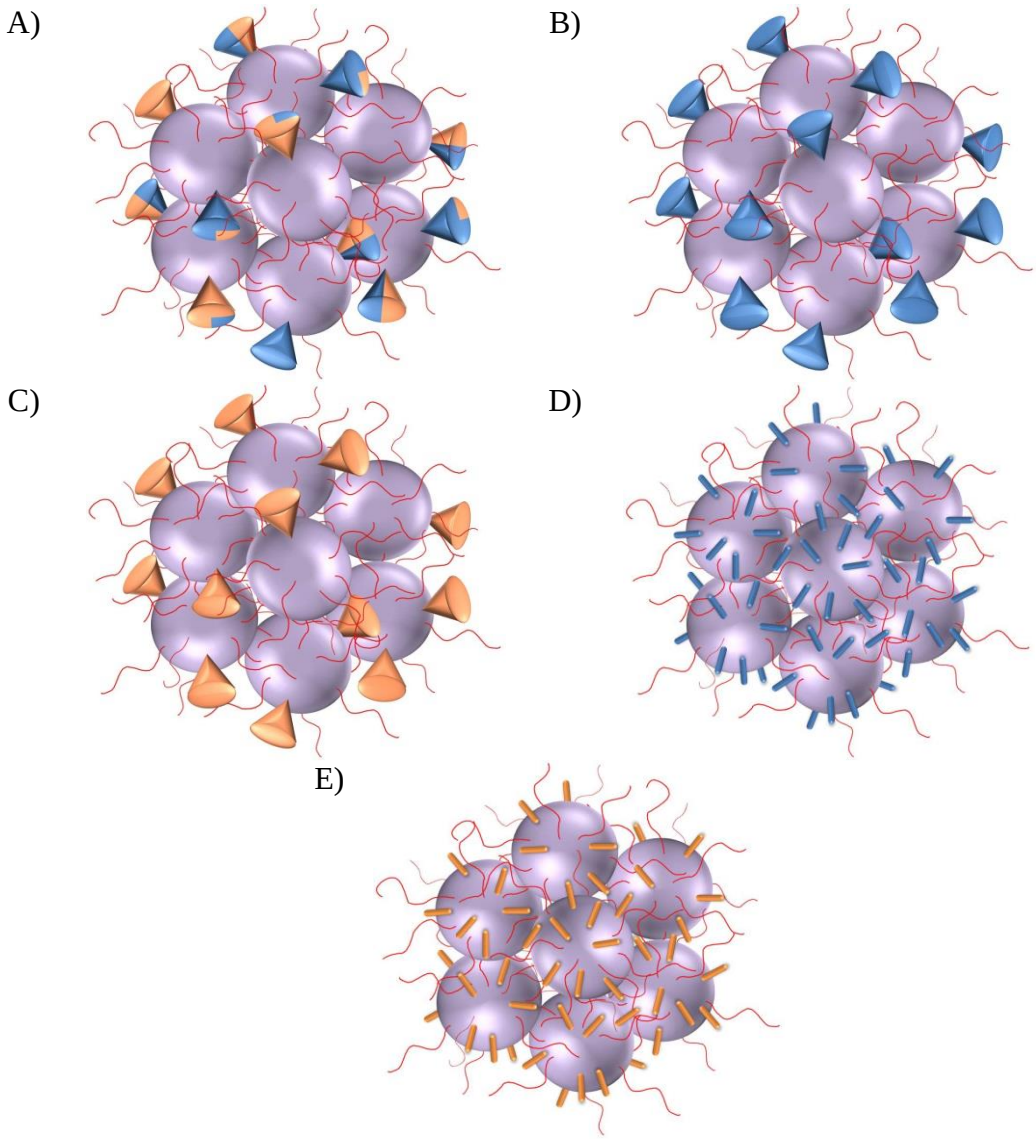

Fig. 6.1 Examples of other materials required to demonstrate the effects of functional group distribution on cellular accumulation; A) G_3-(Am/Bz)/PEG, B) G_3-Bz/PEG, C) G_3-Am/PEG, D) G_0-Bz/PEG and E) G_0-Am/PEG (blue = Bz, orange = Am)

The extremes of G_0-(Am/Bz)/PEG and G_3-(Am/Bz)/PEG were selected to establish a proof-of-concept and a clear difference was seen.

6.4 Biological interactions and outlook

Clear differences between nanoparticles formed from co-initiated HPDs with patchy (G_3) and statistical (G_0) distributions of peripheral functional groups were seen in each of the cellular accumulation studies (ATHP-1, THP-1, +/- collagen). The cellular accumulation ratio (CAR) of patchy and statistically multifunctionalised nanoparticles was monitored using ^{3}[H] radiolabelling and displayed a 3.4-fold increase in CAR for materials with a patchy distribution of surface functional groups, thus demonstrating that functional group distribution affects cellular interaction, which can be tailored using the co-initiated HPD platform. Further cell studies to establish the mechanisms of uptake could involve monitoring CAR of nanoparticles in serum-free experiments to determine whether non-specific protein binding (opsonin adsorption) influences phagocytosis. Another study could draw a comparison between HIV-infected and non-infected macrophage uptake of the nanoparticles; increased phagocytosis is expected for infected macrophages, however, this effect may be enhanced for particles with a patchy distribution of surface functional groups.

There is potential for this research to direct therapeutic nanoparticle design in the future, with this chemistry providing a significant simplification to other reported approaches to patchiness. However, the chemistry presented here is not trivial and even simpler strategies would be required to build towards commercial or clinical applications. Drug encapsulation into these systems was not carried out during this research, and would need to be demonstrated for therapeutic applications. A clear outcome of this research is the detailed study of statistical functionalisation of dendritic macromolecules, which brings many reports of low level modification of dendrimer and dendrimer-like systems into some question.

Overall, this thesis has taken clear steps towards demonstrating the value of patchiness on particles and the modification of biological interactions. Future exploitation will need even

simpler chemistry that can be readily scaled, or the application of this approach will be considerably limited to very rare clinical conditions where no other approach exists to aid therapy. The thesis has shown there is value in following these approaches.

6.5 References

1. H. Ihre, O. L. Padilla De Jesús, and J. M. J. Fréchet, *J. Am. Chem. Soc.*, 2001, **123**, 5908–5917.
2. M. Malkoch, E. Malmström, and A. Hult, *Macromolecules*, 2002, **35**, 8307–8314.
3. S. E. R. Auty, O. Andren, M. Malkoch, and S. P. Rannard, *Chem. Commun.*, 2014, **50**, 6574–6577.
4. S. E. R. Auty, O. C. J. Andrén, F. Y. Hern, M. Malkoch, and S. P. Rannard, *Polym. Chem.*, 2014, **6**, 573–582.
5. F. Y. Hern, S. E. R. Auty, O. C. J. Andren, M. Malkoch, and S. P. Rannard, *Polym. Chem.*, 2017, **8**, 1644–1653.
6. S. García-Gallego, D. Hult, J. V Olsson, and M. Malkoch, *Angew. Chem. Int. Ed. Engl.*, 2015, **54**, 2416–9.
7. P. Stenström, O. C. J. Andrén, and M. Malkoch, *Molecules*, 2016, **21**, 366.
8. F. L. Hatton, *Hyperbranched polydendrons: a new macromolecular architecture*. Springer, 2014.
9. H. E. Rogers (2016), *Exploring Hyperbranched-Polydendron Chemistry and Architecture for Nanomedicine Applications.* PhD thesis, University of Liverpool.

CHAPTER 7

Experimental

7.1 Materials and Methods

7.1.1 Materials

All compounds were purchased from Sigma Aldrich unless otherwise stated and used without further purification. Potassium ethyl xanthogenate, 2-bromoacetic acid, pyridine, 4-dimethylaminopyridine (DMAP), 2,2-dimethoxypropane, N,N'-dicyclohexylcarbodiimide (DCC), benzyl acrylate and 2-(dimethylamino)ethyl acrylate (DMAEA) were purchased from Alfa Aesar and used without further purification. *Para*-toluene sulfonyl ethanol (*p*-TSe) was purchased from Fluorochem and used without further purification. Dichloromethane, hexane and ethyl acetate were HPLC grade and supplied by Fisher Scientific. Analytical TLC was performed on commercial Merck plates coated with silica gel. Flash chromatography was performed using a Grace Reveleris Flash System with Silica gel Flash Cartridges.

7.1.2 Analysis

Nuclear magnetic resonance (NMR): Spectra were recorded using a Bruker Avance 400 spectrometer, operating at 400 MHz for ^{1}H NMR and 100 MHz for ^{13}C NMR, in $CDCl_3$, CD_3OD or D_2O purchased from Goss Scientific. Chemical shifts (δ) are reported in parts per million (ppm) and TMS was used as an internal standard for both ^{1}H and ^{13}C spectra.

Mass Spectrometry (MS): Chemical ionisation (CI) mass spectra were obtained using an Agilent GC/Q-TOF 7200 instrument, using methane CI gas; whilst electrospray ionisation (ESI) mass spectra was obtained using a MicroMass LCT mass spectrometer using electron ionisation and direct infusion syringe pump sampling. All samples were diluted with methanol. Matrix-assisted laser desorption/ionisation - time of flight mass spectrometry (MALDI-TOF MS) sample solutions were prepared with a 2 mg/mL concentration in THF.

Matrix solution was prepared at a concentration of 10 mg/mL in THF and 1 mg/mL Na counter ion solution was prepared. 5 μL of sample solution, 20 μL of matrix solution and 1.5 μL of counter ion was added to an Eppendorf sample tube and homogenised. Solution was deposited on a stainless steel sample plate and the solvent allowed to evaporate. Spectrum acquisitions were conducted on a Bruker UltraFlex MALDI-TOF MS with SCOUT-MTP Ion source (Bruker Daltonics, Bremen) equipped with a N_2-laser (337 nm), a gridless ion source and a reflector. All spectra were acquired using a reflector-positive method with an acceleration voltage of 25 kV and a reflector voltage of 26.3 kV. The detector mass range was set to exclude everything under 1000 Da in order to exclude high intensity peaks from the lower mass range. A total of 1000 shots were performed per sample and the laser intensity was set to the lowest possible value for acquisition of high resolution spectra. The instrument was calibrated using SpheriCal^{TM} calibrants purchased from Polymer Factory Sweden AB. The obtained spectra were analysed with FlexAnalysis Bruker Daltonics, Bremen, version 2.2.

Elemental microanalysis: Recorded on a Thermo FlashEA 1112 series CHNSO elemental analyser.

Size Exclusion Chromatography (SEC): Carried out using a Malvern Viscotek SEC Max equipped with a GPCmax VE2001 autosampler, two Viscotek T6000 columns (and a guard column), a refractive index detector VE3580 and a 270 Dual Detector (light scattering and viscometer) A mobile phase of THF containing 2% triethylamine (v/v) at 35 °C, or DMF containing 0.01 M LiBr at 60 °C, was used as the eluent, with a flow rate of 1mL min^{-1}.

Dynamic light scattering (DLS): Measurements were carried out using a Malvern Zetasizer Nano ZS (4 mW He-Ne laser; wavelength 633 nm), at 25 °C using plastic disposable cuvettes for aqueous dispersions.

Transmission electron microscopy (TEM): Images were recorded using a Hitachi S-4800 FE-SEM at 20 kV. 10 μL of aqueous nanoparticle suspension was pipetted directly onto a Cu (holey carbon) 400 mesh 3 mm TEM grid (Agar Scientific) and blotted with filter paper.

7.2 Chapter 2 compounds

Isopropylidene-2,2-bis(methoxy)propionic Acid **[Acet$_1$-G$_1$-COOH];[1].** 2,2-Bis(hydroxymethyl)-propionic acid (bis-MPA) (100 g, 0.746 mol, 1 equiv.), 2,2-dimethoxypropane (116.7 g, 137.24 mL, 1.12 mol, 1.5 equiv.), and *p*-toluenesulfonic acid monohydrate (7.09 g, 37.0 mmol, 0.05 equiv.) were added to 500 mL of acetone. The reaction mixture was stirred for 2 hours at ambient temperature (clear, colourless). After this time, the catalyst was neutralised by addition of 10 mL NH_4OH:EtOH (1:1 mixture), resulting in salt precipitation. The product was obtained by removal of acetone *in vacuo*, dissolving the crude solid in CH_2Cl_2 (750 mL), washing the organic layer twice with distilled water (2 x 300 mL), drying over $MgSO_4$ and evaporating to dryness. Yield: 100.86 g, white solid, (78%). ^{1}H NMR (400 MHz, $CDCl_3$): δ = 1.22 (s, 3H), 1.42 (s, 3H), 1.45 (s, 3H), 3.68 (d, *J* = 12.1 Hz, 2H), 4.20 (d, *J* = 12.1 Hz, 2H). ^{13}C NMR (100 MHz, $CDCl_3$): δ = 18.47, 21.92, 25.18, 41.86, 65.86, 98.43, 180.31. This compound was prepared by the procedure reported by Ihre *et al*.[1] Spectroscopic data agreed with those reported.

Isopropylidene-2,2-bis(methoxy)propionic Anhydride **[Acet$_2$-G$_1$-Anhy];[2].** [Acet$_1$-G$_1$-COOH];[1] (88.94 g, 0.511 mol, 1 equiv.) and N,N'-Dicyclohexylcarbodiimide (DCC) (52.68 g, 0.255 mol, 0.50 equiv.) were added to 500 mL of CH_2Cl_2. The reaction mixture was stirred at ambient temperature for 48 hours. The precipitated N,N'-dicyclohexylurea (DCU) byproduct was removed by filtration and washed with a small volume of CH_2Cl_2. The crude

product was purified by precipitating the filtrate into 2.5 L of cold hexane (cooled with dry ice bath) with vigorous stirring. Yield: 84.18 g, white viscous oil, (99%). ^{1}H NMR (400 MHz, $CDCl_3$): δ = 1.24 (s, 3H), 1.40 (s, 3H), 1.44 (s, 3H), 3.69 (d, *J* = 12.1 Hz, 4H), 4.21 (d, *J* = 12.1 Hz, 4H). ^{13}C NMR (100 MHz, $CDCl_3$): δ = 17.70, 21.73, 25.56, 43.59, 65.64, 98.42, 169.57. This compound was prepared from [1] according to the procedure reported by Malkoch *et al*.[2] Spectroscopic data agreed with those reported.

General esterification procedure for divergent dendron growth, [Acet$_1$-G$_1$-TSe];[3]. [Acet$_1$-G$_1$-Anhy];[2] (41.88 g, 127 mmol, 1.3 equiv.), *para*-toluene sulfonyl ethanol (*p*-TSe) (19.53 g, 98 mmol, 1 equiv.) and 4-dimethylaminopyridine (DMAP) (2.38 g, 20 mmol, 0.2 equiv.) were dissolved in anhydrous pyridine (40 mL, 5 equiv. per OH-group) and anhydrous CH_2Cl_2 (120 mL 1:3 ratio of pyridine:CH_2Cl_2 (v/v)) under a nitrogen atmosphere. The reaction was left to stir at ambient temperature for 16 hours, monitoring the reaction using TLC to confirm the loss of the starting alcohol. Following this, approximately 40 mL of distilled water was added and stirred vigorously at ambient temperature for an additional 2 hours to quench the excess anhydride. The product was isolated by diluting the mixture with CH_2Cl_2 (1 L) and washing with 1 M $NaHSO_4$ (3 x 400 mL), 1M $NaHCO_3$ (3 x 400 mL), and brine (1 x 400 mL). The organic layer was dried over $MgSO_4$ and evaporated to dryness. Residual solvent was removed under high vacuum overnight. Purification by liquid chromatography on silica was not required for the isolation of [3]. Yield: 33.69 g, colourless viscous oil, (97%). ^{1}H NMR (400 MHz, $CDCl_3$): δ = 1.07 (s, 3H), 1.35 (s, 3H), 1.41 (s, 3H), 2.46 (s, 3H), 3.45 (t, 2H, *J* = 6.2 Hz), 3.56 (d, 2H, *J* = 11.9 Hz), 4.06 (d, 2H, *J* = 11.9 Hz), 4.45 (t, 2H, *J* = 6.2 Hz), 7.38 (d, 1H, *J* = 7.9 Hz), 7.81 (d, 1H, *J* = 7.9 Hz). ^{13}C NMR (100 MHz, $CDCl_3$): δ = 18.26, 21.62, 22.12, 25.09, 41.69, 55.06, 58.03, 65.75, 98.05, 128.17, 130.11, 136.14, 145.28, 173.72. Calcd: $[MH]^+$ ($C_{17}H_{25}O_6S$) = 357.13 Da. Found: CI-MS:

$[MH]^+$ = 357.14 Da. Anal. Calcd for $C_{17}H_{24}O_6S$: C, 57.28; H, 6.79; S, 9.00. Found: C, 57.30; H, 6.81; S, 8.89.

General deprotection procedure for removal of acetonide protecting groups, [$(OH)_2$-G_1-TSe];[4]. DOWEX 50W-X2 (approx. 6 g) was added to a solution of [$Acet_1$-G_1-TSe];[3] (34.73 g, 97 mmol, 1 equiv.) in methanol (350 mL) and allowed to stir at 50 °C for 3 hours. The deprotection was monitored by TLC until total disappearance of the starting material resulted. Once complete, the resin was filtered off and the solution evaporated to dryness. Residual solvent was removed under high vacuum overnight. Yield: 30.49 g, white crystals, (99%). ^{1}H NMR (400 MHz, CD_3OD): δ = 1.05 (s, 3H), 2.47 (s, 3H), 3.15 (s, br, 1H), 3.44 (t, 2H, *J* = 5.8 Hz), 3.73-3.85 (dd, 4H, *J* = 11.6 Hz), 4.53 (t, 2H, *J* = 5.8 Hz), 7.39 (d, 2H, *J* = 8.0 Hz), 7.80 (d, 2H, *J* = 8.0 Hz). ^{13}C NMR (100 MHz, CD_3OD): δ = 17.06, 21.74, 49.65, 55.14, 57.42, 67.96, 128.07, 130.22, 135.55, 145.57, 175.22. Calcd: $[M+Na]^+$ ($C_{14}H_{20}NaO_6S$) = 339.10 Da. Found: ESI-MS: $[M+Na]^+$ = 339.10 Da. Anal. Calcd for $C_{14}H_{20}O_6S$: C, 53.15; H, 6.37; S, 10.14. Found: C, 53.29; H, 6.44; S, 10.01.

[$Acet_2$-G_2-TSe];[5]. [($OH)_2$-G_1-TSe];[4] (14.73 g, 46.56 mmol, 1 equiv.), DMAP (2.56 g, 20.95 mmol, 0.45 equiv.), [2] (46.15 g, 139.68 mmol, 3 equiv.), 38 mL pyridine and 114 mL CH_2Cl_2 were reacted according to the general esterification procedure, resulting in a viscous colourless oil that was purified by liquid chromatography on silica, eluted from EtOAc:hexane (10:90) increasing the polarity to EtOAc:hexane (50:50). Yield: 26.35 g, colourless viscous oil, (90%). ^{1}H NMR (400 MHz, $CDCl_3$): δ = 1.11 (s, 6H), 1.17 (s, 3H), 1.34 (s, 6H), 1.41 (s, 6H), 2.46 (s, 3H), 3.45 (t, 2H, *J* = 6.2 Hz), 3.61 (d, 4H, *J* = 11.9 Hz), 4.13 (d, 4H, *J* = 11.9 Hz), 4.19 (dd, 4H, *J* = 11.1 Hz), 4.45 (t, 2H, *J* = 6.2 Hz), 7.38 (d, 2H, *J* = 8.1 Hz), 7.80 (d, 2H, *J* = 8.1 Hz).^{13}C NMR (100 MHz, $CDCl_3$): δ = 17.37, 18.42, 21.65,

25.68, 42.09, 46.64, 54.83, 58.32, 65.06, 65.98, 65.98, 98.09, 128.05, 130.20, 136.24, 145.24, 171.98, 173.46. Calcd: $[M+Na]^+$ ($C_{30}H_{44}NaO_{12}S$) = 651.73 Da. Found: ESI-MS: $[M+Na]^+$ = 651.20 Da. Anal. Calcd for $C_{30}H_{44}O_{12}S$: C, 57.31; H, 7.05; S, 5.10. Found: C, 58.10; H, 7.16; S, 4.72.

[$(OH)_4$-G_2-TSe];[6]. DOWEX 50W-X2 (approx. 5 g) and $Acet_2$-G_2-TSe [5] (25.26 g, 40.18 mmol, 1 equiv) dissolved in methanol (250 mL) was reacted according to the general deprotection procedure. Yield: 20.72 g, white crystals, (99%). ^{1}H NMR (400 MHz, CD_3OD): δ = 1.13 (s, 9H), 2.46 (s, 3H), 3.58 (s, 2H), 3.64 (dd, 4H, *J* = 11.2 Hz), 4.10 (d, 4H, *J* = 11.2 Hz), 4.43 (t, 2H, *J* = 5.6 Hz), 7.47 (d, 2H, *J* = 8.2 Hz), 7.82 (d, 2H, *J* = 8.2 Hz). ^{13}C NMR (100 MHz, CD_3OD): δ = 17.32, 18.46, 21.54, 25.56, 42.05, 46.66, 54.90, 58.35, 65.06, 66.00, 98.04, 128.15, 130.07, 136.20, 145.22, 172.06, 173.40. Calcd: $[M+Na]^+$ ($C_{24}H_{36}NaO_{12}S$) = 571.18 Da. Found: ESI-MS: $[M+Na]^+$ = 571.20 Da. Anal. Calcd for $C_{24}H_{36}O_{12}S$: C, 52.54; H, 6.61; S, 5.84. Found: C, 52.49; H, 6.56; S, 5.31.

[$Acet_4$-G_3-TSe];[7]. [($OH)_4$-G_2-TSe];[6] (5.89 g, 11 mmol, 1 equiv.), DMAP (0.81 g, 7 mmol, 0.62 equiv.), [2] (21.27 g, 64 mmol, 6 equiv.), 53 mL pyridine and 160 mL CH_2Cl_2 were reacted according to the general esterification procedure, resulting in a viscous colourless oil that was purified by liquid chromatography on silica, eluted from EtOAc:hexane (20:80) increasing the polarity to EtOAc:hexane (60:40). Yield: 12.46 g, colourless viscous oil, (99%). ^{1}H NMR (400 MHz, $CDCl_3$): δ = 1.14 (s, 12H), 1.18 (s, 3H), 1.27 (s, 6H), 1.35 (s, 12H), 1.41 (s, 12H), 2.46 (s, 3H), 3.46 (t, 2H, *J* = 6.0 Hz), 3.6 (d, 8H, *J* = 12.1 Hz) 4.08-4.22 (m, 12H), 4.31 (m, 8H), 4.48 (t, 2H, *J* = 6.0 Hz), 7.39 (d, 2H), 7.82 (d, 2H).^{13}C NMR (100 MHz, $CDCl_3$): δ = 17.25, 17.68, 18.44, 21.67, 22.01, 25.20, 42.05, 46.63, 46.93, 54.74, 58.32, 64.95, 65.76, 65.93, 65.98, 98.07, 128.15, 130.13, 136.23, 145.11,

171.67, 171.88, 173.47. Calcd: $[M+Na]^+$ ($C_{56}H_{84}NaO_{24}S$) = 1195.50 Da. Found: ESI-MS: $[M+Na]^+$ = 1195.50 Da. Anal. Calcd for $C_{56}H_{84}O_{24}S$: C, 57.32; H, 7.22; S, 2.73. Found: C, 57.33; H, 7.18; S, 2.35.

[$(OH)_8$-G_3-TSe];[8]. DOWEX 50W-X2 (approx. 4 g) and $Acet_4$-G_3-TSe [7] (22.66 g, 19 mmol, 1 equiv) dissolved in methanol (300 mL) was reacted according to the general deprotection procedure. Yield: 19.44 g, white crystals, (99%). ^{1}H NMR (400 MHz, CD_3OD): δ = 1.17 (s, 15H), 1.30 (s, 6H), 2.49 (s, 3H), 3.56- 3.73 (m, 18H), 4.14-4.38 (m, 12H), 4.49 (t, 2H, *J* = 5.5 Hz), 7.51 (d, 2H), 7.87 (d, 2H). ^{13}C NMR (100 MHz, CD_3OD): δ = 17.40, 17.71, 18.35, 21.61, 47.74, 47.88, 51.91, 55.75, 59.77, 65.91, 66.15, 67.06, 129.38, 131.30, 138.01, 146.83, 173.33, 173.70, 175.97. Calcd: $[M+Na]^+$ ($C_{44}H_{68}NaO_{24}S$) = 1035.37 Da. Found: ESI-MS: $[M+Na]^+$ = 1035.40 Da. Anal. Calcd for $C_{44}H_{68}O_{24}S$: C, 52.17; H, 6.77; S, 3.17. Found: C, 51.97; H, 6.65; S, 3.15.

2-((Ethoxycarbonothioyl)thio)acetic acid **[Xan-COOH];[9].** Potassium ethyl xanthogenate (53.06 g, 331 mmol) was stirred in acetone (400 mL). A solution of 2-bromoacetic acid (38.35 g, 276 mmol) in acetone (100 mL) was added dropwise over 20 minutes. The reaction was left to stir overnight at ambient temperature. The precipitated potassium bromide by-product was filtered off and washed with a small volume of acetone. The solvent was removed under vacuum. The residue was then diluted in CH_2Cl_2 (300 mL) and washed with brine (3 x 100 mL). The organic phase was dried over $MgSO_4$ and evaporated to give **[9]** as a pale yellow solid. Yield: 36.35g (73%) ^{1}H NMR (400 MHz, $CDCl_3$): δ = 1.43 (t, 3H, *J* = 7.2 Hz), 3.96 (s, 2H), 4.66 (q, 2H, *J* = 7.2 Hz), 9.12 (s, 1H, br). ^{13}C NMR (100 MHz, $CDCl_3$): δ 13.79, 37.56, 70.99, 174.13, 212.0.

2-((Ethoxycarbonothioyl)thio)acetic anhydride **[Xan-Anhy];[10]**. [Xan-COOH];[9] (27.53 g, 152 mmol, 1 equiv.) was dissolved in 100 mL CH_2Cl_2. A solution N,N′-Dicyclohexylcarbodiimide (DCC) (20.76 g, 101 mmol, 0.5 equiv.) in CH_2Cl_2 was slowly added to the mixture, and the reaction allowed to stir at ambient temperature overnight. The reaction was monitored by ^{13}C NMR. Determination of reaction completion resulted by the appearance of the anhydride carbonyl carbon at 163 ppm and the disappearance of the acid carbonyl carbon at 174 ppm. The dicyclohexylurea (DCU) by-product was removed by filtration, washed with a small volume of CH_2Cl_2 and the solvent evaporated under vacuum. Yield: 26.00 g, yellow solid, (99%). ^1H NMR (400 MHz, $CDCl_3$): δ = 1.44 (t, 6H, *J* = 7.1 Hz) 4.07 (s, 4H), 4.67 (q, 4H, *J* = 7.1 Hz). ^{13}C NMR (100 MHz, $CDCl_3$): δ = 13.64, 38.51, 71.28, 163.04, 211.44.

4-(Dimethylamino)pyridinium *p*-toluenesulfonate [**DPTS]** – *p*-toluenesulfonic acid monohydrate (7.80 g, 41 mmol, 1 equiv) was dried by azeotropic distillation with 50 mL anhydrous toluene using a dean-stark head (approximately 4 hours). [Note: the solution turned dusty pink during the loss of water]. Following this, the mixture was cooled to 60 °C and 4-dimethylaminopyridine (DMAP) (5 g, 41 mmol, 1 equiv.) in 30 mL of anhydrous toluene at 60 °C added slowly. An off-white precipitate immediately formed upon addition, and the solution was left to stir at 60 °C for 1 hour. The mixture was then cooled and filtered to yield DPTS. The product was recrystallised once from 1,2-dichloroethane to yield white crystals. Yield: 11.83 g (98%). ^1H NMR (400 MHz, $CDCl_3$): δ = 2.34 (s, 3H), 3.17 (s, 6H), 6.76 (d, *J* = 7.7 Hz, 2H), 7.16 (d, *J* = 8.2 Hz, 2H), 7.81 (d, *J* = 8.2 Hz, 2H), 8.16 (d, *J* = 7.7 Hz, 2H). ^{13}C NMR (100 MHz, $CDCl_3$): δ = 21.34, 40.15, 106.86, 126.00, 128.72, 139.49, 142.76, 157.26. Anal. Calcd for $C_{14}H_{18}N_2O_3S$: C, 57.12; H, 6.16; N, 9.52; S, 10.89. Found:

C, 57.30; H, 6.12; N, 9.51; S, 10.84. This compound was prepared by the procedure reported by Moore and Stupp. The above spectroscopic data agreed with that reported.[3]

General procedure for functionalisation with Xanthate surface groups using DCC/DPTS chemistry, [Xan_1-G_0-TSe];[11]. *Para*-toluenesulfonyl ethanol (*p*-TSe) (2.76 g, 14 mmol, 1 equiv.), [Xan-COOH];[9] (2.50 g, 14 mmol, 1 equiv.) and DPTS (4.47 g, 15 mmol, 1.1 equiv.) were dissolved in CH_2Cl_2 (anhydrous, 35 mL) under a nitrogen atmosphere. Dicyclohexylcarbodiimide (DCC) (3.13 g, 15 mmol, 1.1 equiv.) was added in CH_2Cl_2 (anhydrous, 15 mL) whilst cooling in an ice bath. The reaction was allowed to warm to ambient temperature and the reaction mixture stirred overnight for 16 hours. The precipitated dicyclohexylurea (DCU) by-product was removed by filtration and washed with a small volume of CH_2Cl_2. The crude product was purified by liquid chromatography on silica gel, eluting with hexane gradually increasing to 30:70 ethyl acetate:hexane.. Yield: 3.75 g, yellow oil (75%) ^{1}H NMR (400 MHz, $CDCl_3$): δ = 1.13 (t, 3H, *J* = 7.30 Hz), 2.18 (s, 3H), 3.18 (t, 2H, *J* = 6.1 Hz), 3.42 (s, 2H), 4.19 (t, 2H, *J* = 6.1 Hz), 4.35 (q, 2H, *J* = 7.1 Hz), 7.10 (d, 2H, *J* = 8.1 Hz), 7.52 (d, 2H, *J* = 8.1 Hz). ^{13}C NMR (100 MHz, $CDCl_3$): δ = 13.48, 21.34, 37.26, 54.52, 58.74, 70.62, 127.96, 129.68, 136.00, 144.83, 167.08, 212.14. Calcd: $[M+Na]^+$ ($C_{14}H_{18}NaO_5S_3$) = 385.03. Found ESI-MS: $[M+Na]^+$ = 385.0. Calcd for $C_{14}H_{18}O_5S_3$: C, 46.39; H, 5.01; S, 26.53. Found: C, 46.56; H, 5.00; S, 26.40.

[Xan_2-G_1-TSe];[12]. This compound was prepared by the procedure reported by Auty *et al*.[4] The hydroxyl-terminated dendron [$(OH)_2$-G_1-TSe];[4] (10.23 g, 32 mmol, 2.5 equiv.), [Xan-COOH];[9] (17.55 g, 97 mmol, 7.5 equiv.) and DPTS (3.81 g, 13 mmol, 1 equiv.) were dissolved in CH_2Cl_2 (anhydrous, 100 mL) under a nitrogen atmosphere. DCC (22.01 g, 107 mmol, 8.25 equiv.) was added in CH_2Cl_2 (anhydrous, 50 mL) and the reaction mixture stirred

overnight for 16 hours. The crude product was purified by liquid chromatography on silica gel, eluting with hexane gradually increasing to 40:60 ethyl acetate:hexane to give a viscous oil. Yield: 17.36 g, orange viscous oil (84%) ^{1}H NMR (400 MHz, $CDCl_3$): δ = 1.16 (s, 3H), 1.42 (t, 6H, *J* = 7.1 Hz), 2.46 (s, 3H), 3.44 (t, 2H, *J* = 6.0 Hz), 3.91 (s, 4H), 4.17 (dd, 4H, *J* = 11.0), 4.46 (t, 2H, *J* = 6.0 Hz), 4.65 (q, 4H, *J* = 7.1 Hz), 7.39 (d, 2H, *J* = 8.0 Hz), 7.81 (d, 2H, *J* = 8.0 Hz). ^{13}C NMR (100 MHz, $CDCl_3$): δ = 13.80, 17.52, 21.74, 37.77, 46.22, 54.99, 58.36, 66.13, 70.86, 128.09, 130.12, 136.20, 145.31, 167.26, 171.82, 212.50. Calcd: $[M+Na]^+$ ($C_{24}H_{32}NaO_{10}S_5$) = 663.06. Found ESI-MS: $[M+Na]^+$ = 663.0. Calcd for $C_{24}H_{32}O_{10}S_5$: C, 44.98; H, 5.03; S, 25.02. Found: C, 45.61; H, 5.15; S, 25.68.

[Xan$_4$-G$_2$-TSe];[13]. The hydroxyl-terminated dendron [(OH)$_4$-G$_2$-TSe];[6], [Xan-COOH];[9], DPTS (3.07 g, 10 mmol) and DCC (17.76 g, 86 mmol) were allowed to react according to the general esterification procedure in anhydrous CH_2Cl_2 (200 mL) for 18 hours. The crude product was purified by liquid chromatography on silica gel, eluting with hexane gradually increasing to 50:50 ethyl acetate:hexane. Yield: 14.04 g, orange viscous oil (90%). ^{1}H NMR (400 MHz, $CDCl_3$): δ = 1.20 (s, 3H), 1.25 (s, 6H), 1.42 (t, 12H, *J* = 7.1 Hz), 2.46 (s, 3H), 3.46 (t, 2H, *J* = 5.9 Hz), 3.94 (s, 8H), 4.20 (s, 4H), 4.26 (dd, 8H, *J* = 11.0), 4.46 (t, 2H, *J* = 5.9 Hz), 4.64 (q, 8H, *J* = 7.1 Hz), 7.40 (d, 2H, *J* = 8.0 Hz), 7.82 (d, 2H, *J* = 8.0 Hz). ^{13}C NMR (100 MHz, $CDCl_3$): δ = 13.76, 17.37, 17.90, 21.69, 37.70, 46.44, 46.64 54.85, 58.48, 65.58, 66.24, 70.85, 128.12, 130.24, 136.35, 145.26, 167.36, 171.65, 171.82, 212.56. Calcd: $[M+Na]^+$ ($C_{44}H_{60}NaO_{20}S_9$) = 1219.12. Found MALDI-TOF MS: $[M+Na]^+$ = 1219.1. Calcd for $C_{44}H_{60}O_{20}S_9$: C, 44.13; H, 5.05; S, 24.1. Found: C, 44.83; H, 5.19; S, 24.34.

General procedure for functionalisation with Xanthate surface groups using anhydride chemistry, [Xan$_8$-G$_3$-TSe];[14]. This compound was prepared by the procedure reported by

Auty *et al*.[5] [$(OH)_8$-G_3-TSe];[8] (7.24 g, 7 mmol, 1 equiv.) and DMAP (1.40 g, 11 mmol, 1.6 equiv.) were dissolved in anhydrous pyridine (40 mL). After cooling the mixture in an ice bath, [Xan-Anhy];[10] (25.41 g, 74 mmol, 10.4 equiv.) in anhydrous CH_2Cl_2 (80 mL) was added slowly under a nitrogen atmosphere. After stirring at ambient temperature for 16 hours, approximately 15 mL of distilled water was added and stirred vigorously at ambient temperature for an additional 2 hours to quench the excess anhydride. The product was isolated by diluting the mixture with CH_2Cl_2 (350 mL) and washing with 1 M $NaHSO_4$ (3 x 1200 mL), 1M $NaHCO_3$ (3 x 200 mL), and brine (1 x 200 mL). The organic layer was dried over $MgSO_4$ and evaporated to dryness. Purification by liquid chromatography on silica, eluted from EtOAc:hexane (15:85) increasing the polarity to EtOAc:hexane (50:50). Residual solvent was removed under high vacuum overnight. Yield: 10.10 g, orange viscous oil, (61%). ^{1}H NMR (400 MHz, $CDCl_3$): δ = 1.20-1.30 (m, 21H), 1.42 (t, 24H, *J* = 7.2 Hz), 2.47 (s, 3H), 3.47 (t, 2H, *J* = 5.8 Hz), 3.94 (s, 16H), 4.16-4.36 (m, 28H), 4.49 (t, 2H, *J* = 5.8 Hz), 4.64 (q, 16H, *J* = 7.2 Hz) 7.40 (d, 2H), 7.81 (d, 2H). ^{13}C NMR (100 MHz, $CDCl_3$): δ = 13.67, 17.28, 17.63, 17.89, 21.73, 37.64, 46.27, 46.51, 46.75, 54.71, 58.35, 65.44, 66.23, 70.82, 128.15, 130.26, 136.39, 145.22, 167.46, 171.48, 171.63, 171.68, 212.71. Calcd: $[M+Na]^+$ ($C_{84}H_{116}NaO_{40}S_{17}$) = 2331.22 Da. Found: MALDI-TOF MS: $[M+Na]^+$ = 2331.42 Da. Anal. Calcd for $C_{84}H_{116}O_{40}S_{17}$: C, 43.66; H, 5.06; S, 23.59. Found: C, 44.01; H, 5.04; S, 23.86.

General procedure for deprotection of *para*-toluene sulfonyl ester (TSe) - 1,8-diazabicyclo[5.4.0]undec-7-ene (DBU) (1.3 equiv.) added to xanthate functional dendron dissolved in anhydrous CH_2Cl_2. The reaction was stirred under a nitrogen atmosphere for 16 hours and monitored by using TLC (40:60 ethyl acetate:hexane). The product was isolated by diluting the mixture with CH_2Cl_2 (100 mL) and washing with 1 M $NaHSO_4$ (2 x 100 mL). The organic layer was dried over $MgSO_4$ and evaporated to dryness. The product was then

precipitated three times into hexane:ethyl acetate (9:1). Any residual solvent was removed under high vacuum to yield a viscous oil.

[Xan_2-G_1-COOH];[15]. The removal of the *para*-toluene sulfonyl (*p*-TSe) protecting group was carried out as described above with [Xan_2-G_1-TSe];[12] (4.60 g, 7.18 mmol, 1.0 equiv), and DBU (1.40 mL, 9.33 mmol, 1.3 equiv). Yield: 3.10 g, orange viscous oil (94%). ^{1}H NMR (400 MHz, $CDCl_3$): δ = 1.32 (s, 3H), 1.42 (t, *J* = 7.10, 6H), 2.47 (s, 3H), 3.94 (s, 4H), 4.30 (d, *J* = 11.1 Hz, 2H), 4.36 (d, *J* = 11.1 Hz, 2H), 4.64 (q, *J* = 7.1 Hz, 4H). ^{13}C NMR (100 MHz, $CDCl_3$): δ = 13.74, 17.86, 37.74, 46.06, 66.13, 70.87, 167.45, 177.80, 212.53. Calcd: $[M+Na]^+$ ($C_{15}H_{22}NaO_8S_4$) m/z = 481.02. Found: ESI-MS: $[M+Na]^+$ m/z = 481.00. Anal. Calcd for $C_{15}H_{22}O_8S_4$: C, 39.29; H, 4.84; S, 27.97. Found: C, 40.06; H, 5.06 S, 25.82.

[Xan_4-G_2-COOH];[16]. The removal of the *para*-toluene sulfonyl (*p*-TSe) protecting group was carried out as described above with [Xan_4-G_2-TSe];[13] (5.02 g, 4.18 mmol, 1.0 equiv), and DBU (0.81 mL, 5.43 mmol, 1.3 equiv). Yield: 4.05 g, orange viscous oil (93%). ^{1}H NMR (400 MHz, $CDCl_3$): δ = 1.27 (s, 6H), 1.33 (s, 3H), 1.42 (t, *J* = 7.1 Hz, 12H), 3.94 (s, 8H), 4.21-4.36 (m, 12H), 4.64 (q, *J* = 7.1 Hz, 8H). ^{13}C NMR (100 MHz, $CDCl_3$): δ = 13.67, 17.89, 37.64, 46.46, 65.83, 66.40, 71.00, 167.46, 171.68, 175.13, 212.71. Calcd: $[M+Na]^+$ ($C_{35}H_{50}NaO_{18}S_8$) m/z = 1037.07. Found ESI-MS: $[M+Na]^+$ m/z = 1037.1. Anal. Calcd for $C_{35}H_{50}O_{18}S_8$: C, 41.40; H, 4.96; S, 25.27. Found: C, 42.06; H, 5.15; S, 24.82.

[Xan_8-G_3-COOH];[17]. The removal of the *para*-toluene sulfonyl (*p*-TSe) protecting group was carried out as described above with [Xan_8-G_3-TSe];[14] (9.07 g, 3.93 mmol, 1.0 equiv), and DBU (0.76 mL, 5.10 mmol, 1.3 equiv). Yield: 7.97 g, orange viscous oil (95%). ^{1}H NMR (400 MHz, $CDCl_3$): δ = 1.26 (s, 12H), 1.29 (s, 6H), 1.35 (s, 3H), 1.42 (t, *J* = 7.1 Hz, 24H),

3.95 (s, 16H), 4.21-4.36 (m, 28H), 4.64 (q, *J* = 7.1 Hz, 16H). ^{13}C NMR (100 MHz, $CDCl_3$): δ = 13.70, 17.98, 37.70, 46.41, 66.30, 70.91, 167.70, 171.65, 172.95, 212.57. Calcd: $[M+Na]^+$ ($C_{75}H_{106}NaO_{38}S_{16}$) m/z = 2149.19. Found MALDI-TOF: $[M+Na]^+$ m/z = 2151.7. Anal. Calcd for $C_{75}H_{106}O_{38}S_{16}$: C, 42.32; H, 5.02; S, 28.56. Found: C, 43.15; H, 5.09; S, 23.79.

Dendrimer synthesis by convergent growth; [Xan_{12}-G_2-THPE];[18]. Focal point acid functional dendron [Xan_4-G_2-COOH];[16] (3.94 g, 3.78 mmol, 3.8 equiv.), 1,1,1-tris(4-hydroxyphenyl)ethane (THPE) (0.304 g, 0.994 mmol, 1 equiv.) and DPTS (0.878 g, 2.98 mmol, 3 equiv.) were dissolved in CH_2Cl_2 (anhydrous, 20 mL) under nitrogen. DCC (0.861 g, 4.17 mmol, 4.2 equiv.) in CH_2Cl_2 (anhydrous, 10 mL) was added and the reaction left to stir at ambient temperature for 16 hours. The precipitated DCU by-product was removed by filtration and the product isolated by diluting with CH_2Cl_2 (100 mL) and washing with 1 M $NaHSO_4$ (2 x 100 mL). The organic layer was dried over $MgSO_4$ and the solvent removed *in vacuo*. The product was purified by liquid chromatography on silica gel, eluting with ethyl acetate:hexane (10:90, gradually increasing to 50:50). Yield: 1.46 g, orange viscous oil (44%). ^{1}H NMR (400 MHz, $CDCl_3$): δ = 1.29 (s, 21H), 1.41 (t, *J* = 7.1 Hz, 36H), 1.44 (s, 9H), 3.90 (s, 24H), 4.21-4.36 (m, 24H), 4.42 (s, 12H), 4.63 (q, *J* = 7.1 Hz, 24H), 6.98 (d, *J* = 8.8 Hz), 7.11 (d, *J* = 8.8 Hz). ^{13}C NMR (100 MHz, $CDCl_3$): δ = 13.74, 18.02, 37.61, 46.34, 51.74, 66.26, 70.87, 120.77, 129.82, 146.46, 148.43, 167.53, 171.81, 212.65. Calcd: $[M+Na]^+$ ($C_{125}H_{162}NaO_{54}S_{24}$) m/z = 3317.3. Found MALDI-TOF: $[M+Na]^+$ m/z = 3316.4.

2-Hydroxyethyl-2-bromoisobutyrate, **[HEBiB];[19].** Ethylene glycol (272 mL, 4.85 mol, 50 equiv.) and triethylamine (TEA) (28 mL, 0.20 mol, 2 equiv.) were dissolved in anhydrous THF (100 mL). α-Bromoisobutyryl bromide (12 mL, 97.1 mmol, 1 equiv.) was added dropwise over 30 minutes whilst cooling with an ice bath. The reaction was left to stir at

ambient temperature under a nitrogen atmosphere for 16 hours. The product was isolated by pouring the crude mixture into distilled water (800 mL) and extracting the aqueous phase with CH_2Cl_2 (6 x 100 mL). The combined organic layers were washed with 1 M HCl (pH 4) (2 x 300mL), dried over $MgSO_4$ and evaporated to dryness. Residual solvent was removed under high vacuum overnight. Yield: 15.64 g, pale yellow oil, (76%) ^{1}H NMR (400 MHz, $CDCl_3$): δ = 1.96 (s, 6H), 3.88 (m, *J* = 4.7 Hz, 2H), 4.32 (m, *J* = 4.7 Hz, 2H). ^{13}C NMR (100 MHz, $CDCl_3$): δ = 30.70, 55.86, 60.82, 67.47, 171.94. Calcd: $[M+NH_4]^+$ ($C_6H_{15}BrNO_3$) m/z = 228.02. Found: CI MS: $[M+NH_4]^+$ m/z = 228.02. Anal. Calcd for $C_6H_{11}BrO_3$: C, 34.14; H, 5.25. Found: C, 34.63; H, 5.30. This compound was prepared by Jakubowski *et al.*[6] The above spectroscopic data agreed with that reported.

General procedure for focal point modification to α-bromoisobutyrate moiety, [Xan$_1$-G$_0$-BiB];[20]. [Xan-COOH];[9] (2.42 g, 13 mmol, 1 equiv.), [HEBiB];[19] (2.83 g, 13 mmol, 1 equiv.), and DPTS (4.33 g, 15 mmol, 1.1 equiv.) were dissolved in CH_2Cl_2 (anhydrous, 35 mL) under a nitrogen atmosphere. DCC (3.04 g, 15 mmol, 1.1 equiv.) in CH_2Cl_2 (anhydrous, 15 mL) was added and the reaction left to stir at ambient temperature for 16 hours. The precipitated DCU by-product was removed by filtration and the product isolated by diluting the mixture with CH_2Cl_2 (100 mL), washing with distilled water (2 x 100 mL) and brine (1 x 100 mL). The organic layer was dried over $MgSO_4$ and evaporated to dryness. The residue was purified by liquid chromatography on silica, eluting from ethyl acetate:hexane (10:90), gradually increasing the polarity to ethyl acetate:hexane (30:70). Residual solvent was removed under high vacuum overnight. Yield: 3.74 g, yellow oil, (75%). ^{1}H NMR (400 MHz, $CDCl_3$): δ = 1.42 (t, *J* = 7.1 Hz, 3H), 1.94 (s, 6H), 3.96 (s, 2H), 4.41 (s, 4H), 4.65 (q, *J* = 7.1 Hz, 2H). ^{13}C NMR (100 MHz, $CDCl_3$): δ = 13.48, 30.36, 37.44, 55.09, 62.95, 70.43, 167.46, 171.10, 212.14. Calcd: $[M+Na]^+$ ($C_{11}H_{17}BrNaO_5S_2$) m/z = 394.97. Found: ESI-MS: $[M+Na]^+$

m/z = 395.0 Anal. Calcd for $C_{11}H_{17}BrO_5S_2$: C, 35.39; H, 4.59; S, 17.18. Found: C, 35.76; H, 4.57; S, 16.76.

[Xan_2-G_1-BiB];[21]. [Xan_2-G_1-COOH];[15] (8.25 g, 18 mmol, 1 equiv.), [19] (5.70 g, 27 mmol, 1.5 equiv.), DPTS (1.06 g, 3.6 mmol, 0.2 equiv.), DCC (7.43 g, 36 mmol, 2 equiv.) in anhydrous CH_2Cl_2 (80 mL) were reacted according to the general procedure for focal point modification resulting in a viscous yellow oil that was purified by liquid chromatography on silica, eluting from ethyl acetate:hexane (10:90), gradually increasing the polarity to ethyl acetate:hexane (30:70). Yield: 6.39 g, yellow viscous oil, (55%). ^{1}H NMR (400 MHz, $CDCl_3$): δ = 1.28 (s, 3H), 1.42 (t, *J* = 7.1 Hz, 6H), 1.94 (s, 6H), 3.93 (s, 4H), 4.31 (d, *J* = 11.1 Hz, 2H), 4.35 (d, *J* = 11.1 Hz, 2H), 4.40 (s, 4H), 4.65 (q, *J* = 7.1 Hz, 4H). ^{13}C NMR (100 MHz, $CDCl_3$): δ = 13.67, 17.89, 30.74, 37.84, 46.28, 55.28, 62.76, 63.34, 66.21, 70.82, 167.46, 171.49, 172.06, 212.52. Calcd: $[M+Na]^+$ ($C_{21}H_{31}BrNaO_{10}S_4$) m/z = 673.0. Found: ESI-MS: $[M+Na]^+$ m/z = 673.0 Anal. Calcd for $C_{21}H_{31}BrO_{10}S_4$: C, 38.71; H, 4.80; S, 19.68. Found: C, 40.08; H, 4.98; S, 19.50.

[Xan_4-G_2-BiB];[22]. [Xan_4-G_2-COOH];[16] (6.52 g, 6.42 mmol, 1 equiv.), [19] (2.03 g, 9.63 mmol, 1.5 equiv.), DPTS (0.38 g, 1.28 mmol, 0.2 equiv.), DCC (2.65 g, 12.84 mmol, 2 equiv.) in anhydrous CH_2Cl_2 (60 mL) were reacted according to the general procedure for focal point modification resulting in a viscous orange oil that was purified by liquid chromatography on silica, eluting from ethyl acetate:hexane (20:80), gradually increasing the polarity to ethyl acetate:hexane (60:40). Yield: 4.53 g, orange viscous oil, (58%). ^{1}H NMR (400 MHz, $CDCl_3$): δ = 1.26 (s, 6H), 1.29 (s, 3H), 1.42 (t, *J* = 7.2 Hz, 12H), 1.94 (s, 6H), 3.95 (s, 8H), 4.19-4.36 (m, 12H), 4.36-4.49 (m, 4H), 4.64 (q, *J* = 7.1 Hz, 8H). ^{13}C NMR (100 MHz, $CDCl_3$): δ = 13.67, 17.65, 17.87, 30.74, 37.64, 46.27, 46.67, 55.48, 62.90, 63.34,

65.66, 66.21, 70.82, 167.46, 171.37, 171.67, 171.86, 212.71. Calcd: $[M+Na]^+$ ($C_{41}H_{59}BrNaO_{12}S_8$) m/z = 1229.04. Found: ESI-MS: $[M+Na]^+$ m/z = 1229.17. Anal. Calcd for $C_{41}H_{59}BrO_{20}S_8$: C, 40.75; H, 4.92; S, 21.23. Found: C, 39.69; H, 4.92; S, 18.48.

[Xan$_8$-G$_3$-BiB];[23]. [Xan$_8$-G$_3$-COOH];[17] (3.98 g, 1.87 mmol, 1 equiv.), [19] (0.40 g, 1.87 mmol, 1 equiv.), DPTS (0.61 g, 2.06 mmol, 1.1 equiv.), DCC (0.42 g, 2.06 mmol, 1.1 equiv.) in anhydrous CH_2Cl_2 (40 mL) were reacted according to the general procedure for focal point modification resulting in a viscous orange oil that was purified by liquid chromatography on silica, eluting from ethyl acetate:hexane (15:85), gradually increasing the polarity to ethyl acetate:hexane (50:50). Yield: 2.47 g, orange viscous oil, (57%). ^{1}H NMR (400 MHz, $CDCl_3$): δ = 1.26 (s, 12H), 1.28 (s, 6H), 1.32 (s, 3H), 1.42 (t, *J* = 7.1 Hz, 24H), 1.94 (s, 6H), 3.95 (s, 16H), 4.21-4.38 (m, 28H), 4.21 (s, 4H), 4.64 (q, *J* = 7.1 Hz, 16H). ^{13}C NMR (100 MHz, $CDCl_3$): δ = 13.67, 17.89, 30.74, 37.64, 46.27, 55.48, 60.85, 66.21, 70.82, 167.46, 171.67, 212.71. Calcd: $[M+Na]^+$ ($C_{81}H_{115}BrNaO_{40}S_{16}$) m/z = 2341.17. Found: MALDI-TOF: $[M+Na]^+$ m/z = 2341.4. Anal. Calcd for $C_{81}H_{115}BrO_{40}S_{16}$: C, 41.91; H, 4.99; S, 22.09. Found: C, 43.15; H, 5.14; S, 21.85.

Linear ATRP of *tert*-butyl methacrylate (tBMA) in IPA/H$_2$O with [Xan$_2$-G$_1$-BiB];[21] or [Xan$_4$-G$_2$-BiB];[22]; p[(Xan$_2$-G$_1$)-tBMA$_{50}$];[25] and p[(Xan$_4$-G$_2$)-tBMA$_{50}$];[26]. In a typical synthesis, targeting DP_n = 50 monomer units for the primary chains, [Xan$_2$-G$_1$-BiB];[21] (0.1744 g, 0.281 mmol, 1 equiv.), tBMA (2 g, 14.1 mmol, 50 equiv.) and bpy (0.105 g, 0.563 mmol, 2 equiv.) were placed into a 10 mL round-bottomed flask. IPA/H_2O (92.5/7.5 v/v) was added (50 wt% based on tBMA; 2g, 2.6 mL) and the solution stirred and deoxygenated using a nitrogen purge for 10 minutes. Cu(I)Cl (28 mg, 0.281 mmol, 1 equiv) was added to the flask, whilst maintaining a positive flow of nitrogen, and the solution left to

polymerise at 30 °C. The reaction was terminated when conversion reached >95%, indicated by ^{1}H NMR after 18 hours, by exposure to oxygen and addition of THF. The solution was passed through a neutral alumina column to remove the catalytic system, and precipitated twice into cold hexane. After drying the precipitated sample overnight under high vacuum, the polymer was obtained as a white solid.

Branched ATRP of tBMA in IPA/H_2O with [Xan_2-G_1-BiB];[21] or [Xan_4-G_2-BiB];[22]; p[(Xan_2-G_1)-$tBMA_{50}$-*co*-$EGDMA_{0.8}$];[27] and p[(Xan_4-G_2)-$tBMA_{50}$-*co*-$EGDMA_{0.8}$];[28]. In a typical synthesis, targeting DP_n = 50 monomer units for the primary chains, [Xan_2-G_1-BiB];[21] (0.1744 g, 0.281 mmol, 1 equiv.), tBMA (2 g, 14.1 mmol, 50 equiv.), bpy (0.105 g, 0.563 mmol, 2 equiv.) and bifunctional monomer ethylene glycol dimethacrylate (EGDMA) (45 mg, 0.225 mmol, 0.8 equiv.) were placed into a 10 mL round-bottomed flask. IPA/H_2O (92.5/7.5 v/v) was added (50 wt% based on tBMA, 2g, 2.6 mL) and the solution stirred and deoxygenated using a nitrogen purge for 10 minutes. Cu(I)Cl (28 mg, 0.281 mmol, 1 equiv) was added to the flask, whilst maintaining a positive flow of nitrogen, and the solution was left to polymerise at 30 °C. The reaction was terminated when conversion reached >98%, indicated by ^{1}H NMR after 18 hours, by exposure to oxygen and addition of THF. The solution was passed through a neutral alumina column to remove the catalytic system, and precipitated twice into cold hexane. After drying the precipitated sample overnight under high vacuum, the polymer was obtained as a white solid.

Linear ATRP of *n*-butyl methacrylate (nBMA) in methanol with [Xan_1-G_0-BiB];[20], [Xan_2-G_1-BiB];[21], [Xan_4-G_2-BiB];[22] or [Xan_8-G_3-BiB];[23], targeting DP_n = 50 or 100 monomer units; p[(Xan_2-G_1)-$nBMA_{50}$];[29] and p[(Xan_4-G_2)-$nBMA_{50}$];[30], p[(Xan_8-G_3)-$nBMA_{50}$];[31], p[(Xan_1-G_0)-$nBMA_{100}$];[32] , p[(Xan_2-G_1)-$nBMA_{100}$];[33] ,

p[(Xan$_4$-G$_2$)-nBMA$_{100}$];[34] , p[(Xan$_8$-G$_3$)-nBMA$_{100}$];[35]. In a typical synthesis, targeting DP_n = 100 monomer units for the primary chains, [Xan$_2$-G$_1$-BiB];[21] (46 mg, 0.0702 mmol, 1 equiv.), nBMA (1 g, 7.03 mmol, 100 equiv.) and bpy (22 mg, 0.141 mmol, 2 equiv.) were placed into a 5 mL round-bottomed flask. Methanol was added (50 wt% based on nBMA; 2g, 2.6 mL) and the solution stirred and deoxygenated using a nitrogen purge for 30 minutes. Cu(I)Cl (7 mg, 0.0702 mmol, 1 equiv) was added to the flask, whilst maintaining a positive flow of nitrogen, and the solution left to polymerise at 60 °C. The reaction was terminated when conversion reached >95%, indicated by ^{1}H NMR after 21 hours, by exposure to oxygen and addition of THF. The solution was passed through a neutral alumina column to remove the catalytic system, and precipitated twice into cold petroleum ether (40-60 °C). After drying the precipitated sample overnight under high vacuum, the polymer was obtained as a white solid.

Branched ATRP of nBMA in methanol with [Xan$_1$-G$_0$-BiB];[20], [Xan$_2$-G$_1$-BiB];[21], [Xan$_4$-G$_2$-BiB];[22] or [Xan$_8$-G$_3$-BiB];[23]; p[(Xan$_1$-G$_0$)-nBMA$_{100}$-*co*-EGDMA$_{0.7}$];[36], p[(Xan$_2$-G$_1$)-nBMA$_{100}$-*co*-EGDMA$_{0.8}$];[37], p[(Xan$_4$-G$_2$)-nBMA$_{100}$-*co*-EGDMA$_{0.8}$];[38], p[(Xan$_8$-G$_3$)-nBMA$_{100}$-*co*-EGDMA$_{0.8}$];[39]. In a typical synthesis, targeting DP_n = 100 monomer units for the primary chains, [Xan$_2$-G$_1$-BiB];[21] (92 mg, 0.141 mmol, 1 equiv.), nBMA (2 g, 14.1 mmol, 100 equiv.), bpy (44 mg, 0.281 mmol, 2 equiv.) and EGDMA (22 mg, 0.113 mmol, 0.8 equiv.) were placed into a 10 mL round-bottomed flask. Methanol was added (50 wt% based on nBMA, 2g, 2.6 mL) and the solution stirred and deoxygenated using a nitrogen purge for 30 minutes. Cu(I)Cl (14 mg, 0.141 mmol, 1 equiv) was added to the flask, whilst maintaining a positive flow of nitrogen, and the solution was left to polymerise at 60 °C. The reaction was terminated when conversion reached >98%, indicated by ^{1}H NMR after 24 hours, by exposure to oxygen and addition of THF. The solution was passed through

a neutral alumina column to remove the catalytic system, and precipitated twice into cold petroleum ether (40-60 °C). After drying the precipitated sample overnight under high vacuum, the polymer was obtained as a white solid.

7.3 Chapter 3 compounds

General procedure for Sequential Thiol-Michael addition click reactions - Xanthate peripheral dendron (200mg) was dissolved in anhydrous THF (2 mL) and degassed for 5 minutes under a nitrogen atmosphere. *n*-Butylamine (1 equiv. per xanthate group) was added and the reaction left for 1.5 hrs or until completion by TLC (60:40 hexane:ethyl acetate). 2-(Dimethylamino)ethyl (Am) acrylate (1.5 equiv per thiol) was added and the reaction mixture stirred at ambient temperature for 16 hours. The product was isolated by precipitating twice into hexane. Residual solvent was removed under high vacuum to yield a viscous oil. The partially-functionalised product was then dissolved in anhydrous THF (2 mL) and degassed for 5 minutes under a nitrogen atmosphere. *n*-Butylamine (1.2 equiv per remaining xanthate group) was added and the reaction left for 1.5 hrs or until completion by TLC (60:40 hexane:ethyl acetate). Benzyl (Bz) acrylate (1.5 equiv per thiol) was added and the reaction mixture stirred at ambient temperature for 16 hours. The product was isolated by precipitating twice into hexane. Residual solvent was removed under high vacuum to yield a viscous oil.

General procedure for Simultaneous Thiol-Michael addition click reactions - Xanthate peripheral dendron (200mg) was dissolved in anhydrous THF (2mL) and degassed for 10 minutes under a nitrogen atmosphere. *n*-Butylamine (1.2 equiv. per xanthate group) was added and the reaction left for 1.5 hrs or until completion by TLC (60:40 hexane:ethyl acetate). A stoichiometric mixture of Bz and Am acrylate monomers (1 equiv. per thiol) was added and the reaction mixture stirred at ambient temperature for 16 hours. The product was

isolated by precipitating twice into hexane. Residual solvent was removed under high vacuum to yield a viscous oil.

[Am_x-Bz_y-G_1-TSe]; y=2, [41]; x=1, y=1, [60]; x=2, [40]. The sequential and simultaneous thiol Michael addition click procedures were carried out as described above using [Xan_2-G_1-TSe];[12], (0.2 g, 0.136 mmol) and *n*-butylamine (74 μL, 0.7 mmol, 2.4 equiv.) in 2 mL of anhydrous THF for 1.5 hr, followed by addition of Bz acrylate and Am acrylate and stirred for 16 hours. The product was isolated by precipitating twice into hexane. Residual solvent was removed under high vacuum to yield an orange viscous oil. ^{1}H NMR (400 MHz, $CDCl_3$): δ = 1.14-1.19 (m, 3H), 2.28 (s), 2.45 (s, 3H), 2.54-2.60 (m), 2.62-2.72 (m, 4H), 2.83-2.93 (m, 4H), 3.20-3.26 (m, 4H), 3.43 (t, 2H, *J* = 5.8 Hz), 4.12-4.24 (m), 4.45 (t, 2H, *J* = 5.8 Hz), 5.13 (s), 7.29-7.41 (m), 7.79 (d, 2H, *J* = 8.0 Hz).

[Am_x-Bz_y-G_2-TSe]; y=4, [43]; x=1, y=3, [61]; x=2, y=2, [62]; x=3, y=1, [63]; x=4, [42]. The sequential and simultaneous thiol Michael addition click procedures were carried out as described above using [Xan_4-G_2-TSe];[13], (0.2 g, 0.136 mmol) and *n*-butylamine (79 μL, 0.8 mmol, 4.8 equiv.) in 2 mL of anhydrous THF for 1.5 hr, followed by addition of Bz acrylate and Am acrylate and stirred for 16 hours. The product was isolated by precipitating twice into hexane. Residual solvent was removed under high vacuum to yield an orange viscous oil. ^{1}H NMR (400 MHz, $CDCl_3$): δ = 1.15-1.21 (m, 3H), 1.21-1.30 (m, 6H), 2.28 (s), 2.44 (s, 3H), 2.54-2.61 (m), 2.62-2.73 (m, 4H), 2.83-2.94 (m, 4H), 3.20-3.30 (m, 4H), 3.4-3.48 (m, 2H), 4.13-4.34 (m), 4.45 (m, 2H), 5.13 (s), 7.28-7.41 (m), 7.80 (d, 2H, *J* = 8.6 Hz).

[Am_x-Bz_y-G_3-TSe]; y=8, [45]; x=1, y=7, [64]; x=2, y=6, [65]; x=3, y=5, [66]; x=4, y=4, [67]; x=5, y=3, [68]; x=6, y=2, [69]; x=7, y=1, [70]; x=8, [44]. The sequential and

simultaneous thiol Michael addition click procedures were carried out as described above using [Xan_8-G_3-TSe];[14], (0.2 g, 0.136 mmol) and *n*-butylamine (82 μL, 0.8 mmol, 9.6 equiv.) in 2 mL of anhydrous THF for 1.5 hr, followed by addition of Bz acrylate and Am acrylate and stirred for 16 hours. The product was isolated by precipitating twice into hexane. Residual solvent was removed under high vacuum to yield an orange viscous oil. ^{1}H NMR (400 MHz, $CDCl_3$): δ = 1.16-1.30 (m, 3H), 2.27 (s), 2.45 (s, 3H), 2.52-2.59 (m), 2.61-2.72 (m, 4H), 2.82-2.93 (m, 4H), 3.26 (s, br, 4H), 3.43 (m, 2H), 4.11-4.34 (m), 4.47 (m, 2H), 5.13 (s), 7.28-7.41 (m), 7.80 (d, 2H, *J* = 7.5 Hz).

[Am_x-Bz_y-G_2-THPE]; x=3, y=9, [96]; x=6, y=6, [97]; x=9, y=3, [98] – The sequential and simultaneous thiol Michael addition click procedures were carried out as described above using [Xan_{12}-G_2-THPE];[18], (0.1 g, 0.0303 mmol, 1 equiv.) and *n*-butylamine (43 μL, 0.437 mmol, 14.4 equiv.) in 2 mL of anhydrous THF for 1.5 hr, followed by addition of Bz acrylate and Am acrylate and stirred for 16 hours. The product was isolated by precipitating twice into hexane. Residual solvent was removed under high vacuum to yield an orange viscous oil. ^{1}H NMR (400 MHz, $CDCl_3$): δ = 1.16-1.30 (m, 3H), 2.27 (s), 2.45 (s, 3H), 2.52-2.59 (m), 2.61-2.72 (m, 4H), 2.82-2.93 (m, 4H), 3.26 (s, br, 4H), 3.43 (m, 2H), 4.11-4.34 (m), 4.47 (m, 2H), 5.13 (s), 7.28-7.41 (m), 7.80 (d, 2H, *J* = 7.5 Hz).

General procedure to generate *pseudo*-calibration curves for the sequential deprotection of xanthate-functional dendron-polymer hybrids. Xanthate peripheral LDHs and HPDs (200 mg) dissolved in anhydrous THF (2 mL) and degassed for 5 minutes under a nitrogen atmosphere. Varying molar equivalents of *n*-butylamine were added, based on the theoretical M_n by ^{1}H NMR, and the reaction left to stir for 1.5 hrs. The product was analysed by ^{1}H

NMR and the % of xanthate groups deprotected plotted against equivalents of *n*-butylamine added to generate a *pseudo*-calibration curve.

p[(Am_x-Bz_y-G_1)-$tBMA_{50}$]; x=2, [99]; x=1, y=1, [115]; y=2, [100]. Based on the *pseudo*-calibration curve generated for this material, the sequential and simultaneous thiol Michael addition click procedures were carried out as described above using p[(Xan_2-G_1)-$tBMA_{50}$];[25], and *n*-butylamine in 2 mL of anhydrous THF for 1.5 hr, followed by addition of Bz acrylate and Am acrylate and stirred for 16 hours. The product was isolated by precipitating twice into cold petroleum ether (40-60 °C). Residual solvent was removed under high vacuum to yield a colourless solid.

p[(Am_x-Bz_y-G_2)-$nBMA_{50}$]; y=4, [104]; x=1, y=3, [117]; x=2, y=2, [118]; x=3, y=1, [119]; x=4, [103]. Based on the *pseudo*-calibration curve generated for this material, the sequential and simultaneous thiol Michael addition click procedures were carried out as described above using p[(Xan_4-G_2)-$tBMA_{50}$];[26], and *n*-butylamine in 2 mL of anhydrous THF for 1.5 hr, followed by addition of Bz acrylate and Am acrylate and stirred for 16 hours. The product was isolated by precipitating twice into cold petroleum ether (40-60 °C). Residual solvent was removed under high vacuum to yield a colourless solid.

p[(Am_x-Bz_y-G_1)-$nBMA_{50}$-*co*-$EGDMA_{0.8}$]; x=2, [101]; x=1, y=1, [116]; y=2, [102]. Based on the *pseudo*-calibration curve generated for this material, the sequential and simultaneous thiol Michael addition click procedures were carried out as described above using p[(Xan_2-G_1)-$tBMA_{50}$-*co*-$EGDMA_{0.8}$];[27], and *n*-butylamine in 2 mL of anhydrous THF for 1.5 hr, followed by addition of Bz acrylate and Am acrylate and stirred for 16 hours. The product

was isolated by precipitating twice into cold petroleum ether (40-60 °C). Residual solvent was removed under high vacuum to yield a colourless solid.

p[(Am_x-Bz_y-G_2)-nBMA$_{50}$-*co*-EGDMA$_{0.8}$]; y=4, [106]; x=1, y=3, [120]; x=2, y=2, [121]; x=3, y=1, [122]; x=4, [105]. Based on the *pseudo*-calibration curve generated for this material, the sequential and simultaneous thiol Michael addition click procedures were carried out as described above using p[(Xan_4-G_2)-tBMA$_{50}$-*co*-EGDMA$_{0.8}$];[28], and *n*-butylamine in 2 mL of anhydrous THF for 1.5 hr, followed by addition of Bz acrylate and Am acrylate and stirred for 16 hours. The product was isolated by precipitating twice into cold petroleum ether (40-60 °C). Residual solvent was removed under high vacuum to yield a colourless solid.

p[(Am_x-Bz_y-G_0)-nBMA$_{100}$-*co*-EGDMA$_{0.7}$] (x = 0-1, y = 0-1, x+y = 1);[127]. Based on the *pseudo*-calibration curve generated for this material, the simultaneous thiol Michael addition click procedure was carried out as described above using p[(Xan_1-G_0)-nBMA$_{100}$-*co*-EGDMA$_{0.7}$];[36] (200 mg, 0.0083 mmol, 1 equiv.), and *n*-butylamine (10 μL, 0.1 mmol, 12 equiv.) in 2 mL of anhydrous THF for 1.5 hr, followed by addition of Bz acrylate and Am acrylate and stirred for 16 hours. The product was isolated by precipitating twice into hexane. Residual solvent was removed under high vacuum to yield a colourless solid.

p[(Am_x-Bz_y-G_1)-nBMA$_{100}$-*co*-EGDMA$_{0.8}$] (x = 0-2, y = 0-2, x+y = 2);[128]. Based on the *pseudo*-calibration curve generated for this material, the simultaneous thiol Michael addition click procedure was carried out as described above using p[(Xan_2-G_1)-nBMA$_{100}$-*co*-EGDMA$_{0.8}$];[37] (100 mg, 0.0040 mmol, 1 equiv.), and *n*-butylamine (6 μL, 0.0607 mmol, 15 equiv.) in 2 mL of anhydrous THF for 1.5 hr, followed by addition of Bz acrylate and Am

acrylate and stirred for 16 hours. The product was isolated by precipitating twice into hexane. Residual solvent was removed under high vacuum to yield a colourless solid.

p[(Am_x-Bz_y-G_2)-$nBMA_{100}$-*co*-$EGDMA_{0.8}$] (x = 0-4, y = 0-4, x+y = 4);[128]. Based on the *pseudo*-calibration curve generated for this material, the simultaneous thiol Michael addition click procedure was carried out as described above using p[(Xan_4-G_2)-$nBMA_{100}$-*co*-$EGDMA_{0.8}$];[38] (100 mg, 0.0047 mmol, 1 equiv.), and *n*-butylamine (19 μL, 0.187 mmol, 40 equiv.) in 2 mL of anhydrous THF for 1.5 hr, followed by addition of Bz acrylate and Am acrylate and stirred for 16 hours. The product was isolated by precipitating twice into hexane. Residual solvent was removed under high vacuum to yield a colourless solid.

p[(Am_x-Bz_y-G_3)-$nBMA_{100}$-*co*-$EGDMA_{0.8}$] (x = 0-8, y = 0-8, x+y = 8);[129]. Based on the *pseudo*-calibration curve generated for this material, the simultaneous thiol Michael addition click procedure was carried out as described above using p[(Xan_8-G_3)-$nBMA_{100}$-*co*-$EGDMA_{0.8}$];[39] (100 mg, 0.0051 mmol, 1 equiv.), and *n*-butylamine (13 μL, 0.133 mmol, 26 equiv.) in 2 mL of anhydrous THF for 1.5 hr, followed by addition of Bz acrylate and Am acrylate and stirred for 16 hours. The product was isolated by precipitating twice into hexane. Residual solvent was removed under high vacuum to yield a colourless solid.

7.4 Chapter 4 compounds

[PEG(2K)-BiB];[131]. Monomethoxy poly(ethylene glycol) ($M_w \approx 2000$ g mol^{-1}) (10.25 g, 5.13 mmol, 1 equiv.) was dissolved in THF (anhydrous, 100 mL) at 40 °C, and degassed with dry N_2 for 20 minutes. DMAP (6.26 mg, 0.0512 mmol, 0.01 equiv.) and TEA (1.57 mL, 11 mmol, 2.2 equiv.) were added and the reaction cooled to 0 °C in an ice bath. α-Bromoisobutyryl bromide (1.27 mL, 10 mmol, 2 equiv.) was added dropwise over 20

minutes and a white precipitate immediately formed ($Et_3NH^+Br^-$ salt). After 24 hours, the precipitate was removed by filtration, THF removed and the crude material precipitated twice from acetone into petroleum ether (30-40 °C). ^{1}H NMR (400 MHz, D_2O): δ = 4.34 (m, 2H), 3.59-3.80 (m, 186H), 3.35 (s, 3H), 1.93 (s, 6H).

[PEG(2K)-nBMA$_{100}$]. In a kinetics study, targeting DP_n = 100 monomer units for the primary chains, [PEG(2K)-BiB];[131] (0.302 g, 0.141 mmol, 1 equiv.), nBMA (2 g, 14 mmol, 100 equiv.) and bpy (44 mg, 0.282 mmol, 2 equiv.) were placed into a 10 mL round-bottomed flask. Methanol was added (50 wt% based on nBMA; 2g, 2.6 mL) and the solution stirred and deoxygenated using a nitrogen purge for 30 minutes. Cu(I)Cl (14 mg, 0.141 mmol, 1 equiv) was added to the flask, whilst maintaining a positive flow of nitrogen, and the solution left to polymerise at 60 °C. To determine the kinetics of the reaction, samples (~0.1 mL) were taken at regular intervals and analysed by ^{1}H NMR and SEC. The reaction was terminated when conversion reached >94%, indicated by ^{1}H NMR after 28 hours, by exposure to oxygen and addition of THF. The solution was passed through a neutral alumina column to remove the catalytic system, and precipitated twice into cold petroleum ether (40-60 °C). After drying the precipitated sample overnight under high vacuum, the polymer was obtained as a white solid.

General procedure for the co-initiated branched copolymerisation of nBMA and EGDMA with [Xan$_1$-G$_0$-BiB];[20] and [PEG(2K)-BiB];[131]; p[(PEG(2K))$_{0.99}$-(Xan$_1$-G$_0$)$_{0.01}$-nBMA$_{100}$-*co*-EGDMA$_{0.8}$];[134], p[(PEG(2K))$_{0.925}$-(Xan$_1$-G$_0$)$_{0.075}$-nBMA$_{100}$-*co*-EGDMA$_{0.8}$];[135], p[(PEG(2K))$_{0.9}$-(Xan$_1$-G$_0$)$_{0.1}$-nBMA$_{100}$-*co*-EGDMA$_{0.8}$];[136]. The co-initiated copolymerisation of nBMA and bifunctional monomer EGDMA was carried out with varying molar equivalents of [PEG(2K)-BiB];[131] and [Xan$_1$-G$_0$-BiB];[20] (99:1,

92.5:7.5, 90:10). In a typical synthesis, targeting DP_n = 100 monomer units for the primary chains, [PEG(2K)-BiB];[131], [Xan_1-G_0-BiB];[20], nBMA (5 g, 35 mmol, 100 equiv.), bpy (110 mg, 0.703 mmol, 2 equiv.) and EGDMA (56 mg, 0.280 mmol, 0.8 equiv.) were placed into a 20 mL round-bottomed flask. Methanol was added (50 wt% based on nBMA, 5g, 7.5 mL) and the solution stirred and deoxygenated using a nitrogen purge for 30 minutes. Cu(I)Cl (35 mg, 0.352 mmol, 1 equiv) was added to the flask, whilst maintaining a positive flow of nitrogen, and the solution was left to polymerise at 60 °C. The reaction was terminated when conversion reached >98%, indicated by ^{1}H NMR after 70 hours, by exposure to oxygen and addition of THF. The solution was passed through a neutral alumina column to remove the catalytic system, and precipitated twice into cold petroleum ether (40-60 °C). After drying the precipitated sample overnight under high vacuum, the polymer was obtained as a white solid.

General procedure for the co-initiated branched copolymerisation of nBMA and EGDMA with [Xan_8-G_3-BiB];[23] and [PEG(2K)-BiB];[131]; p[(PEG(2K))$_{0.99}$-(Xan_8-G_3)$_{0.01}$-nBMA$_{100}$-*co*-EGDMA$_{0.8}$];[137], p[(PEG(2K))$_{0.986}$-(Xan_8-G_3)$_{0.014}$-nBMA$_{100}$-*co*-EGDMA$_{0.8}$];[138], p[(PEG(2K))$_{0.95}$-(Xan_8-G_3)$_{0.05}$-nBMA$_{100}$-*co*-EGDMA$_{0.8}$];[139]. The co-initiated copolymerisation of nBMA and bifunctional monomer EGDMA was carried out with varying molar equivalents of [PEG(2K)-BiB];[131] and [Xan_8-G_3-BiB];[23] (99:1, 98.6:1.4, 95:5). In a typical synthesis, targeting DP_n = 100 monomer units for the primary chains, [PEG(2K)-BiB];[131], [Xan_8-G_3-BiB];[23], nBMA (5 g, 35 mmol, 100 equiv.), bpy (110 mg, 0.703 mmol, 2 equiv.) and EGDMA (56 mg, 0.280 mmol, 0.8 equiv.) were placed into a 20 mL round-bottomed flask. Methanol was added (50 wt% based on nBMA, 5g, 7.5 mL) and the solution stirred and deoxygenated using a nitrogen purge for 30 minutes. Cu(I)Cl (35 mg, 0.352 mmol, 1 equiv) was added to the flask, whilst maintaining a positive flow of nitrogen, and the solution was left to polymerise at 60 °C. The reaction was terminated when

conversion reached >98%, indicated by ^{1}H NMR after 72 hours, by exposure to oxygen and addition of THF. The solution was passed through a neutral alumina column to remove the catalytic system, and precipitated twice into cold petroleum ether (40-60 °C). After drying the precipitated sample overnight under high vacuum, the polymer was obtained as a white solid.

General procedure for the deprotection of peripheral xanthate groups of co-initiated HPDs, and subsequent nanoprecipitation and coordination of 3 nm GNPs. Peripheral xanthate groups of each polymer (200 mg, 1 equiv.) were deprotected with excess *n*-butylamine (10 equiv.) in THF (anhydrous, 2 mL) for 1.5 hours. The deprotected polymer was precipitated twice into hexane and dried under vacuum. The deprotected polymer was dissolved in acetone at an initial concentration of 5 mg/mL. The dissolved polymer was rapidly added to water with stirring at ambient temperature. The solvent was allowed to evaporate overnight to give nanoprecipitates with a final concentration of 1 mg/mL of polymer in water. A 1:9 ratio of polymer nanoprecipitates:3 nm GNPs was mixed and stirred for 24 hours, before imaging by TEM.

TEM preparation. TEM grids (3 mm, 400 mesh Cu(holey carbon)) were prepared by pipetting 10 μL of the polymer/GNP samples directly onto the carbon coated side of the grid, and immediately wicking away excess water with filter paper. The grids were allowed to dry for 24 hours before imaging.

7.5 Chapter 5 compounds

Simultaneous multifunctionalisation of p[(PEG(2K))$_{0.9}$-(Xan$_1$-G$_0$)$_{0.1}$-nBMA$_{100}$-*co*-EGDMA$_{0.8}$];[136] to generate p[(PEG(2K))$_{0.9}$-(Am$_{0.5}$-Bz$_{0.5}$-G$_0$)$_{0.1}$-nBMA$_{100}$-*co*-EGDMA$_{0.8}$];[140]. A *pseudo*-calibration curve was generated as described previously, and

applied to the simultaneous thiol Michael addition using p[(PEG(2K))$_{0.9}$-(Xan$_1$-G$_0$)$_{0.1}$-nBMA$_{100}$-*co*-EGDMA$_{0.8}$];[136] (1 g, 0.0602 mmol, 1 equiv.) and *n*-butylamine (59 μL, 0.602 mmol, 10 equiv.) in 10 mL of anhydrous THF for 1.5 hr, followed by addition of Bz acrylate (10 μL, 0.0662 mmol, 1.1 equiv.) and Am acrylate (10 μL, 0.0662 mmol, 1.1 equiv.) and stirred for 16 hours. The product was isolated by precipitating twice into hexane. Residual solvent was removed under high vacuum to yield a colourless solid.

[Bz$_8$-G$_3$-COOH];[141]. 1,8- diazabicyclo[5.4.0]undec-7-ene (DBU) (1.3 equiv.) was added to benzyl functional G$_3$ dendron [Bz$_8$-G$_3$-TSe];[45] (5.82 g, 2 mmol, 1 equiv.) dissolved in anhydrous CH_2Cl_2 (50 mL). The reaction was stirred under a nitrogen atmosphere for 16 hours and monitored by using TLC (40:60 ethyl acetate:hexane). The product was isolated by diluting the mixture with CH_2Cl_2 (350 mL) and washing with 1 M $NaHSO_4$ (2 x 300 mL) and brine (1 x 300 mL). The organic layer was dried over $MgSO_4$ and evaporated to dryness. The product was then precipitated three times into hexane:ethyl acetate (9:1). Any residual solvent was removed under high vacuum to yield a viscous oil. ^{1}H NMR (400 MHz, $CDCl_3$): δ = 1.24 (s, 18H), 1.31 (s, 3H), 2.67 (t, *J* = 7.1 Hz, 16H), 2.88 (t, *J* = 7.1 Hz, 16H), 3.24 (s, 16H), 4.13-4.39 (m, 28H), 5.12 (s, 16H), 7.34 (s, 40H). ^{13}C NMR (100 MHz, $CDCl_3$): δ = 17.71, 27.58, 33.43, 34.34, 65.76, 66.67, 128.59, 170.06, 171.52.

[Bz$_8$-G$_3$-BiB];[142]. [Bz$_8$-G$_3$-COOH];[141] (5.14 g, 1.89 mmol, 1 equiv.), [HEBiB];[19] (0.798 g, 3.78 mmol, 2 equiv.), DPTS (0.611 g, 2.08 mmol, 1.1 equiv.), DCC (0.429 g, 2.08 mmol, 1.1 equiv.) in anhydrous CH_2Cl_2 (50 mL) were reacted according to the general procedure for focal point modification resulting in an orange viscous oil that was purified by liquid chromatography on silica, eluting from DCM, gradually increasing the polarity to methanol:DCM (3:97). Yield: 4.06 g, orange viscous oil, (74%). ^{1}H NMR (400 MHz,

$CDCl_3$): δ = 1.24 (s, 21H), 1.92 (s, 6H), 2.59-2.73 (m, 16H), 2.82-2.95 (m, 16H), 3.24 (s, 16H), 4.11-4.43 (m, 32H), 5.12 (s, 16H), 7.34 (s, 40H). ^{13}C NMR (100 MHz, $CDCl_3$): δ = 17.81, 27.60, 30.83, 33.44, 34.37, 46.56, 49.27, 55.93, 65.73, 66.66, 135.71, 169.80, 171.46.

p[(Bz_8-G_3)-nBMA$_{100}$];[143]. A polymerisation, targeting DP_n = 100 monomer units, was carried out with [Bz_8-G_3-BiB];[142] (0.205 g, 0.0703 mmol, 1 equiv.), nBMA (1 g, 7 mmol, 100 equiv.) and bpy (22 mg, 0.141 mmol, 2 equiv.) were placed into a 5 mL round-bottomed flask. Methanol was added (50 wt% based on nBMA; 1g, 1.6 mL) and the solution stirred and deoxygenated using a nitrogen purge for 30 minutes. Cu(I)Cl (7 mg, 0.0703 mmol, 1 equiv) was added to the flask, whilst maintaining a positive flow of nitrogen, and the solution left to polymerise at 60 °C. The reaction was terminated when conversion reached >95%, indicated by ^{1}H NMR after 70 hours, by exposure to oxygen and addition of THF. The solution was passed through a neutral alumina column to remove the catalytic system, and precipitated twice into cold petroleum ether (40-60 °C). After drying the precipitated sample overnight under high vacuum, the polymer was obtained as a white solid.

Co-initiated branched copolymerisation of nBMA and EGDMA with [Xan_8-G_3-BiB];[23], [Bz_8-G_3-BiB];[142] and [PEG(2K)-BiB];[131] to generate p[(PEG(2K))$_{0.986}$-(Xan_8-G_3)$_{0.007}$-(Bz_8-G_3)$_{0.007}$-nBMA$_{100}$-*co*-EGDMA$_{0.8}$];[144] The co-initiated copolymerisation of nBMA and bifunctional monomer EGDMA was carried out with [PEG(2K)-BiB];[131] (0.745 g, 0.347 mmol, 0.986 equiv.), [Xan_8-G_3-BiB];[23] (5.7 mg, 0.00246 mmol, 0.007 equiv.) and [Bz_8-G_3-BiB];[142] (7.2 mg, 0.00246 mmol, 0.007 equiv.), in a typical synthesis, targeting DP_n = 100 monomer units for the primary chains, nBMA (5 g, 35 mmol, 100 equiv.), bpy (110 mg, 0.703 mmol, 2 equiv.) and EGDMA (56 mg, 0.280 mmol, 0.8 equiv.) were placed into a 20 mL round-bottomed flask. Methanol was added (50

wt% based on nBMA, 5g, 7.5 mL) and the solution stirred and deoxygenated using a nitrogen purge for 30 minutes. Cu(I)Cl (35 mg, 0.352 mmol, 1 equiv) was added to the flask, whilst maintaining a positive flow of nitrogen, and the solution was left to polymerise at 60 °C. The reaction was terminated when conversion reached >98%, indicated by ^{1}H NMR after 72 hours, by exposure to oxygen and addition of THF. The solution was passed through a neutral alumina column to remove the catalytic system, and precipitated twice into cold petroleum ether (40-60 °C). After drying the precipitated sample overnight under high vacuum, the polymer was obtained as a white solid.

p[(PEG(2K))$_{0.986}$-(Am$_8$-G$_3$)$_{0.007}$-(Bz$_8$-G$_3$)$_{0.007}$-nBMA$_{100}$-*co*-EGDMA$_{0.8}$];[145]. Thiol-acrylate Michael addition was carried out as described previously, using p[(PEG(2K))$_{0.986}$-(Xan$_8$-G$_3$)$_{0.007}$-(Bz$_8$-G$_3$)$_{0.007}$-nBMA$_{100}$-*co*-EGDMA$_{0.8}$];[144] (1 g, 0.0611 mmol, 1 equiv.), with an excess of *n*-butylamine (60 μL, 0.611 mmol, 10 equiv.) in 1 mL of anhydrous THF at ambient temperature for 1.5 hr, followed by addition of Am acrylate (139 μL, 0.916 mmol, 15 equiv.) and stirred for 16 hours. The product was isolated by precipitating twice into hexane. Residual solvent was removed under high vacuum to yield a colourless solid.

Cellular accumulation studies

ATHP-1. Collagenated 6-well plates were seeded with 2 x 10^6 THP-1 cells (human monocytic cell line) in Roswell Park Memorial Institute (RPMI) medium supplemented with 200 nM phorbol 12-myristate 13-acetate (PMA) and incubated for 3 days. After 3 days the media was aspirated and replaced with an equal volume of fresh RPMI without PMA and incubated for a further 5 days. Following differentiation, media was aspirated, cells washed (x 3) and replaced with Hanks' balanced salt solution (HBSS) containing each treatment so that the final volume of each nanoformulation was less than 0.5% of the final total volume.

Selected wells were pre-incubated (30 min) and co-incubated with cytochalasin B (5 µg/ml) and the particles, to investigate the mechanisms of particle uptake into ATHP-1 cells. Following 1 or 6 hour incubation extracellular samples were obtained, cells washed with ice-cold HBSS (x 3) and detached/lysed using scintillation fluid and the CAR determined by measuring [^{3}H] radioactivity in the cell lysate via liquid scintillation counting.

THP-1. THP-1 cells were treated as previously described for ATHP-1 cells, but without differentiation (ie without PMA) in collagenated plates. Multiple centrifugation steps were carried out to allow washing of the suspension cells.

Cell-free particle adhesion. Particle adhesion to collagenated and non-collagenated plates was studied for the patchy and statistically multifunctional materials, as previously described, but without the presence of ATHP-1/THP-1 cells.

7.6 References

1. H. Ihre, A. Hult, J. M. J. Fréchet, and I. Gitsov, *Macromolecules*, 1998, **31**, 4061–4068.
2. M. Malkoch, E. Malmström, and A. Hult, *Macromolecules*, 2002, **35**, 8307–8314.
3. J. S. Moore and S. I. Stupp, *Macromolecules*, 1990, **23**, 65–70.
4. S. E. R. Auty, O. Andren, M. Malkoch, and S. P. Rannard, *Chem. Commun.*, 2014, **50**, 6574–6577.
5. S. E. R. Auty, O. C. J. Andrén, F. Y. Hern, M. Malkoch, and S. P. Rannard, *Polym. Chem.*, 2014, **6**, 573–582.
6. W. Jakubowski, J. F. Lutz, S. Slomkowski and Krzysztof Matyjaszewski, J. Polym. Sci. Part A: Polym. Chem., 2005, 7, 1498–1510.